frontiers | Research Topics

Insights in atherosclerosis and vascular medicine: 2021

Edited by
Masanori Aikawa

Published in
Frontiers in Cardiovascular Medicine

ISSN 1664-8714
ISBN 978-2-83251-558-7
DOI 10.3389/978-2-83251-558-7

About Frontiers

Frontiers is more than just an open access publisher of scholarly articles: it is a pioneering approach to the world of academia, radically improving the way scholarly research is managed. The grand vision of Frontiers is a world where all people have an equal opportunity to seek, share and generate knowledge. Frontiers provides immediate and permanent online open access to all its publications, but this alone is not enough to realize our grand goals.

Frontiers journal series

The Frontiers journal series is a multi-tier and interdisciplinary set of open-access, online journals, promising a paradigm shift from the current review, selection and dissemination processes in academic publishing. All Frontiers journals are driven by researchers for researchers; therefore, they constitute a service to the scholarly community. At the same time, the *Frontiers journal series* operates on a revolutionary invention, the tiered publishing system, initially addressing specific communities of scholars, and gradually climbing up to broader public understanding, thus serving the interests of the lay society, too.

Dedication to quality

Each Frontiers article is a landmark of the highest quality, thanks to genuinely collaborative interactions between authors and review editors, who include some of the world's best academicians. Research must be certified by peers before entering a stream of knowledge that may eventually reach the public - and shape society; therefore, Frontiers only applies the most rigorous and unbiased reviews. Frontiers revolutionizes research publishing by freely delivering the most outstanding research, evaluated with no bias from both the academic and social point of view. By applying the most advanced information technologies, Frontiers is catapulting scholarly publishing into a new generation.

What are Frontiers Research Topics?

Frontiers Research Topics are very popular trademarks of the *Frontiers journals series*: they are collections of at least ten articles, all centered on a particular subject. With their unique mix of varied contributions from Original Research to Review Articles, Frontiers Research Topics unify the most influential researchers, the latest key findings and historical advances in a hot research area.

Find out more on how to host your own Frontiers Research Topic or contribute to one as an author by contacting the Frontiers editorial office: frontiersin.org/about/contact

Insights in atherosclerosis and vascular medicine: 2021

Topic editor

Masanori Aikawa — Brigham and Women's Hospital, Harvard Medical School, United States

Citation

Aikawa, M., ed. (2023). *Insights in atherosclerosis and vascular medicine: 2021*. Lausanne: Frontiers Media SA. doi: 10.3389/978-2-83251-558-7

Table of contents

frontiers in Cardiovascular Medicine

BRIEF RESEARCH REPORT
published: 24 September 2021
doi: 10.3389/fcvm.2021.749022

Effects of the Btk-Inhibitors Remibrutinib (LOU064) and Rilzabrutinib (PRN1008) With Varying Btk Selectivity Over Tec on Platelet Aggregation and *in vitro* Bleeding Time

OPEN ACCESS

Edited by:
Rory R. Koenen,
Maastricht University, Netherlands

Reviewed by:
Owen McCarty,
Oregon Health and Science University, United States
Dominik Rath,
Tübingen University Hospital, Germany

***Correspondence:**
Philipp von Hundelshausen
Philipp.von_Hundelshausen@med.uni-muenchen.de

Specialty section:
This article was submitted to Atherosclerosis and Vascular Medicine, a section of the journal Frontiers in Cardiovascular Medicine

Received: *28 July 2021*
Accepted: *31 August 2021*
Published: *24 September 2021*

Citation:
Duan R, Goldmann L, Brandl R, Spannagl M, Weber C, Siess W and von Hundelshausen P (2021) Effects of the Btk-Inhibitors Remibrutinib (LOU064) and Rilzabrutinib (PRN1008) With Varying Btk Selectivity Over Tec on Platelet Aggregation and in vitro Bleeding Time. Front. Cardiovasc. Med. 8:749022. doi: 10.3389/fcvm.2021.749022

***Rundan Duan*[1], *Luise Goldmann*[1], *Richard Brandl*[2], *Michael Spannagl*[3], *Christian Weber*[1,4,5], *Wolfgang Siess*[1,4] *and Philipp von Hundelshausen*[1,4*]**

[1] *Institute for Cardiovascular Prevention, Ludwig-Maximilians-University, Munich, Germany,* [2] *Institute for Vascular Surgery and Phlebology am Marienplatz, Munich, Germany,* [3] *Department of Transfusion Medicine, Cell Therapeutics and Hemostaseology, Ludwig-Maximilians University, Munich, Germany,* [4] *German Centre for Cardiovascular Research, Deutsches Zentrum für Herz-Kreislauf-Forschung (DZHK), Partner Site Munich Heart Alliance, Munich, Germany,* [5] *Department of Biochemistry, Cardiovascular Research Institute Maastricht, Maastricht University, Maastricht, Netherlands*

Background: Bruton tyrosine kinase inhibitors (BTKi) are used in B-cell malignancies and in development against various autoimmune diseases. Since Btk is also involved in specific pathways of platelet activation, BTKi might be considered to target platelet GPVI/GPIb-mediated atherothrombosis and platelet FcγRIIA-dependent immune disorders. However, BTKi treatment of patients with B-cell malignancies is frequently associated with mild bleeding events caused possibly by off-target inhibition of Tec. Here, we compared the platelet effects of two novel BTKi that exhibit a high (remibrutinib) or low (rilzabrutinib) selectivity for Btk over Tec.

Methods and Results: Remibrutinib and rilzabrutinib were pre-incubated with anticoagulated blood. Platelet aggregation and *in vitro* bleeding time (closure time) were studied by multiple electrode aggregometry (MEA) and platelet-function analyzer-200 (PFA-200), respectively. Both BTKi inhibited atherosclerotic plaque-stimulated GPVI-mediated platelet aggregation, remibrutinib being more potent (IC_{50} = 0.03 μM) than rilzabrutinib (IC_{50} = 0.16 μM). Concentrations of remibrutinib (0.1 μM) and rilzabrutinib (0.5 μM), >80% inhibitory for plaque-induced aggregation, also significantly suppressed (>90%) the Btk-dependent pathways of platelet aggregation upon GPVI, von Willebrand factor/GPIb and FcγRIIA activation stimulated by low collagen concentrations, ristocetin and antibody cross-linking, respectively. Both BTKi did not inhibit aggregation stimulated by ADP, TRAP-6 or arachidonic acid. Remibrutinib (0.1 μM) only slightly prolonged closure time and significantly less than rilzabrutinib (0.5 μM).

Conclusion: Remibrutinib and rilzabrutinib inhibit Btk-dependent pathways of platelet aggregation upon GPVI, VWF/GPIb, and FcγRIIA activation. Remibrutinib being more potent and showing a better profile of inhibition of Btk-dependent platelet activation vs. hemostatic impairment than rilzabrutinib may be considered for further development as an antiplatelet drug.

Keywords: atherothrombosis, platelet-aggregation, bleeding, PFA, MEA

INTRODUCTION

Since the first description of a patient with recurrent infections and deficiency of immunoglobulins termed "Agammaglobulinemia" by Ogden Bruton in 1952 (1), it took more than 40 years of research, until Bruton tyrosine kinase (Btk) was identified in 1993 as the responsible protein that is deficient in patients with X-linked agammaglobulinemia (2, 3). Btk belongs to the Tec (tyrosine kinase expressed in hepatocellular carcinoma) family of non-receptor cytoplasmic tyrosine kinase, and contains five different protein interaction domains: an amino terminal pleckstrin homology (PH) domain, a proline-rich Tec homology (TH) domain, the SRC kinase homology (SH) domains SH2 and SH3, and a kinase domain (4). Btk is the best studied member of this tyrosine kinase family and most homologous to Tec, the namesake of this kinase family. Btk plays a crucial role in B-cell receptor function and in immunoglobulin Fc- receptor signaling of monocytes/macrophages and neutrophils (4). Since the approval of ibrutinib, the covalent irreversible first in class Btk inhibitor (BTKi) in 2013 for treatment of certain B-cell malignancies, many more reversible and irreversible BTKi have evolved and the spectrum of diseases that are targeted extends from specific forms of B-cell malignancies to various autoimmune disorders (5). Up to now four BTKi (ibrutinib, acalabrutinib, zanubrutinib, and tirabrutinib) have been approved but at least further eight BTKi are in clinical studies (5).

Btk is expressed not only in B-cells but also in various hematopoietic cells including the megakaryocyte-platelet lineage (6). Btk in platelets is involved in signaling of specific glycoprotein receptors including glycoprotein (GP) VI activation by collagen, GPIb activation by von Willebrand factor (VWF), FcγRIIa activation by IgG immune complexes, and CLEC-2 activation by podoplanin (5). Thus, Btk might be a promising therapeutic target of platelet-related diseases, and BTKi have indeed been proposed as novel antiplatelet drugs as they inhibit selectively platelet GPVI/GPIb-stimulated atherothrombosis (7, 8), platelet FcγRIIA-dependent immune disorders (heparin-induced thrombocytopenia, vaccine-induced immune thrombotic thrombocytopenia) (9, 10), and podoplanin/CLEC-2 mediated venous thrombosis (11, 12). Somewhat surprisingly, XLA patients do not show a bleeding tendency (13). In contrast, mild bleeding events are frequent in patients with B-cell malignancies treated with irreversible covalent BTKi (ibrutinib, acalabrutinib, zanubrutinib, and tirabrutinib) (5). The reasons are not clear but are probably multifactorial. They might be related to the type of diseases treated, but also caused by off-target inhibition as reviewed recently (5).

Beside Btk the homologous kinase Tec is also expressed in platelets. Whereas, FcγRIIa activation and VWF activation of GPIb do not require Tec activation (5, 9), Tec plays a role in GPVI activation. After GPVI-mediated platelet stimulation by high dose collagen, both Btk and Tec support platelet aggregation. Btk-deficient human platelets from patients with XLA and Btk-deficient mouse platelets do not respond to low concentrations of collagen or collagen-related peptide (CRP) indicating that Btk is required for platelet activation after low-degree GPVI stimulation (14, 15). Similar observations have been made by using low Btk-specific concentrations of irreversible BTKi and the reversible BTKi fenebrutinib which inhibits Btk but not Tec and applying human atherosclerotic plaque which also induces only a low-degree activation of GPVI (8, 9, 16–18). After stimulation with high concentrations of collagen, Tec compensates for the absence of Btk (as in XLA patients) or inhibition of Btk (as after platelet pretreatment with Btk-selective concentrations of BTKi) and preserves GPVI-stimulated platelet aggregation. Inhibition of both Tec and Btk abrogates GPVI-activation (15). Since the four approved irreversible covalent BTKi mentioned above have limited selectivity for Btk over Tec as measured by biochemical assays *in vitro* (5), and at higher concentrations prolong bleeding time *in vitro* (19), it is assumed that therapeutic concentrations of these BTKi inhibit in platelets irreversibly Tec in addition to Btk thereby abrogating GPVI signaling. This might contribute to the observed bleeding side effects.

Therefore, we hypothesized that off target effects of BTKi with low Btk selectivity over Tec might explain bleeding of BTKi, and investigated in the present study the effects of two novel BTKi on Btk-mediated pathways of platelet aggregation and bleeding time *in vitro*: the novel selective covalent BTKi remibrutinib (LOU064), a very potent irreversible covalent BTKi, which is highly selective for Btk and barely inhibits Tec (20), and rilzabrutinib (PRN1008) an oral, reversible covalent BTKi which inhibits Btk and Tec with similar IC50 values (21). Both BTKi are in clinical studies of dermatological autoimmune diseases. Rilzabrutinib inhibits very potently Btk and Tec *in vitro* (IC50 values, 1.3 and 0.8 nM, respectively) (22). It forms a reversible covalent bond with Cys481 of Btk, and shows a fast association and a very slow dissociation rate (23). Rilzabrutinib is in clinical trials of pemphigus (24) and idiopathic thrombocytopenic purpura (ITP), a disease exhibiting very low platelet counts ($<$50.000/μl) and bleeding events. Here, it inhibits platelet destruction mainly via the inhibition of autoantibody/FcγR signaling in splenic macrophages (25). Unexpectedly, in a

previous report clinically relevant concentrations of rilzabrutinib showed no inhibition of platelet activation *in vitro* (26).

MATERIALS AND METHODS

Reagents

Remibrutinib (LOU064), rilzabrutinib (PRN1008) and fenebrutinib (GDC-0853) were purchased from MedChem Express (New Jersey, USA). Dimethyl sulfoxide (DMSO) was from Sigma-Aldrich (Taufkirchen, Germany). Collagen was from Takeda (Linz, Austria). ADP, ristocetin, arachidonic acid (AA) and TRAP-6 (Thrombin Receptor Activator Peptide 6) were obtained from Roche Diagnostics (Mannheim, Germany). The anti-CD32 antibody AT10 (monoclonal mouse IgG1), cross-adsorbed F(ab')2-goat anti-mouse IgG (H + L) and the anti-CD9 antibody Ts9 (monoclonal mouse IgG1) were from ThermoFisher Scientific (Waltham, MA, USA).

Declaration of Helsinki

Informed consent was obtained from healthy volunteers, as approved by the Ethics Committee of the Faculty of Medicine of the University of Munich, and in accordance with the ethical principles for medical research involving human subjects, as set out in the Declaration of Helsinki.

Human Atherosclerotic Plaque Homogenates

Atherosclerotic tissue specimens were obtained from patients who underwent endarterectomy for high-grade carotid artery stenosis. Specimen containing lipid-rich soft plaques were collected. The atheromatous plaques were carefully dissected under sterile conditions from other regions of the atherosclerotic tissue. The plaques were weighed, homogenized with a glass pestle and potter, then stored at −80°C (27, 28). Plaque homogenates from 5 patients were pooled.

Blood Collection

Whole blood from healthy donors who had not taken any antiplatelet drug within 2 weeks was collected by cubital venipuncture into blood tubes (double wall) from Verum Diagnostica GmbH (Munich, Germany) containing hirudin as anticoagulant (final hirudin concentration in blood: 200 U/ml corresponding to 15 μg/ml) for platelet aggregation measurements (29) or buffered trisodium citrate/citric acid solution (citrate concentration 0.129 mol/L; S-Monovette 3.8 mL 9NC/PFA from Sarstedt, Nümbrecht, Germany) for closure time measurements with the PFA-200 (30). The blood was kept at room temperature and measurements were performed with 3 h after venipuncture.

Platelet Aggregation in Blood

Multiple electrode aggregometry (MEA) (Roche Diagnostics, Mannheim, Germany) that monitors the change of conductivity between two sets of electrodes (red and blue traces) caused by the attachment of platelets was applied to measure platelet aggregation, as described (29, 31). In brief, 0.9% NaCl (300 μL) was placed in aggregometer cuvettes (06675590, Roche, Mannheim, Germany) with aliquots (300 μL) of hirudin-anticoagulated blood. BTKi or DMSO (solvent control; 0.6 μL) were added, and mixed well with pipet, covered, and incubated for 1 h at 37°C (19). Then, the cuvettes were transferred into the device, platelet stimuli (collagen, ristocetin, AT10 + Fab2, anti-CD9 antibody, TRAP-6, ADP, or AA) were added at concentrations as detailed in the figure legends, stirring was simultaneously started and aggregation was measured for 10 min. Aggregation was recorded in arbitrary units (AU), and cumulative aggregation (AU*min) from 0 to 10 min was measured by quantifying the area under the curve. The traces selected as representative and displayed in the Figures belonged to a specific experiment whose values were closest to the mean.

IC50 values were obtained by non-linear fitting using the following model:

Fifty = (Top + Baseline)/2
Y = Bottom + (Top-Bottom)/(1 + 10^((LogAbsoluteIC50-X)*HillSlope + log((Top-Bottom)/(Fifty-Bottom)-1)))

Closure Time Measurement

The INNOVANCE® PFA-200 System (Siemens Healthcare, Erlangen, Germany), which simulates primary hemostasis *in vitro*, provides rapid and precise assessment of platelet dysfunction and bleeding risk (32, 33). DMSO (0.1%; solvent control) or various concentrations of remibrutinib or rilzabrutinib were pipetted (0.8 μl) into samples of citrate-anticoagulated blood (0.8 ml) (30) and preincubated for 1 h at 37°C. The Dade® PFA Collagen/EPI Test Cartridge was used, and the time of complete plug formation was reported as "closure time." The normal range of closure time is assessed specifically for each test center and was determined to be 84–170 s. The normal range as recommended by the manufacturer (84–160 s) has been slightly modified at our institution to 84–170 s based on the measurement on 54 healthy unselected persons without any medication according to the approved-level consensus guideline from the Clinical and Laboratory Standards Institute (CLSI EP28).

Statistics

The data are shown as mean ± standard deviation (SD) of the indicated number of the experiments. Normal distribution of values was assessed using the Shapiro-Wilk test. Parallel multi-experimental conditions were analyzed by ordinary one-way ANOVA, followed by Bonferroni's test if the normality test was passed, otherwise a Kruskal-Wallis test for unmatched and a Friedman's test for matched observations followed by Dunn's test were used. Side-by side comparisons were analyzed by Wilcoxon matched-pairs signed rank test.

RESULTS

Remibrutinib (LOU064) and Rilzabrutinib (PRN1008) Dose-Dependently Inhibit GPVI-Mediated Platelet Aggregation in Blood Triggered by Atherosclerotic Plaque

Diverse collagen type I and III fibers are the decisive plaque components that induce platelet aggregation via activation of GPVI (27, 28, 34). Blood was incubated with increasing

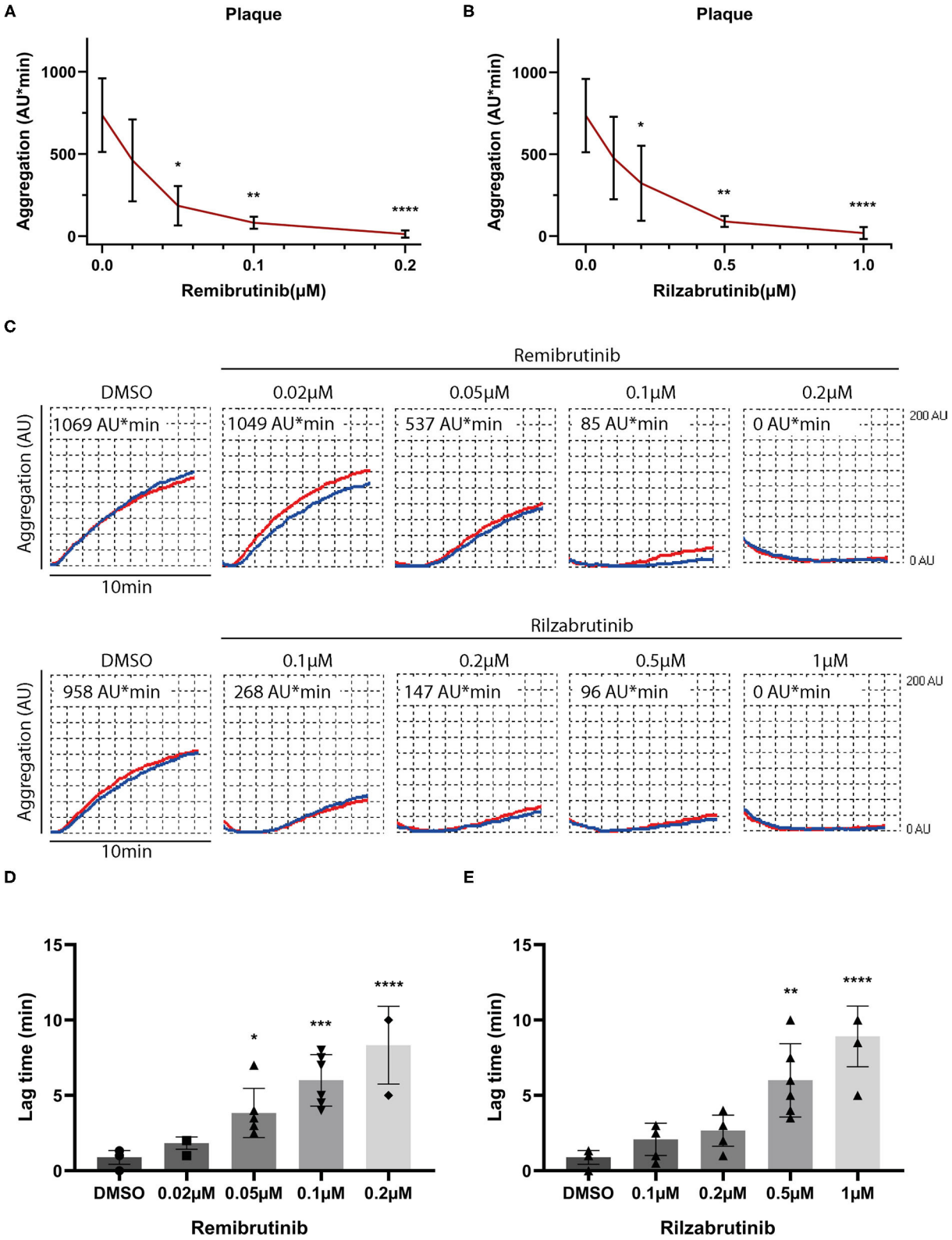

FIGURE 1 | Effects of increasing concentrations of remibrutinib and rilzabrutinib on platelet aggregation in blood stimulated by plaque homogenate. Hirudin anticoagulated blood was preincubated for 1 h at 37°C with solvent control (DMSO, 0.1%), or increasing concentrations of remibrutinib **(A,C,D)** or rilzabrutinib **(B,C,E)**

(Continued)

FIGURE 1 | and aggregation was recorded for 10 min after stimulation by plaque homogenate (833 μg/ml) (19). The dose-response curves of **(A)** remibrutinib and **(B)** rilzabrutinib are shown. **(C)** Representative aggregation traces in red and blue for each electrode, respectively, are shown. **(D,E)** Bar graphs show the dose-dependent delay in aggregation by **(D)** remibrutinib and **(E)** rilzabrutinib. Single data points are shown but are in part not visible due to overlap. Values are mean ± SD ($n = 6$). Statistical analysis was carried out comparing against baseline (without BTKi) using the Friedman test followed by Dunn's test **(A–E)**. *$p < 0.05$, **$p < 0.01$, ***$p < 0.001$, ****$p < 0.0001$.

concentrations of remibrutinib or rilzabrutinib for 1 h prior to plaque stimulation. Remibrutinib and rilzabrutinib inhibited plaque-induced platelet aggregation with IC_{50} values of 0.03 and 0.16 μM, respectively. Remibrutinib (0.2 μM) and rilzabrutinib (1 μM) were able to block plaque-induced platelet aggregation by >90% (**Figures 1A,B**). Accordingly, remibrutinib is more potent than rilzabrutinib.

The aggregation tracings in **Figure 1C** and panels in **Figures 1D,E** show a dose-dependent increase in delay of aggregation (lag time) caused by both inhibitors.

Effects of Remibrutinib and Rilzabrutinib on Platelet Aggregation Stimulated by Collagen, Ristocetin, FcγRIIA- and G-Protein Coupled Receptor-Activation

Next the effects of remibrutinib and rilzabrutinib were investigated on platelet aggregation induced by stimuli known to activate Btk-dependent and Btk-independent platelet signaling pathways. Concentrations of remibrutinib (0.1 μM) and rilzabrutinib (0.5 μM) were chosen that inhibited atherosclerotic plaque-induced platelet aggregation by 89 and 88%, respectively (**Figure 1A**).

Figure 2 shows the results for platelet stimuli that induce aggregation through a Btk-dependent mechanism (5). GPVI-dependent aggregation was inhibited by remibrutinib and rilzabrutinib by 91 and 94%, respectively, on low dose collagen, and by 37 and 41%, respectively, on high dose collagen (**Figures 2A,B**). Glycoprotein Ib/von Willebrand factor (GPIb/VWF)-dependent ristocetin-induced platelet aggregation was blocked by 95% by both BTKi (**Figure 2C**). The inhibitory effects of remibrutinib and rilzabrutinib on GPVI- and GPIb/VWF-dependent platelet aggregation were similar to those of fenebrutinib (0.1 μM) (**Supplementary Figure 2**), which is a reversible and highly selective Btk inhibitor.

Complete suppression of platelet aggregation by both BTKi was also observed on FcγRIIA activation by crosslinking or anti-CD9 antibody stimulation (**Figures 2D,E**). Due to the absence of adenosine 5'-diphosphate (ADP) secretion from platelets (9), anti-CD9 antibody stimulation showed a delayed aggregation response and less maximal aggregation compared with CD32-crosslinking (**Figure 2E**).

Remibrutinib and rilzabrutinib did not compromise Btk-independent pathways of platelet aggregation stimulated by GPCR activation with thrombin receptor-activating peptide (TRAP), arachidonic acid (AA), or ADP under the conditions tested (**Figure 3**).

Effect of Remibrutinib and Rilzabrutinib on *in vitro* Bleeding Time

To investigate whether remibrutinib and rilzabrutinib might impair primary hemostasis, the platelet function analyzer PFA-200 was used. The instrument aspirates citrate-anticoagulated blood under constant vacuum from a reservoir through a capillary and a small hole in a membrane filter which was coated in our experiments with collagen and epinephrine (collagen/epinephrine cartridge). The time required to obtain full occlusion of the aperture is reported as "*in vitro* closure time" (32, 35). The PFA is used for routine screening of patients with potential hemorrhagic risk and is very sensitive to monitor aspirin intake (36, 37).

Closure time was slightly, but significantly prolonged by 0.1 μM remibrutinib (**Figures 4A,B**) which suppressed >85% Btk-dependent platelet aggregation after GPVI activation with low dose collagen and after VWF/GPIb activation with ristocetin (**Figures 1A**, **2A,C**), but it did not exceed the upper limit of the normal range (170 s). Higher concentrations of remibrutinib (0.2 and 0.5 μM) significantly and profoundly prolonged closure time.

For rilzabrutinib it was found that a concentration of 0.2 μM which inhibited GPVI-dependent plaque-stimulated platelet aggregation by 56% (**Figure 1B**) did not affect significantly the closure time. A concentration of 0.5 μM rilzabrutinib equipotent to 0.1 μM remibrutinib suppressed >90% Btk-dependent platelet aggregation after low dose collagen- and ristocetin-stimulated aggregation (**Table 1**; **Figure 2**) and significantly increased closure time by 67% (**Figures 4A,B**). The closure time was significanly more prolonged than by 0.1 μM remibrutinib (**Figure 4B**). A concentration of 1 μM rilzabrutinib prolonged bleeding time maximally. DMSO, the solvent of BTKi, did not affect closure time as shown previously (9), and the DMSO controls showed similar values at the beginning and the end of the experiments (**Figures 4A,B**).

DISCUSSION

We demonstrate here in our study that (i) remibrutinib and rilzabrutinib inhibit and delay dose-dependently atherosclerotic plaque-induced GPVI-mediated platelet aggregation; (ii) remibrutinib (0.1 μM) and rilzabrutinib (0.5 μM) also block Btk-dependent GPVI-, GPIb/VWF- and FcγRIIa-stimulated platelet aggregation; (iii) higher concentrations of remibrutinib (≥0.2 μM) and therapeutic concentrations of rilzabrutinib (≥0.2 μM) prolong the bleeding time *in vitro* as measured by PFA-200.

According to the dose-response curve (**Figures 1A,B**), the potency for platelet inhibition of low degree GPVI-induced

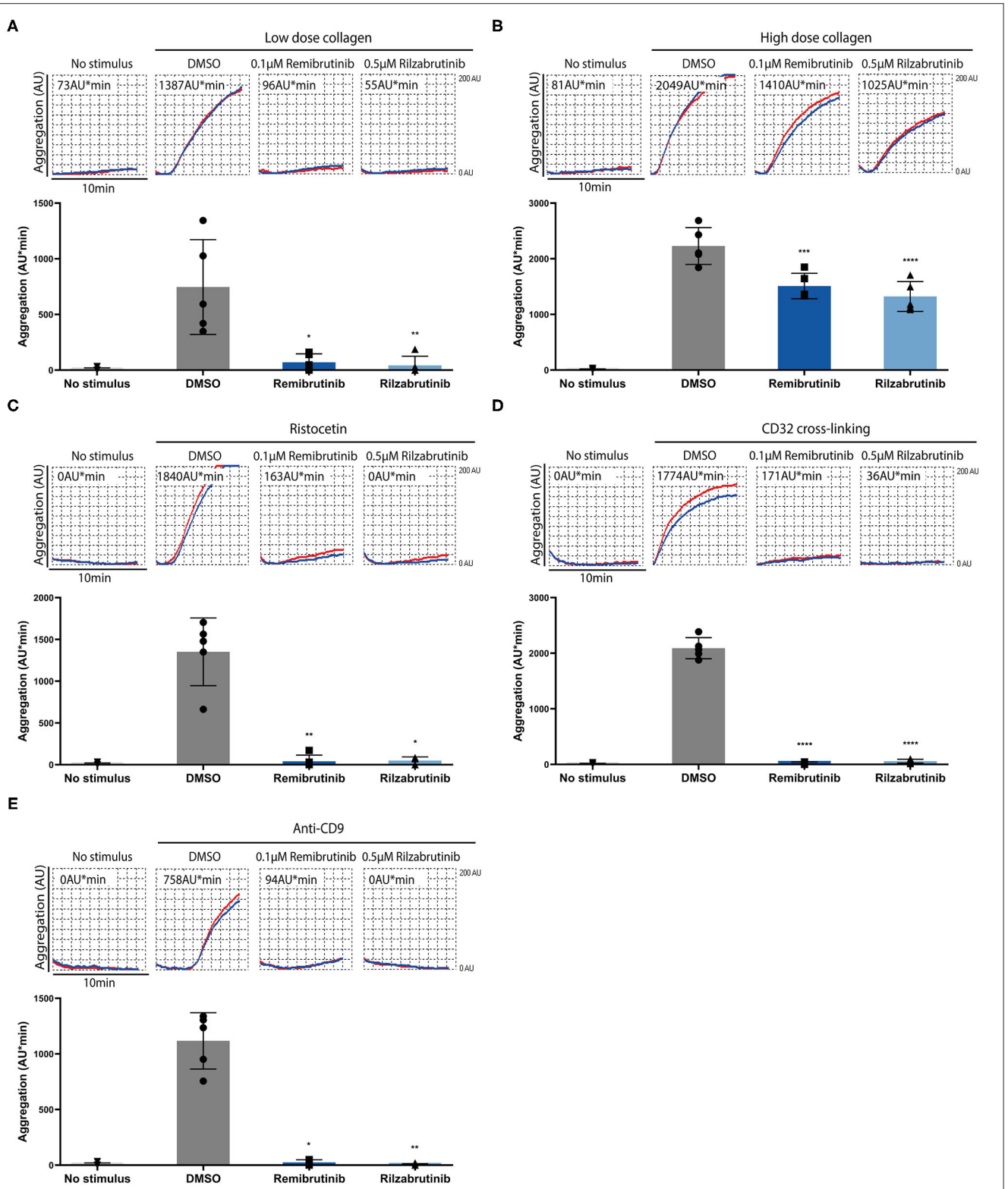

FIGURE 2 | Effects of remibrutinib and rilzabrutinib on platelet aggregation in blood after stimulation by collagen, ristocetin or FcγRIIA activation. Hirudin anticoagulated blood was preincubated for 1 h with DMSO or BTKi (remibrutinib 0.1 μM, rilzabrutinib 0.5 μM) prior to stimulation with **(A)** low dose collagen (0.4–0.6 μg/ml) that was titrated to induce a similar degree of platelet aggregation as plaque homogenate (833 μg/mL) (19), **(B)** high dose collagen (4–6 μg/ml) that was 10× concentrations of the low dose collagen (8, 19), **(C)** ristocetin (0.5 mg/ml), **(D)** CD32 cross-linking (3 min incubation with 2 μg/ml AT10, plus 30 μg/ml Fab2), *(Continued)*

FIGURE 2 | or **(E)** anti-CD9 antibody (1 μg/ml). Representative MEA tracings (top panels) and bar graphs (bottom panels) are shown. Values are shown as mean ± SD ($n = 5$). Statistical analysis was carried out using ordinary one-way ANOVA followed by Bonferroni's test **(B,D)** or Kruskal-Wallis followed by Dunn's test **(A,C,E)**. $^{*}p < 0.05$, $^{**}p < 0.01$, $^{***}p < 0.001$, $^{****}p < 0.0001$.

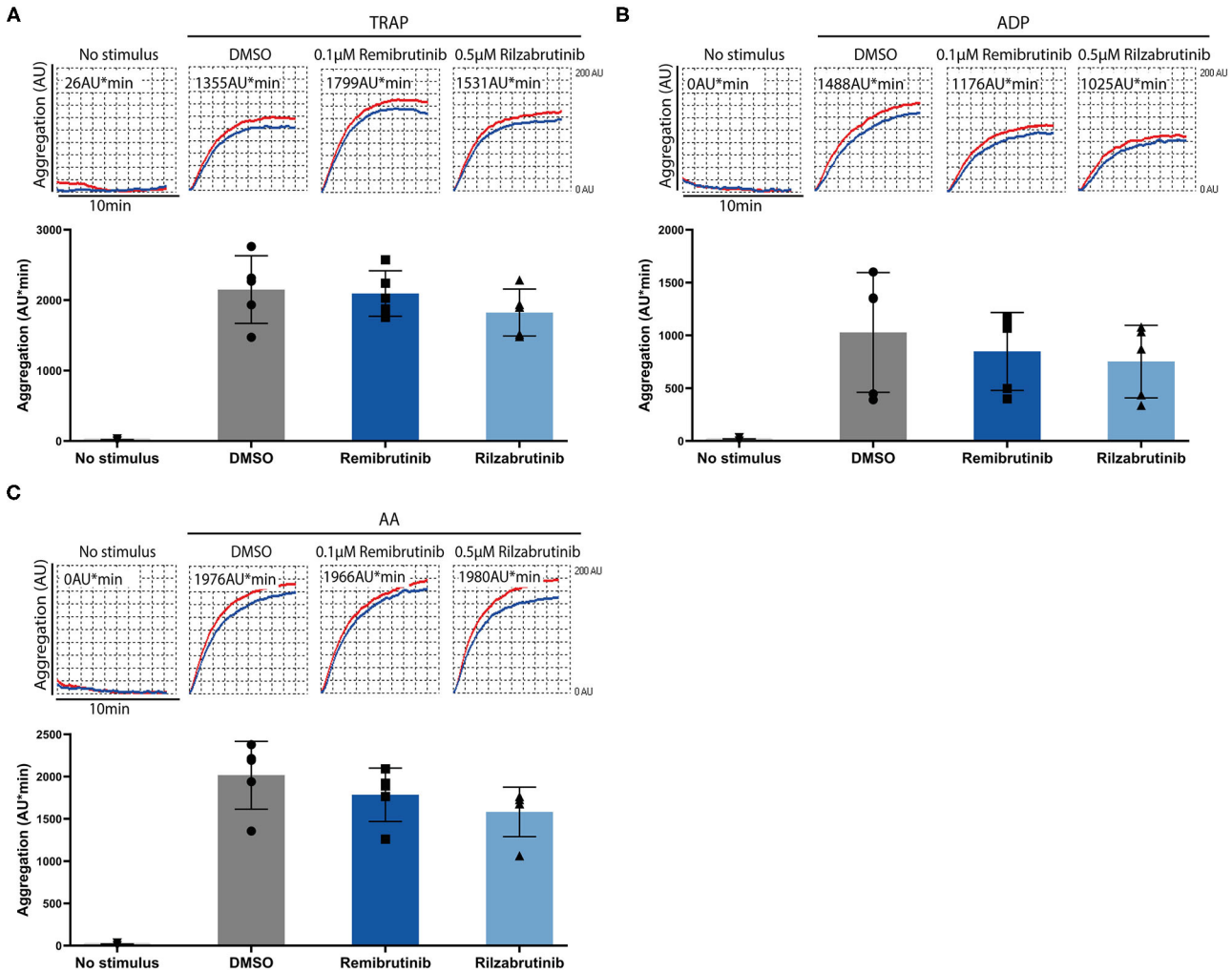

FIGURE 3 | Effects of remibrutinib and rilzabrutinib on platelet aggregation in blood after stimulation by TRAP, ADP, or AA. Hirudin anticoagulated blood samples were pretreated for 1 h at 37°C with solvent control (DMSO, 0.1%), or BTKi (remibrutinib 0.1 μM, rilzabrutinib 0.5 μM) before stimulation with **(A)** TRAP (15 μM), **(B)** ADP (10 μM), or **(C)** AA (0.6 mM). Representative MEA tracings (top panels) and aligned dot blot bar graphs (bottom panels) are shown. Values shown are mean ± SD ($n = 5$). Statistical analysis was carried out using ordinary ANOVA followed by Bonferroni's test **(A,B)** or Kruskal-Wallis test followed by Dunn's test **(C)**, that did not show significant differences.

platelet aggregation of remibrutinib (IC_{50} = 0.03 μM) was 5 times higher than that of rilzabrutinib (IC_{50} = 0.16 μM). Compared with other BTKi (**Table 1**), remibrutinib is only slightly less potent than fenebrutinib (IC_{50} = 0.016 μM) and ibrutinib (IC_{50} = 0.025 μM) and more potent than zanubrutinib, rilzabrutinib, tirabrutinib, acalabrutinib and evobrutinib. The IC_{50} values of remibrutinib (IC_{50} = 0.03 μM) and rilzabrutinib (IC_{50} = 0.16 μM) are 12-times and 2-fold lower than the optimal plasma levels as determined in clinical phase 1 studies, respectively (38, 39). Additionally, both inhibitors induced a dose-dependent increase in delay of atherosclerotic plaque-induced aggregation that was associated with the suppression of aggregation in blood (**Figure 1C**). A delay was also shown in a previous study using ibrutinib- and acalabrutinib-treated washed platelets stimulated by collagen while the maximal aggregation was unaffected (17).

Remibrutinib (0.1 μM) and rilzabrutinib (0.5 μM) significantly suppressed by >90% GPVI-dependent aggregation on low dose collagen, GPIb/VWF-dependent aggregation on ristocetin stimulation, and FcγRIIA-dependent aggregation

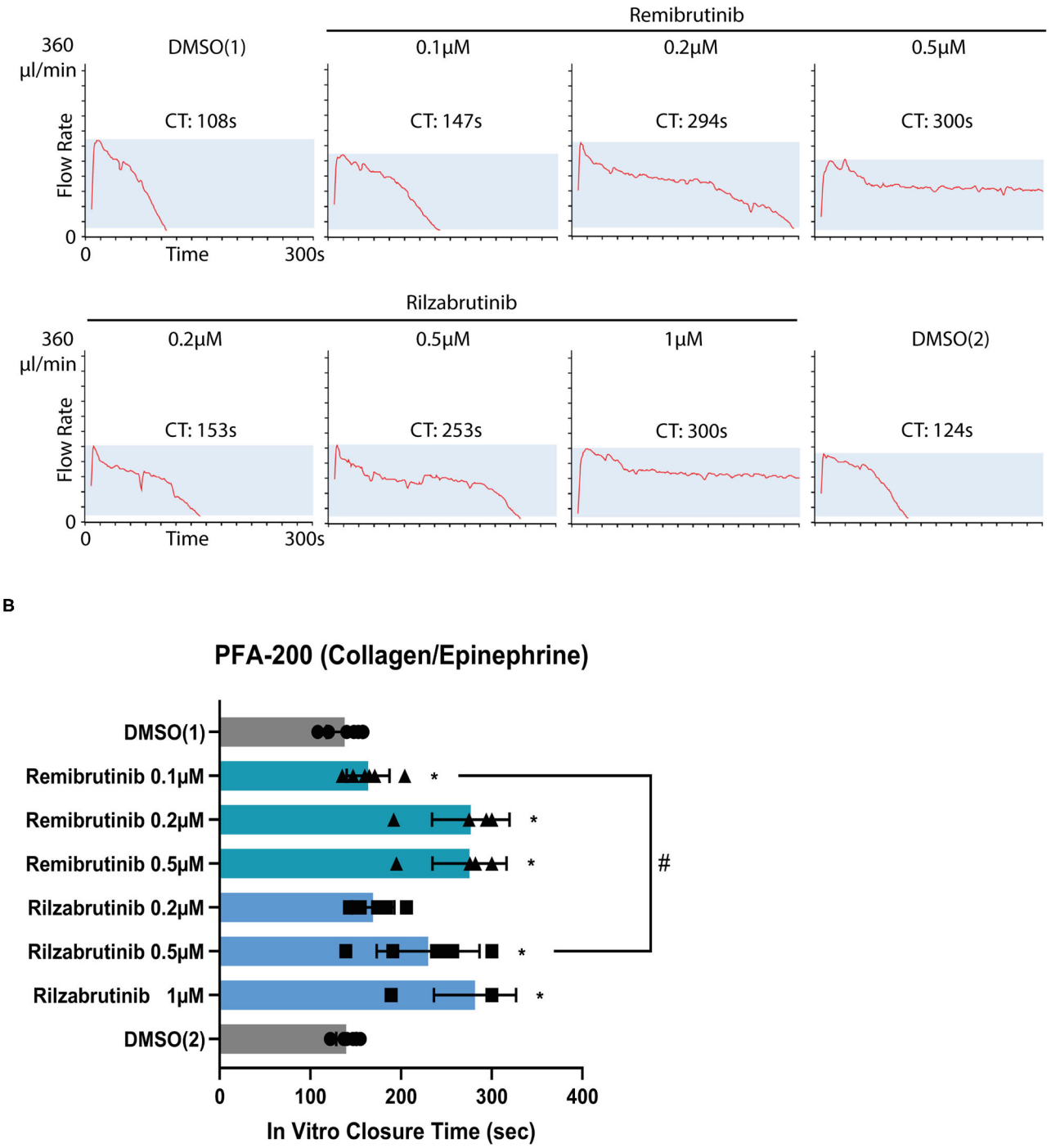

FIGURE 4 | Effect of remibrutinib and rilzabrutinib on bleeding time *in vitro*. Citrate anticoagulated blood samples were pre-incubated for 1 h at 37°C with solvent (DMSO, 0.1%) or increasing concentrations of remibrutinib or rilzabrutinib and then transferred to collagen/epinephrine cartridges. The *in vitro* closure time (CT) was measured with the PFA-200. DMSO (1) and DMSO (2) control samples were measured at the beginning and end of the experiment, respectively. **(A)** Representative PFA-200 tracings. **(B)** The aligned dot plot bar charts show CT values of different concentrations of remibrutinib and rilzabrutinib. Values are mean ± SD ($n = 6$). Statistical analysis was carried out using the Wilcoxon matched-pairs signed rank test comparing against DMSO1 (*$p < 0.05$) or concentrations of remibrutinib (0.1 µM) and rilzabrutinib (0.5 µM) that inhibited Btk-dependent pathways of platelet aggregation by >90% (#$p < 0.05$).

TABLE 1 | IC_{50} values of remibrutinib, rilzabrutinib and other BTK inhibitors for inhibition of low degree GPVI stimulated platelet aggregation, and comparison with therapeutic drug plasma levels.

BTK Inhibitors	IC_{50} (μM)	Therapeutic drug plasma level (μM)
Remibrutinib	0.03*	0.46[a]
Rilzabrutinib	0.16*	0.33[b]
Fenebrutinib	0.016*	0.6[c]
Ibrutinib	0.025#	0.31[d]
Zanubrutinib	0.094#	1.4[e]
Tirabrutinib	0.268#	1.96[f]
Acalabrutinib	0.372#	1.78[g]
Evobrutinib	1.20#	Not known

*Hirudin-anticoagulated blood was pre-incubated with the BTKi for 1 h or 15 min (fenebrutinib, **Supplementary Figure 1**) prior to stimulation with plaque homogenate.*
#Hirudin-anticoagulated blood was pre-incubated with the BTKi for 1 h before stimulation with low collagen concentrations (0.2–0.5 μg/ml). Platelet aggregation was measured by multiple electrode aggregometry (MEA).
[a]Remibrutinib, 100 mg q.d, optimal dose in phase I study (38).
[b]Rilzabrutinib, 300 mg b.i.d (39).
[c]Fenebrutinib, 200 mg q.d (40).
[d]Ibrutinib, 420 mg q.d (41).
[e]Zanubrutinib, 320 mg q.d (42).
[f]Tirabrutinib, 320 mg q.d (43).
[g]Acalabrutinib, 100 mg b.i.d (44).

upon CD32 cross-linking, but it had no effect on TRAP, AA, or ADP stimulation as expected according to the results of previous studies with other BTKi (7, 9, 16, 17), although it has to be stated that a non-existing effect is difficult to prove and may depend on the experimental conditions.

High dose collagen GPVI-dependent aggregation was suppressed to a similar degree of about 30% with remibrutinib (0.1 μM), rilzabrutinib (0.5 μM) and the Btk-selective reversible BTKi fenebrutinib (0.1 μM) (**Supplementary Figure 2**). This may indicate that the concentrations and incubation conditions of remibrutinib and rilzabrutinib used are selective for inhibition of Btk and unlikely to also inhibit Tec in platelets. This is unexpected considering the potent inhibition of Tec by rilzabrutinib *in vitro* (22). Rilzabrutinib by inhibiting Tec in addition to Btk would have shut-off GPVI signaling after high collagen stimulation.

As shown in several studies, low-degree GPVI activation only depends on Btk, while high dose collagen-induced GPVI signaling is also dependent on Tec co-activation (9, 15, 19, 45). In a previous study, 50 nM fenebrutinib was applied and only suppression of platelet aggregation on low but not high dose collagen stimulation was observed (9). Our different results may be explained due to the higher concentration of fenebrutinib (0.1 μM) applied in our study providing a more complete inhibition of Btk.

Our results show that the remibrutinib concentration to fully inhibit Btk-dependent pathways of platelet aggregation (0.1 μM) is lower than the reported maximal plasma level (0.46 μM) in a phase I study after intake of 100 mg q.d. for 12 days (38). Thus, this concentration is expected to block completely Btk-dependent signaling in platelets *in vivo*. The equivalent rilzabrutinib concentration (0.5 μM) is higher than the plasma C_{max} reported in clinical studies after therapeutic dosage for autoimmune diseases (0.33 μM) (**Table 1**) (39). Since the IC_{50} of rilzabrutinib for inhibition of plaque-induced platelet aggregation in blood was lower (0.16 μM), it is likely that therapeutic concentrations of rilzabrutinib inhibit Btk-dependent pathways of platelet aggregation, but not entirely. Our results are in contrast to findings showing no inhibition of ristocetin- and high dose collagen- induced aggregation of platelet-rich plasma from healthy donors and ITP patients pre-incubated with 1 μM rilzabrutinib for 15 min *in vitro* (26, 46). The discrepancy might be explained by differences of the experimental system used (blood vs. PRP), different concentrations of collagen (low vs. high) and exposure times of rilzabrutinib (long vs. short). We selected a long exposure time (1 h), since this might better simulate the *in vivo* situation after absorption of the drug, and previous studies have shown that platelet inhibition with irreversible BTKi increases with the exposure time (17, 19).

Bleeding is a frequent side effect of treatment with certain irreversible BTKi such as ibrutinib and the second generation BTKi acalabrutinib, zanubrutinib, and tirabrutinib used to treat B-cell malignancies (5, 47–49). Exclusive inhibition of Btk should not increase bleeding since XLA patients who are deficient of Btk do not show an impairment of haemostasis (13). It has been discussed that bleeding by these BTKi is related to off-target inhibition of Tec, since this kinase is functionally involved in GPVI-induced platelet activation (8, 15). By comparison, for fenebrutinib, a reversible highly selective BTKi, which is the most selective BTKi and which shows no inhibition of Tec (50), no bleeding events were reported in clinical trials (non-Hodgkin lymphoma, chronic lymphocytic leukemia, rheumatoid arthritis, and systemic lupus erythematosus) (5). Also, fenebrutinib *in vitro*, even at very high concentrations up to 1 μM did not prolong bleeding time measured by the PFA-200 (9).

The reversible BTKi fenebrutinib binds to an inactive conformation of Btk (51). Also, remibrutinib which was developed from fenebrutinib-like scaffolds to bind to the inactive conformation of Btk (20, 51) showed a 175-fold higher affinity for Btk over Tec in binding assays *in vitro* (20). Thus, it was expected that remibrutinib would not increase *in vitro* bleeding time measured by PFA-200, similar to fenebrutinib (9). However, we observed that bleeding times *in vitro* were already slightly but significantly increased after blood incubation with 0.1 μM remibrutinib (which inhibited >90% of Btk-dependent pathways of platelet aggregation), and strongly prolonged by remibrutinib concentrations of 0.2 and 0.5 μM. The results for remibrutinib are similar to a previous study, in which low concentrations of the irreversible BTKi ibrutinib, zanubrutinib, acalabrutinib, and tirabrutinib inhibited GPVI- dependent platelet aggregation by >70%, but 2- to 2.5-fold higher concentrations of these BTKi were required to significantly increase the bleeding time *in vitro* (19). The increase of closure time was similar to that observed after treatment with low dose aspirin (52).

In a phase I placebo controlled clinical trial of remibrutinib (total 156 healthy subjects), mild self-limited bleeding events were observed only in 4 persons in the multiple-ascending dose cohorts with remibrutinib intake for 12 days. These included two

subjects in the 600 mg q.d. cohort with epistaxis and two subjects in the 100 mg cohort with trauma-triggered hematomas (38).

Rilzabrutinib in our study slightly but non-significantly increased at 0.2 μM closure time in the PFA device, the increase was at 0.5 μM pronounced (**Figure 4B**). Potent Tec inhibition could contribute to the increased *in vitro* bleeding time (5); however, the results of the aggregation studies upon stimulation with high concentrations of collagen argue against simultaneous Tec inhibition in platelets by 0.5 μM of rilzabrutinib (see above).

Thus, the mechanisms underlying the increase of closure times elicited by remibrutinib as well as rilzabrutinib are unlikely to involve off-target inhibition of Tec. They could be related to effects on the Btk protein itself. Recently it was found that binding of certain irreversible BTKi (except fenebrutinib) to the kinase domain had long-range allosteric effects on the SH2-and SH3- regulatory domains changing their conformation toward an activated state of the protein (53).

In contrast to remibrutinib, there was not a clear difference of rilzabrutinib concentrations that inhibited Btk-dependent pathways of platelet aggregation in the MEA and robustly increased the closure time in the PFA; the concentration of rilzabrutinib of 0.5 μM does both. Maximal therapeutic concentrations of rilzabrutinib (0.33 μM) are expected to significantly increase the closure time in the PFA device, but no treatment-related bleeding had been noted in the ITP clinical trial with rilzabrutinib (25), although the median platelet count at study entry was only 14.173/μl (25). However, 7% (2/27) of patients treated with rilzabrutinib had treatment-related epistaxis as observed in the latest pemphigus clinical trial (24).

LIMITATIONS

Although our *in vitro* study has the advantage of reducing the complexity of the experimental conditions, and the different effects of the two BTKi studied on platelets in blood are obvious, these data cannot directly be translated into the situation *in vivo*. Clinical studies of platelet function *ex vivo* after oral intake of therapeutic dosage are warranted to approach the *in vivo* effects of remibrutinib and rilzabrutinib on platelets.

CONCLUSION

In the present study we found significant differences of the two BTKi remibrutinib and rilzabrutinib on platelets that would favor remibrutinib as a candidate for further development as an antiplatelet drug to inhibit Btk-dependent platelet activation pathways underlying atherothrombosis and certain platelet-related immune disorders. Since *de novo* protein synthesis in platelets is very limited and because low concentrations of irreversible BTKi such as remibrutinib may covalently inactivate platelet BTK already by a single exposure at low concentrations during absorption, it is likely that low doses of such a selective irreversible BTKi are effective in cardiovascular prevention without affecting the immune system (7, 8, 54). Our study further suggests that off-target effects on Tec are unlike to be involved in the increase of closure time measured by PFA, and may not explain the bleeding side effects elicited by BTKi.

DATA AVAILABILITY STATEMENT

The original contributions presented in the study are included in the article/**Supplementary Material**, further inquiries can be directed to the corresponding author/s.

ETHICS STATEMENT

The studies involving human participants were reviewed and approved by Ethics Committee of the Faculty of Medicine of the University of Munich. Written informed consent for participation was not required for this study in accordance with the national legislation and the institutional requirements.

AUTHOR CONTRIBUTIONS

RD designed and performed experiments, analyzed data, and wrote the manuscript. LG performed experiments and analyzed data. RB provided plaque material. MS supervised experiments and contributed to discussions. CW supervised and contributed to discussions. WS conceived the study, designed experiments, and wrote the manuscript. PH supervised and analyzed experiments and wrote the manuscript. All authors have contributed significantly to this manuscript.

FUNDING

This work was supported by the Deutsche Forschungsgemeinschaft, SFB1123, A2 (PH); RD was sponsored by the Ludwig-Maximilians-University (LMU)-China Scholarship Council (CSC) program.

SUPPLEMENTARY MATERIAL

The Supplementary Material for this article can be found online at: https://www.frontiersin.org/articles/10.3389/fcvm.2021.749022/full#supplementary-material

REFERENCES

1. Bruton OC. Agammaglobulinemia. *Pediatrics.* (1952) 9:722–8.
2. Vetrie D, Vorechovský I, Sideras P, Holland J, Davies A, Flinter F, et al. The gene involved in X-linked agammaglobulinaemia is a member of the src family of protein-tyrosine kinases. *Nature.* (1993) 361:226–33. doi: 10.1038/361226a0
3. Tsukada S, Saffran DC, Rawlings DJ, Parolini O, Allen RC, Klisak I, et al. Deficient expression of a B cell cytoplasmic tyrosine kinase in human X-linked agammaglobulinemia. *Cell.* (1993) 72:279–90. doi: 10.1016/0092-8674(93)90667-F
4. Pal Singh S, Dammeijer F Hendriks RW. Role of Bruton's tyrosine kinase in B cells and malignancies. *Mol Cancer.* (2018) 17:57. doi: 10.1186/s12943-018-0779-z

5. von Hundelshausen P Siess W. Bleeding by Bruton Tyrosine kinase-inhibitors: dependency on drug type and disease. *Cancers.* (2021) 13:1103. doi: 10.3390/cancers13051103
6. Futatani T, Watanabe C, Baba Y, Tsukada S Ochs HD. Bruton's tyrosine kinase is present in normal platelets and its absence identifies patients with X-linked agammaglobulinaemia and carrier females. *Br J Haematol.* (2001) 114:141–9. doi: 10.1046/j.1365-2141.2001.02905.x
7. Busygina K, Jamasbi J, Seiler T, Deckmyn H, Weber C, Brandl R, et al. Oral Bruton tyrosine kinase inhibitors selectively block atherosclerotic plaque–triggered thrombus formation in humans. *Blood.* (2018) 131:2605–16. doi: 10.1182/blood-2017-09-808808
8. Busygina K, Denzinger V, Bernlochner I, Weber C, Lorenz R Siess W. Btk inhibitors as first oral atherothrombosis-selective antiplatelet drugs? *Thromb Haemost.* (2019) 119:1212–21. doi: 10.1055/s-0039-1687877
9. Goldmann L, Duan R, Kragh T, Wittmann G, Weber C, Lorenz R, et al. Oral Bruton tyrosine kinase inhibitors block activation of the platelet Fc receptor CD32a (FcgammaRIIA): a new option in HIT? *Blood Adv.* (2019) 3:4021–33. doi: 10.1182/bloodadvances.2019000617
10. von Hundelshausen P, Lorenz R, Siess W Weber C. Vaccine-induced immune thrombotic thrombocytopenia (VITT): targeting pathomechanisms with Bruton Tyrosine kinase inhibitors. *Thromb Haemost.* (2021). doi: 10.1055/a-1481-3039. [Epub ahead of print].
11. Payne H, Ponomaryov T, Watson SP Brill A. Mice with a deficiency in CLEC-2 are protected against deep vein thrombosis. *Blood.* (2017) 129:2013–20. doi: 10.1182/blood-2016-09-742999
12. Nicolson PL, Welsh JD, Chauhan A, Thomas MR, Kahn ML Watson SP. A rationale for blocking thromboinflammation in COVID-19 with Btk inhibitors. *Platelets.* (2020) 31:685–90. doi: 10.1080/09537104.2020.1775189
13. Shillitoe B Gennery A. X-linked agammaglobulinaemia: outcomes in the modern era. *Clin Immunol.* (2017) 183:54–62. doi: 10.1016/j.clim.2017.07.008
14. Quek LS, Bolen J Watson SP. A role for Bruton's tyrosine kinase (Btk) in platelet activation by collagen. *Curr Biol.* (1998) 8:1137–S1. doi: 10.1016/S0960-9822(98)70471-3
15. Atkinson BT, Ellmeier W Watson SP. Tec regulates platelet activation by GPVI in the absence of Btk. *Blood.* (2003) 102:3592–9. doi: 10.1182/blood-2003-04-1142
16. Bye AP, Unsworth AJ, Desborough MJ, Hildyard CAT, Appleby N, Bruce D, et al. Severe platelet dysfunction in NHL patients receiving ibrutinib is absent in patients receiving acalabrutinib. *Blood Adv.* (2017) 1:2610–23. doi: 10.1182/bloodadvances.2017011999
17. Nicolson PLR, Hughes CE, Watson S, Nock SH, Hardy AT, Watson CN, et al. Inhibition of Btk by Btk-specific concentrations of ibrutinib and acalabrutinib delays but does not block platelet aggregation mediated by glycoprotein VI. *Haematologica.* (2018) 103:2097–108. doi: 10.3324/haematol.2018.193391
18. Jamasbi J, Megens RT, Bianchini M, Uhland K, Munch G, Ungerer M, et al. Cross-linking GPVI-Fc by anti-Fc antibodies potentiates its inhibition of atherosclerotic plaque- and collagen-induced platelet activation. *JACC Basic Transl Sci.* (2016) 1:131–42. doi: 10.1016/j.jacbts.2016.03.008
19. Denzinger V, Busygina K, Jamasbi J, Pekrul I, Spannagl M, Weber C, et al. Optimizing platelet GPVI inhibition versus haemostatic impairment by the Btk inhibitors ibrutinib, acalabrutinib, ONO/GS-4059, BGB-3111 and evobrutinib. *Thromb Haemost.* (2019) 119:397–406. doi: 10.1055/s-0039-1677744
20. Angst D, Gessier F, Janser P, Vulpetti A, Walchli R, Beerli C, et al. Discovery of LOU064 (Remibrutinib), a potent and highly selective covalent inhibitor of Bruton's Tyrosine kinase. *J Med Chem.* (2020) 63:5102–18. doi: 10.1021/acs.jmedchem.9b01916
21. Hill R, Smith P, Krishnarajah J, Bradshaw J, Masjedizadeh M, Bisconte A, et al. Discovery of PRN1008, a novel, reversible covalent btk inhibitor in clinical development for rheumatoid arthritis: abstract number: 1671. *Arthr Rheumatol.* (2015) 67:2062–3.
22. Murrell D, Gourlay S, Hill R, Bisconte A, Francesco M, Smith P, et al. Development of PRN1008, a novel, reversible covalent BTK inhibitor in clinical development for pemphigus. In *Proceedings of the Medical Dermatology Society Annual Meeting, Washington, DC, USA*. (2016). p. 3.
23. Bradshaw JM, McFarland JM, Paavilainen VO, Bisconte A, Tam D, Phan VT, et al. Prolonged and tunable residence time using reversible covalent kinase inhibitors. *Nat Chem Biol.* (2015) 11:525–31. doi: 10.1038/nchembio.1817
24. Murrell DF, Patsatsi A, Stavropoulos P, Baum S, Zeeli T, Kern JS, et al. Proof of concept for the clinical effects of oral rilzabrutinib, the first Bruton tyrosine kinase inhibitor for pemphigus vulgaris: the phase II BELIEVE study. *Br J Dermatol.* (2021). doi: 10.1111/bjd.20431. [Epub ahead of print].
25. Kuter D, Boccia R, Lee E-J, Efraim M, Tzvetkov N, Mayer J, et al. Phase I/II, open-label, adaptive study of oral Bruton Tyrosine kinase inhibitor PRN1008 in patients with relapsed/refractory primary or secondary immune thrombocytopenia. *Blood.* (2019) 134:87–7. doi: 10.1182/blood-2019-122336
26. Langrish CL, Bradshaw JM, Owens TD, Campbell RL, Francesco MR, Karr DE, et al. PRN1008, a reversible covalent BTK inhibitor in clinical development for immune thrombocytopenic purpura. *Blood.* (2017) 130:1052–2. doi: 10.1182/blood.V130.Suppl_1.1052.1052
27. Reininger AJ, Bernlochner I, Penz SM, Ravanat C, Smethurst P, Farndale RW, et al. A 2-step mechanism of arterial thrombus formation induced by human atherosclerotic plaques. *J Am Coll Cardiol.* (2010) 55:1147–58. doi: 10.1016/j.jacc.2009.11.051
28. Penz S, Reininger AJ, Brandl R, Goyal P, Rabie T, Bernlochner I, et al. Human atheromatous plaques stimulate thrombus formation by activating platelet glycoprotein VI. *FASEB J.* (2005) 19:898–909. doi: 10.1096/fj.04-2748com
29. Tóth O, Calatzis A, Penz S, Losonczy H Siess W. Multiple electrode aggregometry: a new device to measure platelet aggregation in whole blood. *Thromb Haemost.* (2017) 96:781–8. doi: 10.1160/TH06-05-0242
30. von Pape K-W, Aland E Bohner J. Platelet function analysis with PFA-100® in patients medicated with acetylsalicylic acid strongly depends on concentration of sodium citrate used for anticoagulation of blood sample??Presented in part at the 43rd annual meeting of the GTH, February 25, 1999, Mannheim, Germany. *Thromb Res.* (2000) 98:295–9. doi: 10.1016/S0049-3848(99)00236-4
31. Bampalis VG, Brantl SA Siess W. Why and how to eliminate spontaneous platelet aggregation in blood measured by multiple electrode aggregometry. *J Thromb Haemost.* (2012) 10:1710–4. doi: 10.1111/j.1538-7836.2012.04819.x
32. Kundu SK, Heilmann EJ, Sio R, Garcia C, Davidson RM Ostgaard RA. Description of an in vitro platelet function analyzer–PFA-100. *Semin Thromb Hemost.* (1995) 21 (Suppl. 2):106–12. doi: 10.1055/s-0032-1313612
33. Favaloro EJ. Clinical utility of the PFA-100. *Semin Thromb Hemost.* (2008) 34:709–33. doi: 10.1055/s-0029-1145254
34. Schulz C, Penz S, Hoffmann C, Langer H, Gillitzer A, Schneider S, et al. Platelet GPVI binds to collagenous structures in the core region of human atheromatous plaque and is critical for atheroprogression in vivo. *Basic Res Cardiol.* (2008) 103:356–67. doi: 10.1007/s00395-008-0722-3
35. Kratzer MAA, Negrescu EV, Hirai A, Yeo YK, Petra F Siess W. The thrombostat system a useful method to test antiplatelet drugs and diets. *Semin Thromb Hemost.* (1995) 21:25–31. doi: 10.1055/s-0032-1313599
36. Marshall PW, Williams AJ, Dixon RM, Growcott JW, Warburton S, Armstrong J, et al. A comparison of the effects of aspirin on bleeding time measured using the Simplate method and closure time measured using the PFA-100, in healthy volunteers. *Br J Clin Pharmacol.* (1997) 44:151–5. doi: 10.1046/j.1365-2125.1997.00639.x
37. Ng KF, Lawmin JC, Tsang SF, Tang WM, Chiu KY. Value of a single preoperative PFA-100 measurement in assessing the risk of bleeding in patients taking cyclooxygenase inhibitors and undergoing total knee replacement. *Br J Anaesth.* (2009) 102:779–84. doi: 10.1093/bja/aep091
38. Kaul M, End P, Cabanski M, Schuhler C, Jakab A, Kistowska M, et al. Remibrutinib (LOU064): a selective potent oral BTK inhibitor with promising clinical safety and pharmacodynamics in a randomized phase I trial. *Clin Transl Sci.* (2021). doi: 10.1111/cts.13005. [Epub ahead of print].
39. Smith PF, Krishnarajah J, Nunn PA, Hill RJ, Karr D, Tam D, et al. A phase I trial of PRN1008, a novel reversible covalent inhibitor of Bruton's tyrosine kinase, in healthy volunteers. *Br J Clin Pharmacol.* (2017) 83:2367–76. doi: 10.1111/bcp.13351
40. Byrd JC, Smith S, Wagner-Johnston N, Sharman J, Chen AI, Advani R, et al. First-in-human phase 1 study of the BTK inhibitor GDC-0853 in relapsed or refractory B-cell NHL and CLL. *Oncotarget.* (2018) 9:13023–13035. doi: 10.18632/oncotarget.24310
41. Chen J, Kinoshita T, Gururaja T, Sukbuntherng J, James D, Lu D, et al. The effect of Bruton's tyrosine kinase (BTK) inhibitors on collagen-induced platelet aggregation, BTK, and tyrosine kinase expressed in hepatocellular carcinoma (TEC). *Eur J Haematol.* (2018) 101:604–12. doi: 10.1111/ejh.13148

42. Tam CS, Trotman J, Opat S, Burger JA, Cull G, Gottlieb D, et al. Phase 1 study of the selective BTK inhibitor zanubrutinib in B-cell malignancies and safety and efficacy evaluation in CLL. *Blood.* (2019) 134:851–9. doi: 10.1182/blood.2019001160
43. Walter HS, Rule SA, Dyer MJ, Karlin L, Jones C, Cazin B, et al. A phase 1 clinical trial of the selective BTK inhibitor ONO/GS-4059 in relapsed and refractory mature B-cell malignancies. *Blood.* (2016) 127:411–9. doi: 10.1182/blood-2015-08-664086
44. Byrd JC, Harrington B, O'Brien S, Jones JA, Schuh A, Devereux S, et al. Acalabrutinib (ACP-196) in relapsed chronic lymphocytic leukemia. *N Engl J Med.* (2016) 374:323–32. doi: 10.1056/NEJMoa1509981
45. Oda A, Ikeda Y, Ochs HD, Druker BJ, Ozaki K, Handa M, et al. Rapid tyrosine phosphorylation and activation of Bruton's tyrosine/Tec kinases in platelets induced by collagen binding or CD32 cross-linking. *Blood.* (2000) 95:1663–70. doi: 10.1182/blood.V95.5.1663.005k44_1663_1670
46. Langrish CL, Bradshaw JM, Francesco MR, Owens TD, Xing Y, Shu J, et al. Preclinical efficacy and anti-inflammatory mechanisms of action of the Bruton Tyrosine kinase inhibitor rilzabrutinib for immune-mediated disease. *J Immunol.* (2021) 206:1454–68. doi: 10.4049/jimmunol.2001130
47. Shatzel JJ, Olson SR, Tao DL, McCarty OJT, Danilov AV DeLoughery TG. Ibrutinib-associated bleeding: pathogenesis, management and risk reduction strategies. *J Thromb Haemost.* (2017) 15:835–47. doi: 10.1111/jth.13651
48. Sibaud V, Beylot-Barry M, Protin C, Vigarios E, Recher C Ysebaert L. Dermatological toxicities of Bruton's Tyrosine kinase inhibitors. *Am J Clin Dermatol.* (2020) 21:799–812. doi: 10.1007/s40257-020-00535-x
49. Sekiguchi N, Rai S, Munakata W, Suzuki K, Handa H, Shibayama H, et al. A multicenter, open-label, phase II study of tirabrutinib (ONO/GS-4059) in patients with Waldenstrom's macroglobulinemia. *Cancer Sci.* (2020) 111:3327–37. doi: 10.1111/cas.14561
50. Crawford JJ, Johnson AR, Misner DL, Belmont LD, Castanedo G, Choy R, et al. Discovery of GDC-0853: a potent, selective, and noncovalent bruton's tyrosine kinase inhibitor in early clinical development. *J Med Chem.* (2018) 61:2227–45. doi: 10.1021/acs.jmedchem.7b01712
51. Gabizon R London N. A fast and clean BTK inhibitor. *J Med Chem.* (2020) 63:5100–1. doi: 10.1021/acs.jmedchem.0c00597
52. Reny JL, De Moerloose P, Dauzat M Fontana P. Use of the PFA-100 closure time to predict cardiovascular events in aspirin-treated cardiovascular patients: a systematic review and meta-analysis. *J Thromb Haemost.* (2008) 6:444–50. doi: 10.1111/j.1538-7836.2008.02897.x
53. Joseph RE, Amatya N, Fulton DB, Engen JA-O, Wales TE, Andreotti AA-O. Differential impact of BTK active site inhibitors on the conformational state of full-length BTK. *eLife*. 9:e60470. doi: 10.7554/eLife.60470
54. Payrastre B Ribes A. Low-dose Btk inhibitors: an 'aspirin' of tomorrow? *Haematologica.* (2021) 106:2–4. doi: 10.3324/haematol.2020.265173

Conflict of Interest: The authors declare that the research was conducted in the absence of any commercial or financial relationships that could be construed as a potential conflict of interest.

Publisher's Note: All claims expressed in this article are solely those of the authors and do not necessarily represent those of their affiliated organizations, or those of the publisher, the editors and the reviewers. Any product that may be evaluated in this article, or claim that may be made by its manufacturer, is not guaranteed or endorsed by the publisher.

frontiers in Cardiovascular Medicine

ORIGINAL RESEARCH
published: 20 October 2021
doi: 10.3389/fcvm.2021.735262

Relationship Between Low Skeletal Muscle Mass and Arteriosclerosis in Western China: A Cross-Sectional Study

Zhenzhen Li[1†], *Xiang Tong*[2†], *Yao Ma*[3], *Ting Bao*[1] *and Jirong Yue*[3*]

[1] Health Management Center, West China Hospital/West China School of Medicine, Sichuan University, Chengdu, China, [2] Department of Respiratory and Critical Care Medicine, West China Hospital/West China School of Medicine, Sichuan University, Chengdu, China, [3] Department of Geriatrics and National Clinical Research Center for Geriatrics, West China Hospital/West China School of Medicine, Sichuan University, Chengdu, China

Objectives: This study explored the prevalence and the correlation between low muscle mass and arteriosclerosis in different gender and age groups, to increase the attention paid to the risk factors of arteriosclerosis in the young and middle-aged population.

Methods: This was an analytical, cross-sectional study. Data were obtained from healthy individuals recruited from the Health Management Center of W Hospital. The brachial-ankle pulse-wave velocity was used as an indicator of arteriosclerosis, and a bioelectrical impedance analysis was used to assess the body composition.

Results: A total of 36,374 subjects (men, 58.4%; women, 41.6%; mean age, 43.74 ± 12.34 years [range, 18–80 years]) participated in this study. The prevalence of low skeletal muscle mass and arteriosclerosis was 17.7 and 53.1%, respectively, in all subjects. Low skeletal muscle mass was significantly associated with arteriosclerosis (OR: 1.435, 95% CI: 1.343–1.533, $P < 0.001$) in all subjects, and the association remained significant in young age (OR: 1.506, 95% CI: 1.353–1.678, $P < 0.001$), middle-age (OR: 1.329, 95% CI: 1.195–1.479, $P < 0.001$), and old age (OR: 1.676, 95% CI: 1.191–2.358, $P = 0.003$), and also significant in men (OR: 1.559, 95% CI: 1.396–1.740, $P < 0.001$) and women (OR: 1.266, 95% CI: 1.143–1.401, $P < 0.001$).

Conclusions and Implications: Our results show that the prevalence of low muscle mass and arteriosclerosis is high in the general population, even among middle-aged people and young people, and confirmed that there is a significant independent association between low skeletal muscle mass and arteriosclerosis in all subjects and in different age and gender subgroups.

Keywords: arteriosclerosis, arterial stiffness, baPWV, low of skeletal muscle mass, sarcopenia

OPEN ACCESS

Edited by:
Johannes A. Schmid, Medical University of Vienna, Austria

Reviewed by:
Rudolf Lucas, Augusta University, United States
Vivek Nanda, University of Alabama at Birmingham, United States

***Correspondence:**
Jirong Yue
yuejirong11@hotmail.com

†These authors have contributed equally to this work and share first authorship

Specialty section:
This article was submitted to Atherosclerosis and Vascular Medicine, a section of the journal Frontiers in Cardiovascular Medicine

Received: *02 July 2021*
Accepted: *23 September 2021*
Published: *20 October 2021*

Citation:
Li Z, Tong X, Ma Y, Bao T and Yue J (2021) Relationship Between Low Skeletal Muscle Mass and Arteriosclerosis in Western China: A Cross-Sectional Study. Front. Cardiovasc. Med. 8:735262. doi: 10.3389/fcvm.2021.735262

INTRODUCTION

It has long been recognized that aging is associated with gradual changes in body composition and unfavorable metabolic alterations. The accumulation of fat and loss of lean muscle mass are important changes that occur in adults as they age. Generally, muscle mass decreases by 3–8% every 10 years after 30 years of age (1), and

muscle strength, the primary component of body function, decreases by 1–2% every year after 50 years of age (2, 3). Sarcopenia is a syndrome characterized by low skeletal muscle mass and strength, which can lead to undesirable health consequences, including physical disability, decreased quality of life, and an increased risk of mortality. A conservative estimate of the prevalence of clinically relevant sarcopenia is that the syndrome currently affects >50 million individuals, and this number is projected to exceed 200 million in the next 40 years (4). The gradual decrease in the skeletal muscle mass is the primary factor that contributes to sarcopenia, and is also the main feature and important pathophysiological change in sarcopenia. A muscle mass loss of >40% is associated with death, and skeletal muscle loss can lead to reduced strength and functional limitations and/or disability (5). However, the pathogenesis of sarcopenia has not yet been fully elucidated. Additionally, sarcopenia may be associated with reduced exercise levels, weakened neuromuscular function, aging-related hormonal changes (including insulin), pro-inflammatory cytokine levels, muscle cell apoptosis, and genetic and nutritional factors (6). These risk factors and pathogenesis are similar to those of other age-related diseases and those involved in atherosclerosis.

Cardiovascular disease (CVD) is the main cause of death worldwide, and is no longer a disease of old age; the incidence rate among young individuals has increased significantly. Arteriosclerosis is the pathological basis of CVD, which is caused by changes in the structure and function of the media, primarily leading to arterial stiffness, especially in the large arteries (7–9). The pathogenesis of arteriosclerosis is complex and may be related to hemodynamic changes, endothelial damage, abnormal lipid metabolism, and chronic inflammation of blood vessel walls caused by physical and chemical damage, eventually leading to the thickening of the arterial intima, vascular stiffness, and luminal stenosis (10). Arteriosclerosis can be considered as the prodromal stage of atherosclerotic disease, or on the contrary, atherosclerosis can be considered as a form of accelerated arteriosclerosis. Nonetheless, arteriosclerosis is an important manifestation of aging-related, subclinical organ damage, and is also a hallmark of cardiovascular disease (11); as such, arteriosclerosis is an excellent predictive tool with added value in the general population (12), which has been established as an independent predictor of cardiovascular events and cardiovascular mortality.

The loss of skeletal muscle mass and arteriosclerosis are two common phenomena associated with aging among middle-aged and older individuals. Some studies have examined the correlation between low skeletal muscle mass and arteriosclerosis (13–16). However, these studies mainly focused on older subjects, and none included populations with a wider range of ages. Although the age of onset of cardiovascular disease and arteriosclerosis has moved forward, young people pay insufficient attention to arteriosclerosis and lack an understanding of the correlation between low muscle mass and arteriosclerosis. This study explored the correlation between low muscle mass and arteriosclerosis in different age groups, to increase the attention paid to the risk factors of arteriosclerosis in the young and middle-aged population, early detection of risk factors, and comprehensive prevention and control measures.

MATERIALS AND METHODS

Participants

All the research subjects in this analytical cross-sectional study were recruited from the Health Management Center of W Hospital. Consecutive participants were recruited between January 1, 2020, and March 31, 2021. The selection criteria were as follows: ability to perform self-care activities of daily living without difficulty or assistance, and willingness to provide informed consent to participate in the research. Individuals with the following comorbidities were excluded: severe malnutrition, history of myocardial infarction, heart failure, stroke, cancer, and severe hepatic or renal dysfunction; the long-term use of corticosteroids and/or diuretics; physical disability (hands, feet, or limbs), diagnosed by the investigators participating in this study, which could affect physical activity or skeletal muscle mass distribution; and weight change >5% in the previous 3 months. All the participants were informed of the purpose and procedures of the study and provided informed written consent. The study protocol was approved by the Biomedical Ethics Committee of the W Hospital (No. 2021-96).

Data Collection

A medical history questionnaire was administered to acquire information about the age, sex, hypertension, diabetes, smoking, and alcohol consumption of the participants. The height of the participants was measured without shoes to an accuracy of 0.1 cm, and the weight of the participants wearing light indoor clothes and without shoes was measured to an accuracy of 0.1 kg. The body mass index (BMI) was calculated by dividing the body weight by height squared (kg/m^2).

The participants assumed a sitting position and after resting for at least 5 min, a mercury sphygmomanometer was used to measure the systolic blood pressure (SBP) and diastolic blood pressure (DBP). The average of two independent blood pressure readings was used, with an interval of 3–5 min between measurements.

After a fast of at least 8 h, a morning blood sample was obtained from the anterior elbow vein and transferred immediately to the central laboratory for analysis. An automated biochemical analyzer was used to measure the fasting blood glucose (FBG) levels. The lipid profiles included total cholesterol, triglycerides, high-density lipoprotein cholesterol, low-density lipoprotein cholesterol (LDL-C), and uric acid.

The skeletal muscle mass was measured by a bio-impedance analysis using an Inbody 570 (BioSpace, Seoul, Korea). The participants stood upright with their arms abducted apart from their trunk and legs spread slightly. Using segmental body composition and skeletal muscle mass, the appendicular skeletal muscle mass index (ASMI) was calculated using the following equation:

$$ASMI = \text{total limb lean mass}/\text{height}^2$$

Arteriosclerosis was measured by trained personnel using an automated brachial-ankle pulse-wave velocity (baPWV)

instrument (Omron Healthcare Co., Ltd., Kyoto, Japan) in accordance with standard procedures in a quiet room with moderate temperature. After the participant rested for 10 min, the measurement was performed with the subject in the supine position. The baPWV, measured through a time-phase analysis, was calculated by estimating the ratio of the distance between the upper chest and the ankle to the time interval between the arm and ankle according to the patient's height (17).

Definitions

Subjects who exhibited an SBP ≥140 mmHg and/or a DBP ≥90 mmHg during the physical examination (18), or who had been previously diagnosed with hypertension by health care professionals, regardless of whether they were taking antihypertensive drugs at the time of the study, were diagnosed with hypertension.

Subjects with an FBG level ≥7.0 mmol/L during the physical examination or had been previously diagnosed with diabetes by health care professionals, regardless of whether they were using hypoglycemic drugs at the time of the study, were diagnosed with diabetes.

According to the Asia Working Group for Sarcopenia (AWGS) recommendation (19), an ASMI <7.0 kg/m^2 in men and <5.7 kg/m^2 in women was classified as "low skeletal muscle mass." A baPWV <1,400 cm/s was defined as normal peripheral arterial elasticity, and baPWV ≥1,400 cm/s was defined as peripheral arteriosclerosis (20).

Statistical Analysis

Statistical analyses were performed using SPSS version 21.0 (IBM Corporation, Armonk, NY, USA). The baseline analysis was performed after dividing the subjects into two different subgroups according to the sex and age, according to the levels of SMI, namely "Low muscle mass" and "Normal." The normality of distributions was tested using the Kolmogorov-Smirnov test. The descriptive data are expressed as numbers and percentages for categorical variables and mean ± standard deviation (SD) for continuous variables. To assess the differences between the groups, *t*-tests were used for ordinal or continuous variables, and the chi-square test for categorical variables.

A multicollinearity diagnostic was conducted to assess the validity of the regression model by calculating the values of tolerance and variance inflation factor (VIF). The values of tolerance >0.1 and VIF <10 were used to indicate the absence of multicollinearity among the dependent variables. The multivariate logistic regression model was performed in all the subjects and different subgroups, such as age groups (age ≤40 years, 40 years < age ≤65 years, and age >65 years) and gender groups, using three models: (a) crude; (b) adjusted for age and sex; and (c) adjusted for age, sex, BMI, hypertension, diabetes, triglyceride, total cholesterol, HDL cholesterol, uric acid, smoking, and alcohol consumption.

The statistical significance was set at $p < 0.05$.

RESULTS

Characteristics of the Study Population

A total of 36,374 subjects (men, 58.4%; women, 41.6%; mean age, 43.74 ± 12.34 years [range, 18–80 years]) participated in this study. The prevalence of low skeletal muscle mass and arteriosclerosis was 17.7 and 53.1% in the overall study population, 18.7 and 30.9% in the youth group (age ≤40 years), 15.1 and 67.6% in the middle-aged group (40 years < Age ≤65 years), 31.2 and 87.1% in the older group (age >65 years) ($P < 0.001$), 12.1 and 59.2% in the group of men, 25.6 and 44.4% in the group of women ($P < 0.001$). **Table 1** summarized the demographic characteristics of all the subjects.

Table 2 summarizes the comparisons between the subjects with and without arteriosclerosis. A total of 19,310 (6.8%) subjects were classified as having arteriosclerosis. Comparing to non- arteriosclerosis subjects, arteriosclerosis subjects were significantly older (48.7 ± 12 years vs. 38.1 ± 10 years, $P < 0.001$), male predominant (65.4 vs. 50.6%, $P < 0.001$), higher BMI (23.9 ± 3.2 vs. 22.9 ± 3.2, $P < 0.001$), while lower muscle mass (18.3 vs. 17%, $P = 0.004$), higher values of hypertension (47.5 vs. 14.4%, $P < 0.001$) and diabetes (9.0 vs. 1.6%, $P < 0.001$), and higher levels of fasting glucose (5.4 ± 1.5 vs. 4.9 ± 0.8, $P < 0.001$), systolic blood pressure (126.1 ± 15.8 vs. 114.5 ± 11.2, $P < 0.001$), diastolic blood pressure (77.4 ± 10.8 vs. 69.3 ± 8.8, $P < 0.001$), triglycerides (1.77 ± 1.57 vs. 1.33 ± 1.1, $P < 0.001$), total cholesterol (4.95 ± 0.95 vs. 4.63 ± 0.87, $P < 0.001$), LDL cholesterol (3.02 ± 0.81 vs. 2.79 ± 0.76, $P < 0.001$), uric acid (353 ± 90 vs. 333 ± 90, $P < 0.001$), lower HDL cholesterol (1.31 ± 0.36 vs. 1.37 ± 0.36, $P < 0.001$), and were more likely to smoke (31.7 vs. 23.4%, $P < 0.001$) and consume alcohol (49.6 vs. 42.2%, $P < 0.001$).

Logistic Regression Analysis

A multicollinearity diagnosis revealed a tolerance of 0.034, VIF of 29.382 for cholesterol, and tolerance of 0.043 and VIF of 23.144 for LDL, thus indicating multicollinearity between cholesterol and LDL; therefore, LDL was excluded.

The results of the univariate analysis showed an association between low skeletal muscle mass and arteriosclerosis (OR: 1.075, 95% CI: 1.019–1.135, $P = 0.008$), and the association remained significant after adjustment for age and sex (OR: 1.241, 95% CI: 1.164–1.322, $P < 0.001$). Similarly, the association was significant in the multiple logistic regression model when other potential confounding factors entered the model (OR: 1.435, 95% CI: 1.343–1.533, $P < 0.001$; **Table 3**).

Subgroup Analysis by Age

For young people (age ≤40 years), the results of the univariate analysis showed an insignificant association between low skeletal muscle mass and arteriosclerosis (OR: 0.923, 95% CI: 0.845–1.007, $P = 0.072$), and the association became significant after adjustment for age and sex (OR: 1.399, 95% CI: 1.272–1.538, $P < 0.001$). The association remained significant after adjustment for other potential confounding factors (OR: 1.506, 95% CI: 1.353–1.678, $P < 0.001$; **Table 3**).

TABLE 1 | Demographic characteristics of all subjects.

	Overall	Subgroups for gender			Subgroups for age			
		Men	Women	*p*	Young	Middle age	Old	*p*
	***n* = 36,374**	***n* = 21,260**	***n* = 15,114**		***n* = 15,772**	***n* = 18,251**	***n* = 2,401**	
Age, years	43.74 ± 12.34	44.27 ± 12.23	43 ± 12.4	<0.001	32.34 ± 4.39	50.1 ± 6.4	70.04 ± 7.3	<0.001
Male, *n* (%)	21,260 (58.4)	/	/	/	8,777 (55.8)	11,000 (60.3)	1,483 (61.8)	<0.001
BMI, kg/m^2	23.34 ± 3.26	24.54 ± 3.01	21.75 ± 2.88	<0.001	22.85 ± 3.5	23.8 ± 3	23.99 ± 3	<0.001
SMI (kg/m^2)	/	7.68 ± 0.65	6.03 ± 0.57	<0.001	/	/	/	/
Low skeletal muscle mass, *n* (%)	6,446 (17.7)	2,579 (12.1)	3,867 (25.6)	<0.001	2,944 (18.7)	2,754 (15.1)	748 (31.2)	<0.001
Arteriosclerosis, *n* (%)	19,310 (53.1)	12,595 (59.2)	6,715 (44.4)	<0.001	4,880 (30.9)	12,338 (67.6)	2,092 (87.1)	<0.001
Hypertension, *n* (%)	11,621 (31.9)	8,523 (40.1)	3,098 (20.5)	<0.001	2,793 (17.8)	7,330 (40.2)	1,499 (62.4)	<0.001
Systolic BP, mmHg	120.70 ± 15.0	123.13 ± 14.5	117.28 ± 15	<0.001	116.5 ± 12.3	122.39 ± 15.16	135.3 ± 17.61	<0.001
Diastolic BP, mmHg	73.6 ± 10.7	76.21 ± 10.63	69.94 ± 10	<0.001	70.67 ± 9.6	75.77 ± 11.08	76.45 ± 10.1	<0.001
Diabetes, *n* (%)	2,009 (5.5)	1,597 (7.5)	412 (2.7)	<0.001	150 (1)	1,368 (7.5)	491 (20.4)	<0.001
Fasting glucose, mmol/L	5.16 ± 1.27	5.28 ± 1.43	4.98 ± 0.97	<0.001	4.83 ± 0.83	5.33 ± 1.39	5.99 ± 1.9	<0.001
Triglyceride, mmol/L	1.56 ± 1.39	1.85 ± 1.61	1.16 ± 0.86	<0.001	1.40 ± 1.39	1.7 ± 1.42	1.55 ± 0.99	<0.001
Total cholesterol, mmol/L	4.80 ± 0.93	4.83 ± 0.92	4.75 ± 0.94	<0.001	4.57 ± 0.86	4.97 ± 0.93	4.95 ± 1.02	<0.001
HDL cholesterol, mmol/L	1.34 ± 0.36	1.19 ± 0.29	1.54 ± 0.36	<0.001	1.34 ± 0.36	1.33 ± 0.37	1.39 ± 0.36	<0.001
LDL cholesterol, mmol/L	2.91 ± 0.8	3 ± 0.78	2.79 ± 0.8	<0.001	2.75 ± 0.75	3.04 ± 0.8	3 ± 0.88	<0.001
Uric acid, μmol/L	/	389.5 ± 79	279.62 ± 60.29	<0.001	345 ± 95.5	341.3 ± 86.16	342.6 ± 82.5	<0.001
Smoking, *n* (%)	10,121 (27.8)	9,858 (46.4)	263 (1.7)	<0.001	3,560 (22.6)	5,909 (32.4)	652 (27.2)	0.002
Alcohol consumption, *n* (%)	16,795 (46.2)	15,519 (73)	1,276 (8.4)	<0.001	7,157 (45.4)	8,794 (48.2)	844 (35.2)	0.015

Values are mean ± SD or valid percentages (n), BMI, body mass index; SMI, skeletal muscle mass index; BP, blood pressure; HDL, high-density lipoprotein; LDL, low-density lipoprotein. Young: Age ≤40 years, Middle-age: 40 years < Age ≤65 years, Old: Age >65 years.

TABLE 2 | Comparisons between subjects with and without arteriosclerosis.

	Arteriosclerosis (*n* = 19,310)	Normal (*n* = 17,064)	*P*
Age, years	48.7 ± 12	38.1 ± 10	<0.001
Male, *n* (%)	65.4 (12,631)	50.6(8,629)	<0.001
BMI, kg/m^2	23.9 ± 3.2	22.9 ± 3.2	<0.001
Low skeletal muscle mass, *n* (%)	3,540 (18.3)	2,906 (17)	0.004
Hypertension, *n* (%)	9,165 (47.5)	2,465 (14.4)	<0.001
Systolic BP, mmHg	126.1 ± 15.8	114.5 ± 11.2	<0.001
Diastolic BP, mmHg	77.4 ± 10.8	69.3 ± 8.8	<0.001
Diabetes, *n* (%)	1,744 (9.0)	265 (1.6)	<0.001
Fasting glucose, mmol/L	5.4 ± 1.5	4.9 ± 0.8	<0.001
Triglyceride, mmol/L	1.77 ± 1.57	1.33 ± 1.1	<0.001
Total cholesterol, mmol/L	4.95 ± 0.95	4.63 ± 0.87	<0.001
HDL cholesterol, mmol/L	1.31 ± 0.36	1.37 ± 0.36	<0.001
LDL cholesterol, mmol/L	3.02 ± 0.81	2.79 ± 0.76	<0.001
Uric acid, μmol/L	353 ± 90	333 ± 90	<0.001
Smoking, *n* (%)	6,121 (31.7)	4,000 (23.4)	<0.001
Alcohol consumption, *n* (%)	9,581 (49.6)	7,214 (42.2)	<0.001

Values are mean ± SD or valid percentages (n), BMI, body mass index; SMI, skeletal muscle mass index; BP, blood pressure; HDL, high-density lipoprotein; LDL, low-density lipoprotein.

For middle-aged people (40 years < Age ≤65 years), the results of the univariate analysis showed a significant association between low skeletal muscle mass and arteriosclerosis (OR: 1.236, 95% CI: 1.130–1.352, $P < 0.001$), and the association was significant after adjustment for age and sex (OR: 1.202, 95% CI: 1.094–1.320, $P < 0.001$). Additionally, the association remained significant after adjustment for other potential confounding factors (OR: 1.329, 95% CI: 1.195–1.479, $P < 0.001$; **Table 3**).

For older people (age >65 years), the results of the univariate analysis showed a significant association between low skeletal muscle mass and arteriosclerosis (OR: 1.682, 95% CI: 1.265–2.236, $P < 0.001$), and the association was significant after

TABLE 3 | Low skeletal muscle mass associated with odds ratio for arteriosclerosis using logistic regression analysis in overall subjects and subgroups.

Subgroups	Model 1		Model 2		Model 3	
	Crude OR [95% CI]	*P*	Crude OR [95% CI]	*P*	Crude OR [95% CI]	*P*
Overall	1.075 [1.019–1.135]	0.008	1.241 [1.164–1.322]	<0.001	1.435 [1.343–1.533]	<0.001
Young	0.923 [0.845–1.007]	0.072	1.399 [1.272–1.538]	<0.001	1.506 [1.353–1.678]	<0.001
Middle-age	1.236 [1.130–1.352]	<0.001	1.202 [1.094–1.320]	<0.001	1.329 [1.195–1.479]	<0.001
Old	1.682 [1.265–2.236]	<0.001	1.598 [1.198–2.132]	0.001	1.676 [1.191–2.358]	0.003
Men	1.598 [1.463–1.745]	<0.001	1.362 [1.237–1.500]	<0.001	1.559 [1.396–1.740]	<0.001
Women	1.038 [0.964–1.117]	0.319	1.222 [1.118–1.336]	<0.001	1.266 [1.143–1.401]	<0.001

Data are presented as odds ratio (95% confidential intervals).
Young: Age ≤40 years, Middle-age: 40 years < Age ≤ 65 years, Old: Age > 65 years.
Model 1: No adjustment.
Model 2: Adjusted by Age and Gender.
Model 3: Adjusted by Age, Gender, BMI, Hypertension, Diabetes, Triglyceride, Total cholesterol, HDL cholesterol, Uric acid, Smoking, Alcohol consumption.

adjustment for age and sex (OR: 1.598, 95% CI: 1.198–2.132, $P = 0.001$). Moreover, the association remained significant after adjustment for other potential confounding factors (OR: 1.676, 95% CI: 1.191–2.358, $P = 0.003$; **Table 3**).

Subgroup Analysis by Sex

For men, the results of the univariate analysis showed a significant association between low skeletal muscle mass and arteriosclerosis (OR: 1.598, 95% CI: 1.463–1.745, $P < 0.001$), and the association was significant after adjustment for age (OR: 1.362, 95% CI: 1.237–1.500, $P < 0.001$). The association remained significant after adjustment for other potential confounding factors (OR: 1.559, 95% CI: 1.396–1.740, $P < 0.001$; **Table 3**).

For women, the results of the univariate analysis showed an insignificant association between low skeletal muscle mass and arteriosclerosis (OR: 1.038, 95% CI: 0.964–1.117, $P = 0.319$). Additionally, the association became significant after adjustment for age (OR: 1.222, 95% CI: 1.118–1.336, $P < 0.001$). Moreover, the association remained significant after adjustment for other potential confounding factors (OR: 1.266, 95% CI: 1.143–1.401, $P < 0.001$; **Table 3**).

The multiple logistic regression model in the overall subjects showed that, among potential risk factors, age (OR: 1.074, 95% CI: 1.071–1.076, $P < 0.001$), hypertension (OR: 3.166, 95% CI: 2.984–3.359, $P < 0.001$), diabetes (OR: 1.884, 95% CI: 1.630–2.176, $P < 0.001$), triglycerides (OR: 1.104, 95% CI: 1.074–1.135, $P < 0.001$), total cholesterol (OR: 1.163, 95% CI: 1.127–1.200, $P < 0.001$), and uric acid (OR: 1.001, 95% CI: 1.000–1.001, $P < 0.001$) were independently associated with arteriosclerosis, except BMI (OR: 0.978, 95% CI: 0.968–0.988, $P < 0.001$), HDL cholesterol (OR: 0.883, 95% CI: 0.803–0.971, $P = 0.010$), smoking (OR: 0.867, 95% CI: 0.814–0.924, $P < 0.001$), and alcohol consumption (OR: 0.962, 95% CI: 0.901–1.027, $P = 0.248$; **Supplementary Table 1**).

The factors associated with the odds ratio for arteriosclerosis using logistic regression analysis in the age (**Supplementary Table 2**) and gender subgroups (**Supplementary Table 3**) are shown in the **Supplementary Table**.

DISCUSSION

This study has a large sample with a large age span (including the entire adult population), and mainly young and middle-aged people. Our results show that the prevalence of low muscle mass and arteriosclerosis is high in the general population, even among middle-aged people and young people, and confirmed that there is a significant independent association between low skeletal muscle mass (assessed according to BIA) and arteriosclerosis (assessed according to baPWV) in all subjects and in different age and gender subgroups.

It is worth noting that in addition to age, several predisposing factors and mechanisms of skeletal muscle mass loss are also believed to be associated with arteriosclerosis, including low levels of physical activity, sedentary lifestyle, chronic inflammatory state, oxidative stress, insulin resistance (IR), and a decline in the testosterone levels (21–27). Age-related chronic low-grade inflammation is an important cause of low muscle mass, which is characterized by elevated levels of tumor necrosis factor-α (TNF-α), C-reactive protein (CRP), and interleukin-6 (IL-6), and increased CRP and IL-6 levels are associated with increased fat levels (28). Inflammatory factors are associated with a decrease in the skeletal muscle mass and strength (29). It is also one of the main signals that induce muscle apoptosis (30). Chronic inflammation leads to programmed cell death (i.e., apoptosis) and hinders muscle protein synthesis, and impaired repair and regeneration are the possible mechanisms of chronic inflammation leading to muscle degradation (31). Chronic inflammation and oxidative stress lead to endothelial dysfunction, collagen and elastin degradation, changes in the composition and hydration state of proteoglycans, and medial calcification, which gradually cause arterial stiffness. Skeletal muscle is not only distributed throughout the exercise system responsible for body functions, but also in various organs, accounting for most of the glucose metabolism in the human body (32). Skeletal muscle is the main organ for glucose homeostasis, and 75% of postprandial glucose uptake is attributed to skeletal muscle. Low skeletal muscle mass may impair glucose homeostasis, reduce insulin sensitivity, and lead to IR, which can increase the blood

pressure and blood lipid levels through a series of reactions and contribute to the process of arteriosclerosis. In addition, hyperglycemia and hyperinsulinemia during IR can increase the risk of arteriosclerosis (33).

At present, the evaluation criteria for low skeletal muscle mass and atherosclerosis are not uniform in different studies, and the results are also inconsistent. In a study involving 208 elderly individuals ≥80 years of age, dual-energy X-ray absorptiometry was used to measure the skeletal muscle mass, pace to assess the muscle function, coronary artery calcification score, and endothelial cell function to assess atherosclerosis, and suggested that sarcopenia is associated with atherosclerosis (34). In another study involving a Japanese cohort >55 years of age, the skeletal muscle mass, determined according to BIA and baPWA was used to assess atherosclerosis, and the results revealed that atherosclerosis and skeletal muscle mass have a negative correlation (35). BaPWV is simply measured by wrapping a pressure cuff around the extremities, which is considered to be a relatively brief, non-invasive, and repeatable method for obtaining data on arterial stiffness (36). Pulse-wave velocity (PWV) is regarded as the gold standard measurement for arterial stiffness and an indicator of vascular damage. A previous meta-analysis reported that PWV is an independent predictor of cardiovascular disease, adverse cardiovascular events, and all-cause mortality (37–39). BIA is also a simple, non-invasive, and reproducible method that can be used for large-scale population screening. It can distinguish between fat mass and fat-free mass. It is widely used to measure the skeletal muscle mass and is one of the few diagnostic criteria for muscle diseases.

Some investigators believe that the loss of skeletal muscle mass is related to arteriosclerosis in men, but not in women. In a study involving 496 middle-aged and elderly patients, the cross-sectional area/weight (CSA/BW) of the middle thigh muscle was used to assess sarcopenia, and the carotid artery intima-media thickness (IMT), and baPWV was used to assess atherosclerosis. The results revealed that the thigh muscle CSA/BW was significantly and negatively associated with carotid IMT and baPWV in men, but not in women (13). In another study involving 427 elderly patients, the skeletal muscle mass in the extremities was assessed, and the radial augmentation index (RAI) was used to assess arteriosclerosis. In patients who were men, the skeletal muscle mass was negatively correlated with RAI; however, this association was not obvious among women (40). However, our findings indicate that a low skeletal muscle mass is associated with atherosclerosis in both men and women. The skeletal muscle mass in women is naturally lower than that in men, and the cut-off values for low skeletal muscle mass are different between the sexes. The diagnostic criteria for low skeletal muscle mass in the above study did not distinguish between the sexes; yet, according to the AWGS recommendation (19), an ASMI <7.0 kg/m^2 in males and <5.7 kg/m^2 in females was classified as "low skeletal muscle mass" in our study. Using the same low skeletal muscle mass cut-off value in different sexes results in more normal women being defined with low skeletal muscle mass, which may cause no relationship between low skeletal muscle mass and arteriosclerosis in women subjects. Our results are consistent with those in a study reported by Ricardo, which involved 75 subjects and ASMI was dichotomized according to the first quintile for men (8.81 kg/m^2) and women (7.57 kg/m^2) (41).

Although there are some studies on the relationship between low skeletal muscle mass and atherosclerosis, most of them only include the older people and lack different age groups, especially young and middle-aged individuals. In modern young people, factors such as high work pressure, fast pace of life, tight schoolwork, staying up late, unscientific diet, and other factors accelerate vascular aging, and CVD is no longer a senile disease. In the recent years, CVD has been trending toward a younger age. The incidence of CVD in people over 25 years of age is gradually increasing, especially among people between 35 and 44 years of age (42). Our research also confirmed that the prevalence of arteriosclerosis in young and middle-aged people is relatively high; nevertheless, this phenomenon has not attracted attention. The increase in sedentary work, changes in lifestyles, and the development of modern transportation have brought convenience to society, greatly reducing the use of labor, and also leading to a decrease in the daily activities, an increasing number of young people have low skeletal muscle, our research found that the prevalence of low skeletal muscle is higher at all ages, unexpectedly, young, and middle-aged people also have higher prevalence; however, people are not aware of this phenomenon. What is more serious is that very little is known about the association between low muscle mass and arteriosclerosis. Therefore, to prevent the occurrence of CVD, it is necessary to pay attention to young and middle-aged individuals, the risk factors need to be detected early, and comprehensive prevention and control is to be exercised.

Among the traditional risk factors for arteriosclerosis, the association between hypertension, diabetes, cholesterol, and arteriosclerosis is significant in all subjects and in different sex or age subgroups, and triglycerides are associated with arteriosclerosis in young and middle-aged people, which is consistent with the hypothesis that increased triglyceride levels favor the development of atherosclerosis (43), however, the association became insignificant in older subjects. The relationship between triglycerides and arteriosclerosis has always been controversial. In the past, atherosclerosis was believed to be a disease characterized by the accumulation of cholesterol instead of triglycerides in the arteries (44). Although most studies point out that triglycerides are directly related to arteriosclerosis, recent studies have suggested that triglycerides are only biomarkers related to arteriosclerosis, and that triglyceride-rich lipoproteins and their residual particles are considered to be one of the main mediators of the link between arteriosclerosis and triglycerides (45). Moreover, the triglyceride levels may fluctuate drastically with diet and exercise; the fasting levels of triglycerides are highly variable, which may depend on the lipid content and the patient's meal time, and population data are biased; therefore, the fasting triglyceride levels are not always positively correlated with atherosclerosis (44, 46). Hypertriglyceridemia is the most difficult lipid disease to evaluate and treat, and is related to several acquired diseases, such as IR. In addition, in a review by Gill et al., the patients with an increased risk of atherosclerotic CVD have a broader spectrum of plasma

lipoprotein abnormalities, especially increased triglyceride-rich remnant particles, in which cholesterol (but not triglycerides) content promotes atherosclerosis (43). Therefore, since most of the people included in our study were young and middle-aged people, and this is a retrospective study and no additional data were collected from the older people, such as comorbidities, statins, or other usage, and no more confounding factors can be corrected. We will establish a prospective cohort for the older group to observe the effects of triglycerides on arteriosclerosis in the future.

From the baseline data, the BMI of the low skeletal muscle mass group was lower than that of the normal group. The BMI is currently the most useful obesity measurement index at the population level, and several previous studies have used BMI to define obesity; however, it cannot distinguish between skeletal muscle and fat; as such, it is not a standardized metric to determine overweight. The individuals with a high BMI may not be obese, but have increased skeletal muscle content, while a normal BMI does not indicate the health status, which may be accompanied by a decreased skeletal muscle mass. Several young people blindly pursue weight loss and often aim to lower their BMI, which is also accompanied by low muscle mass, which may increase the risk of arteriosclerosis. As an important part of the human body, the skeletal muscles play an important role in human function and disease occurrence. Therefore, more importance should be attributed to the body composition analysis in the future, and skeletal muscle mass and body fat should be used as the indicators of obesity rather than BMI.

The population in this study was relatively younger and healthier than similar populations reported in previous studies. The reason for this selective bias is that our study site is a physical examination center of the top hospital in China. Most of the health checkups are healthy people, and patients with diseases or serious illnesses are treated in outpatient clinics or local hospitals. However, the association of low skeletal muscle mass and arteriosclerosis remained exit in this sample. Moreover, the demonstration of the association in this lower-risk population offers strong support for the association exit. Greater effects might have been demonstrated in a higher risk population.

The present study had several limitations. The first of which was its cross-sectional design, which cannot be used to determine causality because it is unclear whether skeletal muscle mass loss precedes atherosclerosis or vice versa. Second, we did not consider some specific and potentially relevant factors, such as comorbidities, statin treatment, physical activity, and inability to correct for confounding factors. Third, single-center studies may be inherently biased. As such, further prospective, multicenter study which included more potentially relevant confounder factors is required.

CONCLUSIONS AND IMPLICATIONS

The prevalence of low skeletal muscle mass and arteriosclerosis was high, and there was a significant independent association between them in all subjects and different age and gender subgroups. The main clinical advantage of this study is that it improved the awareness of the prevalence and correlation of low muscle mass and arteriosclerosis, confirmed the new risk factors related to CVD, and provided new clinical ideas for the prevention of CVD in young and middle-aged people. This will provide a research foundation for multicenter prospective cohort studies in the future.

DATA AVAILABILITY STATEMENT

The original contributions presented in the study are included in the article/**Supplementary Material**, further inquiries can be directed to the corresponding author/s.

ETHICS STATEMENT

The studies involving human participants were reviewed and approved by Biomedical Ethics Committee of the West China Hospital of Sichuan University. The patients/participants provided their written informed consent to participate in this study.

AUTHOR CONTRIBUTIONS

JY, ZL, and XT: study concept and design. ZL and YM: acquisition of data. XT and TB: analysis and interpretation of data. ZL and XT: drafting of the manuscript. JY: critical revision of the manuscript for important intellectual content. All authors contributed to the article and approved the submitted version.

SUPPLEMENTARY MATERIAL

The Supplementary Material for this article can be found online at: https://www.frontiersin.org/articles/10.3389/fcvm.2021.735262/full#supplementary-material

REFERENCES

1. Melton LJ III, Khosla S, Crowson CS, O'Connor MK, O'Fallon WM, Riggs BL. Epidemiology of sarcopenia. *J Am Geriatr Soc.* (2000) 48:625–30. doi: 10.1111/j.1532-5415.2000.tb04719.x
2. Harris T. Muscle mass and strength: relation to function in population studies. *J Nutr.* (1997) 127(5 Suppl):1004s–6. doi: 10.1093/jn/127.5.1004S
3. Metter EJ, Conwit R, Tobin J, Fozard JL. Age-associated loss of power and strength in the upper extremities in women and men. *J Gerontol A Biol Sci Med Sci.* (1997) 52:B267–76. doi: 10.1093/gerona/52A.5.B267
4. Cruz-Jentoft AJ, Baeyens JP, Bauer JM, Boirie Y, Cederholm T, Landi F, et al. Sarcopenia: European consensus on definition and diagnosis: Report of the European Working Group on Sarcopenia in older people. *Age Ageing.* (2010) 39:412–23. doi: 10.1093/ageing/afq034
5. Roubenoff R, Hughes VA. Sarcopenia: current concepts. *J Gerontol A Biol Sci Med Sci.* (2000) 55:M716–24. doi: 10.1093/gerona/55.12.M716
6. Rolland Y, Czerwinski S, Abellan Van Kan G, Morley JE, Cesari M, Onder G, et al. Sarcopenia: its assessment, etiology, pathogenesis, consequences and future perspectives. *J Nutr Health Aging.* (2008) 12:433–50. doi: 10.1007/BF02982704

7. Vlachopoulos C, Xaplanteris P, Aboyans V, Brodmann M, Cífková R, Cosentino F, et al. The role of vascular biomarkers for primary and secondary prevention. A position paper from the European Society of Cardiology Working Group on peripheral circulation: Endorsed by the Association for Research into Arterial Structure and Physiology (ARTERY) Society. *Atherosclerosis.* (2015) 241:507–32. doi: 10.1016/j.atherosclerosis.2015.05.007
8. Siasos G, Oikonomou E, Maniatis K, Georgiopoulos G, Kokkou E, Tsigkou V, et al. Prognostic significance of arterial stiffness and osteoprotegerin in patients with stable coronary artery disease. *Eur J Clin Invest.* (2018) 48. doi: 10.1111/eci.12890
9. Papaioannou TG, Oikonomou E, Lazaros G, Christoforatou E, Vogiatzi G, Tsalamandris S, et al. The influence of resting heart rate on pulse wave velocity measurement is mediated by blood pressure and depends on aortic stiffness levels: insights from the Corinthia study. *Physiol Meas.* (2019) 40:55005. doi: 10.1088/1361-6579/ab165f
10. Mikael LR, Paiva AMG, Gomes MM, Sousa ALL, Jardim P, Vitorino PVO, et al. Vascular aging and arterial stiffness. *Arq Bras Cardiol.* (2017) 109:253–8. doi: 10.5935/abc.20170091
11. Townsend RR. Arterial Stiffness: recommendations and standardization. *Pulse.* (2017) 4(Suppl 1):3–7. doi: 10.1159/000448454
12. Boutouyrie P, Tropeano AI, Asmar R, Gautier I, Benetos A, Lacolley P, et al. Aortic stiffness is an independent predictor of primary coronary events in hypertensive patients: a longitudinal study. *Hypertension.* (2002) 39:10–5. doi: 10.1161/hy0102.099031
13. Ochi M, Kohara K, Tabara Y, Kido T, Uetani E, Ochi N, et al. Arterial stiffness is associated with low thigh muscle mass in middle-aged to elderly men. *Atherosclerosis.* (2010) 212:327–32. doi: 10.1016/j.atherosclerosis.2010.05.026
14. Abbatecola AM, Chiodini P, Gallo C, Lakatta E, Sutton-Tyrrell K, Tylavsky FA, et al. Pulse wave velocity is associated with muscle mass decline: health ABC study. *Age.* (2012) 34:469–78. doi: 10.1007/s11357-011-9238-0
15. Alexandersen P, Tankó LB, Bagger YZ, Jespersen J, Skouby SO, Christiansen C. Associations between aortic calcification and components of body composition in elderly men. *Obesity.* (2006) 14:1571–8. doi: 10.1038/oby.2006.181
16. Ferreira I, Snijder MB, Twisk JW, van Mechelen W, Kemper HC, Seidell JC, et al. Central fat mass versus peripheral fat and lean mass: opposite (adverse versus favorable) associations with arterial stiffness? The Amsterdam Growth and Health Longitudinal Study. *J Clin Endocrinol Metab.* (2004) 89:2632–9. doi: 10.1210/jc.2003-031619
17. Kim DH, Choi JH, Moon JS, Kim HJ, Cha JK. Association between the severity of cerebral small vessel disease, pulsatility of cerebral arteries, and brachial ankle pulse wave velocity in patients with lacunar infarction. *Eur Neurol.* (2010) 64:247–52. doi: 10.1159/000319923
18. Whitworth JA. 2003 World Health Organization (WHO)/International Society of Hypertension (ISH) statement on management of hypertension. *J Hypertens.* (2003) 21:1983–92. doi: 10.1097/00004872-200311000-00002
19. Chen LK, Liu LK, Woo J, Assantachai P, Auyeung TW, Bahyah KS, et al. Sarcopenia in Asia: consensus report of the Asian Working Group for Sarcopenia. *J Am Med Dir Assoc.* (2014) 15:95–101. doi: 10.1016/j.jamda.2013.11.025
20. Xu Y, Li J, Luo Y, Wu Y, Zheng L, Yu J, et al. The association between ankle-brachial index and cardiovascular or all-cause mortality in metabolic syndrome of elderly Chinese. *Hypertens Res.* (2007) 30:613–9. doi: 10.1291/hypres.30.613
21. Sattar N. Do pregnancy complications and CVD share common antecedents? *Atheroscler Suppl.* (2004) 5:3–7. doi: 10.1016/j.atherosclerosissup.2004.03.002
22. Stephens JW, Khanolkar MP, Bain SC. The biological relevance and measurement of plasma markers of oxidative stress in diabetes and cardiovascular disease. *Atherosclerosis.* (2009) 202:321–9. doi: 10.1016/j.atherosclerosis.2008.06.006
23. Hansson GK. Atherosclerosis–an immune disease: the Anitschkov Lecture 2007. *Atherosclerosis.* (2009) 202:2–10. doi: 10.1016/j.atherosclerosis.2008.08.039
24. Brillante DG, O'Sullivan AJ, Howes LG. Arterial stiffness in insulin resistance: the role of nitric oxide and angiotensin II receptors. *Vasc Health Risk Manag.* (2009) 5:73–8. doi: 10.2147/VHRM.S3784
25. Hougaku H, Fleg JL, Najjar SS, Lakatta EG, Harman SM, Blackman MR, et al. Relationship between androgenic hormones and arterial stiffness, based on longitudinal hormone measurements. *Am J Physiol Endocrinol Metab.* (2006) 290:E234–42. doi: 10.1152/ajpendo.00059.2005
26. Hagen JL, Krause DJ, Baker DJ, Fu MH, Tarnopolsky MA, Hepple RT. Skeletal muscle aging in F344BN F1-hybrid rats: I. Mitochondrial dysfunction contributes to the age-associated reduction in VO2max. *J Gerontol A Biol Sci Med Sci.* (2004) 59:1099–110. doi: 10.1093/gerona/59.11.1099
27. Srinivas-Shankar U, Wu F. Frailty and muscle function: role for testosterone? *Front Horm Res.* (2009) 37:133–49. doi: 10.1159/000176050
28. Cesari M, Kritchevsky SB, Baumgartner RN, Atkinson HH, Penninx BW, Lenchik L, et al. Sarcopenia, obesity, and inflammation–results from the Trial of Angiotensin Converting Enzyme Inhibition and Novel Cardiovascular Risk Factors study. *Am J Clin Nutr.* (2005) 82:428–34. doi: 10.1093/ajcn.82.2.428
29. Schaap LA, Pluijm SM, Deeg DJ, Harris TB, Kritchevsky SB, Newman AB, et al. Higher inflammatory marker levels in older persons: associations with 5-year change in muscle mass and muscle strength. *J Gerontol A Biol Sci Med Sci.* (2009) 64:1183–9. doi: 10.1093/gerona/glp097
30. Phillips T, Leeuwenburgh C. Muscle fiber specific apoptosis and TNF-alpha signaling in sarcopenia are attenuated by life-long calorie restriction. *Faseb J.* (2005) 19:668–70. doi: 10.1096/fj.04-2870fje
31. Levine ME, Crimmins EM. The impact of insulin resistance and inflammation on the association between sarcopenic obesity and physical functioning. *Obesity.* (2012) 20:2101–6. doi: 10.1038/oby.2012.20
32. Aubertin-Leheudre M, Lord C, Goulet ED, Khalil A, Dionne IJ. Effect of sarcopenia on cardiovascular disease risk factors in obese postmenopausal women. *Obesity.* (2006) 14:2277–83. doi: 10.1038/oby.2006.267
33. Tanaka KI, Kanazawa I, Sugimoto T. Reduced muscle mass and accumulation of visceral fat are independently associated with increased arterial stiffness in postmenopausal women with type 2 diabetes mellitus. *Diabetes Res Clin Pract.* (2016) 122:141–7. doi: 10.1016/j.diabres.2016.10.014
34. Campos AM, Moura FA, Santos SN, Freitas WM, Sposito AC. Sarcopenia, but not excess weight or increased caloric intake, is associated with coronary subclinical atherosclerosis in the very elderly. *Atherosclerosis.* (2017) 258:138–44. doi: 10.1016/j.atherosclerosis.2017.01.005
35. Kohara K, Okada Y, Ochi M, Ohara M, Nagai T, Tabara Y, et al. Muscle mass decline, arterial stiffness, white matter hyperintensity, and cognitive impairment: Japan Shimanami Health Promoting Program study. *J Cachexia Sarcopenia Muscle.* (2017) 8:557–66. doi: 10.1002/jcsm.12195
36. Sugawara N, Yasui-Furukori N, Umeda T, Kaneda A, Sato Y, Takahashi I, et al. Comparison of ankle-brachial pressure index and pulse wave velocity as markers of cognitive function in a community-dwelling population. *BMC Psychiatry.* (2010) 10:46. doi: 10.1186/1471-244X-10-46
37. Ben-Shlomo Y, Spears M, Boustred C, May M, Anderson SG, Benjamin EJ, et al. Aortic pulse wave velocity improves cardiovascular event prediction: an individual participant meta-analysis of prospective observational data from 17,635 subjects. *J Am Coll Cardiol.* (2014) 63:636–46. doi: 10.1016/j.jacc.2013.09.063
38. Ohkuma T, Ninomiya T, Tomiyama H, Kario K, Hoshide S, Kita Y, et al. Brachial-ankle pulse wave velocity and the risk prediction of cardiovascular disease: an individual participant data meta-analysis. *Hypertension.* (2017) 69:1045–52. doi: 10.1161/HYPERTENSIONAHA.117.09097
39. Vlachopoulos C, Aznaouridis K, Terentes-Printzios D, Ioakeimidis N, Stefanadis C. Prediction of cardiovascular events and all-cause mortality with brachial-ankle elasticity index: a systematic review and meta-analysis. *Hypertension.* (2012) 60:556–62. doi: 10.1161/HYPERTENSIONAHA.112.194779
40. Lee SW, Youm Y, Kim CO, Lee WJ, Choi W, Chu SH, et al. Association between skeletal muscle mass and radial augmentation index in an elderly Korean population. *Arch Gerontol Geriatr.* (2014) 59:49–55. doi: 10.1016/j.archger.2014.01.008
41. Sampaio RA, Sewo Sampaio PY, Yamada M, Yukutake T, Uchida MC, Tsuboyama T, et al. Arterial stiffness is associated with low skeletal muscle mass in Japanese community-dwelling older adults. *Geriatr Gerontol Int.* (2014) 14 (Suppl. 1):109–14. doi: 10.1111/ggi.12206
42. Zhao D, Liu J, Wang M, Zhang X, Zhou M. Epidemiology of cardiovascular disease in China: current features and implications. *Nat Rev Cardiol.* (2019) 16:203–12. doi: 10.1038/s41569-018-0119-4
43. Gill PK, Dron JS, Hegele RA. Genetics of hypertriglyceridemia and atherosclerosis. *Curr Opin Cardiol.* (2021) 36:264–71. doi: 10.1097/HCO.0000000000000839

44. Goldberg IJ, Eckel RH, McPherson R. Triglycerides and heart disease: still a hypothesis? *Arterioscler Thromb Vasc Biol.* (2011) 31:1716–25. doi: 10.1161/ATVBAHA.111.226100
45. Krysa JA, Vine DF, Beilin LJ, Burrows S, Huang RC, Mori TA, et al. ApoB48-remnant lipoproteins are associated with increased cardiometabolic risk in adolescents. *Atherosclerosis.* (2020) 302:20–6. doi: 10.1016/j.atherosclerosis.2020.04.021
46. Generoso G, Janovsky C, Bittencourt MS. Triglycerides and triglyceride-rich lipoproteins in the development and progression of atherosclerosis. *Curr Opin Endocrinol Diabetes Obes.* (2019) 26. doi: 10.1097/MED.0000000000000468

Conflict of Interest: The authors declare that the research was conducted in the absence of any commercial or financial relationships that could be construed as a potential conflict of interest.

Publisher's Note: All claims expressed in this article are solely those of the authors and do not necessarily represent those of their affiliated organizations, or those of the publisher, the editors and the reviewers. Any product that may be evaluated in this article, or claim that may be made by its manufacturer, is not guaranteed or endorsed by the publisher.

frontiers in Cardiovascular Medicine

BRIEF RESEARCH REPORT
published: 01 November 2021
doi: 10.3389/fcvm.2021.782138

Loss of Angiotensin II Type 2 Receptor Improves Blood Pressure in Elastin Insufficiency

Michelle Lin[1], *Robyn A. Roth*[2], *Beth A. Kozel*[3], *Robert P. Mecham*[2] *and Carmen M. Halabi*[1]*

[1] Division of Nephrology, Department of Pediatrics, Washington University School of Medicine, Saint Louis, MO, United States, [2] Department of Cell Biology and Physiology, Washington University School of Medicine, Saint Louis, MO, United States, [3] National Heart, Lung and Blood Institute, National Institutes of Health, Bethesda, MD, United States

There is ample evidence supporting a role for angiotensin II type 2 receptor (AT_2R) in counterbalancing the effects of angiotensin II (ang II) through the angiotensin II type 1 receptor by promoting vasodilation and having anti-inflammatory effects. Elastin insufficiency in both humans and mice results in large artery stiffness and systolic hypertension. Unexpectedly, mesenteric arteries from elastin insufficient ($Eln^{+/-}$) mice were shown to have significant vasoconstriction to AT_2R agonism *in vitro* suggesting that AT_2R may have vasoconstrictor effects in elastin insufficiency. Given the potential promise for the use of AT_2R agonists clinically, the goal of this study was to determine whether AT_2R has vasoconstrictive effects in elastin insufficiency *in vivo*. To avoid off-target effects of agonists and antagonists, mice lacking AT_2R ($Agtr2^{-/Y}$) were bred to $Eln^{+/-}$ mice and cardiovascular parameters were assessed in wild-type (WT), $Agtr2^{-/Y}$, $Eln^{+/-}$, and $Agtr2^{-/Y}$;$Eln^{+/-}$ littermates. As previously published, $Agtr2^{-/Y}$ mice were normotensive at baseline and had no large artery stiffness, while $Eln^{+/-}$ mice exhibited systolic hypertension and large artery stiffness. Loss of AT_2R in $Eln^{+/-}$ mice did not affect large artery stiffness or arterial structure but resulted in significant reduction of both systolic and diastolic blood pressure. These data support a potential vasocontractile role for AT_2R in elastin insufficiency. Careful consideration and investigation are necessary to determine the patient population that might benefit from the use of AT_2R agonists.

Keywords: angiotensin II type 2 receptor, elastin insufficiency, hypertension, vascular stiffness, vascular biology

OPEN ACCESS

Edited by:
Anthony Wayne Orr,
Louisiana State University Health Shreveport, United States

Reviewed by:
Mark C. Chappell,
Wake Forest School of Medicine, United States
Jay S. Mishra,
University of Wisconsin-Madison, United States

***Correspondence:**
Carmen M. Halabi
chalabi@wustl.edu

Specialty section:
This article was submitted to Atherosclerosis and Vascular Medicine, a section of the journal Frontiers in Cardiovascular Medicine

Received: *23 September 2021*
Accepted: *11 October 2021*
Published: *01 November 2021*

Citation:
Lin M, Roth RA, Kozel BA, Mecham RP and Halabi CM (2021) Loss of Angiotensin II Type 2 Receptor Improves Blood Pressure in Elastin Insufficiency. Front. Cardiovasc. Med. 8:782138. doi: 10.3389/fcvm.2021.782138

INTRODUCTION

Elastin (ELN), the main component of elastic fibers, is responsible for conduit arteries' elastic recoil. This recoil is necessary to dampen the pulsatile flow of ventricular ejection at the level of the ascending aorta and transform it into continuous flow at the level of arterioles or small resistance arteries. Elastic fibers are organized into fenestrated concentric sheets or lamellae in blood vessels. Decreased elasticity of large arteries with aging is attributed to fragmentation and thinning of these lamellae and results in increased pulse wave velocity leading to a greater augmentation of the central aortic systolic and pulse pressures (1, 2). Similarly, genetic reduction of elastin through deletion of a single copy of the gene *ELN* (supravalvular aortic stenosis—SVAS, OMIM #185500) or deletion of *ELN* as part of a 25–27 coding gene microdeletion of chromosome 7 (Williams syndrome, OMIM #194050) leads to increased pulse wave velocity and hypertension (3–5).

Similar to humans with SVAS and Williams syndrome, mice hemizygous for the elastin gene ($Eln^{+/-}$) develop large artery stiffness and systolic hypertension (6, 7). Interestingly, the increased large artery stiffness in $Eln^{+/-}$ mice precedes the appearance of hypertension (8) and is not affected by commonly used anti-hypertensives (9). Increased large artery stiffness and central systolic and pulse pressures often lead to structural and functional changes in small resistance arteries that further exacerbate hypertension and a vicious cycle ensues (10). This appears to be the case in elastin insufficiency as recent studies showed altered resistance vessel reactivity that is vascular bed-specific (11–13). Mesenteric arteries (MAs) and middle cerebral arteries (MCAs), but not gastrocnemius feed arteries (GFAs), were found to have impaired endothelial-dependent dilation to acetylcholine due to decreased nitric oxide availability resulting from increased oxidative stress (11, 12, 14). Furthermore, MAs and MCAs, but not GFAs, had an increased contractile response to angiotensin II (ang II) (11, 13). Interestingly, the hypercontractile response of mesenteric arteries to ang II was mediated, at least in part, by the angiotensin II type 2 receptor (AT_2R) as blockade of AT_2R with the antagonist PD123319 decreased the contractile response of MAs to ang II while its activation with novokinin resulted in vasoconstriction (11).

Given the multitude of evidence suggesting a vasodilatory role for AT_2R particularly in disease states and the consideration for the use of AT_2R agonists for patients with COVID-19 and idiopathic pulmonary fibrosis among others (clinicaltrials.gov), we sought to determine the cardiovascular role of AT_2R in elastin insufficiency *in vivo*. We bred elastin insufficient ($Eln^{+/-}$) mice to AT_2R knock-out ($Agtr2^{-/Y}$) mice and examined cardiovascular endpoints. While loss of AT_2R did not affect large artery structure or function, it lowered blood pressure in elastin insufficient mice, suggesting that AT_2R plays a vasocontractile role in elastin insufficiency. This observation has significant therapeutic implications since AT_2R agonists, which may be beneficial in some conditions such as stroke (15, 16), aneurysm formation (17, 18) and myocardial fibrosis (19), would not be appropriate in patients with elastin insufficiency.

MATERIALS AND METHODS

Mice

$Eln^{+/-}$ mice backcrossed into the 129X1/SvJ background (14) over 10 times and the genetic background confirmed by single nucleotide polymorphism genotyping were bred to $Agtr2^{-/-}$ mice maintained on the FVB/n background (20). The $Agtr2^{-/-}$ mice were obtained from Dr. Curt Sigmund, with permission from Dr. Victor Dzau. Tail DNA was used to genotype the mice. Genotyping for *Eln* was done as previously described (21). The following primers were used in one PCR reaction to genotype for *Agtr2*: AT2-F GTGGTCTCACTGTTTTGTTGTC, AT2-R-WT GTATTCAATGGTTCTGACATCC, and AT2-R-KO TGCAATCCATCTTGTTCAATGGC, resulting in a 374 bp product in the WT case and a 570 bp product in the knock-out case. Since *Agtr2* is on the X chromosome and littermates were used for the studies, male mice were used for the physiologic studies to reduce the number of animals needed. Mice were housed under standard conditions with free access to food and water. All surgical procedures were performed in accordance with protocols approved by the Institutional Animal Care and Use Committee of Washington University School of Medicine.

Blood Pressure and Heart Rate Measurement

While sedation is known to lower blood pressure and heart rate, invasive blood pressure measurement provides a more accurate assessment of central arterial pressure compared to tail cuff measurement. Unfortunately, the small caliber and tortuosity of $Eln^{+/-}$ carotid arteries makes blood pressure measurement via telemetry technically challenging, therefore we measured central arterial pressure invasively under sedation. The anesthetic used, isoflurane, has the least effects on the cardiovascular system among commonly used anesthetics (22). Briefly, 3–4 month-old mice were anesthetized with 2% isoflurane and maintained at 37°C using a heating pad and a rectal thermometer for monitoring. The right common carotid artery was exposed and a Millar pressure transducer (model SPR-671) was introduced and advanced to the ascending aorta. After instrumentation was complete, isoflurane anesthesia was reduced to 1.5% and systolic blood pressure, diastolic blood pressure, and heart rate were recorded using the PowerLab data acquisition system (ADInstruments). The average of a 3-min period of stable recording was reported. The data were analyzed using LabChart 8 for Mac software (ADInstruments).

Pressure Myography

Ascending aorta and left common carotid artery of 3–4 month-old mice were excised and placed in physiologic saline solution (PSS) composed of 130 mM NaCl, 4.7 mM KCl, 1.6 mM $CaCl_2$, 1.18 mM $MgSO_4$-$7H_2O$, 1.17 mM KH_2PO_4, 14.8 mM $NaHCO_3$, 5.5 mM dextrose, and 0.026 mM EDTA (pH 7.4). Vessels were cleaned of surrounding fat, mounted on a pressure arteriograph (Danish Myo Technology) and maintained in PSS at 37°C. Vessels were visualized with an inverted microscope connected to a CCD camera and a computerized system, which allows continuous recording of vessel diameter. Intravascular pressure was increased from 0 to 175 mmHg by 25-mmHg increments, the vessel outer diameter was recorded at each step (12 s per step). The average of three measurements at each pressure was reported.

Alexa-633 Hydrazide Staining

Ascending aorta were dissected and frozen in optimal cutting temperature (OCT) compound (Sakura Finetek) at −80°C. Using a cryostat, 3-μm sections were obtained and fixed in 4% paraformaldehyde for 10 min at 4°C. Sections were washed twice with 1 × PBS for 5 min each and then incubated in 1:1,000 of a 2 mM Alexa Fluor 633 hydrazide (Life Technologies) stock in 1% bovine serum albumin (BSA)/1% fish gelatin/0.05% Triton-X in 1 × PBS for 5 min at room temperature. Sections were then washed twice with 1 × PBS for 5 min each. Slides were mounted with DAPI Fluoromount-G (SouthernBiotech) and coverslipped. Images were obtained using a Zeiss Axioskop 50 microscope and QCapture Pro software (Media Cybernetics Inc.).

Transmission Electron Microscopy

After isolation, mesenteric arteries from 3 to 4 month-old mice were fixed in 2.5% glutaraldehyde and 0.1 M sodium cacodylate at 4°C overnight. Vessels were then sent to Washington University's Center for Cellular Imaging for processing and thin sectioning. Images were taken using a JEOL JEM-1400 Plus transmission electron microscope that is equipped with an Advanced Microscopy Techniques XR111 high-speed, 4,000 × 2,000–pixel, phosphor-scintillated, 12-bit charge-coupled device (CCD) camera.

Statistical Analysis

One-way or two-way analysis of variance with Tukey's multiple comparisons test was used to determine differences between genotypes, as indicated in each figure legend. Statistical analyses were run using Prism 9 for Mac OS X (GraphPad Software Inc.). Data are presented as means ± SD. Differences were considered statistically significant when P was equal to or less than 0.05.

RESULTS

Loss of AT_2R Reduces Blood Pressure in Elastin Insufficient Mice

To determine the role, if any, of AT_2R in blood pressure regulation in elastin insufficiency, we bred $Agtr2^{-/Y}$ to $Eln^{+/-}$ mice. As previously reported, loss of AT_2R did not affect blood pressure at baseline (20) and $Eln^{+/-}$ mice exhibited systolic hypertension compared to wild-type (WT) littermates (6) (**Figures 1A–C**). Interestingly, loss of AT_2R in elastin insufficient mice ($Agtr2^{-/Y};Eln^{+/-}$) resulted in reduction of not only systolic, but also diastolic blood pressure (**Figures 1A–C**). Heart rate, body weight and heart weight were not different among the genotypes (**Figures 1D–F**).

Loss of AT_2R Does Not Affect Large Artery Stiffness

One of the characteristic features of elastin insufficiency is large artery stiffness assessed by pressure-diameter curves experimentally in $Eln^{+/-}$ mice and by pulse wave velocity in humans with Williams syndrome (4, 6). To determine whether the improvement in blood pressure in $Agtr2^{-/Y};Eln^{+/-}$ mice was related to an improvement in large artery stiffness, we assessed ascending aorta and carotid artery mechanics in mutant and littermate control mice. As seen in **Figure 2**, loss of AT_2R alone had no effect on large artery stiffness or compliance and it did not ameliorate the large artery stiffness seen in elastin insufficiency.

Conduit and Resistance Arteriolar Structure Is Unaffected by Loss of AT_2R

Ascending aorta of elastin insufficient mice have, on average, two additional lamellar units (7). We examined whether loss of AT_2R has any consequences on large and small artery structure. Fluorescence microscopy using Alexa-633 hydrazide staining of ascending aorta showed that, like WT ascending aorta, $Agtr2^{-/Y}$ ascending aorta have 8–9 lamellar units while $Eln^{+/-}$ ascending aorta have 10–11. Loss of AT2R did not affect lamellar unit number in elastin insufficiency as $Agtr2^{-/Y};Eln^{+/-}$ ascending aortae had 10–11 lamellar units. Representative images are shown in **Figure 3A**. Ultrastructural examination of mesenteric arteries by transmission electron microscopy did not identify an effect of AT_2R on arteriolar wall structure. As previously described, the internal elastic lamina of $Eln^{+/-}$ mesenteric arteries was thinner compared to WT mesenteric arteries, a finding that was not affected by loss of AT_2R (**Figure 3B**).

DISCUSSION

Ang II, the principal effector of the renin-angiotensin system, exerts its functions in physiological and pathological states mainly through two receptors, AT_1R and AT_2R. In hypertension, the pathologic remodeling that occurs, including vasoconstriction, fibrosis, proliferation, and inflammation, has been attributed to ang II's actions through AT_1R. Over the past two to three decades, a great deal of effort has focused on understanding the role of the more elusive AT_2R. Evidence suggests that while its levels are low in the adult cardiovascular system at baseline, AT_2R expression increases significantly in pathological conditions and it is thought to counter-balance the effects of ang II by promoting a vasodilatory, anti-fibrotic, apoptotic, and anti-inflammatory phenotype (23, 24). Often the vasodilatory effect of AT_2R is only evident when the vasoconstrictor action of AT_1R is blocked. At baseline, AT_2R knock-out mice were normotensive but showed an increased pressor response to ang II infusion (20). With the availability of several non-peptide AT_2R agonists, their use is being investigated as a potential therapeutic option in several disease conditions. In this report, based on *in vitro* data suggesting a vasocontractile role for AT_2R in elastin insufficiency, we sought to determine whether AT_2R contributes to elastin insufficiency-mediated hypertension *in vivo*. Using mouse models with genetic loss or insufficiency of AT_2R and ELN, we show that, unlike its protective role in heart failure, myocardial infarction and aneurysms, in the context of elastin insufficiency loss of AT_2R improves blood pressure making its activation a potentially detrimental therapeutic strategy in this disease state.

While initially surprising, the observation that AT_2R may play a vasocontractile role has been made in other models of hypertension. For instance, Touyz et al. (25) showed an enhanced contractile response to ang II in mesenteric arteries from spontaneously hypertensive rats (SHR) compared to Wystar-Kyoto rats (WKY). This response was reduced by AT_2R blockade in young but not old SHR. Similarly, coronary arteries from SHR were found to have enhanced constriction to ang II, that was attributed to the absence of counter-regulatory AT_2R-mediated relaxation and/or a change in the AT_2R phenotype from dilatory to contractile (26).

An interesting observation from our study is that loss of AT_2R decreases both systolic and diastolic blood pressure, while pulse pressure, an indicator of conduit artery stiffness, remains significantly elevated in $Agtr2^{-/y};Eln^{+/-}$ mice compared to WT and $Agtr2^{-/y}$ mice. These data support the large artery pressure-diameter measurements showing that loss of AT_2R does not affect large artery mechanics in elastin insufficiency. Rather, loss of AT_2R likely affects peripheral vascular resistance leading to a reduction in both systolic and diastolic blood pressure.

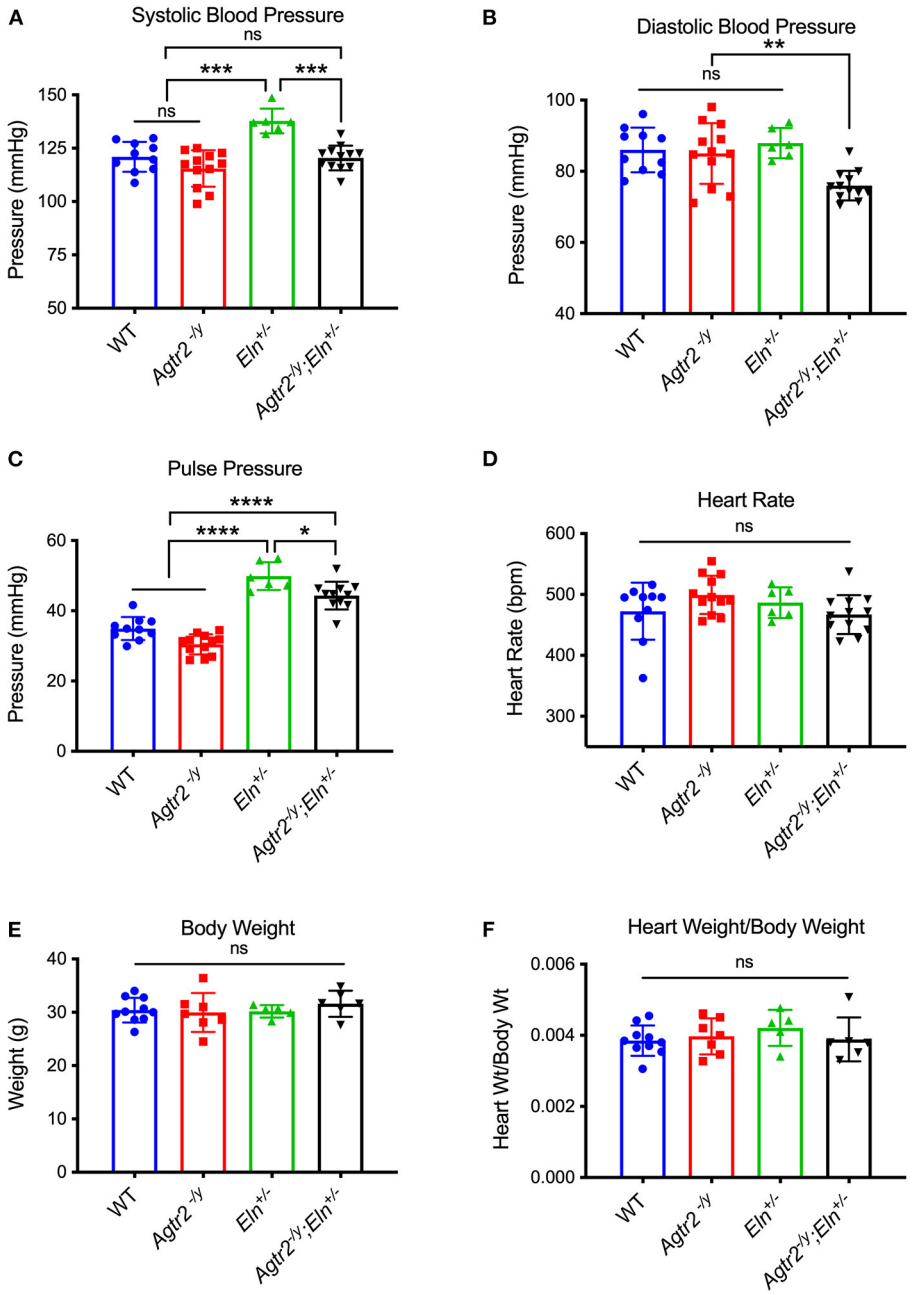

FIGURE 1 | Loss of AT2R leads to a reduction in systolic and diastolic blood pressure in elastin insufficient mice. Systolic **(A)**, diastolic **(B)**, and pulse pressure **(C)** [calculated as systolic–diastolic blood pressure], heart rate **(D)**, body weight **(E)** and heart weight/body weight **(F)** of WT, *Agtr2*$^{-/Y}$, *Eln*$^{+/-}$ and *Agtr2*$^{-/Y}$;*Eln*$^{+/-}$ mice. Data are presented as mean ± standard deviation. One-way analysis of variance with Tukey's multiple comparison test was performed to compare all groups. Significant difference: *$P < 0.05$, **$P < 0.005$, ***$P < 0.001$, and ****$P < 0.0001$, between indicated groups.

Activation of AT_2R by ang II has been shown to increase nitric oxide (NO) production, which activates guanylate cyclase to generate cyclic guanosine monophosphate (cGMP) leading to vasodilation (27, 28). The mechanism by which AT_2R leads to vasoconstriction in elastin insufficiency is unclear at this time. Similar to WT, *Agtr1* is expressed at higher levels than *Agtr2* in *Eln*$^{+/-}$ vessels, and both *Agtr1* and *Agtr2* expression levels were unchanged in aortae and reduced in mesenteric arteries of *Eln*$^{+/-}$ mice (11), making relative changes in receptor levels an unlikely explanation for the observed blood pressure response. It is interesting to note however that, while usually thought of as monomers, G protein-coupled receptors like AT_1R, AT_2R and bradykinin receptor (B_2R) have been shown to heterodimerize and adopt either an enhanced or an altered function. For

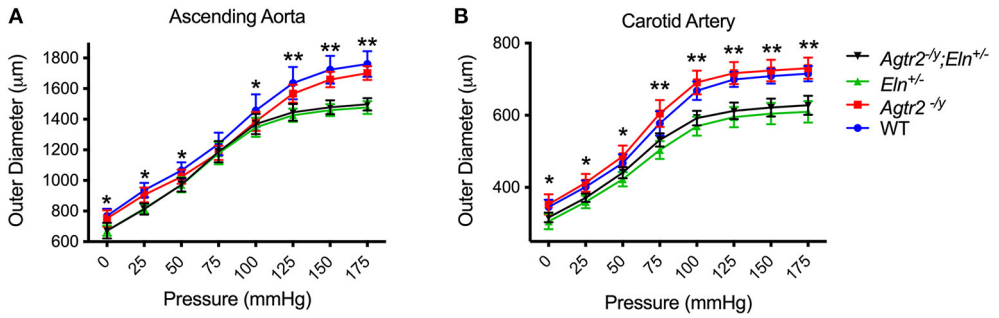

FIGURE 2 | Loss of AT2R does not affect large artery stiffness. Pressure-diameter relationships of ascending aorta **(A)** and carotid arteries **(B)** from WT ($n = 9$–10), *Agtr2*$^{-/Y}$ ($n = 10$–11), *Eln*$^{+/-}$ ($n = 6$) and *Agtr2*$^{-/Y}$;*Eln*$^{+/-}$ ($n = 15$) mice. Data are presented as mean ± standard deviation. Two-way analysis of variance with Tukey's multiple comparison test was performed to compare all groups. Significant difference: *$P < 0.05$ and **$P < 0.005$ between WT or *Agtr2*$^{-/Y}$ vs. *Eln*$^{+/-}$ or *Agtr2*$^{-/Y}$;*Eln*$^{+/-}$.

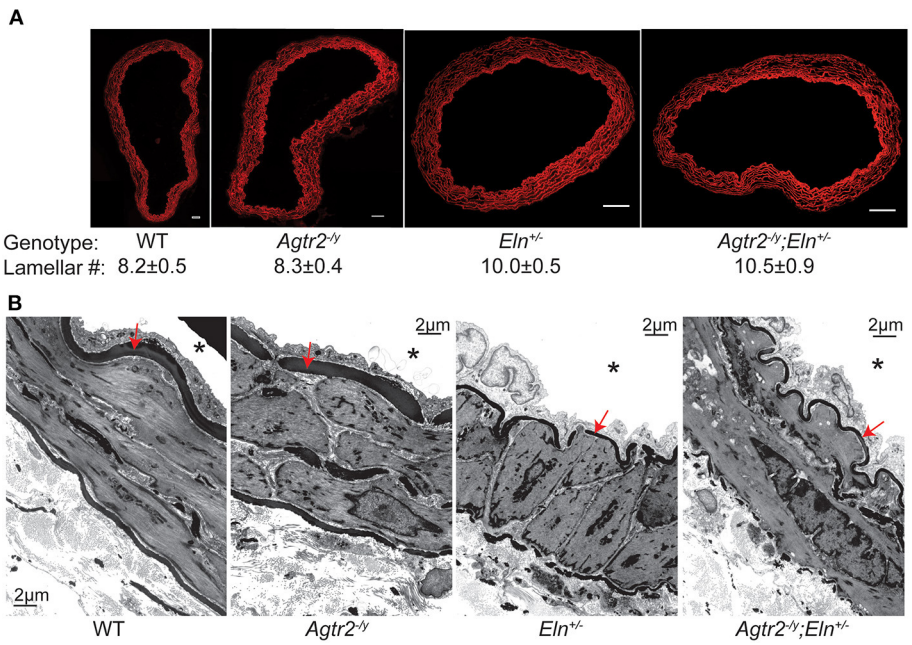

FIGURE 3 | Loss of AT2R does not affect arterial structure. Representative cross sections of Alexa-633 hydrazide-stained ascending aorta from WT, *Agtr2*$^{-/Y}$, *Eln*$^{+/-}$, and *Agtr2*$^{-/Y}$;*Eln*$^{+/-}$ mice along with the respective average lamellar number ± standard error of the mean, $n = 3$–4 per group, scale bar = 50 μm **(A)**. Transmission electron micrographs of mesenteric arteries from all genotypes, *indicates vessel lumen and red arrow indicated internal elastic lamina **(B)**.

instance, heterodimerization of AT_1R and B_2R led to increased activation of Gαq and Gαi, the two major signaling proteins activated by AT_1R (29). This AT_1R-B_2R heterodimerization was shown to contribute to ang II hypersensitivity in pre-eclampsia (30). AT_2R has been shown to dimerize with B_2R leading to enhanced NO and cGMP (27). Since AT_2R expression was reduced in elastin insufficient mesenteric arteries (11), it is interesting to speculate that AT_2R-B_2R dimer formation may be affected, or alternatively, that AT_2R heterodimerizes with AT_1R in elastin insufficiency, resulting in vasoconstriction rather than vasodilation; hypotheses that will be the focus of future investigation.

In summary, using a mouse model of elastin insufficiency-mediated hypertension, here we show that loss of AT_2R improves blood pressure in this model. While the process of elastin insufficiency is distinct, with normal aging older adults develop vascular elastic fiber thinning, systolic hypertension with widened pulse pressure and large artery stiffness, all characteristics of elastin insufficient mice. Therefore, if AT_2R agonists are to be considered for clinical use, carefully designed randomized clinical trials with special attention to patient population and endpoints will be necessary to ensure that they are not contributing to disease, particularly hypertension. AT_2R agonists will likely be useful in a context-specific manner.

DATA AVAILABILITY STATEMENT

The raw data supporting the conclusions of this article will be made available by the authors, without undue reservation.

ETHICS STATEMENT

The animal study was reviewed and approved by Institutional Animal Care and Use Committee of Washington University School of Medicine.

AUTHOR CONTRIBUTIONS

RM, BK, and CH conceived the study design. ML, RR, and CH performed experiments, generated and analyzed data. CH drafted the manuscript. All authors have read and approved the final manuscript.

FUNDING

This work was supported by National Institutes of Health grants K08 HL135400 to CH and R01-HL53325 to RM. Funding for BK came from the Division of Intramural Research of the NIH, ZIA HL006210. Funds were also provided by the Ines Mandl Research Foundation to RM.

ACKNOWLEDGMENTS

We thank Dr. Curt Sigmund for providing the *Agtr2*$^{-/Y}$ mice with permission from Dr. Victor Dzau. We thank James Fitzpatrick and Greg Strout from Washington University's Center for Cellular Imaging that is supported by the Children's Discovery Institute of Washington University and St. Louis Children's Hospital (CDI-CORE-2015-505) for their expertise and assistance with electron microscopy.

REFERENCES

1. Jadidi M, Razian SA, Habibnezhad M, Anttila E, Kamenskiy A. Mechanical, structural, and physiologic differences in human elastic and muscular arteries of different ages: comparison of the descending thoracic aorta to the superficial femoral artery. *Acta Biomater.* (2021) 119:268–83. doi: 10.1016/j.actbio.2020.10.035
2. Laurent S, Boutouyrie P, Asmar R, Gautier I, Laloux B, Guize L, et al. Aortic stiffness is an independent predictor of all-cause and cardiovascular mortality in hypertensive patients. *Hypertension.* (2001) 37:1236–41. doi: 10.1161/01.HYP.37.5.1236
3. Kozel BA, Barak B, Kim CA, Mervis CB, Osborne LR, Porter M, et al. Williams syndrome. *Nat Rev Dis Primers.* (2021) 7:42. doi: 10.1038/s41572-021-00276-z
4. Kozel BA, Danback JR, Waxler JL, Knutsen RH, de Las Fuentes L, Reusz GS, et al. Williams syndrome predisposes to vascular stiffness modified by antihypertensive use and copy number changes in NCF1. *Hypertension.* (2014) 63:74–9. doi: 10.1161/HYPERTENSIONAHA.113.02087
5. Pober BR, Johnson M, Urban Z. Mechanisms and treatment of cardiovascular disease in Williams-Beuren syndrome. *J Clin Investig.* (2008) 118:1606–15. doi: 10.1172/JCI35309
6. Faury G, Pezet M, Knutsen RH, Boyle WA, Heximer SP, McLean SE, et al. Developmental adaptation of the mouse cardiovascular system to elastin haploinsufficiency. *J Clin Investig.* (2003) 112:1419–28. doi: 10.1172/JCI19028
7. Li DY, Faury G, Taylor DG, Davis EC, Boyle WA, Mecham RP, et al. Novel arterial pathology in mice and humans hemizygous for elastin. *J Clin Investig.* (1998) 102:1783–7. doi: 10.1172/JCI4487
8. Le VP, Knutsen RH, Mecham RP, Wagenseil JE. Decreased aortic diameter and compliance precedes blood pressure increases in postnatal development of elastin-insufficient mice. *Am J Physiol Heart Circ.* (2011) 301:H221–9. doi: 10.1152/ajpheart.00119.2011
9. Halabi CM, Broekelmann TJ, Knutsen RH, Ye L, Mecham RP, Kozel BA. Chronic antihypertensive treatment improves pulse pressure but not large artery mechanics in a mouse model of congenital vascular stiffness. *Am J Physiol Heart Circ.* (2015) 309:H1008–16. doi: 10.1152/ajpheart.00288.2015
10. Laurent S, Boutouyrie P. The structural factor of hypertension: large and small artery alterations. *Circ Res.* (2015) 116:1007–21. doi: 10.1161/CIRCRESAHA.116.303596
11. Osei-Owusu P, Knutsen RH, Kozel BA, Dietrich HH, Blumer KJ, Mecham RP. Altered reactivity of resistance vasculature contributes to hypertension in elastin insufficiency. *Am J Physiol Heart Circ.* (2014) 306:H654–66. doi: 10.1152/ajpheart.00601.2013
12. Walker AE, Henson GD, Reihl KD, Morgan RG, Dobson PS, Nielson EI, et al. Greater impairments in cerebral artery compared with skeletal muscle feed artery endothelial function in a mouse model of increased large artery stiffness. *J Physiol.* (2015) 593:1931–43. doi: 10.1113/jphysiol.2014.285338
13. Walker AE, Kronquist EK, Chinen KT, Reihl KD, Li DY, Lesniewski LA, et al. Cerebral and skeletal muscle feed artery vasoconstrictor responses in a mouse model with greater large elastic artery stiffness. *Exp Physiol.* (2019) 104:434–42. doi: 10.1113/EP087453
14. Kozel BA, Knutsen RH, Ye L, Ciliberto CH, Broekelmann TJ, Mecham RP. Genetic modifiers of cardiovascular phenotype caused by elastin haploinsufficiency act by extrinsic noncomplementation. *J Biol Chem.* (2011) 286:44926–36. doi: 10.1074/jbc.M111.274779
15. Jackson-Cowan L, Eldahshan W, Dumanli S, Dong G, Jamil S, Abdul Y, et al. Delayed administration of angiotensin receptor (AT2R) agonist C21 improves survival and preserves sensorimotor outcomes in female diabetic rats post-stroke through modulation of microglial activation. *Int J Mol Sci.* (2021) 22:1356. doi: 10.3390/ijms22031356
16. Shan BS, Mogi M, Iwanami J, Bai HY, Kan-No H, Higaki A, et al. Attenuation of stroke damage by angiotensin II type 2 receptor stimulation via peroxisome proliferator-activated receptor-gamma activation. *Hypertens Res.* (2018) 41:839–48. doi: 10.1038/s41440-018-0082-9
17. Habashi JP, Doyle JJ, Holm TM, Aziz H, Schoenhoff F, Bedja D, et al. Angiotensin II type 2 receptor signaling attenuates aortic aneurysm in mice through ERK antagonism. *Science.* (2011) 332:361–5. doi: 10.1126/science.1192152
18. Lange C, Sommerfeld M, Namsolleck P, Kintscher U, Unger T, Kaschina E. AT2R (Angiotensin AT2 Receptor) agonist, compound 21, prevents abdominal aortic aneurysm progression in the rat. *Hypertension.* (2018) 72:e20–9. doi: 10.1161/HYPERTENSIONAHA.118.11168
19. Dopona EPB, Rocha VF, Furukawa LNS, Oliveira IB, Heimann JC. Myocardial hypertrophy induced by high salt consumption is prevented by angiotensin II AT2 receptor agonist. *Nutr Metab Cardiovasc Dis.* (2019) 29:301–5. doi: 10.1016/j.numecd.2018.11.001
20. Hein L, Barsh GS, Pratt RE, Dzau VJ, Kobilka BK. Behavioural and cardiovascular effects of disrupting the angiotensin II type-2 receptor in mice. *Nature.* (1995) 377:744–7. doi: 10.1038/377744a0
21. Hirano E, Knutsen RH, Sugitani H, Ciliberto CH, Mecham RP. Functional rescue of elastin insufficiency in mice by the human elastin gene: implications for mouse models of human disease. *Circ Res.* (2007) 101:523–31. doi: 10.1161/CIRCRESAHA.107.153510
22. Zhao X, Ho D, Gao S, Hong C, Vatner DE, Vatner SF. Arterial pressure monitoring in mice. *Curr Protoc Mouse Biol.* (2011) 1:105–22. doi: 10.1002/9780470942390.mo100149
23. Lax CJ, Domenighetti AA, Pavia JM, Di Nicolantonio R, Curl CL, Morris MJ, et al. Transitory reduction in angiotensin AT2 receptor expression levels in postinfarct remodelling in rat myocardium. *Clin Exp Pharmacol Physiol.* (2004) 31:512–7. doi: 10.1111/j.1440-1681.2004.04034.x

24. Nio Y, Matsubara H, Murasawa S, Kanasaki M, Inada M. Regulation of gene transcription of angiotensin II receptor subtypes in myocardial infarction. *J Clin Investig.* (1995) 95:46–54. doi: 10.1172/JCI117675
25. Touyz RM, Endemann D, He G, Li JS, Schiffrin EL. Role of AT2 receptors in angiotensin II-stimulated contraction of small mesenteric arteries in young SHR. *Hypertension.* (1999) 33(1 Pt 2):366–72. doi: 10.1161/01.HYP.33.1.366
26. Moltzer E, Verkuil AV, van Veghel R, Danser AH, van Esch JH. Effects of angiotensin metabolites in the coronary vascular bed of the spontaneously hypertensive rat: loss of angiotensin II type 2 receptor-mediated vasodilation. *Hypertension.* (2010) 55:516–22. doi: 10.1161/HYPERTENSIONAHA.109.145037
27. Abadir PM, Periasamy A, Carey RM, Siragy HM. Angiotensin II type 2 receptor-bradykinin B2 receptor functional heterodimerization. *Hypertension.* (2006) 48:316–22. doi: 10.1161/01.HYP.0000228997.88162.a8
28. Li J, Zhao X, Li X, Lerea KM, Olson SC. Angiotensin II type 2 receptor-dependent increases in nitric oxide synthase expression in the pulmonary endothelium is mediated via a G alpha i3/Ras/Raf/MAPK pathway. *Am J Physiol Cell Physiol.* (2007) 292:C2185–96. doi: 10.1152/ajpcell.00204.2006
29. AbdAlla S, Lother H, Quitterer U. AT1-receptor heterodimers show enhanced G-protein activation and altered receptor sequestration. *Nature.* (2000) 407:94–8. doi: 10.1038/35024095
30. AbdAlla S, Lother H, el Massiery A, Quitterer U. Increased AT(1) receptor heterodimers in preeclampsia mediate enhanced angiotensin II responsiveness. *Nature medicine.* (2001) 7:1003–9. doi: 10.1038/nm0901-1003

Conflict of Interest: The authors declare that the research was conducted in the absence of any commercial or financial relationships that could be construed as a potential conflict of interest.

Publisher's Note: All claims expressed in this article are solely those of the authors and do not necessarily represent those of their affiliated organizations, or those of the publisher, the editors and the reviewers. Any product that may be evaluated in this article, or claim that may be made by its manufacturer, is not guaranteed or endorsed by the publisher.

frontiers in Cardiovascular Medicine

ORIGINAL RESEARCH
published: 02 November 2021
doi: 10.3389/fcvm.2021.756098

A Novel Resveratrol Analog Upregulates SIRT1 Expression and Ameliorates Neointima Formation

Baohui Yuan[1,2†], He Liu[1,2†], Xiaoliang Dong[1], Xiaohua Pan[1,2], Xun Sun[3], Jia Sun[1,2*] and Li-Long Pan[1*]*

[1] Wuxi School of Medicine and School of Food Science and Technology, Jiangnan University, Wuxi, China, [2] State Key Laboratory of Food Science and Technology, Jiangnan University, Wuxi, China, [3] School of Pharmacy, Fudan University, Shanghai, China

OPEN ACCESS

Edited by:
Bo Liu,
University of Wisconsin-Madison,
United States

Reviewed by:
Zamaneh Kassiri,
University of Alberta, Canada
Zhao-Jun Liu,
University of Miami, United States

***Correspondence:**
Li-Long Pan
llpan@jiangnan.edu.cn
Jia Sun
jiasun@jiangnan.edu.cn
Xun Sun
sunxunf@shmu.edu.cn

[†] These authors have contributed equally to this work and share first authorship

Specialty section:
This article was submitted to Atherosclerosis and Vascular Medicine, a section of the journal Frontiers in Cardiovascular Medicine

Received: 10 August 2021
Accepted: 11 October 2021
Published: 02 November 2021

Citation:
Yuan B, Liu H, Dong X, Pan X, Sun X, Sun J and Pan L-L (2021) A Novel Resveratrol Analog Upregulates SIRT1 Expression and Ameliorates Neointima Formation. Front. Cardiovasc. Med. 8:756098. doi: 10.3389/fcvm.2021.756098

Neointima formation is a serious complication caused by mechanical trauma to the vessel. (*R*)-4,6-dimethoxy-3-(4-methoxy phenyl)-2,3-dihydro-1H-indanone [(*R*)-TML 104] is a synthesized analog of the natural product resveratrol sesquiterpenes (±)-isopaucifloral F. The present study aimed to investigate the effects and underlying mechanisms of (*R*)-TML104 on neointima formation. Our results showed that (*R*)-TML104 prevented neointima formation based on a carotid artery injury model in mice. Furthermore, (*R*)-TML104 inhibited platelet-derived growth factor-BB (PDGF-BB)-induced vascular smooth muscle cells (VSMC) phenotypic transformation, evidenced by increased α-smooth muscle actin, reduced VSMC proliferation, and migration. Simultaneously, (*R*)-TML104 upregulated sirtuin-1 (SIRT1) expression in VSMC. We further uncovered that SIRT1 expression is critical for the inhibitory effects of (*R*)-TML104 on PDGF-BB-induced VSMC phenotypic transformation *in vitro* and injury-induced neointima formation *in vivo*. Finally, (*R*)-TML104-upregulated SIRT1 inhibited PDGF-BB-induced VSMC phenotypic transformation by downregulating nicotinamide adenine dinucleotide phosphate oxidase 4 expression via decreasing nuclear factor-κB acetylation. Taken together, these results revealed that (*R*)-TML104 upregulates SIRT1 expression and ameliorates neointima formation. Therefore, the application of (*R*)-TML104 may constitute an effective strategy to ameliorate neointima formation.

Keywords: (*R*)-TML104, neointima formation, nicotinamide adenine dinucleotide phosphate oxidase 4, nuclear factor-κB, vascular smooth muscle cells, reactive oxygen species, SIRT1

INTRODUCTION

Cardiovascular diseases are the major cause of death worldwide (1). Although surgery is a commonly used strategy to treat cardiovascular disease, the surgical process may cause vascular inflammation, potentially leading to endothelial damage and subsequent neointima formation (2, 3). Neointima formation may result in vascular restenosis (2–4). The underlying mechanisms of neointima formation remain unclear. However, current medical therapies for inhibiting neointima formation are still scarce, making the development of novel strategies a necessity.

Phenotypic transformation of the vascular smooth muscle cells (VSMC) plays a vital role in neointima formation and can be triggered by oxidative stress, which stems from the excessive

production of reactive oxygen species (ROS) (5, 6). The major source of ROS in VSMC is the nicotinamide adenine dinucleotide phosphate (NADPH) oxidase (NOX) family (7). Additionally, the NOX-derived ROS can be modulated by sirtuin-1 (SIRT1) (8, 9). Platelet-derived growth factor-BB (PDGF-BB) is a major driving factor of the VSMC phenotypic transformation involved in neointima formation (10). During neointima formation, vascular stabilizing factors are attenuated, including SIRT1, a NAD (+)-dependent histone deacetylase (11, 12). Meanwhile, accumulating evidence suggests that various transcription factors are regulated by SIRT1, including nuclear factor-κB (NF-κB) (13, 14). Additionally, NF-κB activation is a pathological hallmark of VSMC phenotypic transformation (15, 16). The NF-κB activity can be mediated by sirtuin-1 (SIRT1)-mediated deacetylation (11, 17). Therefore, upregulation of SIRT1 may be a potential strategy for inhibiting VSMC phenotypic transformation.

Resveratrol, an active polyphenol compound, is found in red wine, grapes, and peanuts, and exhibits antioxidant and anti-inflammatory effects (18, 19). Resveratrol has attracted massive attention for its health benefits, including its advantageous effects on vascular diseases (20–22). It had also been shown that the beneficial properties of resveratrol are involved in multiple signaling pathways and oxygen species genes (23, 24). Several studies have indicated that numerous resveratrol analogs have better effects than resveratrol on improving disease (25, 26). In this study, we evaluated the effect of (*R*)-4, 6-dimethoxy-3-(4-methoxy phenyl)-2, 3-dihydro-1H-indanone [(*R*)-TML104], a synthetic analog of resveratrol sesquiterpenes (±)-isopaucifloral F (**Supplementary Figure 1A**), on neointima formation.

MATERIALS AND METHODS

Animal Model

Male C57BL/6J mice (25–30 g, 12 weeks, JOINN Lab, Suzhou, China) were maintained in a pathogen-free environment. Food and water were freely available under a controlled temperature (24 ± 1°C) with a 12/12 h dark/light cycle. We used a carotid artery injury mouse model, according to previously described protocols (2). Briefly, after mice were anesthetized with sodium pentobarbital (80 mg/kg, intraperitoneally), a midline neck incision was made, and the left carotid artery was exposed by blunt dissection. We then used blood vessel clamps to interrupt blood flow to the carotid arteries and made a lateral incision near the point of bifurcation of the external and internal carotid arteries. A guide wire (0.38 mm in diameter, NO.C-SF-15-15; Cook, Bloomington, USA) was inserted into the arterial lumen facing the aortic arch and rotated back and forth three times. After carefully removing the guide wire, the blood vessel was ligated at the lateral incision and the clamp was removed to restore blood flow. After vascular injury was induced, freshly prepared (*R*)-TML104 (10, 20 mg/kg) and atorvastatin (20 mg/kg) were administered daily by gastric gavage to the model group mice. (*R*)-TML104 and atorvastatin were both dissolved with saline. Mice were euthanized 28 days post-surgery by an overdose of sodium pentobarbital (150 mg/kg) via intraperitoneal injection.

Antibodies and Reagents

Antibodies against α-smooth muscle actin (α-SMA, A11111) and β-Actin (AC026) were purchased from Abclonal (Wuhan, China). Antibodies against Ac-p65 (ab19870), NF-κB (ab16502), NOX1 (ab131088), NOX2 (ab129068), NOX4 (ab133303), proliferating cell nuclear antigen (PCNA, ab92552), cyclin D1 (ab134175), and SIRT1 (ab110304) were obtained from Abcam (Cambridge, UK). PDGF-BB was purchased from R&D (Minneapolis, USA). Goat anti-Mouse IgG (H+L) Cross-Adsorbed Secondary Antibody-Alexa Fluor 647 (A21235) and Goat anti-Rabbit IgG (H+L) Cross-Adsorbed Secondary Antibody-Alexa Fluor 555 (A21428) were purchased from Thermo Fisher Scientific (MA, USA). (*R*)-TML104 was synthesized and provided by Dr. Xun Sun's laboratory at the School of Pharmacy (Fudan University, China). Atorvastatin (MB1021) and resveratrol (MB1199) were purchased from Meilun Bio (Dalian, China). BAY 11-7082 (S1523) and N-acetyl-L-cysteine (S0077) was purchased from Beyotime (Shanghai, China). 4′,6-diamidino-2-phenylindole (DAPI) was purchased from Solarbio (Beijing, China).

Histological and Morphometric Analysis

Fresh arteries samples were fixed in a 4% paraformaldehyde solution for 24 h and embedded in paraffin. The vascular tissue was cut into 5 μm sections, which were stained with hematoxylin and eosin (H&E) (G1120; Solarbio, China) for morphological analysis. Image-Pro Plus software (version 6.0, Media Cybernetics, MD, USA) was used to determine neointima formation. A mean value was generated from five independent sections of each artery sample.

Immunofluorescence Staining

The 5 μm slices were cut from paraffin-embedded blocks and placed on microscope slides. Briefly, the sections were microwaved in the citric acid buffer to retrieve antigens for 30 min. Sections were then permeabilized with 0.1% Triton X-100 for 15 min and blocked with 1% bovine serum albumin for 30 min, incubated with primary antibody at 4°C overnight. The following antibodies were used: PCNA (1:100), cyclin D1 (1:100), α-SMA (1:100), SIRT1 (1:100). Afterward, sections were washed with PBS and incubated with appropriate secondary antibody (1:100 dilution; Alexa Fluor Plus 555) for 1 h at room temperature. Nuclei were then stained with DAPI. The images were obtained using a Zeiss LSM880 microscope (Zeiss, Gottingen, Germany). The integrated optical density values were obtained using the ImageJ Pro Plus software (version 6.0, Media Cybernetics).

Cell Culture

Rat VSMC were enzymatically isolated from the Sprague-Dawley rats according to the protocols previously described (2). For functional studies, the cells were used between passages 3 and 5. VSMC were maintained in Dulbecco's Modified Eagle's Medium (DMEM, Hyclone, USA) supplemented with 10% fetal bovine serum (FBS, Hyclone, USA). Primary VSMC were maintained at 37°C under humidified 5% CO_2/95% air atmosphere and their identity were confirmed using α-smooth muscle actin antibody.

MTT Assay

The viability of VSMC was determined with 3-(4,5-Dimethyl-2-thiazolyl)-2, 5-diphenyl-2H-tetrazolium (MTT) bromide assay kit (C0009S; Beyotime Institute of Biotechnology, Shanghai, China). Briefly, the VSMC were plated in a 96-well microplate (5,000 cells/well). After the VSMC were incubated with different concentrations of (*R*)-TML104 for 24 h. Then, MTT reagent was added into the medium for a further 4 h. Next, the supernatant was then discarded, and dimethyl sulfoxide (DMSO) was added to solubilize the formazan crystals. The absorbance was measured at 570 nm with a microtiter plate reader (BIO-TEK, Winooski, VT, USA).

EdU Assay

We used a 5-Ethynyl-2′-Deoxyuridine (EdU) incorporation assay (C0071S; Beyotime Institute of Biotechnology, Shanghai, China) to detect the proliferation of VSMC. Briefly, VSMC were seeded in 96-well plates. After growing to 60% confluence, the cells were serum-starved for 24 h. After the VSMC were incubated with different concentrations of (*R*)-TML104 for 4 h and subsequently treated with PDGF-BB for 24 h, and then incubated with EdU for 2 h. Next, the cells were fixed with 4% paraformaldehyde (P0099; Beyotime Institute of Biotechnology, Shanghai, China) for 30 min, permeabilized with 0.1% Triton X-100 for 10 min, and the cells were stained with Hoechst 33342 (50 μL/well) for 10 min. The images were captured using fluorescence microscopy (Nikon Eclipse Ti-S, Tokyo, Japan). The ratio of EdU-positive cells (EdU-stained cells/Hoechst-stained cells×100%) was determined using a fluorescence microscope (Nikon Eclipse Ti-S, Tokyo, Japan).

Cell Wound Assay

VSMC were seeded in a 6-well plate and scraped with a sterile tip in a straight line. The cells were immediately washed with cold phosphate buffer saline (PBS). After growing to 60% confluence, the cells were serum-starved for 24 h. After the VSMC were incubated with different concentrations of (*R*)-TML104 for 4 h and subsequently treated with PDGF-BB for 24 h. The images were taken by light microscopy (Olympus Optical Co, Tokyo, Japan). Wound healing images were analyzed using ImageJ Pro Plus software.

Transwell Assay

The migration assay was performed using a transwell chamber (8 μm pore size, Corning costar, 3422, USA). Briefly, VSMC were seeded into each well of the upper chamber, and PBS or PDGF-BB were loaded into the bottom chamber. After growing to 60% confluence, the cells were serum-starved for 24 h. After the VSMC were incubated with different concentrations of (*R*)-TML104 for 4 h and subsequently treated with PDGF-BB for 18 h, the transwell membranes were fixed with 4% paraformaldehyde for 15 min. The membranes were stained with a 0.1% crystal violet solution for 10 min. The non-migrating cells on the top surface of the membrane were scraped with a cotton swab. Images were captured using light microscopy to quantify the average number of migrated cells. Five randomly chosen high-power fields (×200) in three independent experiments were used to calculate the average number of migrated cells. The migratory cells were evaluated by ImageJ Pro Plus software.

Western Blot Analysis

VSMC were homogenized in lysis RIPA buffer on ice for 30 min and then centrifuged at 12,000 g for 15 min at 4°C. Protein concentrations were determined by using a BCA Protein Assay Kit (Cat.P0010; Beyotime Biotechnology, Shanghai, China). Equal amounts of protein were then separated in sodium dodecyl sulfate-polyacrylamide gel electrophoresis (SDS-PAGE) electrophoresis and then transferred onto polyvinylidene fluoride (PVDF) membranes. After being blocked with 5% skim milk plus tris-buffered saline for 1 h, the membrane was incubated with a primary antibody. The following antibodies were used: Ac-p65 (1:1000), NF-κB (1:2000), NOX1 (1:2000), NOX2 (1:2000), NOX4 (1:2000), PCNA (1:1000), cyclin D1 (1:1000), α-SMA (1:500), SIRT1 (1:1000), and β-Actin (1:10000) at 4°C overnight. The next day, the membrane was washed three times and then incubated with secondary antibodies (1:5000) for 1 h. Finally, the immunoreactive proteins were visualized using a chemiluminescence reagent (Millipore, Billerica, MA, USA). Signals were detected using a chemiluminescence system (Bio-Rad, Hercules, CA, USA). The β-Actin loading control was used for quantifying protein expression levels.

ROS Detection and H_2O_2 Measurement

The dye, 2, 7-dichlorofluorescein diacetate (DCFH-DA, S0033S; Beyotime Institute of Biotechnology, China) was served as a fluorescence probe to detect intracellular ROS. Briefly, VSMC were incubated with DCFH-DA in a dark container at 37°C for 30 min. The cells were washed three times with PBS and finally analyzed using the FACSCalibu flow cytometry system (BD Biosciences, San Jose, CA, USA). The relative mean fluorescence intensity of each sample was analyzed using Flow Jo software version 10 (Tree Star Inc., Ashland, OR, USA). Intracellular H_2O_2 levels were detected using a Hydrogen Peroxide Assay Kit (S0038, Beyotime Institute of Biotechnology, Shanghai, China) according to the manufacturer's instructions. Briefly, scrape the lysed VSMC with a pipette tip and transfer cell lysate to a microcentrifuge tube. The cells were sufficiently homogenized and then centrifuged at 12 000 g for 5 min at 4°C. The supernatant was then incubated with a detection reagent for 30 min. The H_2O_2 production was assessed by using a microtiter plate reader.

RNA Isolation and Quantitative Real-Time PCR

To determine the mRNA expression levels of genes, total RNA was isolated from VSMC using TRIzol reagent (Life Technologies, MA, USA), and cDNA was synthesized using a Prime Script RT reagent Kit according to the manufacturer's instructions. SYBR Green PCR reagents (Yeasen, Shanghai, China) were used to determine the relative expression of all gene transcripts by a Real-Time PCR Detection System (Applied Biosystems, Foster City, CA, USA). The expression of sample genes was quantified by the level of the β-Actin gene. The specific

primers of NOX1, NOX2, NOX4, and β-Actin were available in **Supplementary Table 1**.

Lentivirus Production and siRNA Transfection

The SIRT1 short hairpin was linearized plasmid and ligated into the pLVX vector. Lentivirus was produced by co-transfection of the SIRT1 lentiviral construct, the packaging plasmid psPAX2, and the envelope plasmid pMD2.G into HEK-293 T cells using Lipofectamine 3000 (Invitrogen, Carlsbad, CA, USA). The virus supernatant was harvested at 24 h and 48 h after transfection and stored at 4°C until the concentration step. The supernatant was filtered through a 0.45 μM filter and then centrifuged at 100,000 g for 2 h. The collected virus pellet was stored at −80°C. The mature antisense sequences of sh-SIRT1-1 and sh-SIRT1-2 were available in **Supplementary Table 2**. NOX4 or SIRT1 knockdown in VSMC was carried out by transfecting NOX4 or SIRT1 small interfering RNA (siRNA). The siRNA (20 nM) was transfected into VSMC using Lipofectamine 3000. All sequences of siRNAs were synthesized by Gene Pharma (Shanghai, China) and available in **Supplementary Table 3**.

Statistics Analysis

Data were expressed as mean ± SD. Differences among three or more groups were determined using analysis of variance (ANOVA) followed by Tukey's *post-hoc* test. All statistical analyses were performed using GraphPad Prism (version 7.04; GraphPad Software Inc., San Francisco, CA, USA). Statistical significance was defined as $^{*}p < 0.05$, $^{**}p < 0.01$, $^{***}p < 0.001$.

RESULTS

(*R*)-TML104 Mitigates Injury-Induced Neointima Formation *in vivo*

To investigate whether (*R*)-TML104 affected injury-induced neointima formation, we treated the mice with two doses of (*R*)-TML104 (10, 20 mg/kg) after injury. (*R*)-TML104 treatment significantly decreased injury-induced neointimal area (**Figure 1A**). Meanwhile, (*R*)-TML104 treatment mitigated injury-induced downregulating α-SMA protein expression and upregulating PCNA and cyclin D1 expression (**Figure 1B**). Among the doses examined, (*R*)-TML104 at 20 mg/kg exhibited optimal protective effects and we used this dose for subsequent studies. To further confirm the function of (*R*)-TML104 on neointima formation, we used atorvastatin as a positive control. Interestingly, (*R*)-TML104 exhibits more prominent beneficial effects on neointima formation than atorvastatin at the same dosage (**Figures 1A,B**). Collectively, these findings demonstrate that (*R*)-TML104 could mitigate neointima formation *in vivo*.

(*R*)-TML104 Inhibits PDGF-BB-Induced VSMC Phenotypic Transformation *in vitro*

Phenotypic transformation of VSMC plays a vital role in neointima formation (27, 28). To investigate whether (*R*)-TML104 affects PDGF-BB-induced VSMC phenotypic transformation, we first detected the cytotoxicity of (*R*)-TML104 on VSMC. The MTT assay showed that (*R*)-TML104 (1-10 μM) had no significant effect on the viability of VSMC (**Supplementary Figure 1B**). As shown in **Figure 2A**, (*R*)-TML104 concentration-dependently reversed PDGF-BB-induced the expression of α-SMA, PCNA, and cyclin D1. Among the doses examined, (*R*)-TML104 at 10 μM exhibited optimal inhibitory effects yet no cytotoxic effect and we used this dose for subsequent studies. Meanwhile, the EdU assay showed that (*R*)-TML104 could inhibit PDGF-BB-mediated VSMC proliferation (**Figure 2C**). Followingly, the cell wound assay and transwell assay showed that (*R*)-TML104 could abolish PDGF-BB-induced VSMC migration (**Figure 2D** and **Supplementary Figure 1C**).

To further explore the effects of (*R*)-TML104 on VSMC phenotypic transformation, we chose atorvastatin and resveratrol as positive controls (29, 30). Notably, the protective effect of (*R*)-TML104 was similar to that of atorvastatin (**Figures 2B–D** and **Supplementary Figure 1C**). Moreover, we observed that resveratrol abolished PDGF-BB-induced the expression of PCNA and α-SMA (**Supplementary Figure 1D**). Interestingly, (*R*)-TML104 at the same dosage exhibited greater protective effects on these changes than resveratrol. Collectively, these results indicate that (*R*)-TML104 could inhibit PDGF-BB-induced VSMC phenotype transformation *in vitro*.

(*R*)-TML104 Inhibits PDGF-BB-Induced VSMC Phenotypic Transformation by Upregulating SIRT1 *in vitro*

Resveratrol has beneficial effects on vascular disease by activating SIRT1 (31). SIRT1 has emerged as a critical target for VSMC phenotypic transformation (2, 12, 17). We hypothesized that (*R*)-TML104 inhibits PDGF-BB-mediated VSMC phenotypic transformation by modulating SIRT1. We then detected the expression of SIRT1 in VSMC in response to PDGF-BB. We found that SIRT1 expression was time-dependently and dose-dependently upregulated by (*R*)-TML104 treatment (**Supplementary Figures 2A,B**). Interestingly, (*R*)-TML104 exerted more significant effects on SIRT1 expression than resveratrol at the same dosage (**Figure 2B**).

Our results showed that PDGF-BB decreased SIRT1 expression in VSMC, which is restored by (*R*)-TML104 treatment (**Figure 3A**). Next, we knocked down the expression of SIRT1 in VSMC by siRNA transfection. SIRT1 siRNA, but not control siRNA, markedly decreased (*R*)-TML104-mediated SIRT1 expression and abolished the inhibitory effects of (*R*)-TML104 on VSMC phenotypic transformation, as evidenced by increased PCNA expression (**Figure 3A**), decreased α-SMA expression (**Figure 3A**), increased EdU-positive (**Figure 3B**) and migrating cells (**Figure 3C**). Thus, our findings indicate that (*R*)-TML104 inhibits PDGF-BB-induced VSMC phenotypic transformation via upregulating SIRT1 *in vitro*.

(*R*)-TML104 Mitigates Injury-Induced Neointima Formation by Upregulating SIRT1 *in vivo*

To investigate whether the inhibitory effects of (*R*)-TML104 on neointima formation were mediated by SIRT1 *in vivo*,

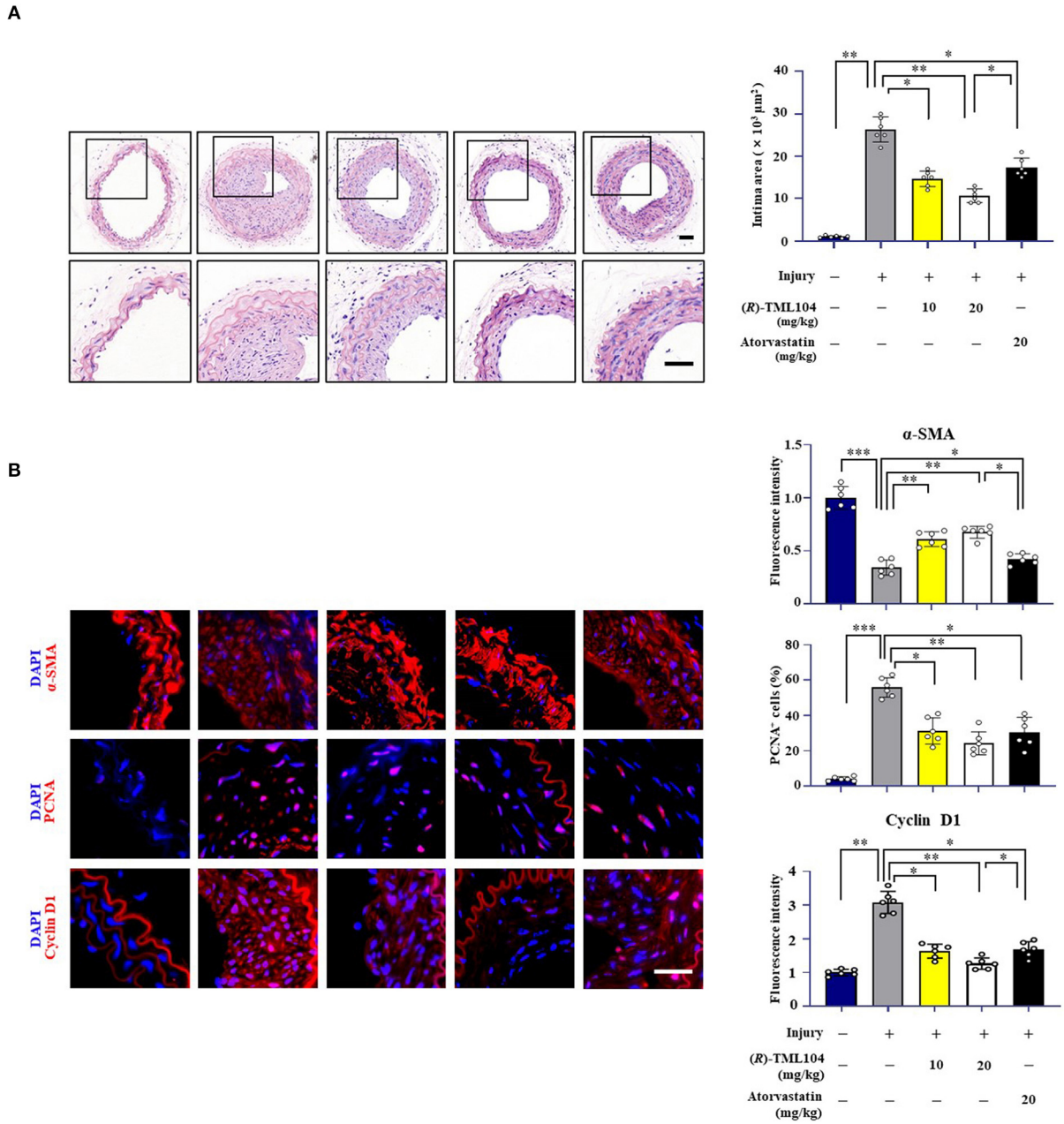

FIGURE 1 | (*R*)-TML104 mitigates injury-induced neointima formation *in vivo*. **(A)** Hematoxylin and Eosin (H&E) staining of sections at 28 days after injury (Scale bar: 50 μm). **(B)** Immunofluorescence staining of α-SMA, PCNA, and cyclin D1 on sections of carotid arteries from mice. Scale bar: 50 μm, Data shown are means ± S.D ($n = 6$). $^{*}p < 0.05$, $^{**}p < 0.01$, $^{***}p < 0.001$.

we then investigated the expression of SIRT1 in mice. We found that SIRT1 expression was decreased in vascular tissue after injury, which was reversed by (*R*)-TML104 treatment (**Figure 4B**). Next, we delivered lentiviral shRNA to specific SIRT1 knockdown in mice. Lentiviral SIRT1 shRNA, but not control shRNA, markedly decreased (*R*)-TML104-mediated SIRT1 expression and significantly abolished the protective effect of (*R*)-TML104 on neointima formation (**Figure 4A**). Moreover, immunofluorescence staining showed that (*R*)-TML104-mediated PCNA, cyclin D1 and α-SMA expression was abolished by genetic SIRT1 knockdown (**Figure 4B**). These data demonstrate that (*R*)-TML104 inhibits neointima formation by upregulating the expression of SIRT1 *in vivo*.

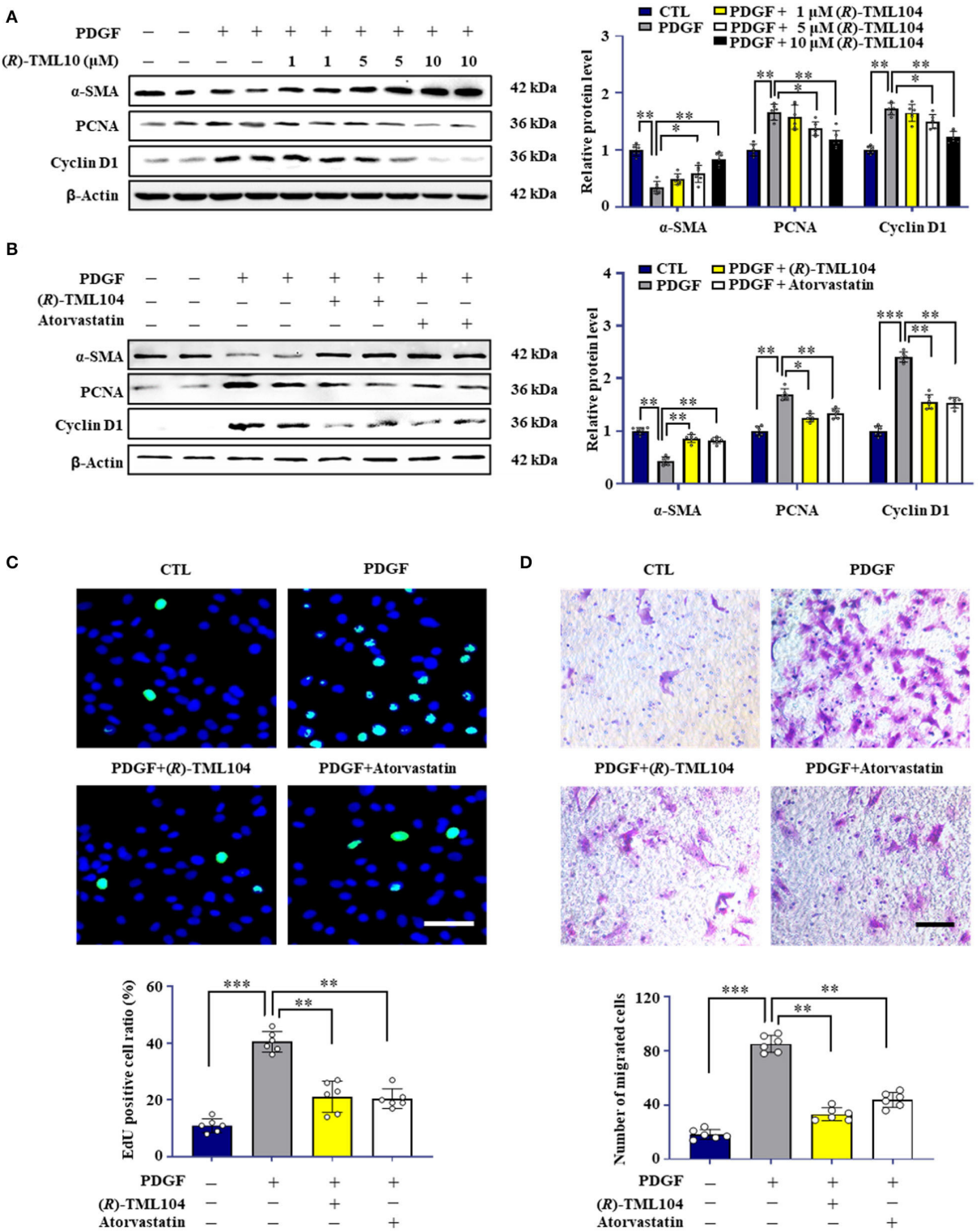

FIGURE 2 | (*R*)-TML104 inhibits PDGF-BB-induced VSMC phenotypic transformation *in vitro*. **(A)** VSMC were pretreated with (*R*)-TML104 for 4 h and then stimulated with PDGF-BB (20 ng/mL) for 24 h. The protein levels of α-SMA, PCNA, and cyclin D1 were determined by western blotting. **(B)** The protein levels of α-SMA, PCNA, and cyclin D1 were determined by western blotting. **(C)** DNA synthesis in VSMC determined with EdU incorporation assay. Blue fluorescence (Hoechst 33342) showed cell nuclei and green fluorescence (EdU) stands for cells with DNA synthesis. **(D)** Transwell assay was performed to determine the migration of VSMC. Scale bar: 50 μm, Data shown are means ± S.D ($n = 6$). $^{*}p < 0.05$, $^{**}p < 0.01$, $^{***}p < 0.001$.

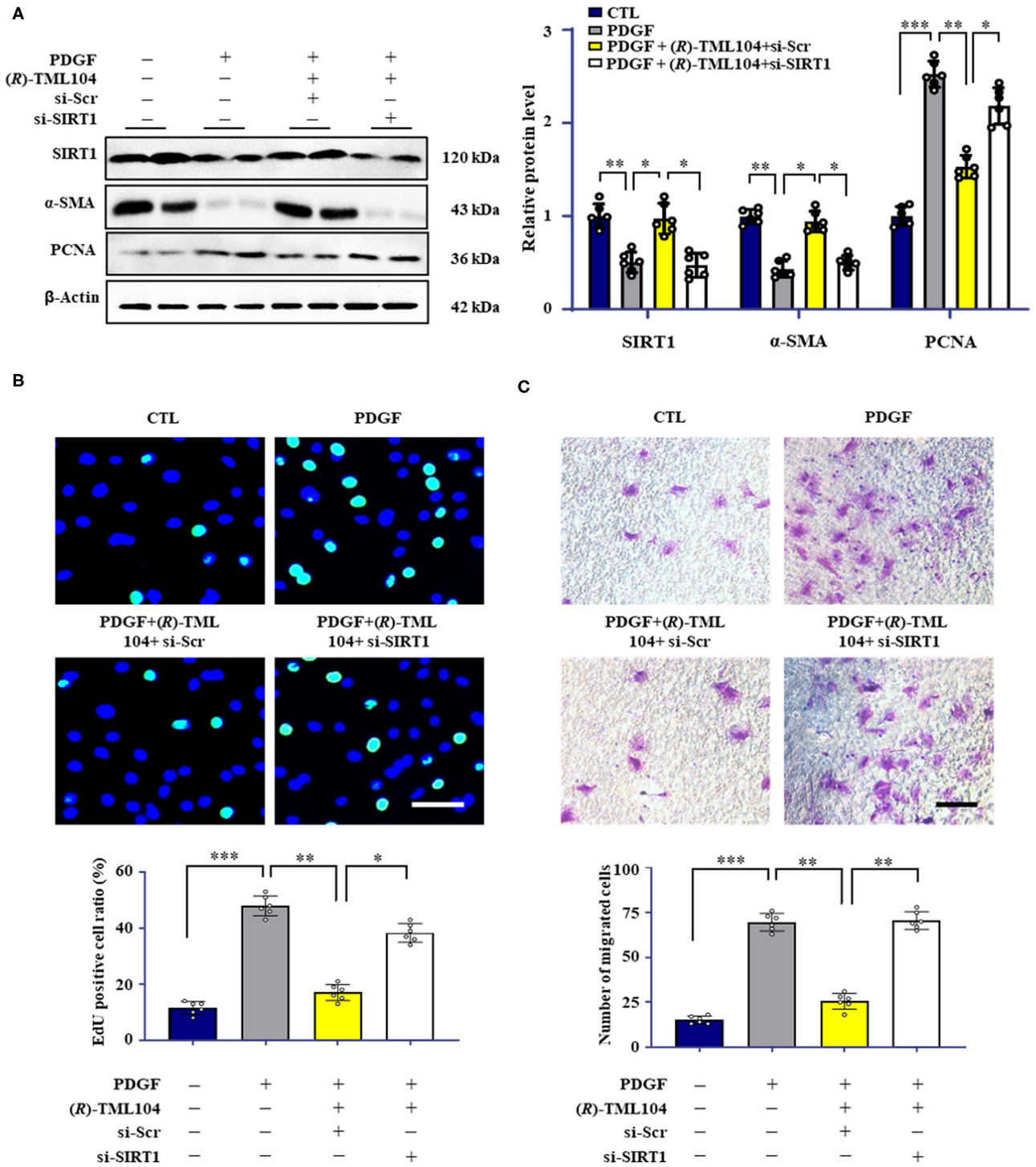

FIGURE 3 | (*R*)-TML104 inhibits PDGF-BB-induced VSMC phenotypic transformation by upregulating SIRT1 *in vitro*. **(A)** VSMC were pre-treated with (*R*)-TML104 (10 μM) for 4 h and then stimulated with PDGF-BB (20 ng/mL) for 24 h. The SIRT1, α-SMA, and PCNA protein levels were determined by western blotting. **(B)** DNA synthesis was determined by the EdU incorporation assay. **(C)** VSMC migration was determined by transwell assay. Scale bar: 50 μm, Data shown are means ± S.D ($n = 6$). $^{*}p < 0.05$, $^{**}p < 0.01$, $^{***}p < 0.001$.

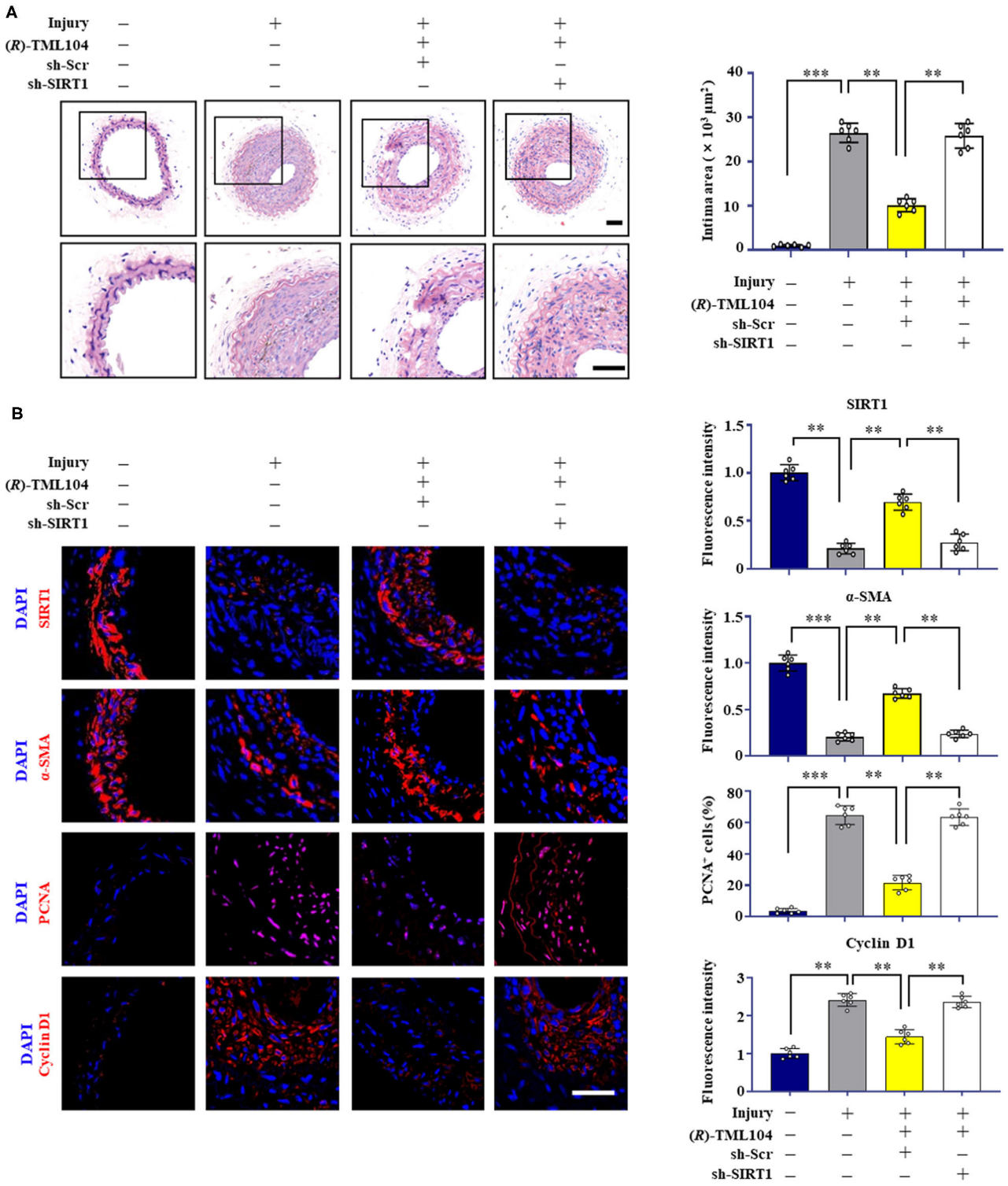

FIGURE 4 | (*R*)-TML104 mitigates injury-induced neointima formation by upregulating SIRT1 *in vivo*. **(A)** After vascular injury, (*R*)-TML104 (20 mg/kg) was administered by gastric gavage to mice for 4 weeks. H&E staining of the sections of arterial neointima area. **(B)** Immunofluorescence staining of SIRT1, α-SMA, PCNA, and cyclin D1 on sections of carotid arteries from mice. Scale bar: 50 μm, Data shown are means ± S.D ($n = 6$) $^{**}p < 0.01$, $^{***}p < 0.001$.

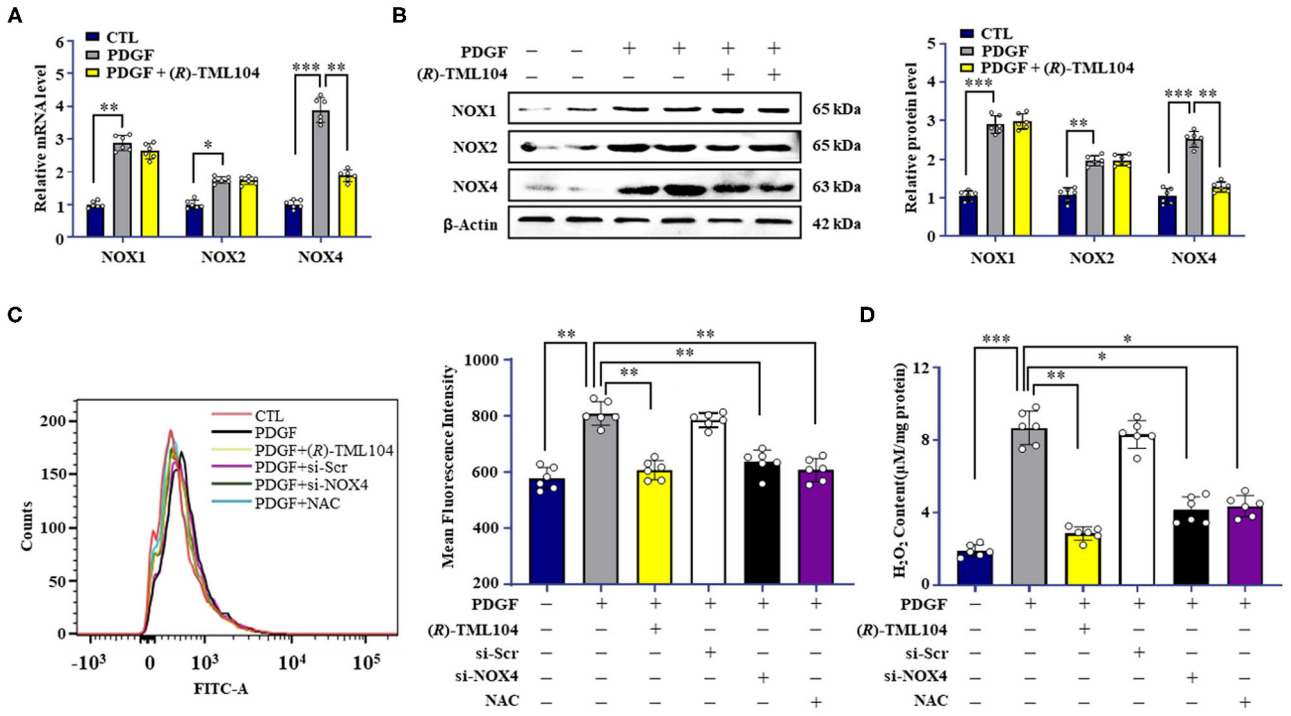

FIGURE 5 | (*R*)-TML104 inhibits PDGF-BB-mediated VSMC phenotypic transformation by modulating NOX4. **(A)** VSMC were pretreated with (*R*)-TML104 (10 μM) for 4 h and then stimulated with PDGF-BB (20 ng/mL) for 6 h. Using real-time PCR, we measured NOX1, NOX2, NOX4 mRNA levels. **(B)** The NOX1, NOX2, and NOX4 protein levels were determined by western blotting. **(C)** ROS were quantitated by flow cytometry. **(D)** H_2O_2 concentrations were determined with a hydrogen peroxide assay. Data shown are means ± S.D ($n = 6$). $^*p < 0.05$, $^{**}p < 0.01$, $^{***}p < 0.001$.

(*R*)-TML104 Inhibits PDGF-BB-Mediated VSMC Phenotypic Transformation by Modulating NOX4

It is reported that NOX-derived ROS plays a critical role in VSMC phenotypic transformation (32–34). In addition, SIRT1 can modulate the generation of ROS via regulating NOX expression (9, 35). To examine whether (*R*)-TML104 could modulate PDGF-BB-induced NOX expression in VSMC, the expression of NOX1, NOX2, and NOX4 in VSMC was measured. NOX1, NOX2, and NOX4 were all significantly higher both at the protein and mRNA level in VSMC in response to PDGF-BB when compared with control groups (**Figures 5A,B**). Intriguingly, (*R*)-TML104 treatment specifically inhibited the PDGF-BB-induced NOX4 expression, but not NOX1 or NOX2 expression both at the protein and mRNA level (**Figures 5A,B**). In addition, (*R*)-TML104 treatment also markedly reduced PDGF-BB-induced production of ROS (**Figure 5C**) and H_2O_2 (**Figure 5D**).

Next, we investigated the effect of NOX4 on VSMC phenotypic transformation, a NOX4-targeted siRNA was used to knock down the NOX4 expression. As expected, NOX4 siRNA, but not control siRNA, markedly decreased PDGF-BB-induced Nox4 expression in VSMC (**Supplementary Figure 3A**). PDGF-BB-induced the production of H_2O_2 (**Figure 5C**) and ROS (**Figure 5D**) was reduced by NOX4 siRNA. Moreover, NOX4 knockdown mimicked the inhibitory effects of (*R*)-TML104 on VSMC phenotypic transformation, as evidenced by decreased PCNA expression, increased α-SMA expression (**Supplementary Figure 3A**), reduced EdU-positive (**Supplementary Figure 3B**) and migrating cells (**Supplementary Figures 3C,D**).

To detect the role of ROS in PDGF-BB-induced VSMC phenotypic transformation, VSMC were treated with a ROS scavenger, N-acetyl-L-cysteine (NAC, 2 mM). Our results showed that NAC treatment significantly alleviated the PDGF-BB-increased ROS (**Figure 5C**) and H_2O_2 levels (**Figure 5D**). Meanwhile, NAC mimicked the inhibitory effects of (*R*)-TML104 on PDGF-BB-induced VSMC phenotypic transformation (**Supplementary Figure 3A**), proliferation (**Supplementary Figure 3B**) and migration (**Supplementary Figures 3C,D**). Collectively, these results suggest that (*R*)-TML104 inhibits PDGF-BB-induced VSMC phenotypic transformation through the NOX4-ROS signaling pathway.

(*R*)-TML104 Regulates NOX4 by Modulating NF-κB Activation

Previous studies have shown that SIRT1 can regulate NOX4 expression (9, 36). We hypothesized that (*R*)-TML104-mediated NOX4 expression is regulated by SIRT1 in VSMC. Next, we measured the expression of NOX4 in VSMC by Western blot. It showed that SIRT1 knockdown by siRNA reversed (*R*)-TML104-mediated NOX4 expression in VSMC (**Figure 6A**). It is well-established that NF-κB activation is a crucial modulator of NOX4 expression (16, 37). In addition, NF-κB activation can

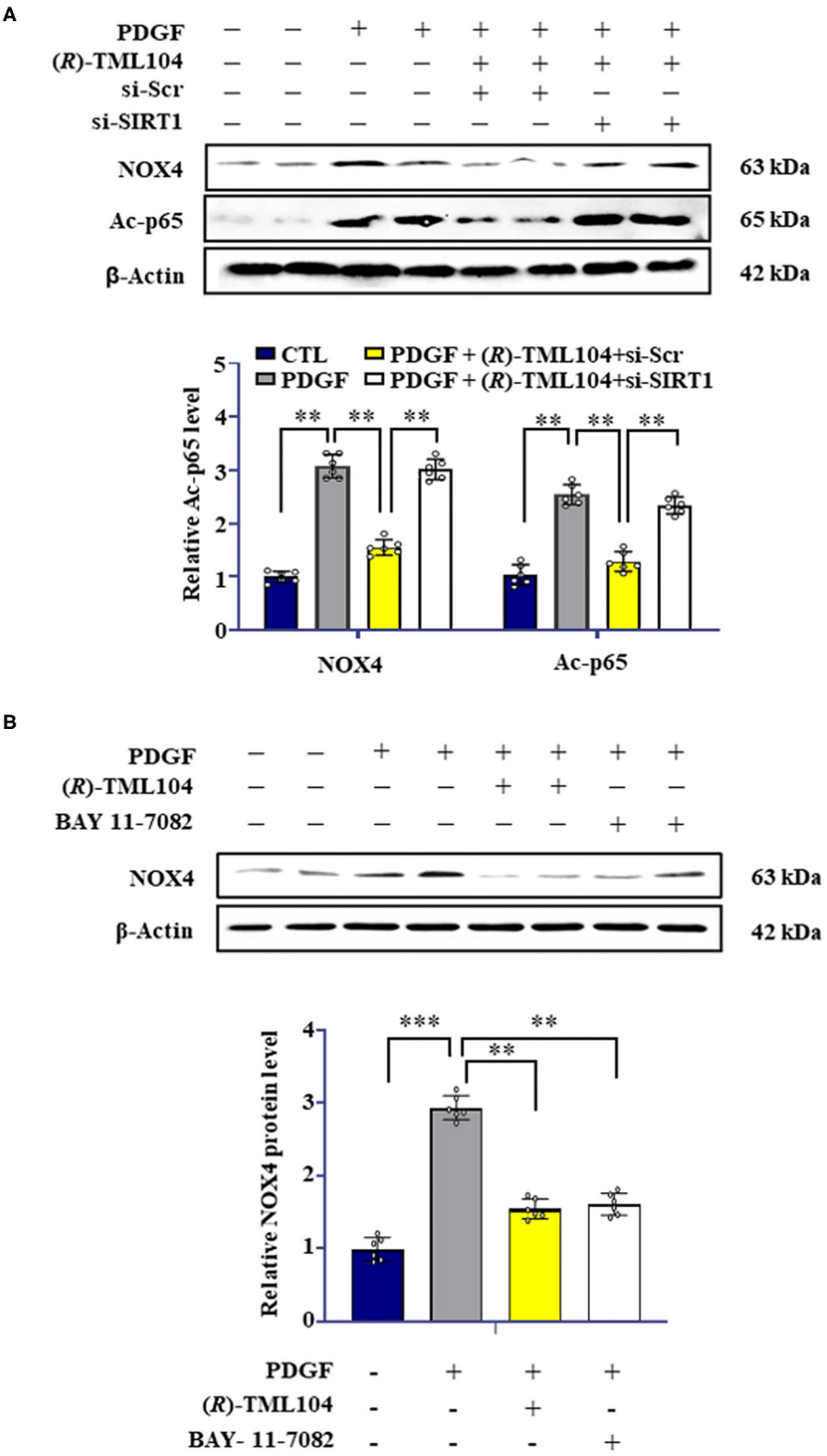

FIGURE 6 | (*R*)-TML104 regulates NOX4 by modulating NF-κB activation. **(A)** VSMC were pretreated with (*R*)-TML104 (10 μM) for 4 h and then stimulated with PDGF-BB (20 ng/mL) for 4 h. The NOX4 and Ac-p65 protein levels were determined by western blotting. **(B)** The NOX4 protein levels were determined by western blotting. Data shown are means ± S.D ($n = 6$). $^{**}p < 0.01$, $^{***}p < 0.001$.

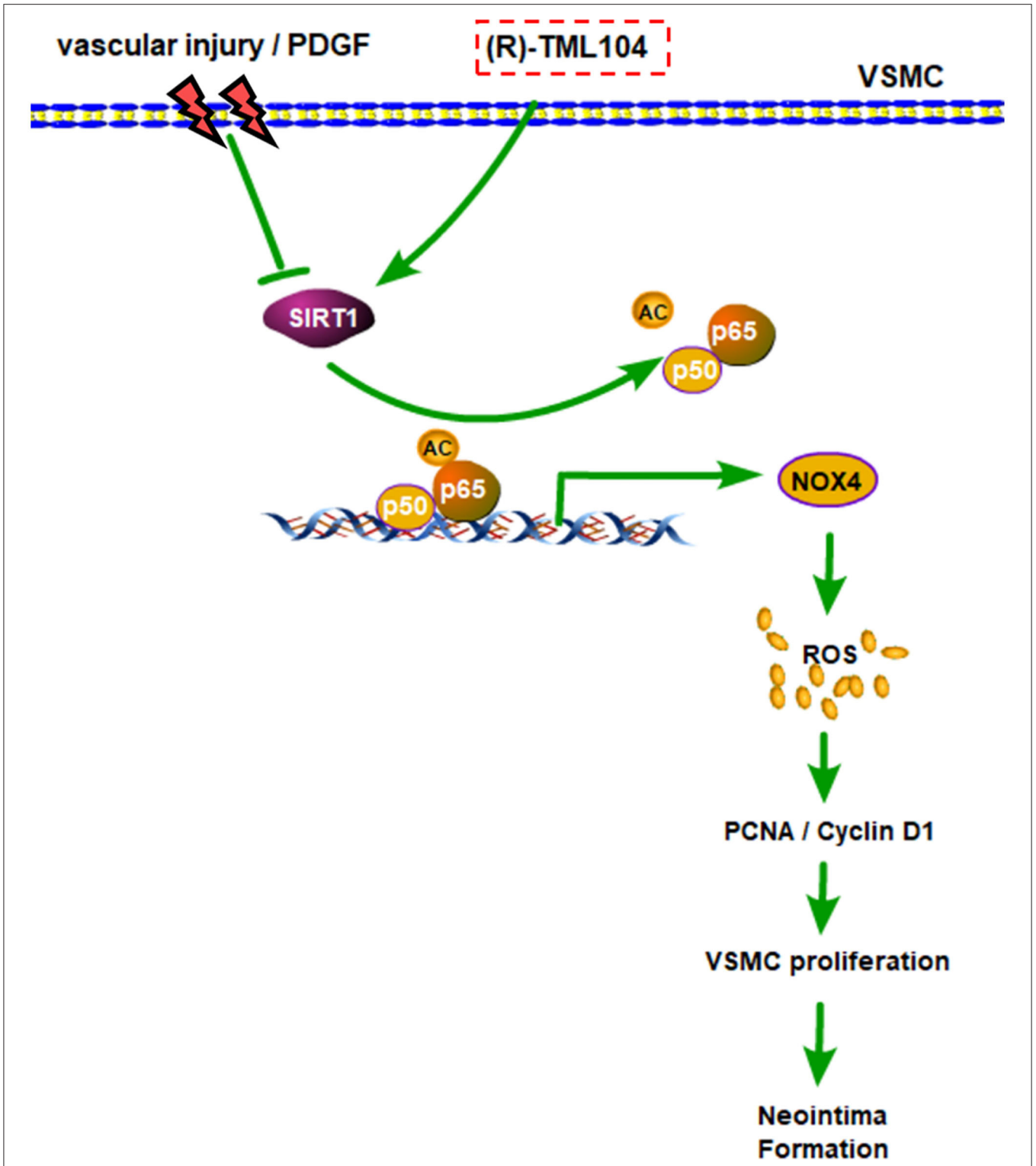

FIGURE 7 | A schematic representation of modulatory effects of (*R*)-TML104 on neointima formation after injury. Our results showed that (*R*)-TML104 ameliorates neointima formation in a SIRT1-dependent mechanism. SIRT1 is decreased in VSMC by arterial injury *in vivo* or PDGF-BB *in vitro*. (*R*)-TML104 upregulates SIRT1 expression, and SIRT1 subsequently suppresses NOX4 expression by reducing NF-κB acetylation, thereby mitigates neointima formation. By this means, the treatment with (*R*)-TML104 could inhibit neointima formation in mice.

be regulated by SIRT1-mediated deacetylation (38). Next, we investigated the status of NF-κB acetylation in VSMC. We found that NF-κB acetylation was increased in response to PDGF-BB, which is abolished by (*R*)-TML104 treatment. We then examined whether (*R*)-TML104-increased SIRT1 modulated NF-κB acetylation in VSMC. Next, we knocked down the expression of SIRT1 in VSMC by siRNA transfection. Our results showed that SIRT1 knockdown abolished the inhibitory effect of (*R*)-TML104 on the acetylation of NF-κB (**Figure 6A**).

To assess the role of NF-κB in NOX4 expression in VSMC, we used BAY 11-7082 (NF-κB inhibitor) to inhibit NF-κB activation. BAY 11-7082 treatment, similarly to (*R*)-TML104, suppressed PDGF-BB-induced NOX4 expression (**Figure 6B**). Collectively, these observations suggest that (*R*)-TML104-upregulated SIRT1 inhibits PDGF-BB-induced VSMC phenotypic transformation by downregulating NOX4 expression via decreasing NF-κB acetylation.

DISCUSSION

In the current study, we demonstrated that (*R*)-TML104 could prevent neointima formation *in vivo*. Furthermore, (*R*)-TML104 inhibited PDGF-BB-induced VSMC phenotypic transformation *in vitro*. We also found that SIRT1 expression is critical for (*R*)-TML104 to exert its protective effects. Finally, (*R*)-TML104 inhibited PDGF-BB-induced VSMC phenotypic transformation through NOX4 modulation via decreasing NF-κB acetylation. In summary, we found that (*R*)-TML104 against neointima formation and upregulates SIRT1 expression (**Figure 7**).

Previous work has demonstrated that resveratrol can protect from vascular disease (39). We hypothesized that (*R*)-TML104 could prevent vascular diseases, which was confirmed by our results showing that (*R*)-TML104 inhibited PDGF-BB-induced VSMC phenotypic transformation and injury-induced neointima formation. Next, we used atorvastatin as a positive control *in vivo* (40). Interestingly, the protective effects of (*R*)-TML104 against neointima formation were better than atorvastatin at the same dosage. We speculate that this superior effect of (*R*)-TML104 *in vivo* may be due to the key role of SIRT1, a well-known regulatory target of resveratrol, in the process of neointima formation (41). The expression of SIRT1 has been reported to decrease in neointima formation (2). In line with this observation, our data showed that SIRT1 decreases in VSMC in response to PDGF-BB, increased by (*R*)-TML104.

Increasing evidence has suggested that NOX4-derived ROS is crucial to the proliferation of several cell types (42, 43). A previous study showed that NOX4-derived ROS promote neointima formation (15, 44, 45). Consistently, our results showed that PDGF-BB increased NOX4-derived ROS levels, which was abolished by treatment with NOX4 siRNA or (*R*)-TML104. Consequently, we concluded that NOX4 down-regulation is responsible for the anti-oxidative effects of (*R*)-TML104 that confer vascular protection. In contrast, Chandrika showed that NOX4-derived ROS play an inhibitory role in the differentiation phenotypic of diabetic atherosclerosis (46). The diversity in NOX4-derived ROS functions may depend on specific environmental stimuli. Future work is needed to elucidate the complex role of NOX4-derived ROS in the development of vascular disease.

SIRT1 has been reported to regulate NOX4 expression in various biological processes (47, 48). Similarly, we found that (*R*)-TML104-increased SIRT1 inhibited PDGF-BB-induced NOX4 expression in VSMC, whereas SIRT1 knockdown abolished (*R*)-TML104-mediated inhibitory effects on NOX4 expression. Therefore, the fact that (*R*)-TML104 inhibits the PDGF-BB-induced expression of NOX4 likely depends on SIRT1 expression in VSMC. Previous studies have highlighted the influence of NF-κB-induced oxidative stress on the modulation of VSMC phenotypic transformation (30). In addition, NOX4 expression can be regulated by NF-κB activation (16). Hence, we evaluated whether (*R*)-TML104-reduced oxidative stress was associated with NF-κB activation. We found that (*R*)-TML104-increased SIRT1 inhibited NOX4 expression by reducing the acetylation status of NF-κB. This result is consistent with a previous report that SIRT1 regulated NOX4 expression by attenuating NF-κB acetylation in pancreatic cancer cachexia (9).

PDGF-BB is not the only factor that drives the injury-induced neointima formation (49, 50). A limitation in our study is that only PDGF-BB was used *in vitro* mechanistic study. The effect of (*R*)-TML104 on other factors-induced VSMC proliferation would be investigated as a follow-up study.

In summary, our data revealed that (*R*)-TML104-increased SIRT1 expression led to a reduction in NF-κB acetylation, thereby inhibit PPDGF-BB-induced VSMC phenotypic transformation by down-regulating NOX4 expression. Taken together, our findings suggest that (*R*)-TML104 may be an important therapeutic drug to prevent neointima formation.

DATA AVAILABILITY STATEMENT

The original contributions presented in the study are included in the article/**Supplementary Material**, further inquiries can be directed to the corresponding author/s.

ETHICS STATEMENT

The animal study was reviewed and approved by Experimental Animal Center of Jiangnan University.

AUTHOR CONTRIBUTIONS

L-LP, XS, and JS designed the project. BY and HL performed the experiments. XD and XP performed the majority of the data analysis. L-LP and XD performed the final manuscript. All authors edited the manuscript.

FUNDING

The work was supported by funds from the National Natural Science Foundation of China (Grant nos: 81973322, 82122068, 80270666, and 81870439), the Natural Science Foundation for Distinguished Young Scholars of Jiangsu Province (Grant no: BK20200026), Jiangsu Province Recruitment

Plan for High-level, Innovative and Entrepreneurial Talents (Innovative Research Team), Wuxi Social Development Funds for International Science & Technology Cooperation (Grant no: WX0303B010518180007PB), Jiangsu Province "Six Summit Talents" program (Grant no: YY-038), Jiangsu Province Qing Lan Project, the Fundamental Research Funds for the Central Universities (Grant nos: JUSRP221037 and JUSRP22007), and Collaborative Innovation Center of Food Safety and Quality Control in Jiangsu Province and Wuxi Taihu Talent Project. Shanghai Municipal Committee of Science and Technology (Grant no: 17JC1400200).

ACKNOWLEDGMENTS

We thank Doctor Chengfei Wu (School of Food Science and Technology) for assistance with the experiment technique.

SUPPLEMENTARY MATERIAL

The Supplementary Material for this article can be found online at: https://www.frontiersin.org/articles/10.3389/fcvm.2021.756098/full#supplementary-material

REFERENCES

1. Zhou SS, Jin JP, Wang JQ, Zhang ZG, Freedman JH, Zheng Y, et al. miRNAS in cardiovascular diseases: potential biomarkers, therapeutic targets and challenges. *Acta Pharmacol Sin.* (2018) 39:1073–84. doi: 10.1038/aps.2018.30
2. Zhang SM, Zhu LH, Chen HZ, Zhang R, Zhang P, Jiang DS, et al. Interferon regulatory factor 9 is critical for neointima formation following vascular injury. *Nat Commun.* (2014) 5:5160. doi: 10.1038/ncomms6160
3. Bubb KJ, Aubdool AA, Moyes AJ, Lewis S, Drayton JP, Tang O, et al. Endothelial C-type natriuretic peptide is a critical regulator of angiogenesis and vascular remodeling. *Circulation.* (2019) 139:1612–28. doi: 10.1161/CIRCULATIONAHA.118.036344
4. Johnson JL, Dwivedi A, Somerville M, George SJ, Newby AC. Matrix metalloproteinase (MMP)-3 activates MMP-9 mediated vascular smooth muscle cell migration and neointima formation in mice. *Arterioscler Thromb Vasc Biol.* (2011) 31:e35–44. doi: 10.1161/ATVBAHA.111.225623
5. Vendrov AE, Sumida A, Canugovi C, Lozhkin A, Hayami T, Madamanchi NR, et al. NOXA1-dependent NADPH oxidase regulates redox signaling and phenotype of vascular smooth muscle cell during atherogenesis. *Redox Biol.* (2019) 21:101063. doi: 10.1016/j.redox.2018.11.021
6. Shi Y, Li S, Song Y, Liu P, Yang Z, Liu Y, et al. Nrf-2 signaling inhibits intracranial aneurysm formation and progression by modulating vascular smooth muscle cell phenotype and function. *J Neuroinflammation.* (2019) 16:185. doi: 10.1186/s12974-019-1568-3
7. Garcia-Redondo AB, Aguado A, Briones AM, Salaices M. NADPH oxidases and vascular remodeling in cardiovascular diseases. *Pharmacol Res.* (2016) 114:110–20. doi: 10.1016/j.phrs.2016.10.015
8. Zhou B, Qiu Y, Wu N, Chen AD, Zhou H, Chen Q, et al. FNDC5 attenuates oxidative stress and NLRP3 inflammasome activation in vascular smooth muscle cells via activating the AMPK-SIRT1 signal pathway. *Oxid Med Cell Longev.* (2020) 2020:6384803. doi: 10.1155/2020/6384803
9. Dasgupta A, Shukla SK, Vernucci E, King RJ, Abrego J, Mulder SE, et al. SIRT1-NOX4 signaling axis regulates cancer cachexia. *J Exp Med.* (2020) 217:e20190745. doi: 10.1084/jem.20190745
10. Tang L, Dai F, Liu Y, Yu X, Huang C, Wang Y, et al. RhoA/ROCK signaling regulates smooth muscle phenotypic modulation and vascular remodeling via the JNK pathway and vimentin cytoskeleton. *Pharmacol Res.* (2018) 133:201–12. doi: 10.1016/j.phrs.2018.05.011
11. Kong P, Yu Y, Wang L, Dou YQ, Zhang XH, Cui Y, et al. circ-Sirt1 controls NF-kappaB activation via sequence-specific interaction and enhancement of SIRT1 expression by binding to miR-132/212 in vascular smooth muscle cells. *Nucleic Acids Res.* (2019) 47:3580–93. doi: 10.1093/nar/gkz141
12. Shu YN, Dong LH, Li H, Pei QQ, Miao SB, Zhang F, et al. CKII-SIRT1-SM22α loop evokes a self-limited inflammatory response in vascular smooth muscle cells. *Cardiovasc Res.* (2017) 113:1198–207. doi: 10.1093/cvr/cvx048
13. Yu Q, Dong L, Li Y, Liu G. SIRT1 and HIF1alpha signaling in metabolism and immune responses. *Cancer Lett.* (2018) 418:20–6. doi: 10.1016/j.canlet.2017.12.035
14. Shin NR, Ko JW, Kim JC, Park G, Kim SH, Kim MS, et al. Role of melatonin as an SIRT1 enhancer in chronic obstructive pulmonary disease induced by cigarette smoke. *J Cell Mol Med.* (2020) 24:1151–6. doi: 10.1111/jcmm.14816
15. Wu W, Zhang W, Choi M, Zhao J, Gao P, Xue M, et al. Vascular smooth muscle-MAPK14 is required for neointimal hyperplasia by suppressing VSMC differentiation and inducing proliferation and inflammation. *Redox Biol.* (2019) 22:101137. doi: 10.1016/j.redox.2019.101137
16. Xu T, Shao L, Wang A, Liang R, Lin Y, Wang G, et al. CD248 as a novel therapeutic target in pulmonary arterial hypertension. *Clin Transl Med.* (2020) 10:e175. doi: 10.1002/ctm2.175
17. Dou YQ, Kong P, Li CL, Sun HX, Li WW, Yu Y, et al. Smooth muscle SIRT1 reprograms endothelial cells to suppress angiogenesis after ischemia. *Theranostics.* (2020) 10:1197–212. doi: 10.7150/thno.39320
18. Rauf A, Imran M, Butt MS, Nadeem M, Peters DG, Mubarak MS. Resveratrol as an anti-cancer agent: a review. *Crit Rev Food Sci Nutr.* (2018) 58:1428–47. doi: 10.1080/10408398.2016.1263597
19. Zambrano A, Molt M, Uribe E, Salas M. Glut 1 in cancer cells and the inhibitory action of resveratrol as a potential therapeutic strategy. *Int J Mol Sci.* (2019) 20:3374. doi: 10.3390/ijms20133374
20. Ma Y, Liu S, Shu H, Crawford J, Xing Y, Tao F. Resveratrol alleviates temporomandibular joint inflammatory pain by recovering disturbed gut microbiota. *Brain Behav Immun.* (2020) 87:455–64. doi: 10.1016/j.bbi.2020.01.016
21. Dyck GJB, Raj P, Zieroth S, Dyck JRB, Ezekowitz JA. The effects of resveratrol in patients with cardiovascular disease and heart failure: a narrative review. *Int J Mol Sci.* (2019) 20:904. doi: 10.3390/ijms20040904
22. Tellone E, Galtieri A, Russo A, Giardina B, Ficarra S. Resveratrol: a focus on several neurodegenerative diseases. *Oxid Med Cell Longev.* (2015) 2015:392169. doi: 10.1155/2015/392169
23. Zhuang Y, Wu H, Wang X, He J, He S, Yin Y. Resveratrol attenuates oxidative stress-induced intestinal barrier injury through PI3K/Akt-mediated Nrf2 signaling pathway. *Oxid Med Cell Longev.* (2019) 2019:7591840. doi: 10.1155/2019/7591840
24. Cosin-Tomas M, Senserrich J, Arumi-Planas M, Alquezar C, Pallas M, Martin-Requero A, et al. Role of resveratrol and selenium on oxidative stress and expression of antioxidant and anti-aging genes in immortalized lymphocytes from Alzheimer's disease patients. *Nutrients.* (2019) 11:1764. doi: 10.3390/nu11081764
25. Chen Y, Zheng Z, Li C, Pan Y, Tang X, Wang XJ. Synthetic imine resveratrol analog 2-methoxyl-3,6-dihydroxyl-IRA ameliorates colitis by activating protective Nrf2 pathway and inhibiting NLRP3 expression. *Oxid Med Cell Longev.* (2019) 2019:7180284. doi: 10.1155/2019/7180284
26. Hosoda R, Hamada H, Uesugi D, Iwahara N, Nojima I, Horio Y, et al. Different antioxidative and antiapoptotic effects of piceatannol and resveratrol. *J Pharmacol Exp Ther.* (2021) 376:385–96. doi: 10.1124/jpet.120.000096
27. Wu JH, Zhou YF, Hong CD, Chen AQ, Luo Y, Mao L, et al. Semaphorin-3A protects against neointimal hyperplasia after vascular injury. *EBioMedicine.* (2019) 39:95–108. doi: 10.1016/j.ebiom.2018.12.023
28. Yang F, Chen Q, He S, Yang M, Maguire EM, An W, et al. miR-22 Is a novel mediator of vascular smooth muscle cell phenotypic modulation and neointima formation. *Circulation.* (2018) 137:1824–41. doi: 10.1161/CIRCULATIONAHA.117.027799
29. Bruder-Nascimento T, Callera GE, Montezano AC, Belin de Chantemele EJ, Tostes RC, Touyz RM. Atorvastatin inhibits pro-inflammatory actions of

aldosterone in vascular smooth muscle cells by reducing oxidative stress. *Life Sci.* (2019) 221:29–34. doi: 10.1016/j.lfs.2019.01.043
30. Wan W, Ding Y, Xie Z, Li Q, Yan F, Budbazar E, et al. PDGFR-β modulates vascular smooth muscle cell phenotype via IRF-9/SIRT-1/NF-κB pathway in subarachnoid hemorrhage rats. *J Cereb Blood Flow Metab.* (2019) 39:1369–80. doi: 10.1177/0271678X18760954
31. Ma S, Feng J, Zhang R, Chen J, Han D, Li X, et al. SIRT1 activation by resveratrol alleviates cardiac dysfunction via mitochondrial regulation in diabetic cardiomyopathy mice. *Oxid Med Cell Longev.* (2017) 2017:4602715. doi: 10.1155/2017/4602715
32. Luo X, Yang D, Wu W, Long F, Xiao C, Qin M, et al. Critical role of histone demethylase Jumonji domain-containing protein 3 in the regulation of neointima formation following vascular injury. *Cardiovasc Res.* (2018) 114:1894–906. doi: 10.1093/cvr/cvy176
33. Dong X, Wu D, Zhang Y, Jia L, Pan X, Sun J, et al. Cathelicidin modulates vascular smooth muscle cell phenotypic switching through ROS/IL-6 pathway. *Antioxidants.* (2020) 9:491. doi: 10.3390/antiox9060491
34. Fernandes DC, Wosniak J, Gonçalves RC, Tanaka LY, Fernandes CG, Zanatta DB, et al. PDIA1 acts as master organizer of NOX1/NOX4 balance and phenotype response in vascular smooth muscle. *Free Radic Biol Med.* (2021) 162:603–14. doi: 10.1016/j.freeradbiomed.2020.11.020
35. Zhang W, Huang Q, Zeng Z, Wu J, Zhang Y, Chen Z. Sirt1 inhibits oxidative stress in vascular endothelial cells. *Oxid Med Cell Longev.* (2017) 2017:7543973. doi: 10.1155/2017/7543973
36. Wang D, Li Y, Wang N, Luo G, Wang J, Luo C, et al. 1α,25-dihydroxyvitamin D prevents renal oxidative damage via the PARP1/SIRT1/NOX4 pathway in Zucker diabetic fatty rats. *Am J Physiol Endocrinol Metab.* (2020) 318:E343–56. doi: 10.1152/ajpendo.00270.2019
37. Ji ML, Jiang H, Zhang XJ, Shi PL, Li C, Wu H, et al. Preclinical development of a microRNA-based therapy for intervertebral disc degeneration. *Nat Commun.* (2018) 9:5051. doi: 10.1038/s41467-018-07360-1
38. Shen G, Ren H, Shang Q, Zhang Z, Zhao W, Yu X, et al. miR-128 plays a critical role in murine osteoclastogenesis and estrogen deficiency-induced bone loss. *Theranostics.* (2020) 10:4334–48. doi: 10.7150/thno.42982
39. Wang Z, Wu Y, Wang J, Zhang C, Yan H, Zhu M, et al. Effect of resveratrol on modulation of endothelial cells and macrophages for rapid vascular regeneration from electrospun poly (epsilon-caprolactone) scaffolds. *ACS Appl Mater Interfaces.* (2017) 9:19541–51. doi: 10.1021/acsami.6b16573
40. Intagliata S, Modica MN, Santagati LM, Montenegro L. Strategies to improve resveratrol systemic and topical bioavailability: an update. *Antioxidants.* (2019) 8:244. doi: 10.3390/antiox8080244
41. Li L, Zhang HN, Chen HZ, Gao P, Zhu LH, Li HL, et al. SIRT1 acts as a modulator of neointima formation following vascular injury in mice. *Circ Res.* (2011) 108:1180–9. doi: 10.1161/CIRCRESAHA.110.237875
42. Mondol AS, Tonks NK, Kamata T. Nox4 redox regulation of PTP1B contributes to the proliferation and migration of glioblastoma cells by modulating tyrosine phosphorylation of coronin-1C. *Free Radic Biol Med.* (2014) 67:285–91. doi: 10.1016/j.freeradbiomed.2013.11.005
43. Peshavariya HM, Chan EC, Liu GS, Jiang F, Dusting GJ. Transforming growth factor-beta1 requires NADPH oxidase 4 for angiogenesis *in vitro* and *in vivo*. *J Cell Mol Med.* (2014) 18:1172–83. doi: 10.1111/jcmm.12263
44. Zhang WX, Tai GJ, Li XX, Xu M. Inhibition of neointima hyperplasia by the combined therapy of linagliptin and metformin via AMPK/Nox4 signaling in diabetic rats. *Free Radic Biol Med.* (2019) 143:153–63. doi: 10.1016/j.freeradbiomed.2019.07.030
45. Chen D, Zang YH, Qiu Y, Zhang F, Chen AD, Wang JJ, et al. BCL6 attenuates proliferation and oxidative stress of vascular smooth muscle cells in hypertension. *Oxid Med Cell Longev.* (2019) 2019:5018410. doi: 10.1155/2019/5018410
46. Di Marco E, Gray SP, Kennedy K, Szyndralewiez C, Lyle AN, Lassegue B, et al. NOX4-derived reactive oxygen species limit fibrosis and inhibit proliferation of vascular smooth muscle cells in diabetic atherosclerosis. *Free Radic Biol Med.* (2016) 97:556–67. doi: 10.1016/j.freeradbiomed.2016.07.013
47. Chen A, Chen Z, Xia Y, Lu D, Yang X, Sun A, et al. Liraglutide attenuates NLRP3 inflammasome-dependent pyroptosis via regulating SIRT1/NOX4/ROS pathway in H9c2 cells. *Biochem Biophys Res Commun.* (2018) 499:267–72. doi: 10.1016/j.bbrc.2018.03.142
48. Zhang H, Zhai Z, Wang Y, Zhang J, Wu H, Wang Y, et al. Resveratrol ameliorates ionizing irradiation-induced long-term hematopoietic stem cell injury in mice. *Free Radic Biol Med.* (2013) 54:40–50. doi: 10.1016/j.freeradbiomed.2012.10.530
49. Qin ZX, Yu P, Qian DH, Song MB, Tan H, Yu Y, et al. Hydrogen-rich saline prevents neointima formation after carotid balloon injury by suppressing ROS and the TNF-α/NF-κB pathway. *Atherosclerosis.* (2012) 220:343–50. doi: 10.1016/j.atherosclerosis.2011.11.002
50. Yue H, Febbraio M, Klenotic PA, Kennedy DJ, Wu Y, Chen S, et al. CD36 enhances vascular smooth muscle cell proliferation and development of neointimal hyperplasia. *Arterioscler Thromb Vasc Biol.* (2019) 39:263–75. doi: 10.1161/ATVBAHA.118.312186

Conflict of Interest: The authors declare that the research was conducted in the absence of any commercial or financial relationships that could be construed as a potential conflict of interest.

Publisher's Note: All claims expressed in this article are solely those of the authors and do not necessarily represent those of their affiliated organizations, or those of the publisher, the editors and the reviewers. Any product that may be evaluated in this article, or claim that may be made by its manufacturer, is not guaranteed or endorsed by the publisher.

frontiers in Cardiovascular Medicine

ORIGINAL RESEARCH
published: 05 November 2021
doi: 10.3389/fcvm.2021.764337

MFAP4 Deficiency Attenuates Angiotensin II-Induced Abdominal Aortic Aneurysm Formation Through Regulation of Macrophage Infiltration and Activity

Bartosz Pilecki[1†], Paulo V. S. D. de Carvalho[1,2,3†], Katrine L. Kirketerp-Møller[1†], Anders Schlosser[1], Karin Kejling[1], Magdalena Dubik[1], Nicklas P. Madsen[1], Jane Stubbe[4], Pernille B. L. Hansen[4,5], Thomas L. Andersen[6,7], Jesper B. Moeller[1,8], Niels Marcussen[6], Vasco Azevedo[2], Svend Hvidsten[9], Christina Baun[9], Guo-Ping Shi[10], Jes S. Lindholt[11] and Grith L. Sorensen[1]*

[1] Department of Cancer and Inflammation Research, Institute of Molecular Medicine, University of Southern Denmark, Odense, Denmark, [2] Department of General Biology, Institute of Biological Sciences, Federal University of Minas Gerais (UFMG), Belo Horizonte, Brazil, [3] Department of Mathematics and Informatics, University of Southern Denmark, Odense, Denmark, [4] Department of Cardiovascular and Renal Research, Institute of Molecular Medicine, University of Southern Denmark, Odense, Denmark, [5] Cardiovascular, Renal and Metabolism, Innovative Medicines and Early Development Biotech Unit, AstraZeneca, Gothenburg, Sweden, [6] Department of Pathology, Odense University Hospital, Odense, Denmark, [7] Pathology Research Unit, Institute of Clinical Research and Institute of Molecular Medicine, University of Southern Denmark, Odense, Denmark, [8] Danish Institute for Advanced Study, University of Southern Denmark, Odense, Denmark, [9] Department of Nuclear Medicine, Odense University Hospital, Odense, Denmark, [10] Department of Medicine, Brigham and Women's Hospital and Harvard Medical School, Boston, MA, United States, [11] Department of Thoracic, Heart and Vascular Surgery, Odense University Hospital, Odense, Denmark

Objective: Abdominal aortic aneurysm (AAA) is a common age-related vascular disease characterized by progressive weakening and dilatation of the aortic wall. Microfibrillar-associated protein 4 (MFAP4) is an extracellular matrix (ECM) protein involved in the induction of vascular remodeling. This study aimed to investigate if MFAP4 facilitates the development of AAA and characterize the underlying MFAP4-mediated mechanisms.

Approach and Results: Double apolipoprotein E- and *Mfap4*-deficient ($ApoE^{-/-}Mfap4^{-/-}$) and control apolipoprotein E-deficient ($ApoE^{-/-}$) mice were infused subcutaneously with angiotensin II (Ang II) for 28 days. *Mfap4* expression was localized within the adventitial and medial layers and was upregulated after Ang II treatment. While Ang II-induced blood pressure increase was independent of *Mfap4* genotype, $ApoE^{-/-}Mfap4^{-/-}$ mice exhibited significantly lower AAA incidence and reduced maximal aortic diameter compared to $ApoE^{-/-}$ littermates. The $ApoE^{-/-}Mfap4^{-/-}$ AAAs were further characterized by reduced macrophage infiltration, matrix metalloproteinase (MMP)-2 and MMP-9 activity, proliferative activity, collagen content, and elastic membrane disruption. MFAP4 deficiency also attenuated activation of integrin- and TGF-β-related signaling within the adventitial layer of

OPEN ACCESS

Edited by:
Emiel Van Der Vorst, Institute for Molecular Cardiovascular Research (IMCAR), Germany

Reviewed by:
Judith Sluimer, Maastricht University, Netherlands
Vivek Nanda, University of Alabama at Birmingham, United States

***Correspondence:**
Bartosz Pilecki
bpilecki@health.sdu.dk

†These authors have contributed equally to this work and share first authorship

Specialty section:
This article was submitted to Atherosclerosis and Vascular Medicine, a section of the journal Frontiers in Cardiovascular Medicine

Received: *25 August 2021*
Accepted: *15 October 2021*
Published: *05 November 2021*

Citation:
Pilecki B, de Carvalho PVSD, Kirketerp-Møller KL, Schlosser A, Kejling K, Dubik M, Madsen NP, Stubbe J, Hansen PBL, Andersen TL, Moeller JB, Marcussen N, Azevedo V, Hvidsten S, Baun C, Shi G-P, Lindholt JS and Sorensen GL (2021) MFAP4 Deficiency Attenuates Angiotensin II-Induced Abdominal Aortic Aneurysm Formation Through Regulation of Macrophage Infiltration and Activity. Front. Cardiovasc. Med. 8:764337. doi: 10.3389/fcvm.2021.764337

AAA tissues. Finally, MFAP4 stimulation promoted human monocyte migration and significantly upregulated MMP-9 activity in macrophage-like THP-1 cells.

Conclusion: This study demonstrates that MFAP4 induces macrophage-rich inflammation, MMP activity, and maladaptive remodeling of the ECM within the vessel wall, leading to an acceleration of AAA development and progression. Collectively, our findings suggest that MFAP4 is an essential aggravator of AAA pathology that acts through regulation of monocyte influx and MMP production.

Keywords: abdominal aortic aneurysm, extracellular matrix, inflammation, macrophage, matrix metalloproteinases

INTRODUCTION

Abdominal aortic aneurysm (AAA) is a focal pathological dilation of the aorta associated with substantial morbidity and mortality due to the potentially fatal consequence of aortic rupture (1). AAA incidence has been observed to decline in some European populations (2), possibly due to benefits of screening programs (3, 4) or changes in population trends of cardiovascular risk factors. However, AAA mortality has not declined globally (5). Pathological mechanisms driving the formation of AAA include inflammation, smooth muscle cell (SMC) apoptosis, neovascularization, and extracellular matrix (ECM) degradation (1), which contribute to vascular remodeling and weakening of the aortic wall. The current clinical approach to treatment includes open or endovascular surgical repair when the aortic diameter has attained sufficient expansion linked to a high probability of rupture, and no validated pharmacological therapy against AAA exists (6, 7). Most AAAs of lesser diameter continue to grow and will eventually require surgical repair, highlighting a need to improve the knowledge of the mechanisms involved in development and progression of aortic aneurysms.

We have previously shown that microfibrillar-associated protein 4 (MFAP4) is an ECM protein with relatively high expression in the heart and arteries and that systemic MFAP4 levels vary with cardiovascular disease (8, 9) as well as fibrotic disease (10–12). We have demonstrated that MFAP4 binds specifically to the ECM fibrils, fibrillin, elastin, and collagen (13) and that it can activate various cells through RGD-dependent integrin ligation and downstream focal adhesion kinase (FAK)-dependent signaling (14). Unchallenged MFAP4-deficient mice exhibit mild pulmonary airspace enlargement (15) but otherwise appear healthy. However, when subjected to carotid artery ligation, *Mfap4*-deficient mice show delayed neointimal formation as well as reduced proliferation, apoptosis and inflammatory infiltration within the arterial wall (16).

Based on these observations, we hypothesized that MFAP4 might aggravate AAA formation and progression. We used a murine model of AAA development based on angiotensin II (Ang II) infusion in double apolipoprotein E- and *Mfap4*-deficient ($ApoE^{-/-}Mfap4^{-/-}$) mice and control apolipoprotein E-deficient ($ApoE^{-/-}$) littermates as well as cell culture studies to establish a mechanistic role of MFAP4 in AAA pathophysiology.

MATERIALS AND METHODS

Additional details on the methods are provided in the **Supplementary Material**.

Experimental Animals

Mfap4-deficient ($Mfap4^{-/-}$) mice were generated in-house as previously described (16) and crossbred with C57BL/6N mice (Charles River Laboratories International) for >10 generations before they were used for experiments.

ApoE-deficient (B6.129P2-$Apoe^{tm1Unc}$/J, stock nr 002052, $ApoE^{-/-}$) mice were obtained from Jackson Laboratory and back-crossed to the C57BL/6N background. $ApoE^{-/-}$ mice and double *ApoE*- and *Mfap4*-deficient ($ApoE^{-/-}Mfap4^{-/-}$) littermate mice were produced by $ApoE^{-/-}Mfap4^{+/-}$ breeding pairs.

The mice were housed in separate single cages during the course of the experiment. All animal experiments were approved by the National Animal Experiments Inspectorate of Denmark (permit numbers 2012-15-2934-00047 and 2015-15-0201-00474).

Induction of AAA

Experimental AAAs were induced using a continuous infusion of Ang II as described previously (17). This model shows a strong male gender preference, recapitulating the much higher incidence of human AAA in men than in women (18). Therefore, this study only included male mice in accordance with the guidelines described in the ATVB Council Statement (19). Male $ApoE^{-/-}Mfap4^{-/-}$ and littermate $ApoE^{-/-}$ control mice were fed western diet 1 week before surgery and throughout the experiment. At the age of 10–12 weeks, subcutaneous osmotic minipumps (Alzet® Model 2004, DURECT™ Corporation, Cupertino, CA, USA) were installed via a mid-scapular incision under mild anesthesia (2% isoflurane, IsoFlo® vet, Orion Pharma, Nivå, Denmark) supplemented with analgesia (subcutaneous injection of 5 μg/g carprofen, Rimadyl, Pfizer, Ballerup, Denmark). Adequacy of anesthesia was monitored throughout the procedure by the toe pinch reflex.

The pumps delivered saline or Ang II (Calbiochem, Merck Millipore, Darmstadt, Germany) at 1,000 ng/kg/min

for 9, 21, and 28 days. The body weight and overall well-being were regularly monitored for all mice throughout the treatment period.

Mice were euthanized by CO_2/O_2 asphyxiation. Abdominal aortic tissue and/or serum was sampled and snap-frozen 9 days after surgery. Aortic diameter (AD) was measured 28 days after surgery. AAA severity was scored as previously described (20). The cardiovascular system was perfused with sterile PBS and the hearts were dissected, rinsed with sterile PBS and weighed. The aortas were carefully isolated from the heart to the iliac bifurcation, cleaned from fat and connective tissue, weighed, mounted on black wax and measured. The parts of the aortas with a maximum diameter were subsequently fixed in 4% (v/w) formaldehyde for 24 h, rinsed in PBS and paraffin-embedded.

Aortic Diameter Measurements

Maximal AAA diameter in dissected aortas from *ApoE*$^{-/-}$ and *ApoE*$^{-/-}$*Mfap4*$^{-/-}$ mice was measured using a 5 mm measuring scale (Ted Pella, Inc., Redding, CA, USA) and a Canon EOS 6D camera. The measurements were performed in affected regions using Adobe® Photoshop® CC2018 (San Jose, CA, USA) in a blinded manner by two independent investigators. AAA was defined as a diameter increase >50% compared to the average aortic diameter of saline-infused mice.

RNA *in situ* Hybridization

In situ hybridization was performed using a modified version of the RNAScope 2.5 high-definition procedure (Advanced Cell Diagnostics, Newark, CA, USA). Mouse aortic tissues were hybridized with 20 probe pairs (421391, Advanced Cell Diagnostics) targeting nucleotides 98-1231 of mouse Mfap4 mRNA (accession number NM_029568.2) followed by branched DNA signal amplification and tyramide enhancement visualized with Liquid Permanent Red (Agilent). The sections were subsequently immunostained with anti-α-smooth muscle actin (α-SMA) antibodies (Agilent) detected with anti-mouse BrightVision horseradish peroxidase (ImmunoLogic, Duiven, the Netherlands) and visualized with Deep Space Black (BIocare Medical, Pacheco, CA, USA).

Immunohistochemistry

Four μm-thick serial sections were stained with hematoxylin and eosin (H&E), Verhoeff-Van Gieson, Picrosirius red and for: α-SMA, cleaved caspase-3, CD45, F4/80, Ki67, MMP-9, MMP-2, CD31, CD11b, phosphorylated (p)FAK, pSMAD2, pSMAD3, and MFAP4 (**Supplementary Table 1**). All immunostainings were counter-stained with hematoxylin. The stainings were performed on a Dako Autostainer Universal Staining System (Dako, Denmark A/S, Glostrup, Denmark). Stained sections were scanned at 20x magnification using NanoZoomer-XR (Hamamatsu Photonics, Hamamatsu, Japan).

Morphometric Analysis

The scanned images were analyzed in a blinded manner using Adobe Photoshop or ImageJ.

Ki67-positive nuclei, CD31-positive microvessels, and MMP-9-positive cells were quantified as cells per section. Collagen, α-SMA, cleaved caspase-3, CD45, F4/80, CD11b, MFAP4, MMP-2, pSMAD2, pSMAD3, and pFAK stainings were quantified as staining-positive area using automated color threshold analysis. Elastic fiber degradation was assessed as a percentage of destroyed Verhoeff van Gieson-positive tissue area. Briefly, the damaged regions showing degradation of proper elastic lamellar structure were delineated and presented as a fraction of a total intima-media area. All analyses were performed in a blinded manner. Representative images of isotype control stainings are shown in **Supplementary Figure 1**. Representative images of entire aortic sections are shown in **Supplementary Figure 2**.

Immunofluorescence

Four μm-thick serial sections were deparaffinized, subjected to antigen retrieval with citrate buffer (pH 6.0), blocked with 3% BSA and subsequently double-stained for Ki-67 and CD45 or Ki-67 and α-SMA (**Supplementary Table 1**). The sections were counterstained with DAPI and mounted using Fluorescent Mounting Medium (Dako). Fluorescent images were visualized and acquired using Olympus BX63 microscope (Olympus) and X-cite 120LED (Lumen Dynamics) with an Olympus DP80 camera and analyzed using ImageJ.

Measurement of Serum MFAP4

Serum levels of mouse MFAP4 were measured using a modified AlphaLISA immunoassay (Perkin Elmer, Waltham, MA, USA) as described previously (8). The two utilized anti-MFAP4 monoclonal antibodies (HG-HYB 7-14 and HG-HYB 7-18) had been raised against human recombinant MFAP4 and cross-react with the murine MFAP4 homolog due to very high sequence similarity. Data are presented as U/ml. When measured in human serum, 1 U/ml of MFAP4 corresponds to a concentration of 38 ng/ml.

THP-1 Cell Culture and Stimulation

THP-1 human monocyte leukemia cell line (ATCC) was grown in RPMI-1640 medium (Gibco, TermoFisher) supplemented with 10% FBS (Sigma-Aldrich), 5,000 U/ml penicillin, 5,000 μg/ml streptomycin, and 200 mM L-glutamine (all from Gibco) at 37°C and 5% CO_2 humidity. The cells were subcultured every second-third day.

MaxiSorp 96-well plates were coated overnight at 4°C with human serum albumin (HSA) or immobilized MFAP4 (both 10 μg/ml). The cells seeded (40.000 cells/well) and differentiated with 5 nM phorbol 12-myristate 13-acetate (PMA; Sigma) for 48 h, equilibrated with complete medium for 24 h, and serum-starved for 48 h. The cells were then stimulated with 20 ng/ml TNF (R&D Systems) for 48 h. Zymography on culture supernatants was performed essentially as described above. Cell proliferation rate was assessed using WST-1 assay (Sigma) according to the manufacturer's instructions. Cell viability was assessed by CytoTox-ONE™ Homogeneous Membrane Integrity Assay (Promega) according to the manufacturer's instructions. The zymography results were normalized to the cell proliferation index.

SMC Culture and Stimulation

Fetal human primary aortic SMCs (Cell Applications) were grown in Smooth Muscle Cell Growth Medium (Cell Applications) supplemented with 5,000 U/ml penicillin and 5,000 μg/ml streptomycin. Cells from passages 3–10 were used.

The cells were seeded at HSA- and MFAP4-coated plates essentially as described above (16.800 cells/well), starved overnight in Smooth Muscle Cell Basal Medium (Cell Applications) and stimulated with indicated concentrations of TNF or Ang II for 24 h. Zymography on culture supernatants was performed essentially as described above.

Human Monocyte Isolation

Human peripheral blood mononuclear cells were isolated from buffy coats obtained from the local blood bank (permit nr DP086) using Ficoll-Paque Plus density gradient centrifugation (GE Healthcare). Briefly, the samples were layered over 15 ml of Ficoll and centrifuged brake-free for 25 min at 800 g at room temperature. The interface was removed and washed twice with PBS containing 2% FBS and 1 mM EDTA. The cells were resuspended in PBS containing 2% FBS and 1 mM EDTA. The monocytes were enriched using the EasySep™ Human CD14 Positive Selection Kit (Stemcell Technologies) according to the manufacturer's instructions. The purity of isolated monocytes was tested by flow cytometry immediately after isolation by staining with anti-CD14-FITC antibody (BD Biosciences) and was >97% in all experiments.

Monocyte Migration Assay

The lower sides of the Transwell inserts with 5.0 μm pores (Corning) were coated with 10 μg/cm^2 MFAP4 or HSA overnight at 4°C, washed with PBS, blocked with 10 mg/ml HSA for 1 h at room temperature and washed again. The monocytes were seeded in the upper chamber (100.000 cells/insert) in serum-free RPMI medium containing 0.5% FBS. In some experiments, the cells were pre-incubated with anti-integrin $\alpha_V\beta_3$, anti-integrin $\alpha_V\beta_5$ (both from Merck Millipore), or isotype control antibody (Thermo Fisher) for 30 min at room temperature before seeding. The lower chamber contained serum-free RPMI medium with 0.5% FBS ± 100 ng/ml human recombinant CCL-2 (R&D

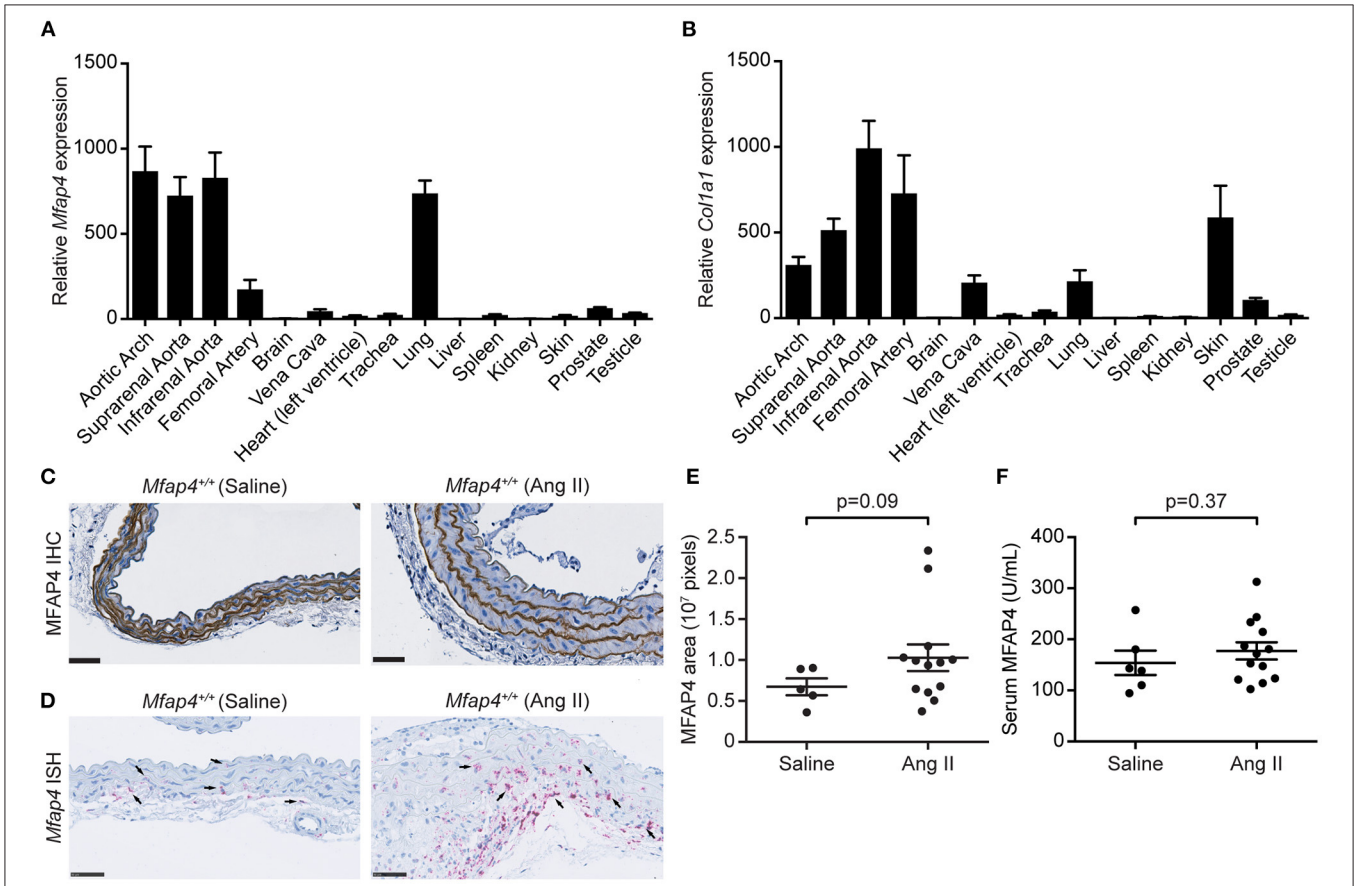

FIGURE 1 | MFAP4 expression in normal aorta and AAA tissue. **(A,B)** Quantitative real-time PCR analysis of **(A)** *Mfap4* and **(B)** *Col1a1* mRNA transcripts in C57BL/6N mouse tissues ($n = 7$). Expression levels are normalized against eukaryotic 18S rRNA and presented as means + SEM. **(C,D)** Representative images of **(C)** MFAP4 immunohistochemical staining (IHC) and **(D)** *Mfap4 in situ* hybridization staining (ISH) in abdominal aortic sections in saline-infused and Ang II-infused *ApoE*$^{-/-}$ (*Mfap4*$^{+/+}$) mice. Black arrows indicate examples of positive cells. $n = 5$–13. Scale bar = 50 μm. **(E)** Semi-quantitation of MFAP4 IHC staining intensity in the aortas of saline- and Ang II-infused *ApoE*$^{-/-}$ mice. **(F)** MFAP4 concentration in serum from saline- and Ang II-infused *ApoE*$^{-/-}$ mice. Data are analyzed with Mann-Whitney *U*-test.

Systems). The cells were allowed to migrate for 3 h, after which the upper sides of the filters were washed with PBS and swiped with a cotton swab to remove any non-migrated cells. The lower sides of the filters were then stained with Hemacolor (Sigma) and divided into four fields. The migrated cells in each field were counted in a blinded manner by two independent investigators.

Statistical Analysis

The normality of data was assessed using Shapiro-Wilk test. Levene's test was used to assess equality of variances. Non-normally distributed data were analyzed using Mann-Whitney *U*-test. Normally distributed data were analyzed using one-way ANOVA or Student's *t*-test. Comparisons of aneurysm incidence were performed using Fisher's exact test. Data are presented as means + SEM unless otherwise stated. Significance was accepted if $p < 0.05$. All statistical analyses were performed using GraphPad Prism (GraphPad.com).

RESULTS

MFAP4 Expression in Normal Aorta and AAA

Initially, we performed RT-qPCR analysis to assess the relative *Mfap4* mRNA levels in the aorta as well as 19 additional tissues from wild-type C57BL/6N mice. The relative expression levels of *Mfap4* were highest in the lung and arteries (**Figure 1A**). MFAP4

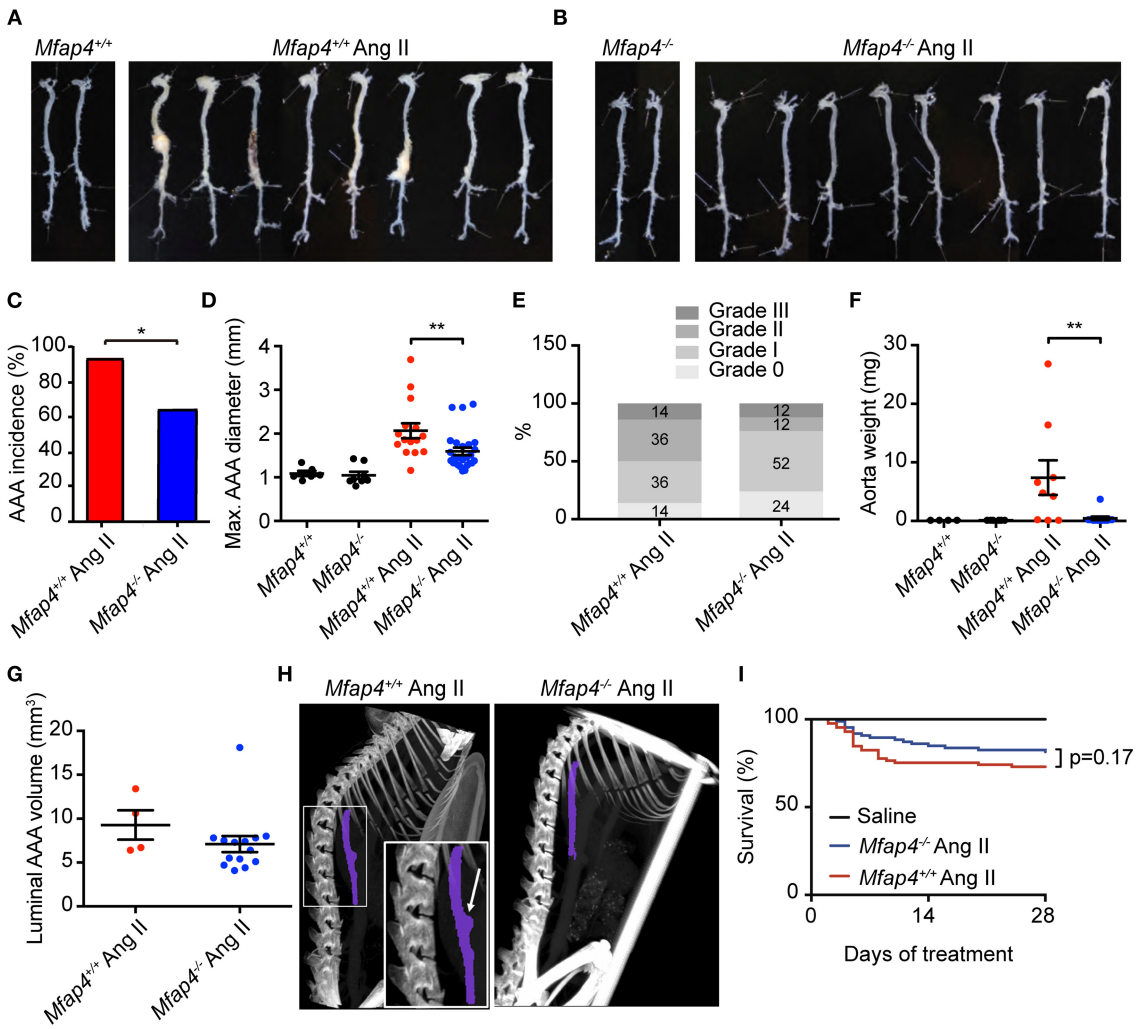

FIGURE 2 | *Mfap4* deficiency attenuates Ang II-induced AAA development. **(A,B)** Representative photographs of dissected aortic segments from the aortic arch to the iliac bifurcation from **(A)** *ApoE*$^{-/-}$ (*Mfap4*$^{+/+}$) and **(B)** *ApoE*$^{-/-}$*Mfap4*$^{-/-}$ (*Mfap4*$^{-/-}$) mice infused with saline (left panels) or Ang II (right panels) for 28 days. **(C)** AAA incidence. $n = 15$ (*Mfap4*$^{+/+}$ Ang II), 26 (*Mfap4*$^{-/-}$ Ang II). **(D)** Quantification of maximal AAA diameter. $n = 6$–8 (saline), 15–26 (Ang II). **(E)** AAA severity scoring. $n = 14$ (*Mfap4*$^{+/+}$ Ang II), 25 (*Mfap4*$^{-/-}$ Ang II). **(F)** Quantification of dissected aorta weight. $n = 4$–6 (saline), 9–12 (Ang II). **(G)** Quantification of luminal AAA volume assessed by micro-CT. $n = 4$ (*Mfap4*$^{+/+}$ Ang II), 14 (*Mfap4*$^{-/-}$ Ang II). **(H)** Representative micro-CT images of the vascular luminal volume spanning a distance of 4 vertebrae after 28 days of Ang II infusion. Purple color demarks the investigated region of interest. The arrow indicates an aortic AAA. **(I)** Survival analysis. *$p < 0.05$, **$p < 0.01$, analyzed with Fisher's exact test **(C)** or Mann-Whitney *U*-test **(D–F)**.

is an ECM molecule with the capacity to bind various ECM fibers including collagen (21). In line with this, the tissue expression profile of type I collagen (*Col1a1*) mRNA resembled the *Mfap4* expression profile (**Figure 1B**).

In agreement with previous observations (16), MFAP4 was predominantly localized to the arterial elastic fibers by immunohistochemistry, and this localization was unaltered after 28 days of Ang II infusion (**Figure 1C**). To identify *Mfap4*-expressing cells, we performed *in situ* hybridization staining for *Mfap4* transcript that revealed that *Mfap4* mRNA is expressed in adventitial cells (presumably adventitial fibroblasts) and medial SMCs and that it is upregulated upon AAA infusion (**Figure 1D** and **Supplementary Figure 3**). Ang II-induced AAA development did not significantly impact MFAP4 deposition within the aortic ECM (**Figure 1E**) or circulating serum MFAP4 levels (**Figure 1F**).

Mfap4 Deficiency Does Not Affect HR, MAP, and Heart Weight Development After Ang II Infusion

Following, we assessed the changes in basic physiological parameters after Ang II infusion. We have previously reported that MAP is not affected by *Mfap4* ablation in unchallenged mice when measured over periods of minutes-to-hours 5 days after placing indwelling catheters (16). In the present study, HR and MAP were measured continuously for 7 days using indwelling catheters in conscious $ApoE^{-/-}$ and $ApoE^{-/-}Mfap4^{-/-}$ mice infused with Ang II. A significantly increased HR and a tendency for increased MAP was observed in the active night period (6 p.m. to 6 a.m.) compared to the day period (6 a.m. to 6 p.m.) for both $ApoE^{-/-}$ and $ApoE^{-/-}Mfap4^{-/-}$ mice after Ang II treatment. However, we did not observe any significant differences in either HR or MAP between Ang II-infused $ApoE^{-/-}$ and $ApoE^{-/-}Mfap4^{-/-}$ mice (**Supplementary Figures 4A,B**). Likewise, heart weight and heart-to-body weight ratio were significantly increased after Ang II infusion but not influenced by *Mfap4* genotype (**Supplementary Figures 4C,D**).

Mfap4 Deficiency Attenuates Ang II-Induced AAA Development

We next asked whether MFAP4 plays a role in the development of Ang II-induced AAA. As expected, none of the saline-infused mice developed AAAs. In contrast, 28 day-long Ang II infusion caused suprarenal AAA development, with $ApoE^{-/-}Mfap4^{-/-}$ mice showing a significantly lower incidence rate (62%) compared to 93% incidence rate in $ApoE^{-/-}$ mice (**Figures 2A–C**). Moreover, Ang II-infused $ApoE^{-/-}Mfap4^{-/-}$ mice exhibited significantly lower maximal outer AAA diameter compared to $ApoE^{-/-}$ *mice* (**Figure 2D**) as well as ameliorated AAA severity (**Figure 2E**). The dissected aorta weight was significantly reduced from 7.4 ± 3.0 mg in Ang II-treated $ApoE^{-/-}$ mice to 0.4 ± 0.3 mg in $ApoE^{-/-}Mfap4^{-/-}$ mice (**Figure 2F**). A similar trend was observed in the vascular luminal volume between $ApoE^{-/-}$ and $ApoE^{-/-}Mfap4^{-/-}$ mice when measured over a distance of four specific vertebrae using micro-CT in a limited number of samples (**Figures 2G,H**). On the other hand, there was no significant difference in survival (caused by early aneurysm rupture) between $ApoE^{-/-}$ and $ApoE^{-/-}Mfap4^{-/-}$ mice (**Figure 2I**). In addition, no effect of Ang II infusion or MFAP4 deficiency was observed on serum total cholesterol or triglyceride levels (**Supplementary Figure 5**).

Mfap4 Deficiency Reduces Macrophage Infiltration, MMP Activity, and FAK Activation in Ang II-Induced AAAs

Following, we evaluated the MFAP4-dependent changes in the inflammatory responses within the aortic wall. Ang II-induced inflammatory infiltration, quantified as the CD45-positive area, was significantly attenuated within the aortas of $ApoE^{-/-}Mfap4^{-/-}$ mice compared to $ApoE^{-/-}$ littermates (**Figures 3A,B**). Moreover, Ang II-infused $ApoE^{-/-}Mfap4^{-/-}$ mice showed a potent reduction in CD11b-positive area in the aortas of Ang II-infused $ApoE^{-/-}Mfap4^{-/-}$ mice compared to $ApoE^{-/-}$ littermates (**Figures 3C,D**), suggesting monocytes/macrophages to be the affected leukocyte type. We confirmed this by staining for another macrophage marker F4/80, which yielded comparable results (data not shown). Furthermore, CD11b-positive area analyzed exclusively within the adventitial layer was also significantly lowered in Ang II-infused $ApoE^{-/-}Mfap4^{-/-}$ mice compared to $ApoE^{-/-}$ littermates (**Supplementary Figure 6**).

We further analyzed aortic tissue lysates (collected at day 9) by zymography to investigate MMP activity in Ang II-infused mice (**Figure 3E**). We observed a significant decrease in both MMP-2 (**Figure 3F**) and MMP-9 (**Figure 3G**) activity in Ang II-infused $ApoE^{-/-}Mfap4^{-/-}$ mice compared to $ApoE^{-/-}$ littermates. To confirm that, we analyzed MMP protein expression in aortic sections and found that both MMP-2 and MMP-9 expression, localized predominantly in the adventitial layer, were significantly decreased in Ang II-infused $ApoE^{-/-}Mfap4^{-/-}$ mice compared to $ApoE^{-/-}$ littermates (**Figures 3H–K**). These results suggest that MFAP4 promotes inflammatory responses in macrophages during AAA development.

As integrin receptors serve as main MFAP4 cellular ligands, we stained AAA sections for pFAK as a proxy for activation of integrin signaling pathways. We observed that total pFAK-positive adventitial area as well as pFAK-positive area normalized to adventitial area were significantly reduced in Ang II-infused $ApoE^{-/-}Mfap4^{-/-}$ mice compared to $ApoE^{-/-}$ littermates (**Figures 3L,M** and not shown).

Mfap4 Deficiency Reduces Cellular Proliferation, Apoptosis, and Microvessel Number in Ang II-Induced AAAs

Medial α-SMA-positive area remained unchanged between Ang II-infused $ApoE^{-/-}$ and $ApoE^{-/-}Mfap4^{-/-}$ mice (**Figures 4A,B**).

We then investigated the degree of cellular apoptosis and proliferation within the vessel wall. Ang II infusion resulted in an overall increase in both cleaved caspase 3-positive area and Ki-67 positive cell number. Apart

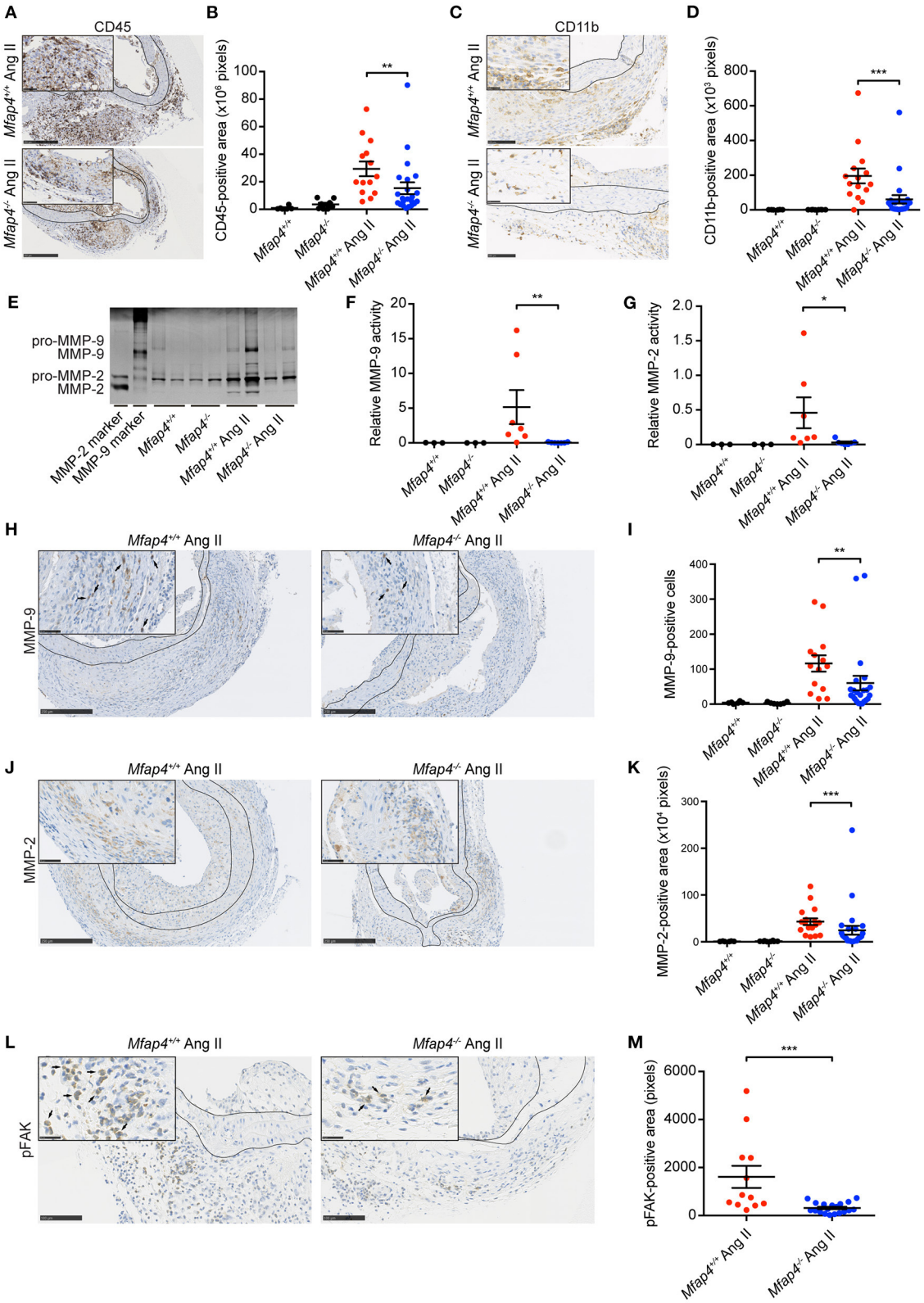

FIGURE 3 | *Mfap4* deficiency reduces macrophage infiltration, MMP activity, and FAK activation in Ang II-induced AAAs. **(A–D)** Morphometric analysis of **(A,B)** CD45 and **(C,D)** CD11b stainings of aortic sections of *ApoE*$^{-/-}$ (*Mfap4*$^{+/+}$) and *ApoE*$^{-/-}$*Mfap4*$^{-/-}$ (*Mfap4*$^{-/-}$) mice after 28 days of Ang II infusion. $n = 6–8$ (saline), 14–24

(Continued)

FIGURE 3 | (Ang II). **(E–G)** Representative MMP zymogram **(E)** of aortic lysates from saline- and Ang II-infused mice after 9 days with corresponding densitometric quantification of **(F)** MMP-9 and **(G)** MMP-2 activity. $n = 3–7$. **(H–M)** Morphometric analysis of **(H,I)** MMP-9, **(J,K)** MMP-2, and **(L,M)** phosphorylated FAK (pFAK) stainings of aortic sections of $ApoE^{-/-}$ ($Mfap4^{+/+}$) and $ApoE^{-/-}Mfap4^{-/-}$ ($Mfap4^{-/-}$) mice after 28 days of Ang II infusion. Black arrows indicate examples of positive cells. Black lines delineate borders between intimal, medial and adventitial layers. $n = 6–8$ (saline), 12–26 (Ang II). Representative pictures are shown. Scale bar = 250 μm/50 μm **(A,H,J)**, 100 μm/25 μm **(B,L)**. $^{*}p < 0.05$, $^{**}p < 0.01$, $^{***}p < 0.001$, analyzed with Mann-Whitney *U*-test.

from few isolated cells found throughout the tissue, the majority of cleaved caspase 3-positive staining was localized within the media at the sites of SMC degeneration. Ang II-induced apoptosis was significantly attenuated in $ApoE^{-/-}Mfap4^{-/-}$ mice compared to $ApoE^{-/-}$ littermates (**Figures 4C,D**).

On the other hand, Ki-67-positive cells were found throughout the vessel wall but predominantly in the adventitial layer. Ki-67 positive cell number was significantly reduced in Ang II-infused $ApoE^{-/-}Mfap4^{-/-}$ mice compared to $ApoE^{-/-}$ littermates (**Figures 4E,F**). Moreover, double immunofluorescent staining revealed that while single SMA-positive medial SMCs stained positive for Ki-67 (**Figure 4G**), the vast majority of Ki67-positive cells were CD45-positive infiltrating leukocytes (**Figure 4H**).

CD31-positive microvessels were essentially undetectable in aortic tissues from control mice, while numerous capillary vessels were observed in Ang II-infused aortas after 28 days. Ang II-infused $ApoE^{-/-}Mfap4^{-/-}$ mice exhibited a 78% reduction in the observed number of microvessels compared to $ApoE^{-/-}$ mice (**Supplementary Figure 7**).

Mfap4 Deficiency Limits Elastic Membrane Disruption as Well as Collagen Deposition and Associated Fibrotic Signaling in Ang II-Induced AAAs

Ang II infusion resulted in elastic membrane disruption that was significantly attenuated in $ApoE^{-/-}Mfap4^{-/-}$ mice compared to $ApoE^{-/-}$ littermates (**Figures 5A,B**).

We also analyzed AAA-linked fibrotic changes within the vessel wall. Ang II treatment induced adventitial collagen deposition that was significantly decreased in Ang II-infused $ApoE^{-/-}Mfap4^{-/-}$ mice compared to $ApoE^{-/-}$ littermates (**Figures 5C,D**). To investigate the related mechanisms, we stained AAA sections for pSMAD2 and pSMAD3, key mediators of pro-fibrotic TGF-β signaling. While the medial pSMAD-positive area was modestly influenced by MFAP4 genotype (**Supplementary Figure 8**), both the pSMAD2- and pSMAD3-positive area in the adventitia were highly reduced in Ang II-infused $ApoE^{-/-}Mfap4^{-/-}$ mice compared to $ApoE^{-/-}$ littermates (**Figures 5E–H**), showing that activation of TGF-β-dependent downstream signaling is significantly attenuated by MFAP4 deficiency.

MFAP4 Promotes Monocyte Chemotaxis

To confirm our *in vivo* findings and better understand the molecular mechanisms behind MFAP4-mediated regulation of inflammatory infiltration, we evaluated the role of MFAP4 in chemotaxis of blood monocytes. We observed that MFAP4 alone was able to stimulate directional monocyte migration and that this increase could be inhibited by blocking integrin $\alpha_V\beta_3$ but not integrin $\alpha_V\beta_5$ (**Figures 6A,B**). We observed a similar tendency for monocyte chemotaxis toward CCL-2, although it did not reach statistical significance (**Figures 6A,B**).

MFAP4 Stimulation Induces MMP-9 Activity in Macrophage-Like Cells *in vitro*

Finally, we investigated if MFAP4 has a direct effect on MMP production in SMCs and macrophage-like cells. We stimulated fetal aortic SMCs and PMA-differentiated THP-1 cells with immobilized MFAP4 with or without TNF co-stimulation. MMP-2 activity in fetal aortic SMCs was independent of MFAP4 regardless of TNF or Ang II stimulation (**Supplementary Figure 9A**). Conversely, we observed that while TNF stimulation resulted in an overall increase in MMP-9 activity in PMA-differentiated THP-1 cells, co-stimulation with MFAP4 significantly potentiated MMP-9 activity when compared to TNF stimulation alone (**Figure 6C**). THP-1 cell proliferation or viability after TNF stimulation were not significantly influenced by MFAP4 (**Supplementary Figures 9B,C**).

DISCUSSION

In the present study, we evaluated the role of MFAP4 in AAA pathology in mice. We showed that MFAP4 is abundantly expressed in the arteries and that its mRNA expression is upregulated after Ang II infusion. Furthermore, we demonstrated that Ang II-induced AAA formation is attenuated in *Mfap4*-deficient mice due to reduced macrophage infiltration, MMP activity, integrin signaling and vascular remodeling. We also showed that MFAP4 directly induces monocyte migration and MMP-9 activity. Thus, MFAP4 contributes to the weakening of the aortic wall and aggravates vascular pathology in an Ang II-driven model of AAA (**Figure 7**).

MFAP4 is a structural and functional component of elastic fibers throughout the body, abundantly present within the vascular ECM. Such expression pattern sets MFAP4 apart from the "matricellular" proteins, described to be non-structural, cell-activating ECM proteins that are virtually absent during homeostasis but show a dynamic upregulation during vascular pathogenesis (22). The present study supports a permissive role for MFAP4 in the induction of pathological

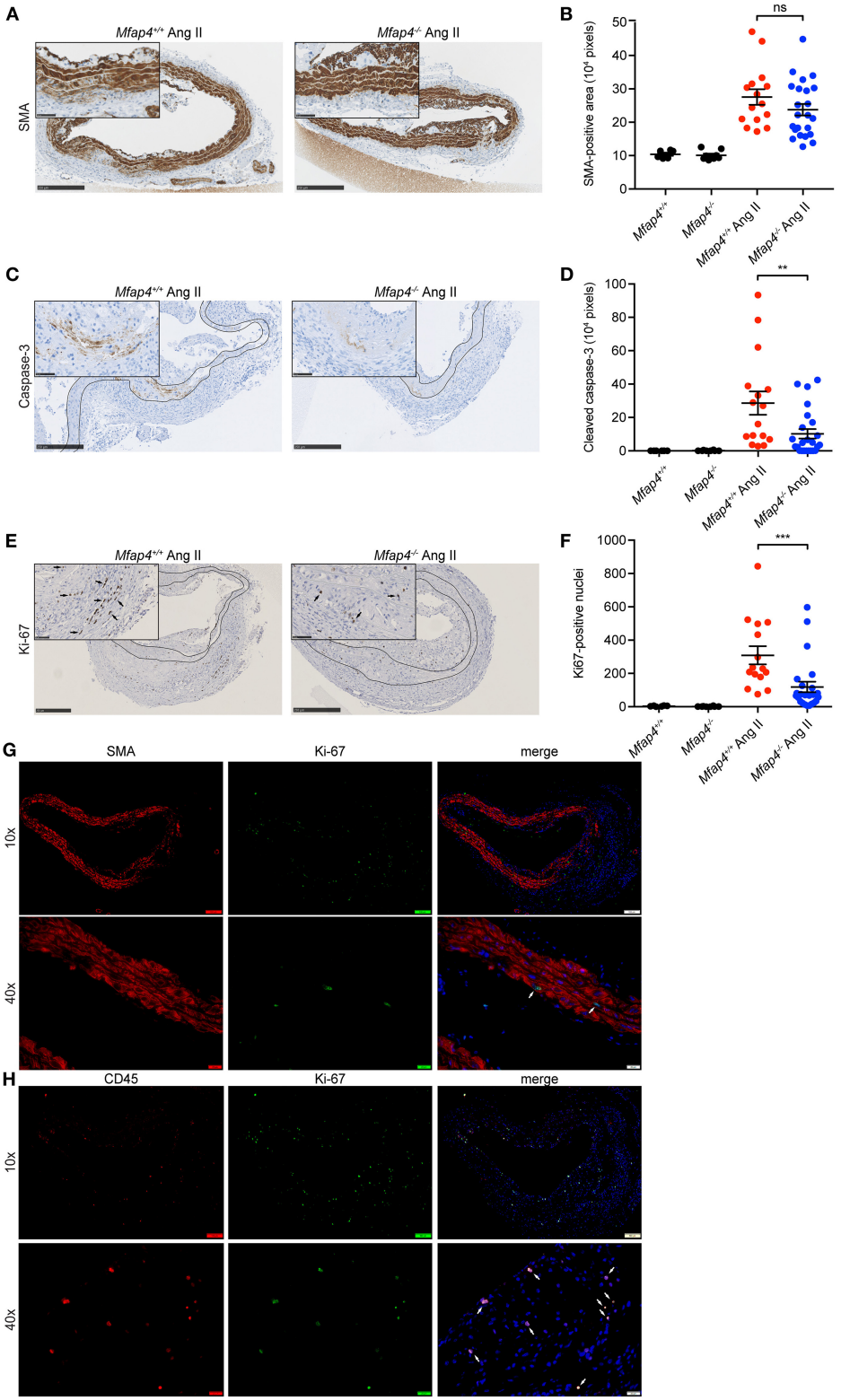

FIGURE 4 | *Mfap4* deficiency reduces cellular proliferation and apoptosis in Ang II-induced AAAs. Morphometric analysis of **(A,B)** α-smooth muscle actin (SMA), **(C,D)** cleaved caspase-3, and **(E,F)** Ki-67 stainings of aortic sections of *ApoE*$^{-/-}$ (*Mfap4*$^{+/+}$) and *ApoE*$^{-/-}$*Mfap4*$^{-/-}$ (*Mfap4*$^{-/-}$) mice after 28 days of Ang II infusion. Black arrows indicate examples of positive cells. Black lines delineate borders between intimal, medial and adventitial layers. **(G,H)** Double immunofluorescent staining of Ki-67 and SMA **(G)** or CD45 **(H)**. White arrows indicate examples of double-positive cells. $n = 6$–8 (saline), 15–26 (Ang II). Representative pictures are shown. Scale bar = 250 μm/50 μm **(A,C,E)**, 100 μm/20 μm **(G,H)**. $^{**}p < 0.01$, $^{***}p < 0.001$, analyzed with Mann-Whitney *U*-test. ns, non-significant.

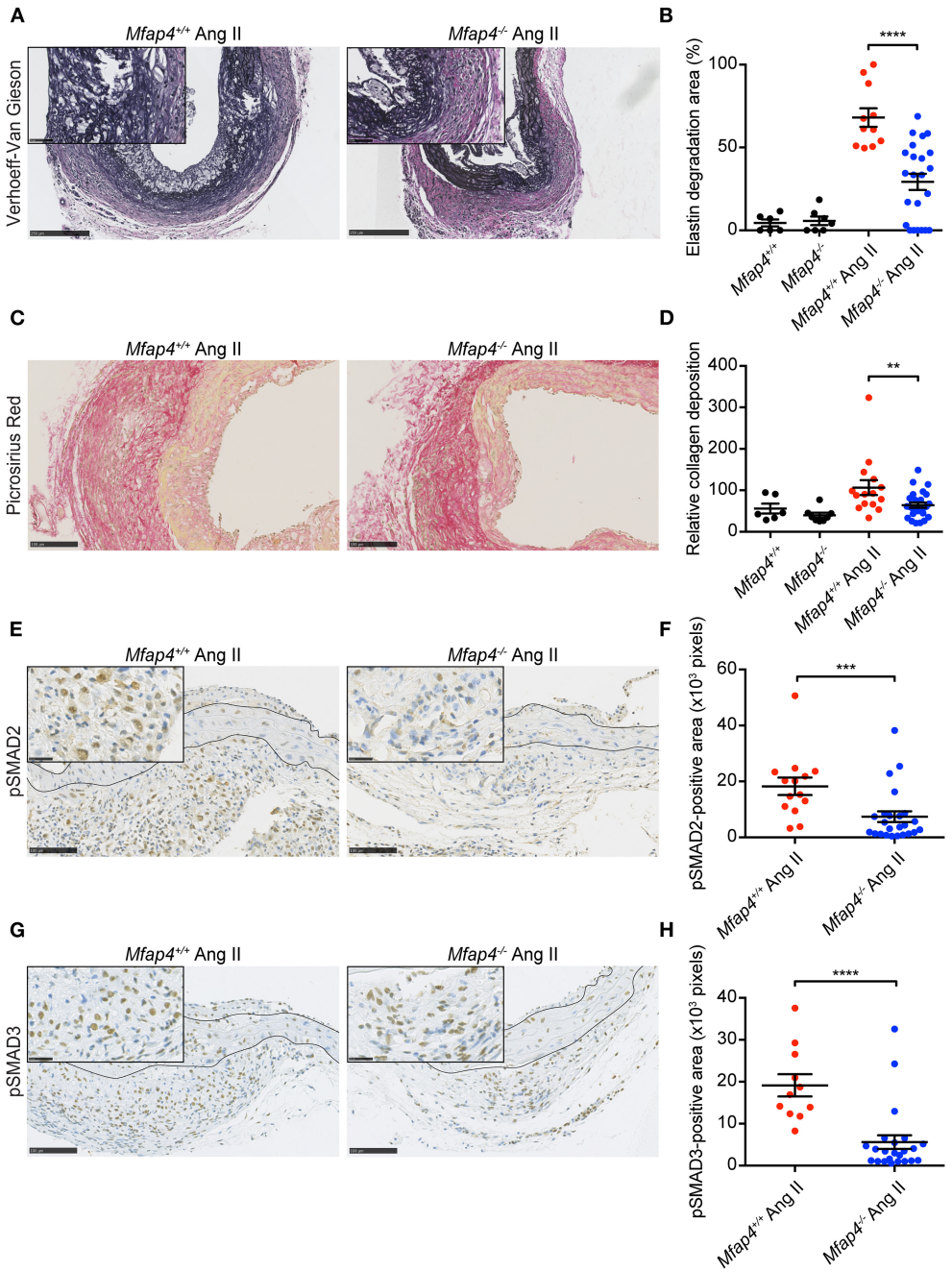

FIGURE 5 | *Mfap4* deficiency limits elastic membrane disruption, collagen deposition and fibrotic signaling in Ang II-induced AAAs. Morphometric analysis of **(A,B)** elastin (Verhoeff-Van Gieson) staining, **(C,D)** collagen (Picrosirius Red) staining, **(E,F)** phosphorylated SMAD2 (pSMAD2) staining and **(G,H)** phosphorylated SMAD3 (pSMAD3) staining of aortic sections of *ApoE*$^{-/-}$ (*Mfap4*$^{+/+}$) and *ApoE*$^{-/-}$*Mfap4*$^{-/-}$ (*Mfap4*$^{-/-}$) mice after 28 days of Ang II infusion. Black lines delineate borders between intimal, medial and adventitial layers. n = 6–8 (saline), 11–26 (Ang II). Representative pictures are shown. Scale bar = 250 μm/50 μm **(A)**, 100 μm **(C)**, 100 μm/25 μm **(E,G)**. $^{**}p < 0.01$, $^{***}p < 0.001$, $^{****}p < 0.0001$, analyzed with Mann-Whitney *U*-test.

vascular remodeling, previously established for outward arterial remodeling in neointima formation (16). The eliciting factors in MFAP4-mediated AAA progression may be the disease-related upregulation of integrin expression as well as concomitant growth factor signaling, known to potentiate the integrin-dependent cellular responses (23). Indeed, RGD-dependent integrin expression is induced and correlates to the degree of vascular inflammation in the Ang II-induced AAA model (24), suggesting it to be a primary driver of MFAP4-mediated effects.

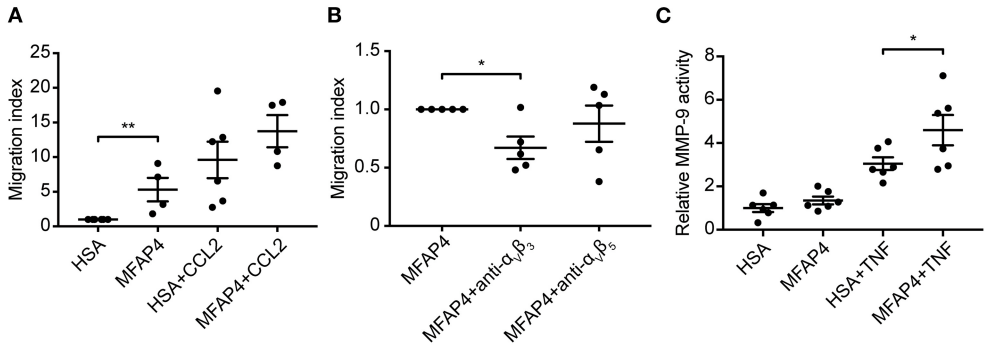

FIGURE 6 | MFAP4 induces monocyte migration and MMP-9 activity in macrophage-like cells *in vitro*. **(A)** MFAP4 acts as a haptoattractant for human blood monocytes. **(B)** MFAP4-dependent monocyte directional migration can be inhibited by anti-integrin $\alpha_V\beta_3$ antibody. **(C)** MFAP4 stimulation potentiates TNF-induced MMP-9 activity in differentiated THP-1 macrophage-like cells. $n = 4$–6 independent experiments. $^*p < 0.05$, $^{**}p < 0.01$, analyzed with paired *t*-test and repeated measures ANOVA followed by Bonferroni's test.

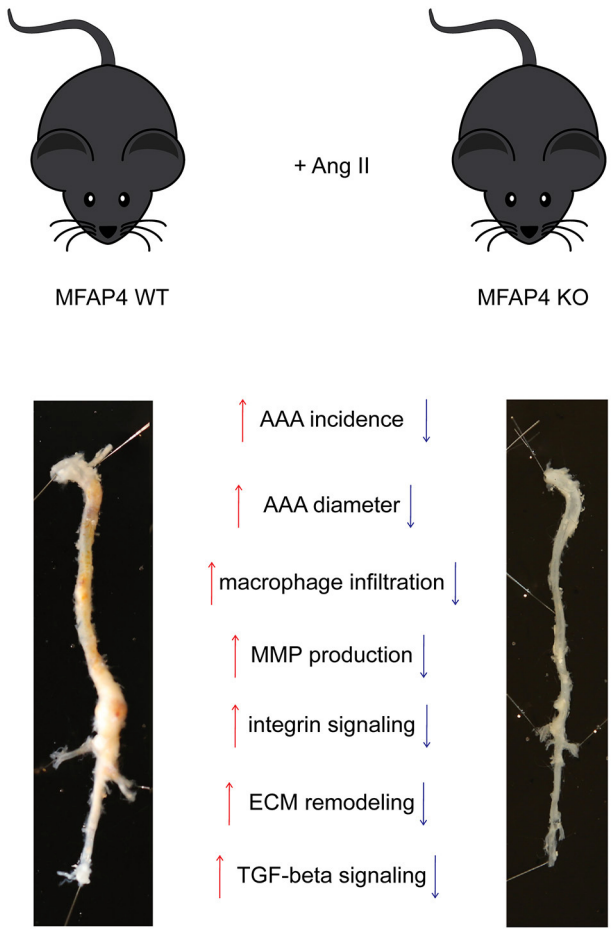

FIGURE 7 | MFAP4 deficiency protects against Ang II-induced AAA pathology. Overview of the identified actions of MFAP4 in Ang II-induced AAA.

MFAP4 has previously been localized to the vessel wall, but the exact aortic cell types responsible for its production and deposition have not been investigated in detail. By using *in situ* hybridization, we showed that MFAP4 transcript expression localized predominantly to adventitial cells (possibly fibroblasts) and to a lesser extent also to medial cells (vascular SMCs). Our findings are in line with recent single cell RNAseq data, where MFAP4 was found to be expressed mainly in various fibroblast subpopulations and only to a minor degree by mural cells such as vascular SMCs and pericytes (25, 26). Further investigations are needed to confirm the expression of MFAP4 in adventitial fibroblasts and identify the specific fibroblast subset responsible for MFAP4 upregulation in AAA.

The hallmark pathology of AAA is the destruction of elastic lamellae within the aortic media, associated with vessel expansion. While multiple MMPs have been reported as necessary in this aspect of AAA formation, MMP-2 and MMP-9 play a particularly important role (17), and the absence of either MMP-2 and MMP-9 is associated with lower incidence of experimental AAAs (27). In the present study, we showed that MFAP4 deficiency significantly decreased both MMP-2 and MMP-9 expression and activity. These MFAP4-dependent differences appeared to be of sufficient magnitude to infer significant changes in elastin integrity.

The cellular sources of MMPs include mesenchymal cells as well as macrophages and other leukocytes, with MMP-2 and MMP-9 predominantly derived from vascular SMCs and macrophages, respectively (28–30). Importantly, integrin $\alpha_V\beta_3$ has been reported to promote cellular production of MMPs (31). We found that MFAP4 effectively stimulated MMP-9 activity in differentiated THP-1 cells *in vitro*. Conversely, vascular SMC production of MMP-2 seemed to be independent of MFAP4. While the observed effects might be cell type-specific and depend e.g., on integrin abundance and activation status, they imply an essential role for MFAP4 in driving MMP-9 production in macrophages.

MFAP4 engagement in MMP synthesis has previously been reported in human skin, where MFAP4 appeared to protect collagen integrity by reducing MMP-12 activity after UV light exposure (32). Moreover, MFAP4 is known to accelerate

tropoelastin assembly into elastic fibers (13), and *Mfap4*-deficient mice develop a mild age-induced airspace enlargement linked to loss of alveolar surface (15), both indicating that MFAP4 contributes to ECM stability. These previous observations suggest that the role of MFAP4 may change from maintenance of proper tissue architecture during normal homeostatic conditions toward promotion of inflammation and remodeling in pathological settings.

Monocytes and macrophages play a critical role in vascular injury. Macrophages, arising mainly from circulating monocytes, constitute a major inflammatory cell type within AAA lesions (33). Monocyte adhesion, migration, and MMP-9 production are all increased in AAA patients and lead to aneurysm expansion (34). Here we demonstrated that Ang II-driven macrophage recruitment was significantly limited in *Mfap4*-deficient mice and that MFAP4 directly promoted haptotactic migration of monocytes via integrin $\alpha_V\beta_3$ ligation. In line with that, integrin $\alpha_V\beta_3$ blockade has been previously reported to attenuate monocyte/macrophage infiltration both *in vitro* and within the vessel wall (35, 36). Further supporting our observations, the crucial mediator of integrin signaling FAK has been shown to stimulate macrophage motility and MMP synthesis in experimental AAA. Importantly, activated FAK has been localized predominantly to adventitial macrophages and only rarely to medial SMCs (37). In agreement with that, we found that MFAP4 promotes FAK activation specifically in the adventitia. Taken together, these findings strongly suggest that MFAP4-integrin interaction and subsequent downstream FAK signaling promote monocyte/macrophage recruitment and activation.

Circulatory MFAP4 has been previously associated with fibrotic deposition and cirrhosis in hepatitis C as well as other conditions leading to fibrogenesis of the liver (10, 11). Moreover, direct induction of collagen synthesis in white blood cells after treatment with MFAP4 has been demonstrated (38). Together, these observations imply that MFAP4 may directly affect collagen synthesis. In agreement with that, we observed the MFAP4-dependent increase in adventitial pSMAD staining in Ang II-induced AAA. Phosphorylation of SMAD2 and SMAD3 is a key step in pro-fibrotic signaling leading to collagen deposition (39). Indeed, MFAP4 deficiency has been shown to attenuate kidney and cardiac fibrosis (40, 41), further underlining MFAP4 involvement in fibrotic tissue remodeling. Importantly, upregulation of pSMADs and other crucial components of the TGF-β signaling pathway has been reported in AAA patient samples (42). As TGF-β signaling is mostly suggested to exert a protective role in AAA pathology (43), this dysregulated, exaggerated response might be a compensatory mechanism to the pathological changes happening in the aortic wall.

MFAP4 is a ligand for integrins $\alpha_V\beta_3$ and $\alpha_V\beta_5$, known inducers of neovascularization (44). Angiogenesis has been associated with the risk of AAA rupture and complications (45) and is suggested to result mainly from the growth factor signaling inferred by inflammatory cells accumulating within the vessel wall (46). Therefore, the observed reduction of aortic microvessel number in *Mfap4*-deficient animals was expected. However, we did not further investigate the mechanistic role of MFAP4 in angiogenesis in this study.

Several studies have supported that clinical MFAP4 levels may be influenced by the presence of vascular aneurysms. However, the pattern of MFAP4 regulation has shown inconsistency (47–49), and a role of MFAP4 in clinical AAA remains unknown. We have recently shown that high plasma MFAP4 is associated with reduced risk of undergoing later surgical repair in AAA (50); however, this observation needs validation in an independent cohort.

An imbalance of the renin-angiotensin system has been associated with the pathogenesis of AAA (51), and Ang II-induced AAA formation in $ApoE^{-/-}$ mice shares many characteristic features of the human disease, including chemokine generation, macrophage infiltration, and neovascularization (18). However, weaknesses of our study include that we only used a single model of AAA formation and thus cannot rule out whether the observed MFAP4-mediated effects are exclusively dependent on Ang II treatment. Particularly, Ang II infusion also results in development of atherosclerosis, and the importance of MFAP4 in atherosclerosis-independent AAA model remains to be investigated. On the other hand, as significant atherosclerotic lesions are first observed beyond 28 days of Ang II treatment (52), and the AAA lesions can be induced (although with lowered incidence) also in normolipidemic mice (53), it seems that atherosclerosis might develop independently of AAA. Also, we have not addressed if MFAP4, apart from its direct haptotactic effects, can promote monocyte migration indirectly through upregulation of chemokine expression or integrin receptor availability. Finally, we did not investigate thrombus formation and biomechanical properties, which also contribute to AAA formation (54) and could be affected by the observed *Mfap4*-deficient phenotype.

In conclusion, our study provides evidence that MFAP4 deficiency alleviates macrophage accumulation and MMP production, leading to attenuated AAA formation. Even though contemporary interventions have considerably reduced the mortality of AAA (55, 56), the remaining high mortality rate warrants the search for new pharmacological approaches against AAA progression. Our findings strongly indicate that MFAP4 aggravates vascular inflammation and remodeling, suggesting that MFAP4 targeting may be a novel potential therapeutic avenue for vascular inflammatory diseases.

DATA AVAILABILITY STATEMENT

The raw data supporting the conclusions of this article will be made available by the authors, without undue reservation.

ETHICS STATEMENT

The animal study was reviewed and approved by National Animal Experiments Inspectorate of Denmark.

AUTHOR CONTRIBUTIONS

AS, JS, G-PS, and GS conceived the study. BP, PC, KK-M, AS, KK, MD, NPM, SH, and CB performed the experiments and

analyzed the data. JS, PH, TA, JM, NM, and VA participated in data analysis. BP, PC, KK-M, and GS wrote the manuscript. All authors revised and approved the manuscript.

FUNDING

This work was supported by Novo Nordisk Fonden—project grants in clinical and translational medicine (22360), the Danish Research Council (7016-00038B), the Lundbeck Foundation (R164-2013-15355), Th. Maigaards eftf. Fru Lily Benthine Lunds Fond af 1.6.1978, Familien Hede Nielsens Fond, Snedkermester Sophus Jacobsen og Hustru Astrid Jacobsens Fond, Beckett Fonden, Fonden til Lægevidenskabens Fremme, Fondsbørsvekselerer Henry Hansen og Hustru Karla Hansen Født Vestergaards Legat, Frimodt-Heineke Fonden, and Torben og Alice Frimodts Fond.

ACKNOWLEDGMENTS

We thank Lisbet Mortensen and Lone Christiansen (Department of Pathology, Odense University Hospital, Odense, Denmark) for performing tissue processing and immunohistochemical stainings, Karen Bentsen (Biomedical Laboratory, Institute of Molecular Medicine, University of Southern Denmark, Odense, Denmark) for performing serum lipid measurements, Vivi Monrad (Department of Cardiovascular and Renal Research, Institute of Molecular Medicine, University of Southern Denmark, Odense, Denmark) for performing the catheter insertions for blood pressure measurement, Malene Hykkelbjerg Nielsen (Department of Pathology, Odense University Hospital, Odense, Denmark) for performing ISH stainings, Bente Finsen (Department of Neurobiology Research, Institute of Molecular Medicine, University of Southern Denmark, Odense, Denmark) for access to the fluorescent microscope, and Vicki Nielsen, Charlotte Skouboe and especially Tine D. Rasmussen (Department of Cancer and Inflammation Research, Institute of Molecular Medicine, University of Southern Denmark, Odense, Denmark) for expert technical assistance.

SUPPLEMENTARY MATERIAL

The Supplementary Material for this article can be found online at: https://www.frontiersin.org/articles/10.3389/fcvm.2021.764337/full#supplementary-material

REFERENCES

1. Nordon IM, Hinchliffe RJ, Loftus IM, Thompson MM. Pathophysiology and epidemiology of abdominal aortic aneurysms. *Nat Rev Cardiol.* (2011) 8:92–102. doi: 10.1038/nrcardio.2010.180
2. Anjum A, Powell JT. Is the incidence of abdominal aortic aneurysm declining in the 21st century? Mortality and hospital admissions for England & wales and Scotland. *Eur J Vasc Endovasc Surg.* (2012) 43:161–6. doi: 10.1016/j.ejvs.2011.11.014
3. Cosford PA, Leng GC. Screening for abdominal aortic aneurysm. *Cochrane Database Syst Rev.* (2007). 2:CD002945. doi: 10.1002/14651858.CD002945.pub2
4. Ashton HA, Buxton MJ, Day NE, Kim LG, Marteau TM, Scott RA, et al. The multicentre aneurysm screening study (mass) into the effect of abdominal aortic aneurysm screening on mortality in men: a randomised controlled trial. *Lancet.* (2002) 360:1531–9. doi: 10.1016/S0140-6736(02)11522-4
5. Sidloff D, Stather P, Dattani N, Bown M, Thompson J, Sayers R, et al. Aneurysm global epidemiology study. *Circulation.* (2014) 129:747–53. doi: 10.1161/CIRCULATIONAHA.113.005457
6. Golledge J, Muller J, Daugherty A, Norman P. Abdominal aortic aneurysm: pathogenesis and implications for management. *Arterioscler Thromb Vasc Biol.* (2006) 26:2605–13. doi: 10.1161/01.ATV.0000245819.32762.cb
7. Robertson L, Atallah E, Stansby G. Pharmacological treatment of vascular risk factors for reducing mortality and cardiovascular events in patients with abdominal aortic aneurysm. *Cochrane Database Syst Rev.* (2017) 1:CD010447. doi: 10.1002/14651858.CD010447.pub3
8. Wulf-Johansson H, Lock Johansson S, Schlosser A, Trommelholt Holm A, Rasmussen LM, Mickley H, et al. Localization of microfibrillar-associated protein 4 (mfap4) in human tissues: clinical evaluation of serum mfap4 and its association with various cardiovascular conditions. *PLoS ONE.* (2013) 8:e82243. doi: 10.1371/journal.pone.0082243
9. Hemstra LE, Schlosser A, Lindholt JS, Sorensen GL. Microfibrillar-associated protein 4 variation in symptomatic peripheral artery disease. *J Transl Med.* (2018) 16:159. doi: 10.1186/s12967-018-1523-6
10. Bracht T, Molleken C, Ahrens M, Poschmann G, Schlosser A, Eisenacher M, et al. Evaluation of the biomarker candidate mfap4 for non-invasive assessment of hepatic fibrosis in hepatitis c patients. *J Transl Med.* (2016) 14:201. doi: 10.1186/s12967-016-0952-3
11. Molleken C, Sitek B, Henkel C, Poschmann G, Sipos B, Wiese S, et al. Detection of novel biomarkers of liver cirrhosis by proteomic analysis. *Hepatology.* (2009) 49:1257–66. doi: 10.1002/hep.22764
12. Sækmose S, Mössner B, Christensen P, Lindvig K, Schlosser A, Holst R, et al. Microfibrillar-associated protein 4: a potential biomarker for screening for liver fibrosis in a mixed patient cohort. *PLoS ONE.* (2015) 10:e0140418. doi: 10.1371/journal.pone.0140418
13. Pilecki B, Holm AT, Schlosser A, Moeller JB, Wohl AP, Zuk AV, et al. Characterization of microfibrillar-associated protein 4 (mfap4) as a tropoelastin- and fibrillin-binding protein involved in elastic fiber formation. *J Biol Chem.* (2016) 291:1103–14. doi: 10.1074/jbc.M115.681775
14. Pilecki B, Schlosser A, Wulf-Johansson H, Trian T, Moeller JB, Marcussen N, et al. Microfibrillar-associated protein 4 modulates airway smooth muscle cell phenotype in experimental asthma. *Thorax.* (2015) 70:862–72. doi: 10.1136/thoraxjnl-2014-206609
15. Holm AT, Wulf-Johansson H, Hvidsten S, Jorgensen PT, Schlosser A, Pilecki B, et al. Characterization of spontaneous air space enlargement in mice lacking microfibrillar-associated protein 4. *Am J Physiol Lung Cell Mol Physiol.* (2015) 308:L1114–24. doi: 10.1152/ajplung.00351.2014
16. Schlosser A, Pilecki B, Hemstra LE, Kejling K, Kristmannsdottir GB, Wulf-Johansson H, et al. Mfap4 promotes vascular smooth muscle migration, proliferation and accelerates neointima formation. *Arterioscler Thromb Vasc Biol.* (2016) 36:122–33. doi: 10.1161/ATVBAHA.115.306672
17. Daugherty A, Manning MW, Cassis LA. Angiotensin ii promotes atherosclerotic lesions and aneurysms in apolipoprotein E–deficient mice. *J Clin Investig.* (2000) 105:1605–12. doi: 10.1172/JCI7818
18. Daugherty A, Rateri DL, Cassis LA. Role of the renin-angiotensin system in the development of abdominal aortic aneurysms in animals and humans. *Ann N Y Acad Sci.* (2006) 1085:82–91. doi: 10.1196/annals.1383.035
19. Robinet P, Milewicz DM, Cassis LA, Leeper NJ, Lu HS, Smith JD. Consideration of sex differences in design and reporting of experimental arterial pathology studies-statement from ATVB council. *Arterioscler Thromb Vasc Biol.* (2018) 38:292–303. doi: 10.1161/ATVBAHA.117.309524
20. Daugherty A, Manning MW, Cassis LA. Antagonism of at2 receptors augments angiotensin ii-induced abdominal aortic aneurysms and atherosclerosis. *Br J Pharmacol.* (2001) 134:865–70. doi: 10.1038/sj.bjp.0704331

21. Lausen M, Lynch N, Schlosser A, Tornøe I, Sækmose S, Teisner B, et al. Microfibril-associated protein 4 is present in lung washings and binds to the collagen region of lung surfactant protein d. *J Biol Chem.* (1999) 274:32234–40. doi: 10.1074/jbc.274.45.32234
22. Bornstein P. Matricellular proteins: an overview. *J Cell Commun Signal.* (2009) 3:163–5. doi: 10.1007/s12079-009-0069-z
23. Giancotti FG, Tarone G. Positional control of cell fate through joint integrin/receptor protein kinase signaling. *Annu Rev Cell Dev Biol.* (2003) 19:173–206. doi: 10.1146/annurev.cellbio.19.031103.133334
24. Kitagawa T, Kosuge H, Chang E, James ML, Yamamoto T, Shen B, et al. Integrin-targeted molecular imaging of experimental abdominal aortic aneurysms by (18)f-labeled Arg-Gly-Asp positron-emission tomography. *Circ Cardiovasc Imaging.* (2013) 6:950–6. doi: 10.1161/CIRCIMAGING.113.000234
25. Muhl L, Genove G, Leptidis S, Liu J, He L, Mocci G, et al. Single-cell analysis uncovers fibroblast heterogeneity and criteria for fibroblast and mural cell identification and discrimination. *Nat Commun.* (2020) 11:3953. doi: 10.1038/s41467-020-18511-8
26. He L, Vanlandewijck M, Mae MA, Andrae J, Ando K, Del Gaudio F, et al. Single-cell RNA sequencing of mouse brain and lung vascular and vessel-associated cell types. *Sci Data.* (2018) 5:180160. doi: 10.1038/sdata.2018.160
27. Longo MG, Xiong W, Greiner TC, Zhao Y, Fiotti N, Baxter TB. Matrix metalloproteinases 2 and 9 work in concert to produce aortic aneurysms. *J Clin Investig.* (2002) 110:625–632. doi: 10.1172/JCI0215334
28. Newby AC. Metalloproteinase expression in monocytes and macrophages and its relationship to atherosclerotic plaque instability. *Arterioscl Throm Vas.* (2008) 28:U2108–20. doi: 10.1161/ATVBAHA.108.173898
29. Davis V, Persidskaia R, Baca-Regen L, Itoh Y, Nagase H, Persidsky Y, et al. Matrix metalloproteinase-2 production and its binding to the matrix are increased in abdominal aortic aneurysms. *Arterioscler Thromb Vasc Biol.* (1998) 18:1625–33. doi: 10.1161/01.ATV.18.10.1625
30. Thompson RW, Holmes DR, Mertens RA, Liao S, Botney MD, Mecham RP, et al. Production and localization of 92-kilodalton gelatinase in abdominal aortic aneurysms. An elastolytic metalloproteinase expressed by aneurysm-infiltrating macrophages. *J Clin Invest.* (1995) 96:318–26. doi: 10.1172/JCI118037
31. Bendeck MP, Irvin C, Reidy M, Smith L, Mulholland D, Horton M, et al. Smooth muscle cell matrix metalloproteinase production is stimulated via alpha(v)beta(3) integrin. *Arterioscler Thromb Vasc Biol.* (2000) 20:1467–72. doi: 10.1161/01.ATV.20.6.1467
32. Kasamatsu S, Hachiya A, Fujimura T, Sriwiriyanont P, Haketa K, Visscher MO, et al. Essential role of microfibrillar-associated protein 4 in human cutaneous homeostasis and in its photoprotection. *Sci Rep.* (2011) 1:164. doi: 10.1038/srep00164
33. Raffort J, Lareyre F, Clement M, Hassen-Khodja R, Chinetti G, Mallat Z. Monocytes and macrophages in abdominal aortic aneurysm. *Nat Rev Cardiol.* (2017) 14:457–71. doi: 10.1038/nrcardio.2017.52
34. Samadzadeh KM, Chun KC, Nguyen AT, Baker PM, Bains S, Lee ES. Monocyte activity is linked with abdominal aortic aneurysm diameter. *J Surg Res.* (2014) 190:328–34. doi: 10.1016/j.jss.2014.03.019
35. Brilha S, Wysoczanski R, Whittington AM, Friedland JS, Porter JC. Monocyte adhesion, migration, and extracellular matrix breakdown are regulated by integrin alphavbeta3 in mycobacterium tuberculosis infection. *J Immunol.* (2017) 199:982–91. doi: 10.4049/jimmunol.1700128
36. Bishop GG, McPherson JA, Sanders JM, Hesselbacher SE, Feldman MJ, McNamara CA, et al. Selective alpha(v)beta(3)-receptor blockade reduces macrophage infiltration and restenosis after balloon angioplasty in the atherosclerotic rabbit. *Circulation.* (2001) 103:1906–11. doi: 10.1161/01.CIR.103.14.1906
37. Harada T, Yoshimura K, Yamashita O, Ueda K, Morikage N, Sawada Y, et al. Focal adhesion kinase promotes the progression of aortic aneurysm by modulating macrophage behavior. *Arterioscl Throm Vas.* (2017) 37:156–65. doi: 10.1161/ATVBAHA.116.308542
38. Sun H, Zhu Y, Pan H, Chen X, Balestrini JL, Lam TT, et al. Netrin-1 regulates fibrocyte accumulation in the decellularized fibrotic sclerodermatous lung microenvironment and in bleomycin-induced pulmonary fibrosis. *Arthr Rheumatol.* (2016) 68:1251–61. doi: 10.1002/art.39575
39. Itoh S, Itoh F, Goumans MJ, ten Dijke P. Signaling of transforming growth factor-beta family members through Smad proteins. *Eur J Biochem.* (2000) 267:6954–67. doi: 10.1046/j.1432-1327.2000.01828.x
40. Pan Z, Yang K, Wang H, Xiao Y, Zhang M, Yu X, et al. MFAP4 deficiency alleviates renal fibrosis through inhibition of NF-κB and TGF-beta/Smad signaling pathways. *FASEB J.* (2020) 34: 14250–63. doi: 10.1096/fj.202001026R
41. Wang HB, Yang J, Shuai W, Yang J, Liu LB, Xu M, et al. Deletion of microfibrillar-associated protein 4 attenuates left ventricular remodeling and dysfunction in heart failure. *J Am Heart Assoc.* (2020) 9:e015307. doi: 10.1161/JAHA.119.015307
42. IJpma A, Te Riet L, van de Luijtgaarden KM, van Heijningen PM, Burger J, Majoor-Krakauer D, et al. Inflammation and TGF-beta signaling differ between abdominal aneurysms and occlusive disease. *J Cardiovasc Dev Dis.* (2019) 6:38. doi: 10.3390/jcdd6040038
43. Quintana RA, Taylor WR. Cellular mechanisms of aortic aneurysm formation. *Circ Res.* (2019) 124:607–18. doi: 10.1161/CIRCRESAHA.118.313187
44. Hodivala-Dilke K. Avβ3 integrin and angiogenesis: a moody integrin in a changing environment. *Curr Opin Cell Biol.* (2008) 20:514–9. doi: 10.1016/j.ceb.2008.06.007
45. Choke E, Cockerill GW, Dawson J, Wilson RW, Jones A, Loftus IM, et al. Increased angiogenesis at the site of abdominal aortic aneurysm rupture. *Ann N Y Acad Sci.* (2006) 1085:315–9. doi: 10.1196/annals.1383.007
46. Ucuzian AA, Gassman AA, East AT, Greisler HP. Molecular mediators of angiogenesis. *J Burn Care Res.* (2010) 31:158. doi: 10.1097/BCR.0b013e3181c7ed82
47. Kidholm C, Beck H, Madsen J, Palstrøm N, Lindholt J, Rasmussen L. Preliminary analysis of proteome alterations in non-aneurysmal, internal mammary artery tissue from patients with abdominal aortic aneurysms. *PLoS ONE.* (2018) 13:e0192957. doi: 10.1371/journal.pone.0192957
48. Modrego J, López-Farré AJ, Martínez-López I, Muela M, Macaya C, Serrano J, et al. Expression of cytoskeleton and energetic metabolism-related proteins at human abdominal aortic aneurysm sites. *J Vasc Surg.* (2012) 55:1124–33. doi: 10.1016/j.jvs.2011.10.033
49. Pilop C, Aregger F, Gorman RC, Brunisholz R, Gerrits B, Schaffner T, et al. Proteomic analysis in aortic media of patients with Marfan syndrome reveals increased activity of calpain 2 in aortic aneurysms. *Circulation.* (2009) 120:983–91. doi: 10.1161/CIRCULATIONAHA.108.843516
50. Lindholt JS, Madsen M, Kirketerp-Moller KL, Schlosser A, Kristensen KL, Andersen CB, et al. High plasma microfibrillar-associated protein 4 is associated with reduced surgical repair in abdominal aortic aneurysms. *J Vasc Surg.* (2020) 71:1921–9. doi: 10.1016/j.jvs.2019.08.253
51. Lu H, Rateri DL, Cassis LA, Daugherty A. The role of the renin-angiotensin system in aortic aneurysmal diseases. *Curr Hypertens Rep.* (2008) 10:99–106. doi: 10.1007/s11906-008-0020-3
52. Saraff K, Babamusta F, Cassis LA, Daugherty A. Aortic dissection precedes formation of aneurysms and atherosclerosis in angiotensin ii-infused, apolipoprotein e-deficient mice. *Arterioscler Thromb Vasc Biol.* (2003) 23:1621–6. doi: 10.1161/01.ATV.0000085631.76095.64
53. Deng GG, Martin-McNulty B, Sukovich DA, Freay A, Halks-Miller M, Thinnes T, et al. Urokinase-type plasminogen activator plays a critical role in angiotensin ii-induced abdominal aortic aneurysm. *Circ Res.* (2003) 92:510–7. doi: 10.1161/01.RES.0000061571.49375.E1
54. Michel JB, Martin-Ventura JL, Egido J, Sakalihasan N, Treska V, Lindholt J, et al. Novel aspects of the pathogenesis of aneurysms of the abdominal aorta in humans. *Cardiovasc Res.* (2011) 90:18–27. doi: 10.1093/cvr/cvq337
55. Johansson M, Zahl PH, Siersma V, Jorgensen KJ, Marklund B, Brodersen J. Benefits and harms of screening men for abdominal aortic aneurysm in Sweden: a registry-based cohort study. *Lancet.* (2018) 391:2441–7. doi: 10.1016/S0140-6736(18)31031-6
56. Lindholt JS, Sogaard R. Population screening and intervention for vascular disease in Danish men (viva): a randomised controlled trial. *Lancet.* (2017) 390:2256–65. doi: 10.1016/S0140-6736(17)32250-X

Conflict of Interest: AS and GS are inventors of patents owned by the University of Southern Denmark WO2014114298 and EP17199552.5. PH is employed by Astra Zeneca.

The remaining authors declare that the research was conducted in the absence of any commercial or financial relationships that could be construed as a potential conflict of interest.

Publisher's Note: All claims expressed in this article are solely those of the authors and do not necessarily represent those of their affiliated organizations, or those of the publisher, the editors and the reviewers. Any product that may be evaluated in this article, or claim that may be made by its manufacturer, is not guaranteed or endorsed by the publisher.

frontiers in Cardiovascular Medicine

ORIGINAL RESEARCH
published: 17 November 2021
doi: 10.3389/fcvm.2021.759666

Combination of Exercise Testing Criteria to Diagnose Lower Extremity Peripheral Artery Disease

*Olivier Stivalet[1], Anita Paisant[2], Dihia Belabbas[2], Alexis Le Faucheur[3], Philippe Landreau[1], Estelle Le Pabic[4], Loukman Omarjee[1,5] and Guillaume Mahé[1,3,4,6]**

[1] Vascular Medicine Unit, CHU Rennes, Rennes, France, [2] Radiology Department, CHU Rennes, Rennes, France, [3] University of Rennes 2, M2S-EA 7470, Rennes, France, [4] Institut National de la Santé Et de la Recherche Médicale (INSERM), CIC1414, Rennes, France, [5] Vascular Medicine, Centre Hospitalier de Redon, Redon, France, [6] University of Rennes 1, Rennes, France

Objectives: Nothing is known about the interest of the combination of exercise tests to diagnose Lower-extremity Peripheral Artery Disease (LEPAD). The aim of this study was to assess if combining exercise testing criteria [post-exercise Ankle-Brachial Index (ABI) + exercise-oximetry (exercise-TcPO2)] improves the detection of lower limbs arterial stenoses as compared with post-exercise ABI using American Heart Association (AHA) criteria, or exercise-TcPO2 alone.

Material and Methods: In a prospective monocentric study, consecutive patients with exertional-limb pain and normal resting-ABI referred to our vascular center (Rennes, France) were assessed from May 2016 to February 2018. All included patients had a computed tomography angiography (CTA), a resting-ABI, a post-exercise ABI and an exercise-TcPO2. AHA post-exercise criteria, new validated post-exercise criteria (post-exercise ABI decrease ≥18.5%, post-exercise ABI decrease <0.90), and Delta from Rest of Oxygen Pressure (Total-DROP) ≤-15mmHg (criterion for exercise-TcPO2) were used to diagnose arterial stenoses ≥50%. For the different combinations of exercise testing criteria, sensitivity or specificity or accuracies were compared with McNemar's test.

Results: Fifty-six patients (mean age 62 ± 11 years old and 84% men) were included. The sensitivity of the combination of exercise testing criteria (post-exercise ABI decrease ≥18.5%, or post-exercise ABI decrease <0.90 or a Total-DROP ≤-15mmHg) was significantly higher (sensitivity = 81% [95% CI, 71–92]) than using only one exercise test (post-exercise AHA criteria (sensitivity = 57% [43–70]) or exercise-TcPO2 alone (sensitivity = 59% [45–72]).

Conclusions: Combination of post-exercise ABI with Exercise-TcPO2 criteria shows better sensitivity to diagnose arterial stenoses compared with the AHA post-exercise criteria alone or Exercise-TcPO2 criteria used alone. A trend of a better accuracy of this combined strategy was observed but an external validation should be performed to confirm this diagnostic strategy.

Keywords: peripheral artery disease (PAD), exercise test, ankle brachial index (ABI), transcutaneous oxygen pressure (TcPO2), claudication

OPEN ACCESS

Edited by:
Marat V. Ezhov, Ministry of Health of the Russian Federation, Russia

Reviewed by:
Vihang Narkar, University of Texas Health Science Center at Houston, United States
Jun-Ichiro Koga, Kyushu University, Japan

***Correspondence:**
Guillaume Mahé
maheguillaume@yahoo.fr

Specialty section:
This article was submitted to Atherosclerosis and Vascular Medicine, a section of the journal Frontiers in Cardiovascular Medicine

Received: *16 August 2021*
Accepted: *07 October 2021*
Published: *17 November 2021*

Citation:
Stivalet O, Paisant A, Belabbas D, Le Faucheur A, Landreau P, Le Pabic E, Omarjee L and Mahé G (2021) Combination of Exercise Testing Criteria to Diagnose Lower Extremity Peripheral Artery Disease. Front. Cardiovasc. Med. 8:759666. doi: 10.3389/fcvm.2021.759666

INTRODUCTION

Lower Extremity Peripheral Artery Disease (LEPAD) affects more than 235 million people worldwide (1). The ankle-brachial index at rest (Resting-ABI) is a clinical means recommended by the guidelines of the American Heart Association (AHA) to diagnose the presence and severity of LEPAD regardless of the symptoms reported by the patients (2).

In patients with exertional limb pain relieved by rest and a resting-ABI >0.90, exercise testing with post-exercise ABI measurements is recommended by the AHA (2). The AHA statement proposed two different post-exercise criteria to diagnose LEPAD: either a post-exercise ABI decrease >20% or a post-exercise pressure decrease >30 mmHg. Exercise oximetry (exercise-TcPO2) has also been proposed to diagnose lower limbs arterial stenoses (3–5). Several studies have shown that exercise-TcPO2 using the Delta from Resting Oxygen Pressure (DROP) value is accurate to diagnose arterial stenoses of ≥50% assessed by computed tomography angiography (CTA) or angiography as a gold standard (3–5). Aday et al. has shown that post-exercise ABI <0.90 shows a better sensitivity than each of the AHA criteria taken separately (6). We have previously found that in patients with a normal resting-ABI, cut off values of post-exercise ABI decrease ≥18.5% or DROP ≤-15 mmHg have similar area under the curves (AUC) to detect LEPAD (i.e., arterial stenoses≥50%) (7). AUCs for post-exercise ABI decrease ≥18.5% and DROP ≤-15 mmHg were 0.67[0.53–0.78] and 0.67[0.53–0.78] respectively (7). We and others have previously demonstrated that discrepancies for the diagnosis of LEPAD exist between exercise criteria (Ankle pressure, post-exercise ABI and exercise-TcPO2) (8–10). Indeed, using a criterion patient can be considered as a LEPAD patient whereas using another criterion the same patient can be considered as a patient without LEPAD.

To date, nothing is known about the interest of the combination of exercise testing criteria to diagnose LEPAD in clinical practice. We hypothesize that the combination of exercise testing criteria could improve the detection of LEPAD in patients with exertional limb symptoms and a resting-ABI >0.90. The aim of this study was to assess if the sensitivity of the combination of exercise testing criteria is higher than the sensitivity of post-exercise ABI using the AHA criteria, or exercise-TcPO2 alone in patients with exertional limb symptoms and a resting-ABI > 0.90.

METHODS

Ethical Standards

The study was conducted from May 2016 to February 2018 and approved by an institutional review board (IRB) from the University Hospital of Rennes (ref.17.12). All participants gave written informed consent. The study protocol conforms to the ethical guidelines of the 1975 Declaration of Helsinki. The Exercise Peripheral Artery Disease (PAD) study was registered with the American National Institutes of Health database under reference n° NCT03186391.

Study Design

This is a monocentric study on consecutive patients referred to our vascular unit (University Hospital, Rennes, France) for exertional limb pain suspected of LEPAD. In this population, we selected patients with at least one limb with a resting-ABI >0.90, who had a CTA performed within 3 months of the exercise appointment. In our clinical practice, we systematically perform an exercise-TcPO2 test immediately followed by a second exercise test to measure the post-exercise ankle pressure and post-exercise ABI. Patients who were unable to walk on a treadmill or suffering from heart disease contraindicating an exercise test were not included.

Patient Demographic Characteristics

Variables collected included age, gender, body mass index, comorbidities, and medications (statins, anti-hypertension treatment, antiplatelet, antidiabetic oral treatment, or insulin).

There were 15 patients (17 limbs with an ABI >0.90) who had undergone peripheral artery procedures before our study such as bypass, stent, or angioplasty on the limb included in the evaluation.

ABI Measurement

After a careful clinical evaluation, a measurement of resting-ABI was performed according to AHA recommendations (2) using a hand-held Doppler probe (8 MHz; Basic Atys Medical™, Soucieu en Jarrest, France) by a trained vascular medicine physician. Briefly, the patient was at rest for 10 min in the supine position, relaxed, head and heels supported, in a room with a comfortable temperature (21°C) (11). The following counterclockwise sequence was used for the systolic arterial pressure measurement: "right brachial artery, right posterior tibial artery, right dorsalis pedis artery, left posterior tibial artery, left dorsalis pedis artery, left brachial artery, and right brachial artery" as mentioned by AHA Guidelines (2). The resting-ABI was calculated by dividing the highest pressure of the limb (dorsalis pedis or posterior tibial pressures) by the highest arm pressure as recommended (12). For the brachial artery, contrary to the AHA guidelines, we used an automatic blood pressure monitor (Carescape™ Dinamap V100; GE Healthcare) in order to have the same procedure to measure the pressure at rest and after exercise (7).

Treadmill Test

A treadmill walking test (3.2 km/h, 10% slope) was used up to a maximal distance of 1053m (20 min). This test was used for both the exercise-TcPO2 measurement, which was performed first, and for the post-exercise pressure measurements. A minimal recovery period of 10 min was required between the two exercise tests. The patients were asked to inform the physician when and where (buttock, thigh, calf, or other) the pain appeared during the test. Exercise was stopped for both tests according to the limitation of the patient.

Exercise-TcPO2 Measurement

Briefly, measurement of TcPO2 was performed using calibrated TcPO2 electrodes (TCOM/TcPO2; PF 6000TcPO2/CO2 Unit;

Perimed; Jarfalla, Sweden). A reference electrode (chest electrode) was placed between the scapulae and the spine to measure systemic changes in TcPO2 during exercise (3, 13, 14). One electrode was positioned on each buttock, 4 to 5 cm behind the bony prominence of the trochanter, and one electrode on each calf (3, 13, 14). Exercise was performed on a treadmill at a 10% slope and a speed of up to 3.2 km/h (13). Exercise was discontinued at the request of the patient or, by protocol, up to a maximum exercise duration of 20 min. The measurement from the TcPO2 electrodes was used to calculate the Delta from Resting Oxygen Pressure (DROP) index, which was expressed in mmHg (14). We define Total DROP as the lowest DROP value between proximal and distal electrodes on each limb. DROP was recorded in real-time by the in-house Oxymonitor (version 2019.01.05) free Software (https://imagemed.univ-rennes1.fr/en/oxymonitor/download.php) as previously described (15). As defined in a previous study, we considered a Total DROP $\leq$-15 mmHg accurate to diagnose arterial stenoses of $\geq$50% assessed by computed tomography angiography (CTA) as a gold standard (7).

Post-exercise Pressure and Post-exercise ABI Measurements

Two persons performed the measurements: one at the brachial level with the automatic blood pressure device (Carescape™ Dinamap V100; GE Healthcare) and one at the limb level with the handheld Doppler (7, 16).

Post-exercise pressures were assessed on the same arteries as it was for the resting-ABI measurement (16). When the resting-ABI was measured, a black pen was used to mark the skin area where the highest limb pressure had been recorded with a hand-held Doppler. Following exercise, we were sure that we were in the correct area to perform the post-exercise pressure measurement and if there was no arterial flow it meant that the pressure was 0 mmHg (17). The highest ankle pressure of each limb at rest was assessed, beginning with the more symptomatic limb. Post-exercise pressures were assessed within 1 min after the termination of walking (18).

Arterial Stenoses Quantification Using CTA

Computed tomography angiography was performed in all subjects within 3 months before or after the post-exercise ABI and exercise-TcPO2 measurements to confirm the arterial stenotic lesions. The methodology is similar to the one previously published by our team (7). CTA was performed with a 64-slice CT scanner (Discovery CT 750 High Definition; GE Healthcare, Milwaukee, WI, USA), 100-kV tube voltage, and an automatic modulation of mAs (80–500 mAs). The scanning range was planned with a scout view and included the entire vascular tree from the abdominal aorta to ankles. A total of 120 ml or 1.5 ml/kg of iobitridol 350 mgI/ml (Xenetix®, Guerbet, Roissy, France) was administered with an automated injector at a flow rate of 4 ml/sec. There was systematically a 3D MIP reconstruction (Maximum Intensity Projection) and a 2D multiplanar reconstruction (MPR). CTA data were transferred to a computer workstation (Advantage Workstation, AW 4.6; GE Medical Systems) for analysis. The reformatted 1.25-mm axial images, multiplanar reformats and Vessel Analysis© software (GE Healthcare, Milwaukee, WI, USA) were used to determine the grade of stenosis. The referring doctor of the patient ordered CTA at his or her discretion. CTA, used as gold standard, was performed to detect luminal arterial stenoses in each patient in our facility. Significant stenoses ($\geq$50% of the diameter) at each artery level (aorta, common iliac artery, external iliac artery, internal iliac artery, common femoral artery, superficial femoral artery, popliteal artery on both sides) were reported by two blinded radiologists (AP and DB) who were unaware of the results of the exercise tests appointment. Infrapopliteal artery stenoses were not assessed. In case of variability higher than 10% for $\geq$50% stenoses between the two radiologists, a new interpretation was performed with both. The percent stenoses were calculated as follows by each physician: 100 x [1 – (diameter of the lumen at the site of the stenosis/diameter of the normal lumen)]. Finally, the degree of stenoses at each artery level used for the statistical analyses was calculated as the mean of the quantification performed by both physicians or, in the case of a third interpretation, a third measurement was used.

Data Analysis

Post-exercise pressure decrease, post-exercise ABI were calculated and results of exercise-TcPO2 were analyzed without knowing the results of CTA. Right Total DROP allows the detection of flow-reducing lesions in the following arteries: the aorta, the right common iliac artery, the right external iliac artery, the right common femoral artery, the right superficial femoral artery, and the right popliteal artery. Left Total DROP allows the detection of flow-reducing lesions in the following arteries: the aorta, the left common iliac artery, the left external iliac artery, the left common femoral artery, the left superficial femoral artery, and the left popliteal artery (14).

Statistical Analyses

Results are expressed as mean $\pm$ standard deviation. Continuous variables were expressed as mean and 95% confidence interval (CI), and categorical variables as numbers (percentages). Then, sensitivity, specificity, positive predictive value, and negative predictive value were calculated with their respective 95% CI. For the different combinations of exercise testing criteria, sensitivity, or specificity or accuracies were compared with McNemar's test. Statistical analyses were performed with SAS software, v.9.4® (SAS Institute, Cary, NC, USA). For all statistical tests, a two-tailed probability level of $p \leq 0.05$ was used to indicate statistical significance.

RESULTS

Among 307 patients, 56 patients (83.9% men) met all criteria (at least one limb with ABI > 0.90 and exertional limb pain and CTA perform within 3 months) to be included in this prospective study (**Figure 1**). Characteristics of patients are presented in **Table 1**. The average age and body mass index were 62 $\pm$ 11 years old, 26.5 $\pm$ 5.1 kg/m^2, respectively. Among the limbs with a resting-ABI > 0.90 ($n = 86$), 53 limbs had arterial stenoses. Among these 53 limbs, 85 stenoses were identified as follows: 3 on the aorta, 22

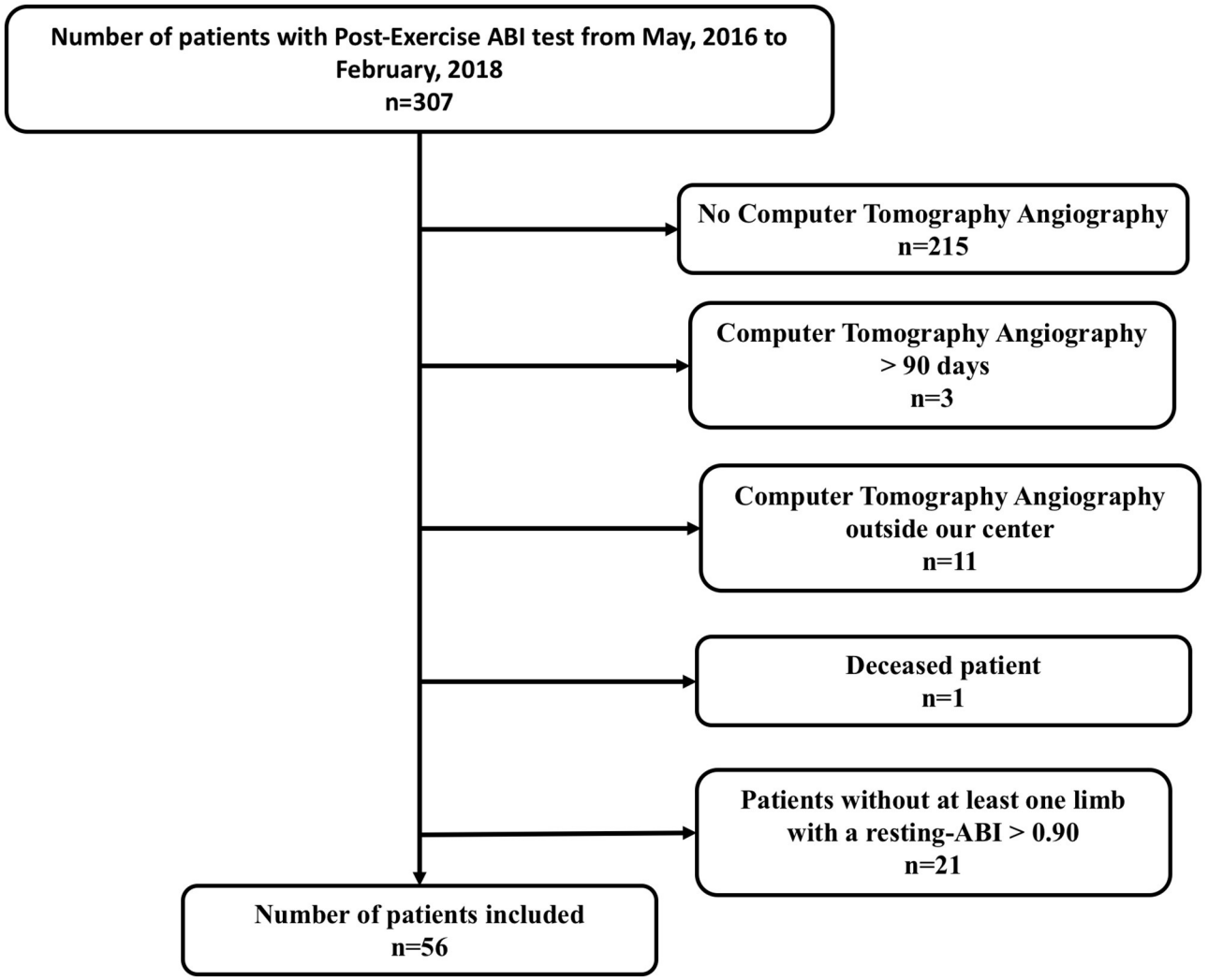

FIGURE 1 | Flow chart. ABI, Ankle-Brachial Index.

on the common iliac artery, 4 on the external iliac artery, 23 on the internal iliac artery, 3 on the common femoral artery, 18 on the superficial femoral, and 12 on the popliteal artery.

Among limbs with a normal resting-ABI ($n = 86$), **Table 2** shows the results of the different exercise tests to detect limbs of patients with or without arterial stenoses ≥50% detected with CTA. **Figure 2** shows for limbs of patients with a resting-ABI >0.90 and an arterial stenosis ≥50% ($n = 53$) along with the proportion of patients' limbs with arterial stenoses detected by the different criteria or combinations of criteria.

We show that the sensitivity of the combination of exercise criteria (post-exercise ABI decrease ≥18.5%, or post-exercise ABI < 0.90 or a Total DROP ≤-15 mmHg) is greater than the sensitivity of the AHA criteria (post-exercise ABI decrease >20% or post-exercise pressure >30 mmHg) or the sensitivity of exercise-TcPO2 alone.

The sensitivity, specificity, positive and negative predictive values (95% CI), and accuracies are presented in **Tables 2**, **3**. Globally, the increase of the number of exercise criteria increases the accuracy of the tests. The highest accuracy is found for the combination of three exercise criteria (post-exercise ABI decrease ≥18.5%, or post-exercise ABI < 0.90 or a Total DROP ≤-15mmHg). This accuracy is statistically better than the accuracy of post exercise pressure >30 mmHg ($p = 0.0035$) and Exercise TcPO2 criterion ($p = 0.0201$). A trend to an improvement of the accuracy was also observed as compared with the combination of post-exercise ABI decrease >20% or post-exercise ankle pressure decrease >30 mmHg ($p = 0.0593$).

There were discrepancies between AHA criteria (post-exercise ABI decrease >20% or post-exercise ankle pressure decrease > 30 mmHg) and the combination of post-exercise ABI with Exercise-TcPO2. The characteristics of patients are described in

TABLE 1 | Population characteristics.

Clinical characteristics	*n* = 56
Age, y, mean ± standard deviation	62 ± 11
Male sex, no., (%)	47 (83.9%)
Body mass index, kg/m^2, mean ± standard deviation	26.5 ± 5.1
Comorbidities, (history of), no. (%)	
Current smoker, no. (%)	21 (37.5%)
History of smoking, no. (%)	45 (80.4%)
Hypercholesterolemia, no. (%)	34 (60.7%)
Diabetes, no. (%)	10 (17.9%)
Peripheral artery vascular surgery*, no. (%)	19 (33.9%)
Hypertension, no. (%)	37 (66.1%)
History of coronaropathy, no. (%)	17 (30.4%)
History of stroke, no. (%)	9 (16.1%)
Current medications, no. (%)	
Statins, no. (%)	32 (57.1%)
Anti-Hypertension treatments, no. (%)	38 (67.8%)
Antiplatelets, no. (%)	42 (75%)
Anti-diabetic oral treatments, no. (%)	8 (14.3%)
Resting Ankle-Brachial index	
Resting ankle-brachial index (right), mean [CI 95%]	1.03 [0.78–1.28]
Resting ankle-brachial index (left), mean [CI 95%]	0.95 [0.74–1.16]
Indication of the treadmill test, no. (%)	
Exertional limb pain, no. (%)	52 (92.9%)
Muscle fatigability (limbs), no. (%)	4 (7.1%)

** Peripheral artery Vascular surgery from aorta and/or more distal iliac or leg arteries.*

Table 4. Ten patients (12 limbs) who had arterial stenosis ≥50% had discrepancies between AHA criteria (i.e., post-exercise ABI decrease >20% or post-exercise ankle pressure decrease >30 mmHg) and combination of post-exercise ABI with Exercise-TcPO2 [post-exercise ABI < 0.90 or post-exercise ABI decrease ≥18.5% or exercise-TcPO2 (Total DROP) ≤-15 mmHg]. Five out of twelve limbs (42%) had stenosis localized at the internal iliac artery level. Only one patient (1 limb) stopped the test due to exertional limb pain localized on the limb with an arterial stenosis ≥50%. Seven patients stopped for pain on both limbs (3 patients/5 limbs) or pain on the other limb (4 patients/4 limbs). The last two patients (2 limbs) were not limited on the treadmill (1053m). There was no case of a limb considered as diseased with the AHA criteria (i.e., post-exercise ABI decrease >20% or post-exercise ankle pressure decrease >30 mmHg) and not diseased with the combination of post-exercise ABI with Exercise-TcPO2 criteria.

Nine patients (10 limbs) were identified neither by the AHA criteria nor by the combination of post-exercise ABI with Exercise-TcPO2 (post-exercise ABI < 0.90 or post-exercise ABI decrease ≥18.5% or exercise-TcPO2 (Total DROP) ≤-15 mmHg). The characteristics of patients are described in **Table 5**. Four patients (5 limbs) were not limited on the treadmill test (1053m). Three patients (3 limbs) stopped due to contralateral pain and two stopped due to fatigue (1 patient/1 limb) and vertigo (1 patient/1 limb).

DISCUSSION

To our knowledge, this is the first study designed to evaluate the diagnostic value of a combination of exercise testing criteria including post-exercise ABI and exercise-TcPO2 criteria to detect arterial stenoses ≥50% in patients with normal resting-ABI. This study shows that the sensitivity of the combination of exercise criteria (post-exercise ABI decrease ≥18.5%, or post-exercise ABI < 0.90 or a Total DROP ≤−15 mmHg) is statistically better than the sensitivity of the AHA criteria (post-exercise ABI decrease >20%, or post-exercise pressure >30 mmHg) or the sensitivity of exercise-TcPO2 alone.

For patients with a normal resting-ABI suspected of LEPAD, the AHA recommends to perform a post-exercise ABI using a post-exercise ABI decrease >20%, and/or a post-exercise pressure > 30 mmHg as criteria to diagnose LEPAD (Class IIa; Level of Evidence A) (2). A previous study had shown a dissonance between these two criteria (19). Previous studies about the accuracy of exercise tests to diagnose LEPAD were conducted in the 80s and suffer from many bias (7, 19–21). Therefore, in a previous paper, we defined new criteria of post-exercise ABI (post-exercise ABI decrease ≥18.5%) and exercise-TcPO2 criterion (Total DROP ≤-15 mmHg) with a current treadmill test (3.2 km/h and 10% grade) performed in clinical routine to detect significant arterial stenosis (7). In the meantime, Aday et al. has confirmed that post-exercise ABI < 0.90 was also a good candidate to diagnose LEPAD (6, 7). In case of incompressible lower limb arteries, the resting-ABI and post-exercise ABI can be falsely reassuring. In this context, the exercise-TcPO2 can be of interest (14, 22). In this study, we show for the first time that a combination of exercise tests improves diagnosis of arterial stenoses ≥50% in patients suspected of having LEPAD (i.e., with exertional limb symptoms) with normal resting-ABI.

Some authors might think that there is no interest to use several exercise tests for cost and time issues, but our study demonstrates a synergy between both exercise tests. Furthermore, performing these two exercise tests might finally reduce the number of CTA that are performed to find the etiology of the exertional limb symptoms.

In our study, the sensitivity is higher for the combination of the new exercise criteria (post-exercise ABI decrease ≥18.5%, or post-exercise ABI < 0.90) with exercise-TcPO2 [81%(71–92)] or without exercise-TcPO2 [68%(55–81)] than the sensitivity of AHA criteria (post-exercise ABI decrease >20%, or post-exercise pressure >30mmHg) [57%(43–70)] with a slightly lower specificity [73%(58–88) vs. 76%(61–90) for AHA criteria] without exercise-TcPO2 and a lower specificity with exercise-TcPO2 [61% (44–77)]. The AHA criteria (post-exercise ABI decrease >20%, or post-exercise pressure >30 mmHg) and the exercise-TcPO2 (Total DROP ≤-15 mmHg) seems to have similar sensitivity [57%(43–70) and 59%(45–72)], but specificity of exercise-TcPO2 is slightly lower [70%(54–89%) vs. 76%(61–90) for AHA criteria]. To comfort our results and study the statistical significance, an

TABLE 2 | Diagnosis performances of the different exercise criteria to diagnose lower extremity peripheral artery disease.

Population (n = 56) Limbs with a resting-ABI >0.90 (n = 86)	Sensitivity (95%CI)	Specificity (95%CI)	Positive predictive value (95%CI)	Negative predictive value (95%CI)	Accuracy (95%CI)
Post-exercise ABI decrease >20% *or* Post-exercise ankle pressure decrease >30 mmHg	57% [43–70]	76% [61–90]	79% [66–92]	52% [38–66]	64% [54–74]
Exercise-TcPO2 (Total DROP) ≤-15 mmHg	59% [45–72]	70% [54–85]	76% [63–89]	51% [37–66]	63% [53–73]
Post-exercise ABI decrease ≥18.5%	62% [49–75]	76% [61–90]	81% [68–93]	56% [41–70]	67% [57–77]
Post-exercise ABI <0.90	62% [49–75]	73% [58–88]	79% [66–91]	55% [40–69]	66% [56–76]
Post-exercise ABI <0.90 *or* Post-exercise ABI decrease ≥18.5%	68% [55–81]	73% [58–88]	80% [68–92]	59% [44–74]	70% [60–80]
Post-exercise ABI decrease >20% *or* Post-exercise ankle pressure decrease >30 mmHg *or* Exercise-TcPO2 (Total DROP) ≤-15 mmHg	74% [62–86]	64% [47–80]	77% [65–88]	60% [44–76]	70% [60–80]
Post-exercise ABI decrease ≥18.5% *or* Exercise-TcPO2 (Total DROP) ≤-15 mmHg	77% [66–89]	64% [47–80]	77% [66–89]	64% [47–80]	72% [63–82]
Post-exercise ABI <0.90 *or* Exercise-TcPO2 (Total DROP) ≤-15 mmHg	77% [66–89]	61% [44–77]	76% [65–87]	63% [46–79]	71% [61–81]
Post-exercise ABI <0.90 *or* Post-exercise ABI decrease ≥18.5% *or* Exercise-TcPO2 (Total DROP) ≤-15 mmHg	81% [71–92]	61% [44–77]	77% [66–88]	67% [50–84]	73% [64–83]

ABI, Ankle-Brachial Index; TcPO2, Transcutaneous Oxygen Pressure measurements; DROP, Delta from Rest Oxygen Pressure; CI, Confidence Interval.

TABLE 3 | Comparisons of the accuracies of the different tests.

Accuracy								
Post-exercise ABI <0.90 *or* post-exercise ABI decrease ≥18.5% or exercise-TcPO2 (Total DROP) ≤-15 mmHg	**Post-exercise ABI <0.90**	**Post-exercise ABI decrease >20%**	**Post-exercise ankle pressure decrease >30 mmHg**	**Post-exercise ABI decrease ≥18.5%**	**Exercise-TcPO2 (Total DROP) ≤-15 mmHg**	**Post-exercise ABI decrease >20% *or* post-exercise ankle pressure decrease >30 mmHg**	**Post-exercise ABI <0.90 *or* post-exercise ABI decrease ≥18.5%**	***p* value**
73% [64–83]	66% [56–76]							0.1088
73% [64–83]		64% [54–74]						0.0593
73% [64–83]			52% [42–63]					0.0035
73% [64–83]				67% [57–77]				0.1967
73% [64–83]					63% [53–73]			0.0201
73% [64–83]						64% [54–74]		0.0593
73% [64–83]							70% [60–80]	0.3657

ABI, Ankle-Brachial Index; DROP, Delta from Resting Oxygen Pressure.

external validation remains to be performed. Of interest, the sensitivity of post-exercise ABI decrease >20% [57%(43–70)] was significantly better than the sensitivity of post-exercise pressure >30mmHg [28%(16–40), 95%CI] confirming previous suggestions that the use of a post-exercise ankle pressure decrease > 30 mm Hg to diagnose PAD should not be proposed anymore (23).

Unfortunately, the combination of post-exercise ABI with exercise-TcPO2 did not detect all limbs with an arterial stenosis ≥50% (i.e., 18.8% limbs were missed). Of interest, in none of these cases, patients stopped the treadmill due to exertional limb symptom on the limb with an arterial stenosis ≥50%. This suggests that to be informative, exercise tests and their diagnosis criteria have to be symptom-limited to be accurate as suggested in previous papers (24–26).

Based on the literature and our results, we suggest in order to diagnose LEPAD in patients with exertional limb symptoms that first, the physician should perform resting-ABI. Second, in case of resting-ABI > 0.90, physicians should perform post-exercise ABI measurements or exercise-TcPO2 on a treadmill test of 3.2km/h and 10% grade with the following cut-offs: post-exercise ABI decrease of ≥18.5%; post-exercise ABI < 0.90; and Total DROP

TABLE 4 | Characteristics of patients of which there were discrepancies between the American Heart Association (AHA) post-exercise criteria (negative for the diagnosis) and the combination of post-exercise ankle-brachial index (ABI) with Exercise oximetry (TcPO2) (positive for the diagnosis).

Limbs with a resting ABI > 0.90 and an arterial stenosis ≥50%	Gender	Age (years)	Location of arterial stenosis ≥50%	Resting-ABI of the limb	Diabetes	Vascular surgery	MWD (meter) first test	Cause of stopping for first test	MWD (meter) second test	Cause of stopping for second test
1	Woman	74	Aorta	0.96	No	No	1,053	None	1,053	None
2	Woman	60	Aorta	0.97	No	No	1,053	None	1,053	None
3	Man	49	CIA	0.91	No	Yes	208	Exertional contralateral limb pain	211	Exertional contralateral limb pain
4	Man	67	CIA	1.05	No	No	61	Exertional both limbs pain and dyspnea	59	Exertional both limbs pain and dyspnea
5	Man	69	IIA, CIA, CFA, SFA, PA	1.47	Yes	No	285	Exertional both limbs pain	330	Exertional both limbs pain
6	Man	69	IIA, CIA, CFA, SFA, PA	1.53	Yes	No	285	Exertional both limbs pain	330	Exertional both limbs pain
7	Man	44	IIA	1.15	No	No	108	Exertional contralateral limb pain	110	Exertional contralateral limb pain
8	Man	58	IIA	0.94	No	No	205	Exertional both limbs pain	198	Exertional both limbs pain
9	Man	58	IIA, CIA, CFA, SFA, PA	0.94	No	No	205	Exertional both limbs pain	198	Exertional both limbs pain
10	Man	65	SFA	0.93	No	No	345	Exertional contralateral limb pain	284	Exertional contralateral limb pain
11	Man	77	SFA	1.19	No	No	133	Exertional limb pain	218	Exertional limb pain
12	Man	49	SFA, PA	1.07	No	No	244	Painful sore on the contralateral limb	389	Exertional both limbs pain

CIA, common iliac artery; IIA, internal iliac artery; CFA, common femoral artery; SFA, superficial femoral artery; PA, popliteal artery; MWD, Maximal walking distance; Vascular surgery, graft, angioplastia or stenting. Joined lines in blue correspond to a same patient.

TABLE 5 | Characteristics of patients of which neither AHA post-exercise criteria nor the combination of post-exercise ABI with Exercise-TcPO2 detect arterial stenosis ≥50%.

Limbs with a resting ABI > 0.90 and an arterial stenosis ≥50%	Gender	Age (years)	Location of arterial stenosis ≥50%	Resting-ABI of the limb	Diabetes	Vascular surgery	MWD (meter) first test	Cause of stopping for first test	MWD (meter) second test	Cause of stopping for second test
1	Man	63	CIA	1.06	No	No	478	Vertigo	1,053	None
2	Man	70	CIA	1.05	No	No	1,053	None	1,053	None
3	Man	70	CIA	0.99	No	No	1,053	None	1,053	None
4	Man	84	CIA, SFA	0.98	Yes	No	285	Dyspnea	254	Dyspnea
5	Man	58	CIA, SFA	1.13	No	No	235	Exertional contralateral limb pain	333	Exertional both limbs pain
6	Man	72	IIA	1.02	No	No	1,053	Exertional contralateral limb pain	1,053	Exertional contralateral limb pain
7	Woman	76	IIA	1.05	No	No	98	Exertional contralateral limb pain	98	Exertional contralateral limb pain
8	Man	51	SFA	1.96	No	No	1,053	None	1,053	None
9	Man	82	PA	1.66	No	No	281	Exertional contralateral limb pain	358	Exertional contralateral limb pain
10	Man	77	PA	1.12	Yes	No	93	General fatigue	68	General fatigue

CIA, common iliac artery; IIA, internal iliac artery; CFA, common femoral artery; SFA, superficial femoral artery; PA, popliteal artery; MWD, Maximal walking distance; Vascular surgery, graft, angioplastia or stenting. Joint lines in blue correspond to a same patient.

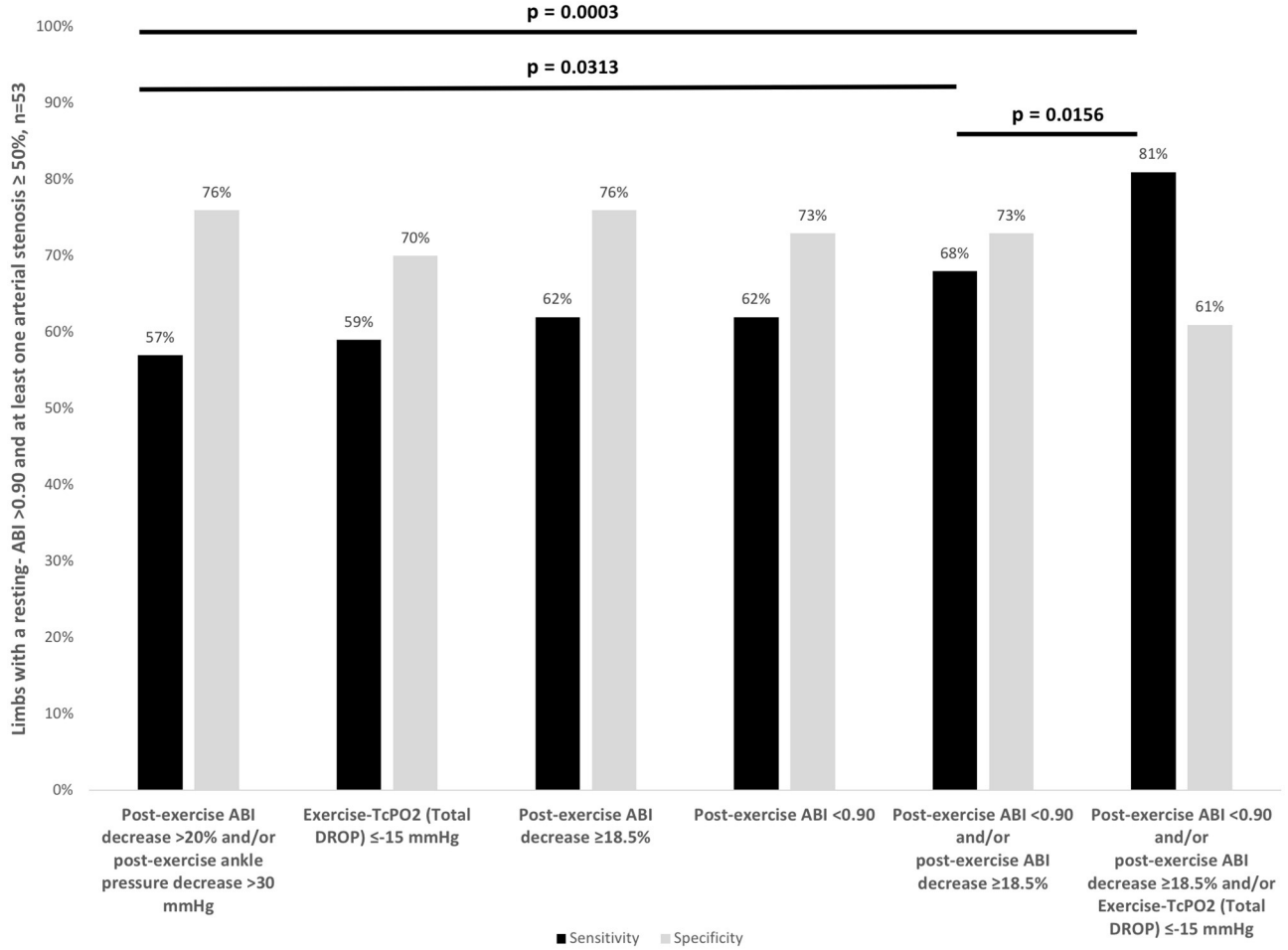

FIGURE 2 | Sensitivity and specificity of exercise tests criteria to diagnose Lower Extremity Peripheral Artery Disease (LEPAD) in patients with an ABI >0.90 and at least one arterial stenosis ≥50%. CI, confidence interval; ABI, Ankle-Brachial Index; DROP, Delta from Resting Oxygen Pressure.

index of ≤-15mmHg (7). Third, if the test is normal, a second exercise testing should be performed. This could either be post-exercise ABI if exercise-TCPO2 was done first. or exercise-TcPO2 if post-exercise ABI was performed first.

Limits

Our study has several limitations. First, we used an automatic blood pressure monitor to assess brachial blood pressure at rest and after exercise. We know that the AHA guidelines recommend performing all pressure measurements with a handheld Doppler at rest (2). However, our objective was that this new diagnosis strategy can be used in clinical practice where in most cases, only one person is devoted to perform the measurement. In that case and based on previous work from Gardner and Montgomery, we have decided to use an automatic blood pressure measurement to perform as quickly as possible the different pressure measurements because pressure can return to normal value very quickly in some patients (27). In order to avoid any bias, we applied the same method at rest. Second, it was not possible to assess the reproducibility of the different tests. However, our reproducibility to perform resting-ABI and the reproducibility of exercise-TcPO2 have been previously reported as good (20, 28). Third, characterization of stenoses has been made with CTA rather than Doppler ultrasound (DUS) in order to allow a double reading of the CTA rather than one reading/operator with the DUS. In a meta-analysis, the reported sensitivity and specificity of CTA to detect aorto-iliac stenoses >50% were 96 and 98%, respectively, with similar sensitivity (97%) and specificity (94%) for the femoropopliteal region (29). Digital subtraction angiography was not retained as a gold standard due to its invasive nature. Fourth, we decided to consider the presence of LEPAD according to the presence of at least one arterial stenosis ≥50% according to the most common practice in the literature (30–37). Fifth, we assess the presence of stenoses on the aorto-iliac and femoro-popliteal tract without studying infrapopliteal arteries. Indeed, we decided not to explore the distal arterial axis due to: (i) the absence of an evaluation of the 3 arterials axis by the resting-ABI (posterior and anterior

tibial artery only), (ii) an arterial stenosis ≥50% on one calf arterial axis could not formally be correlated to an abnormal resting-ABI and formally linked to an intermittent claudication, and iii) degree of infra-popliteal artery stenoses is not assessed, only their permeability. Finally, this last limitation is similar for all exercise tests.

CONCLUSION

Our study shows that the sensitivity of a combination of post-exercise criteria (post-exercise ABI decrease ≥18.5%, or post-exercise ABI < 0.90) with exercise-TcPO2 (Total DROP ≤-15 mmHg) is significantly improved as compared with the use of AHA criteria (post-exercise ABI decrease >20%, or post-exercise pressure >30 mmHg) alone. A trend of a better accuracy of this combined strategy was observed but an external validation should be performed to confirm this diagnostic strategy.

DATA AVAILABILITY STATEMENT

The raw data supporting the conclusions of this article will be made available by the authors, without undue reservation.

ETHICS STATEMENT

The studies involving human participants were reviewed and approved by Institutional Review Board (IRB) from the University Hospital of Rennes (ref.17.12). The patients/participants provided their written informed consent to participate in this study.

AUTHOR CONTRIBUTIONS

OS and GM: protocol conception and design, data interpretation, and drafting of the paper. OS, PL, LO, and GM: data acquisition. OS, AP, DB, ELP, ALF, and GM: data analysis and writing of the paper. Each author revised the report and approved the submitted version of the manuscript. Each author has agreed both to be personally accountable for his/her own contribution and to ensure that questions related to the accuracy or integrity of any part of the work, even those in which the author was not personally involved, are appropriately investigated, resolved, and the resolved outcome documented in the literature. All authors contributed to the article and approved the submitted version.

FUNDING

The Article Processing Charges (APC) were funded by CHU Rennes.

ACKNOWLEDGMENTS

Several parts of the method section of this manuscript are similar to method sections described in our previous studies.

REFERENCES

1. Fowkes FGR, Rudan D, Rudan I, Aboyans V, Denenberg JO, McDermott MM, et al. Comparison of global estimates of prevalence and risk factors for peripheral artery disease in 2000 and 2010: a systematic review and analysis. *Lancet.* (2013) 382:1329–40. doi: 10.1016/S0140-6736(13)61249-0
2. Gerhard-Herman MD, Gornik HL, Barrett C, Barshes NR, Corriere MA, Drachman DE, et al. 2016 AHA/ACC guideline on the management of patients with lower extremity peripheral artery disease: a report of the American College of Cardiology/American Heart Association Task Force on Clinical Practice Guidelines. *Circulation.* (2016) 69:e71–126. doi: 10.1161/CIR.0000000000000471
3. Abraham P, Picquet J, Vielle B, Sigaudo-Roussel D, Paisant-Thouveny F, Enon B, et al. Transcutaneous oxygen pressure measurements on the buttocks during exercise to detect proximal arterial ischemia: comparison with arteriography. *Circulation.* (2003) 107:1896–900. doi: 10.1161/01.CIR.0000060500.60646.E0
4. Abraham P, Picquet J, Bouyé P. L'Hoste P, Enon B, Vielle B, Saumet JL. Transcutaneous oxygen pressure measurements (tcpO2) at ankle during exercise in arterial claudication. *Int Angiol.* (2005) 24:80–8.
5. Koch C, Chauve E, Chaudru S, Le Faucheur A, Jaquinandi V, Mahé G. Exercise transcutaneous oxygen pressure measurement has good sensitivity and specificity to detect lower extremity arterial stenosis assessed by computed tomography angiography. *Medicine.* (2016) 95:e4522. doi: 10.1097/MD.0000000000004522
6. Aday AW, Kinlay S, Gerhard-Herman MD. Comparison of different exercise ankle pressure indices in the diagnosis of peripheral artery disease. *Vasc Med.* (2018) 23:541–8. doi: 10.1177/1358863X18781723
7. Stivalet O, Paisant A, Belabbas D, Omarjee L, Le Faucheur A, Landreau P, et al. Exercise testing criteria to diagnose lower extremity peripheral artery disease assessed by computed-tomography angiography. *PLoS ONE.* (2019) 14:e0219082. doi: 10.1371/journal.pone.0219082
8. Mahé G, Catillon F, Tollenaere Q, Stivalet O, Guilcher A, Le Pabic E, et al. Confirmation of discrepancies between exercise oximetry and American Heart Association post-exercise criteria to diagnose peripheral artery disease in patients with normal ankle-brachial index at rest. *Pflugers Arch.* (2020) 472:321–2. doi: 10.1007/s00424-020-02360-x
9. Mahé G, Catillon F, Tollenaere Q, Jéhannin P, Guilcher A, Le Pabic E, et al. Discordance of peripheral artery disease diagnosis using exercise transcutaneous oxygen pressure measurement and post-exercise ankle-brachial index. *Sci Rep.* (2020) 10:7419. doi: 10.1038/s41598-020-64276-x
10. Abraham P, Hersant J, Ramondou P, Picquet J, Feuilloy M, Henni S, et al. Comparison of exercise oximetry and ankle pressure measurements for patients with intermittent claudication: an observational study of 433 patients. *Pflugers Arch.* (2020) 472:293–301. doi: 10.1007/s00424-019-02340-w
11. Chaudru S, de Müllenheim P-Y, Le Faucheur A, Kaladji A, Jaquinandi V, Mahé G. Training to perform ankle-brachial index: systematic review and perspectives to improve teaching and learning. *Eur J Vasc Endovasc Surg.* (2016) 51:240–7. doi: 10.1016/j.ejvs.2015.09.005
12. Aboyans V, Criqui MH, Abraham P, Allison MA, Creager MA, Diehm C, et al. Measurement and interpretation of the ankle-brachial index: a scientific statement from the American Heart Association. *Circulation.* (2012) 126:2890–909. doi: 10.1161/CIR.0b013e318276fbcb
13. Mahé G, Kaladji A, Le Faucheur A, Jaquinandi V. Internal iliac artery stenosis: diagnosis and how to manage it in 2015. *Front Cardiovasc Med.* (2015) 2:33. doi: 10.3389/fcvm.2015.00033
14. Mahe G, Kalra M, Abraham P, Liedl DA, Wennberg PW. Application of exercise transcutaneous oxygen pressure measurements for detection of proximal lower extremity arterial disease: a case report. *Vasc Med.* (2015) 20:251–5. doi: 10.1177/1358863X14567030
15. Poulin A, Guilcher A, Omarjee L, Jaquinandi V, Gandon Y, Mahe G, et al. Validation of a software to perform exercise oximetry to diagnose

arterial stenosis of the lower limbs. *Atherosclerosis.* (2018) 278:325–7. doi: 10.1016/j.atherosclerosis.2018.08.025
16. Mahé G, Boge G, Bura-Rivière A, Chakfé N, Constans J, Goueffic Y, et al. Disparities between international guidelines (AHA/ESC/ESVS/ESVM/SVS) concerning lower extremity arterial disease: consensus of the french society of vascular medicine (SFMV) and the French Society for Vascular and Endovascular Surgery (SCVE). *Ann Vasc Surg.* (2021) 72:1–56. doi: 10.1016/j.avsg.2020.11.011
17. Mahé G, Jaquinandi V. Diagnosis of lower limb peripheral artery disease. *Presse Med.* (2018) 47:47–55. doi: 10.1016/j.lpm.2017.09.021
18. Stivalet O, Laneelle D, Omarjee L, Mahe G. Post-exercise criteria to diagnose lower extremity peripheral artery disease: Which one should I use in my practice? *Vasc Med.* (2019) 24:76–7. doi: 10.1177/1358863X18811932
19. Mahe G, Pollak AW, Liedl DA, Cohoon KP, Mc Carter C, Rooke TW, et al. Discordant diagnosis of lower extremity peripheral artery disease using american heart association postexercise guidelines. *Medicine (Baltimore).* (2015) 94:e1277. doi: 10.1097/MD.0000000000001277
20. Ouriel K, McDonnell AE, Metz CE, Zarins CK. Critical evaluation of stress testing in the diagnosis of peripheral vascular disease. *Surgery.* (1982) 91:686–93.
21. Laing SP, Greenhalgh RM. Standard exercise test to assess peripheral arterial disease. *Br Med J.* (1980) 280:13–6. doi: 10.1136/bmj.280.6206.13
22. Mahé G, Ouedraogo N, Leftheriotis G, Vielle B, Picquet J, Abraham P. Exercise treadmill testing in patients with claudication, with and without diabetes. *Diabet Med.* (2011) 28:356–62. doi: 10.1111/j.1464-5491.2010.03208.x
23. Mahé G, Lanéelle D, Le Faucheur A. Postexercise ankle-brachial index testing to diagnose peripheral artery disease. *JAMA.* (2021) 325:89. doi: 10.1001/jama.2020.22475
24. Paul E, Jaquinandi V, Larralde A, Schnell F, Mahé G. Contribution of the maximal exercise test to diagnosis the vascular origin of leg pain in athletes. *J Med Vasc.* (2018) 43:379–83. doi: 10.1016/j.jdmv.2018.10.001
25. Stivalet O, Lanéelle D, Mahé G, Jaquinandi V, Omarjee L. Time to redefine post-exercise pressure decrease and post-exercise ankle-brachial index to diagnose peripheral artery disease. *Scand J Med Sci Sports.* (2018) 28:2457–8. doi: 10.1111/sms.13293
26. Bruneau A, Le Faucheur A, Mahe G, Vielle B, Leftheriotis G, Abraham P. Endofibrosis in athletes: is a simple bedside exercise helpful or sufficient for the diagnosis? *Clin J Sport Med.* (2009) 19:282–6. doi: 10.1097/JSM.0b013e3181b20456
27. Gardner AW, Montgomery PS. Comparison of three blood pressure methods used for determining ankle/brachial index in patients with intermittent claudication. *Angiology.* (1998) 49:723–8. doi: 10.1177/000331979804901003
28. Bouyé P, Picquet J, Jaquinandi V, Enon B, Leftheriotis G, Saumet J-L, et al. Reproducibility of proximal and distal transcutaneous oxygen pressure measurements during exercise in stage 2 arterial claudication. *Int Angiol.* (2004) 23:114–21.
29. Met R, Bipat S, Legemate DA, Reekers JA, Koelemay MJW. Diagnostic performance of computed tomography angiography in peripheral arterial disease: a systematic review and meta-analysis. *JAMA.* (2009) 301:415–24. doi: 10.1001/jama.301.4.415
30. Allen J, Oates CP, Henderson J, Jago J, Whittingham TA, Chamberlain J, et al. Comparison of lower limb arterial assessments using color-duplex ultrasound and ankle/brachial pressure index measurements. *Angiology.* (1996) 47:225–32. doi: 10.1177/000331979604700302
31. Clairotte C, Retout S, Potier L, Roussel R, Escoubet B. Automated ankle-brachial pressure index measurement by clinical staff for peripheral arterial disease diagnosis in nondiabetic and diabetic patients. *Diabetes Care.* (2009) 32:1231–6. doi: 10.2337/dc08-2230
32. de Groote P, Millaire A, Deklunder G, Marache P, Decoulx E, Ducloux G. Comparative diagnostic value of ankle-to-brachial index and transcutaneous oxygen tension at rest and after exercise in patients with intermittent claudication. *Angiology.* (1995) 46:115–22. doi: 10.1177/000331979504600204
33. Guo X, Li J, Pang W, Zhao M, Luo Y, Sun Y, et al. Sensitivity and specificity of ankle-brachial index for detecting angiographic stenosis of peripheral arteries. *Circ J.* (2008) 72:605–10. doi: 10.1253/circj.72.605
34. Lijmer JG, Hunink MG, van den Dungen JJ, Loonstra J, Smit AJ, ROC analysis of noninvasive tests for peripheral arterial disease. *Ultrasound Med Biol.* (1996) 22:391–8. doi: 10.1016/0301-5629(96)00036-1
35. Niazi K, Khan TH, Easley KA. Diagnostic utility of the two methods of ankle brachial index in the detection of peripheral arterial disease of lower extremities. *Catheter Cardiovasc Interv.* (2006) 68:788–92. doi: 10.1002/ccd.20906
36. Sumner DS, Strandness DE. The relationship between calf blood flow and ankle blood pressure in patients with intermittent claudication. *Surgery.* (1969) 65:763–71.
37. Wikström J, Hansen T, Johansson L, Lind L. Ahlström H. Ankle brachial index <09 underestimates the prevalence of peripheral artery occlusive disease assessed with whole-body magnetic resonance angiography in the elderly. *Acta Radiol.* (2008) 49:143–9. doi: 10.1080/02841850701732957

Conflict of Interest: The authors declare that the research was conducted in the absence of any commercial or financial relationships that could be construed as a potential conflict of interest.

Publisher's Note: All claims expressed in this article are solely those of the authors and do not necessarily represent those of their affiliated organizations, or those of the publisher, the editors and the reviewers. Any product that may be evaluated in this article, or claim that may be made by its manufacturer, is not guaranteed or endorsed by the publisher.

frontiers in Cardiovascular Medicine

ORIGINAL RESEARCH
published: 18 November 2021
doi: 10.3389/fcvm.2021.788645

Neuraminidase 1 Exacerbating Aortic Dissection by Governing a Pro-Inflammatory Program in Macrophages

Qian Wang[1†], Zhaoyang Chen[2†], Xiaoping Peng[3,4†], Zeqi Zheng[3,4†], Aiping Le[1†], Junjie Guo[5], Leilei Ma[6], Hongtao Shi[6], Kang Yao[6], Shuning Zhang[6], Zhenzhong Zheng[3,4] and Jianbing Zhu[3,4]*

[1] Department of Blood Transfusion, The First Affiliated Hospital of Nanchang University, Nanchang, China, [2] Department of Cardiology, Union Hospital, Fujian Medical University, Fuzhou, China, [3] Department of Cardiology, The First Affiliated Hospital of Nanchang University, Nanchang, China, [4] Department of Cardiology, Jiangxi Hypertension Research Institute, Nanchang, China, [5] Department of Cardiology, Affiliated Hospital of Qingdao University, Qingdao, China, [6] Department of Cardiology, Shanghai Institute of Cardiovascular Diseases, Zhongshan Hospital, Fudan University, Shanghai, China

Inflammation plays an important role in aortic dissection (AD). Macrophages are critically involved in the inflammation after aortic injury. Neuraminidases (NEUs) are a family of enzymes that catalyze the cleavage of terminal sialic acids from glycoproteins or glycolipids, which is emerging as a regulator of macrophage-associated immune responses. However, the role of neuraminidase 1 (NEU1) in pathological vascular remodeling of AD remains largely unknown. This study sought to characterize the role and identify the potential mechanism of NEU1 in pathological aortic degeneration. After β-aminopropionitrile monofumarate (BAPN) administration, NEU1 elevated significantly in the lesion zone of the aorta. Global or macrophage-specific NEU1 knockout (NEU1 CKO) mice had no baseline aortic defects but manifested improved aorta function, and decreased mortality due to aortic rupture. Improved outcomes in NEU1 CKO mice subjected to BAPN treatment were associated with the ameliorated vascular inflammation, lowered apoptosis, decreased reactive oxygen species production, mitigated extracellular matrix degradation, and improved M2 macrophage polarization. Furthermore, macrophages sorted from the aorta of NEU1 CKO mice displayed a significant increase of M2 macrophage markers and a marked decrease of M1 macrophage markers compared with the controls. To summarize, the present study demonstrated that macrophage-derived NEU1 is critical for vascular homeostasis. NEU1 exacerbates BAPN-induced pathological vascular remodeling. NEU1 may therefore represent a potential therapeutic target for the treatment of AD.

Keywords: NEU1, aortic dissection, vascular remodeling, macrophage polarization, MMP

OPEN ACCESS

Edited by:
Ryuichi Morishita, Osaka University, Japan

Reviewed by:
Yasushi Fujio, Osaka University, Japan
Tlili Barhoumi, King Abdullah International Medical Research Center (KAIMRC), Saudi Arabia

***Correspondence:**
Jianbing Zhu
ncdxzjb2020@outlook.com

[†] These authors have contributed equally to this work

Specialty section:
This article was submitted to Atherosclerosis and Vascular Medicine, a section of the journal Frontiers in Cardiovascular Medicine

Received: *03 October 2021*
Accepted: *20 October 2021*
Published: *18 November 2021*

Citation:
Wang Q, Chen Z, Peng X, Zheng Z, Le A, Guo J, Ma L, Shi H, Yao K, Zhang S, Zheng Z and Zhu J (2021) Neuraminidase 1 Exacerbating Aortic Dissection by Governing a Pro-Inflammatory Program in Macrophages. Front. Cardiovasc. Med. 8:788645. doi: 10.3389/fcvm.2021.788645

INTRODUCTION

Aortic dissection (AD) is a fatal surgical emergency characterized by acute-onset chest or back pain with few, if any, preceding signs (1). The mortality rate is 60–70% in the first 24 h (2). Anatomically, when the intima of the aorta is damaged and ruptured for various reasons, the flow of blood through the tears and separated the media into two layers, leading to the further destruction of the aortic wall (3). Despite new concepts regarding the diagnosis, classification, and treatment of AD have been developed recently (4), little is known about the pathological and molecular mechanisms before and after the onset of AD due to its sudden and unpredictable nature (5). Therefore, ongoing research is emergency for elucidating the pathophysiology of AD and developing diagnostic and therapeutic intervention methods.

The pathophysiology of AD has gradually been elucidated. In addition to mutations in some genes involved in extracellular matrix metabolism and smooth muscle cytoskeleton, some high-risk factors for AD have also been confirmed, including long-term hypertension, dyslipidemia, smoking, giant cell arteritis, etc. These non-genetic factors suggest that the inflammation may make the aorta susceptible to AD (6). Inflammatory cells infiltrate the injured site of the aorta to remove necrotic cells and damaged tissue; however, the excessive inflammation may play a role in aneurysm formation after dissection (7). Although the degeneration of the media is a fundamental pathological change of AD, the degeneration only weakens the media, and most cases of AD form intimal tears at the beginning. Further studies have shown that the inflammation is an important mechanism leading to intimal damage and mid-layer degeneration (8). Moreover, an analysis of gene expression changes in human dissecting tissues using cDNA microarrays confirmed that the inflammation was involved in the pathogenesis of disease (9). Indeed, numerous studies confirmed that inflammatory cytokines and chemokines, including interleukin (IL)-6, granulocyte colony-stimulating factor, granulocyte macrophage colony-stimulating factor, IL-17, chemokine (C–X–C motif) ligand 1, and C–C motif chemokine ligand 2, play essential roles in AD pathogenesis (10–12). IL-6-STAT3 signaling pathway promotes AD induced by angiotensin (Ang) II *via* the Th17/IL-17 axis in mice (13).

Different types of immune cells infiltrated in the lesion area of the AD aorta, among which macrophages are the most abundant cell type (14). Evidence from animal models and patients showed marked infiltration of macrophages at the site of tears (15). Animal model studies revealed the importance of signaling amplification loops between macrophages and fibroblasts *via* IL-6 and monocyte/macrophage chemokine (MCP-1) in AD tissues (10). Macrophage-associated cytokine signaling may be the targets to prevent the development and progression of AD. For example, Socs3 in macrophages modulates the stress response of macrophages and vascular smooth muscle cells (VSMCs) and promotes the healing of damaged aortic walls and preventing AD development in mice, whereas macrophage Socs3 knockout mice showed premature activation of cell proliferation, increased inflammatory response, and the conversion of macrophages to a pro-inflammatory phenotype (5).

Neuraminidases (NEUs), also known as sialidases, are a family of enzymes that cleave sialic acid on the surfaces of cells. NEU1 is the most abundant and ubiquitous of the four mammalian sialidases with a wide tissue distribution (16). In addition to participating in catabolism of glycoproteins and glycolipids *in vivo*, an increasing body of literature suggests that NEU1 also plays an important role in the immune system, especially in the macrophage-related inflammation (17). For example, animal studies have found that sialidase deficiency leads to reduced macrophage effect, whereas the upregulation of NEU1 expression during the differentiation of monocytes into macrophages helps to enhance the phagocytosis of these cells (18). Recently, a study has shown that NEU1 regulates the activation of TLR receptors on macrophages, to be specific, binding of the ligand to TLR induces NEU1 activity, leading to the desalivation of the receptor, which in turn induces receptor activation, nitric oxide, and pro-inflammatory cytokine production (19). Given inflammatory macrophage triggering AD and NEU1 governing macrophage polarization, whether NEU1 is involved in the pathogenesis of AD through the regulation of macrophages has not been reported.

In the present study, we observed that the NEU1 expression was markedly upregulated in aortic tissues from β-aminopropionitrile monofumarate (BAPN)-induced AD mice. Deletion of NEU1 (either global or specifically in macrophage) all manifested improved aorta function, vascular remodeling, and decreased mortality due to aortic rupture. Mechanically, improved outcomes in NEU1 CKO mice were associated with the improved vascular inflammation, which at least in part by promoting the polarization of M2 macrophages. Therefore, it is proposed that NEU1 may be a potential therapeutic target for AD.

METHODS

Animals

$NEU1^{F/F}$ mice, $LysM^{Cre}$, and NEU1 KO mice (C57BL/6) were purchased from Shanghai Biomodel Organism Co, Shanghai, China. NEU1 gene is comprised of five coding exons 2–6. To generate $NEU1^{F/F}$ mice, a donor vector containing exon 2 flanked by two loxP sites and two homology arms were used as the homologous recombination mediated repairing template. $NEU1^{F/F}$ mice were hybridized with $LysM^{Cre}$ mice to generate $NEU1^{F/F}$, $LysM^{Cre}$ (NEU1 CKO) mice. All experiment animals were male considering the feature of less sex hormone variations and high incidence of thoracic aortic dissection (TAD). Age/weight-matched wild-type (WT) mice served as controls. NEU1 KO, $NEU1^{F/F}$ mice, and NEU1 CKO mice aged 4 weeks were administrated with BAPN in the drinking water with 1 g/kg/day for 4 weeks to induce TAD. All mice shared standard chow and water and were maintained with an alternating 12-h light/dark cycle. All animal procedures were performed in accordance with the protocols approved by the Animal Care and Use Committee of The First Affiliated Hospital of Nanchang University.

Immunofluorescence Staining

Vascular tissue was firstly fixed with 4% paraformaldehyde (PFA) at room temperature for 2 h. After phosphate-buffered saline (PBS) washing, they were dehydrated with 30% sucrose overnight and embedded in optimum cutting temperature (OCT) solution (Sakura Finetek Inc., Torrance, CA, USA). Before the experiment, the frozen sections (7 μm) were dried at room temperature and fixed in cold acetone solution for 10 min. Sections were sealed with 3% bovine serum albumin (BSA) for 2 h to prevent non-specific binding. COL1A1 (1:200; NBP1-30054; Novus, St. Louis, MO, USA), CD68 (1:200, AB283654; Abcam, Cambridge, UK), inducible nitric oxide synthase (iNOS) (1:200, AB178945; Abcam, Cambridge, UK), arginase-1 (Arg-1) (1:200, 93668; Cell Signaling Technology, Danvers, MA, USA), and NEU1 (1:500, sc-166824; Santa Cruz Biotechnology, Santa Cruz, CA, USA) were incubated at 4°C overnight. An appropriate secondary antibody (1:500) was taken and incubated at room temperature for 2 h. The 4′,6-diamidino-2-phenylindole (DAPI) staining was performed after full rinse-washing. Finally, it was sealed with anti-fade reagent and observed by laser scanning confocal microscope (Carl Zeiss, Oberkochen, Germany). For cell immunofluorescence test, sorted macrophages were cultured on a coverslip placed in 12-well plate. Before the experiment, the slides were fixed with 4% PFA for 30 min, rinsed with PBS, and remaining procedures were according to the frozen sections. The primary antibody used was as follows: iNOS (1:200, AB178945, Abcam, Cambridge, UK) and Arg-1 (1:200, 93668; Cell Signaling Technology, Danvers, MA, USA).

Dihydroethidium Staining

Dihydroethidium (DHE) assay kit (S0063, Beyotime, Shanghai, China) was used to measure superoxide anions in aorta sections of $NEU1^{F/F}$ and NEU1 CKO mice. Each group of sections was exposed to DHE (10 μM) for 30 min at 37°C. After washing with PBS three times, samples were visualized by confocal microscopy (Olympus Corp., Tokyo, Japan).

Hematoxylin and Eosin Staining

Hematoxylin and Eosin Kit (ab245880, Abcam, Cambridge, UK) was used for the pathology study of the aorta. Briefly, sections were deparaffinized and hydrated in distilled water. Then, sections were placed in adequate Mayer's Hematoxylin (Lillie's Modification) to completely cover tissue section and incubated for 5 min. Furthermore, slides were rinsed in two changes of distilled water to remove excess stain. Later, slides were applied with adequate bluing reagent to completely cover tissue section and incubated for 10–15 s. Then slides were rinsed in two changes of distilled water and dipped in absolute alcohol and blot off the excess, applied with adequate Eosin Y Solution (Modified Alcoholic) to completely cover tissue section to excess and incubated for 2–3 min. Furthermore, slides were rinsed using absolute alcohol and dehydrated in three changes of absolute alcohol. Clear slides were mounted in synthetic resin.

Van Gieson's Staining

Van Gieson's Staining Kit (ab150667, Abcam, Cambridge, UK) was used for the study of the elastin degradation. Briefly, sections were deparaffinized and hydrated in distilled water. Then slides were placed in Elastic Stain Solution for 15 min, rinsed in running tap water until no excess stain remains on slides, and were dipped in differentiating solution 15–20 times and rinsed in tap water. Slides were checked microscopically for proper differentiation, rinsed in running tap water, placed in sodium thiosulfate solution for 1 min, and rinsed in running tap water. Stained slides were placed in Van Gieson's solution (ab150667, Abcam, Cambridge, UK) for 2–5 min, rinsed in two changes of 95% alcohol, and dehydrated in absolute alcohol. Clear slides were mounted in synthetic resin.

TUNEL

Cell Death Detection Kit (C1088, Beyotime, Shanghai, China) was used for cell apoptosis studies. The TUNEL staining was performed according to the instructions of the manufacturer. First, the frozen sections of vascular tissue were fixed with 4% PFA for 30 min and incubated with 0.5% Triton X-100 at room temperature for 5 min. The TUNEL detection solution was added and incubated at 37°C for 60 min in dark. The tissue sections were observed by confocal microscopy. For each aortic treatment, images were captured from three randomly selected views. The number of positive cells and the total number of nuclei in each image were quantitatively analyzed.

RNA Extraction and Quantitative Real-Time PCR

Total RNA was extracted from aortic tissue using the TRIzol reagent (Invitrogen, Carlsbad, CA, USA), and RNA was isolated from sorting macrophages using the RNeasy Plus Micro Kit (74034, QIAGEN, Hilden, Germany), according to the instructions of the manufacturer. RNA samples (1 μg) were subsequently reverse-transcribed into cDNA with a reverse transcription reagent kit (RR036A, Takara Bio Inc., Kusatsu, Japan), and the resulting cDNA was amplified by RT-PCR using the SYBR Green Mix (11201ES08; Yeasen, Shanghai, China). Each sample was analyzed in triplicate and normalized to a reference RNA. Relative expression levels were quantitated using the ΔΔCt method.

Western Blotting

The protein concentrations of aortic tissue lysates were determined using a Pierce BCA Protein Assay Kit (Pierce Biotechnology, Waltham, MA, USA). Equal amounts of samples were loaded and separated on 10% SDS-PAGE. Then, the proteins were transferred to nitrocellulose membranes, incubated with 5% skimmed milk for 2 h at room temperature, and incubated with primary antibodies overnight at 4°C. Primary antibodies were used as follows: NEU1 (1:500, sc-166824, Santa Cruz Biotechnology, Santa Cruz, CA, USA) and GAPDH (1:1000, 5174s, Cell Signaling Technology, Danvers, MA, USA) Then, the membranes were incubated with the corresponding secondary antibodies. The blots were visualized using a chemiluminescence reagent. Densitometric analysis for each band was performed using the ImageJ software (National Institutes of Health, Bethesda, MD, USA).

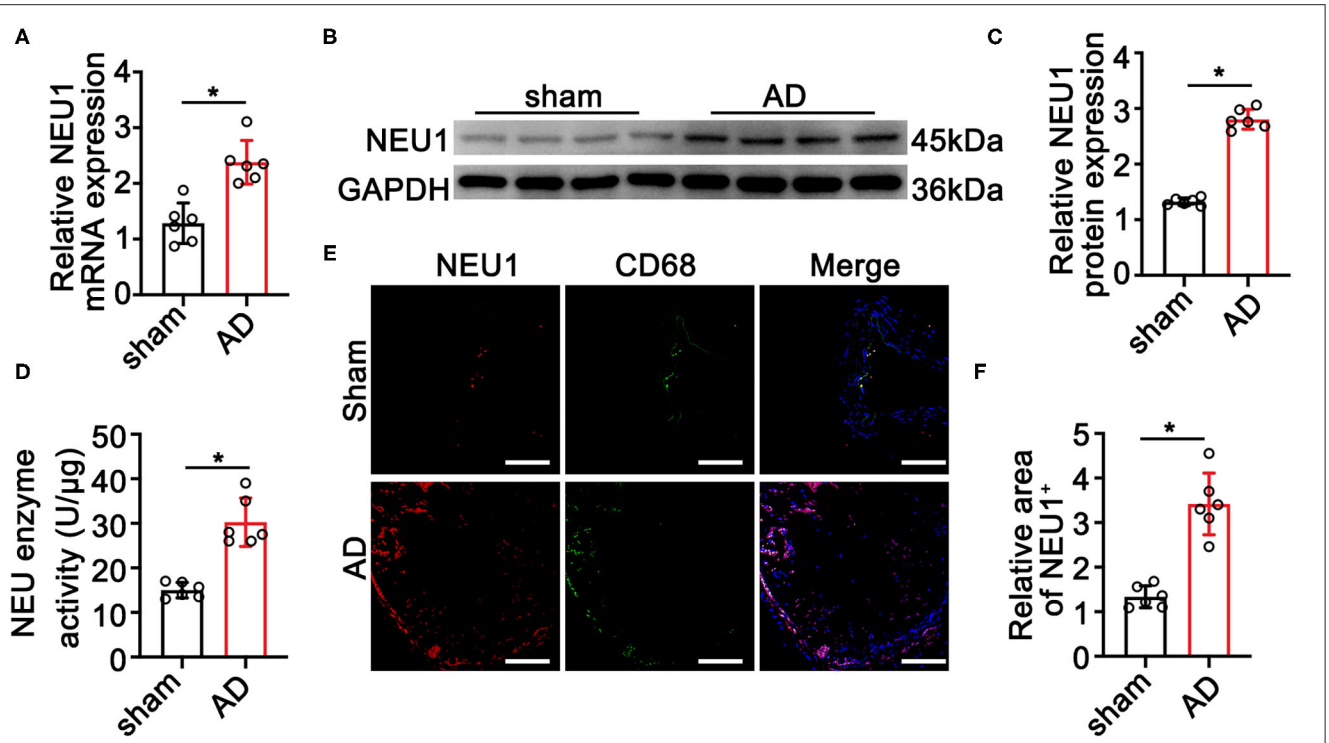

FIGURE 1 | Neuraminidase 1 (NEU1) expression increases in aortic dissecting (AD) tissues. **(A)** Quantitative results of NEU1 mRNA level in aortas of mice subjected to BAPN induction for 4 weeks ($n = 6$ mice per group). **(B,C)** Representative western blots and quantitative results of NEU1 level in aortas of mice subjected to BAPN induction for 4 weeks ($n = 6$ mice per group). **(D)** The neuraminidase enzyme activity of AD in mice by ELISA ($n = 6$ aortas per group). **(E,F)** Immunofluorescence staining with anti-NEU1 (red) and anti-CD68 (green) antibody in slices from the indicated mice aortas ($n = 6$ mice aortas per group; scale bar: 50 μm). Data are presented as mean ± SEM. **(A,C,D,F)** unpaired two-tailed *t*-test. BAPN, β-aminopropionitrile monofumarate; NEU1, neuraminidase 1. $^*p < 0.05$.

Flow Cytometry

Macrophages were analyzed and sorted using a fluorescence-activated cell sorter (FACS) (BD Biosciences, San Jose, CA, USA) as previously described. Briefly, the AD tissues were dissected, carefully cut into small pieces, and enzymatically digested with collagenase II (1.5 mg/ml), elastase (0.25 mg/ml), and DNase I (0.5 mg/ml) for 1 h at 37°C. After digestion, the tissues were passed through 70-μm cell strainers. After washing, anti-CD16/32 antibody was used to block the non-specific binding. Fixable viability stain 510 (564406, BD Biosciences, San Jose, CA, USA) and the following antibodies were used for flow cytometry: CD45-APC-Cy7 (557659, BD Biosciences), CD11b-PE-Cy7 (552850, BD Biosciences), F4/80-BV421 (565411, BD Biosciences), CD86-PE (553692, BD Biosciences), and CD206-APC (565250, BD Biosciences). For flow cytometric sorting, cells were resuspended in the FACS buffer at 20×10^6 cells/ml and separated on a MoFlo High-Performance Cell Sorter (Dako Cytomation, Carpinteria, CA, USA). The results were expressed as the absolute number of cells per mg of tissue. Data were analyzed with the FlowJo software (FlowJo LLC, Ashland, OR, USA).

Statistical Analysis

All data are presented as the mean ± SEM and analyzed in GraphPad Prism 8.0 (GraphPad Software, San Diego, CA). Data normality was determined by the Shapiro–Wilk test. The significant differences between different data were calculated by unpaired two-tailed *t*-test (for two groups) and one-way or two-way ANOVA (for more than two groups) followed by the Tukey's and Dunnett's multiple comparisons test. The *p*-value lower than 0.05 were considered statistically significant.

RESULTS

NEU1 Expression Increases in Aortic Dissecting Tissues

To elucidate the role of NEU1 in AD development, we detected the expression of NEU1 in AD tissues. As shown in **Figures 1A–C**, the mRNA and protein levels of NEU1 were dramatically higher in AD vessels than in normal controls. The NEU1 activity was also elevated in dissecting aortas compared with the controls (**Figure 1D**). Since NEU1 was reported to highly expressed in macrophages in atherosclerosis vessels (20), we therefore speculated that NEU1 may also highly expressed in macrophages in AD vessels. CD68 and NEU1 immunofluorescence staining revealed NEU1 was mainly located in $CD68^+$ macrophages in dissecting aortas (**Figures 1E,F**). Collectively, these results revealed that NEU1 may play a role in AD development.

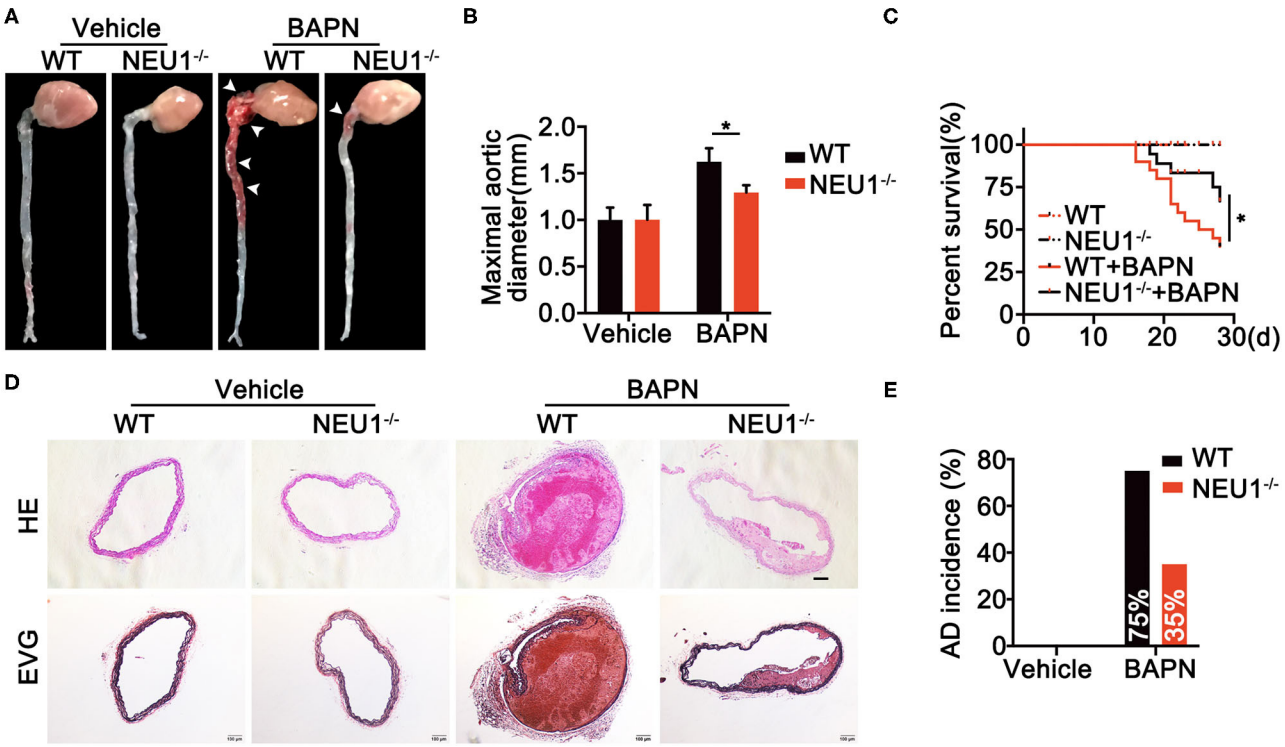

FIGURE 2 | Global NEU1 deletion mitigates BAPN-induced AD development. **(A–E)**, C57BL/6 wild-type and NEU1 KO mice were subjected to BAPN induction. **(A)** Representative macrographs of the aortas. **(B)** Maximal aortic diameter ($n = 8$, $^*p < 0.05$). **(C)** Kaplan–Meier survival analysis of indicated groups ($n = 20$, $^*p < 0.05$). **(D)** Representative HE and EVG staining of the aorta. **(E)** AD incidence in indicated groups ($n = 20$). AD, aortic dissecting; BAPN, β-aminopropionitrile monofumarate; EVG, Elastic Van Gieson's staining; HE, hematoxylin and eosin; KO, knockout; NEU1, neuraminidase 1.

Global NEU1 Deletion Mitigates BAPN-Induced AD Development

To further discern the role of NEU1 in AD development, a murine AD model was established using 4-week BAPN drinking in C57BL/6-WT and NEU1 KO mice (**Supplementary Figure 1A**). Interestingly, BAPN administration prompted AD formation, increased maximal aortic diameters, and provoked a remarkable mortality (**Figures 2A–C**), the effects of which were greatly attenuated by NEU1 KO, with little effect at base line (**Figures 2A–C**). Moreover, hematoxylin and Verhoeff–van Gieson staining demonstrated that NEU1 deletion mitigated BAPN-induced dissecting aneurysm formation and elastic fiber degradation (**Figure 2D**). Additionally, AD incidence was also alleviated in NEU1 KO mice (35%) compared with WT controls (75%) (**Figure 2E**). These findings denoted the benefit of NEU1 deficiency in AD development.

Macrophage-Specific NEU1 Deletion Mitigates BAPN-Induced AD Development

Since NEU1 was identified to highly localized in macrophages in lesion area of vessels as shown in **Figure 1E**, we therefore utilized macrophage NEU1 KO mice (**Supplementary Figure 1B**) to establish AD model. Coincidently, BAPN administration prompted AD formation, increased maximal aortic diameters, and provoked a remarkable mortality (**Figures 3A–C**), the effects of which were greatly attenuated by Mac-NEU1 KO (**Figures 3A–C**). Moreover, hematoxylin and Verhoeff–van Gieson staining demonstrated that macrophage NEU1 deletion mitigated BAPN-induced dissecting aneurysm formation and elastic fiber degradation (**Figure 3D**). Additionally, AD incidence was also decreased in NEU1 CKO mice (30%) compared with controls (60%) (**Figure 3E**). These findings denoted the benefit of macrophage NEU1 deficiency in AD development.

NEU1 Depletion Suppresses BAPN-Induced Inflammation

Given the role of NEU1 in the inflammation and the localization of NEU1 in macrophages, we therefore detected both pro- and anti-inflammatory factors. Protein and mRNA analysis revealed that BAPN administration enhanced the expression of pro-inflammatory factors like IL-6, IL-1β, tumor necrosis factor (TNF)-α, matrix metalloproteinase (MMP)-2, and MMP-9 in $NEU1^{F/F}$ mice, whereas Mac-NEU1 KO partly reversed the inflammatory state (**Figures 4A–E,I**). Meanwhile, the expression of anti-inflammatory factors like IL-10, IL-4, and transforming growth factor (TGF)-β was higher in NEU1 CKO mice than those in $NEU1^{F/F}$ mice following BAPN treatment (**Figures 4F–H,I**).

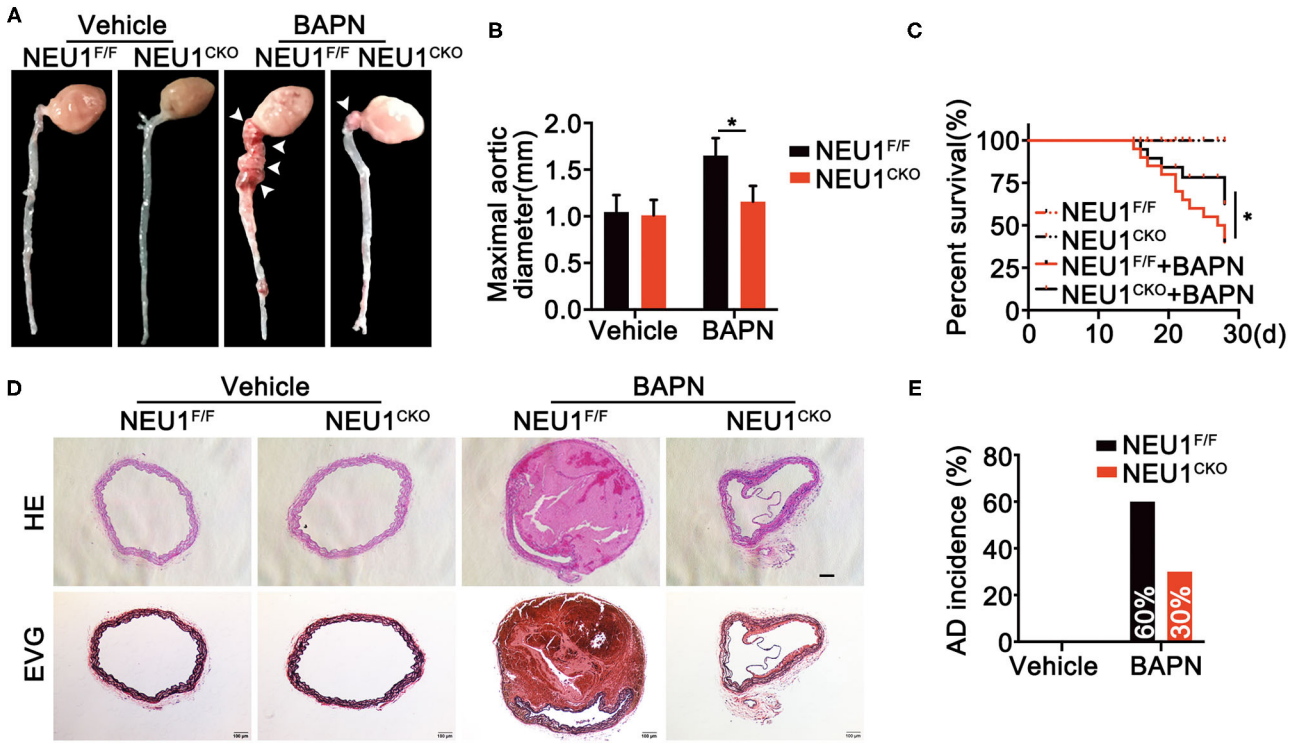

FIGURE 3 | Macrophage-specific NEU1 knockout (NEU1 CKO) deficiency mitigates BAPN-induced AD development. **(A–E)**, NEU1$^{F/F}$ and NEU1 CKO mice were subjected to BAPN induction. **(A)** Representative macrographs of the aortas. **(B)** Maximal aortic diameter ($n = 9$, $^*p < 0.05$). **(C)** Kaplan–Meier survival analysis of indicated groups ($n = 20$, $^*p < 0.05$). **(D)** Representative HE and EVG staining of the aorta. **(E)** AD incidence in indicated groups ($n = 20$). AD, aortic dissecting; BAPN, β-aminopropionitrile monofumarate; HE, hematoxylin and eosin; KO, knockout; NEU1, neuraminidase 1.

Moreover, the exacerbated cell apoptosis, extracellular matrix (ECM) degradation, MMP 2/9 activity, and reactive oxygen species (ROS) production by BAPN administration were rescued by NEU1 deletion in macrophage (**Figures 4J–M**). NEU1 deficiency alone affects little in aortic function (**Figures 4A–M**). The above results demonstrated that NEU1 promoted the inflammation, apoptosis, and ROS production, thus leading to the progression of AD.

NEU1 Deletion Promotes the M2 Polarization of Macrophages

Neuraminidase 1 was realized to regulate the inflammation of aorta; we therefore studied the role of NEU1 in macrophage polarization. Flow cytometry analysis of the BAPN-induced aorta revealed that NEU1 deletion promoted the polarization of macrophage from pro-inflammatory to anti-inflammatory state (**Figures 5A–D**). Immunofluorescence staining of the aorta also displayed that the pro-inflammatory marker iNOS was decreased, and the anti-inflammatory marker Arg-1 was increased by NEU1 depletion in BAPN-induced mice (**Figures 5E,F**). The mRNA analysis of the macrophages sorted by flow cytometry was coincidence with the previous results (**Figures 5G,H**). Furthermore, we sorted the macrophages from WT and NEU1 CKO mice and subjected to Ang II treatment for 24 h. Immunofluorescence staining revealed that NEU1-deficient macrophages were prone to M2 polarization (**Figures 5I,J**). Our findings demonstrated that the critical role of NEU1 in macrophage polarization.

DISCUSSION

In this study, we found that NEU1 expression was significantly upregulated in dissecting tissues from BAPN-induced AD mice. Additionally, using genetically KO mice, we demonstrated that NEU1 played an important role in the development of AD. Furthermore, the elevated NEU1 expression in macrophages promotes the M1 macrophage polarization. Therefore, NEU1 may become a potential therapeutic target for AD.

Neuraminidases are a family of four different enzymes, NEU1, NEU2, NEU3, and NEU4, which remove the terminal sialic acids from glycoproteins or glycolipids (21). Among the four sialidases, the lysosomal NEU1 has been shown to assume a vital role in immune cells (22). The immune inflammatory response plays an important role in the development of AD. However, whether NEU1 could affect the pathogenesis of AD remains unknown. Previous studies suggest that NEU1 is closely associated with the progression of several cardiovascular diseases. Lipopolysaccharide (LPS), NEU1, and IL-1β act in a positive feedback loop as enhancers of inflammation in monocytes/macrophages and may therefore

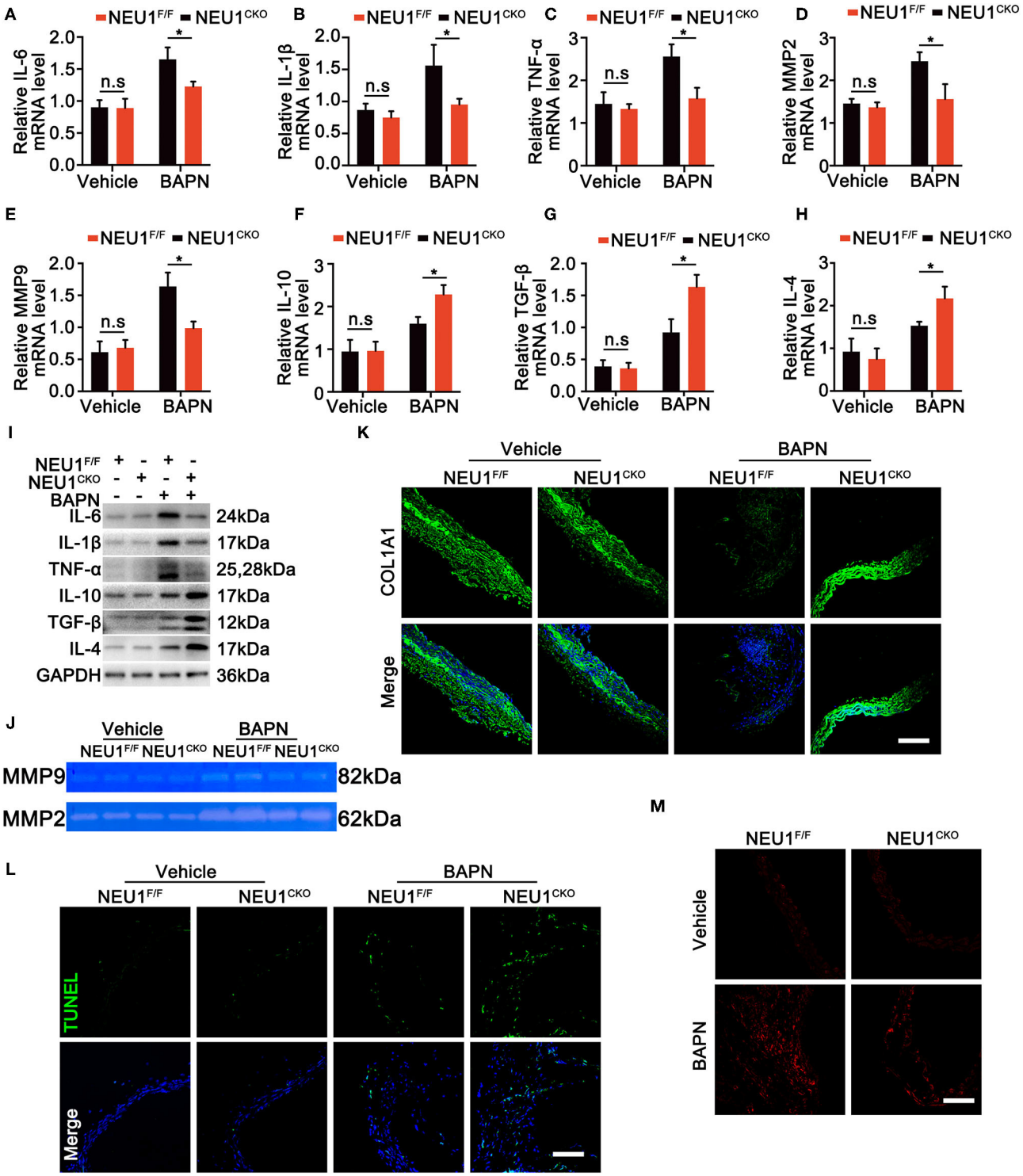

FIGURE 4 | NEU1 depletion suppressed BAPN-induced inflammation. **(A–H)** Quantitative mRNA levels of pro- and anti-inflammatory factors in aortas of NEU1$^{F/F}$ and NEU1 CKO mice subjected to BAPN induction for 4 weeks ($n = 6$ per group). **(I)** Representative western blots of pro- and anti-inflammatory factors in aortas of NEU1$^{F/F}$ and NEU1 CKO mice subjected to BAPN induction for 4 weeks ($n = 6$ per group). **(J)** Gelatin zymogram analysis of MMP2 and MMP9 activity levels in aortas of NEU1$^{F/F}$ and NEU1 CKO mice subjected to BAPN induction for 4 weeks. **(K)** Immunofluorescence images of COL1A1 in aortas of NEU1$^{F/F}$ and NEU1 CKO mice subjected to BAPN induction for 4 weeks (scale bar: 50 μm). **(L)** TUNEL staining of aortas from NEU1$^{F/F}$ and NEU1 CKO mice subjected to BAPN induction (scale bar: 50 μm). **(M)** DHE staining of aortas from NEU1$^{F/F}$ and NEU1 CKO mice subjected to BAPN induction for 4 weeks (scale bar: 50 μm). BAPN, β-aminopropionitrile monofumarate; DHE, dihydroethidium; KO, knockout; MMP, matrix metalloproteinase; NEU1, neuraminidase 1; NEU1 CKO, macrophage-specific NEU1 knockout. *$p < 0.05$.

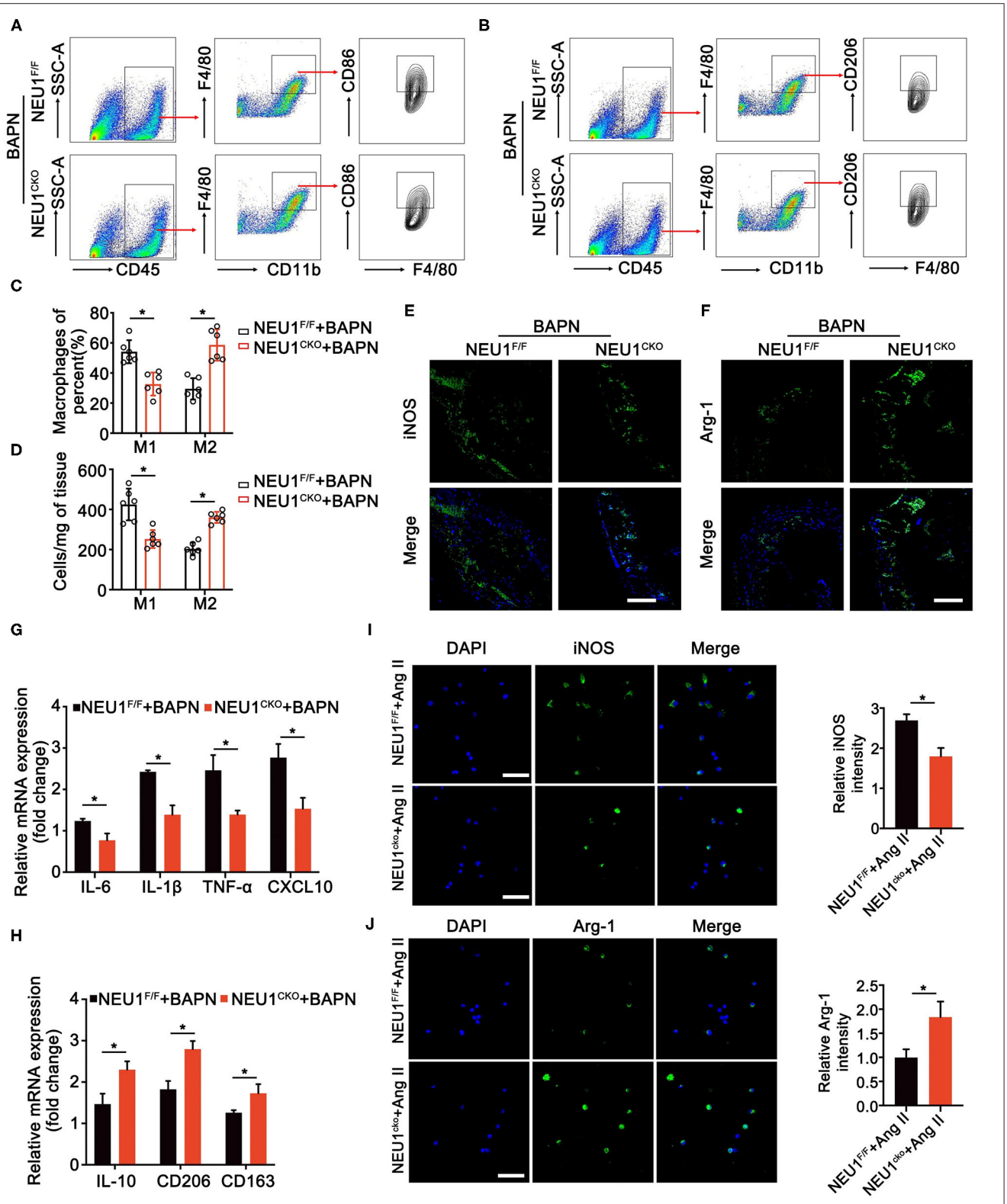

FIGURE 5 | NEU1 deletion promotes the polarization of macrophages. **(A,B)** Gating strategy for $CD45^+CD11b^+F4/80^+$ $CD86^+$ M1 macrophages and $CD45^+CD11b^+$ $F4/80^+$ $CD206^+$ M2 macrophages in aortas of NEU1 CKO mice and their controls. **(C,D)** Quantification of the $CD86^+$ and $CD206^+$ macrophages. **(E,F)** Immunofluorescence images of $iNOS^+$ and Arg-1^+ macrophages in aortas of $NEU1^{F/F}$ and NEU1 CKO mice subjected to BAPN induction for 4 weeks (scale bar: 50 μm). **(G,H)** mRNA levels of M1 and M2 markers in macrophages sorted by flow cytometry of $NEU1^{F/F}$ and NEU1 CKO mice subjected to BAPN induction for 4

(Continued)

FIGURE 5 | weeks ($n = 6$, $^*p < 0.05$). **(I,J)** Macrophages sorted from NEU1$^{F/F}$ and NEU1 CKO mice, and subjected to Ang II treatment for 24 h. Immunofluorescence images of iNOS$^+$ and Arg-1$^+$ macrophages by Ang II treatment (scale bar: 50 μm). Ang, angiotensin; Arg-1, arginase-1; BAPN, β-aminopropionitrile monofumarate; DHE, dihydroethidium; iNOS, inducible nitric oxide synthase; KO, knockout; NEU1, neuraminidase 1; NEU1 CKO, macrophage-specific NEU1 knockout.

promote atherosclerosis and plaque instability (20). In addition, upregulation of NEU1 after ischemia/reperfusion (I/R) promotes heart failure by promoting monocyte/macrophage inflammation and enhancing myocardial hypertrophy (23). Based on the above evidence, we speculated whether NEU1 could also participated in the pathogenesis of AD by regulating macrophages.

Considering the elevated NEU1 expression in the aortic tissues of AD mice, we hypothesized the involvement of NEU1 in AD development. Our studies proved that NEU1 deficiency mitigated the AD. Recent investigations provide evidence that NEU1 was mainly expressed in macrophages (20), which is consistent with our immunofluorescence findings. We further obtained NEU1 CKO mice by hybridization of NEU1$^{F/F}$ mice with LysM^{cre} mice to explore the effect of macrophage-derived NEU1 on AD. NEU1 CKO mice also showed significant improvement in aortic injury, consistent with the results of global NEU1 KO mice. Collectively, these observations suggested elevated NEU1 expression in dissecting tissues (especially in macrophages) contributed to aortic vascular remodeling.

Inflammation, apoptosis, ECM degradation, and oxidative stress are responsible for the pathogenesis of AD (24). In our study, we found that the pro-inflammatory factors were significantly decreased in the aortic tissues of NEU1 CKO mice. The dysfunction of VSMCs, including the imbalance between proliferation and apoptosis, is deemed to promote the vascular remodeling (25, 26). We also observed the decreased apoptosis of VSMCs compared with the controls. In addition, VSMCs are the main source of ECM proteins (24, 27). *In vivo* results showed that NEU1 CKO mice significantly reduced collagen 1 degradation in the vascular wall. Moreover, a series of evidence suggested that ROS plays a crucial role in the development of AD (28). Indeed, our results showed that the ROS production in aortic tissues was significantly reduced when NEU1 was deficient in macrophage. Taken together, our data suggest that NEU1 accelerates the development of AD by enhancing inflammatory response, cell apoptosis, oxidative stress, and ECM degradation.

We further investigated how NEU1 in macrophages promotes inflammation in the local microenvironment. Studies have shown that Ang II promotes the inflammatory response of local tissues by regulating the recruitment and polarization of macrophages, and thus induces the onset of AD in humans and experimental animals (8). We therefore tested whether NEU1 KO in macrophages could also affect the occurrence and development of AD by changing the polarization state of macrophages. Flow cytometry and immunofluorescence staining revealed that macrophage NEU1 KO significantly reduced the M1 macrophages and upregulated the M2 macrophages. The macrophages in the aortic tissues were sorted by flow cytometry and detected by q-PCR, and the results showed that when NEU1 was knocked out, the pro-inflammatory-related (M1-like) gene was significantly downregulated, whereas the anti-inflammatory-related (M2-like) gene was significantly upregulated. In addition, to further confirm these findings, we extracted macrophages from the NEU1$^{F/F}$ mice and their controls. After Ang II treatment, stained with M1 and M2 macrophage markers, it was confirmed that NEU1 promoted the onset of dissection by regulating macrophage into M1 phenotype.

In summary, we showed that NEU1 was upregulated in aortic tissues (especially in CD68$^+$ macrophages) from the BAPN-induced AD mouse model. Moreover, the genetic deletion retarded AD progression by directly suppressing the production of pro-inflammatory macrophages. Collectively, these data suggest that NEU1 may potentially serve as a new therapeutic target for AD.

DATA AVAILABILITY STATEMENT

The raw data supporting the conclusions of this article will be made available by the authors, without undue reservation.

ETHICS STATEMENT

The animal study was reviewed and approved by the Ethics Committee of The First Affiliated Hospital of Nanchang University.

AUTHOR CONTRIBUTIONS

QW, ZC, XP, ZZ, AL, and JZ designed the study and revised critically the manuscript. QW, ZC, XP, ZZ, AL, JG, LM, HS, and KY performed experiments. KY and SZ provided materials, performed measurements, and analyzed data. ZZ and KY wrote the manuscript. All authors approved final version of manuscript submitted.

FUNDING

This study was supported by National Natural Science Foundation of China (Grant Nos. 81800324, 81960061, and 81600241), Natural Science Foundation of Jiangxi Province (Grant Nos. 20192ACBL21040 and 20204BCJ23017), Key Project of Science and Technology Research Funds of Department of Education of Jiangxi Province (Grant Nos. GJJ170136 and GJJ170005), and Science Project of Department of Health Commission of Jiangxi Province (Grant No. 20203094).

SUPPLEMENTARY MATERIAL

The Supplementary Material for this article can be found online at: https://www.frontiersin.org/articles/10.3389/fcvm.2021.788645/full#supplementary-material

REFERENCES

1. Vaideeswar P, Kundu S, Singaravel S, Tyagi S. Spontaneous aortic rupture: report of two cases with review of literature. *Indian J Pathol Microbiol.* (2021) 64:152–4. doi: 10.4103/IJPM.IJPM_382_20
2. Yang YY, Li LY, Jiao XL, Jia LX, Zhang XP, Wang YL, et al. Intermittent hypoxia alleviates beta-aminopropionitrile monofumarate induced thoracic aortic dissection in C57BL/6 mice. *Eur J Vasc Endovasc Surg.* (2020) 59:1000–10. doi: 10.1016/j.ejvs.2019.10.014
3. Santos LCF, de Paiva MAF, Santana MVL, Mendes R, Tenorio PP. Could we adopt serum Tenascin-C assays to determine prognosis in aortic aneurysms and dissections?. *J Vasc Bras.* (2021) 20:e20200165. doi: 10.1590/1677-5449.200165
4. Juraszek A, Czerny M, Rylski B. Update in aortic dissection. *Trends Cardiovasc Med.* (2021) 8:8. doi: 10.1016/j.tcm.2021.08.008
5. Ohno-Urabe S, Aoki H, Nishihara M, Furusho A, Hirakata S, Nishida N, et al. Role of macrophage socs3 in the pathogenesis of aortic dissection. *J Am Heart Assoc.* (2018) 7:389. doi: 10.1161/JAHA.117.007389
6. Nienaber CA, Clough RE. Management of acute aortic dissection. *Lancet.* (2015) 385:800–11. doi: 10.1016/S0140-6736(14)61005-9
7. Wu D, Choi JC, Sameri A, Minard CG, Coselli JS, Shen YH, et al. Inflammatory cell infiltrates in acute and chronic thoracic aortic. *Dissection Aorta.* (2013) 1:259–67. doi: 10.12945/j.aorta.2013.13-044
8. Wang X, Zhang H, Ge Y, Cao L, He Y, Sun G, et al. AT1R regulates macrophage polarization through YAP and regulates aortic dissection incidence. *Front Physiol.* (2021) 12:644903. doi: 10.3389/fphys.2021.644903
9. Muller BT, Modlich O, Prisack HB, Bojar H, Schipke JD, Goecke T, et al. Gene expression profiles in the acutely dissected human aorta. *Eur J Vasc Endovasc Surg.* (2002) 24:356–64. doi: 10.1053/ejvs.2002.1731
10. Tieu BC, Lee C, Sun H, Lejeune W, Recinos A 3rd, Ju X, et al. An adventitial IL-6/MCP1 amplification loop accelerates macrophage-mediated vascular inflammation leading to aortic dissection in mice. *J Clin Invest.* (2009) 119:3637–51. doi: 10.1172/JCI38308
11. Anzai A, Shimoda M, Endo J, Kohno T, Katsumata Y, Matsuhashi T, et al. Adventitial CXCL1/G-CSF expression in response to acute aortic dissection triggers local neutrophil recruitment and activation leading to aortic rupture. *Circ Res.* (2015) 116:612–23. doi: 10.1161/CIRCRESAHA.116.304918
12. Son BK, Sawaki D, Tomida S, Fujita D, Aizawa K, Aoki H, et al. Granulocyte macrophage colony-stimulating factor is required for aortic dissection/intramural haematoma. *Nat Commun.* (2015) 6:6994. doi: 10.1038/ncomms7994
13. Ju X, Ijaz T, Sun H, Ray S, Lejeune W, Lee C, et al. Interleukin-6-signal transducer and activator of transcription-3 signaling mediates aortic dissections induced by angiotensin II via the T-helper lymphocyte 17-interleukin 17 axis in C57BL/6 mice. *Arterioscler Thromb Vasc Biol.* (2013) 33:1612–21. doi: 10.1161/ATVBAHA.112.301049
14. Kibler WB, Goldberg C, Chandler TJ. Functional biomechanical deficits in running athletes with plantar fasciitis. *Am J Sports Med.* (1991) 19:66–71. doi: 10.1097/00042752-199107000-00021
15. Liu J, Yang Y, Liu X, Widjaya AS, Jiang B, Jiang Y. Macrophage-biomimetic anti-inflammatory liposomes for homing and treating of aortic dissection. *J Control Release.* (2021) 337:224–35. doi: 10.1016/j.jconrel.2021.07.032
16. Chen QQ, Ma G, Liu JF, Cai YY, Zhang JY, Wei TT, et al. Neuraminidase 1 is a driver of experimental cardiac hypertrophy. *Eur Heart J.* (2021) 2021:ehab347. doi: 10.1093/eurheartj/ehab347
17. Seyrantepe V, Poupetova H, Froissart R, Zabot MT, Maire I, Pshezhetsky AV. Molecular pathology of NEU1 gene in sialidosis. *Hum Mutat.* (2003) 22:343–52. doi: 10.1002/humu.10268
18. Khan A, Das S, Sergi C. Therapeutic potential of NEU1 in Alzheimer's disease *via* the immune system. *Am J Alzheimers Dis Other Demen.* (2021) 36:1533317521996147. doi: 10.1177/1533317521996147
19. Abdulkhalek S, Amith SR, Franchuk SL, Jayanth P, Guo M, Finlay T, et al. NEU1 sialidase and matrix metalloproteinase-9 cross-talk is essential for Toll-like receptor activation and cellular signaling. *J Biol Chem.* (2011) 286:36532–49. doi: 10.1074/jbc.M111.237578
20. Sieve I, Ricke-Hoch M, Kasten M, Battmer K, Stapel B, Falk CS, et al. A positive feedback loop between IL-1beta, LPS and NEU1 may promote atherosclerosis by enhancing a pro-inflammatory state in monocytes and macrophages. *Vascul Pharmacol.* (2018) 103–5:16–28. doi: 10.1016/j.vph.2018.01.005
21. Sieve I, Munster-Kuhnel AK, Hilfiker-Kleiner D. Regulation and function of endothelial glycocalyx layer in vascular diseases. *Vascul Pharmacol.* (2018) 100:26–33. doi: 10.1016/j.vph.2017.09.002
22. Pshezhetsky AV, Ashmarina LI. Desialylation of surface receptors as a new dimension in cell signaling. *Biochemistry.* (2013) 78:736–45. doi: 10.1134/S0006297913070067
23. Heimerl M, Sieve I, Ricke-Hoch M, Erschow S, Battmer K, Scherr M, et al. Neuraminidase-1 promotes heart failure after ischemia/reperfusion injury by affecting cardiomyocytes and invading monocytes/macrophages. *Basic Res Cardiol.* (2020) 115:62. doi: 10.1007/s00395-020-00821-z
24. Xiao Y, Sun Y, Ma X, Wang C, Zhang L, Wang J, et al. MicroRNA-22 inhibits the apoptosis of vascular smooth muscle cell by targeting p38MAPKalpha in vascular remodeling of aortic dissection. *Mol Ther Nucleic Acids.* (2020) 22:1051–62. doi: 10.1016/j.omtn.2020.08.018
25. McMurtry MS, Bonnet S, Wu X, Dyck JR, Haromy A, Hashimoto K, et al. Dichloroacetate prevents and reverses pulmonary hypertension by inducing pulmonary artery smooth muscle cell apoptosis. *Circ Res.* (2004) 95:830–40. doi: 10.1161/01.RES.0000145360.16770.9f
26. Liao WL, Tan MW, Yuan Y, Wang GK, Wang C, Tang H, et al. Brahma-related gene 1 inhibits proliferation and migration of human aortic smooth muscle cells by directly up-regulating Ras-related associated with diabetes in the pathophysiologic processes of aortic dissection. *J Thorac Cardiovasc Surg.* (2015) 150:1292–301 e2. doi: 10.1016/j.jtcvs.2015.08.010
27. Zhang J, Liu F, He YB, Zhang W, Ma WR, Xing J, et al. Polycystin-1 downregulation induced vascular smooth muscle cells phenotypic alteration and extracellular matrix remodeling in thoracic aortic dissection. *Front Physiol.* (2020) 11:548055. doi: 10.3389/fphys.2020.548055
28. Fan LM, Douglas G, Bendall JK, McNeill E, Crabtree MJ, Hale AB, et al. Endothelial cell-specific reactive oxygen species production increases susceptibility to aortic dissection. *Circulation.* (2014) 129:2661–72. doi: 10.1161/CIRCULATIONAHA.113.005062

Conflict of Interest: The authors declare that the research was conducted in the absence of any commercial or financial relationships that could be construed as a potential conflict of interest.

Publisher's Note: All claims expressed in this article are solely those of the authors and do not necessarily represent those of their affiliated organizations, or those of the publisher, the editors and the reviewers. Any product that may be evaluated in this article, or claim that may be made by its manufacturer, is not guaranteed or endorsed by the publisher.

frontiers in Cardiovascular Medicine

ORIGINAL RESEARCH
published: 24 November 2021
doi: 10.3389/fcvm.2021.753711

Single-Cell Transcriptome Profiles Reveal Fibrocytes as Potential Targets of Cell Therapies for Abdominal Aortic Aneurysm

Bolun Li[1†], Xiaomin Song[1†], Wenjun Guo[1], Yangfeng Hou[1], Huiyuan Hu[1,2], Weipeng Ge[1], Tianfei Fan[1], Zhifa Han[1,3], Zhiwei Li[1], Peiran Yang[4], Ran Gao[1], Hongmei Zhao[1*] and Jing Wang[1]*

[1] State Key Laboratory of Medical Molecular Biology, Department of Pathophysiology, Institute of Basic Medical Sciences, Chinese Academy of Medical Sciences, Peking Union Medical College, Beijing, China, [2] First Clinical College, Xi'an Jiaotong University, ShaanXi, China, [3] Department of Basic Medical Sciences, School of Medicine, Tsinghua University, Beijing, China, [4] State Key Laboratory of Medical Molecular Biology, Department of Physiology, Institute of Basic Medical Sciences, Chinese Academy of Medical Sciences, Peking Union Medical College, Beijing, China

OPEN ACCESS

Edited by:
Ha Won Kim,
Augusta University, United States

Reviewed by:
Xiaochun Long,
Augusta University, United States
Ting Zhou,
University of Wisconsin-Madison, United States

***Correspondence:**
Hongmei Zhao
hongmeizhao@ibms.pumc.edu.cn
Ran Gao
ggrr1991@outlook.com

[†]These authors have contributed equally to this work and share first authorship

Specialty section:
This article was submitted to Atherosclerosis and Vascular Medicine, a section of the journal Frontiers in Cardiovascular Medicine

Received: *05 August 2021*
Accepted: *22 October 2021*
Published: *24 November 2021*

Citation:
Li B, Song X, Guo W, Hou Y, Hu H, Ge W, Fan T, Han Z, Li Z, Yang P, Gao R, Zhao H and Wang J (2021) Single-Cell Transcriptome Profiles Reveal Fibrocytes as Potential Targets of Cell Therapies for Abdominal Aortic Aneurysm. Front. Cardiovasc. Med. 8:753711. doi: 10.3389/fcvm.2021.753711

Abdominal aortic aneurysm (AAA) is potentially life-threatening in aging population due to the risk of aortic rupture and a lack of optimal treatment. The roles of different vascular and immune cells in AAA formation and pathogenesis remain to be future characterized. Single-cell RNA sequencing was performed on an angiotensin (Ang) II-induced mouse model of AAA. Macrophages, B cells, T cells, fibroblasts, smooth muscle cells and endothelial cells were identified through bioinformatic analyses. The discovery of multiple subtypes of macrophages, such as the re-polarization of $Trem2^{+}Acp5^{+}$ osteoclast-like and M2-like macrophages toward the M1 type macrophages, indicates the heterogenous nature of macrophages during AAA development. More interestingly, we defined $CD45^{+}COL1^{+}$ fibrocytes, which was further validated by flow cytometry and immunostaining in mouse and human AAA tissues. We then reconstituted these fibrocytes into mice with Ang II-induced AAA and found the recruitment of these fibrocytes in mouse AAA. More importantly, the fibrocyte treatment exhibited a protective effect against AAA development, perhaps through modulating extracellular matrix production and thus enhancing aortic stability. Our study reveals the heterogeneity of macrophages and the involvement of a novel cell type, fibrocyte, in AAA. Fibrocyte may represent a potential cell therapy target for AAA.

Keywords: abdominal aortic aneurysm, single cell sequencing, fibrocytes, cell therapy, cell atlas

INTRODUCTION

Abdominal aortic aneurysm (AAA) is an aging-related vascular disease. During the progression of AAA, the aneurysm slowly expands and acutely causes vessel rupture without any symptom and warning in advance, resulting in high mortality. For patients with ruptured AAAs, endovascular repair or open repair are the main clinical remedies. However, even undergoing intervention for repair, the in-hospital mortality is still as high as 53.1% (1). New therapies, such cell or stem cell therapies, have been proposed but have encountered difficulties in their development. Therefore, it is necessary to investigate the mechanism of AAA formation and identify the novel biomarkers or therapies to diagnose and treat AAA patients.

Previous studies revealed that AAA was caused by chronic inflammation and an imbalance between synthesis and degradation of extracellular matrix (ECM) composed of elastin and collagen (2, 3). Chronic inflammation is characterized by infiltration of a variety of immune cells. Macrophages have been most widely studied (3, 4) as main inflammatory cells. Besides macrophages, the roles of B cells (5), T cells (6), and mast cells (7, 8) in AAA formation have also been reported, while the function of other immune cells like natural killer (NK) T cells in AAA formation is still rarely studied.

In addition to inflammation, another essential pathological feature of AAA is the dysregulation of ECM proteins that are mainly synthesized by vascular smooth muscle cells (SMCs) and adventitial fibroblasts. SMC apoptosis has been identified as a hallmark of AAA pathology (9). Matrix metalloproteinases (MMPs) are mainly produced by SMCs, fibroblasts and infiltrated macrophages. Increased MMPs lead to matrix degradation, loss of aortic wall integrity, AAA expansion and rupture. The balance of ECM synthesis and degradation is critical for the stability of AAA (2, 10). Fibroblasts, as the major matrix-producing cell population, can transform into myofibroblasts to produce ECMs (11).

In addition to the classical vascular and immune cells, recent evidence suggests that circulating fibrocytes are the bone-marrow derived precursors of fibroblasts and can regulate the ECM (12). Fibrocytes are found in the plaques of atherosclerosis (13). In ischemic cardiomyopathy, fibrocytes can be recruited and involved in the fibrosis (14). Given these possible functions of fibrocytes, they may constitute another essential cell population in AAA formation.

To determine the specific cell types and further explore the molecular mechanisms, we performed single-cell RNA sequencing (scRNA-seq) of mouse AAA tissues, in which different cell types and subtypes in AAA can be defined by unique transcriptomes.

MATERIALS AND METHODS

Animal Model

To induce AAA, 8-week-old *ApoE*$^{-/-}$ male mice (C57BL/6J, Beijing Vital River Laboratory Animal Technology Co., Ltd. Beijing) were anesthetized with 200 mg/kg ketamine and 10 mg/kg xylazine by intraperitoneal injection, and infused with 1,000 ng/kg/min Ang II (A9525-50MG sigma-Aldrich) or saline with alzet osmotic mini-pumps (Alzet model 2004, DURECT Corp., Cupertino, CA) for 28 days. To evaluate the effect of fibrocytes, 8×10^6 fibrocytes were injected into mice via tail vein on days 7 and 21 after Ang II-infusion (1.6×10^7 in total). GFP-labeled fibrocytes were injected with the same protocol to trace them *in vivo*. All animal experiments were approved by the Research Ethics Committee of Peking Union Medical College.

Single-Cell RNA-seq and Analysis

A single-cell cDNA library was generated as previously described (15). For the isolation of individual cells, both control and AAA mice were anesthetized with ketamine (200 mg/kg) and xylazine (10 mg/kg) by intraperitoneal injection. The normal aorta (one whole aorta from one mouse) or aneurysm tissue (one piece of the supra-renal part with aneurysm from one AAA mouse) were dissected and digested for 15 min at 37°C in PBS containing 200 U/ml collagenase I (SCR103, Sigma Aldrich, Germany), 0.05 U/ml elastase (E1250, Sigma Aldrich, Germany), 5 U/ml neutral protease (LS02111, Worthington, USA), and 0.3 U/ml deoxyribonuclease I (M6101, Promega, USA). The tissue digestion was stopped with DMEM containing 10% FBS (10099141, Gibco, USA.) and the mixture was filtered through a 40 μm cell strainer (15-1040, Biologix, China) to obtain single-cell suspensions. Using the method of 7-amino-actinomycin D (7-AAD) positive cells staining, living aortic cells (7-AAD negative cells) were sorted using a Moflo-XDP (Beckman, USA). Cell suspensions (∼10,000 single cells) were next loaded on the Chromium Single Cell Controller (10X Genomics) to generate a single cell and gel bead emulsion (GEM). Single-cell sequencing library preparation was performed according to the instructions of Chromium single cell 3' library & Gel bead kit v2 (10X Genomics). Libraries were sequenced by Illumina Hiseq X Ten in paired-end to reach ∼50,000 reads per single-cell (Novo Generation Bioinformatics Technology Co., Ltd.).

The 10X Genomics single-cell transcriptome sequencing data were filtered by removing bases with a mass less than 3 at the beginning and end of the reads, using a CellRanger software suite version 3.0.2 pipeline (16). The filtered reads were aligned to the MM10 mouse reference genome by STAR. For further analysis and statistics, based on the barcode and gene expression matrix, single-cell data were log-normalized and filtered by the R 3.6.0 package Seurat 3.2.3 (17, 18), with the following parameters: unique gene count per cell >500, cell counts per gene >3 (0.1% of the total cell amount), and percentage of mitochondrial genes <0.05. After the control and AAA samples were combined, the UMAP and automated cluster detection algorithms were performed stepwise. The resolution for cluster identification was set as 0.5. DEGs were identified by the Wilcox test with default parameters and $p<0.05$. DEGs from each cluster were sorted by $\log_e$-fold change relative to the other clusters. Then, the DEGs of which log-fold change was more than 0 were selected and used for GO analysis by ClusterProfiler 3.14.3 (https://guangchuangyu.github.io/software/clusterProfiler/). The enriched function or pathway were further clustered to predict the most likely function of the specific cluster. Alternatively, to detect the possible polarization or differentiation process among different clusters, Monocle 2.14.0 (19) was used for the trajectory analysis. The co-expression level of n genes was calculated by $\sqrt[n]{e_1 \times e_2 \times \cdots \times e_n}$ (e_n means the expression of the nth gene) and the accuracy is confirmed by ROC curve. Velocyto.R v0.6 package were then used for calculating RNA velocity of each single cells and further visualization.

Flow Cytometry

For flow cytometry analyses, single-cell suspensions of mouse aortae were prepared according to the previous protocol (20) and stained with following antibodies: 7AAD (00-6993-50, eBioscience, USA), Fluorescent isothiocyanate (FITC) anti-mouse-α-SMA (ab8211, Abcam, United Kingdom),

PE-anti-mouse-CD34 (551387, BD, USA), FITC-anti-mouse-CD68 (MA1-82739, Invitrogen, USA), PE-anti-mouse-NK1.1 (ab269324, Abcam, United Kingdom), FITC-anti-mouse-CD19 (11-0193-82, eBioscience, USA), PE-anti-mouse-CD21 (12-0211-82, eBioscience, USA), PE-anti-mouse-CD45 (12-0451-82, eBioscience, USA), and Collagen I (ab88147, Abcam, United Kingdom; at room temperature for 30 min) with Alexa Fluor 488 goat anti-mouse antibody (A32723, Invitrogen, at room temperature for 30 min). Flow cytometry results were analyzed by using FlowJo 7.6 software (FlowJo, LLC., Ashland, Oregon). Statistical analysis was further performed by GraphPad Prism 8.0.

Isolation and Culture of Bone Marrow-Derived Fibrocytes

Bone marrow-derived fibrocytes were obtained by *in vitro* differentiation of spleen cells as previously described (21). Spleen cells were isolated from 8-week $ApoE^{-/-}$ or generic GFP male mice as previously described (22). Briefly, spleens were separated, minced and digested at 37°C. Spleen cells were isolated using a 70 μm cell strainer (15-1070, Biologix, China) and cultured in 3 ml of RPMI-1640 (31800-500, Solarbio, China) with L-Glutamine, 20% fetal bovine serum (10099-141, Gibco, Australia), penicillin–streptomycin (P1400, Solarbio, China). After 3 days, the medium was changed into Fibrolife basal media (LM-0001, Lifeline Cell Technology, USA) with 25 ng/ml of murine macrophage colony-stimulating factor (M-CSF) (315-02, PeproTech, USA) and 50 ng/ml of murine interleukin (IL)-13 (210-13, PeproTech, USA) and cells were cultured in a humidified incubator containing 5% CO_2 at 37°C for 10 days. To detect whether cells were induced differentiation, we observed the morphological changes under microscopy (Nikon, Tokyo, Japan). Following 10 to 14 days, the adherent cells were harvested and used to injected to mice and immunofluorescence staining.

Human Aortic Tissue

Human aortic tissue extracts were prepared from the abdominal aortic aneurysm patient (Peking Union Medical College Hospital and Beijing Anzhen Hospital) and from the body of the deceased donor with no detectable vascular disease (Peking Union Medical College Volunteer Corpse Donation Reception Station). Age and gender were matched (**Supplementary Tables S1, S2**). The human donor aortic tissues obtained were approved by the institutional review board of institute of basic medical sciences, Chinese academy of medical sciences. The abdominal aortic aneurysm tissue obtained were approved by the institutional review board of Peking Union Medical College Hospital and Beijing Anzhen Hospital.

Hematoxylin and Eosin (H&E) Staining and Elastin Staining

The mouse aortae were embedded in optical cutting temperature (OCT) compound (4583, Sakura, Netherlands) and the frozen sections were used for H&E staining, Elastin staining or immunofluorescence staining. H&E staining and Elastin staining were performed by using H&E staining kit (G1120, Solarbio, China) elastic staining Kit (HT25A, Sigma-aldrich, Germany) according to the manufactures' instructions.

Immunofluorescence Staining

For immunofluorescence staining, the sections for mouse aortae and human aortae or cells seed in 35 mm glass bottom dish were fixed with 4% paraformaldehyde for 10 min and permeabilized with 1% Triton X-100 for 15 min. Then the sections blocked with 1% bovine serum albumin for 30 min at room temperature and incubated with mouse monoclonal collagen I (ab88147, Abcam, United Kingdom, 1:100 dilution) and rabbit polyclonal CD45 (ab10558, Abcam, United Kingdom, 1:100 dilution) antibodies overnight at 4°C. After washing with PBS three times, sections were incubated Alexa Fluor 488-conjugated goat anti-mouse IgG (H+L) secondary antibody (A-11008, Invitrogen, USA, 1:1,000), Alexa Fluor 594 conjugated goat anti-rabbit IgG(H+L) highly cross-adsorbed secondary antibody (A-11037, Invitrogen, USA, 1:1,000 dilution) for 40 min at room temperature. Finally, sections were mounted with ProLong Gold antifade reagent with DAPI (ab104139, Abcam, United Kingdom). Pictures were taken by confocal microscopy (LSM780, Zeiss).

Quantification and Statistical Analysis

For animal experiments, the exact number of mice used in each experiment is reported in the figure legends. Normality tests were conducted first. Then, comparisons between two groups were made with an unpaired two-tailed *t*-test or non-parametric test. Comparisons among groups with two factors were made with two-way ANOVA, and $p < 0.05$ was considered statistically significant. Data were presented as mean ± standard error of the mean (SEM).

RESULTS

Aortic and Aneurysmal Cell Populations Revealed by scRNA-seq

To explore the cell types involved in AAA, apolipoprotein E–deficient ($ApoE^{-/-}$) male mice were implanted with Ang II osmotic pump for 4 weeks to induce AAA or underwent sham surgery, and the tissues were collected for scRNA-seq (**Figure 1A**). After alignment (**Supplementary Figure S1A**) and quality control (**Supplementary Figures S1B,C**), 7,914 and 9,338 cells from control and AAA groups were combined and included in the subsequent analysis. Unsupervised clustering by Seurat R package revealed 15 distinct clusters (**Figure 1B**). In accordance with the canonical markers, the clusters were fibroblasts (Cluster 0, 2, 3; $Cd34^{+}Pdgfra^{+}$), macrophages [Cluster 1, 4; $Cd68^{+}Ptprc^{+}$ (encoding *Cd45*)], SMC [Cluster 5; $Acta2^{+}$ (encoding α-SMA) $Cd34^{-}Pdgfra^{-}$], endothelial cells (ECs) [Cluster 6; $Pecam1^{+}$ (encoding *Cd31*), T cells (Cluster 7; $Cd3e^{+}Cd8a^{+}$), B cells (Cluster 8; $Cd19^{+}$), lymphatic endothelial cells (Cluster 12; $Lyve1^{+}Pecam1^{+}$), and proliferating cells (Cluster 9; $Top2a^{+}Mki67^{+}$)] (**Figure 1C**). Consistent with previous studies, among all cell types, the proportion of immune cells significantly increased in the AAA group, especially macrophages and B cells (**Figures 1D,E**). By contrast, fibroblasts

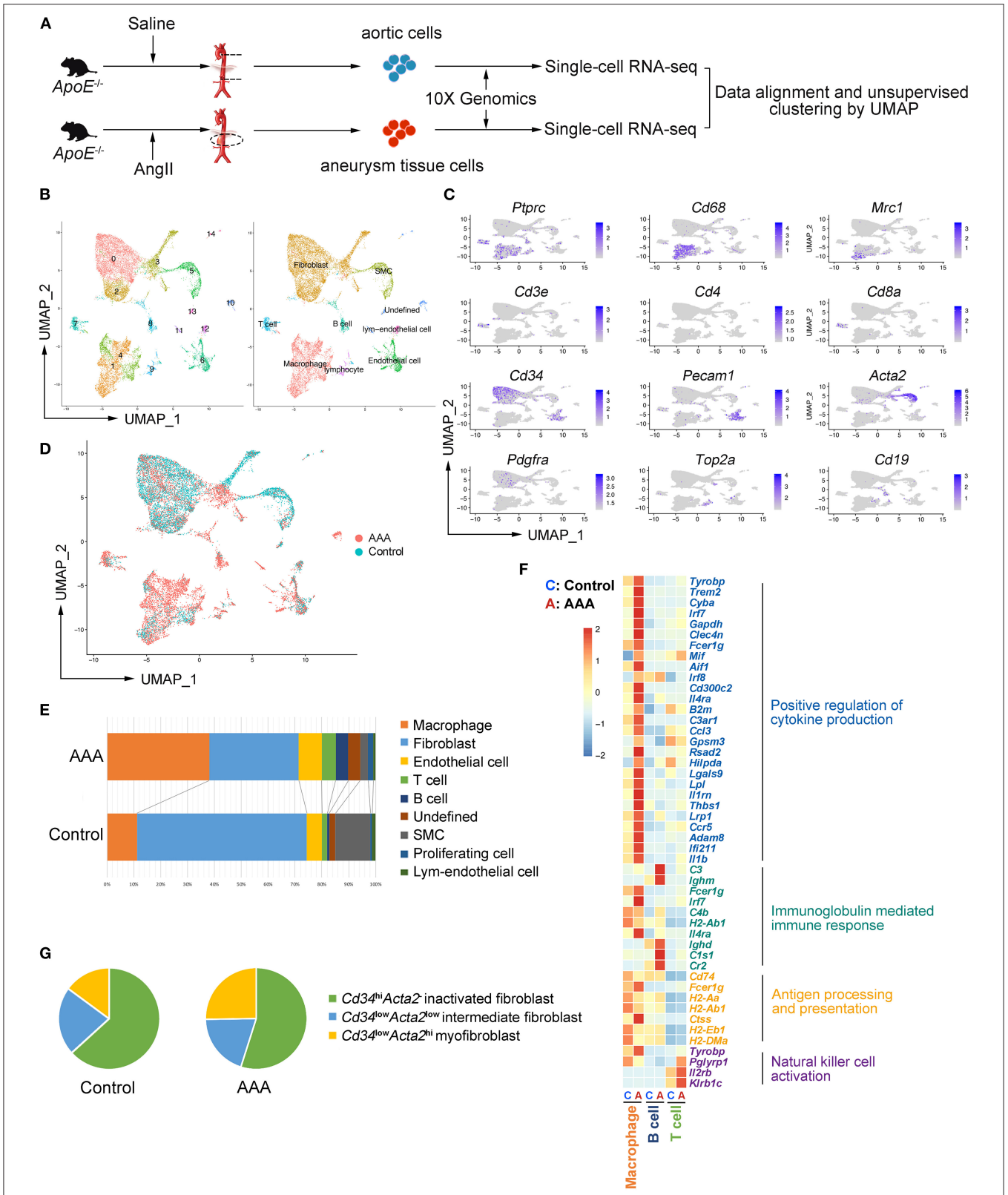

FIGURE 1 | Aortic and aneurysmal cell populations revealed by scRNA-seq. **(A)** Schematic diagram of the experimental design. **(B)** Uniform manifold approximation and projection (UMAP) representation of the aligned gene expression data from saline-treated (control, $n = 7,914$, in blue) and Ang II-treated (AAA, $n = 9,338$, in red)

(Continued)

FIGURE 1 | aortae of apolipoprotein E (*ApoE*$^{-/-}$) mice, showing partition of 15 distinct clusters (left panel) and cell identities (right panel). **(C)** The expression of marker genes exhibited on UMAP plot (gene expression log-normalized by Seurat). **(D)** UMAP representation of cells showing cellular origins. **(E)** Stacked column chart of the proportion of each identified cell type in control and AAA group individually (Control vs. AAA). **(F)** Heatmap of key genes differentially expressed after Ang II infusion (in the left panel) and the associated Gene Ontology (GO) pathway enrichment (in the right panel). Heatmap showed the relative expression level in each cluster. **(G)** Pie chart of the proportion of fibroblast subtypes in control and AAA groups (Control vs. AAA). SMC: smooth muscle cell.

and SMCs were reduced after 4-week of Ang II-exposure (**Figures 1D,E**).

To assess the robustness of the dataset and explore the cellular mechanisms of AAA formation, differentially expressed gene (DEG) were determined by comparing each cell type between AAA and control groups and Gene Ontology (GO) analyses were performed. We found that the functions of "positive regulation of cytokine production," "regulation of inflammatory response," and "antigen processing and presentation" (**Figure 1F**; **Supplementary Figure S2A**) was upregulated in macrophages in AAA. Moreover, B cells in this dataset were predicted to be activated to plasma cells with the high expression level of *Cr2* (encoding *Cd21*) and *Ighm*, and the upregulated genes of B cells were mainly enriched in the function of "immunoglobulin mediated immune response." As for T cells, "natural killer cell activation" was upregulated with increased expression of *Klrb1c* and *Il2rb* in AAA pathogenesis. To validate the results from scRNA-seq analyses, the cells were analyzed by flow cytometry, which confirmed the infiltration of macrophages, and the activation of B cells and NK T cells in AAA (**Supplementary Figures S3A–C**).

Fibroblasts were composed of three clusters (Clusters 0, 2 and 3). The highly expressed genes (HEGs) among these clusters and potential functions of these cells were analyzed. The typical fibroblast functions such as "extracellular matrix organization" and "extracellular structure organization" were enriched in all of the three clusters. HEGs of Cluster 0 were mainly enriched in the function of "transmembrane receptor protein serine/threonine kinase signaling pathway" (**Supplementary Figure S2B**). By contrast, the specifically enriched GO functions of Clusters 2 and 3 were "connective tissue development" and "wound healing" (**Supplementary Figures S2C,D**). Further analysis based on the gene expression patterns determined Cluster 0 as the inactivated fibroblasts, with higher expression of *Cd34* but no expression of *Acta2* (**Supplementary Figure S2E**). By contrast, Cluster 3, with higher expression level of *Acta2* and lower expression level of *Cd34* compared with Cluster 0, was regarded as myofibroblasts (11). Cluster 2 could be the intermediate types between Cluster 0 and 3. In addition, scRNA-seq data showed that the proportion of *Acta2*$^{+}$ myofibroblasts increased significantly (**Figure 1G**) in AAA, which was validated by flow cytometry analysis (**Supplementary Figure S3D**).

In terms of vascular cells, SMCs involved in the function of "regulation of apoptotic signaling pathway" were upregulated in AAA, which was consistent with the increased SMC death in AAA (**Supplementary Figure S2E**). Furthermore, ECM-related functions were enriched in SMCs in the AAA group, suggesting that the SMCs underwent phenotypic transformation in AAA (**Supplementary Figure S2E**). In addition, GO analysis of DEGs of ECs suggested that the upregulated functions were related to leukocyte migration and EC proliferation (**Supplementary Figure S2F**), which was consistent with the previous reported function of ECs in AAA formation.

Heterogeneity and Re-polarization of Macrophage Subtypes in AAA

As the largest and most varied population in our scRNA-seq data, we focused on macrophages (Clusters 1 and 4) and re-clustered them by Seurat (**Figures 1C–E**). We observed four main clusters (Clusters 0–3) (**Figure 2A**). Using canonical markers and HEGs to analyze the macrophage subtypes, we identified *Trem2*$^{+}$*Acp5*$^{+}$ osteoclast-like macrophages (Cluster 0), *Mrc1*$^{+}$*Cd163*$^{+}$ M2-like macrophages (Cluster 1), *Il1b*$^{+}$*Ccr2*$^{+}$ M1-like macrophages (Cluster 2), and *Cd34*$^{+}$*Col1a2*$^{+}$ bone marrow-derived fibrocyte (21, 23) (Cluster 3) (**Figure 2A**; **Supplementary Figure S4A**). To define the specific gene expression features and potential functions, HEG and GO analyses were performed on three subtypes of macrophages (**Figure 2B**). Osteoclast-like macrophages (Cluster 0) expressing high levels of *Trem2*, *Tyrobp*, *Plin2*, and *Lpl* were enriched in the function of "apoptotic cell clearance" and "lipid storage," suggesting that osteoclast-like macrophages could be involved in lipid deposition and the phagocytosis of apoptotic cells or lipid. In M2-like macrophages (Cluster 1), C-C motif chemokine (CCL) genes (*Ccl8, Ccl6, Ccl24, Ccl9* and *Ccl12*) were highly expressed, and their enriched function was "mononuclear cell migration," implying that M2-like macrophages might contribute to the recruitment of mononuclear cells by producing chemokines in AAA pathogenesis. Furthermore, the enriched function of "tissue remodeling" related genes were also highly expressed in M2-like macrophages, which is consistent with the previous reported phenotypic characteristics of M2 macrophages (24). In M1-like macrophages (Cluster 2), HEGs were mainly enriched in the function of "regulation of cytokine biosynthetic process" and "antigen processing and presentation." Combining with the high expression of *Il1b* and *Ccr2*, these cells have been predicted to be the most important pro-inflammatory cells in AAA pathogenesis.

To further analyze the changes of macrophage subtypes between control and AAA groups, DEG and GO analyses were performed on each macrophage subtype. In osteoclast-like macrophages, the genes upregulated in AAA were enriched in the function of "NADH dehydrogenase complex assembly," "ATP metabolic process," and "glycolytic process" (**Figure 2C**; **Supplementary Figure S4B**). In M2-like macrophages, the function of "positive regulation of cytokine production" and "tissue remodeling" were upregulated (**Figure 2C**). On the other hand, upregulated pro-inflammatory factors, such as *Il1b* and *Thbs1*, were enriched in the function of "positive regulation of cytokine production" in M1-like macrophages. In addition, the

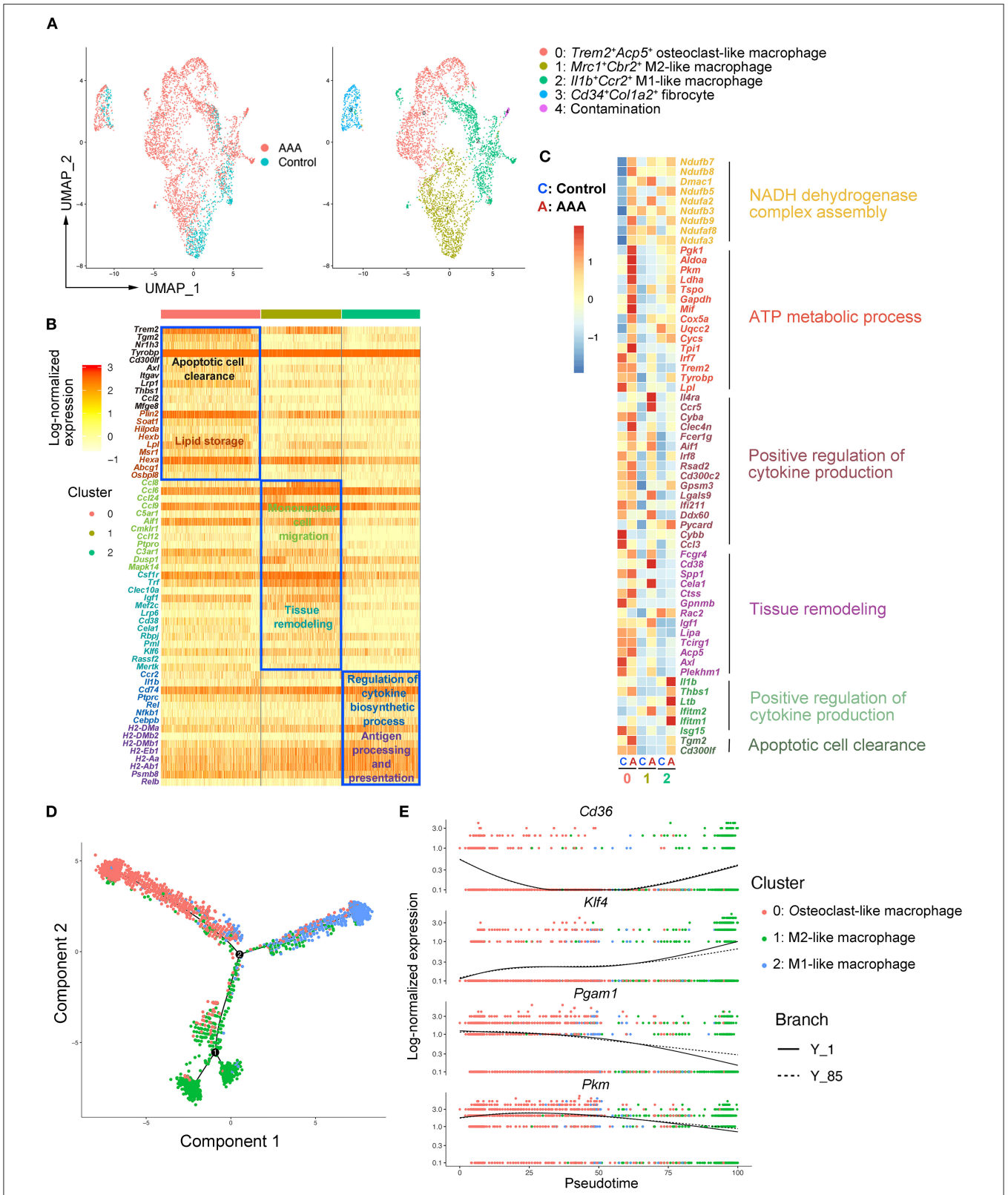

FIGURE 2 | Heterogeneity and re-polarization of macrophage subtypes in AAA. **(A)** Uniform manifold approximation and projection (UMAP) representation of the aligned gene expression data in macrophages separated from **Figure 1B**. **(B)** Heatmap of highly expressed genes (HEGs) from three subtypes of macrophages in **(A)**.

(Continued)

FIGURE 2 | (C) Heatmap of key genes differentially expressed (in the left panel) after Ang II infusion and the associated GO pathway enrichment (in the right panel). Heatmap showed the relative expression level in each cluster of macrophages. **(D)** Pseudo-time plot by trajectory analysis of three clusters of macrophages (Cluster 0: *Trem2*$^+$*Acp5*$^+$ macrophages; Cluster 1: *Mrc1*$^+$*Cbr2*$^+$ M2-like macrophages; Cluster 2: *Il1b*$^+$*Ccr2*$^+$ M1-like macrophages). **(E)** The expression of key genes in pseudo-time plot.

expression of genes related to "apoptotic cell clearance" were also increased in M1-like macrophages. More interestingly, we found that the mode of ATP metabolism in osteoclast-like macrophages might be shifted to glycolysis (**Supplementary Figure S4B**), which is typical of M1 macrophages (25). Moreover, the upregulated functions of M2-like macrophages were similar to the signature functions of M1-like macrophages. These data together suggest a connection between the three subtypes, which was clarified by trajectory analysis with the Monocle2 R package. As shown in **Figure 2D**, we found the tendency of transition among different macrophages. As shown by the RNA velocity, we found that osteoclast-like macrophages and M2-like macrophages tended to polarize to M1-like (**Supplementary Figures S5A,B**). Key genes related to the macrophage polarization were significantly changed among these three subtypes of macrophages. For example, *Klf4* (26) was highly expressed in M2 compared to M1 cells and was reported to play a crucial role in macrophage polarization (**Figure 2E**). Deficiency of *Klf4* could evoke a partial loss of M2 but gain of M1. Moreover, the expression of *Cd36* declined from M2 to M1 (**Figure 2E**), which was proven to be essential for fatty acid uptake and metabolism of M2 macrophages (27). By contrast, the expression of *Pkm* and *Pgam1* related to glycolysis and gluconeogenesis, increased during the M2 to M1 transition (**Figure 2E**). The high levels of *Pkm* and *Pgam1* in M1 macrophages indicate that M1 macrophages are glycolytic (25), which was consistent with our GO analysis above (**Figure 2C**). Taken together, we identified three subtypes of macrophages in aortic and aneurysmal tissues and we thus proposed that the osteoclast-like and M2-like macrophages might polarize toward M1 type in AAA pathogenesis.

Identification of Fibrocytes That Were Distinct From Macrophages in AAA

While analyzing the subtypes of macrophages, a remarkable population of *Cd34*$^+$*Col1a2*$^+$ bone marrow-derived fibrocytes (Cluster 3) were found in control aorta and AAA tissues, and tended to increase in AAA (**Figure 2A**; **Supplementary Figures S6A,B**). When performing HEG analysis on fibrocytes compared with the three subtypes of macrophages, we found that the expression pattern of fibrocytes was exceedingly distinct from macrophages (**Figure 3A**). ECM-related genes were highly expressed in fibrocytes, such as collagen (*Col1a1, Col1a2, Col3a1, Col5a, Col4a1,* etc.), elastin (*Eln*), matrix metalloproteinases (*Mmp2, Mmp3*, etc.), and periostin (*Postn*) (**Figure 3A**). GO analysis of HEGs suggested fibrocyte functions such as ECM organization, collagen related process and response to growth factor and wounding (**Figure 3B**), similar to the functions of fibroblasts (**Supplementary Figures S2B–D**). Further trajectory analysis of fibrocytes and macrophages revealed that there might be no connection or transition between the fibrocytes and three subtypes of macrophages (**Figure 3C**). Taken together, we identified fibrocytes in AAA tissues, whose gene expression patterns and functions were different from those of macrophages.

Identification and Function of Fibrocytes in AAA Pathogenesis

Bone marrow–derived fibrocytes are differentiated from circulating CD14$^+$ peripheral blood mononuclear cells (PBMCs) and co-express markers of hematopoietic stem cells (CD34$^+$), monocyte lineage (CD11b$^+$), leukocyte (CD45$^+$), and stromal cells (collagen I$^+$). These characterizations are used to identify fibrocytes (23, 28). In our scRNA-seq analysis, marker genes distinguishing fibrocytes from macrophages were retrieved and combined with the canonical markers to identify fibrocytes from other cell types. Among all cell types, the fibrocyte features distinct from macrophages were remarkably similar with fibroblasts, but the fibrocytes also exhibited leukocyte-like features. This suggests that fibroblasts represent a unique cell type (**Figure 4A**). For screening the markers of fibrocytes, we calculated the co-expression levels (details in Methods) of the fibroblast features (i.e., *Cd34*, *Col1a2*, *Meg3*, *Aebp1*, *Dcn*, *Igfbp7*, and *Nbl1*) and the leukocyte-like features (*Cd45*) and assessed the accuracy and specificity of different feature combinations by ROC curve. The result showed that the combination of *Cd45* and *Col1a2* showed a high specificity (>95%) for identifying fibrocytes with a co-expression level of more than 0.25 (**Figure 4B**). Fibrocytes were newly identified by co-expression of *Ptprc* and *Col1a2*, and distributed among macrophage, fibroblast and smooth muscle cell clusters (**Supplementary Figures S6C,D**). Furthermore, we adopted and analyzed a previous single cell RNA-seq dataset from human ascending thoracic aortic aneurysm (29) (ATAA) to validate our current findings in mice. By calculating the co-expression level of *PTPRC* and *COL1A2,* fibrocytes were also detected in the ATAA dataset. Fibrocytes were mainly distributed among macrophage, fibroblast and smooth muscle cell clusters in the embedding space (**Supplementary Figures S7A,B**), which is consistent with our results. In addition, the proportions of fibrocytes tended to increase in ATAA patients (**Supplementary Figure S7C**). Next, the transcriptomic changes of fibrocytes in AAA were analyzed. In terms of the classic markers of fibrocytes, the hematopoietic stem cell- and immune cell-like features (i.e., *Cd34*, *Ptprc*, *Itgam*) were decreased but the stromal feature (*Col1a2*) was increased (**Figure 4C**). DEG analysis of our data showed the upregulation of *Ccl8, Gm2564, Aif1,* and *Lgals3* in fibrocytes, which were enriched in the function of "monocyte chemotaxis." The expression levels of *Timp1, Tyrobp, Mif, Col1a1, and C3* were increased, and they were enriched in the function of "response

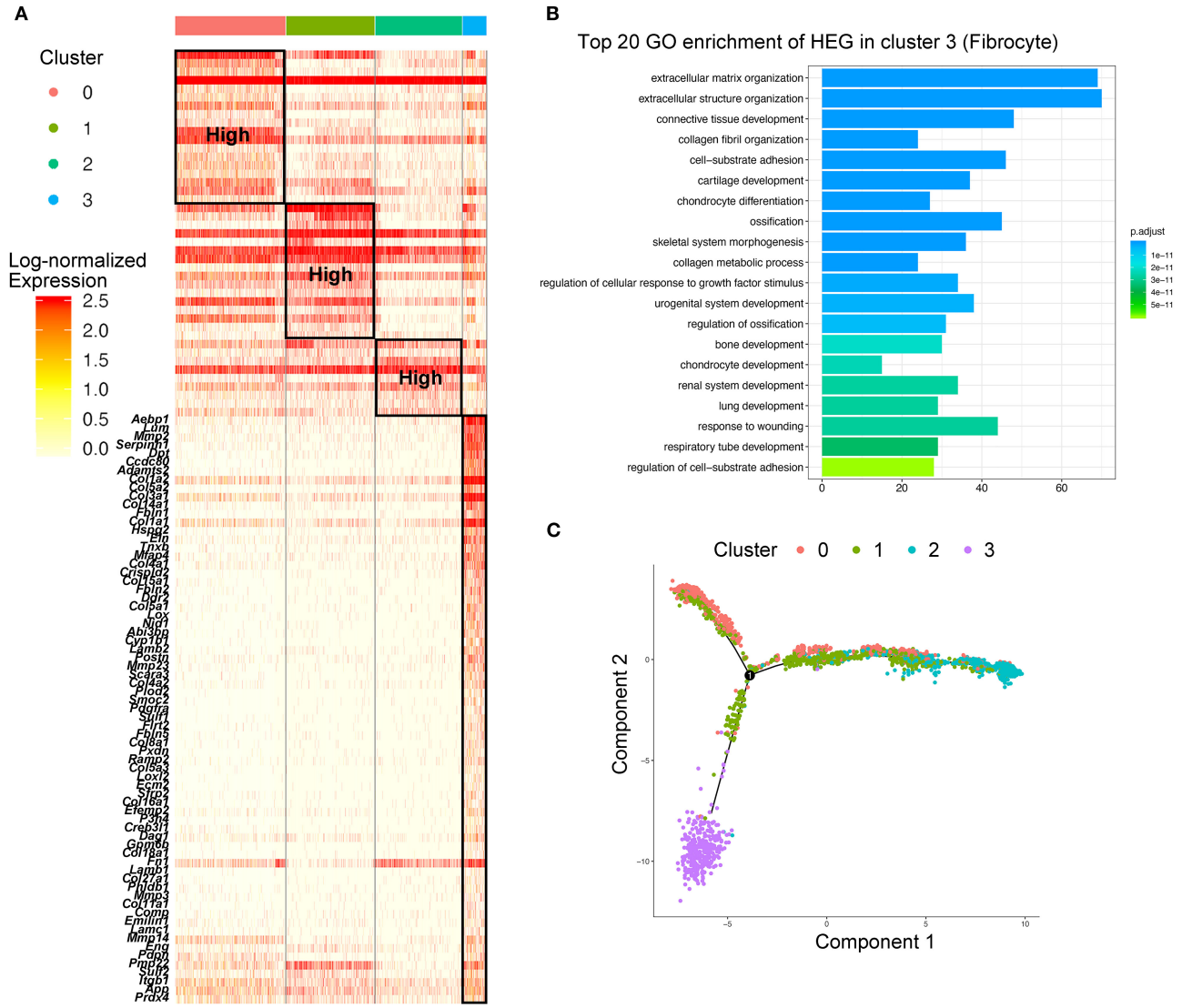

FIGURE 3 | Identification of fibrocytes that were distinct from macrophages in AAA. **(A)** Heatmap of highly expressed genes (HEGs) from three subtypes of macrophages and fibrocytes (Cluster 3), The HEGs of fibrocytes compared with macrophage subtypes were labeled (lower part), and the HEGs of macrophage subtypes (upper part) were the same as **Figure 2B**. **(B)** Bar plot of Gene Ontology (GO) pathway enrichment of the HEGs in fibrocytes. **(C)** Pseudo-time plot by trajectory analysis of three clusters of macrophages (Cluster 0: *Trem2*$^{+}$*Acp5*$^{+}$ macrophages; Cluster 1: *Mrc1*$^{+}$*Cbr2*$^{+}$ M2-like macrophages; Cluster 2: *Il1b*$^{+}$*Ccr2*$^{+}$ M1-like macrophages; Cluster 3: *Cd34*$^{+}$*Col1a2*$^{+}$ fibrocytes).

to wounding" (**Figures 4D,E**). These data together suggest the response and recruitment of fibrocytes to the AAA lesion. In addition, ECM and collagen-related functions were upregulated in fibrocytes during AAA formation (**Figure 4E**), which were similar to fibroblast functions (**Supplementary Figures S2B–D**). Further combining with the ATAA single cell dataset, DEGs of fibrocytes caused by aortic aneurysms were overlapped with those in our dataset and determined. Specifically, *Timp1*, *Sfrp2*, and *Sfrp4* were upregulated in both human and mouse samples (**Figure 4F**). These genes are known to be closely related to AAA formation (30–32). Further trajectory analysis between fibroblasts and fibrocytes showed fibrocytes were similar with inactivated fibroblasts and might be differentiated toward myofibroblasts (**Supplementary Figure S5D**), consistent with their role as the fibroblast progenitor. Taken together, we hypothesized that fibrocytes are recruited to AAA tissues and tend to transform toward fibroblasts to influence AAA pathogenesis by mediating ECMs remodeling.

In order to validate the existence and localization of fibrocytes, co-immunofluorescence staining was performed and the results showed that numerous CD45^{+}COL1^{+} fibrocytes were significantly increased in both mouse (**Figures 5A,B**) and human (**Figures 5C,D**) AAA tissues, suggestive of fibrocytes mainly in the adventitia. Co-localization of CD45 and elastin layers

showed that $CD45^+$ cells were mainly localized in the adventitia (**Supplementary Figure S8**), further indicating the localization of fibrocytes in the adventitia. Flow cytometry data further confirmed the increase of fibrocytes in mouse AAA tissues (**Supplementary Figure S9**).

Alleviation of Ang II-Induced AAA Formation by Reconstitution of Fibrocytes

Fibrocytes have been reported to play essential roles in wound healing, atherogenesis, and lung diseases (21, 23, 33, 34), but their role in AAA is not understood. To test the hypothesized roles of fibrocytes in AAA formation, bone marrow-derived fibrocytes were administered into Ang II-treated mice on days 7 and 21 by tail-vein injection (**Figure 6A**). Bone marrow-derived fibrocytes were produced from spleen monocytes and cultured with IL-13 (50 ng/ml) and M-CSF (25 ng/ml) for 10 days (**Supplementary Figure S10**). GFP-labeled fibrocytes from GFP-transgenic mice were then injected into Ang II-infused mice (non-GFP) to trace the cells *in vivo*. By co-staining GFP with fibrocyte markers, GFP-labeled fibrocytes were found to be recruited to AAA tissues (**Supplementary Figure S11**). More importantly, reconstitution of fibrocytes significantly attenuated AAA formation, demonstrated by a decrease in AAA incidence and mortality (**Figures 6B,C**), reduced lesion diameters (**Figures 6D–F**) and diminished elastin degradation (**Figures 6G,H**). Taken together, our data suggest that fibrocytes attenuate Ang II-induced AAA formation.

DISCUSSION

We performed scRNA-seq analysis of aortic tissues from Ang II-induced AAA mouse model and found infiltration and activation of pro-inflammatory cells such as macrophages, B cells and NK T cells in the AAA tissue. Additionally, myofibroblast activation, SMC apoptosis, and EC dysfunction were also indicated by the results of scRNA-seq. We focused on the heterogeneity of macrophage subtypes, and discovered the repolarization of M2-like and $Trem2^+$ osteoclast-like macrophages toward M1-like macrophages, highlighting a critical role of this process in AAA pathogenesis. More importantly, we identified fibrocytes from scRNA-seq analysis and confirmed the recruitment of fibrocytes and their protective effect in AAA formation. Thus, our study has identified specific cell populations critical to AAA and provided evidence supporting these cells as targets for intervention.

Despite the rapidly growing number of single-cell sequencing studies, only a few single-cell datasets of AAA have been published, including data from ATAA patients (29), the elastase model (35) and the $CaCl_2$ model (36). Hadi et al. conducted scRNA-seq on Ang II-induced AAA tissues and showed the expression of Nertin-1 in different cell types without in-depth analysis on the heterogeneity of cell populations. We performed scRNA-seq in Ang II-induced AAA tissues and obtained consistent findings with previously reported results. For example, B cells have been reported to play a crucial role by producing abundant inflammatory factors in AAA (37). Depletion of B cells using anti-CD20 could suppress the formation of AAA and evoke the infiltration of immunosuppressive cells (38). Consistently, we found the activation and increase of B cells, which was confirmed by flow cytometry in AAA. Similarly, the activation of NK T cells has been demonstrated to aggravate AAA formation (39), which is also consistent with our scRNA-seq and flow cytometry results. Apoptosis of SMCs has become the hallmark of AAA, which is also confirmed in our scRNA-seq data in terms of cell proportions and function analysis. Moreover, both previous studies and our scRNA-seq results showed the vital function of ECs in the recruitment of inflammatory cells during AAA formation. The consistent results from our and previous studies support the important roles of these cell types in AAA.

Our scRNA-seq analysis revealed the heterogeneities of three macrophage subtypes and found the increase of $Trem2^+$ osteoclast-like macrophages in AAA tissues. These data were consistent to the previous reports that osteoclast-like macrophages were increased in AAA lesions, and the inhibition of osteoclastogenic differentiation diminished AAA formation (40–42). In addition, based on the gene expression patterns and trajectory analysis, we proposed the re-polarization of osteoclast-like macrophages and M2-like macrophages toward the M1 type. However, it remains unclear when and how re-polarization takes place in AAA formation, which deserves to be further investigated. Besides promoting inflammation (**Supplementary Figure S2A**), infiltrated macrophages can also influence ECM degradation by secreting proteases, such as cathepsins and MMPs (43, 44). It has been reported that cathepsin S was highly expressed in AAA lesions, and deficiency of cathepsin S attenuated AAA formation by preventing SMC apoptosis and proliferation of inflammatory cells. Consistently, our scRNA-seq data showed an upregulated expression of cathepsins in different macrophages. Specifically, cathepsins S and B were most highly expressed in osteoclast-like macrophages and the expression levels were increased in AAA (**Supplementary Figure S6A**). Similarly, the expression of a series of cathepsins was upregulated in M2-like macrophages, including *Ctsa, Ctsb, Ctsc, Ctsd* (**Supplementary Figure S12**). In addition, previous studies have reported that MMP9 and MMP12 produced by macrophages contribute to AAA (45, 46). Our data showed that *Mmp9* was highly expressed in M2-like macrophages, and *Mmp12* and *Mmp14* were highly expressed in osteoclast-like macrophages correspondingly (**Supplementary Figure S6A**). These data together suggest the vital roles of different types of macrophages in AAA formation by differentially regulating inflammation and ECMs remodeling.

Fibrocytes are bone marrow-derived cells maturing in spleen. Fibrocytes are recruited to injured sites and differentiated toward fibroblasts (23). Previous studies have proposed their roles in wound healing, atherosclerogensis, and lung diseases (21, 33, 34, 47, 48). Reconstitution of fibrocytes could accelerate wound healing by upregulating collagen-related genes (23). Similarly, reconstitution of $Postn^{-/-}$ fibrocytes diminished bleomycin-induced lung fibrosis (48). In vascular pathology, fibrocytes were found to be involved in the atherosclerotic plaque formation (33, 47). In our study,

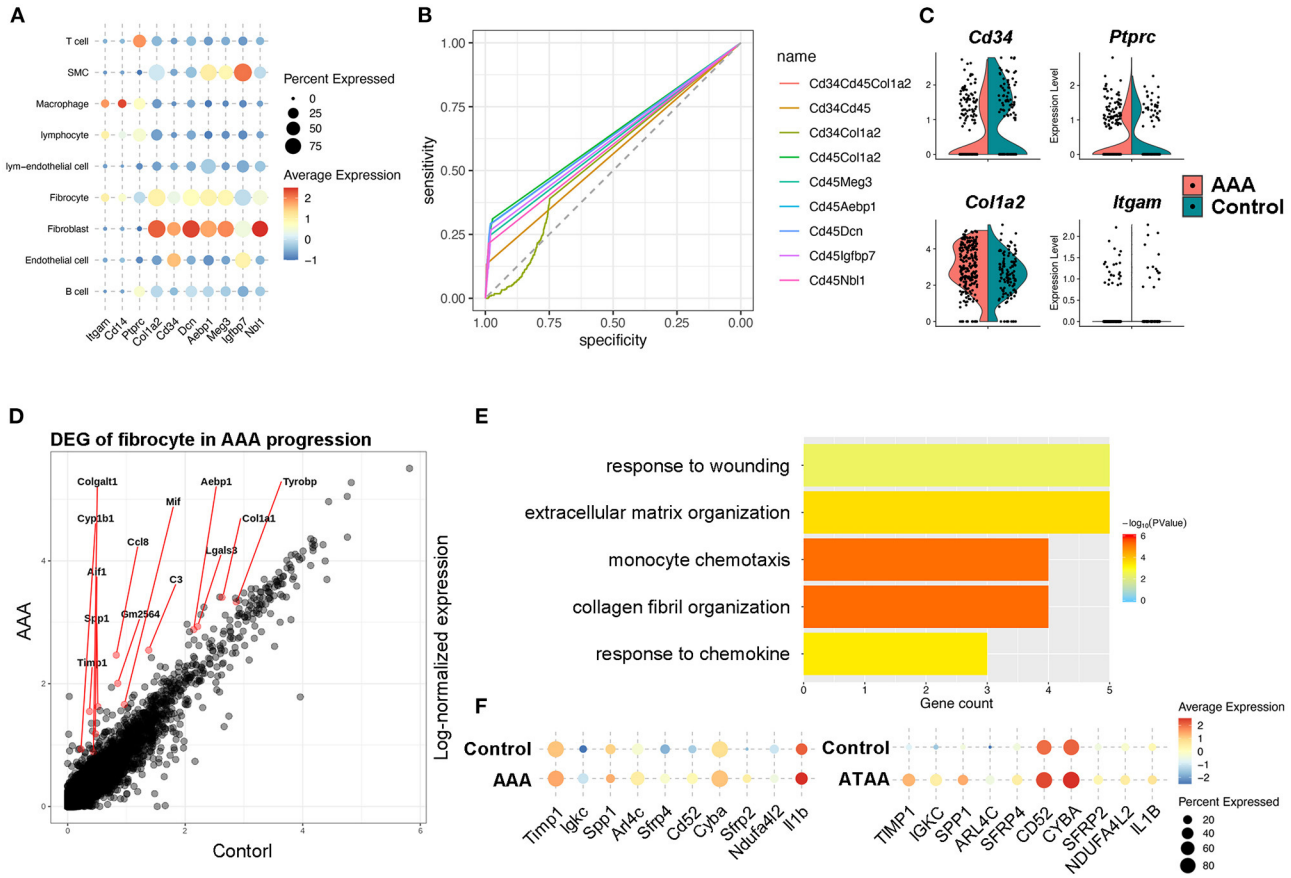

FIGURE 4 | Identification and function of fibrocytes in AAA pathogenesis. **(A)** Dot plot showing the expression of classic fibrocyte markers and the top 5 highly expressed genes compared with macrophages. **(B)** The ROC curve identifying the sensitivity and specificity of the co-expression of distinct marker genes. **(C)** Violin plots of the expression levels of the classic marker genes that identify fibrocytes during Ang II infusion. **(D)** Differentially expressed genes (DEGs) of fibrocytes during Ang II infusion. **(E)** Bar plot of Gene Ontology (GO) pathway enrichment of DEGs in fibrocytes. **(F)** Dot plot showing the expression of 10 shared DEGs in Ang II model and human ATAA.

the reconstitution of fibrocytes reduced the incidence and mortality of Ang II-induced AAA, and attenuated elastin degradation and AAA formation. In our study, we found the activation of fibroblast toward myofibroblast with high *Acta2* expression in AAA (**Figure 1G**). Importantly, single cell trajectory analyses revealed fibrocytes, as another source, tended to be differentiated toward fibroblasts and then myofibroblasts (**Supplementary Figure S5D**). The results suggested that the increased myofibroblasts in the AAA group may result from the activation of adventitial fibroblast as well as the recruited and increased fibrocytes. In previous studies, the activation and differentiation of fibroblast toward myofibroblast is a well-established phenomenon during which fibroblasts mature and acquire the contractile feature. This phenotypic transition contributes to vascular pathology by producing inflammatory factors, such as IL-6 and monocyte chemoattractant protein-1 (49, 50). In terms of the source of myofibroblasts, they have been reported to be differentiated from not only fibroblasts, but also from SMCs and fibrocytes (51), which are consistent with our observations. For the underlying mechanism of transition process, previous studies have revealed the roles of TGFβ, hypoxia, angiotension II, endothelin-1, IL-6, hyperhomocysteinemia (HHcy), cylindromatosis (CYLD), nicotinamide adenine dinucleotide phosphate (NADPH) oxidase 4 (Nox4), and Fizzl (50, 52–55). The enhanced expression of ECM-related genes (i.e., *Col1a1* and *Timp1*) and WNT antagonists (i.e. *Sfrp2* and *Sfrp4*) in fibrocytes (**Figure 4F**) suggests a protective effect in AAA formation. Additionally, these genes are involved in the TGFβ pathway (56), indicating the transition of fibrocytes to myofibroblasts. The specific mechanisms by which fibrocytes modulate AAA formation need to be further characterized in the future.

In conclusion, this study identified important roles of macrophage subtypes and fibrocytes in AAA by scRNA-seq. Reconstitution experiment with cell tracing confirmed that fibrocytes were recruited and attenuated AAA formation. As clinical treatment for AAA lacks breakthrough, our data provide the theoretical underpinning for fibrocytes as a new approach for cell therapy for AAA treatment or post-operative protection, where fibrocytes can maintain aortic homeostasis and reduce

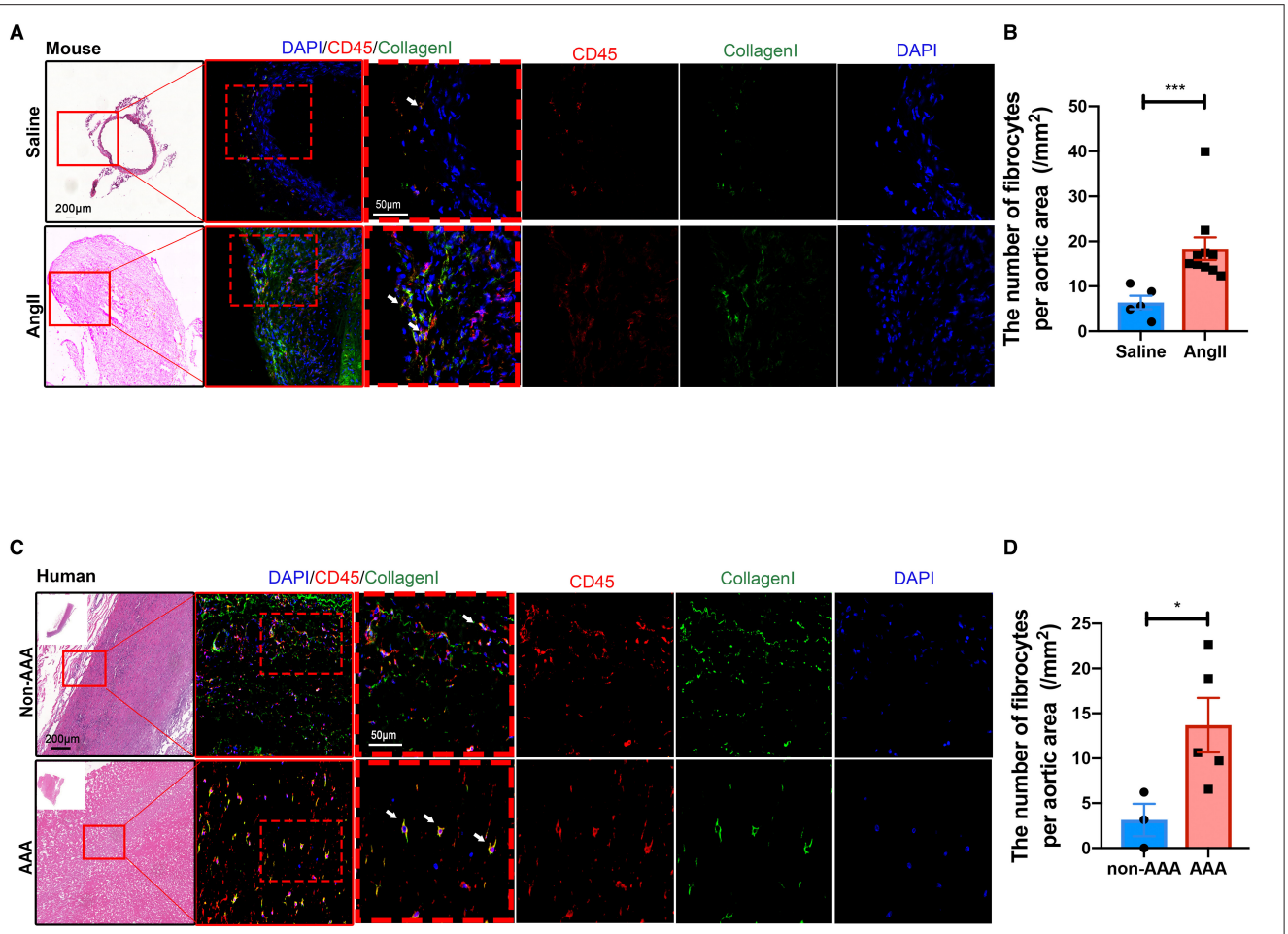

FIGURE 5 | Validation and localization of fibrocytes in AAA. **(A)** Representative images of H&E staining and the immunofluorescence images of normal aorta and AAA tissue from mice stained with COL1 (green) and CD45 (red). **(B)** Quantification of the number of fibrocytes per aortic area (/mm^2). The quantitative data were shown as mean ± SEM, and the difference between the groups was evaluated by Mann-Whitney test. (Saline: $n = 5$; Ang II: $n = 10$). **(C)** Representative images of H&E staining and the immunofluorescence images of normal aorta and AAA tissue from human stained with COL1 (green) and CD45 (red). **(D)** Quantification of the number of fibrocytes per aortic area (/mm^2). The quantitative data were shown as mean ± SEM, and the difference between the groups was evaluated by Mann-Whitney test. $^*p < 0.05$, and $^{***}p < 0.001$. (non-AAA: $n = 3$; AAA: $n = 5$).

the mortality due to AAA. Additionally, human fibrocytes can be easily derived from PBMCs for autologous cell therapy, providing a new and feasible strategy for future treatment of AAA.

LIMITATION

This study has some limitations. First, we have one AAA mouse versus one saline control for scRNA-seq. Multiple biological replicates in scRNA-seq will more conductive to exploring the heterogeneities of cell types in AAA. However, we did validation experiments to confirm cell heterogeneity in our scRNA-seq data, which were consistent with other scRNA-seq studies (29, 35, 36). The changes among the different cell types in AAA were confirmed by flow cytometry (**Supplementary Figure S3**). The involvement of fibrocytes in AAA pathogenesis were confirmed by reconstitution experiments in mice (**Figure 6**). Nevertheless, the results suggested that the cell types analyzed by scRNA-seq data were critical in progression of AAA. Second, the cell types captured and their proportions might be affected by the different enzyme digestion strategies used for obtaining single-cell suspensions, as shown in the previous scRNA-seq studies of vessel tissues (29, 35, 36). In our study, based on our preliminary experiments, we optimized the enzymatic strategy [PBS containing 200 U/ml collagenase I (Sigma Aldrich), 0.05 U/ml elastase (Sigma Aldrich), 5 U/ml neutral protease (Worthington), and 0.3 U/ml deoxyribonuclease I (Promega)]. Our results showed that the cell types and the proportions were similar with the single cell dataset of the $CaCl_2$ model (36). In addition, the cleanliness of dissected adventitia can also affect the cell types and its proportions. In this study, we kept more adventitial tissue to acquire complete cell atlas of the aorta, which might have resulted in more fibroblasts in this dataset. Taken together, these factors may have caused

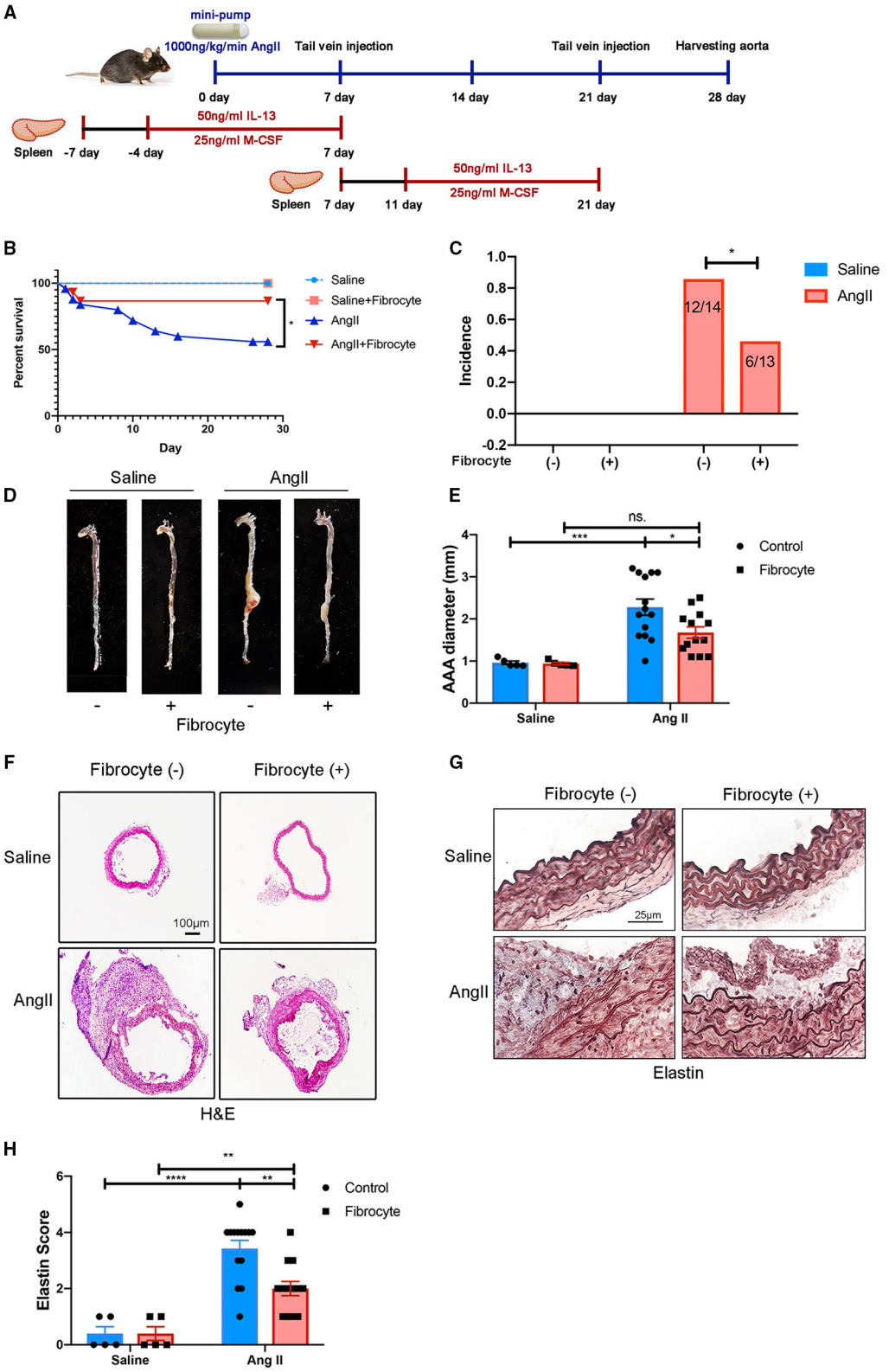

FIGURE 6 | Alleviation of Ang II-induced AAA formation by reconstitution of fibrocytes. **(A)** Schematic diagram of the fibrocytes reconstitution experiment. **(B)** Survival curves of control and Ang II-infused mice with or without fibrocytes reconstitution [Fibrocyte (–): $n = 5$ for control mice and $n = 25$ for Ang II-infusion mice; Fibrocyte

(Continued)

FIGURE 6 | (+): $n = 5$ for control mice and $n = 15$ for Ang II-infusion mice]. **(C)** The incidence rate of AAA in control and Ang II-infused mice with or without fibrocytes reconstitution. Fisher exact method was used to test for statistical significance. **(D)** Representative images of whole aortae. **(E)** Quantification of AAA diameter (mm). **(F)** Representative images of H&E staining of abdominal aortae. Scale bar = 250 μm. **(G)** Representative images of elastin staining in four groups of mice. Scale bar = 25μm. **(H)** Quantification of the elastin score. The quantitative data were shown as mean ± SEM, and the difference between multiple groups was evaluated by two-way ANOVA. $^{*}p < 0.05$, $^{**}p < 0.01$, $^{***}p < 0.001$, and $^{****}p < 0.0001$. [Fibrocyte (–): $n = 5$ for control mice and $n = 14$ for Ang II-infusion mice; Fibrocyte (+): $n = 5$ for control mice and $n = 13$ for Ang II-infusion mice].

the relatively low numbers of vascular smooth muscle cells in the control saline group. Therefore, the method of obtaining single-cell suspensions should be continually optimized in future studies. Finally, we only performed scRNA-seq study in Ang II-induced AAA mouse model. Different animal AAA models show multiple differences in anatomic positions, histological features, and pathological mechanisms. None of the experimental rodent models developed to date is exactly identical to human AAAs. Therefore, our findings need to be confirmed in AAAs from different animal models and perhaps human tissues in the future.

DATA AVAILABILITY STATEMENT

The datasets presented in this study can be found in online repositories. The names of the repository/repositories and accession number(s) can be found at: https://ngdc.cncb.ac.cn/gsa/PRJCA006049.

ETHICS STATEMENT

The studies involving human participants were reviewed and approved by the Institutional Review Board of Peking Union Medical College Hospital and Beijing Anzhen Hospital. The patients/participants provided their written informed consent to participate in this study. The animal study was reviewed and approved by the Research Ethics Committee of Peking Union Medical College.

AUTHOR CONTRIBUTIONS

BL, XS, RG, and JW designed the study. XS, RG, HZ, YH, WGu, WGe, HH, and TF performed the experiments. BL, HZ, XS, ZH, and ZL analyzed the data. BL, PY, HZ, and JW wrote the manuscript. All authors read and approved the final manuscript.

FUNDING

This study was financially supported by Chinese Academy of Medical Sciences Innovation Fund for Medical Sciences (2021-1-I2M-016) (to RG); the National Natural Science Foundation of China Grants 82100514 (to RG); the National Key Research and Development Program of China grants 2019YFA0801804 (to JW); Thousand Young Talents Program of China (to JW).

SUPPLEMENTARY MATERIAL

The Supplementary Material for this article can be found online at: https://www.frontiersin.org/articles/10.3389/fcvm.2021.753711/full#supplementary-material

REFERENCES

1. Karthikesalingam A, Holt PJ, Vidal-Diez A, Ozdemir BA, Poloniecki JD, Hinchliffe RJ, et al. Mortality from ruptured abdominal aortic aneurysms: clinical lessons from a comparison of outcomes in England and the USA. *Lancet.* (2014) 383:963–9. doi: 10.1016/S0140-6736(14)60109-4
2. Quintana RA, Taylor WR. Cellular mechanisms of aortic aneurysm formation. *Circ Res.* (2019) 124:607–18. doi: 10.1161/CIRCRESAHA.118.313187
3. Dale MA, Ruhlman MK, Baxter BT. Inflammatory cell phenotypes in AAAs: their role and potential as targets for therapy. *Arterioscler Thromb Vasc Biol.* (2015) 35:1746–55. doi: 10.1161/ATVBAHA.115.305269
4. Raffort J, Lareyre F, Clement M, Hassen-Khodja R, Chinetti G, Mallat Z. Monocytes and macrophages in abdominal aortic aneurysm. *Nat Rev Cardiol.* (2017) 14:457–71. doi: 10.1038/nrcardio.2017.52
5. Furusho A, Aoki H, Ohno-Urabe S, Nishihara M, Hirakata S, Nishida N, et al. Involvement of B cells, immunoglobulins, and syk in the pathogenesis of abdominal aortic aneurysm. *J Am Heart Assoc.* (2018) 7:e007750. doi: 10.1161/JAHA.117.007750
6. Galle C, Schandene L, Stordeur P, Peignois Y, Ferreira J, Wautrecht JC, et al. Predominance of type 1 CD4+ T cells in human abdominal aortic aneurysm. *Clin Exp Immunol.* (2005) 142:519–27. doi: 10.1111/j.1365-2249.2005.02938.x
7. Tsuruda T, Kato J, Hatakeyama K, Kojima K, Yano M, Yano Y, et al. Adventitial mast cells contribute to pathogenesis in the progression of abdominal aortic aneurysm. *Circ Res.* (2008) 102:1368–77. doi: 10.1161/CIRCRESAHA.108.173682
8. Mayranpaa MI, Trosien JA, Fontaine V, Folkesson M, Kazi M, Eriksson P, et al. Mast cells associate with neovessels in the media and adventitia of abdominal aortic aneurysms. *J Vasc Surg.* (2009) 50:388–95. doi: 10.1016/j.jvs.2009.03.055
9. Lopez-Candales A, Holmes DR, Liao S, Scott MJ, Wickline SA, Thompson RW. Decreased vascular smooth muscle cell density in medial degeneration of human abdominal aortic aneurysms. *Am J Pathol.* (1997) 150:993–1007.
10. Isselbacher EM. Thoracic and abdominal aortic aneurysms. *Circulation.* (2005) 111:816–28. doi: 10.1161/01.CIR.0000154569.08857.7A
11. Hinz B, Phan SH, Thannickal VJ, Prunotto M, Desmouliere A, Varga J, et al. Recent developments in myofibroblast biology: paradigms for connective tissue remodeling. *Am J Pathol.* (2012) 180:1340–55. doi: 10.1016/j.ajpath.2012.02.004
12. Keeley EC, Mehrad B, Strieter RM. Fibrocytes: bringing new insights into mechanisms of inflammation and fibrosis. *Int J Biochem Cell Biol.* (2010) 42:535–42. doi: 10.1016/j.biocel.2009.10.014
13. Zulli A, Buxton BF, Black MJ, Hare DL. CD34 Class III positive cells are present in atherosclerotic plaques of the rabbit model of atherosclerosis. *Histochem Cell Biol.* (2005) 124:517–22. doi: 10.1007/s00418-005-0072-2
14. Haudek SB, Xia Y, Huebener P, Lee JM, Carlson S, Crawford JR, et al. Bone marrow-derived fibroblast precursors mediate ischemic cardiomyopathy in mice. *Proc Natl Acad Sci USA.* (2006) 103:18284–9. doi: 10.1073/pnas.0608799103
15. Xie T, Wang Y, Deng N, Huang G, Taghavifar F, Geng Y, et al. Single-cell deconvolution of fibroblast heterogeneity in mouse pulmonary fibrosis. *Cell Rep.* (2018) 22:3625–40. doi: 10.1016/j.celrep.2018.03.010

16. Zheng GX, Terry JM, Belgrader P, Ryvkin P, Bent ZW, Wilson R, et al. Massively parallel digital transcriptional profiling of single cells. *Nat Commun.* (2017) 8:14049. doi: 10.1038/ncomms14049
17. Satija R, Farrell JA, Gennert D, Schier AF, Regev A. Spatial reconstruction of single-cell gene expression data. *Nat Biotechnol.* (2015) 33:495–502. doi: 10.1038/nbt.3192
18. Butler A, Hoffman P, Smibert P, Papalexi E, Satija R. Integrating single-cell transcriptomic data across different conditions, technologies, and species. *Nat Biotechnol.* (2018) 36:411–20. doi: 10.1038/nbt.4096
19. Trapnell C, Cacchiarelli D, Grimsby J, Pokharel P, Li S, Morse M, et al. The dynamics and regulators of cell fate decisions are revealed by pseudotemporal ordering of single cells. *Nat Biotechnol.* (2014) 32:381–6. doi: 10.1038/nbt.2859
20. Kim K, Shim D, Lee JS, Zaitsev K, Williams JW, Kim KW, et al. Transcriptome analysis reveals nonfoamy rather than foamy plaque macrophages are proinflammatory in atherosclerotic murine models. *Circ Res.* (2018) 123:1127–42. doi: 10.1161/CIRCRESAHA.118.312804
21. Maekawa T, Osawa Y, Izumi T, Nagao S, Takano K, Okada Y, et al. Myeloproliferative leukemia protein activation directly induces fibrocyte differentiation to cause myelofibrosis. *Leukemia.* (2017) 31:2709–16. doi: 10.1038/leu.2017.112
22. Crawford JR, Pilling D, Gomer RH. Improved serum-free culture conditions for spleen-derived murine fibrocytes. *J Immunol Methods.* (2010) 363:9–20. doi: 10.1016/j.jim.2010.09.025
23. Kao HK, Chen B, Murphy GF, Li Q, Orgill DP, Guo L. Peripheral blood fibrocytes: enhancement of wound healing by cell proliferation, re-epithelialization, contraction, and angiogenesis. *Ann Surg.* (2011) 254:1066–74. doi: 10.1097/SLA.0b013e3182251559
24. Russell DG, Huang L, VanderVen BC. Immunometabolism at the interface between macrophages and pathogens. *Nat Rev Immunol.* (2019) 19:291–304. doi: 10.1038/s41577-019-0124-9
25. O'Neill LA, Pearce EJ. Immunometabolism governs dendritic cell and macrophage function. *J Exp Med.* (2016) 213:15–23. doi: 10.1084/jem.20151570
26. Liao X, Sharma N, Kapadia F, Zhou G, Lu Y, Hong H, et al. Kruppel-like factor 4 regulates macrophage polarization. *J Clin Invest.* (2011) 121:2736–49. doi: 10.1172/JCI45444
27. Huang SCC, Everts B, Ivanova Y, O'Sullivan D, Nascimento M, Smith AM, et al. Cell-intrinsic lysosomal lipolysis is essential for alternative activation of macrophages. *Nat Immunol.* (2014) 15:846–55. doi: 10.1038/ni.2956
28. Bellini A, Mattoli S. The role of the fibrocyte, a bone marrow-derived mesenchymal progenitor, in reactive and reparative fibroses. *Lab Invest.* (2007) 87:858–70. doi: 10.1038/labinvest.3700654
29. Li Y, Ren P, Dawson A, Vasquez HG, Ageedi W, Zhang C, et al. Single-cell transcriptome analysis reveals dynamic cell populations and differential gene expression patterns in control and aneurysmal human aortic tissue. *Circulation.* (2020) 142:1374–88. doi: 10.1161/CIRCULATIONAHA.120.046528
30. Lemaitre V, Soloway PD, D'Armiento J. Increased medial degradation with pseudo-aneurysm formation in apolipoprotein E-knockout mice deficient in tissue inhibitor of metalloproteinases-1. *Circulation.* (2003) 107:333–8. doi: 10.1161/01.CIR.0000044915.37074.5C
31. Krishna SM, Seto SW, Jose RJ, Li J, Morton SK, Biros E, et al. Wnt signaling pathway inhibitor sclerostin inhibits angiotensin II-induced aortic aneurysm and atherosclerosis. *Arterioscler Thromb Vasc Biol.* (2017) 37:553–66. doi: 10.1161/ATVBAHA.116.308723
32. van Andel H, Kocemba KA, Spaargaren M, Pals ST. Aberrant Wnt signaling in multiple myeloma: molecular mechanisms and targeting options. *Leukemia.* (2019) 33:1063–75. doi: 10.1038/s41375-019-0404-1
33. Medbury HJ, Tarran SL, Guiffre AK, Williams MM, Lam TH, Vicaretti M, et al. Monocytes contribute to the atherosclerotic cap by transformation into fibrocytes. *Int Angiol.* (2008) 27:114–23. doi: 10.1016/S1567-5688(08)70207-1
34. Nikam VS, Schermuly RT, Dumitrascu R, Weissmann N, Kwapiszewska G, Morrell N, et al. Treprostinil inhibits the recruitment of bone marrow-derived circulating fibrocytes in chronic hypoxic pulmonary hypertension. *Eur Respir J.* (2010) 36:1302–14. doi: 10.1183/09031936.00028009
35. Zhao G, Lu H, Chang Z, Zhao Y, Zhu T, Chang L, et al. Single-cell RNA sequencing reveals the cellular heterogeneity of aneurysmal infrarenal abdominal aorta. *Cardiovasc Res.* (2021) 117:1402–16. doi: 10.1093/cvr/cvaa214
36. Yang H, Zhou T, Stranz A, DeRoo E, Liu B. Single-Cell RNA sequencing reveals heterogeneity of vascular cells in early stage murine abdominal aortic aneurysm-brief report. *Arterioscler Thromb Vasc Biol.* (2021) 41:1158–66. doi: 10.1161/ATVBAHA.120.315607
37. Meher AK, Johnston WF, Lu G, Pope NH, Bhamidipati CM, Harmon DB, et al. B2 cells suppress experimental abdominal aortic aneurysms. *Am J Pathol.* (2014) 184:3130–41. doi: 10.1016/j.ajpath.2014.07.006
38. Schaheen B, Downs EA, Serbulea V, Almenara CC, Spinosa M, Su G, et al. B-cell depletion promotes aortic infiltration of immunosuppressive cells and is protective of experimental aortic aneurysm. *Arterioscler Thromb Vasc Biol.* (2016) 36:2191–202. doi: 10.1161/ATVBAHA.116.307559
39. van Puijvelde GHM, Foks AC, van Bochove RE, Bot I, Habets KLL, de Jager SC, et al. CD1d deficiency inhibits the development of abdominal aortic aneurysms in LDL receptor deficient mice. *PLoS ONE.* (2018) 13:e0190962. doi: 10.1371/journal.pone.0190962
40. Takei Y, Tanaka T, Kent KC, Yamanouchi D. Osteoclastogenic differentiation of macrophages in the development of abdominal aortic aneurysms. *Arterioscler Thromb Vasc Biol.* (2016) 36:1962–71. doi: 10.1161/ATVBAHA.116.307715
41. Byon CH, Sun Y, Chen J, Yuan K, Mao X, Heath JM, et al. Runx2-upregulated receptor activator of nuclear factor kappaB ligand in calcifying smooth muscle cells promotes migration and osteoclastic differentiation of macrophages. *Arterioscler Thromb Vasc Biol.* (2011) 31:1387–96. doi: 10.1161/ATVBAHA.110.222547
42. Cochain C, Vafadarnejad E, Arampatzi P, Pelisek J, Winkels H, Ley K, et al. Single-cell rna-seq reveals the transcriptional landscape and heterogeneity of aortic macrophages in murine atherosclerosis. *Circ Res.* (2018) 122:1661–74. doi: 10.1161/CIRCRESAHA.117.312509
43. Pyo R, Lee JK, Shipley JM, Curci JA, Mao DL, Ziporin SJ, et al. Targeted gene disruption of matrix metalloproteinase-9 (gelatinase B) suppresses development of experimental abdominal aortic aneurysms. *J Clin Invest.* (2000) 105:1641–9. doi: 10.1172/JCI8931
44. Qin YW, Cao X, Guo J, Zhang Y, Pan L, Zhang H, et al. Deficiency of cathepsin S attenuates angiotensin II-induced abdominal aortic aneurysm formation in apolipoprotein E-deficient mice. *Cardiovasc Res.* (2012) 96:401–10. doi: 10.1093/cvr/cvs263
45. Thompson RW, Holmes DR, Mertens RA, Liao S, Botney MD, Mecham RP, et al. Production and localization of 92-kilodalton gelatinase in abdominal aortic aneurysms. An elastolytic metalloproteinase expressed by aneurysm-infiltrating macrophages. *J Clin Invest.* (1995) 96:318–26. doi: 10.1172/JCI118037
46. Curci JA, Liao S, Huffman MD, Shapiro SD, Thompson RW. Expression and localization of macrophage elastase (matrix metalloproteinase-12) in abdominal aortic aneurysms. *J Clin Invest.* (1998) 102:1900–10. doi: 10.1172/JCI2182
47. Hillebrands JL, Onuta G, Rozing J. Role of progenitor cells in transplant arteriosclerosis. *Trends Cardiovasc Med.* (2005) 15:1–8. doi: 10.1016/j.tcm.2004.10.002
48. Just SA, Lindegaard H, Hejbol EK, Davidsen JR, Bjerring N, Hansen SWK, et al. Fibrocyte measurement in peripheral blood correlates with number of cultured mature fibrocytes in vitro and is a potential biomarker for interstitial lung disease in Rheumatoid Arthritis. *Respir Res.* (2017) 18:141. doi: 10.1186/s12931-017-0623-9
49. Enzerink A, Vaheri A. Fibroblast activation in vascular inflammation. *J Thromb Haemost.* (2011) 9:619–26. doi: 10.1111/j.1538-7836.2011.04209.x
50. Liu Z, Luo H, Zhang L, Huang Y, Liu B, Ma K, et al. Hyperhomocysteinemia exaggerates adventitial inflammation and angiotensin II-induced abdominal aortic aneurysm in mice. *Circ Res.* (2012) 111:1261–73. doi: 10.1161/CIRCRESAHA.112.270520
51. McAnulty RJ. Fibroblasts and myofibroblasts: their source, function and role in disease. *Int J Biochem Cell Biol.* (2007) 39:666–71. doi: 10.1016/j.biocel.2006.11.005
52. Shi Y, O'Brien JE, Jr., Fard A, Zalewski A. Transforming growth factor-beta 1 expression and myofibroblast formation during arterial repair. *Arterioscler Thromb Vasc Biol.* (1996) 16:1298–305. doi: 10.1161/01.ATV.16.10.1298

53. Misra S, Fu AA, Misra KD, Shergill UM, Leof EB, Mukhopadhyay D. Hypoxia-induced phenotypic switch of fibroblasts to myofibroblasts through a matrix metalloproteinase 2/tissue inhibitor of metalloproteinase-mediated pathway: implications for venous neointimal hyperplasia in hemodialysis access. *J Vasc Interv Radiol.* (2010) 21:896–902. doi: 10.1016/j.jvir.2010.02.030
54. An SJ, Boyd R, Zhu M, Chapman A, Pimentel DR, Wang HD. NADPH oxidase mediates angiotensin II-induced endothelin-1 expression in vascular adventitial fibroblasts. *Cardiovasc Res.* (2007) 75:702–9. doi: 10.1016/j.cardiores.2007.02.015
55. Yu B, Liu Z, Fu Y, Wang Y, Zhang L, Cai Z, et al. CYLD deubiquitinates nicotinamide adenine dinucleotide phosphate oxidase 4 contributing to adventitial remodeling. *Arterioscler Thromb Vasc Biol.* (2017) 37:1698–709. doi: 10.1161/ATVBAHA.117.309859
56. Akhmetshina A, Palumbo K, Dees C, Bergmann C, Venalis P, Zerr P, et al. Activation of canonical Wnt signalling is required for TGF-beta-mediated fibrosis. *Nat Commun.* (2012) 3:735. doi: 10.1038/ncomms1734

Conflict of Interest: The authors declare that the research was conducted in the absence of any commercial or financial relationships that could be construed as a potential conflict of interest.

Publisher's Note: All claims expressed in this article are solely those of the authors and do not necessarily represent those of their affiliated organizations, or those of the publisher, the editors and the reviewers. Any product that may be evaluated in this article, or claim that may be made by its manufacturer, is not guaranteed or endorsed by the publisher.

frontiers in Cardiovascular Medicine

REVIEW
published: 06 December 2021
doi: 10.3389/fcvm.2021.770574

Mitochondrial Dynamics: Pathogenesis and Therapeutic Targets of Vascular Diseases

Yi Luan[1], *Kai-Di Ren*[2,3], *Ying Luan*[4], *Xing Chen*[1]* *and Yang Yang*[1]*

[1] Department of Translational Medicine Center, The First Affiliated Hospital of Zhengzhou University, Zhengzhou, China, [2] Department of Pharmacy, The First Affiliated Hospital of Zhengzhou University, Zhengzhou, China, [3] Henan Key Laboratory of Precision Clinical Pharmacy, Zhengzhou University, Zhengzhou, China, [4] Department of Physiology and Neurobiology, School of Basic Medical Sciences, Zhengzhou University, Zhengzhou, China

Vascular diseases, particularly atherosclerosis, are associated with high morbidity and mortality. Endothelial cell (EC) or vascular smooth muscle cell (VSMC) dysfunction leads to blood vessel abnormalities, which cause a series of vascular diseases. The mitochondria are the core sites of cell energy metabolism and function in blood vessel development and vascular disease pathogenesis. Mitochondrial dynamics, including fusion and fission, affect a variety of physiological or pathological processes. Multiple studies have confirmed the influence of mitochondrial dynamics on vascular diseases. This review discusses the regulatory mechanisms of mitochondrial dynamics, the key proteins that mediate mitochondrial fusion and fission, and their potential effects on ECs and VSMCs. We demonstrated the possibility of mitochondrial dynamics as a potential target for the treatment of vascular diseases.

Keywords: cardiovascular disease (CVDs), vascular diseases, mitochondrial dynamics, fusion, fission

OPEN ACCESS

Edited by:
Masanori Aikawa,
Brigham and Women's Hospital and Harvard Medical School, United States

Reviewed by:
Sudhahar Varadarajan,
Augusta University, United States
Beatrice Charreau,
Université de Nantes, France

***Correspondence:**
Yang Yang
yangyangbio@163.com
Xing Chen
chenxing1212@163.com

Specialty section:
This article was submitted to Atherosclerosis and Vascular Medicine, a section of the journal Frontiers in Cardiovascular Medicine

Received: *04 September 2021*
Accepted: *25 October 2021*
Published: *06 December 2021*

Citation:
Luan Y, Ren K-D, Luan Y, Chen X and Yang Y (2021) Mitochondrial Dynamics: Pathogenesis and Therapeutic Targets of Vascular Diseases. Front. Cardiovasc. Med. 8:770574. doi: 10.3389/fcvm.2021.770574

INTRODUCTION

Cardiovascular disease (CVD) is the leading cause of death worldwide (1). Vascular diseases, particularly atherosclerosis, are initiated at an early stage in life and remain asymptomatic for a long period until they reach advanced stages (2). Among vascular diseases, atherosclerosis is a pathologic process of lipid accumulation, scarring, and inflammation in the vascular wall, particularly the subendothelial (intimal) space of arteries, which leads to vascular wall thickening, luminal stenosis, and calcification (3). Endothelial cell (EC) activation or dysfunction is an early symptom of vascular diseases that occur at the lesion-prone sites of arterial blood vessels, where ECs display pro-inflammatory and prothrombotic phenotypes and reduced barrier function. Notably, ECs are extremely sensitive to oxidative stress and respond rapidly to altered environments, such as changes in oxygen levels, pathogen stimulation, and damaging endogenous stimuli (4). In addition, the direct contact between ECs and circulating immune cells triggers immune reactions (5). Another substance that plays an important role in blood vessel function is nitric oxide (NO). NO is a signaling molecule in the vascular system, in which blood vessels control blood flow by sending signals to the vessels to vasodilate. NO could also slow the deposition of atherosclerotic plaque on the blood vessel wall (6).

Other mechanisms and stimuli also affect the function of blood vessels. Blood flow promotes the production of adhesive molecules, which recruit inflammatory cells (7). Besides, the migration of vascular smooth muscle cells (VSMCs) also facilitates atherosclerosis progression (5). Several

vascular diseases ultimately lead to myocardial infarction, stroke, and peripheral artery disease (8). The etiology of vascular diseases is complex; thus, several risk factors may contribute to their progression, including dyslipidemia, diabetes, smoking, hypertension, oxidative stressors, angiotensin II, systemic infection, and inflammation (9). Nonetheless, an effective cure for vascular diseases still lacks partially because of the complex etiology of the diseases in spite of recent advances (4).

The occurrence of vascular diseases is related to the loss of energy metabolism; notably, the mitochondria are the core sites of cell energy metabolism (10). The mitochondria are important in endothelial and smooth muscle function (11, 12). Mitochondria are composed of a central mitochondrial matrix surrounded by two inner and outer mitochondrial membranes, and eukaryotic mitochondrial respiratory chain is composed of complex. Compounds I, II, III, IV and complex V (ATP synthase), ubiquinone, coenzyme Q and cytochrome C are located in the inner membrane of mitochondria. Mitochondrial respiratory chain oxidative phosphorylation is responsible for more than 90% of oxygen consumption and provides more than 95% of body energy. Supply, the mitochondrial matrix is the main site of the tricarboxylic acid cycle and fatty acid β oxidation. Apart from its capacity for ATP production, the mitochondria also modulate reactive oxygen species (ROS) generation, calcium regulation, cell death, and survival (13, 14). The function of the mitochondria is affected by mitochondrial dynamics, including fusion and fission, interaction with the endoplasmic reticulum (ER), and mitophagy (**Figure 1**). Mitochondrial dysfunction leads to cell senescence, inflammation, and apoptosis, which are characteristics of vascular diseases (15). In addition, mitochondrial dysfunction can be triggered by DNA damage, which is closely related to several risk factors of CVDs (16). In this review, we summarize the correlation between vascular diseases and mitochondrial dynamics with emphasis on the detailed function of mitochondrial dynamics in specific vascular disease forms and the potential therapeutic approach of mitochondrial dynamics in vascular diseases.

REGULATION OF MITOCHONDRIAL DYNAMICS

More and more evidences indicate the role of mitochondrial dynamics in vascular function and the pathogenesis of vascular diseases. The mitochondria are highly dynamic organelles whose structure and distribution affect metabolism despite being recognized as isolated organelles (17). The nature of the dynamic network depends on the proper balance between mitochondrial fusion and fission (18). Its balance can be destroyed by environmental stimuli, developmental status, and cellular metabolic demands. The recently identified molecular mediators of mitochondrial fusion and fission, as well as post-translational modification (PTM) by an extensive set of kinases, phosphatases, and ubiquitination mediators, bring a new slight on the mechanism of mitochondrial dynamics (**Table 1**) (19).

Mitochondrial Fusion Proteins

Mechanically, mitochondrial fusion at the outer mitochondrial membrane is controlled by the transmembrane GTPases, MFN 1 and MFN2, and fusion at the inner membrane is controlled by optic atrophy protein 1 (OPA1) (20, 21). Besides, fission is regulated by DRP1 and fission-1 (FIS1) (22, 23). Mitochondrial fusion is regulated by the coordinated action of conserved GTPase proteins, including MFN1 and MFN2, and these transmembrane GTPases located in the outer membrane of the mitochondria are responsible for the regulation of the mitochondrial fusion by forming homodimeric or heterodimeric, antiparallel, coiled-coil linkages between adjacent mitochondria and C-terminal domains (24) (**Figure 2**). MFN1 and MFN2 deficiencies lead to a remarkable decrease in mitochondrial fusion (25). Additionally, MFN2 mediates cell apoptosis and mitochondrial autophagy (26). OPA1, a dynamin-related GTPase embedded in the inner membrane or intermembrane of the mitochondria, is involved in mitochondrial intima fusion and mitochondrial cristae remodeling (20). OPA1 harbors two forms (i.e., long and short OPA1 proteins) with distinguished functions (27). The long form of OPA1 located in the inner membrane, which is responsible for intimal fusion, can be cleaved into short form under the digestion of the intestinal peptidase, OMA1, and the i-AAA proteolytic enzyme, YME1L, to induce mitochondrial fragmentation and fission in the membrane space (19).

Mitochondrial Fission Proteins

Mitochondrial fission in mammalian cells is manipulated by DRP1, FIS1, mitochondrial fission factor (MFF), and mitochondrial dynamic proteins of 49 and 51 kDa (MiD49/51) as shown in **Figure 2** (24). DRP1, a GTPase located in the cytoplasm, mediates mitochondrial fission at the outer membrane (28). DRP1 is encoded by the *DNM1L* gene and contains a GTPase region, an intermediate region, a polytropic region, and a GTPase effector region from the N-terminal to the C-terminal, which are involved in the physical constriction of the mitochondria (the early step of fission) (29). Notably, DRP1 needs to bind with other receptor proteins, such as FIS1, to embed on the outer membrane of the mitochondria because of its lack of lipid-interacting hydrophobic transmembrane domain (30). However, FIS1 depletion has minimal effect on the transfer of DRP1 to the mitochondria in mammalian cells (31). A multitude of receptors is involved in the recruitment of DRP1 to the mitochondria to trigger fission (32). Mid49/51 are involved in DRP1 translocation in this fission machinery (30). In addition, DRP1 activity is regulated by PTMs, such as acetylation and phosphorylation (32). DRP1 activity is modulated by two serine phosphorylation sites with opposing functions; that is, DRP1 activity can be activated by phosphorylation at serine 616 but inhibited by phosphorylation at serine 637 (33). Each serine phosphorylation is catalyzed by a different kinase and phosphatase; thus, mitochondrial fission is linked to key cellular processes (**Table 1**). For instance, the DRP1 phosphorylation at serine 616 mediated by the mitotic initiator, cyclin B1–cyclin-dependent kinase (CDK1), links mitochondrial fission to cell division (34). The phosphorylation mediated by calcium-calmodulin-dependent kinase (CamK) coordinates fission to

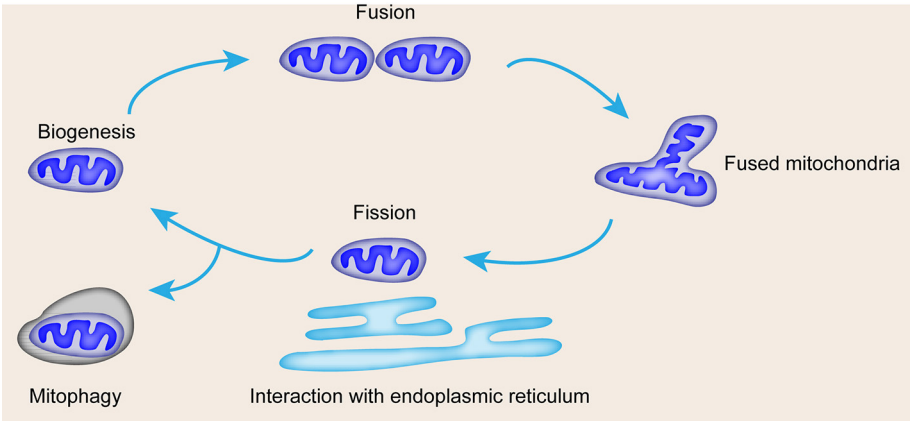

FIGURE 1 | Mitochondrial life cycle and contribution of mitochondrial dynamics and mitophagy to quality control. Mitochondrial dynamics include biogenesis, fusion for mass increase, fission for number increase, interaction with ER, and mitophagy.

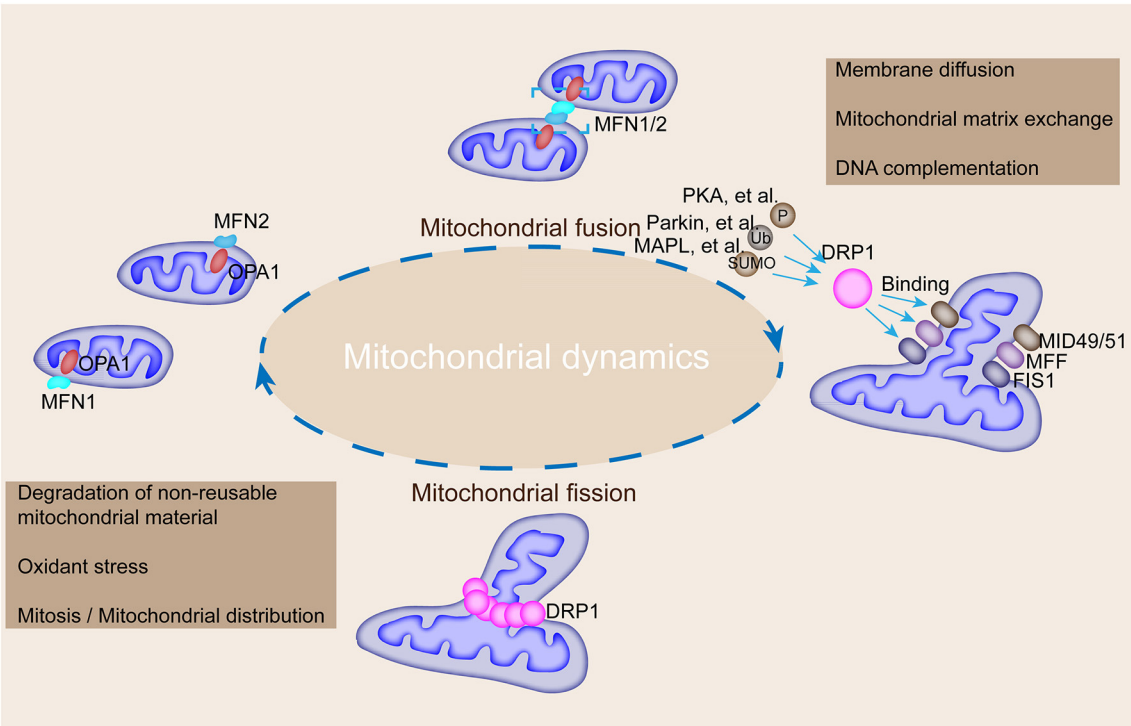

FIGURE 2 | Mechanisms underlying the regulation of mitochondrial fusion and fission and their roles in modulating mitochondrial morphology. MFN1, MFN2, and OPA1 mediate mitochondrial fusion, whereas DRP1 interacts with FIS1, MFF, and MiD49/51 to participate in mitochondrial fission. DRP1 could be modified by phosphorylation, ubiquitination, and SUMOylation by corresponding enzymes to promote its binding with FIS1, MFF, and MiD49/51. Mitochondrial fusion is accompanied by membrane diffusion, matrix exchange, and DNA complementation, and fission is accompanied by the degradation of non-reusable mitochondrial material, oxidative stress, and mitosis.

intracellular calcium (35). The serine ratio between the 616 and 637 sites modulates DRP1 activity and reflects the polymerized influence of several kinases and phosphatases (36). DRP1 activity is also modulated by the ubiquitin ligases, membrane-associated RING-CH protein 5 and small ubiquitin-like modifier type 1 (37). DRP1 acetylation regulates the activity of itself and contributes to metabolic stress-associated cardiomyocyte death and dysfunction (38). Previous studies depicted that DRP1 forms a dimer or tetramer under basic conditions and further self-assembles into a larger polymer structure in the fission process.

Multiple PTMs of human mitochondrial proteins, such as phosphorylation (in MFN1, MFN2, and OPA1), acetylation

TABLE 1 | Mediators involved in the regulation of mitochondria fission and fusion.

Mediator	Function in mitochondrial dynamics	Role of mediator in vascular diseases
Fusion mediators		
Mitofusin-1	GTPase in outer mitochondrial membrane that tethers adjacent mitochondria	Atherosclerosis
Mitofusin-2	GTPase in outer mitochondrial membrane that tethers adjacent mitochondria	Pulmonary arterial hypertension, arterial restenosis, and atherosclerosis
Optic atrophy 1	GTPase in inner mitochondrial membrane that mediates fusion	
Fission mediator: DRP1	Cytosolic GTPase that translocates to the outer mitochondrial membrane when activated	Patent ductus arteriosus, pulmonary arterial hypertension, and atherosclerosis
Fusogenic and fissogenic lipids		
Phosphatidic acid	Generated by mitochondrial phospholipase D; promotes assembly of fusogenic mediators	
Diacylglycerol	Lipin-1, a protease that hydrolyzes phosphatidic acid, generates diacylglycerol, which promotes fission	
Transcription factors		
PGC-1α	Mediator of mitochondrial biogenesis and transcriptional coactivator of mitofusin-2	Pulmonary arterial hypertension
HIF1α	Hypoxic transcription factor that also promotes DRP1 activation and fission	Pulmonary arterial hypertension
Post-translational regulators of DRP1		
Cyclin B–cyclin-dependent kinase1	Serine–threonine kinase that initiates mitosis and also activates DRP1 by phosphorylation of DRP1 serine 616	Pulmonary arterial hypertension
Aurora A kinase	Serine-threonine kinase, regulating mitotic entry, chromosomal segregation, and DRP1 activation	
Calcium-calmodulin–dependent kinase	Activates DRP1	Patent ductus arteriosus
Calcineurin	Serine-threonine protein phosphatase that activates DRP1 by dephosphorylating DRP1 serine 637	
Protein kinase A	Causes cyclic AMP–dependent phosphorylation of DRP1 at serine 637, which inhibits fission	
SENP5	Moves to the mitochondria during mitosis and desumoylates DRP1, which leads to the activation of DRP1	

(in MFN1, MFN2, and OPA1), methylation (in MFN1 and OPA1), and ubiquitination (in MFN1, MFN2, and OPA1) have been detected by mass spectrometry-based proteomics (39). However, the modulation of PTM in mitochondrial fusion proteins is largely uncharacterized compared with that in DRP1. For instance, the PTMs of MFN2 (phosphorylation and ubiquitination) are observed in hearts with cardiomyopathy. PINK1-dependent MFN2 phosphorylation induces Parkin translocation to the outer mitochondrial membrane upon membrane depolarization, which subsequently promotes Parkin-mediated MFN2 ubiquitination in adult cardiomyocytes (40). Also, Parkin-mediated MFN2 ubiquitination leads to MFN2 degradation, which results in the selective removal of damaged mitochondria by mitophagy in adult cardiomyocytes (41).

Mitochondrial miRNAs

Apart from proteins, mitochondrial miRNAs (mitomiRs) modulate the translational activity of the mitochondrial genome and mitochondrial function (42). Mitochondrial fission/fusion can also be regulated by mitomiRs. Notably, miR-146a, miR-34a, and miR-181a may regulate mitochondrial dynamics by targeting Bcl-2 (42). Other mitomiRs can also directly target mitochondrial fusion/fission proteins. miR-484 suppresses FIS1-mediated fission and apoptosis in cardiomyocytes by decreasing FIS1 expression. Mitochondrial fission is also suppressed by the miR-30-mediated downregulation of DRP1 and p53 (43).

Regulators of Mitochondrial Dynamics

Mitochondrial fusion and fission can also be mediated by peroxisome proliferator-activated receptor γ co-activator 1α (PGC-1α), which is a modulator of mitochondrial fusion by acting as a transcriptional coactivator of MFN2 (44, 45). The assembly of fission apparatus also needs the assistance of the ER directly in contact with the mitochondria to form a microdomain that facilitates the assembly of DRP1, MEF, and proapoptotic proteins (46). The lipids produced by mitochondrial phospholipase D, especially phosphatidic acid, guide mitochondrial dynamics (47).

The cooperation of mitochondrial fusion and fission maintains the fundamental integrity and normal functioning of the mitochondria, including energy metabolism, ROS generation, and apoptosis regulation (48). Fusion favors mitochondrial interconnection, mitochondrial DNA mixing, signal transduction, and metabolite exchange (49). Mitochondrial fission facilitates the elimination of damaged mitochondria by dividing the mitochondria into daughter mitochondria to maintain the normal function of the mitochondria (50). However, the perturbation of mitochondrial fusion and fission

breaks their balance and consequently leads to the accumulation of damaged and non-functional mitochondria (48).

Mitochondrial dynamics play an important role in the morphology, function, and distribution of mitochondria. Fusion and fission regulate mitochondrial shape, length, and number. The balance between mitochondrial fusion and fission controls mitochondrial morphology. Mitochondrial shape affects the ability of cells to distribute their mitochondria to specific subcellular locations. Fusion and fission allow the mitochondrial exchange of lipid membranes and intramitochondrial content, which is crucial for maintaining the health of a mitochondrial population (51). For instance, MFN1 and MFN2 ablation in fibroblasts induce reduced respiratory capacity and great heterogeneity in mitochondrial shape and membrane potential (52).

ENDOTHELIAL FUNCTION AND THE MITOCHONDRIA

The proper function of the mitochondria in the arterial wall is critical in all atherogenesis-related key cell types, including ECs, VSMCs, and macrophages, which are responsible for massive lipid storage via phagocytosis, as well as pro-inflammatory status maintenance in a lesion (53). Normal endothelium is a dynamic organ that regulates vascular tone by balancing the production of vasodilators and vasoconstrictors in response to a variety of stimuli (54). The endothelial mitochondria act as critical signaling organelles that play a crucial role in endothelial function, including subcellular location, dynamics, biogenesis, mitophagy, autophagy, ROS; therefore, mitochondrial dysfunction facilitates atherosclerosis development (55, 56). Endothelial dysfunction is a pathological condition characterized by an imbalance between substances with vasodilating, antimitogenic, and antithrombogenic properties (endothelium-derived relaxing factors) and substances with vasoconstricting, prothrombotic, and proliferative characteristics (endothelium-derived contracting factors) (57). ECs play important roles in the maintenance of vascular homeostasis by modulating vasodilation, platelet activation, and leukocyte adhesion (58). Therefore, the dysfunction of EC leads to increased vascular tension and atherosclerosis, followed by systemic hypertension, and increased incidence of ischemia and stroke. Moreover, mitochondrial dysfunction is involved in the formation of oxidative stress conditions in atherosclerosis, which facilitate inflammatory response and lesion development (59).

In pulmonary ECs, DRP-1 activation, which induces mitochondrial fission, stimulates angiogenesis by promoting cell proliferation and migration and inhibiting apoptosis (60). Endothelial dysfunction contributes to the development of nearly all vascular diseases (10). Even though ECs have low mitochondrial content, mitochondrial dynamics act as a pivotal orchestrator of EC homeostasis under normal conditions; damage in mitochondrial dynamics participates in endothelial dysfunction and diverse vascular diseases. Endothelial dysfunction leads to altered mitochondrial morphology, reduced network extent, and increased FIS1 protein expression compared with ECs from healthy volunteers (61).

VASCULAR SMOOTH MUSCLE CELL FUNCTION AND THE MITOCHONDRIA

VSMCs are the main constitutive stromal cells of the vascular wall that engage in a variety of different structural and physiological functions (62). VSMCs are crucial components of blood vessels and the major determinants of vasotone (62). This critical and tightly regulated function is granted by the contractile phenotype of VSMCs. VSMCs can switch to a synthetic dedifferentiated phenotype characterized by increased proliferative and migratory capabilities in response to certain cues. The VSMC phenotypic switch is implicated in the pathogenesis of vascular diseases (63). During the progression of atherosclerosis, VSMCs are subjected to a phenotype switch that can internalize atherogenic LDL particles, such as oxidized LDL or desialylated LDL, for lipid accumulation to migrate to lesion sites (64, 65). Cells with lipid particle accumulation are recognized as "foam cells" and manifest as atherosclerotic plaques (66). The association between VSMCs and mitochondrial dysfunction in atherosclerosis has been discussed before.

Mitochondrial dysfunction characterized by decreased oxidative phosphorylation is a striking phenotype of VSMCs isolated from atherosclerosis (13). In addition, a multitude amount of energy and oxygen-free radicals are required for the impairment of nuclear and mitochondrial DNAs in VSMCs, which further promotes DNA damage, genomic instability, and mitochondrial damage (67). Mitochondrial fission and fusion also affect VSMC function (68). Mitochondrial fission is an integral process in cell migration, and controlling mitochondrial fission can limit VSMC migration and pathological intimal hyperplasia by altering mitochondrial energetics and ROS levels (69). For instance, mitofusin (MFN) 2 is an important suppressor of VSMC proliferation (70). In addition, the link between mitochondrial dynamics and VSMC senescence can be mediated by Krüppel-like factor 5 (Klf5), an essential transcriptional factor of cardiovascular remodeling. Klf5 downregulation induces VSMC senescence through eIF5a depletion and mitochondrial fission (71).

MACROPHAGE AND MONOCYTE FUNCTION AND THE MITOCHONDRIA

Macrophage mitochondrial fission is essential for the continued removal of apoptotic cells and plays a protective role in advanced atherosclerosis (72). In macrophage-enriched murine atherosclerosis lesion areas, the level of dynamin-related protein-1 (DRP1) is downregulated and MFN2 is upregulated as the lesion progresses. Inhibiting macrophage mitochondrial fission results in a dramatic increase in the necrotic core area and the accumulation of apoptotic cells in the advanced stage of atherosclerosis; thus, macrophage mitochondrial fusion/fission could be a potential therapeutic target to prevent lesion necrosis and stabilize advanced plaques (73).

Human CD14+ monocytes exhibit reduced mitochondrial fission and increased mitochondrial fusion for metabolic adaptation upon lipopolysaccharide stimulation. Notably, mitochondrial dynamics affect the inflammatory responses of CD14+ monocytes.

MITOCHONDRIAL DYNAMICS IMBALANCE

Many studies have pointed out the beneficial effects of mitochondrial fusion in oxidative phosphorylation. Mitochondrial fusion maintains normal mitochondrial function by protecting from mitochondrial DNA loss and maintaining the synthesis of mitochondrial proteins (74). In addition, mitochondrial fusion events can attenuate the damage of DNA and protein contents and restore damaged mitochondria by "functional complementation" (75). Mitochondrial fusion damage can lead to increased mitochondrial fission and fragmentation, which induce oxidative phosphorylation and cell apoptosis attenuated by mitochondrial division (76). For example, DRP1 gene mutation in mice can damage mitochondrial function and induce mitophagy, which contribute to heart enlargement and failure (77). Mitochondrial division inhibitor 1 (Mdivi-1) is a selective cell-permeable inhibitor of mitochondrial division DRP1 and mitochondrial division dynamin I. Mdivi-1 attenuates mitophagy and enhances apoptosis. Also, DRP1 inhibition with Mdivi-1 protects the injured heart and brain from ischemia (78, 79). Mitochondrial fission seems harmful in this perspective; however, the deletion of myocardial DRP1 gene can lead to division disorders, which result in dysfunctional mitochondria and ultimately lead to heart failure and death (80). Mitochondrial dynamics proteins have been genetically alerted in vascular cells. For example, in VSMCs, the overexpression of the phospho-deficient mutation, MFN2-S442A, increases the inhibitory effects of MFN2 on cell proliferation, as well as neointimal hyperplasia and restenosis, in rat carotid artery balloon injury model (70).

Excessive mitochondrial fragmentation often occurs in most vascular diseases and thus could be a promising therapeutic target for these diseases (81). The promotion of mitochondrial fusion and the inhibition of mitochondrial fission guide the different fates of the heart (82). MFN2 upregulation, besides DRP1 downregulation, maintains mitochondrial function through the elimination of excessive mitochondrial fragmentation (83). Mitochondrial fusion promoter, M1 (2 mg/kg), as an intervention in rat ischemia–reperfusion (I/R), reduces infarct size and exerts a beneficial effect toward ischemia (84). This result demonstrated that increased mitochondrial fusion brings about a beneficial impact on myocardial I/R injury.

However, excessive mitochondrial fusion causes serious diseases (85). Point mutation in mitochondrial carrier protein, SLC25A46, promotes the protein's rapid degradation and the stable recruitment of MFN2 and MFN1 complexes to the mitochondria and ultimately leads to over-fusion and the phenotype of cerebellopontine hypoplasia (86). Additionally, excessive mitochondrial fusion results in elevated oxidative stress and abnormal Ca^{2+} homeostasis, which eventually cause arrhythmia, particularly atrial fibrillation (87). Therefore, the balance between mitochondrial fusion and fission plays a vital role in the normal function of the vascular system.

PATHOGENESIS OF VASCULAR DISEASES

Structurally, the normal artery is composed of three layers (88). The inner layer lined by a monolayer of ECs is closely contacted with blood; the middle layer composed of VSMCs is located at the complex extracellular matrix; and the outer layer of arteries is composed of mast cells, nerve endings, and microvessels (89). Direct contact with blood makes ECs especially vulnerable to damages caused by molecules (90). ECs act as ideal protection because they sense alterations in external stimuli and directly respond or transmit signals; EC dysfunction leads to the pathogenesis of almost all types of vascular diseases (91). Despite the low mitochondrial content of ECs, mitochondrial dynamics is a key endothelial homeostasis coordinator under normal conditions (10).

Atherosclerosis is the leading cause of vascular diseases and responsible for almost 50% of all cardiovascular deaths, and the mechanism of atherosclerosis has been well studied. Its pathogenesis comprises respective mechanisms during different disease stages (8). It is initiated through atherosclerotic lesion formation with a phenotype of endothelial dysfunction (92). The endothelium provides the functional link between blood circulation and the vessel wall. Local disturbance to the arterial endothelium leads to cell activation, which promotes the recruitment of circulating immune cells and increases permeability for circulating lipoprotein particles (93). Low-density lipoprotein (LDL), especially in its modified atherogenic form, is the main source of lipids that accumulate in the arterial wall (94). Several studies have confirmed the close association between the mitochondria and the different stages of atherosclerosis (95).

MITOCHONDRIAL DYNAMICS AND VASCULAR DISEASES

Multiple factors are responsible for vascular diseases, including the infiltration, differentiation, and transformation of monocytes to active lipid foam cells, as well as VSMC migration to the intima (96). ROS production in the mitochondria is a key factor in vascular diseases (97).

Mitochondrial dynamics plays an important role in the progression of vascular diseases (**Figure 3**). Mitochondrial fragmentation and FIS1 expression are increased in patients with type 2 diabetes (98). DRP1 and FIS1 accumulate in human aortic ECs after high glucose treatment (99). Alterations in mitochondrial dynamics are correlated with the production of mitochondrial ROS, which affects the pathogenesis of vascular diseases (100). FIS1 and DRP1 inhibition can block the production of mitochondrial ROS and mitochondrial network; hence, mitochondrial fission has a vital role in vascular diseases (37).

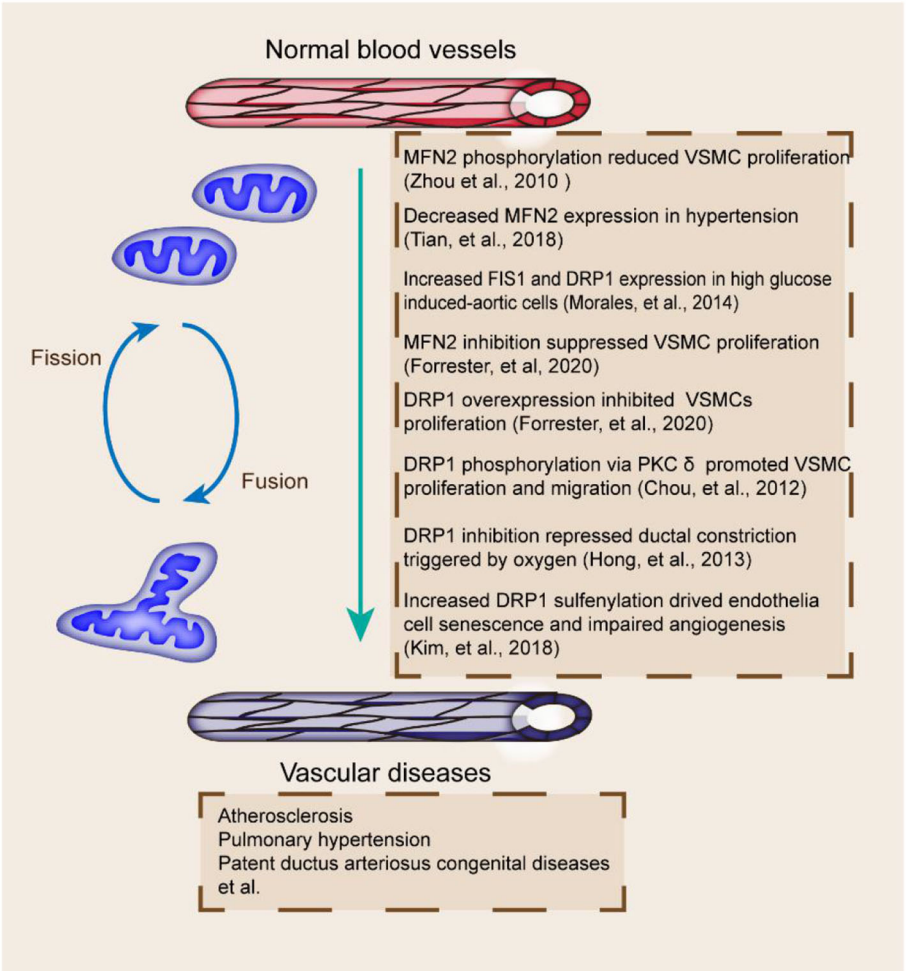

FIGURE 3 | Mitochondrial fusion and fission proteins and vascular diseases. Fission and fusion imbalances are related to multiple vascular abnormalities, including MFN2 decrease and PTM, DRP1 inhibition and phosphorylation, and dysregulated FIS1 and DRP1 (70, 99, 104, 106, 114, 118, 122). The effects of proteins involved in the pathogenesis of vascular diseases are included.

TABLE 2 | Role of mitochondrial dynamics protein in vascular diseases.

Mediator	Cellular phenotype	Vascular disease involving abnormalities of mitochondrial dynamics
Fusion mediators		
Mitofusin-1	VSMC proliferation and migration	Atherosclerosis
Mitofusin-2	VSMC proliferation and migration, proliferation of pulmonary artery smooth muscle cells,	Pulmonary arterial hypertension, arterial restenosis, Atherosclerosis, arterial restenosis
Optic atrophy 1		Hypertension
Fission mediator		
DRP1	VSMC proliferation, phenotypic alterations of VSMCs, apoptosis	Patent ductus arteriosus, pulmonary arterial hypertension, Atherosclerosis,
FIS1	Increased FIS1 in Endothelial dysfunction,	

The coordination of mitochondrial fusion and fission is essential for the maintenance of mitochondrial quantity and quality. Mitochondrial fragmentation occurs in vascular diseases (**Table 2**). Functional ductus arteriosus closure, initially induced by oxygen-dependent vasoconstriction shortly after birth, is dependent on mitochondrial fission (97). DRP1 perturbation is associated with endothelial dysfunction (101). DRP1-mediated mitochondrial fission exerts a critical function in the acute constriction of the ductus arteriosus to O^2 and participates in the subsequent anatomic closure of the ductus arteriosus (102). Mitochondrial fission also seems indispensable for angiogenesis in ECs (103). The loss of protein disulfide isomerase active 1 in ECs induces mitochondrial fragmentation and mitochondrial ROS elevation by increasing Cys644 sulfenylation and DRP1

activity, which impair endothelium-dependent vasorelaxation and angiogenesis (104). DRP1 depletion in mice also leads to defective efferocytosis and has pathologic consequences in the thymus after dexamethasone treatment and in the advanced atherosclerotic lesions of fat-fed LDLR$^{-/-}$ mice (105). DRP1 overexpression or MFN2 inhibition also leads to endothelial dysfunction and the inhibition of VSMC proliferation (106). The decreased expression of MFN1 and MFN2 promotes atherosclerosis in animal models (107).

The functions of MFN1 and MFN2 in ECs have also been addressed (108). Interestingly, the expression of MFNs could be stimulated in ECs when exposed to the angiogenic mitogen, vascular endothelial growth factor (VEGF) (109). The knockdown of MFN1 and MFN2 prevents the endothelial migration and differentiation induced by VEGF (110). Additionally, the diverse roles of MFNs in ECs were measured (111). MFN2 inhibition exclusively attenuates the production of basal and stress-induced ROS (96). MFN1 ablation particularly blocks VEGF signal transduction and suppresses NO production (23). Interestingly, the role of MFNs in vascular pathology is tightly related to metabolic stress (112).

Mitochondrial fission is indispensable for VSMC proliferation and migration, as well as pathophysiological processes, such as the premature closure of open arterial ducts and pulmonary hypertension (113). On the occasion of oxidative stress and angiotensin II stimulation, activated protein kinase C δ phosphorylates DRP1, which leads to mitochondrial fission and ROS-stimulated VSMC proliferation and migration (114). Therefore, the pharmacological inhibition of DRP1 could be used as a therapeutic target.

Emerging evidence implied that alteration in mitochondrial dynamics is accompanied by acute I/R. Several researches have observed that reduced OPA1 and MFN2 and increased DRP1 in cardiomyocytes simulate I/R. I/R stimulation in HL-1 cells induces mitochondrial fission through DRP1; the transfection of the fusion protein or DRP1 dominate-negative mutant protects from I/R injury (115). Moreover, OPA1 mild overexpression transgenic mice are resistant to muscular atrophy and I/R damage in the heart and brain. In spite of the well-known impact of mitochondrial fission and fusion balance on cardiac I/R injury, no study has shown a direct indication of their potential role in ischemic myopathy in peripheral artery disease.

Mitochondrial fusion and fission are also implicated in the abdominal aortic aneurysm (AAA). Angiotensin II stimulation (one of the main methods to induce AAA) in cultured rat aortic VSMCs induces mitochondrial fission. DRP1 expression was enhanced in human AAA samples compared with age-matched healthy controls (116). Furthermore, DRP1 inhibition protects from AAA development, as assessed by the diameters of the abdominal aorta as well as histological observation. Protection against AAA by DRP1 inhibition is accompanied by reduced stress response and senescence. Therefore, DRP1-mediated mitochondrial fission potentially stimulates the proinflammatory phenotypic alterations of VSMCs and contributes to the pathogenesis of AAA development.

As an impeditive vascular disease, pulmonary arterial hypertension is induced by several factors, including disordered oxygen sensing and dysregulated mitochondrial dynamics in pulmonary artery smooth muscle cells (117). Pulmonary arterial hypertension is believed to be contributed by excessive cell proliferation and impaired apoptosis accompanied by vasoconstriction, inflammation, and thrombosis (92). Pulmonary arterial hypertension is accompanied by reduced MFN2 and excessive DRP1 caused by increased hypoxia inducible factor 1 alpha (HIF-1α) activation and decreased PGC-1α activity (118). MFN2 mediates the proliferation of pulmonary artery smooth muscle cells in hypoxic pulmonary hypertension via the PI3K/Akt pathway (119). HIF-1α activation induces DRP1-dependent mitochondrial fission and an imbalance in fusion and fission in normal pulmonary artery smooth muscle cells (120). The decrease in MFN2 in pulmonary arterial hypertension leads to mitochondrial fragmentation and proliferation (121).

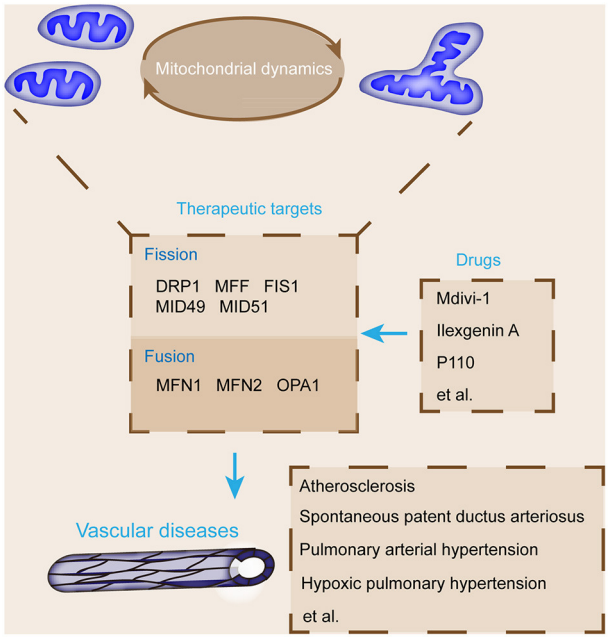

FIGURE 4 | Summary of key mitochondrial dynamic regulatory proteins and major pharmacological agents that target these proteins for the treatment of vascular diseases. The targeting agents of mitochondrial fusion and fission proteins, such as DRP1 and MFN1, protect from vascular diseases, including pulmonary arterial hypertension, atherosclerosis, and ductus arteriosus closure.

DRP1 inhibition represses the ductal constriction triggered by oxygen (122). Oxygen induces the PTM of DRP1 mediated by cyclin B1-CDK1 and CamK to trigger mitochondrial fission (123). Although the continuous inhibition of DRP1 impedes structural closure in an *in vitro* model of human open ductus arteriosus, the previous study still has not elucidated whether damaged mitochondria result in spontaneous patent ductus arteriosus (122).

MiRNA expression alteration contributes to ischemic heart disease by regulating the expression of various key mitochondrial elements involved in cell survival and death. MiR-762 and miR-210 are elevated whereas miR-1 is downregulated in myocardial

infarction. miR-762 knockdown alleviates myocardial I/R injury in mice. The upregulation of miR-15/16 and miR-195 modulate cardiomyocyte survival and myocardial infarction by inhibiting ATP levels and inducing mitochondrial fusion. In addition, miR-15 inhibition protects against I/R injury *in vivo* by targeting pyruvate dehydrogenase kinase 4 and serum/glucocorticoid-regulated kinase 1, which are responsible for mitochondrial function and apoptosis, respectively (124). miRNAs also regulate foam cell formation and subsequent plaque formation. miR-302a suppresses foam cell formation, which would aggravate atheromatic plaque by increasing the activity of ABCA1, which induces the efflux of cholesterol out of macrophages.

MITOCHONDRIAL DYNAMIC REGULATORY PROTEINS AS THERAPEUTIC TARGETS

Supporting materials relate mitochondrial fusion and fission to vascular diseases; emerging studies elucidated the protective effects of mitochondrial fusion and fission modulators on vascular diseases (**Figure 3**) (125). The pharmacological inhibition of DRP1 relieves plaque formation and lessens the accumulation of macrophages in the plaques of the ApoE$^{-/-}$ mouse model of carotid artery injury induced with wire (126). DRP1 seems to be a promising novel therapeutic target for atherosclerosis (106). As a selective cell-permeable inhibitor of mitochondrial division, Mdivi-1 treatment can dramatically reduce atherosclerotic lesion formation in streptozotocin-induced diabetic ApoE$^{-/-}$ mice (127). Mdivi-1 inhibits VSMC proliferation and migration through the attenuation of ROS production and DRP1 phosphorylation (128). Moreover, the anti-proliferation effect of Mdivi-1 is dependent on G2/M cell cycle arrest and independent on cyclin B1/CDK1-mediated DRP1 phosphorylation in arterial smooth muscle cells (118). Another example is ilexgenin A, a novel pentacyclic triterpenoid that exerts anti-atherosclerotic activity to reduce atherosclerosis in apolipoprotein E-deficient mice. Ilexgenin A hinders mitochondrial fission and induces DRP1 degradation dependent on Nrf2-induced proteasome subunit beta 5 in ECs, which contribute to the restraint of mitochondrial fission and thus relieve endothelial dysfunction (129). These findings provide the theoretical basis for the future development of ilexgenin A as a potential agent for atherosclerosis treatment. Mdivi-1 or congeners could also be used to maintain ductus arteriosus patency in infants awaiting congenital heart surgery (120). In addition, Mdivi-1 administration facilitates premature senescence and destroys the angiogenic function of human umbilical cord vein ECs by promoting the production of mitochondrial ROS and reducing autophagy flux (78). Therefore, DRP1 may be a promising therapeutic target for vascular repair (**Figure 4**).

CONCLUDING REMARKS

Mitochondrial dynamics is associated with the pathogenesis of various vascular diseases and provides potential therapeutic targets (12, 56, 97, 98). Further identification prior to trial on potential therapeutic agents related to mitochondrial dynamics is indispensable to determine proper molecular targets and definitions and confirm the optimal and effective doses for mitochondrial fusion and fission modulators (130, 131). Extra modulators for mitochondrial fusion and fission are required (121, 132). For example, a recently designed inhibitor, P110, can inhibit DRP1 activation and fission by blocking the interaction between DRP1 and FIS1 (133).

In spite of the development of pharmacological agents that target fusion and fission for the prevention and treatment of vascular diseases, several obstacles remain to be solved to achieve this goal (87, 103, 104). First, the therapeutic agent needs to have specificity to target the organ and ascertain the duration time (134). Second, mitochondrial fusion and fission are vital for the proper functioning of the mitochondria and normal cells; hence, the manipulation of fusion and fission might have detrimental effects on normal cells. Besides, the application of such therapeutic agents is limited to temporary acute conditions rather than chronic conditions. Moreover, off-target effects should also be minimized. The off-target effects of these pharmacological agents are often caused by the recognition of the binding sites of the drug by other biomacromolecules, including receptors, enzymes, ion channels, transporters, and genes. This occurrence is still an important issue in the study of vascular related inhibitors.

In addition to energy metabolism, the mitochondria have multidimensional influence on cells and the vascular system. For example, the regulation of mitochondrial calcium homeostasis and mitophagy can affect vascular development and functional maintenance, but related molecular mechanisms still need further theoretical support (71, 105, 106). Whether mitochondrial homeostasis can cooperate with other mitochondrial functions to jointly affect vascular development and disease, as well as how key proteins play roles in this dynamic interaction process, needs further study. Mitochondrial dynamic regulatory proteins, such as FIS1, have a variety of functions. Their effects on vascular function still need to be studied in depth if these proteins will be used as therapeutic targets for vascular diseases.

AUTHOR CONTRIBUTIONS

YY and YL conceptualized, wrote the manuscript, and created Figures. YL, XC, and K-DR contributed to the writing of the manuscript. YY, XC, and YL reviewed and modified the manuscript. All authors approved the final version of the manuscript.

FUNDING

This work was supported by the National Natural Science Foundation of China (No. 31900502), the Henan Medical Science and Technology Joint Building Program (No. LHGJ20190236), and Key scientific Research project of Henan Universities (No. 21A310027).

REFERENCES

1. Hammam N, Becher H, Andersen J, Manns PJ, Whittaker JL, Pritchard L. Early indicators of cardiovascular disease are evident in children and adolescents with cerebral palsy. *Disabil Health J.* (2021) 14:101112. doi: 10.1016/j.dhjo.2021.101112
2. Akawi N, Checa A, Antonopoulos AS, Akoumianakis I, Daskalaki E, Kotanidis CP, et al. Fat-secreted ceramides regulate vascular redox state and influence outcomes in patients with cardiovascular disease. *J Am Coll Cardiol.* (2021) 77:2494–513. doi: 10.1016/j.jacc.2021.03.314
3. Mitchell ME, Sidawy AN. The pathophysiology of atherosclerosis. *Semin Vasc Surg.* (1998) 11:134–41.
4. Deng HT, Liu HL, Zhai BB, Zhang K, Xu GC, Peng XM, et al. Vascular endothelial growth factor suppresses TNFSF15 production in endothelial cells by stimulating miR-31 and miR-20a expression via activation of Akt and Erk signals. *FEBS Open Bio.* (2017) 7:108–17. doi: 10.1002/2211-5463.12171
5. Kim J, Kang Y, Kojima Y, Lighthouse JK, Hu X, Aldred MA, et al. An endothelial apelin-FGF link mediated by miR-424 and miR-503 is disrupted in pulmonary arterial hypertension. *Nat Med.* (2013) 19:74–82. doi: 10.1038/nm.3040
6. Gimbrone MA Jr, Garcia-Cardena G. Endothelial cell dysfunction and the pathobiology of atherosclerosis. *Circ Res.* (2016) 118:620–36. doi: 10.1161/CIRCRESAHA.115.306301
7. Fei Y, Hou J, Xuan W, Zhang C, Meng X. The relationship of plasma miR-503 and coronary collateral circulation in patients with coronary artery disease. *Life Sci.* (2018) 207:145–51. doi: 10.1016/j.lfs.2018.06.001
8. Bi R, Ding F, He Y, Jiang L, Jiang Z, Mei J, et al. miR-503 inhibits platelet-derived growth factor-induced human aortic vascular smooth muscle cell proliferation and migration through targeting the insulin receptor. *Biomed Pharmacother.* (2016) 84:1711–6. doi: 10.1016/j.biopha.2016.10.081
9. Ogita H, Kunimoto S, Kamioka Y, Sawa H, Masuda M, Mochizuki N. EphA4-mediated Rho activation via Vsm-RhoGEF expressed specifically in vascular smooth muscle cells. *Circ Res.* (2003) 93:23–31. doi: 10.1161/01.RES.0000079310.81429.C8
10. Tang X, Luo YX, Chen HZ, Liu DP. Mitochondria, endothelial cell function, and vascular diseases. *Front Physiol.* (2014) 5:175. doi: 10.3389/fphys.2014.00175
11. Kluge MA, Fetterman JL, Vita JA. Mitochondria and endothelial function. *Circ Res.* (2013) 112:1171–88. doi: 10.1161/CIRCRESAHA.111.300233
12. Park SY, Gifford JR, Andtbacka RH, Trinity JD, Hyngstrom JR, Garten RS, et al. Cardiac, skeletal, and smooth muscle mitochondrial respiration: are all mitochondria created equal? *Am J Physiol Heart Circ Physiol.* (2014) 307:H346–352. doi: 10.1152/ajpheart.00227.2014
13. Moulis M, Grousset E, Faccini J, Richetin K, Thomas G, Vindis C. The multifunctional sorting protein PACS-2 controls mitophagosome formation in human vascular smooth muscle cells through mitochondria-ER contact sites. *Cells.* (2019) 8:638. doi: 10.3390/cells8060638
14. Luan Y, Luan Y, Yuan RX, Feng Q, Chen X, Yang Y. Structure and Function of Mitochondria-Associated Endoplasmic Reticulum Membranes (MAMs) and Their Role in Cardiovascular Diseases. *Oxid Med Cell Longev.* (2021) 2021:4578809. doi: 10.1155/2021/4578809
15. Zhunina OA, Yabbarov NG, Grechko AV, Starodubova AV, Ivanova E, Nikiforov NG, et al. The role of mitochondrial dysfunction in vascular disease, tumorigenesis, and diabetes. *Front Mol Biosci.* (2021) 8:671908. doi: 10.3389/fmolb.2021.671908
16. Daiber A, Steven S, Vujacic-Mirski K, Kalinovic S, Oelze M, Di Lisa F, et al. Regulation of vascular function and inflammation via cross talk of reactive oxygen and nitrogen species from mitochondria or NADPH oxidase-implications for diabetes progression. *Int J Mol Sci.* (2020) 21:3405. doi: 10.3390/ijms21103405
17. Fukuda N, Yago N. Population dynamics of mitochondria. I A model for the role to ACTH in the degradation of adrenocortical mitochondria. *J Theor Biol.* (1974) 46:21–30. doi: 10.1016/0022-5193(74)90138-6
18. Bereiter-Hahn J, Voth M. Dynamics of mitochondria in living cells: shape changes, dislocations, fusion, and fission of mitochondria. *Microsc Res Tech.* (1994) 27:198–219. doi: 10.1002/jemt.1070270303
19. Liu X, Hajnoczky G. Altered fusion dynamics underlie unique morphological changes in mitochondria during hypoxia-reoxygenation stress. *Cell Death Differ.* (2011) 18:1561–72. doi: 10.1038/cdd.2011.13
20. Polyakov VY, Soukhomlinova MY, Fais D. Fusion, fragmentation, and fission of mitochondria. *Biochemistry (Mosc).* (2003) 68:838–49. doi: 10.1023/A:1025738712958
21. Vasquez-Trincado C, Garcia-Carvajal I, Pennanen C, Parra V, Hill JA, Rothermel BA, et al. Mitochondrial dynamics, mitophagy and cardiovascular disease. *J Physiol.* (2016) 594:509–25. doi: 10.1113/JP271301
22. Hunter AM, Kottachchi D, Lewis J, Duckett CS, Korneluk RG, Liston P, et al. novel ubiquitin fusion system bypasses the mitochondria and generates biologically active Smac/DIABLO. *J Biol Chem.* (2003) 278:7494–9. doi: 10.1074/jbc.C200695200
23. Lee JY, Kapur M, Li M, Choi MC, Choi S, Kim HJ, et al. MFN1 deacetylation activates adaptive mitochondrial fusion and protects metabolically challenged mitochondria. *J Cell Sci.* (2014) 127(Pt 22):4954–63. doi: 10.1242/jcs.157321
24. Bockler S, Chelius X, Hock N, Klecker T, Wolter M, Weiss M, et al. Fusion, fission, and transport control asymmetric inheritance of mitochondria and protein aggregates. *J Cell Biol.* (2017) 216:2481–98. doi: 10.1083/jcb.201611197
25. Arribat Y, Broskey NT, Greggio C, Boutant M, Conde Alonso S, Kulkarni SS, et al. Distinct patterns of skeletal muscle mitochondria fusion, fission and mitophagy upon duration of exercise training. *Acta Physiol (Oxf).* (2019) 225:e13179. doi: 10.1111/apha.13179
26. Ciarlo L, Vona R, Manganelli V, Gambardella L, Raggi C, Marconi M, et al. Recruitment of mitofusin 2 into "lipid rafts" drives mitochondria fusion induced by Mdivi-1. *Oncotarget.* (2018) 9:18869–84. doi: 10.18632/oncotarget.24792
27. Westermann B. Mitochondrial dynamics in model organisms: what yeasts, worms and flies have taught us about fusion and fission of mitochondria. *Semin Cell Dev Biol.* (2010) 21:542–9. doi: 10.1016/j.semcdb.2009.12.003
28. Varadi A, Johnson-Cadwell LI, Cirulli V, Yoon Y, Allan VJ, Rutter GA. Cytoplasmic dynein regulates the subcellular distribution of mitochondria by controlling the recruitment of the fission factor dynamin-related protein-1. *J Cell Sci.* (2004) 117(Pt 19):4389–400. doi: 10.1242/jcs.01299
29. Santel A, Frank S. Shaping mitochondria: The complex posttranslational regulation of the mitochondrial fission protein DRP1. *IUBMB Life.* (2008) 60:448–55. doi: 10.1002/iub.71
30. Zhou BH, Wei SS, Jia LS, Zhang Y, Miao CY, Wang HW. Drp1/Mff signaling pathway is involved in fluoride-induced abnormal fission of hepatocyte mitochondria in mice. *Sci Total Environ.* (2020) 725:138192. doi: 10.1016/j.scitotenv.2020.138192
31. Yoon YS, Yoon DS, Lim IK, Yoon SH, Chung HY, Rojo M, et al. Formation of elongated giant mitochondria in DFO-induced cellular senescence: involvement of enhanced fusion process through modulation of Fis1. *J Cell Physiol.* (2006) 209:468–80. doi: 10.1002/jcp.20753
32. Scarpelli PH, Tessarin-Almeida G, Vicoso KL, Lima WR, Borges-Pereira L, Meissner KA, et al. Melatonin activates FIS1, DYN1, and DYN2 Plasmodium falciparum related-genes for mitochondria fission: mitoemerald-GFP as a tool to visualize mitochondria structure. *J Pineal Res.* (2019) 66:e12484. doi: 10.1111/jpi.12484
33. Ko HJ, Tsai CY, Chiou SJ, Lai YL, Wang CH, Cheng JT, et al. The phosphorylation status of Drp1-Ser637 by PKA in mitochondrial fission modulates mitophagy via PINK1/Parkin to exert multipolar spindles assembly during mitosis. *Biomolecules.* (2021) 11:424. doi: 10.3390/biom11030424
34. Chen C, Huang J, Shen J, Bai Q. Quercetin improves endothelial insulin sensitivity in obese mice by inhibiting Drp1 phosphorylation at serine 616 and mitochondrial fragmentation. *Acta Biochim Biophys Sin (Shanghai).* (2019) 51:1250–7. doi: 10.1093/abbs/gmz127
35. Bo T, Yamamori T, Suzuki M, Sakai Y, Yamamoto K, Inanami O. Calmodulin-dependent protein kinase II (CaMKII) mediates radiation-induced mitochondrial fission by regulating the phosphorylation of dynamin-related protein 1 (Drp1) at serine 616. *Biochem Biophys Res Commun.* (2018) 495:1601–7. doi: 10.1016/j.bbrc.2017.12.012
36. Lee Y, Kwon I, Jang Y, Song W, Cosio-Lima LM, Roltsch MH. Potential signaling pathways of acute endurance exercise-induced cardiac autophagy

and mitophagy and its possible role in cardioprotection. *J Physiol Sci.* (2017) 67:639–54. doi: 10.1007/s12576-017-0555-7
37. MacVicar TD, Lane JD. Impaired OMA1-dependent cleavage of OPA1 and reduced DRP1 fission activity combine to prevent mitophagy in cells that are dependent on oxidative phosphorylation. *J Cell Sci.* (2014) 127(Pt 10):2313–25. doi: 10.1242/jcs.144337
38. Hu Q, Zhang H, Gutierrez Cortes N, Wu D, Wang P, Zhang J, et al. Increased Drp1 acetylation by lipid overload induces cardiomyocyte death and heart dysfunction. *Circ Res.* (2020) 126:456–70. doi: 10.1161/CIRCRESAHA.119.315252
39. Adaniya SM. J OU, Cypress MW, Kusakari Y, Jhun BS. Posttranslational modifications of mitochondrial fission and fusion proteins in cardiac physiology and pathophysiology. *Am J Physiol Cell Physiol.* (2019) 316:C583–604. doi: 10.1152/ajpcell.00523.2018
40. Chen Y, Dorn GW 2nd. PINK1-phosphorylated mitofusin 2 is a parkin receptor for culling damaged mitochondria. *Science.* (2013) 340:471–5. doi: 10.1126/science.1231031
41. Gegg ME, Cooper JM, Chau KY, Rojo M, Schapira AH, Taanman JW. Mitofusin 1 and mitofusin 2 are ubiquitinated in a PINK1/parkin-dependent manner upon induction of mitophagy. *Hum Mol Genet.* (2010) 19:4861–70. doi: 10.1093/hmg/ddq419
42. Song R, Hu XQ, Zhang L. Mitochondrial MiRNA in cardiovascular function and disease. *Cells.* (2019) 8:1475. doi: 10.3390/cells8121475
43. Li J, Donath S, Li Y, Qin D, Prabhakar BS Li P. miR-30 regulates mitochondrial fission through targeting p53 and the dynamin-related protein-1 pathway. *PLoS Genet.* (2010) 6:e1000795. doi: 10.1371/journal.pgen.1000795
44. Zhloba AA, Subbotina TF, Alekseevskaia ES, Moiseeva OM, Gavriluk ND, Irtuga OB. The metabolic and protein markers of dysfunction of mitochondria in patients with cardio-vascular diseases. *Klin Lab Diagn.* (2015) 60:35–41. doi: 10.18821/0860-2084-2015-60-7-35-41
45. Forte M, Schirone L, Ameri P, Basso C, Catalucci D, Modica J, et al. The role of mitochondrial dynamics in cardiovascular diseases. *Br J Pharmacol.* (2021) 178:2060–76. doi: 10.1111/bph.15068
46. Han XJ, Lu YF Li SA, Kaitsuka T, Sato Y, Tomizawa K, Nairn AC, et al. CaM kinase I alpha-induced phosphorylation of Drp1 regulates mitochondrial morphology. *J Cell Biol.* (2008) 182:573–85. doi: 10.1083/jcb.200802164
47. Luo J, Shen S. Lipoic acid alleviates schistosomiasis-induced liver fibrosis by upregulating Drp1 phosphorylation. *Acta Trop.* (2020) 206:105449. doi: 10.1016/j.actatropica.2020.105449
48. Arduino DM, Esteves AR, Cardoso SM. Mitochondrial fusion/fission, transport and autophagy in Parkinson's disease: when mitochondria get nasty. *Parkinsons Dis.* (2011) 2011:767230. doi: 10.4061/2011/767230
49. Karbowski M. Mitochondria on guard: role of mitochondrial fusion and fission in the regulation of apoptosis. *Adv Exp Med Biol.* (2010) 687:131–42. doi: 10.1007/978-1-4419-6706-0_8
50. Grohm J, Plesnila N, Culmsee C. Bid mediates fission, membrane permeabilization and peri-nuclear accumulation of mitochondria as a prerequisite for oxidative neuronal cell death. *Brain Behav Immun.* (2010) 24:831–8. doi: 10.1016/j.bbi.2009.11.015
51. Li D, Yang S, Xing Y, Pan L, Zhao R, Zhao Y, et al. Novel insights and current evidence for mechanisms of atherosclerosis: mitochondrial dynamics as a potential therapeutic target. *Front Cell Dev Biol.* (2021) 9:673839. doi: 10.3389/fcell.2021.673839
52. Baumann K. Organelle dynamics: fusing for stability. *Nat Rev Mol Cell Biol.* (2010) 11:391. doi: 10.1038/nrm2910
53. Masi S, Virdis A. Targeting mitochondria in age-related vascular changes: a new arrow to the bow of antioxidant treatment? *Hypertension.* (2018) 71:1023–5. doi: 10.1161/HYPERTENSIONAHA.118.10869
54. Pearson JD. Normal endothelial cell function. *Lupus.* (2000) 9:183–8. doi: 10.1191/096120300678828299
55. Wang X, Wang Y, Zhang L, Zhang D, Bai L, Kong W, et al. L-Cystathionine protects against homocysteine-induced mitochondria-dependent apoptosis of vascular endothelial cells. *Oxid Med Cell Longev.* (2019) 2019:1253289. doi: 10.1155/2019/1253289
56. Luan Y, Feng Q, Chen X, Ren KD, Yang Y. Emerging role of mitophagy in the heart: therapeutic potentials to modulate mitophagy in cardiac diseases. *Oxid Med Cell Longev.* (2021) 2021:13. doi: 10.1155/2021/3259963
57. Flammer AJ, Anderson T, Celermajer DS, Creager MA, Deanfield J, Ganz P, et al. The assessment of endothelial function: from research into clinical practice. *Circulation.* (2012) 126:753–67. doi: 10.1161/CIRCULATIONAHA.112.093245
58. Forte M, Stanzione R, Cotugno M, Bianchi F, Marchitti S, Rubattu S. Vascular ageing in hypertension: focus on mitochondria. *Mech Ageing Dev.* (2020) 189:111267. doi: 10.1016/j.mad.2020.111267
59. Markin AM, Khotina VA, Zabudskaya XG, Bogatyreva AI, Starodubova AV, Ivanova E, et al. Disturbance of mitochondrial dynamics and mitochondrial therapies in atherosclerosis. *Life (Basel).* (2021) 11:165. doi: 10.3390/life11020165
60. Caja S, Enriquez JA. Mitochondria in endothelial cells: sensors and integrators of environmental cues. *Redox Biol.* (2017) 12:821–7. doi: 10.1016/j.redox.2017.04.021
61. Shenouda SM, Widlansky ME, Chen K, Xu G, Holbrook M, Tabit CE, et al. Altered mitochondrial dynamics contributes to endothelial dysfunction in diabetes mellitus. *Circulation.* (2011) 124:444–53. doi: 10.1161/CIRCULATIONAHA.110.014506
62. Badran A, Nasser SA, Mesmar J, El-Yazbi AF, Bitto A, Fardoun MM, et al. Reactive oxygen species: modulators of phenotypic switch of vascular smooth muscle cells. *Int J Mol Sci.* (2020) 21:8764. doi: 10.3390/ijms21228764
63. Maddaluno M, Grassia G, Di Lauro MV, Parisi A, Maione F, Cicala C, et al. Bindarit inhibits human coronary artery smooth muscle cell proliferation, migration and phenotypic switching. *PLoS ONE.* (2012) 7:e47464. doi: 10.1371/journal.pone.0047464
64. Quintero M, Colombo SL, Godfrey A, Moncada S. Mitochondria as signaling organelles in the vascular endothelium. *Proc Natl Acad Sci U S A.* (2006) 103:5379–84. doi: 10.1073/pnas.0601026103
65. Lopes RA, Neves KB, Pestana CR, Queiroz AL, Zanotto CZ, Chignalia AZ, et al. Testosterone induces apoptosis in vascular smooth muscle cells via extrinsic apoptotic pathway with mitochondria-generated reactive oxygen species involvement. *Am J Physiol Heart Circ Physiol.* (2014) 306:H1485–1494. doi: 10.1152/ajpheart.00809.2013
66. Busija DW, Rutkai I, Dutta S, Katakam PV. Role of mitochondria in cerebral vascular function: energy production, cellular protection, and regulation of vascular tone. *Compr Physiol.* (2016) 6:1529–48. doi: 10.1002/cphy.c150051
67. Brock M, Samillan VJ, Trenkmann M, Schwarzwald C, Ulrich S, Gay RE, et al. AntagomiR directed against miR-20a restores functional BMPR2 signalling and prevents vascular remodelling in hypoxia-induced pulmonary hypertension. *Eur Heart J.* (2014) 35:3203–11. doi: 10.1093/eurheartj/ehs060
68. Zhang X, Chen W, Li J, Qi S, Hong S, Wang Y, et al. Involvement of mitochondrial fission in calcium sensing receptor-mediated vascular smooth muscle cells proliferation during hypertension. *Biochem Biophys Res Commun.* (2018) 495:454–60. doi: 10.1016/j.bbrc.2017.11.048
69. Wang L, Yu T, Lee H, O'Brien DK, Sesaki H, Yoon Y. Decreasing mitochondrial fission diminishes vascular smooth muscle cell migration and ameliorates intimal hyperplasia. *Cardiovasc Res.* (2015) 106:272–83. doi: 10.1093/cvr/cvv005
70. Zhou W, Chen KH, Cao W, Zeng J, Liao H, Zhao L, et al. Mutation of the protein kinase A phosphorylation site influences the anti-proliferative activity of mitofusin 2. *Atherosclerosis.* (2010) 211:216–23. doi: 10.1016/j.atherosclerosis.2010.02.012
71. Ma D, Zheng B, Liu HL, Zhao YB, Liu X, Zhang XH, et al. Klf5 down-regulation induces vascular senescence through eIF5a depletion and mitochondrial fission. *PLoS Biol.* (2020) 18:e3000808. doi: 10.1371/journal.pbio.3000808
72. Yarbro JR, Emmons RS, Pence BD. Macrophage immunometabolism and inflammaging: roles of mitochondrial dysfunction, cellular senescence, CD38, and NAD. *Immunometabolism.* (2020) 2:e200026. doi: 10.20900/immunometab20200026
73. Umezu R, Koga JI, Matoba T, Katsuki S, Wang L, Hasuzawa N, et al. Macrophage (Drp1) dynamin-related protein 1 accelerates intimal thickening after vascular injury. *Arterioscler Thromb Vasc Biol.* (2020) 40:e214–26. doi: 10.1161/ATVBAHA.120.314383
74. Li T, Zheng F, Cheung M, Wang F, Fu C. Fission yeast mitochondria are distributed by dynamic microtubules in a motor-independent manner. *Sci Rep.* (2015) 5:11023. doi: 10.1038/srep11023

75. Di Pietro V, Lazzarino G, Amorini AM, Signoretti S, Hill LJ, Porto E, et al. Fusion or fission: the destiny of mitochondria in traumatic brain injury of different severities. *Sci Rep.* (2017) 7:9189. doi: 10.1038/s41598-017-09587-2
76. Arimura SI. Fission and fusion of plant mitochondria, and genome maintenance. *Plant Physiol.* (2018) 176:152–61. doi: 10.1104/pp.17.01025
77. Chen WR, Zhou YJ, Sha Y, Wu XP, Yang JQ, Liu F. Melatonin attenuates vascular calcification by inhibiting mitochondria fission via an AMPK/Drp1 signalling pathway. *J Cell Mol Med.* (2020) 24:6043–54. doi: 10.1111/jcmm.15157
78. Sharp WW, Fang YH, Han M, Zhang HJ, Hong Z, Banathy A, et al. Dynamin-related protein 1 (Drp1)-mediated diastolic dysfunction in myocardial ischemia-reperfusion injury: therapeutic benefits of Drp1 inhibition to reduce mitochondrial fission. *FASEB J.* (2014) 28:316–26. doi: 10.1096/fj.12-226225
79. Zhang N, Wang S, Li Y, Che L, Zhao Q. A selective inhibitor of Drp1, mdivi-1, acts against cerebral ischemia/reperfusion injury via an anti-apoptotic pathway in rats. *Neurosci Lett.* (2013) 535:104–9. doi: 10.1016/j.neulet.2012.12.049
80. Wu J, Chen H, Qin J, Chen N, Lu S, Jin J, et al. Baicalin improves cardiac outcome and survival by suppressing Drp1-mediated mitochondrial fission after cardiac arrest-induced myocardial damage. *Oxid Med Cell Longev.* (2021) 2021:8865762. doi: 10.1155/2021/8865762
81. Tan DX, Chen XX, Bai TZ, Zhang J, Li ZF. Sevoflurane up-regulates microRNA-204 to ameliorate myocardial ischemia/reperfusion injury in mice by suppressing Cotl1. *Life Sci.* (2020) 259:118162. doi: 10.1016/j.lfs.2020.118162
82. Wang Z, Wang Z, Wang T, Yuan J, Wang X, Zhang Z. Inhibition of miR-34a-5p protected myocardial ischemia reperfusion injury-induced apoptosis and reactive oxygen species accumulation through regulation of Notch Receptor 1 signaling. *Rev Cardiovasc Med.* (2019) 20:187–97. doi: 10.31083/j.rcm.2019.03.545
83. Qin Y, Li A, Liu B, Jiang W, Gao M, Tian X, et al. Mitochondrial fusion mediated by fusion promotion and fission inhibition directs adult mouse heart function toward a different direction. *FASEB J.* (2020) 34:663–75. doi: 10.1096/fj.201901671R
84. Lees JG, Kong AM, Chen YC, Sivakumaran P, Hernandez D, Pebay A, et al. Mitochondrial fusion by M1 promotes embryoid body cardiac differentiation of human pluripotent stem cells. *Stem Cells Int.* (2019) 2019:6380135. doi: 10.1155/2019/6380135
85. Chen L, Chen H. Effect of Mahuang Gancao Ganjiang decoction on fusion and fission of mitochondria and apoptosis of lymphocytes in mice under cold stress. *Evid Based Complement Alternat Med.* (2017) 2017:5132963. doi: 10.1155/2017/5132963
86. Zhang ZQ, Zhang CZ, Shao B, Pang DH, Han GZ, Lin L. Effects of abnormal expression of fusion and fission genes on the morphology and function of lung macrophage mitochondria in SiO2-induced silicosis fibrosis in rats *in vivo*. *Toxicol Lett.* (2019) 312:181–7. doi: 10.1016/j.toxlet.2019.04.029
87. Wang X, Liu X, Chen Y, Wang H, Zhang R, Zhang Q, et al. Calreticulin regulated intrinsic apoptosis through mitochondria-dependent and independent pathways mediated by ER stress in arsenite exposed HT-22 cells. *Chemosphere.* (2020) 251:126466. doi: 10.1016/j.chemosphere.2020.126466
88. Yu E, Mercer J, Bennett M. Mitochondria in vascular disease. *Cardiovasc Res.* (2012) 95:173–82. doi: 10.1093/cvr/cvs111
89. Lo J, Plutzky J. The biology of atherosclerosis: general paradigms and distinct pathogenic mechanisms among HIV-infected patients. *J Infect Dis.* (2012) 205 Suppl 3:S368–374. doi: 10.1093/infdis/jis201
90. Lermant A, Murdoch CE. Cysteine glutathionylation acts as a redox switch in endothelial cells. *Antioxidants (Basel).* (2019) 8:315. doi: 10.3390/antiox8080315
91. Dedkova EN Ji X, Lipsius SL, Blatter LA. Mitochondrial calcium uptake stimulates nitric oxide production in mitochondria of bovine vascular endothelial cells. *Am J Physiol Cell Physiol.* (2004) 286:C406–415. doi: 10.1152/ajpcell.00155.2003
92. Lin CF, Chang YH Yu FC, Tsai CT, Chen CC, Liu HY, Chien LN. Risk of heart failure following drug-eluting stent implantation in patients with non-ST-elevation myocardial infarction. *Atherosclerosis.* (2021) 316:84–9. doi: 10.1016/j.atherosclerosis.2020.10.012
93. Gomibuchi H, Okazaki M, Iwai S, Kumai T, Kobayashi S, Oguchi K. Development of hyperfibrinogenemia in spontaneously hypertensive and hyperlipidemic rats: a potentially useful animal model as a complication of hypertension and hyperlipidemia. *Exp Anim.* (2007) 56:1–10. doi: 10.1538/expanim.56.1
94. Davidson SM, Duchen MR. Endothelial mitochondria: contributing to vascular function and disease. *Circ Res.* (2007) 100:1128–41. doi: 10.1161/01.RES.0000261970.18328.1d
95. Ballinger SW, Patterson C, Knight-Lozano CA, Burow DL, Conklin CA, Hu Z, et al. Mitochondrial integrity and function in atherogenesis. *Circulation.* (2002) 106:544–9. doi: 10.1161/01.CIR.0000023921.93743.89
96. Liu X, Zheng Z, Yu L, Hu J, Li X. Down-regulation of protein phosphatase 2A catalytic subunit involved in mitochondria fission/fusion dynamics imbalance and functional impairment induced by Human tau. *Zhongguo Yi Xue Ke Xue Yuan Xue Bao.* (2020) 42:297–306. doi: 10.3881/j.issn.1000-503X.12163
97. Khraiwesh H, Lopez-Dominguez JA, Lopez-Lluch G, Navas P, de Cabo R, Ramsey JJ, et al. Alterations of ultrastructural and fission/fusion markers in hepatocyte mitochondria from mice following calorie restriction with different dietary fats. *J Gerontol A Biol Sci Med Sci.* (2013) 68:1023–34. doi: 10.1093/gerona/glt006
98. Zheng J, Lu C. Oxidized LDL causes endothelial apoptosis by inhibiting mitochondrial fusion and mitochondria autophagy. *Front Cell Dev Biol.* (2020) 8:600950. doi: 10.3389/fcell.2020.600950
99. Morales PE, Torres G, Sotomayor-Flores C, Pena-Oyarzun D, Rivera-Mejias P, Paredes F, et al. GLP-1 promotes mitochondrial metabolism in vascular smooth muscle cells by enhancing endoplasmic reticulum-mitochondria coupling. *Biochem Biophys Res Commun.* (2014) 446:410–6. doi: 10.1016/j.bbrc.2014.03.004
100. Gbel J, Engelhardt E, Pelzer P, Sakthivelu V, Jahn HM, Jevtic M, et al. Mitochondria-endoplasmic reticulum contacts in reactive astrocytes promote vascular remodeling. *Cell Metab.* (2020) 31:791–808.e798. doi: 10.1016/j.cmet.2020.03.005
101. Li J, Wang Y, Wang Y, Wen X, Ma XN, Chen W, et al. Pharmacological activation of AMPK prevents Drp1-mediated mitochondrial fission and alleviates endoplasmic reticulum stress-associated endothelial dysfunction. *J Mol Cell Cardiol.* (2015) 86:62–74. doi: 10.1016/j.yjmcc.2015.07.010
102. Shang X, Li J, Yu R, Zhu P, Zhang Y, Xu J, et al. Sepsis-related myocardial injury is associated with Mst1 upregulation, mitochondrial dysfunction and the Drp1/F-actin signaling pathway. *J Mol Histol.* (2019) 50:91–103. doi: 10.1007/s10735-018-09809-5
103. She H, Zhu Y, Deng H, Kuang L, Fang H, Zhang Z, et al. Protective effects of dexmedetomidine on the vascular endothelial barrier function by inhibiting mitochondrial fission via ER/mitochondria contact. *Front Cell Dev Biol.* (2021) 9:636327. doi: 10.3389/fcell.2021.636327
104. Kim YM, Youn SW, Sudhahar V, Das A, Chandhri R, Cuervo Grajal H, et al. Redox regulation of mitochondrial fission protein Drp1 by protein disulfide isomerase limits endothelial senescence. *Cell Rep.* (2018) 23:3565–78. doi: 10.1016/j.celrep.2018.05.054
105. Wang Y, Subramanian M, Yurdagul A Jr, Barbosa-Lorenzi VC, Cai B, de Juan-Sanz J, et al. Mitochondrial fission promotes the continued clearance of apoptotic cells by macrophages. *Cell.* (2017) 171:331–345.e322. doi: 10.1016/j.cell.2017.08.041
106. Forrester SJ, Preston KJ, Cooper HA, Boyer MJ, Escoto KM, Poltronetti AJ, et al. Mitochondrial fission mediates endothelial inflammation. *Hypertension.* (2020) 76:267–76. doi: 10.1161/HYPERTENSIONAHA.120.14686
107. de Brito OM, Scorrano L. Mitofusin 2: a mitochondria-shaping protein with signaling roles beyond fusion. *Antioxid Redox Signal.* (2008) 10:621–33. doi: 10.1089/ars.2007.1934
108. Liu X, Liu Z, Hou W, Wang K, Ding W, Chen D, et al. Changes in mitochondria fusion protein-2 hepatic expression in conditions of liver cirrhosis and acute on chronic liver failure. *Zhonghua Gan Zang Bing Za Zhi.* (2014) 22:671–5. doi: 10.3760/cma.j.issn.1007-3418.2014.09.008
109. Garonna E, Botham KM, Birdsey GM, Randi AM, Gonzalez-Perez RR, Wheeler-Jones CP. Vascular endothelial growth factor receptor-2 couples cyclo-oxygenase-2 with pro-angiogenic actions of leptin on human endothelial cells. *PLoS ONE.* (2011) 6:e18823. doi: 10.1371/journal.pone.0018823

110. Lugus JJ, Ngoh GA, Bachschmid MM, Walsh K. Mitofusins are required for angiogenic function and modulate different signaling pathways in cultured endothelial cells. *J Mol Cell Cardiol*. (2011) 51:885–93. doi: 10.1016/j.yjmcc.2011.07.023
111. Trevisan T, Pendin D, Montagna A, Bova S, Ghelli AM, Daga A. Manipulation of mitochondria dynamics reveals separate roles for form and function in mitochondria distribution. *Cell Rep*. (2018) 23:1742–53. doi: 10.1016/j.celrep.2018.04.017
112. Chandhok G, Lazarou M, Neumann B. Structure, function, and regulation of mitofusin-2 in health and disease. *Biol Rev Camb Philos Soc*. (2018) 93:933–49. doi: 10.1111/brv.12378
113. Zeng JW, Chen BY, Lv XF, Sun L, Zeng XL, Zheng HQ, et al. Transmembrane member 16A participates in hydrogen peroxide-induced apoptosis by facilitating mitochondria-dependent pathway in vascular smooth muscle cells. *Br J Pharmacol*. (2018) 175:3669–84. doi: 10.1111/bph.14432
114. Chou CH, Lin CC, Yang MC, Wei CC, Liao HD, Lin RC, et al. GSK3beta-mediated Drp1 phosphorylation induced elongated mitochondrial morphology against oxidative stress. *PLoS ONE*. (2012) 7:e49112. doi: 10.1371/journal.pone.0049112
115. Jin JY, Wei XX, Zhi XL, Wang XH, Meng D. Drp1-dependent mitochondrial fission in cardiovascular disease. *Acta Pharmacol Sin*. (2021) 42:655–64. doi: 10.1038/s41401-020-00518-y
116. Wang X, Li S, Liu L, Jian Z, Cui T, Yang Y, et al. Role of the aryl hydrocarbon receptor signaling pathway in promoting mitochondrial biogenesis against oxidative damage in human melanocytes. *J Dermatol Sci*. (2019) 96:33–41. doi: 10.1016/j.jdermsci.2019.09.001
117. Chan DC. Mitochondrial dynamics and its involvement in disease. *Annu Rev Pathol*. (2020) 15:235–59. doi: 10.1146/annurev-pathmechdis-012419-032711
118. Tian L, Potus F, Wu D, Dasgupta A, Chen KH, Mewburn J, et al. Increased Drp1-mediated mitochondrial fission promotes proliferation and collagen production by right ventricular fibroblasts in experimental pulmonary arterial hypertension. *Front Physiol*. (2018) 9:828. doi: 10.3389/fphys.2018.00828
119. Li D, Li X, Guan Y, Guo X. Mitofusin-2-mediated tethering of mitochondria and endoplasmic reticulum promotes cell cycle arrest of vascular smooth muscle cells in G0/G1 phase. *Acta Biochim Biophys Sin (Shanghai)*. (2015) 47:441–50. doi: 10.1093/abbs/gmv035
120. Feng W, Wang J, Yan X, Zhang Q, Chai L, Wang Q, et al. ERK/Drp1-dependent mitochondrial fission contributes to HMGB1-induced autophagy in pulmonary arterial hypertension. *Cell Prolif*. (2021) 54:e13048. doi: 10.1111/cpr.13048
121. Ryan J, Dasgupta A, Huston J, Chen KH, Archer SL. Mitochondrial dynamics in pulmonary arterial hypertension. *J Mol Med (Berl)*. (2015) 93:229–42. doi: 10.1007/s00109-015-1263-5
122. Hong Z, Kutty S, Toth PT, Marsboom G, Hammel JM, Chamberlain C, et al. Role of dynamin-related protein 1 (Drp1)-mediated mitochondrial fission in oxygen sensing and constriction of the ductus arteriosus. *Circ Res*. (2013) 112:802–15. doi: 10.1161/CIRCRESAHA.111.300285
123. Xu S, Wang P, Zhang H, Gong G, Gutierrez Cortes N, Zhu W, et al. CaMKII induces permeability transition through Drp1 phosphorylation during chronic beta-AR stimulation. *Nat Commun*. (2016) 7:13189. doi: 10.1038/ncomms13189
124. Hullinger TG, Montgomery RL, Seto AG, Dickinson BA, Semus HM, Lynch JM, et al. Inhibition of miR-15 protects against cardiac ischemic injury. *Circ Res*. (2012) 110:71–81. doi: 10.1161/CIRCRESAHA.111.244442
125. Ong SB, Kalkhoran SB, Cabrera-Fuentes HA, Hausenloy DJ. Mitochondrial fusion and fission proteins as novel therapeutic targets for treating cardiovascular disease. *Eur J Pharmacol*. (2015) 763(Pt A):104–14. doi: 10.1016/j.ejphar.2015.04.056
126. Fernandez-Calle R, Vicente-Rodriguez M, Pastor M, Gramage E, Di Geronimo B, Zapico JM, et al. Pharmacological inhibition of Receptor Protein Tyrosine Phosphatase beta/zeta (PTPRZ1) modulates behavioral responses to ethanol. *Neuropharmacology*. (2018) 137:86–95. doi: 10.1016/j.neuropharm.2018.04.027
127. Cassidy-Stone A, Chipuk JE, Ingerman E, Song C, Yoo C, Kuwana T, et al. Chemical inhibition of the mitochondrial division dynamin reveals its role in Bax/Bak-dependent mitochondrial outer membrane permeabilization. *Dev Cell*. (2008) 14:193–204. doi: 10.1016/j.devcel.2007.11.019
128. Lee DS, Kim JE. PDI-mediated S-nitrosylation of DRP1 facilitates DRP1-S616 phosphorylation and mitochondrial fission in CA1 neurons. *Cell Death Dis*. (2018) 9:869. doi: 10.1038/s41419-018-0910-5
129. Li Y, Yang J, Chen MH, Wang Q, Qin MJ, Zhang T, et al. Ilexgenin A inhibits endoplasmic reticulum stress and ameliorates endothelial dysfunction via suppression of TXNIP/NLRP3 inflammasome activation in an AMPK dependent manner. *Pharmacol Res*. (2015) 99:101–15. doi: 10.1016/j.phrs.2015.05.012
130. Cao J, Remaley AT, Guan W, Devaraj S, Tsai MY. Performance of novel low-density lipoprotein-cholesterol calculation methods in predicting clinical and subclinical atherosclerotic cardiovascular disease risk: the multi-ethnic study of atherosclerosis. *Atherosclerosis*. (2021) 327:1–4. doi: 10.1016/j.atherosclerosis.2021.04.018
131. Kuzmicic J, Del Campo A, Lopez-Crisosto C, Morales PE, Pennanen C, Bravo-Sagua R, et al. Mitochondrial dynamics: a potential new therapeutic target for heart failure. *Rev Esp Cardiol*. (2011) 64:916–23. doi: 10.1016/j.rec.2011.05.022
132. Gomez E, Vercauteren M, Kurtz B, Ouvrard-Pascaud A, Mulder P, Henry JP, et al. Reduction of heart failure by pharmacological inhibition or gene deletion of protein tyrosine phosphatase 1B. *J Mol Cell Cardiol*. (2012) 52:1257–64. doi: 10.1016/j.yjmcc.2012.03.003
133. Filichia E, Hoffer B, Qi X, Luo Y. Inhibition of Drp1 mitochondrial translocation provides neural protection in dopaminergic system in a Parkinson's disease model induced by MPTP. *Sci Rep*. (2016) 6:32656. doi: 10.1038/srep32656
134. Ishihara T, Ban-Ishihara R, Maeda M, Matsunaga Y, Ichimura A, Kyogoku S, et al. Dynamics of mitochondrial DNA nucleoids regulated by mitochondrial fission is essential for maintenance of homogeneously active mitochondria during neonatal heart development. *Mol Cell Biol*. (2015) 35:211–23. doi: 10.1128/MCB.01054-14

Conflict of Interest: The authors declare that the research was conducted in the absence of any commercial or financial relationships that could be construed as a potential conflict of interest.

Publisher's Note: All claims expressed in this article are solely those of the authors and do not necessarily represent those of their affiliated organizations, or those of the publisher, the editors and the reviewers. Any product that may be evaluated in this article, or claim that may be made by its manufacturer, is not guaranteed or endorsed by the publisher.

frontiers in Cardiovascular Medicine

SYSTEMATIC REVIEW
published: 20 December 2021
doi: 10.3389/fcvm.2021.738654

Chronic Stress A Potential Suspect Zero of Atherosclerosis: A Systematic Review

Ling-bing Meng[1,2], *Yuan-meng Zhang*[3], *Yue Luo*[4], *Tao Gong*[5]* and *De-ping Liu*[1,2]*

[1] Department of Cardiology, National Center of Gerontology, Institute of Geriatric Medicine, Beijing Hospital, Chinese Academy of Medical Sciences, Beijing, China, [2] Graduate School of Peking Union Medical College and Chinese Academy of Medical Sciences, Beijing, China, [3] Department of Internal Medicine, The Third Medical Centre of Chinese People's Liberation Army (PLA) General Hospital, The Training Site for Postgraduate of Jinzhou Medical University, Beijing, China, [4] Department of Respiratory, The First Affiliated Hospital of Jinzhou Medical University, Jinzhou, China, [5] Department of Neurology, National Center of Gerontology, National Center of Gerontology, Institute of Geriatric Medicine, Beijing Hospital, Chinese Academy of Medical Sciences, Beijing, China

OPEN ACCESS

Edited by:
Yi Yang,
First Affiliated Hospital of Jilin University, China

Reviewed by:
Achuthan Raghavamenon, Amala Cancer Research Centre, India
Fu-Liang Zhang, First Affiliated Hospital of Jilin University, China

***Correspondence:**
De-ping Liu
liudeping@263.net
Tao Gong
mac0852@163.com

Specialty section:
This article was submitted to Atherosclerosis and Vascular Medicine, a section of the journal Frontiers in Cardiovascular Medicine

Received: *09 July 2021*
Accepted: *29 November 2021*
Published: *20 December 2021*

Citation:
Meng L-b, Zhang Y-m, Luo Y, Gong T and Liu D-p (2021) Chronic Stress A Potential Suspect Zero of Atherosclerosis: A Systematic Review. Front. Cardiovasc. Med. 8:738654. doi: 10.3389/fcvm.2021.738654

Atherosclerosis (AS) is a chronic vascular inflammatory disease, in which the lipid accumulation in the intima of the arteries shows yellow atheromatous appearance, which is the pathological basis of many diseases, such as coronary artery disease, peripheral artery disease and cerebrovascular disease. In recent years, it has become the main cause of death in the global aging society, which seriously endangers human health. As a result, research on AS is increasing. Lesions of atherosclerosis contain macrophages, T cells and other cells of the immune response, together with cholesterol that infiltrates from the blood. Recent studies have shown that chronic stress plays an important role in the occurrence and development of AS. From the etiology of disease, social, environmental and genetic factors jointly determine the occurrence of disease. Atherosclerotic cardio-cerebrovascular disease (ASCVD) is often caused by chronic stress (CS). If it cannot be effectively prevented, there will be biological changes in the body environment successively, and then the morphological changes of the corresponding organs. If the patient has a genetic predisposition and a combination of environmental factors triggers the pathogenesis, then chronic stress can eventually lead to AS. Therefore, this paper discusses the influence of chronic stress on AS in the aspects of inflammation, lipid metabolism, endothelial dysfunction, hemodynamics and blood pressure, plaque stability, autophagy, ferroptosis, and cholesterol efflux.

Keywords: chronic stress, atherosclerosis, inflammation, lipid metabolism, endothelial function, plaque stability

INTRODUCTION

Atherosclerosis (AS) is considered as a non-specific inflammatory disease, mainly involving the intima and medial layer of the arterial wall, which is the pathological basis of various cardiovascular and cerebrovascular diseases (1, 2). Cardiovascular disease is still the leading cause of death worldwide, with an increasing prevalence in developing countries (3). In recent years, the rapid economic development in China has led to the change of lifestyle and the aggravation of population

aging (4). The incidence and prevalence of chronic non-communicable diseases, such as hypertension, hyperlipidemia, diabetes, hyperuricemia, and chronic psychological stress, are increasing year by year, and the AS caused by these diseases is also becoming more and more serious (5–9). AS is the main cause of atherosclerotic cardiovascular disease (ASCVD), which is the leading cause of disability and death among urban and rural residents in China (10). In China, cardiovascular diseases account for about 45% of the deaths of the population, causing a serious medical burden and becoming a major public health problem (11). What's more, the incidence of ASCVD in China continues to rise. As is the main cause of ASCVD (12). The pathophysiological development of AS is closely related to the mutation and abnormal expression of genes, including fms-like tyrosine kinase-1 (Flt-1), tumor necrosis factor-α (TNF-α), apolipoprotein A-I (apo A-I), Vascular Endothelial Growth Factor (VEGF), and Angiogenin (ANG). Previous studies have shown that low expression of Flt-1 could predict the development of endothelial injury, which leads to the development of AS (13). In addition, the stronger the proliferative ability of endothelial progenitor cells (EPCs), the lower the vulnerability of vascular endothelium. Thus, TNF-α overexpression damages the vascular endothelium by disrupting the proliferation process of EPCs (14). The mutation of the anti-atherosclerosis gene, apo A-I, could accelerate the apoptosis of vascular endothelial cells by down-regulating the levels of endothelial nitric oxide synthase (eNOS) and heme oxygenase-1, and eventually lead to the formation of atherosclerotic plaque (15). The expression of VEGF and ANG could promote the regeneration of vascular endothelial cells (16, 17). Therefore, the abnormal expression of VEGF and ANG might play an important role in the occurrence and development of AS (18–20). The up-regulation of "VEGF and ANG" plays a significant role in the development of AS. Compared with the normal artery tissues, the expression of "VEGF and ANG" were higher in the AS tissues. The main biological function of ANG is to promote angiogenesis, which promotes plaque instability (21). VEGF is the strongest known factor promoting angiogenesis, which could promote endothelial cell mitosis and proliferation, increase vascular permeability and promote endothelial cell migration (22). Furthermore, VEGF could promote intimal hyperplasia and aggravate AS by promoting monocyte activation, adhesion, and migration and increasing permeability of endothelial cells (23). However, one of the important reasons for the current inability to effectively control the occurrence and recurrence of ASCVD is that the occurrence and progress of atherosclerotic stenosis and vulnerable plaques cannot be detected in time, dynamically monitored, and effectively controlled, which is also the main research field for ASCVD in China and abroad (24–26). So it is imperative to explore the risk factors for the occurrence and development of atherosclerosis for the early diagnosis and precise treatment of ASCVD (27).

Chronic stress induces changes in organisms that increase the risk of atherosclerotic diseases, including heart disease, stroke, and transient ischemic attack (8, 28). The report shows that stress increases the risk of cardiovascular disease (29). A large amount of evidence confirms that chronic stress plays a significant role in the occurrence and development of AS, but the specific mechanism is still unclear (30–33). The purpose of this paper is to provide a comprehensive review of studies on the effects of chronic stress in healthy individuals and patients with cardiovascular disease (CVD). This study focuses on the research progress of the relationship between chronic stress and AS in the aspects of inflammation, lipid metabolism, endothelial dysfunction, hemodynamics and blood pressure, plaque stability, autophagy, ferroptosis, and cholesterol efflux.

Abbreviations: AS, Atherosclerosis; ASCVD, Atherosclerotic cardio-cerebrovascular disease; Flt-1, fms-like tyrosine kinase-1; TNF-α, tumor necrosis factor-α; apo A-I, apolipoprotein A-I; VEGF, Vascular Endothelial Growth Factor; ANG, Angiogenin; EPCs, endothelial progenitor cells; eNOS, endothelial nitric oxide synthase; CVD, cardiovascular disease; ICAM-1, intercellular adhesion molecule-1; CRP, C-reactive protein; ApoE, apolipoprotein E; SNS, Sympathetic Nervous System; NE, noradrenaline; NPY, Nerve Peptide Y; ET, endothelin; MAPKs, mitogen activated protein kinases; HMGB1, High Mobility Group Box 1; DPP4, dipeptidyl peptidase-4; GLP-1, glucagon-like peptide-1; APN, adiponectin; LDLC, low density lipoprotein cholesterol; VLDLC, very low density lipoprotein cholesterol; NPY, Neuropeptide Y; CRH, corticosteroid releasinghormone; AVP, vasopressin; RCT, Reverse cholesterol transport; HDL, high-density lipoprotein; ROS, Reactive oxygen species; EPC, endothelial progenitor cell; SP1, Sp1 Transcription Factor; HDL, high-density lipoprotein; ABCA1, ATP-binding cassette transporters A1; ABCG1, ATP-binding cassette transporters G1.

METHODS

Our systematic review is a new method of literature synthesis. It systematically and comprehensively collects the published and unpublished studies on a specific clinical problem, and uses the principles and methods of strict evaluation of clinical epidemiology to select the literatures that meet the quality standards for qualitative combination, so as to draw reliable comprehensive conclusions. This systematic review was conducted in accordance with the Preferred Reporting Items for Systematic Reviews statement guidelines. A protocol was developed prior to commencing this review on PROSPERO. The procedure of searching the references in the databases was manifested in the flow diagram (**Figure 1**; **Table 1**).

Search Strategy

This systematic review focused on the period 2011–2021. Main focus of this paper is on basic medical research about the AS and chronic stress. Researches included in this paper were screened by keyword searches in PubMed, MEDLINE, EMBASE, and Cochrane Library databases. These databases were searched using a combination of subject headings (such as MeSH) and filters (such as Time) when available. We reviewed references of included studies to identify pertinent studies. We imposed no language restriction. The keywords included "chronic stress," "atherosclerosis," "inflammation," "lipid metabolism," "endothelial function," and "plaque stability." And the strings of terms were "(chronic stress[Title/Abstract]) AND (atherosclerosis[Title/Abstract])," "(Atherosclerosis[Title/Abstract]) AND (plaque stability [Title/Abstract])," "(Atherosclerosis[Title/Abstract]) AND (inflammation[Title/Abstract])," "(Atherosclerosis[Title/Abstract]) AND (lipid metabolism[Title/Abstract]),"

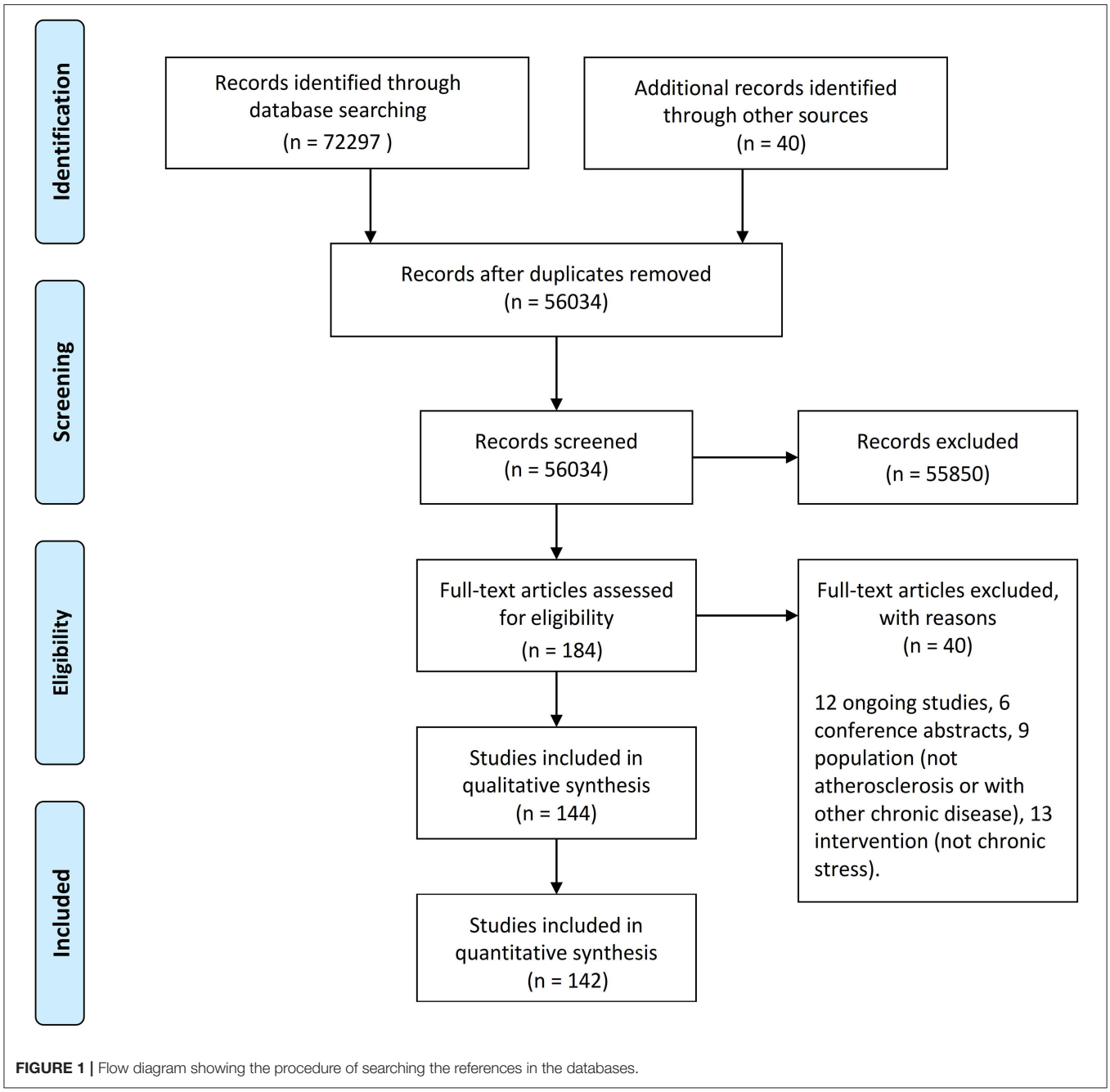

FIGURE 1 | Flow diagram showing the procedure of searching the references in the databases.

"(Atherosclerosis[Title/Abstract]) AND (endothelial function[Title/Abstract])," "(Atherosclerosis[Title/Abstract]) AND (autophagy [Title/Abstract])," "(Atherosclerosis[Title/Abstract]) AND (ferroptosis [Title/Abstract])," "(Atherosclerosis[Title/Abstract]) AND (cholesterol efflux [Title/Abstract])."

Inclusion and Exclusion Criteria

Two reviewers independently assessed records identified from the search for eligibility. Any discrepancies were resolved by consensus. We included any studies referring to chronic stress and atherosclerosis. The researches mainly included the basic medical study with molecular exploration. Outcomes must be objectively measured "atherosclerosis." We accepted 2011–2021 duration of intervention.

We excluded studies with confounding chronic conditions such as "ventricular remodeling, arrhythmia, Peripheral hemangitis."

Study Quality

Study quality was assessed by two reviewers based on the seven domains defined by the Cochrane Collaboration's tool for

TABLE 1 | Literature search tracking sheet.

Date of search	Database	Years searched	Search terms	Strings of terms	#HITS
20/05/21	PubMed, MEDLINE,MBASE, and Cochrane Library	2011–01/2021	Chronic stress	None used	52888
22/05/21	PubMed, MEDLINE,MBASE, and Cochrane Library	2011–01/2021	Chronic stress; atherosclerosis	(chronic stress[Title/Abstract]) AND (atherosclerosis[Title/Abstract])	182
23/05/21	PubMed, MEDLINE,MBASE, and Cochrane Library	2011–01/2021	Atherosclerosis; plaque stability	(Atherosclerosis[Title/Abstract]) AND (plaque stability[Title/Abstract])	655
24/05/21	PubMed, MEDLINE,MBASE, and Cochrane Library	2011–01/2021	Atherosclerosis; inflammation	(Atherosclerosis[Title/Abstract]) AND (inflammation[Title/Abstract])	12619
25/05/21	PubMed, MEDLINE,MBASE, and Cochrane Library	2011–01/2021	Atherosclerosis; lipid metabolism	(Atherosclerosis[Title/Abstract]) AND (lipid metabolism[Title/Abstract])	1706
25/05/21	PubMed, MEDLINE,MBASE, and Cochrane Library	2011–01/2021	Atherosclerosis; endothelial function	(Atherosclerosis[Title/Abstract]) AND (endothelial function[Title/Abstract])	1898
20/10/21	PubMed, MEDLINE,MBASE, and Cochrane Library	2011–10/2021	Atherosclerosis; autophagy	(Atherosclerosis[Title/Abstract]) AND (autophagy[Title/Abstract])	956
20/10/21	PubMed, MEDLINE,MBASE, and Cochrane Library	2011–10/2021	Atherosclerosis; ferroptosis	(Atherosclerosis[Title/Abstract]) AND (ferroptosis[Title/Abstract])	68
20/10/21	PubMed, MEDLINE,MBASE, and Cochrane Library	2011–10/2021	Atherosclerosis; cholesterol efflux	(Atherosclerosis[Title/Abstract]) AND (cholesterol efflux[Title/Abstract])	1325

assessing risk of bias. Namely, (1) random sequence generation; (2) allocation concealment; (3) blinding of participants and personnel; (4) blinding of outcome assessment; (5) incomplete outcome data; (6) selective reporting; and (7) other biases, including baseline imbalance, early stopping and bias due to vested financial interest or academic bias.

Potential publication bias across studies was assessed using a funnel plot.

Data Extraction

One author extracted all the data, and two authors reviewed the data for accuracy. The following data was collected: all papers about the association between "chronic stress" and "atherosclerosis."

RESULTS AND DISCUSSION

Chronic Stress Accelerating Atherosclerosis *via* Inflammation

Although the specific biological mechanisms by which chronic stress increases cardiovascular disease risk remain unclear (34). However, chronic low-grade inflammatory load appears as a possible link because chronic stress exacerbates this load and leads to early progression of atherosclerosis and thrombotic complications (35–37). Inflammation plays a key role in the overall atherosclerotic step, involving the accumulation of foam cells, the formation of fatty stripe tissue and fibrous plaques, the rupture of acute plaques, and the formation of thrombus (38–40). Persistence of inflammation is necessary for plaque development and instability, and plays a decisive role in the pathogenesis and progression of coronary artery disease (41–44). Animal experiments have shown that the levels of intercellular adhesion molecule-1 (ICAM-1), the reactant C-reactive protein (CRP) in the acute phase, and the pro-inflammatory cytokine are significantly increased in apolipoprotein E (ApoE) knockout mice preconditioned by chronic stress (45, 46). Plenty of evidence shows that chronic stress could activate inflammation in the brain and surrounding areas (47, 48). Some researchers believe that stress might activate the Sympathetic Nervous System (SNS) to release noradrenaline (NE) and Nerve Peptide Y (NPY), and these two stress hormones further promote the phosphorylation of mitogen activated protein kinases (MAPKs) or the release of High Mobility Group Box 1 (HMGB1), thereby inducing systemic inflammation to accelerate the development of CVD (49). Chronic stress alters the dynamic balance of the sympathetic and vagal nervous systems. Decrease of vagal tone could promote inflammation. It has been found that chronic stress could enhance the activity of dipeptidyl peptidase-4 (DPP4) in plasma and reduce plasma glucagon-like peptide-1 (GLP-1) and adiponectin (APN) concentrations, thus promoting the development of inflammation (50–52). However, whether it is possible to reduce the promoting effect of chronic stress on atherosclerosis through the targeted inhibition of some cellular inflammatory factors remains to be further studied.

It has been proved that chronic stress and its related diseases anxiety and depression interact with inflammatory response (53). IL-6 is an important inflammatory factor, and its changes represent the body's defense response to chronic stress and help the body adapt to the environment (54). And IL-6 is a kind of polypeptide cytokines with immunomodulatory effects, mainly produced by mononuclear macrophages and T lymphocytes. In the central nervous system, both neurons and glial cells produce this factor (55). Study has shown that IL-6 is involved in the occurrence and development of atherosclerosis in hypertensive patients, and the size of cerebral infarction is positively correlated with the level of serum IL-6 (56). At the same time, IL-6 might promote the progression of atherosclerosis. Studies have shown that IL-6, a pro-inflammatory factor, is elevated in the

serum of patients with chronic stress (57). Serum IL-6 increased significantly after chronic stress, and the increase was more obvious in the high-fat diet group. Cortisol acts as an anti-inflammatory, and as IL-6 levels rise in the body, so do cortisol levels. Studies have shown that chronic stress can promote the development of AS through high levels of cortisol mediated by IL-6 (58). IL-6 could promote platelet activation, accelerate the coagulation process, cause endothelial and smooth muscle cell necrosis, and accelerate the formation of AS. IL-6 could damage the vascular endothelium and interfere with uptake of low-density lipoprotein (LDL) by macrophages, resulting in lipid accumulation in the vascular wall and leading to AS (59).

Disorder of Lipid Metabolism in Atherosclerosis Under Chronic Stress

Studies have shown that chronic stress-induced hyperlipidemia and oxidative damage can contribute to the development of atherosclerosis (60). Although atherosclerosis is a chronic inflammatory disease, currently, more and more evidence manifested that atherosclerosis is a complex systematic pathology, and hyperlipidemia is a major risk factor for changes in intimal and media thickness during atherosclerosis (41). Experiments have found that compared with the control group, the high concentrations of serum total cholesterol, triglyceride, low density lipoprotein cholesterol (LDLC), and very low density lipoprotein cholesterol (VLDLC) could increase the atherosclerosis index in the chronic stress group, while the concentration of high density lipoprotein cholesterol did not change significantly (61–65). Chronic stress caused by long-term social pressure leads to obesity to some extent. Obesity is the result of excessive accumulation of fat (66). Scientific studies have shown that obesity can increase the incidence of cardiovascular and cerebrovascular diseases (67, 68). However, the accumulation of subcutaneous fat was not associated with an increased risk of cardiovascular disease. One study found that chronic stress promoted the accumulation of visceral fat, which in turn led to atherosclerosis and cardiovascular events, rather than the accumulation of subcutaneous fat (69). The chronic stress might stimulate the production of glucocorticoid, which can promote visceral obesity, and accompanied by a series of metabolic disorders, including dyslipidemia, impaired glucose tolerance and insulin resistance, unstable or elevated blood pressure (70–73). These factors will be harmful to the arteries, and promote the development of atherosclerosis (67, 74). Other studies have found that Neuropeptide Y (NPY) is a mediator of vascular lipid metabolism disorder under chronic stress and a risk factor for stress-induced lipid metabolic syndrome and atherosclerosis (75–78). Understanding how neuropeptide Y and its homologous receptors regulate lipid metabolism may provide new ideas for the study of the mechanism and treatment of atherosclerosis (79, 80). A large number of studies have shown that hyperlipidemia, induced by chronic stress, is closely related to atherosclerosis (60, 81–83). Therefore, the understanding of lipid metabolism under stress state has important guiding significance for the study of the relationship between chronic stress and atherosclerosis.

Effect of Chronic Stress on Endothelial Dysfunction in Atherosclerosis

Studies have shown that stress is a risk factor for cardiovascular disease (CVD) (84–86). However, the underlying mechanism is not clear. Studies have shown that mental stress activates the sympathetic nervous system (87), which might cause a range of adverse cardiovascular effects, including increased blood pressure, increased heart rate, and endothelial dysfunction. The endothelial dysfunction represent an important link between chronic stress and cardiovascular disease (CVD) risk (46, 88). Recent data from human and animal stress model studies highlight the critical role of endothelial dysfunction in stress-induced cardiovascular disease (89). It was found that under chronic stress, thoracic aortic rings exhibited high sensitivity to vasoconstrictors by inhibiting nitric oxide synthase activity or removing endothelial cells (90–92). Chronic stress could reduce NO production and induce physiological and biological changes of blood vessels, leading to endothelial dysfunction and the progression of atherosclerotic plaques (93, 94). One study examined the effect of vascular endothelial dysfunction on subclinical atherosclerotic plaques by measuring arterial elasticity by observing changes in the percentage of intima-media. The results showed that the loss of endothelial cells could affect the percentage of intima-media and induce atherosclerosis. It has also been found that poor vascular endothelial function will increase the incidence of atherosclerosis (95, 96). Endothelial dysfunction is an important cause of atherosclerosis. Stress can directly inhibit the vasodilator function of endothelial cells. Patients with long-term chronic psychological stress may develop impaired vascular endothelial function. Maintaining homeostasis is a new way to prevent and treat atherosclerosis.

Variation of Hemodynamics and Blood Pressure Under Chronic Stress

Chronic stress is associated with increased cardiovascular risk, including increased incidence of atherosclerosis, myocardial ischemia, coronary heart disease, and death. The association between stress and cardiovascular dysfunction represents an important node for therapeutic interventions for cardiovascular disease, especially in the aging population, where hypertension is a well-known risk factor (97). Chronic stress plays a very important role in the development of hypertension, and its mechanisms are known to involve long-term abnormal neurological and endocrine activity, such as significantly elevated levels of corticosteroids, cortisol, epinephrine, norepinephrine, and angiotensin. Initially, the sympathetic nerve-adrenal medulla system is an important factor in the development of hypertension. Under chronic stress, plasma adrenaline, norepinephrine, and dopamine increase rapidly (98). It is now clear that in hypertension, the sympathetic nervous system activity is increased, and sympathetic excitation causes small arteriovenous contractions, leading to an increase in diastolic/systolic blood pressure (99–101). Catecholamine is an important humoral factor in the sympathetic adrenal myeloid system, which can cause constriction of peripheral blood vessels and increase diastolic

pressure. The renin-angiotensin-aldosterone system also plays an important role in chronic stress by inducing increased angiotensin levels, regulating catecholamine secretion, and increasing blood pressure (102–105). Sympathetic excitation is known to increase angiotensin II production by stimulating proximal cells and beta receptors in local tissues to promote renin secretion. Finally, on the hypothalamic-pituitary-adrenal axis (106, 107), chronic psychological stress stimulates the secretion of corticosteroid releasinghormone (CRH) and vasopressin (AVP) in the hypothalamus, which promotes the secretion of corticotropic hormone. Glucocorticoids are important factors in maintaining the normal response of the circulatory system to catecholamines. Glucocorticoid deficiency was associated with significantly reduced response, decreased myocardial contractibility, decreased output, and decreased blood pressure (108). In addition, endothelin (ET) was also an important factor regulating cardiovascular function, and plays an important role in maintaining vascular tension and cardiovascular system homeostasis. As endodermal vascular active factors, endothelin has the strongest and most lasting effect among the endogenous vasoconstrictor peptides. The endothelium could contract vessels and promote endothelial cell proliferation by releasing endothelin. Hypertension and diabetes could lead to endothelial dysfunction and promote release of endothelin (109). The levels of endothelin in patients with diabetes and coronary heart disease were higher than those in control group. The level of endothelin increased significantly in diabetic patients with coronary heart disease. These results demonstrate that endothelin is a good response to vascular endothelial disease regardless of the primary etiology. One study suggests that plasma endothelin levels in atherosclerotic patients are proportional to the severity of atherosclerotic vascular lesions. The more damaged vessels, the higher the endothelin level (110). Endothelin might be an independent risk factor for atherosclerosis. Endothelin causes coronary artery dysfunction, promotes coronary artery wall remodeling, platelet activation, and aggregation (111).

Reduced Plaque Stability by Chronic Stress

Chronic stress could reduce the intimal mediators of atherosclerosis and accelerate plaque instability by promoting apoptosis and neovascularization (28). In our current study, chronic stress increased plaque vulnerability, characterized by thinning of the fibrous cap, larger lipid nuclei, increased macrophages and neovascularization, but fewer smooth muscle cells and elastic fibers (112–114). Thus, chronic stress may not induce larger plaque areas, but rather lead to advanced atherosclerotic lesions. So, how does chronic stress affect the stability of atherosclerotic plaque? Levels of inflammation and oxidative stress, which can be exacerbated by chronic stress, have been shown to be associated with atherosclerotic plaque instability (115, 116).

The Effect of Chronic Stress on Atherosclerosis *via* Autophagy

Autophagy is a self-protective cellular catabolic pathway involved in protein and organelle degradation (117, 118). Autophagy plays an important role in inhibiting inflammation and apoptosis, and in promoting efferocytosis and cholesterol efflux, and in maintaining cellular metabolic homeostasis. Autophagy is related to oxidative stress, inflammation, and foam cell formation, further promoting atherosclerosis. Therefore, autophagic homeostasis is essential for the development and outcome of atherosclerosis (119). Atherosclerotic lesions are continuously challenged by stressful insults such as DNA damaging molecules, ROS, oxidized lipids, inflammatory cytokines, hypoxia, etc. and will respond in three different ways: either fight (autophagy), adapt (senescence), or die (apoptosis/necrosis). All the three pathways are interconnected and negatively control each other. Atherosclerosis is the progressive buildup of plaque in the arterial wall ultimately resulting in rupture and thrombosis manifesting (120). Moderate activation of autophagy prevents macrophages and vascular smooth muscle cells (VSMCs) from forming foam cells and preventing the progression of atherosclerotic plaques (121, 122). Stimulation of autophagy suppresses vascular smooth muscle cell senescence, whereas inhibition of autophagy promotes it (123). Autophagy is an evolutionarily conserved process in eukaryotes that processes the turnover of intracellular substances. In patients, excessive autophagy activation leads to cell death, plaque instability, or even plaque rupture (119, 124). Abnormal autophagy regulation may lead to atherosclerosis (125).

The Relationship Between Atherosclerosis and Ferroptosis

Ferroptosis is a newly identified form of regulated cell death characterized by the iron-dependent accumulation of lipid hydroperoxides to lethal levels (126), this type of cell death was found to have molecular characteristics distinct from other forms of regulated cell death (127), which exhibits distinct features from apoptosis, necrosis and autophagy in morphology, biochemistry, and genetics (128, 129). Ferroptosis is a type of autophagy-dependent cell death (130). Emerging mechanisms of ferroptosis is related to disease (131). Ferroptosis is closely related to atherosclerosis, and might occur during the initiation and development of AS (129). Apoptosis, necrosis and autophagy-dependent cell death are the three major types of cell death. Traditionally, necrosis is thought as a passive and unregulated form of cell death. However, certain necrosis can also occur in a highly regulated manner, referring to regulated necrosis. Depending on the signaling pathways, regulated necrosis can be further classified as necroptosis, pyroptosis, ferroptosis, parthanatos, and CypD-mediated necrosis. endothelial progenitor cell (EPC)-EVs transferred miR-199a-3p to inhibit Sp1 Transcription Factor (SP1), thus repressing ferroptosis of endothelial cells and retarding the occurrence of AS (132). Inhibition of ferroptosis could alleviate AS through attenuating lipid peroxidation and endothelial dysfunction in AECs (129, 133). Therefore, ferroptosis as a central gene in human coronary atherosclerosis (134).

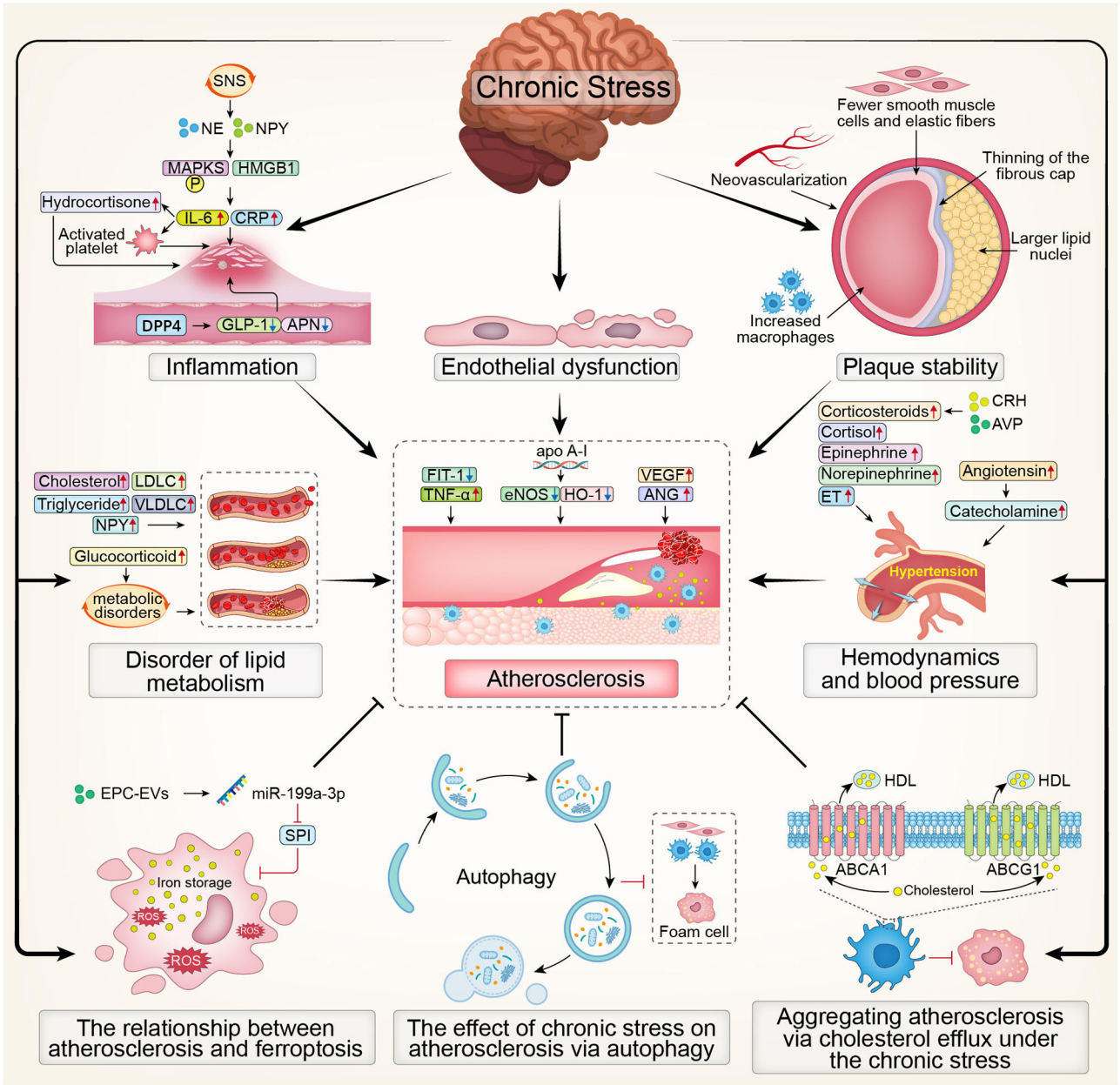

FIGURE 2 | The overview map presenting the effect of chronic stress on atherosclerosis. SNS, Sympathetic Nervous System; NE, noradrenaline; NPY, Nerve Peptide Y; MAPKS, mitogen activated protein kinases; HMGB1, High Mobility Group Box 1; CRP, C-reactive protein; IL-6, interleukin; DPP4, dipeptidyl peptidase-4; GLP-1, glucagon-like peptide-1; APN, adiponectin; LDLC, low density lipoprotein cholesterol; VLDLC, very low density lipoprotein cholesterol; Flt-1, fms-like tyrosine kinase-1; TNF-α, tumor necrosis factor-α; eNOS, endothelial nitric oxide synthase; HO-1, Hemeoxygenase-1; VEGF, Vascular Endothelial Growth Factor; ANG, Angiogenin; CRH, corticosteroid releasinghormone; AVP, vasopressin; ET, endothelin; ROS, Reactive oxygen species; EPC, endothelial progenitor cell; SP1, Sp1 Transcription Factor; HDL, high-density lipoprotein; ABCA1, ATP-binding cassette transporters A1; ABCG1, ATP-binding cassette transporters G1.

Aggregating Atherosclerosis *via* Cholesterol Efflux Under the Chronic Stress

Cholesterol is an important lipid for maintaining cell membrane fluidity and generation of various hormones and bile acids. Thus, it is critical to maintain cholesterol homeostasis including absorption, trafficking, biosynthesis, and efflux. Dysregulation of cholesterol homeostasis may lead to human disorders (135). The phenomena of lipid accumulation, inflammation, oxidative stress, hypoxia, and insulin resistance commonly associated with AS lesions can regulate the expression of cholesterol transporter, and then regulate intracellular cholesterol efflux, affecting the occurrence, and development of As. Cholesterol efflux is a key step in cholesterol reverse transport (136). The reverse cholesterol transport, a process that removes excess

cholesterol from peripheral tissues/cells including macrophages to circulating HDL, is one of the main mechanisms responsible for anti-atherogenic properties of HDL. Reverse cholesterol transport (RCT) may counteract the pathogenic events leading to the formation and development of atheroma, by promoting the high-density lipoprotein (HDL)-mediated removal of cholesterol from the artery wall (137, 138). The key proteins of reverse cholesterol transport-ATP-binding cassette transporters A1 (ABCA1) and G1 (ABCG1)-mediate the cholesterol efflux from macrophages and prevent their transformation into foam cells (139). The formation of foam cells is a typical pathological feature of early atherosclerosis, the imbalance of cholesterol metabolism homeostasis of macrophages runs through the whole process of foam cell formation.

Atherosclerosis is characterized by significant aggregation of macrophage foam cells in atherosclerotic plaques and associated pro-inflammatory responses in pathological cells. Results from animal and human studies suggest that in these cells, especially in diseased macrophages, dyshomeostasis plays a key role in the pro-inflammatory response. The cholesterol efflux pathway also inhibits the accumulation of cholesterol esters in macrophages, namely the formation of macrophage foam cells (140). Cholesterol efflux is a key link in regulating the cholesterol dynamic balance of macrophages, which is of great significance in reducing intracellular cholesterol accumulation, preventing the formation of foam cells and the occurrence of As. Cholesterol efflux pathways exert anti-inflammatory and anti-atherogenic effects by suppressing proliferation of hematopoietic stem and progenitor cells, and inflammation and inflammasome activation in macrophages. Therefore, atherosclerosis can be prevented by promoting cholesterol efflux from macrophages (141, 142).

In summary, the overview map presented the effect of chronic stress on atherosclerosis (**Figure 2**).

CONCLUSION

Chronic stress is the cause of atherosclerotic cardiovascular and cerebrovascular diseases. If it cannot be effectively prevented, biological changes in the body environment will occur successively, such as inflammation, lipid metabolism, endothelial function, hemodynamics and other changes, and then morphologic changes of the corresponding organs will appear. If the patient has a genetic predisposition, and at the same time the environmental factors work together to activate the pathogenic mechanism, then the chronic stress factors will eventually lead to the development of atherosclerotic cardiovascular disease.

DATA AVAILABILITY STATEMENT

The original contributions presented in the study are included in the article/supplementary material, further inquiries can be directed to the corresponding author/s.

AUTHOR CONTRIBUTIONS

L-bM was major contributor in writing and was involved in critically revising manuscript for important intellectual content. TG and D-pL made substantial contributions to research conception and designed the draft of the research process. YL and Y-mZ were major contributors in submitting the manuscript and they gave the technical support in the methods. All authors read and approved the final manuscript.

FUNDING

The present study was funded by the National Key R&D Program of China (Grant Nos. 2020YFC2003000 and 2020YFC2003001), Chinese Academy of Medical Sciences, CAMS Innovation Fund for Medical Sciences (Grant No. 2018-I2M-1-002), and National Natural Science Foundation of China (Grant Nos. 31271097 and 51672030).

ACKNOWLEDGMENTS

The authors would like to thank Xiao-Meng Yu for his assistance and suggestions during the submitting process.

REFERENCES

1. Allahverdian S, Ortega C, Francis GA. Smooth muscle cell-proteoglycan-lipoprotein interactions as drivers of atherosclerosis. *Handb Exp Pharmacol.* (2020). doi: 10.1007/164_2020_364
2. Yin K, Liang S, Tang X, Li M, Yuan J, Wu M, et al. The relationship between intracranial arterial dolichoectasia and intracranial atherosclerosis. *Clin Neurol Neurosurg.* (2020) 200:106408. doi: 10.1016/j.clineuro.2020.106408
3. Cainzos-Achirica M, Glassner K, Zawahir HS, Dey AK, Agrawal T, Quigley E, et al. Inflammatory bowel disease and atherosclerotic cardiovascular disease: JACC review topic of the week. *J Am Coll Cardiol.* (2020) 76:2895–905. doi: 10.1016/j.jacc.2020.10.027
4. De Winter G. Aging as disease. *Med Health Care Philos.* (2015) 18:237–43. doi: 10.1007/s11019-014-9600-y
5. Song P, Rudan D, Zhu Y, Fowkes F, Rahimi K, Fowkes F, et al. Global, regional, and national prevalence and risk factors for peripheral artery disease in 2015: an updated systematic review and analysis. *Lancet Glob Health.* (2019) 7:e1020–30. doi: 10.1016/S2214-109X(19)30255-4
6. Sharif K, Watad A, Coplan L, Amital H, Shoenfeld Y, Afek A. Psychological stress and type 1 diabetes mellitus: what is the link. *Expert Rev Clin Immunol.* (2018) 14:1081–8. doi: 10.1080/1744666X.2018.1538787
7. Bernstein CN. Psychological stress and depression: risk factors for IBD. *Dig Dis.* (2016) 34:58–63. doi: 10.1159/000442929
8. Marin MF, Lord C, Andrews J, Juster RP, Sindi S, Arsenault-Lapierre G, et al. Chronic stress, cognitive functioning and mental health. *Neurobiol Learn Mem.* (2011) 96:583–95. doi: 10.1016/j.nlm.2011.02.016
9. Ioachimescu AG. Diabetes and atherosclerotic cardiovascular disease. *Endocrinol Metab Clin North Am.* (2018) 47:xiii–xiv. doi: 10.1016/j.ecl.2017.12.002
10. Tang X, Zhang D, He L, Wu N, Si Y, Cao Y, et al. Performance of atherosclerotic cardiovascular risk prediction models in a rural Northern Chinese population: results from the Fangshan Cohort Study. *Am Heart J.* (2019) 211:34–44. doi: 10.1016/j.ahj.2019.01.009
11. Low Wang CC, Hess CN, Hiatt WR, Goldfine AB. Clinical update: cardiovascular disease in diabetes mellitus: atherosclerotic cardiovascular disease and heart failure in type 2 diabetes mellitus - mechanisms,

management, and clinical considerations. *Circulation.* (2016) 133:2459–502. doi: 10.1161/CIRCULATIONAHA.116.022194
12. Yang X, Li J, Hu D, Chen J, Li Y, Huang J, et al. Predicting the 10-Year risks of atherosclerotic cardiovascular disease in Chinese population: the China-PAR project (prediction for ASCVD risk in China). *Circulation.* (2016) 134:1430–40. doi: 10.1161/CIRCULATIONAHA.116.022367
13. Mitsides N, Cornelis T, Broers N, Diederen N, Brenchley P, Heitink-Ter Braak N, et al. Inflammatory and angiogenic factors linked to longitudinal microvascular changes in hemodialysis patients irrespective of treatment dose intensity. *Kidney Blood Press Res.* (2017) 42:905–18. doi: 10.1159/000485048
14. Zhang Y, Liu H, Tang W, Qiu Q, Peng J. Resveratrol prevents TNF-α-induced VCAM-1 and ICAM-1 upregulation in endothelial progenitor cells via reduction of NF-κB activation. *J Int Med Res.* (2020) 48:300060520945131. doi: 10.1177/0300060520945131
15. Xu W, Qian M, Huang C, Cui P, Li W, Du Q, et al. Comparison of mechanisms of endothelial cell protections between high-density lipoprotein and apolipoprotein A-I mimetic peptide. *Front Pharmacol.* (2019) 10:817. doi: 10.3389/fphar.2019.00817
16. Apte RS, Chen DS, Ferrara N. VEGF in signaling and disease: beyond discovery and development. *Cell.* (2019) 176:1248–64. doi: 10.1016/j.cell.2019.01.021
17. Fagiani E, Christofori G. Angiopoietins in angiogenesis. *Cancer Lett.* (2013) 328:18–26. doi: 10.1016/j.canlet.2012.08.018
18. Jaipersad AS, Lip GY, Silverman S, Shantsila E. The role of monocytes in angiogenesis and atherosclerosis. *J Am Coll Cardiol.* (2014) 63:1–11. doi: 10.1016/j.jacc.2013.09.019
19. Braile M, Marcella S, Cristinziano L, Galdiero MR, Modestino L, Ferrara AL, et al. VEGF-A in cardiomyocytes and heart diseases. *Int J Mol Sci.* (2020) 21:5294. doi: 10.3390/ijms21155294
20. Marino M, Del Bo' C, Tucci M, Klimis-Zacas D, Riso P, Porrini M. Modulation of adhesion process, E-selectin and VEGF production by anthocyanins and their metabolites in an *in vitro* model of atherosclerosis. *Nutrients.* (2020) 12:655. doi: 10.20944/preprints202001.0113.v1
21. Gürses KM, Yalçin MU, Koçyigit D, Beşler MS, Canpinar H, Evranos B, et al. The association between serum angiogenin and osteopontin levels and coronary collateral circulation in patients with chronic total occlusion. *Anatol J Cardiol.* (2019) 22:77–84. doi: 10.14744/AnatolJCardiol.2019.88555
22. Melincovici CS, Boşca AB, Suşman S, Mărginean M, Mihu C, Istrate M, Moldovan IM, et al. Vascular endothelial growth factor (VEGF) - key factor in normal and pathological angiogenesis. *Rom J Morphol Embryol.* (2018) 59:455–67. Available online at: https://pubmed.ncbi.nlm.nih.gov/30173249/
23. Ahmed S, Ahmed A, Säleby J, Bouzina H, Lundgren J, Rådegran G. Elevated plasma tyrosine kinases VEGF-D and HER4 in heart failure patients decrease after heart transplantation in association with improved haemodynamics. *Heart Vessels.* (2020) 35:786–99. doi: 10.1007/s00380-019-01548-1
24. Song P, Rudan D, Wang M, Chang X, Rudan I. National and subnational estimation of the prevalence of peripheral artery disease (PAD) in China: a systematic review and meta-analysis. *J Glob Health.* (2019) 9:010601. doi: 10.7189/jogh.09.010601
25. Rosenblit PD. Extreme atherosclerotic cardiovascular disease (ASCVD) risk recognition. *Curr Diab Rep.* (2019) 19:61. doi: 10.1007/s11892-019-1178-6
26. Hussain A, Ballantyne CM, Saeed A, Virani SS. Triglycerides and ASCVD risk reduction: recent insights and future directions. *Curr Atheroscler Rep.* (2020) 22:25. doi: 10.1007/s11883-020-00846-8
27. Sun GZ, Ye N, Wu SJ, Zhou Y, Sun YX. 10-year ASCVD risk is positively correlated with depressive symptoms in a large general population. *BMC Psychiatry.* (2019) 19:125. doi: 10.1186/s12888-019-2114-7
28. Yu ZM, Deng XT, Qi RM, Xiao LY, Yang CQ, Gong T. Mechanism of chronic stress-induced reduced atherosclerotic medial area and increased plaque instability in rabbit models of chronic stress. *Chin Med J.* (2018) 131:161–70. doi: 10.4103/0366-6999.222322
29. Iob E, Steptoe A. Cardiovascular disease and hair cortisol: a novel biomarker of chronic stress. *Curr Cardiol Rep.* (2019) 21:116. doi: 10.1007/s11886-019-1208-7
30. Kovaleva M, Spangler S, Clevenger C, Hepburn K. Chronic stress, social isolation, and perceived loneliness in dementia caregivers. *J Psychosoc Nurs Ment Health Serv.* (2018) 56:36–43. doi: 10.3928/02793695-20180329-04
31. Kattoor AJ, Pothineni N, Palagiri D, Mehta JL. Oxidative stress in atherosclerosis. *Curr Atheroscler Rep.* (2017) 19:42. doi: 10.1007/s11883-017-0678-6
32. Libby P, Buring JE, Badimon L, Hansson GK, Deanfield J, Bittencourt MS, et al. Atherosclerosis. *Nat Rev Dis Primers.* (2019) 5:56. doi: 10.1038/s41572-019-0106-z
33. Esler M. Mental stress and human cardiovascular disease. *Neurosci Biobehav Rev.* (2017) 74:269–76. doi: 10.1016/j.neubiorev.2016.10.011
34. Ferrucci L, Fabbri E. Inflammageing: chronic inflammation in ageing, cardiovascular disease, and frailty. *Nat Rev Cardiol.* (2018) 15:505–22. doi: 10.1038/s41569-018-0064-2
35. Furman D, Campisi J, Verdin E, Carrera-Bastos P, Targ S, Franceschi C, et al. Chronic inflammation in the etiology of disease across the life span. *Nat Med.* (2019) 25:1822–32. doi: 10.1038/s41591-019-0675-0
36. Raggi P, Genest J, Giles JT, Rayner KJ, Dwivedi G, Beanlands RS, et al. Role of inflammation in the pathogenesis of atherosclerosis and therapeutic interventions. *Atherosclerosis.* (2018) 276:98–108. doi: 10.1016/j.atherosclerosis.2018.07.014
37. Pant S, Deshmukh A, Gurumurthy GS, Pothineni NV, Watts TE, Romeo F, et al. Inflammation and atherosclerosis–revisited. *J Cardiovasc Pharmacol Ther.* (2014) 19:170–8. doi: 10.1177/1074248413504994
38. Wolf D, Ley K. Immunity and inflammation in atherosclerosis. *Circ Res.* (2019) 124:315–27. doi: 10.1161/CIRCRESAHA.118.313591
39. Geovanini GR, Libby P. Atherosclerosis and inflammation: overview and updates. *Clin Sci.* (2018) 132:1243–52. doi: 10.1042/CS20180306
40. Zhu Y, Xian X, Wang Z, Bi Y, Chen Q, Han X, et al. Research progress on the relationship between atherosclerosis and inflammation. *Biomolecules.* (2018) 8:80. doi: 10.3390/biom8030080
41. Fioranelli M, Bottaccioli AG, Bottaccioli F, Bianchi M, Rovesti M, Roccia MG. Stress and inflammation in coronary artery disease: a review psychoneuroendocrineimmunology-based. *Front Immunol.* (2018) 9:2031. doi: 10.3389/fimmu.2018.02031
42. Bäck M, Yurdagul A Jr, Tabas I, Öörni K, Kovanen PT. Inflammation and its resolution in atherosclerosis: mediators and therapeutic opportunities. *Nat Rev Cardiol.* (2019) 16:389–406. doi: 10.1038/s41569-019-0169-2
43. Shah PK. Inflammation, infection and atherosclerosis. *Trends Cardiovasc Med.* (2019) 29:468–72. doi: 10.1016/j.tcm.2019.01.004
44. Ruparelia N, Choudhury R. Inflammation and atherosclerosis: what is on the horizon. *Heart.* (2020) 106:80–5. doi: 10.1136/heartjnl-2018-314230
45. Chumaeva N, Hintsanen M, Pulkki-Råback L, Jokela M, Juonala M, Lehtimäki T, et al. Interleukin-6 gene polymorphism, chronic stress and atherosclerosis: interleukin-6-174G>C polymorphism, chronic stress and risk of early atherosclerosis in the Cardiovascular Risk in Young Finns Study. *J Psychosom Res.* (2014) 76:333–8. doi: 10.1016/j.jpsychores.2014.01.007
46. Kershaw KN, Lane-Cordova AD, Carnethon MR, Tindle HA, Liu K. Chronic stress and endothelial dysfunction: the multi-ethnic study of atherosclerosis (MESA). *Am J Hypertens.* (2017) 30:75–80. doi: 10.1093/ajh/hpw103
47. Yao BC, Meng LB, Hao ML, Zhang YM, Gong T, Guo ZG. Chronic stress: a critical risk factor for atherosclerosis. *J Int Med Res.* (2019) 47:1429–40. doi: 10.1177/0300060519826820
48. Rohleder N. Stimulation of systemic low-grade inflammation by psychosocial stress. *Psychosom Med.* (2014) 76:181–9. doi: 10.1097/PSY.0000000000000049
49. Liu YZ, Wang YX, Jiang CL. Inflammation: the common pathway of stress-related diseases. *Front Hum Neurosci.* (2017) 11:316. doi: 10.3389/fnhum.2017.00316
50. Lei Y, Yang G, Hu L, Piao L, Inoue A, Jiang H, et al. Increased dipeptidyl peptidase-4 accelerates diet-related vascular aging and atherosclerosis in ApoE-deficient mice under chronic stress. *Int J Cardiol.* (2017) 243:413–20. doi: 10.1016/j.ijcard.2017.05.062
51. Yang G, Lei Y, Inoue A, Piao L, Hu L, Jiang H, et al. Exenatide mitigated diet-induced vascular aging and atherosclerotic plaque growth in ApoE-deficient mice under chronic stress. *Atherosclerosis.* (2017) 264:1–10. doi: 10.1016/j.atherosclerosis.2017.07.014

52. Halaris A. Co-morbidity between cardiovascular pathology and depression: role of inflammation. *Mod Trends Pharmacopsychiatry.* (2013) 28:144–61. doi: 10.1159/000343981
53. Bauer ME, Teixeira AL. Inflammation in psychiatric disorders: what comes first. *Ann NY Acad Sci.* (2019) 1437:57–67. doi: 10.1111/nyas.13712
54. Wang YL, Han QQ, Gong WQ, Pan DH, Wang LZ, Hu W, et al. Microglial activation mediates chronic mild stress-induced depressive- and anxiety-like behavior in adult rats. *J Neuroinflammation.* (2018) 15:21. doi: 10.1186/s12974-018-1054-3
55. Hunter CA, Jones SA. IL-6 as a keystone cytokine in health and disease. *Nat Immunol.* (2015) 16:448–57. doi: 10.1038/ni.3153
56. Tyrrell DJ, Goldstein DR. Ageing and atherosclerosis: vascular intrinsic and extrinsic factors and potential role of IL-6. *Nat Rev Cardiol.* (2021) 18:58–68. doi: 10.1038/s41569-020-0431-7
57. Molnar DS, Moore J, O'Leary DD, MacNeil AJ, Wade TJ. Perfectionistic cognitions, Interleukin-6, and C-Reactive protein: a test of the perfectionism diathesis stress model. *Brain Behav Immun Health.* (2021) 13:100211. doi: 10.1016/j.bbih.2021.100211
58. Okutsu M, Lira VA, Higashida K, Peake J, Higuchi M, Suzuki K. Corticosterone accelerates atherosclerosis in the apolipoprotein E-deficient mouse. *Atherosclerosis.* (2014) 232:414–9. doi: 10.1016/j.atherosclerosis.2013.11.076
59. Luo P, Shi W, Wang Y, Ma H, Liu T, Yan D, et al. Raloxifene inhibits IL-6/STAT3 signaling pathway and protects against high-fat-induced atherosclerosis in ApoE(-/-) mice. *Life Sci.* (2020) 261:118304. doi: 10.1016/j.lfs.2020.118304
60. Devaki M, Nirupama R, Yajurvedi HN. Chronic stress-induced oxidative damage and hyperlipidemia are accompanied by atherosclerotic development in rats. *Stress.* (2013) 16:233–43. doi: 10.3109/10253890.2012.719052
61. Neves VJ, Moura MJ, Tamascia ML, Ferreira R, Silva NS, Costa R, et al. Proatherosclerotic effects of chronic stress in male rats: altered phenylephrine sensitivity and nitric oxide synthase activity of aorta and circulating lipids. *Stress.* (2009) 12:320–7. doi: 10.1080/10253890802437779
62. Poznyak A, Grechko AV, Poggio P, Myasoedova VA, Alfieri V, Orekhov AN. The diabetes mellitus-atherosclerosis connection: the role of lipid and glucose metabolism and chronic inflammation. *Int J Mol Sci.* (2020) 21:1835. doi: 10.3390/ijms21051835
63. Meng LB, Qi R, Xu L, Chen Y, Yu Z, Guo P, et al. The more critical murderer of atherosclerosis than lipid metabolism: chronic stress. *Lipids Health Dis.* (2018) 17:143. doi: 10.1186/s12944-018-0795-4
64. Çimen I, Kocatürk B, Koyuncu S, Tufanli Ö, Onat UI, Yildirim AD, et al. Prevention of atherosclerosis by bioactive palmitoleate through suppression of organelle stress and inflammasome activation. *Sci Transl Med.* (2016) 8:358ra126. doi: 10.1126/scitranslmed.aaf9087
65. Ou L, Li X, Chen B, Ge Z, Zhang J, Zhang Y, et al. Recombinant human cytoglobin prevents atherosclerosis by regulating lipid metabolism and oxidative stress. *J Cardiovasc Pharmacol Ther.* (2018) 23:162–73. doi: 10.1177/1074248417724870
66. Bullon P, Newman HN, Battino M. Obesity, diabetes mellitus, atherosclerosis and chronic periodontitis: a shared pathology via oxidative stress and mitochondrial dysfunction. *Periodontology.* (2014) 64:139–53. doi: 10.1111/j.1600-0757.2012.00455.x
67. Shively CA, Register TC, Clarkson TB. Social stress, visceral obesity, and coronary artery atherosclerosis: product of a primate adaptation. *Am J Primatol.* (2009) 71:742–51. doi: 10.1002/ajp.20706
68. Ortega-Montiel J, Posadas-Romero C, Ocampo-Arcos W, Medina-Urrutia A, Cardoso-Saldaña G, Jorge-Galarza E, et al. Self-perceived stress is associated with adiposity and atherosclerosis. The GEA Study. *BMC Public Health.* (2015) 15:780. doi: 10.1186/s12889-015-2112-8
69. Peters A, McEwen BS. Stress habituation, body shape and cardiovascular mortality. *Neurosci Biobehav Rev.* (2015) 56:139–50. doi: 10.1016/j.neubiorev.2015.07.001
70. Palumbo ML, Prochnik A, Wald MR, Genaro AM. Chronic stress and glucocorticoid receptor resistance in asthma. *Clin Ther.* (2020) 42:993–1006. doi: 10.1016/j.clinthera.2020.03.002
71. Chiba S, Numakawa T, Ninomiya M, Richards MC, Wakabayashi C, Kunugi H. Chronic restraint stress causes anxiety- and depression-like behaviors, downregulates glucocorticoid receptor expression, and attenuates glutamate release induced by brain-derived neurotrophic factor in the prefrontal cortex. *Prog Neuropsychopharmacol Biol Psychiatry.* (2012) 39:112–9. doi: 10.1016/j.pnpbp.2012.05.018
72. Vyas S, Rodrigues AJ, Silva JM, Tronche F, Almeida OF, Sousa N, et al. Chronic stress and glucocorticoids: from neuronal plasticity to neurodegeneration. *Neural Plast.* (2016) 2016:6391686. doi: 10.1155/2016/6391686
73. Horchar MJ, Wohleb ES. Glucocorticoid receptor antagonism prevents microglia-mediated neuronal remodeling and behavioral despair following chronic unpredictable stress. *Brain Behav Immun.* (2019) 81:329–40. doi: 10.1016/j.bbi.2019.06.030
74. Hui N, Morris MJ, Allison MA, Tsai MY, Rye KA, Tabet F, et al. Lipoprotein (a) and the risk of elevated depressive symptoms: The Multi-Ethnic Study of Atherosclerosis. *J Psychiatr Res.* (2020) 133:119–24. doi: 10.1016/j.jpsychires.2020.12.022
75. Sun WW, Zhu P, Shi YC, Zhang CL, Huang XF, Liang SY, et al. Current views on neuropeptide Y and diabetes-related atherosclerosis. *Diab Vasc Dis Res.* (2017) 14:277–84. doi: 10.1177/1479164117704380
76. Tan C, Green P, Tapoulal N, Lewandowski AJ, Leeson P, Herring N. The role of neuropeptide Y in cardiovascular health and disease. *Front Physiol.* (2018) 9:1281. doi: 10.3389/fphys.2018.01281
77. Zheng YL, Wang WD, Li MM, Lin S, Lin HL. Updated role of neuropeptide Y in nicotine-induced endothelial dysfunction and atherosclerosis. *Front Cardiovasc Med.* (2021) 8:630968. doi: 10.3389/fcvm.2021.630968
78. Wu WQ, Peng S, Wan XQ, Lin S, Li LY, Song ZY. Physical exercise inhibits atherosclerosis development by regulating the expression of neuropeptide Y in apolipoprotein E-deficient mice. *Life Sci.* (2019) 237:116896. doi: 10.1016/j.lfs.2019.116896
79. Abe K, Kuo L, Zukowska Z. Neuropeptide Y is a mediator of chronic vascular and metabolic maladaptations to stress and hypernutrition. *Exp Biol Med.* (2010) 235:1179–84. doi: 10.1258/ebm.2010.009136
80. Vähätalo LH, Ruohonen ST, Ailanen L, Savontaus E. Neuropeptide Y in noradrenergic neurons induces obesity in transgenic mouse models. *Neuropeptides.* (2016) 55:31–7. doi: 10.1016/j.npep.2015.11.088
81. Park K, Li Q, Evcimen ND, Rask-Madsen C, Maeda Y, Maddaloni E, et al. Exogenous insulin infusion can decrease atherosclerosis in diabetic rodents by improving lipids, inflammation, and endothelial function. *Arterioscler Thromb Vasc Biol.* (2018) 38:92–101. doi: 10.1161/ATVBAHA.117.310291
82. Han Y, Lin M, Wang X, Guo K, Wang S, Sun M, et al. Basis of aggravated hepatic lipid metabolism by chronic stress in high-fat diet-fed rat. *Endocrine.* (2015) 48:483–92. doi: 10.1007/s12020-014-0307-x
83. Takahashi K, Yamada T, Tsukita S, Kaneko K, Shirai Y, Munakata Y, et al. Chronic mild stress alters circadian expressions of molecular clock genes in the liver. *Am J Physiol Endocrinol Metab.* (2013) 304:E301–9. doi: 10.1152/ajpendo.00388.2012
84. Aboa-Eboulé C, Brisson C, Maunsell E, Mâsse B, Bourbonnais R, Vézina M, et al. Job strain and risk of acute recurrent coronary heart disease events. *JAMA.* (2007) 298:1652–60. doi: 10.1001/jama.298.14.1652
85. Bairey Merz CN, Dwyer J, Nordstrom CK, Walton KG, Salerno JW, Schneider RH. Psychosocial stress and cardiovascular disease: pathophysiological links. *Behav Med.* (2002) 27:141–7. doi: 10.1080/08964280209596039
86. De Bacquer D, Pelfrene E, Clays E, Mak R, Moreau M, de Smet P, et al. Perceived job stress and incidence of coronary events: 3-year follow-up of the Belgian Job Stress Project cohort. *Am J Epidemiol.* (2005) 161:434–41. doi: 10.1093/aje/kwi040
87. Hjemdahl P, Fagius J, Freyschuss U, Wallin BG, Daleskog M, Bohlin G, et al. Muscle sympathetic activity and norepinephrine release during mental challenge in humans. *Am J Physiol.* (1989) 257:E654–4. doi: 10.1152/ajpendo.1989.257.5.E654
88. Ross R. The pathogenesis of atherosclerosis: a perspective for the (1990s). *Nature.* (1993) 362:801–9. doi: 10.1038/362801a0
89. Golbidi S, Frisbee JC, Laher I. Chronic stress impacts the cardiovascular system: animal models and clinical outcomes. *Am J Physiol Heart Circ Physiol.* (2015) 308:H1476–98. doi: 10.1152/ajpheart.00859.2014

90. Ghiadoni L, Bruno RM. The endothelium as a target for chronic stress. *Am J Hypertens.* (2017) 30:19–20. doi: 10.1093/ajh/hpw116
91. Stanley SC, Brooks SD, Butcher JT, d'Audiffret AC, Frisbee SJ, Frisbee JC. Protective effect of sex on chronic stress- and depressive behavior-induced vascular dysfunction in BALB/cJ mice. *J Appl Physiol.* (2014) 117:959–70. doi: 10.1152/japplphysiol.00537.2014
92. Balkaya M, Prinz V, Custodis F, Gertz K, Kronenberg G, Kroeber J, et al. Stress worsens endothelial function and ischemic stroke via glucocorticoids. *Stroke.* (2011) 42:3258–64. doi: 10.1161/STROKEAHA.110.607705
93. Dikalov SI, Mayorov VI, Panov AV. Physiological levels of nitric oxide diminish mitochondrial superoxide. Potential role of mitochondrial dinitrosyl iron complexes and nitrosothiols. *Front Physiol.* (2017) 8:907. doi: 10.3389/fphys.2017.00907
94. Yang HJ, Kim KY, Kang P, Lee HS, Seol GH. Effects of Salvia sclarea on chronic immobilization stress induced endothelial dysfunction in rats. *BMC Complement Altern Med.* (2014) 14:396. doi: 10.1186/1472-6882-14-396
95. Mausbach BT, Roepke SK, Ziegler MG, Milic M, von Känel R, Dimsdale JE, et al. Association between chronic caregiving stress and impaired endothelial function in the elderly. *J Am Coll Cardiol.* (2010) 55:2599–606. doi: 10.1016/j.jacc.2009.11.093
96. Chumaeva N, Hintsanen M, Ravaja N, Juonala M, Raitakari OT, Keltikangas-Järvinen L. Chronic stress and the development of early atherosclerosis: moderating effect of endothelial dysfunction and impaired arterial elasticity. *Int J Environ Res Public Health.* (2009) 6:2934–49. doi: 10.3390/ijerph6122934
97. Goodson ML, Packard A, Buesing DR, Maney M, Myers B, Fang Y, et al. Chronic stress and Rosiglitazone increase indices of vascular stiffness in male rats. *Physiol Behav.* (2017) 172:16–23. doi: 10.1016/j.physbeh.2016.03.031
98. Imperatore R, Palomba L, Cristino L. Role of orexin-A in hypertension and obesity. *Curr Hypertens Rep.* (2017) 19:34. doi: 10.1007/s11906-017-0729-y
99. Bohuslavova R, Cerychova R, Papousek F, Olejnickova V, Bartos M, Görlach A, et al. HIF-1α is required for development of the sympathetic nervous system. *Proc Natl Acad Sci USA.* (2019) 116:13414–23. doi: 10.1073/pnas.1903510116
100. DeLalio LJ, Sved AF, Stocker SD. Sympathetic nervous system contributions to hypertension: updates and therapeutic relevance. *Can J Cardiol.* (2020) 36:712–20. doi: 10.1016/j.cjca.2020.03.003
101. Esler M. The sympathetic nervous system in hypertension: back to the future. *Curr Hypertens Rep.* (2015) 17:11. doi: 10.1007/s11906-014-0519-8
102. Lezama-Martínez D, Valencia-Hernández I, Flores-Monroy J, Martínez-Aguilar L. Combination of β adrenergic receptor block and renin-angiotensin system inhibition diminished the angiotensin ii-induced vasoconstriction and increased bradykinin-induced vasodilation in hypertension. *Dose Response.* (2017) 15:1559325817737932. doi: 10.1177/1559325817737932
103. Wang C, Luo Z, Carter G, Wellstein A, Jose PA, Tomlinson J, et al. NRF2 prevents hypertension, increased ADMA, microvascular oxidative stress, and dysfunction in mice with two weeks of ANG II infusion. *Am J Physiol Regul Integr Comp Physiol.* (2018) 314:R399–406. doi: 10.1152/ajpregu.00122.2017
104. Holbein WW, Blackburn MB, Andrade MA, Toney GM. Burst patterning of hypothalamic paraventricular nucleus-driven sympathetic nerve activity in ANG II-salt hypertension. *Am J Physiol Heart Circ Physiol.* (2018) 314:H530–41. doi: 10.1152/ajpheart.00560.2017
105. Ishigaki S, Ohashi N, Matsuyama T, Isobe S, Tsuji N, Iwakura T, et al. Melatonin ameliorates intrarenal renin-angiotensin system in a 5/6 nephrectomy rat model. *Clin Exp Nephrol.* (2018) 22:539–49. doi: 10.1007/s10157-017-1505-7
106. O'Connor DB, Green JA, Ferguson E, O'Carroll RE, O'Connor RC. Effects of childhood trauma on cortisol levels in suicide attempters and ideators. *Psychoneuroendocrinology.* (2018) 88:9–16. doi: 10.1016/j.psyneuen.2017.11.004
107. Tang AR, Rabi DM, Lavoie KL, Bacon SL, Pilote L, Kline GA. Prolonged hypothalamic-pituitary-adrenal axis activation after acute coronary syndrome in the GENESIS-PRAXY cohort. *Eur J Prev Cardiol.* (2018) 25:65–72. doi: 10.1177/2047487317734323
108. Ewart CK, Elder GJ, Jorgensen RS, Fitzgerald ST. The role of agonistic striving in the association between cortisol and high blood pressure. *Psychosom Med.* (2017) 79:416–25. doi: 10.1097/PSY.0000000000000412
109. Barton M, Yanagisawa M. Endothelin: 30 years from discovery to therapy. *Hypertension.* (2019) 74:1232–65. doi: 10.1161/HYPERTENSIONAHA.119.12105
110. Pernow J, Shemyakin A, Böhm F. New perspectives on endothelin-1 in atherosclerosis and diabetes mellitus. *Life Sci.* (2012) 91:507–16. doi: 10.1016/j.lfs.2012.03.029
111. Li MW, Mian MO, Barhoumi T, Rehman A, Mann K, Paradis P, et al. Endothelin-1 overexpression exacerbates atherosclerosis and induces aortic aneurysms in apolipoprotein E knockout mice. *Arterioscler Thromb Vasc Biol.* (2013) 33:2306–15. doi: 10.1161/ATVBAHA.113.302028
112. Roth L, Rombouts M, Schrijvers DM, Lemmens K, De Keulenaer GW, Martinet W, et al. Chronic intermittent mental stress promotes atherosclerotic plaque vulnerability, myocardial infarction and sudden death in mice. *Atherosclerosis.* (2015) 242:288–94. doi: 10.1016/j.atherosclerosis.2015.07.025
113. Giannarelli C, Rodriguez DT, Zafar MU, Christoffel D, Vialou V, Peña C, et al. Susceptibility to chronic social stress increases plaque progression, vulnerability and platelet activation. *Thromb Haemost.* (2017) 117:816–8. doi: 10.1160/TH16-10-0817
114. Mury P, Chirico EN, Mura M, Millon A, Canet-Soulas E, Pialoux V. Oxidative stress and inflammation, key targets of atherosclerotic plaque progression and vulnerability: potential impact of physical activity. *Sports Med.* (2018) 48:2725–41. doi: 10.1007/s40279-018-0996-z
115. Nation DA, Gonzales JA, Mendez AJ, Zaias J, Szeto A, Brooks LG, et al. The effect of social environment on markers of vascular oxidative stress and inflammation in the Watanabe heritable hyperlipidemic rabbit. *Psychosom Med.* (2008) 70:269–75. doi: 10.1097/PSY.0b013e3181646753
116. Legein B, Temmerman L, Biessen EA, Lutgens E. Inflammation and immune system interactions in atherosclerosis. *Cell Mol Life Sci.* (2013) 70:3847–69. doi: 10.1007/s00018-013-1289-1
117. Shao BZ, Han BZ, Zeng YX, Su DF, Liu C. The roles of macrophage autophagy in atherosclerosis. *Acta Pharmacol Sin.* (2016) 37:150–6. doi: 10.1038/aps.2015.87
118. Kraft C, Martens S. Mechanisms and regulation of autophagosome formation. *Curr Opin Cell Biol.* (2012) 24:496–501. doi: 10.1016/j.ceb.2012.05.001
119. Xu J, Kitada M, Ogura Y, Koya D. Relationship between autophagy and metabolic syndrome characteristics in the pathogenesis of atherosclerosis. *Front Cell Dev Biol.* (2021) 9:641852. doi: 10.3389/fcell.2021.641852
120. Evans TD, Jeong SJ, Zhang X, Sergin I, Razani B. TFEB and trehalose drive the macrophage autophagy-lysosome system to protect against atherosclerosis. *Autophagy.* (2018) 14:724–6. doi: 10.1080/15548627.2018.1434373
121. Grootaert MO, da Costa Martins PA, Bitsch N, Pintelon I, De Meyer GR, Martinet W, et al. Defective autophagy in vascular smooth muscle cells accelerates senescence and promotes neointima formation and atherogenesis. *Autophagy.* (2015) 11:2014–32. doi: 10.1080/15548627.2015.1096485
122. Li BH, Yin YW, Liu Y, Pi Y, Guo L, Cao XJ, et al. TRPV1 activation impedes foam cell formation by inducing autophagy in oxLDL-treated vascular smooth muscle cells. *Cell Death Dis.* (2014) 5:e1182. doi: 10.1038/cddis.2014.146
123. Grootaert M, Moulis M, Roth L, Martinet W, Vindis C, Bennett MR, et al. Vascular smooth muscle cell death, autophagy and senescence in atherosclerosis. *Cardiovasc Res.* (2018) 114:622–34. doi: 10.1093/cvr/cvy007
124. Miao J, Zang X, Cui X, Zhang J. Autophagy, hyperlipidemia, and atherosclerosis. *Adv Exp Med Biol.* (2020) 1207:237–64. doi: 10.1007/978-981-15-4272-5_18
125. Kim KH, Lee MS. Autophagy–a key player in cellular and body metabolism. *Nat Rev Endocrinol.* (2014) 10:322–37. doi: 10.1038/nrendo.2014.35
126. Weiland A, Wang Y, Wu W, Lan X, Han X, Li Q, et al. Ferroptosis and its role in diverse brain diseases. *Mol Neurobiol.* (2019) 56:4880–93. doi: 10.1007/s12035-018-1403-3
127. Hirschhorn T, Stockwell BR. The development of the concept of ferroptosis. *Free Radic Biol Med.* (2019) 133:130–43. doi: 10.1016/j.freeradbiomed.2018.09.043
128. Hu H, Chen Y, Jing L, Zhai C, Shen L. The link between ferroptosis and cardiovascular diseases: a novel target for treatment. *Front Cardiovasc Med.* (2021) 8:710963. doi: 10.3389/fcvm.2021.710963

129. Bai T, Li M, Liu Y, Qiao Z, Wang Z. Inhibition of ferroptosis alleviates atherosclerosis through attenuating lipid peroxidation and endothelial dysfunction in mouse aortic endothelial cell. *Free Radic Biol Med.* (2020) 160:92–102. doi: 10.1016/j.freeradbiomed.2020.07.026
130. Zhou B, Liu J, Kang R, Klionsky DJ, Kroemer G, Tang D. Ferroptosis is a type of autophagy-dependent cell death. *Semin Cancer Biol.* (2020) 66:89–100. doi: 10.1016/j.semcancer.2019.03.002
131. Stockwell BR, Jiang X, Gu W. Emerging mechanisms and disease relevance of ferroptosis. *Trends Cell Biol.* (2020) 30:478–90. doi: 10.1016/j.tcb.2020.02.009
132. Li L, Wang H, Zhang J, Chen X, Zhang Z, Li Q. Effect of endothelial progenitor cell-derived extracellular vesicles on endothelial cell ferroptosis and atherosclerotic vascular endothelial injury. *Cell Death Discov.* (2021) 7:235. doi: 10.1038/s41420-021-00610-0
133. Ouyang S, You J, Zhi C, Li P, Lin X, Tan X, et al. Ferroptosis: the potential value target in atherosclerosis. *Cell Death Dis.* (2021) 12:782. doi: 10.1038/s41419-021-04054-3
134. Zhou Y, Zhou H, Hua L, Hou C, Jia Q, Chen J, et al. Verification of ferroptosis and pyroptosis and identification of PTGS2 as the hub gene in human coronary artery atherosclerosis. *Free Radic Biol Med.* (2021) 171:55–68. doi: 10.1016/j.freeradbiomed.2021.05.009
135. Guo S, Li L, Yin H. Cholesterol homeostasis and liver X receptor (LXR) in atherosclerosis. *Cardiovasc Hematol Disord Drug Targets.* (2018) 18:27–33. doi: 10.2174/1871529X18666180302113713
136. Hafiane A, Gasbarrino K, Daskalopoulou SS. The role of adiponectin in cholesterol efflux and HDL biogenesis and metabolism. *Metab Clin Exp.* (2019) 100:153953. doi: 10.1016/j.metabol.2019.153953
137. Favari E, Chroni A, Tietge UJ, Zanotti I, Escolà-Gil JC, Bernini F. Cholesterol efflux and reverse cholesterol transport. *Handb Exp Pharmacol.* (2015) 224:181–206. doi: 10.1007/978-3-319-09665-0_4
138. Annema W, Tietge UJ. Role of hepatic lipase and endothelial lipase in high-density lipoprotein-mediated reverse cholesterol transport. *Curr Atheroscler Rep.* (2011) 13:257–65. doi: 10.1007/s11883-011-0175-2
139. Demina EP, Miroshnikova VV, Schwarzman AL. Role of the ABC transporters A1 and G1, key reverse cholesterol transport proteins, in atherosclerosis. *Mol Biol.* (2016) 50:223–30. doi: 10.1134/S0026893316020047
140. Groenen AG, Halmos B, Tall AR, Westerterp M. Cholesterol efflux pathways, inflammation, and atherosclerosis. *Crit Rev Biochem Mol Biol.* (2021) 56:426–39. doi: 10.1080/10409238.2021.1925217
141. Ren K, Li H, Zhou HF, Liang Y, Tong M, Chen L, et al. Mangiferin promotes macrophage cholesterol efflux and protects against atherosclerosis by augmenting the expression of ABCA1 and ABCG1. *Aging.* (2019) 11:10992–1009. doi: 10.18632/aging.102498
142. Ou X, Gao JH, He LH, Yu XH, Wang G, Zou J, et al. Angiopoietin-1 aggravates atherosclerosis by inhibiting cholesterol efflux and promoting inflammatory response. *Biochim Biophys Acta Mol Cell Biol Lipids.* (2020) 1865:158535. doi: 10.1016/j.bbalip.2019.158535

Conflict of Interest: The authors declare that the research was conducted in the absence of any commercial or financial relationships that could be construed as a potential conflict of interest.

Publisher's Note: All claims expressed in this article are solely those of the authors and do not necessarily represent those of their affiliated organizations, or those of the publisher, the editors and the reviewers. Any product that may be evaluated in this article, or claim that may be made by its manufacturer, is not guaranteed or endorsed by the publisher.

frontiers in Cardiovascular Medicine

ORIGINAL RESEARCH
published: 20 December 2021
doi: 10.3389/fcvm.2021.752305

Stressor-Induced "Inflammaging" of Vascular Smooth Muscle Cells via Nlrp3-Mediated Pro-inflammatory Auto-Loop

Jaqueline Herrmann[1,2], *Mengdi Xia*[1,3], *Manasa Reddy Gummi*[1], *Anna Greco*[1], *Annika Schacke*[1], *Markus van der Giet*[1]*, *Markus Tölle*[1] *and Mirjam Schuchardt*[1]

[1] *Department of Nephrology and Medical Intensive Care, Charité – Universitätsmedizin Berlin, Cooperate Member of Freie Universität and Humboldt Universität, Berlin, Germany,* [2] *Department of Chemistry, Biochemistry and Pharmacy, Freie Universität Berlin, Berlin, Germany,* [3] *Department of Nephrology, Second Clinical Medical Institution of North Sichuan Medical College (Nanchong Central Hospital), Nanchong, China*

OPEN ACCESS

Edited by:
Masuko Ushio-Fukai,
Augusta University, United States

Reviewed by:
Delphine Gomez,
University of Pittsburgh, United States
David Anthony Tulis,
The Brody School of Medicine at East Carolina University, United States
Margreet R. De Vries,
Leiden University Medical Center, Netherlands

***Correspondence:**
Markus van der Giet
markus.vandergiet@charite.de

Specialty section:
This article was submitted to Atherosclerosis and Vascular Medicine, a section of the journal Frontiers in Cardiovascular Medicine

Received: *02 August 2021*
Accepted: *29 November 2021*
Published: *20 December 2021*

Citation:
Herrmann J, Xia M, Gummi MR, Greco A, Schacke A, van der Giet M, Tölle M and Schuchardt M (2021) Stressor-Induced "Inflammaging" of Vascular Smooth Muscle Cells via Nlrp3-Mediated Pro-inflammatory Auto-Loop. Front. Cardiovasc. Med. 8:752305. doi: 10.3389/fcvm.2021.752305

Calcification of the vessel wall as one structural pathology of aged vessels is associated with high cardiovascular mortality of elderly patients. Aging is linked to chronic sterile inflammation and high burden of reactive oxygen species (ROS), leading to activation of pattern recognition receptors (PRRs) such as Nlrp3 in vascular cells. The current study investigates the role of PRR activation in the calcification of vascular smooth muscle cells (VSMCs). Therefore, *in vitro* cell culture of primary rat VSMCs and *ex vivo* aortic stimulations were used to analyze osteogenic, senescence and inflammatory markers via real-time PCR, *in situ* RNA hybridization, Western Blot, photometric assays and histological staining. Induction of ROS and DNA-damage by doxorubicin induces a shift of VSMC phenotype toward the expression of osteogenic, senescence and inflammatory proteins. Induction of calcification is dependent on Nlrp3 activity. Il-1β as a downstream target of Nlrp3 induces the synthetic, pro-calcifying VSMC phenotype. Inhibition of PRR with subsequent reduction of chronic inflammation might be an interesting target for reduction of calcification of VSMCs, with subsequent reduction of cardiovascular mortality of patients suffering from vessel stiffness.

Keywords: calcification, senescence, inflammation, Nlrp3, smooth muscle cell

INTRODUCTION

Cardiovascular disease (CVD) is the most critical age-related cause of death. Almost 70% of patients with new CVD are over 75 years old, so that the age might be the most prominent cardiovascular risk factor (1). One sign of structural pathology of the vessel wall associated with vascular aging is medial calcification, leading to increased vessel stiffness and pulse-wave velocity (2, 3). Medial calcification is common in patients with other comorbidities as e.g., chronic kidney disease (CKD) (2, 4, 5). Until now, no therapy exists to effectively reduce the increased cardiovascular risk associated with vessel calcification (3).

In particular involved in calcification of the medial layer of the vessel wall is the accumulation of senescent vascular smooth muscle cells (VSMCs) with a senescence-associated secretory phenotype (SASP) (6). Senescent cells express typical senescence markers [e.g., p53/p21, lysosomal senescence-associated β-galactosidase activity (SA-β-Gal), γH2A.X], and show an increased

vulnerability to exogenous stressors (7–9). VSMCs physiologically have a contractile phenotype and express specific VSMC marker proteins (e.g., SM22α, Myh11, Cnn1, Acta2). Due to phenotype plasticity, VSMCs can adapt an osteoblast-like phenotype characterized by decreased expression of VSMC markers and increased expression of osteoblast markers e.g., core binding factor alpha-1 (Cbfa-1), tissue non-specific alkaline phosphatase (Alp), osteopontin (Opn), and bone morphogenetic protein-2 (Bmp-2) (9, 10). Recently, Shanahan's group pointed out that the DNA damage-induced calcification is dependent on activation of Cbfa1 in VSMCs (11). They found Cbfa1 to be involved in DNA damage response and therefore bridging osteogenic transition and apoptosis in the mineralization process (11).

During physiological aging, a chronic sterile inflammation, known as "inflammaging," develops. This "inflammaging" is primarily based on mechanisms of the innate immune system that involve activation of pattern recognition receptors (PRRs) (12, 13). PRRs are a link between inflammation and cellular senescence. PRRs are mainly transmembrane toll-like receptors (Tlrs) and cytoplasmic Nod-like receptor (Nlr) inflammasomes (14). The Nlrp3 is the best characterized inflammasome and is expressed in VSMCs (15). The activation of Nlr inflammasomes induces the secretion of Il-1 cytokines e.g., Il-1β (16). Il-1β has strong pro-inflammatory effects by activating different Il-1 receptors (Il-1Rs). It induces the expression of other pro-inflammatory cytokines, especially Il-6, and can increase its own expression by a positive feedback mechanism (17). Cytokines and chemokines as major pro-inflammatory mediators can contribute to chronic inflammation and senescence (18).

Doxorubicin (DOX) is an anthracycline antitumor drug (19). DOX is known to induce several kinds of DNA damages by intercalation, generation of free radicals, DNA-binding, alkylation and cross-linking, DNA strands separation, influenced helicase activity and inhibition of topoisomerase II (19). Previous studies have not only investigated effects of DOX on stress-induced senescence (20) but also, induction of Alp activity upon DOX treatment; however, only after seven days of treatment (20). In addition, recent studies have shown the important role of DNA-damage response and the Cbfa1-dependent link to the calcification process of VSMCs (9, 11). Cobb et al. pointed out that the DNA damage-induced calcification is dependent on activation of Cbfa1 in VSMCs (11). They found Cbfa1 to be involved in DNA damage response and therefore bridging osteogenic transition and apoptosis in the mineralization process (11).

However, there are no detailed studies on the relationship of stress-induced senescence as e.g., caused by DOX, subsequent activation of Nlrp3-dependent pro-inflammatory signaling and calcification in VSMCs. We aim to show that stressor-induced senescence in VSMCs results in a pro-inflammatory response and induction of calcification. Accordingly, we used DOX as stressor. We are aware that DOX might not reflect the whole spectrum of senescence induction in VSMCs; however, DNA damage, upregulated under treatment with DOX, is a known and well-documented inducer of cellular senescence (9, 11).

Therefore, the current study investigates the effects of the stressor DOX on the initiation of processes of acute "inflammaging" and vascular calcification. The increase in calcification upon DOX treatment was dependent on the activation of the Nlrp3 inflammasome. Il-1β as Nlrp3 downstream effector amplifies its own expression. The initial stressor-induced acute "inflammaging" process then can be continued via a Nlrp3 inflammasome-mediated auto-inflammatory loop resulting in SASP and calcification of VSMCs.

Abbreviations: Acta2, Actin alpha 2; Alp, Alkaline Phosphatase; Asc, Apoptosis-Associated Speck-like Protein Containing a Caspase-Recruitment Domain; ATM, Ataxia–Telangiectasia Mutated; BCA, Bicinchonic Acid; Bmp-2, Bone Morphogenetic Protein-2; Calc M, Calcification Medium; Cbfa-1, Core Binding Factor alpha 1; Cnn1, Calponin; Ctrl M, Control Medium; CVD, Cardiovascular Disease; DAMP, Damage Associated Molecular Pattern; DHE, Dihydroethidium; DMEM, Dulbecco's Modified Eagle Medium; DOX, Doxorubicin; FCS, Fetal Calf Serum; Il-1β, Interleukin 1 β; Il-6, Interleukin 6; Myh11, Myosin Heavy Chain 11; Nlr, Nod-like Receptor; Nlrp3, Nod-like receptor family pyrin domain containing 3; Opn, Osteopontin; PBS, Phosphate Buffered Saline; PRRs, Pattern Recognition Receptors; ROS, Reactive Oxygen Species; Tlr, Toll-like Receptor; SA-β-Gal, Senescence Associated β-Galactosidase; SASP, Senescence Associated Secretory Phentoype; Sm22α, Smooth Muscle Protein 22-alpha; VSMCs, Vascular Smooth Muscle Cells.

MATERIALS AND METHODS

All cell culture components were obtained from Biochrom AG and Bio and Sell. DOX was obtained from Thermo Fisher. Recombinant rat Il-6 and Il-1β were purchased from PeproTech. VAS2870 was obtained from Sigma Aldrich and MCC950 from Invivogen. Tiron was purchased from Biozol and TAK242 from Biomol.

Animals

All experiments with animals were done under minimal animal suffering and in accordance with the EU Directive 2010/63/EU. The experiments were approved by the Landesamt fuer Gesundheit und Soziales Berlin (T0211/02), Germany and the Charité - Universitätsmedizin Berlin, Germany.

Wistar rats were purchased from Janvier Labs. $Nlrp3^{-/-}$ and $Nlrp3^{+/+}$ (genetic background: C57BL/6) were bred at the Charité-Universitätsmedizin Berlin animal facility.

Euthanasia of animals was accomplished with intraperitoneal injection of sodium pentobarbital (rats: 400 mg/kg body weight, mice: 200 mg/kg body weight).

VSMCs Cell Culture

Primary rat VSMCs from aortic tissue (aortic arch and thoracic aorta) of Wistar rats (mean age 4 months, male/female) were cultured by the outgrowth technique described previously (21). VSMCs at passages 3 to 7 were used for experiments. Cells were cultured in a humidified incubator at 37°C with 5% carbon dioxide. If not stated otherwise, VSMCs were cultured in Dulbecco Modified Eagle Medium (DMEM) containing 1 g/l glucose, supplemented with 10% fetal calf serum (FCS), penicillin (100 U/ml) and streptomycin (0.1 mg/ml) (culture medium). For gene expression, ROS detection, protein secretion and immunohistology experiments, cells were serum-starved for

24 h and stimulated using DMEM with 4.5 g/l glucose (w/o phenol red), supplemented with 1% glutamine, penicillin (100 U/ml) and streptomycin (0.1 mg/ml).

Preparation of Aortic Rings for *ex vivo* Experiments

For *ex vivo* stimulation of aortic tissue, the adventitia was removed. Thoracic aortas of rats (mean age 4 months, male) or Nlrp3$^{-/-}$ and Nlrp3$^{+/+}$ mice (mean age 11 months, male/female) were dissected into aortic rings of equal size and incubated in a well-plate with the respective stimulation medium for 24 h or 14 days, respectively. Each stimulation contained several aortic rings from different aortic parts (aortic arch, different segments of descending aorta proximal to distal), which were equally distributed between stimulation and respective controls. The incubation procedure of the tissue took place in a humidified incubator at 37°C and 5% carbon dioxide.

In vitro and *ex vivo* Calcification

Calcification was induced by exposing VSMCs or aortic rings (rat and mice) to DMEM containing 4.5 g/l glucose, supplemented with 15% FCS, 284 μmol/l ascorbic acid and 5 mmol/l inorganic phosphate, penicillin (100 U/ml) and streptomycin (0,1 mg/ml) [Calcification Medium (Calc M)]. As Control Medium (Ctrl M) served DMEM containing 4.5 g/l glucose, supplemented with antibiotics. Calcification was induced over 14 days of stimulation with Ctrl M, Calc M and in co-stimulation with DOX (10 or 100 nmol/l), Il-6 (100 ng/ml), Il-β (100 ng/ml) and MCC950 (50 μmol/l). Medium was replaced every two to three days.

Gene Expression

VSMCs were serum-starved for 24 h prior to stimulation for 48 h. Cells were washed after stimulation with phosphate buffered saline (PBS) on ice and lysed with RLT™ cell lysis buffer (Qiagen). RNA was isolated according to the RNeasy™ Mini kit protocol (Qiagen). The RNA was reverse transcribed using the High-Capacity cDNA Reverse Transcription Kit™ (Applied Biosystems) according to the manufacturer's instructions. For the quantitative determination of mRNA expression, the iQ™ SYBR Green SuperMix and the CFX384 real-time PCR detection system (Biorad, CFX software version 3.1) were used. The oligonucleotides (**Supplementary Table 1**) were synthesized by TibMolBiol. Each sample was performed as technical duplicate for real-time PCR. β-actin and Gapdh were used as housekeeper genes for normalization. Analysis was performed with the ΔΔCT-method.

Measurement of Alp Activity

After stimulation, VSMCs were lysed and scraped in 0.2% Triton X/PBS lysis buffer. Alp activity was assessed using a p-nitrophenyl phosphate-based Alp Assay Kit (Abcam) according to the manufacturer's recommendations. Protein content was determined with the bicinchoninic acid (BCA) protein assay kit (Pierce) and was used for normalization. Photometric measurements were conducted with a Multiskan Spectrum (Thermo Electron Corporation).

Quantification of Calcium Content

For quantification of calcification, VSMCs or aortic rings were decalcified in 0.6 mol/l HCl overnight or for 24 h, respectively. After decalcification, cells were washed with PBS and lysed in 0.1 mol/l NaOH/0.1% SDS buffer. The protein content was quantified using BCA protein assay kit (Pierce). Aortic rings were dried and weighed. Calcium content was quantified using the colorimetrical o-cresolphthalein method (Colorimetric Calcium Assay, ScienCell) according to the manufacturer's recommendation. Photometric measurements were conducted with a Multiskan Spektrum (Thermo Electron Corporation). Protein content (*in vitro*) or aortic dry weight (*ex vivo*) was used for normalization, respectively.

Histological Staining of Calcium Deposits

Upon stimulation of VSMCs for 14 days, the cells were fixed with 4% buffered formaldehyde, washed with PBS and distilled deionized water and treated with Alizarin Red solution (2%, pH 4.2) for 20 min, then washed again and imaged.

Upon stimulation of aortic rings for 14 days, the tissue was fixed overnight, transferred to 70% ethanol, and embedded in paraffin via automatic procedure. The aortas were serially cut into 4 μm sections, stained with Alizarin Red solution (0.5%, pH 4.2) and imaged. For all histological imaging, the Axiovert 200M microscope (Zeiss) with Zen2 software (Blue edition, Zeiss) was used.

ROS Staining

VSMCs were seeded in 8-well slides (LabTec, Thermo Fisher, μ-slide, Ibidi), serum-starved for 24 h, and stimulated for 30 min as indicated. Afterwards, cells were washed and treated with 30 μmol/l dihydroethidium (DHE) (Molecular Probes) for 30 min. Cells were fixed with cold formalin (4%) for 5 min and subsequently washed with PBS. LabTec were mounted with ProLong™ Gold antifade mount (Thermo Fisher) and stored in the dark until imaging. For μ-slides, wells were covered with PBS and immediately imaged. A more detailed description of the staining procedure and data analysis can be found in the **Supplementary Material**. For all imaging of fluorescence stainings, an Axiovert 200M microscope (Zeiss) with Zen2 software (Blue edition, Zeiss) was used.

Immunohistology and mRNA *in situ* Staining

VSMCs were stained for SA-β-Gal activity, histone γH2A.X, Bmp-2, Opn and p21 mRNA according to a previously published protocol (22) with some modifications. Briefly, cells were seeded in 8-well LabTec chamber slides (Thermo Fisher) or μ-slide (Ibidi), serum-starved for 24 h and stimulated for 48–72 h. Cells were stained for the desired target and imaged. A more detailed description of the staining procedure and data analysis can be found in the **Supplementary Material**. Quantification of fluorescence intensity was done with Zen2 (Blue edition, Zeiss) and Fiji/ImageJ.

Western Blot

VSMCs were stimulated with DOX (500 and 1,000 nmol/l) and Il-1β (100 ng/ml) in cell culture medium for 48 h. For protein extraction, cells were washed with ice-cold PBS and lysed in cold RIPA buffer (Thermo Fisher Scientific). Protein content was assessed with BCA protein assay kit (Pierce). 15–10 μg protein per lane (p21: 15 μg, all others 10 μg) was applied on the respective gel. Protein samples were mixed and dissolved in 4× Laemmli buffer (Biorad) and heated to 95°C for 15 min. The proteins were separated on 12% TGX Gels (Biorad) and transferred onto a polyvinylidene difluoride membrane. The membranes were immunoblotted overnight at 4°C with primary antibodies: rabbit anti-p21 (1:2,500, ab109199, Abcam), rabbit anti-Alp (1:500, 7H11L3, Invitrogen), rabbit anti-Cbfa1 (1:1,1000, sc-10758, Santa Cruz), and mouse anti-β-actin (1:5,000 8H10D10, Cell Signaling Technology). After washing five times for five min each with TBST, the membranes were incubated with conjugated fluorescent secondary antibodies [anti-rabbit-StarBright Blue700 (1:2,500, #12004162, Biorad) and anti-mouse-StarBright Blue520 (1:2,500, #12005867)]. The bands were visualized using a ChemiDoc MP Imaging System (Biorad).

Luminex™

VSMCs were serum-starved for 24 h prior to stimulation with Il-1β (100 ng/ml) and respective antagonists [VAS2870 (10 μM), MCC950 (50 μM), Tiron (10 mM), TAK242 (10 μM)] for 48 h. Rat aortic rings were stimulated with DOX (1000 nmol/l) and MCC950 (50 μM) for 24 h. After stimulation, supernatant was collected for cytokine quantification. Cytokine concentrations in the supernatant were determined using the Milliplex™ Cytokine Kit (Millipore) according to the manufacturer's instructions. Measurements were conducted using the Bio-Plex device and respective Bio-Plex software (version 6.1, Biorad). Cells were washed with cold PBS and lysed in NP40 buffer, followed by protein quantification using BCA protein assay kit (Pierce). Aortic rings were dried and weighed for normalization.

Statistical Analysis

Data are provided as mean ± SEM of at least 3 independent experiments. Statistical analysis was performed using GraphPad Prism software (version 6.0). The one-way Anova with multiple comparisons or Wilcoxon matched paired test were applied to evaluate differences between treatment groups. A p-value < 0.05 was considered as statistically significant.

RESULTS

Stressor-Induced Calcification With Osteogenic Transition

Stimulation with calcifying medium robustly induced calcification of VSMCs after 14 d (**Figure 1A**). Co-stimulation with DOX significantly and dose-dependently reinforced calcification of VSMCs *in vitro*: quantification (**Figure 1A**) shows a significant and dose-dependent induction of calcification under co-stimulation of calcification medium and DOX. This is also visualized by Alizarin Red staining (**Figure 1B**). To confirm these *in vitro* findings, an *ex vivo* setting using aortic rings was conducted. Calcium content of rat aortic rings was quantified upon 14 d of stimulation, and calcification was visualized via Alizarin Red staining (**Figures 1C,D**). DOX stimulation in calcifying medium dose-dependently increases calcium deposition *ex vivo*.

Further evidence for the pro-calcifying potential of DOX derives from mRNA detection of osteogenic markers as Bmp-2, Cbfa1 and Opn, all of them significantly increased upon DOX stimulation. VSMC marker as Acta2, Cnn1, Myh11, and SM22α slightly, but not significantly, decreased under stimulation with DOX (**Figure 2A**). The osteogenic transition is further confirmed by detection of Alp activity increase upon DOX treatment (**Figure 2B**). The induction of calcification markers after stimulation with DOX was confirmed by *in situ* hybridization analysis for Bmp-2 and Opn. Both markers were visualized via fluorescence staining and quantified by counting signal dots per whole image (**Figure 2C**). Although DOX influences cell behavior and growth, the cytotoxicity of DOX in our cell model did not reach statistical significance in the used setting (**Supplementary Figure 1**).

Stressor-Induced Induction of "Inflammaging"

Il-1β and Il-6 are known essential components of the SASP (23). Therefore, we investigated the effect of DOX on the expression of both cytokines. DOX induced Il-1β and Il-6 mRNA expression in VSMCs (**Figure 3A**). It is already known from the literature that the Nlrp3 inflammasome is involved in the phenotype switching of VSMCs and in Il-β production (15). Therefore, we measured the mRNA expression of Nlrp3, its cofactor Asc and the associated enzyme caspase-1 that cleaves the preform of Il-1β (pre-Il-1β) into active Il-1β. The mRNA expression of all three proteins was significantly increased upon DOX stimulation (**Figure 3A**). Also, the secretion of Il-1β was significantly upregulated after DOX stimulation, while no significant secretion of Il-6 was found upon DOX treatment. The DOX-induced Il-1β secretion was reduced by co-stimulation with Nlrp3 inhibitor MCC950 (**Figure 3B**). As Il-1β and Il-6 are both components of the SASP, we tested the pro-calcifying potential of both substances and found Il-1β to significantly induce calcification, whereas Il-6 did not exhibit calcifying potential in our model (**Figure 3C**). To validate the role of the Nlrp3 inflammasome for calcification, we used an *ex vivo* setting with aortic rings from $Nlrp3^{-/-}$ and respective control mice ($Nlrp3^{+/+}$). While DOX significantly induced aortic calcification in $Nlrp3^{+/+}$, the effect is lost in aortas from $Nlrp3^{-/-}$ mice (**Figure 3D**).

To further verify the involvement of Il-1β as effector molecule of the Nlrp3 inflammasome and of Il-6, we investigated their effect on mRNA expression of inflammation, senescence and calcification markers using real-time PCR and *in situ* hybridization. Il-1β significantly induces the expression of Il-6 and, in the context of a very potent pro-inflammatory auto-loop, Il-1β itself. In addition, Il-1β induces the expression of Nlrp3 (**Figure 4A**). Upon Il-1β treatment, VSMCs release

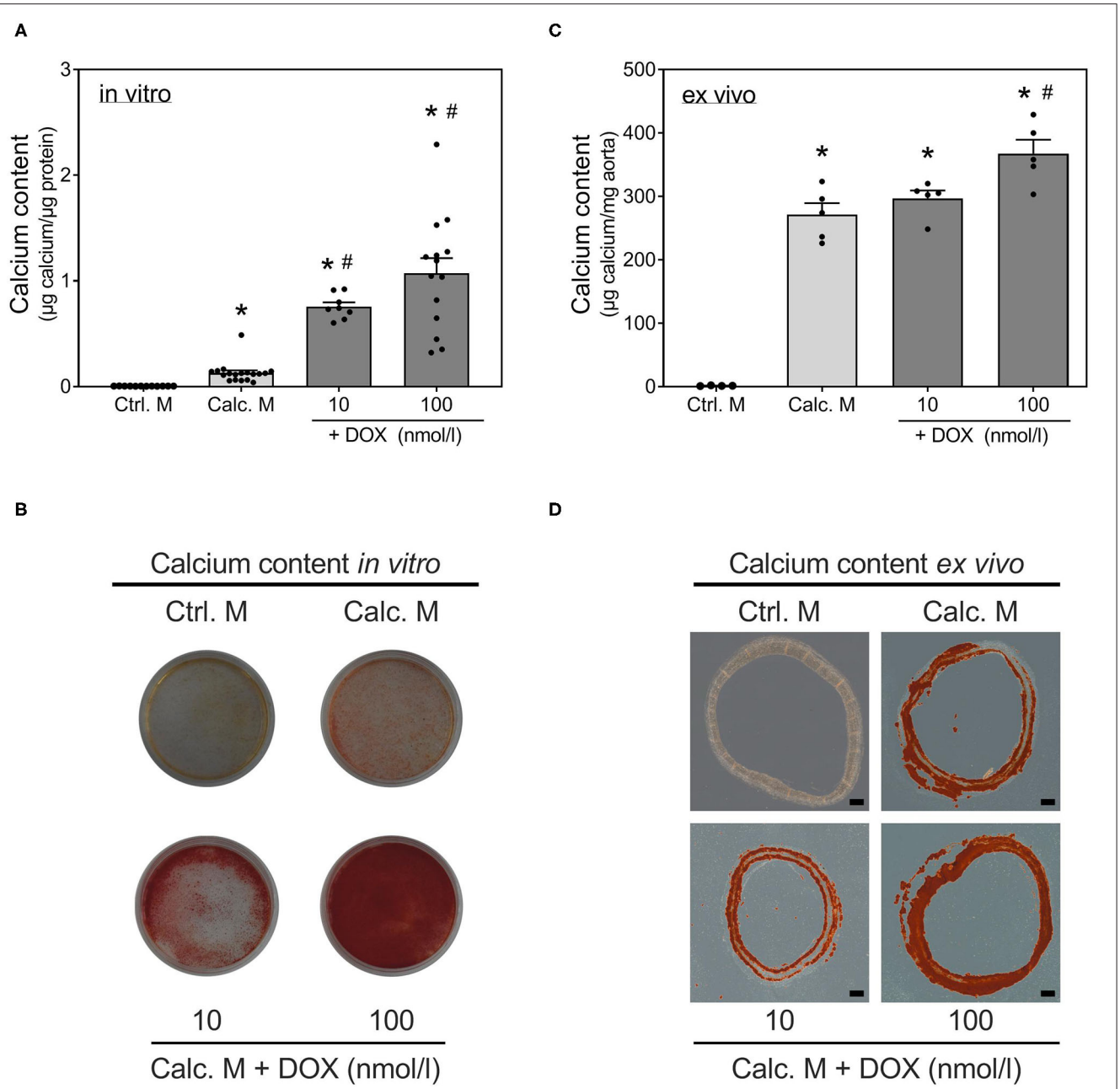

FIGURE 1 | Induction of calcification with doxorubicin. VSMCs **(A,B)** or rat aortic rings **(C,D)** were stimulated with control medium or calcification medium supplemented with DOX as indicated for 14 d. Calcium content was quantified with o-cresolphthalein **(A,C)** and normalized to protein content (µg) **(A)** or aortic weight (mg) **(C)**. Calcium deposits were stained with Alizarin Red **(B,D)**. Data represent mean ± SEM, $n \geq 3$, $^*p < 0.05$ vs. indicated control, $\#p < 0.05$ vs. calcification medium. Pictures show one representative experiment of $n \geq 3$ **(B,D)**, the scale bar indicates a 200 µm section **(D)**.

Il-6 (**Figure 4B**). While the Il-1β-induced expression of the osteogenic marker Bmp-2 increased, the VSMCs marker SM22α, Acta2, and Cnn1 decreased upon Il-1β (**Figure 4C**). The increased mRNA expression of Bmp-2 upon Il-1β stimulation was confirmed by *in situ* hybridization technique. While for Opn mRNA expression via real-time PCR no significant effect could be detected, the *in situ* hybridization found a slight induction (**Figure 4D**).

As already shown in **Figures 1–4**, both DOX and Il-1β induce several markers of calcification. In addition, the protein expression of Cbfa1 and Alp, detected via Western Blot, is increased upon DOX and Il-1β, respectively (**Figures 5A,B**). However, the effects of Il-1β and DOX on senescence markers differ in our experimental model. As shown in **Figure 5C**, ROS (superoxide production) is significantly increased by DOX and Il-1β. ROS are one inducer of DNA damage, which can

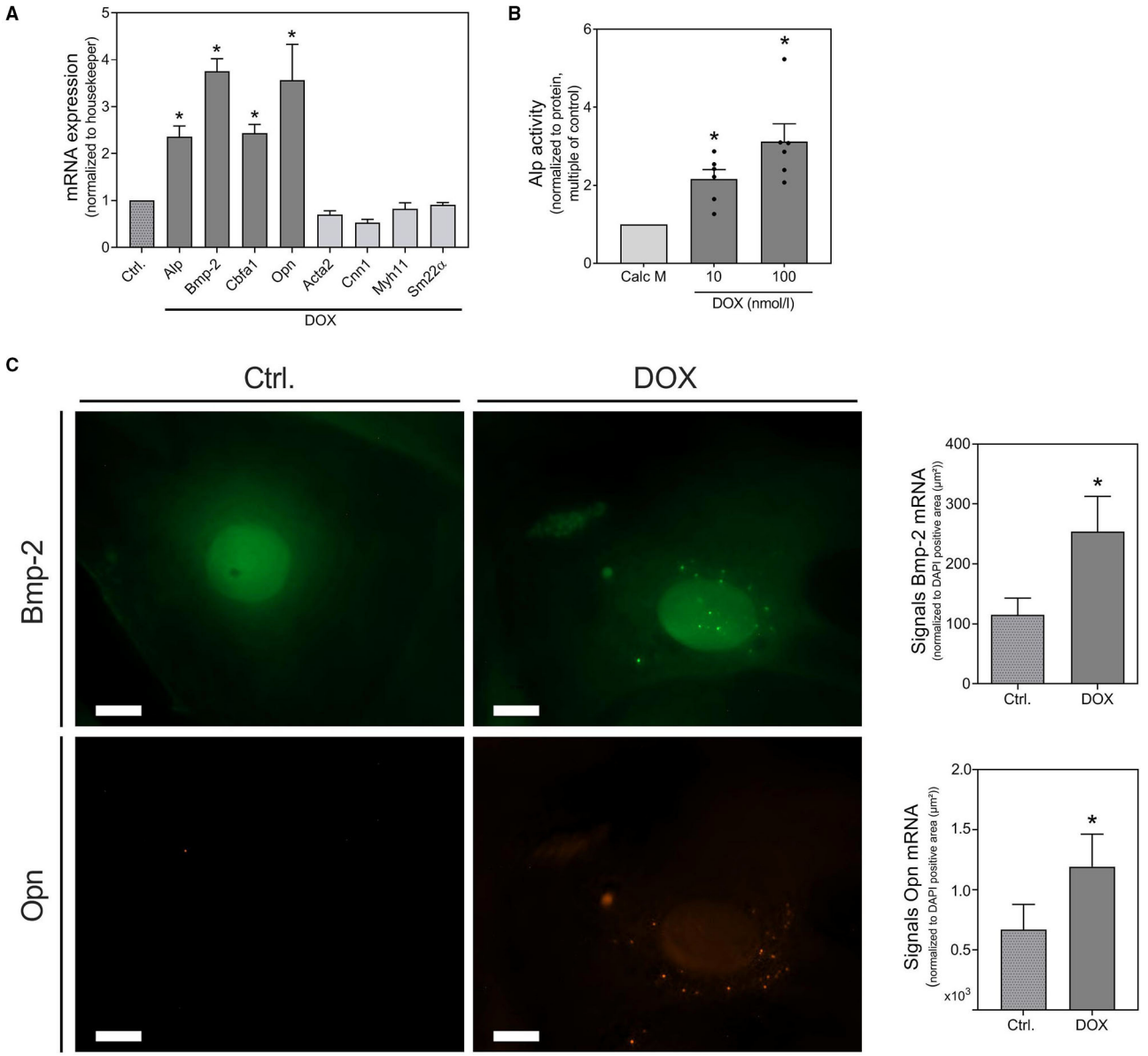

FIGURE 2 | Induction of osteoblastic trans-differentiation by doxorubicin. VSMCs were stimulated in quiescence medium **(A,C)** or calcification medium **(B)** with DOX as indicated or 1,000 nmol/l for 48 h **(A,C)** or 14 d **(B)**. mRNA expression was measured with quantitative real-time PCR **(A)**. Measured thresholds of the respective targets were normalized to the corresponding threshold of housekeeper gene actin before normalization to control **(A)**. Alp activity was measured with a p-nitrophenyl phosphate-based Alp Assay and normalized to protein content (µg/µl) before normalization to control **(B)**. mRNA expression of Bmp-2 and Opn were visualized with RNA *in situ* hybridization staining and were quantified by counting signal dots per whole image, normalized to the DAPI positive cell core area per image (µm^2) **(C)**. Data represent mean ± SEM, $n \geq 3$, $^*p < 0.05$ vs. control. Pictures show a section of a representative experiment of $n \geq 3$, the scale bar indicates a 10 µm section **(C)**. Full representative images are shown in **Supplementary Table 3**.

result in double-strand DNA breaks. A marker of double-strand DNA breaks, the formation of γH2A.X, was significantly increased upon DOX treatment, while it is not affected by Il-1β stimulation (**Figure 5C**). In line, while DOX stimulation results in upregulated expression of the senescence markers p21 and SA-β-Gal, both were not induced by Il-1β (**Figure 5C**). This could be confirmed by p21 protein detection via Western Blot (**Figure 5D**). mRNA detection via real-time PCR confirmed the findings of increased p21 mRNA expression upon DOX (**Figure 5E**) and no effect on p21 expression upon Il-1β treatment (**Figure 5F**). Neither DOX nor Il-1β induced p16 mRNA expression in our cell model (**Figures 5E,F**).

Involved Signaling Pathway

As Il-1β strongly stimulates its own expression, we tested possible mediators of the signaling pathway involved in Il-1β-induced

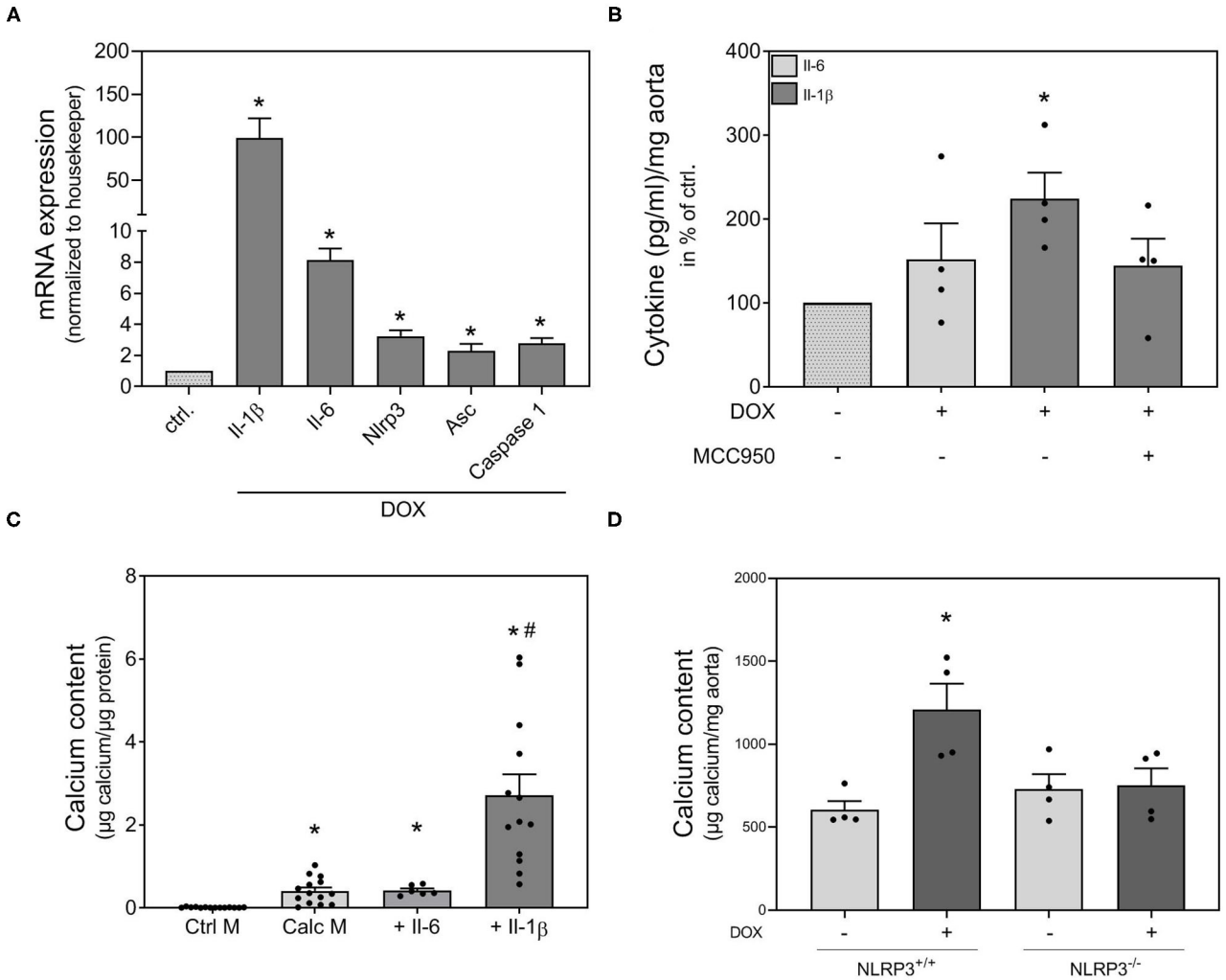

FIGURE 3 | Involvement of Nlrp3 in doxorubicin induced calcification. VSMCs **(A,C)** were stimulated as indicated with 1,000 nmol/l DOX **(A)**, 100 ng/ml Il-1β **(C)** and 100 ng/ml Il-6 **(C)** for 48 h **(A)** or 14 d **(C)** in quiescence medium **(A)**, control medium (Ctrl. M) **(C)** or calcification medium (Calc M) **(C)**. Aortic rings from rats were stimulated in quiescence medium with 1,000 nmol/l DOX and MCC950 (50 µM) as indicated for 24 h **(B)**. Aortic rings from Nlrp3$^{-/-}$ mice and respective controls were stimulated for 14 d in calcification medium with DOX (100 nmol/l) as indicated **(D)**. mRNA expression was measured with quantitative real time PCR **(A)**. Measured thresholds of the respective targets were normalized to the corresponding threshold of housekeeper gene actin before normalization to control **(A)**. Protein secretion was assessed with Luminex™ and normalized to aortic weight (mg) **(B)**. Calcium content was quantified with *o*-cresolphthalein **(C,D)** and normalized to protein content (µg) **(C)** or aortic weight **(D)**. Data represent mean ± SEM, $n \geq 3$, $^*p < 0.05$ vs. control, $\#p < 0.05$ vs. Calc M.

SASP activation. A schema of the Nlrp3 inflammasome activation and the therefore used antagonists is provided in **Figure 6A**. MCC950 was used as Nlrp3 inhibitor. It is already known from the literature that Tlrs work as one initial stimulus for Nlrp3 assembly and that the activation of Tlr2 and Tlr4 are involved in Il-1β release (24, 25). A previous study by our own working group has shown that the Tlr4 is constitutively active in our VSMCs cell model, whereas the Tlr2 is subsequently activated (26). Therefore, we tested the Tlr4 inhibitor TAK242. As increased ROS production serves as second stimulus for Nlrp3 activation (25), we also tested tiron as ROS scavenger. In VSMCs, the NADPH oxidase is one of the leading ROS producers (27). Therefore, the Nox1 inhibitor VAS2870 was also used. Both, Tlr2 as well as Tlr4 expression (first stimulus) and Nox1 expression (second stimulus), were induced in VSMCs upon Il-1β stimulation (**Figure 6B**). Both signals for Nlrp3 assembly could be significantly diminished by co-treatment with VAS2870 and tiron (**Figures 6C,D**). Nlrp3 mRNA expression itself was also diminished by tiron and MCC950 co-treatment, while VAS2870 and TAK242 have no significant effect (**Figure 6E**). Downstream, the Il-1β expression is significantly blocked by VAS2870, tiron, TAK242, and MCC950 (**Figure 6F**). The secretion of Il-6 could be significantly reduced by inhibition of ROS via tiron and Nlpr3 inhibition via MCC950 (**Figure 6G**). To verify the role of the Nlrp3-dependent pathway, we also tested Nlrp3 inhibition with MCC950 for calcification as endpoint. As shown in **Figure 6H**,

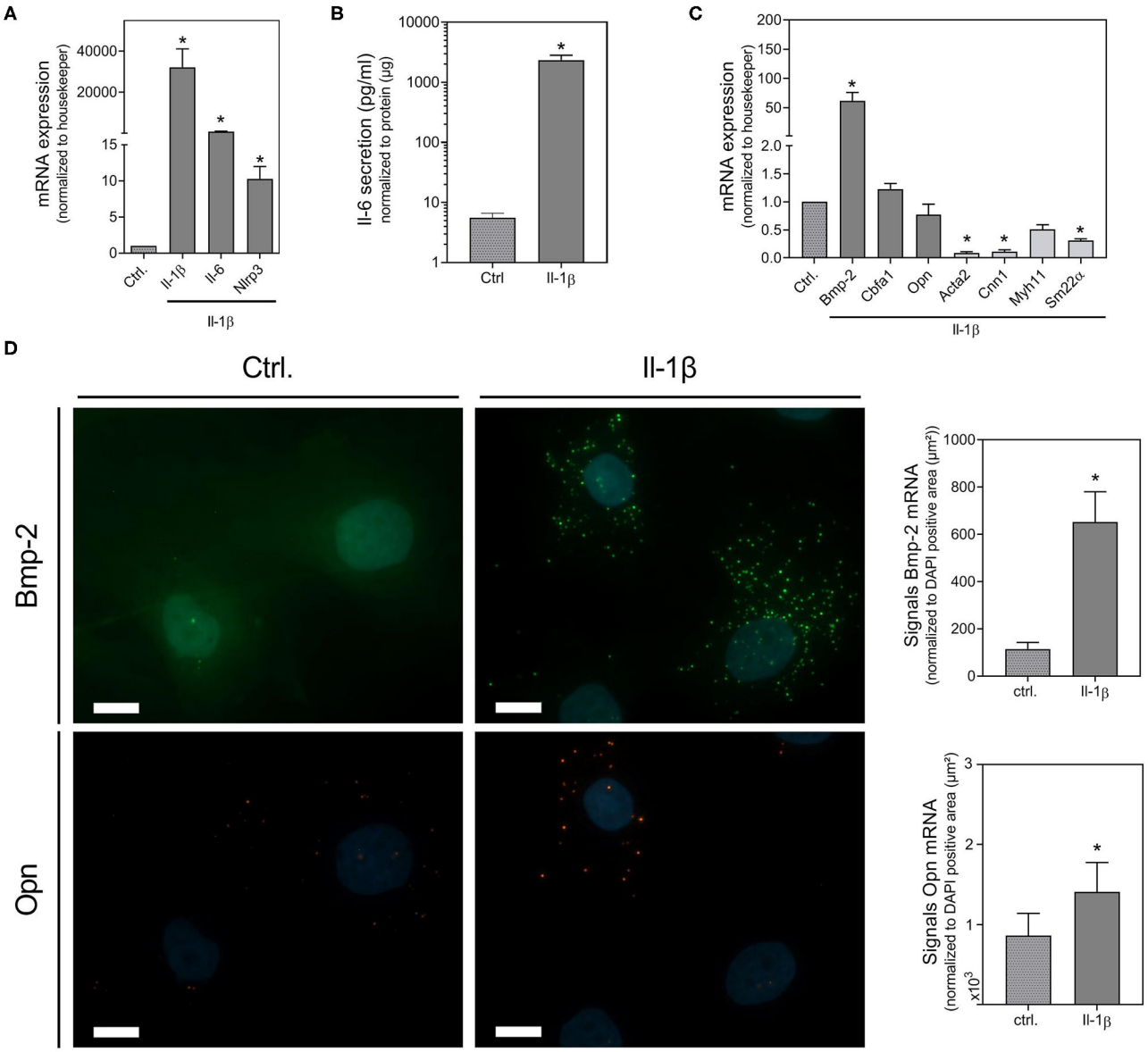

FIGURE 4 | Il-1β induced changes in osteoblastic and pro-inflammatory gene expression and protein secretion. VSMCs were stimulated for 48 h with 100 ng/ml Il-1β. mRNA expression was measured with quantitative real-time PCR **(A,C)**. Measured thresholds of the respective targets were normalized to the corresponding average threshold of housekeeper genes actin and Gapdh before normalization to control **(A,C)**. Secretion of Il-6 was measured with Luminex™ and normalized to protein content (µg) **(B)**. Expression of Bmp-2, Opn were visualized with RNA *in situ* hybridization staining and were quantified by counting signal dots per whole image, normalized to the DAPI positive cell core area per image (μm^2) **(D)**. Data represent mean ± SEM, $n \geq 3$, $^*p < 0.05$ vs. control, pictures show a section of a representative experiment of $n \geq 3$, the scale bar indicates a 10 µm section **(D)**. Full representative images are shown in **Supplementary Table 4**.

both the DOX-and Il-β-induced calcifications are significantly inhibited by MCC950 co-treatment.

DISCUSSION

In the current study, we investigated the effect of ROS induction, DNA damage, and inflammation on the process of cellular senescence and calcification in *in vitro* and *ex vivo* models using rat VSMCs and thoracic aortas from rats and mice. After induction of ROS and DNA-damage by the primary stressor, the Nlrp3 inflammasome is activated with a subsequent auto-inflammatory loop driven by its effector molecule Il-1β.

As primary stressor molecule for VSMCs the anthracycline DOX was used. It has already been shown in literature that DOX causes DNA damage via induction of double strand breaks and ROS and promotes cellular senescence (20). Bielak-Zmijewska et al. investigated several markers of senescence in VSMCs upon DOX treatment (20). Although DOX might not

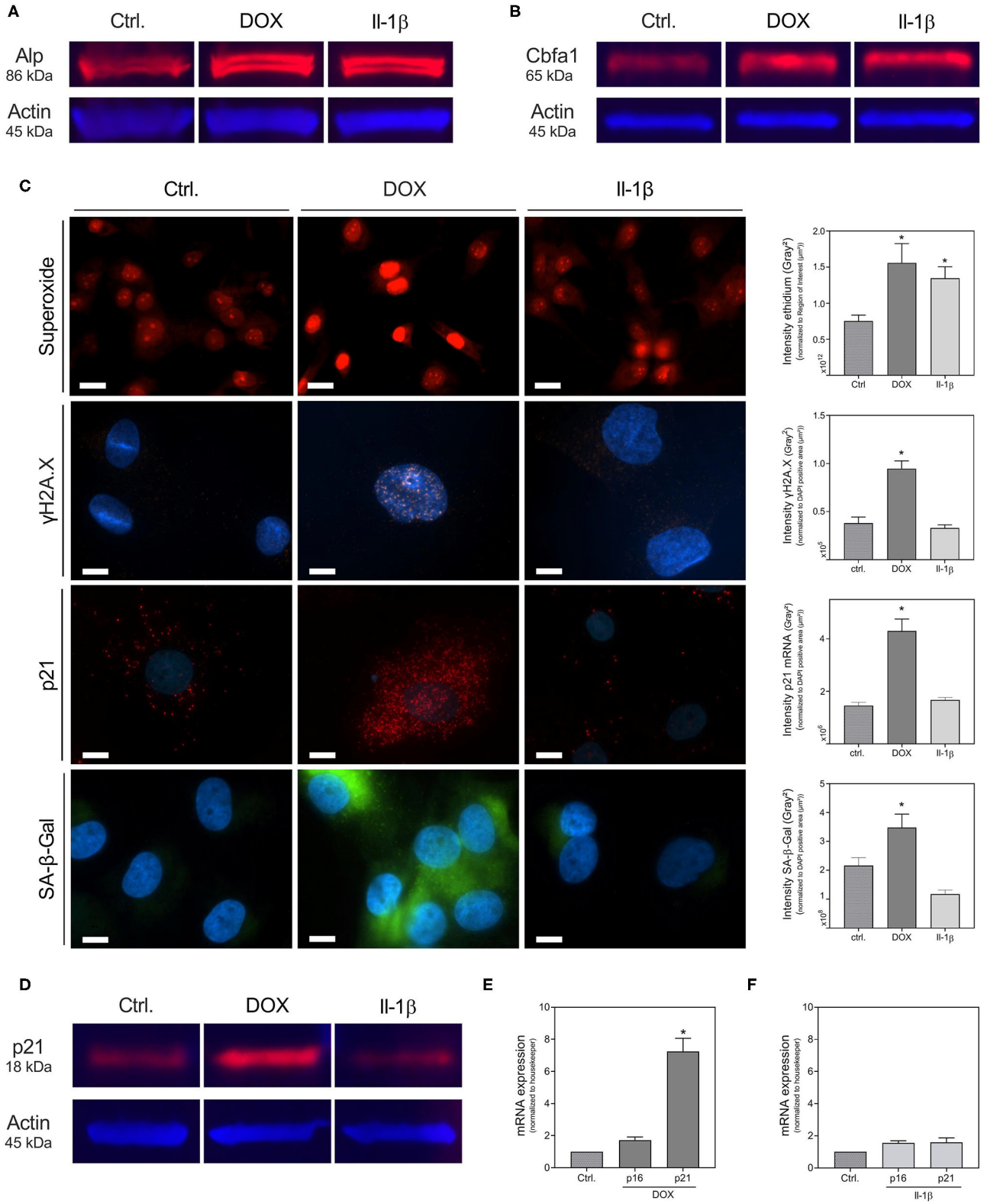

FIGURE 5 | Formation of calcification markers, reactive oxygen species and senescence upon DOX and Il-1β treatment. VSMCs were stimulated for 30 min (superoxide), 48 h [**(A,B)**, γH2A.X, p21 *in situ* **(D–F)**], or 72 h (SA-β-Gal) with 100 ng/ml Il-1β or 1000 nmol/l DOX in quiescence medium **(C,E,F)** or culture medium

(Continued)

FIGURE 5 | (A,B,D). Formation of superoxide was assessed with DHE, expression of γH2A.X was analyzed immunohistochemically, mRNA expression of p21 was assessed with RNA *in situ* hybridization and formation of SA-β-Gal was assessed with Spider staining **(C)**. For quantification of the expression of γH2A.X, mRNA expression of p21 and formation of SA-β-Gal, intensity of the respective fluorescence signal was measured after application of a threshold procedure as described in the supplement and the signal intensity then normalized to the DAPI positive cell core area per image (μm^2). For quantification of DHE, regions of interest were detected with a threshold procedure as described in the supplement and measured intensity was normalized to the area of interest detected by the threshold procedure. Alp protein, Cbfa1 protein and p21 protein were assessed with Western Blot **(A,B,D)**. mRNA expression was measured with quantitative real-time PCR **(E,F)**. Measured thresholds of the respective targets were normalized to actin **(E)** or the corresponding average threshold of housekeeper genes actin and Gapdh **(F)** before normalization to control. Data represent mean ± SEM, $n \geq 3$, $^*p < 0.05$ vs. Control. The Western Blots show a representative experiment of $n = 3$. Full blots are shown in **Supplementary Figures 3–5**. Pictures show a section of a representative experiment of $n \geq 3$, the scale bar indicates a 10 μm section (γH2A.X, p21, SA-β-Gal) or a 20 μm section (superoxide). Full representative images are shown in **Supplementary Tables 3–5**.

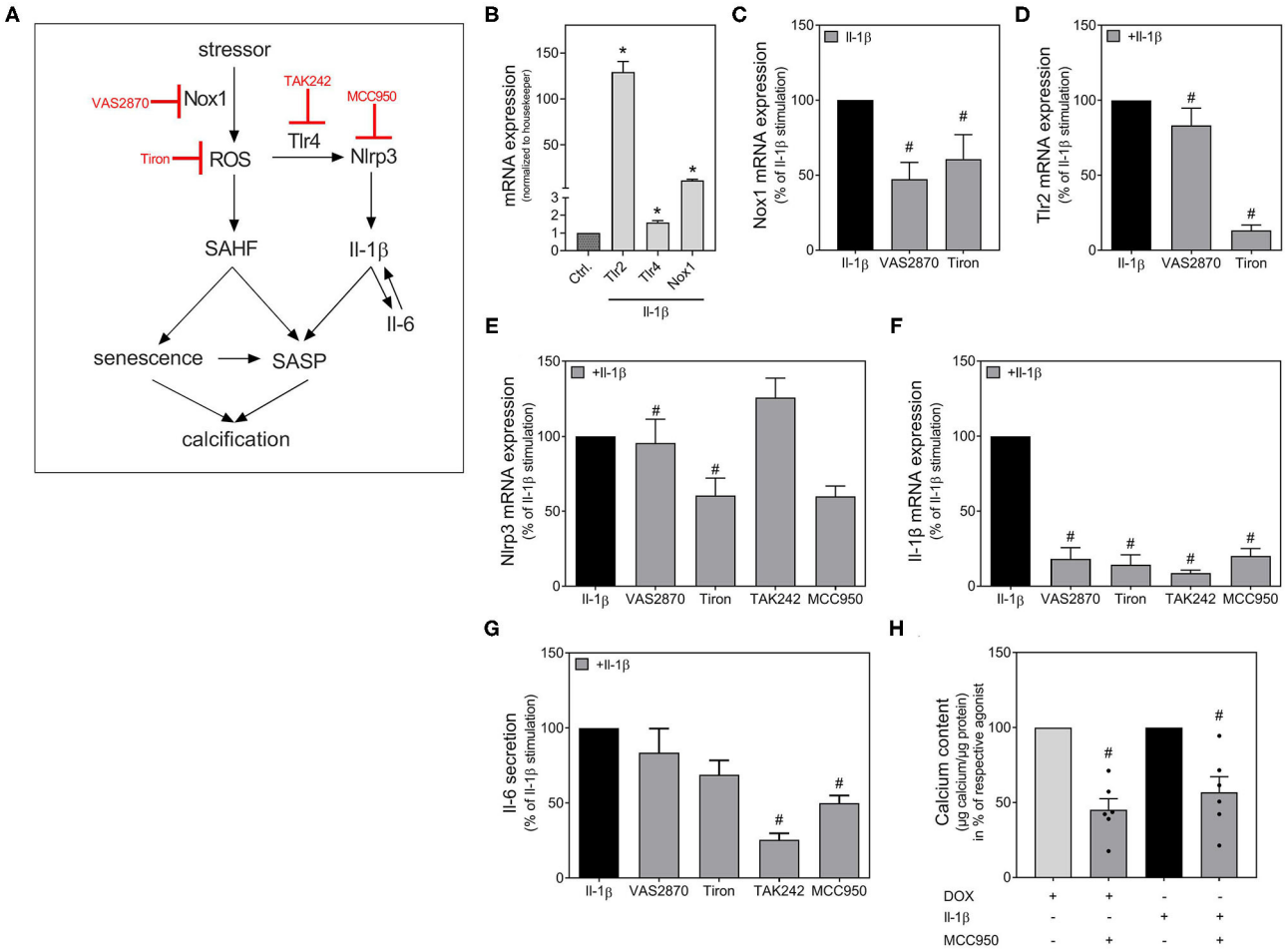

FIGURE 6 | Possible signaling pathways in Nlrp3 dependent calcification. Scheme with inhibitors used **(A)**. VSMC were stimulated for 48 h **(B–G)** or 14 d **(H)** with Il-1β (100 ng/ml), DOX (100 nmol/l), VAS2870 (10 μM), MCC950 (50 μM), TAK242 (10 μM) or Tiron (10 mM) as indicated. mRNA expression was measured with quantitative real-time PCR **(B–F)**. Measured thresholds of the respective targets were normalized to the corresponding average threshold of housekeeper genes actin and Gapdh before normalization to control **(B–F)**. Secretion of Il-6 was measured with Luminex™ and normalized to protein content (μg) **(G)**. Calcium content was quantified with *o*-cresolphthalein and normalized to protein content (μg) **(H)**. Data represent mean ± SEM, $n \geq 3$, $^*p < 0.05$ vs. Control, $^{\#}p < 0.05$ vs. Respective agonist (100 ng/ml Il-1β or 100 nmol/l DOX).

reflect the whole spectrum of senescence induction in VSMCs, DNA damage is a known and well-documented inducer of cellular senescence (9, 11). As shown recently by Shanahan's group, the formation of nuclei positive for γH2A.X and ATM in VSMCs is induced by calcium phosphate and correlates with the induction seen by other DNA damagers as DOX and hydrogen peroxide treatments (9). γH2A.X is a marker of double-strand DNA breaks, which are specific domains of facultative heterochromatin that contribute to silencing of genes promoting proliferation in senescent cells and are one known marker of senescence-associated heterochromatin foci (SAHF) (28). The phosphorylation of γH2A.X by ATM is a

key response mechanism to DNA damage, which can result in the activation of senescence pathways, including p21 (29). In line, in our experimental model treatment with DOX also induces DNA damage as γH2A.X and increases senescence markers p21 and SA-β-Gal. SA-β-Gal catalyzes the hydrolysis of β-galactosidase to monosaccharides in senescent cells. Cellular senescence is a dynamically regulated process, with activation of the p53/p21 and p16 pathways (30). In our experimental setting the p53/p21 pathway was upregulated by DOX, whereas p16 was not significantly affected (mRNA expression). While the senescence growth arrest via the p16 pathway seems not reversible, the p53-induced growth arrest is reversible upon p53 inactivation (31).

As in the previous study by Bielak-Zmijewska et al. only limited markers and only seven days of stimulation were investigated to study induction of calcification by DOX (20), we aimed to investigate DOX as primary stressor of DNA damage and senescence in order to analyze pro-inflammatory response and induction of calcification in VSMCs. In our experimental setting using primary VSMCs from rat thoracic aortas, DOX induces mineralization of VSMCs detected via calcium quantification and Alizarin Red staining after 14 days. The calcification induction was verified in an *ex vivo* setting using thoracic aortic rings. Analysis of the mRNA expression via real-time PCR and partly also *in situ* hybridization, enzyme activity and Western Blot confirmed the findings of osteogenic transformation of VSMCs; osteogenic markers as Cbfa1, Alp, Bmp-2, and Opn increase upon DOX treatment.

Senescent cells also have a metabolic active and pro-inflammatory phenotype termed as SASP. Cytokines of the Il-1 family and Il-6 are known to be part of this SASP (32). Furthermore, the induction of senescence by cytokines of the Il-1 family, e.g., Il-1β was investigated in cell culture and animal models (33). A microarray study has shown that senescent VSMCs reveal differential regulation of Matrix Gla Protein, Bmp-2, Osteoprotegerin, and Il-1β (34). In our own previous work, we demonstrated that plasma concentrations of Il-1β and Il-6 were significantly increased in rats treated with azathioprine, another known cellular stressor and ROS inducer, over a 24-weeks period of treatment (35). Increased expression of Il-1β and Il-6 was also detected in the aortas of treated rats, which were associated with increased expression of the osteogenic proteins Bmp-2, Alp and Cbfa1 (35). Therefore, we examined the effect of DOX on the expression of Il-1β and Il-6. The mRNA expression of Il-1β and Il-6 were significantly increased upon DOX stimulation, with higher induction for Il-1β. The Nlrp3 inflammasome, the most widely characterized inflammasome and known to be expressed in VSMCs (15), serves as most significant source of Il-1β production (16). Beside Nlr inflammasomes, transmembrane Tlrs are the main types of PRRs (14). The activation of PRRs mainly induces sterile inflammation associated with extensive transcriptional pro-inflammatory cellular reprogramming (36). This is temporarily useful in acute situations, while chronic activation is detrimental (37). Due to their potent pro-inflammatory potency, the Nlrp3 activation and assembly is a strictly controlled process with an initial stimulus e.g., activation of Tlr, and a second stimulus e.g., increased production of ROS (25). Subsequent activation of caspase-1 leads to cleavage and activation of pro-Il-1β into its active form Il-1β (25). PRRs are a link between the innate immune system, inflammation, and cellular senescence. VSMCs express small inflammasomes with low and slow onset, but long-lasting activity leading to a continuous release of Il-1 cytokines (15, 38). This mainly induces cellular hyperactivity and chronic sterile inflammation, which can maintain itself independently of the initial trigger (39). The cells retain their full viability and include Il-1 cytokines in the repertoire of their pro-inflammatory secretome (39). It was already shown that inflammasomes are involved in the calcification process and age-related diseases (40–42). In calcified VSMCs, Nlrp3, its cofactor Asc, and the cleavage enzyme caspase-1 are upregulated with subsequent Il-1β production, while Nlrp3 inhibition prevents *in vitro* calcification (38). In our experimental model, the expression of Nlrp3, Asc as well as caspase-1 is significantly upregulated upon DOX stimulation in VSMCs. Simultaneously, the expression of Tlr2 and Nox1 also increases. The NADPH oxidase, with Nox1 as one subunit, is one of the major sources for superoxide anion release in VSMCs (43). In VSMCs, the Tlr4 is constitutively active, while the Tlr2 is upregulated upon an inflammatory response (26).

As already known from a previous study by Wen et al., Il-1β can promote osteogenic differentiation and induction of calcification of VSMCs (38). In line, in our experimental setting, both Il-1β and DOX induce VSMC calcification. The DOX-induced mineralization could be significantly reduced by MCC950. This could be confirmed in the *ex vivo* setting with Nlrp3$^{-/-}$ mice, where the calcification induction by DOX is also inhibited compared to control mice. This finding is comparable to our previous results regarding the stressor azathioprine, whose calcifying effect could also no longer be seen in aortic rings from Nlrp3$^{-/-}$ mice (35). Therefore, Il-1β appears to be a very important effector cytokine, especially for the maintenance of a SASP after primary initiation of the SASP by the induction of "inflammaging" due to a cellular stressor. Thus, Il-1 cytokines might become an essential part of the respective pathogenesis by forming an auto-inflammatory loop, independent of the initial trigger.

Il-1β increases its own expression as well as the expression and secretion of Il-6. Moreover, Il-1β also enhances the expression of relevant components of the signaling pathway, particularly Tlr2, Nox1 and Nlrp3, also shown to be involved in DOX-mediated "inflammaging." Yet, in contrast to the DOX-induced effects in VSMCs, Il-1β does not affect the expression of senescence markers, such as p21 or SA-β-Gal, nor induces DNA breaks detected via γH2A.X in our model using primary rat VSMCs. In contrast, a recent study found induction of senescence in a co-treatment of Il-1β and phosphate in human umbilical cord VSMCs (42). Different effects on calcification were also seen for Il-6 when the origin of VSMCs differs: while pro-calcifying effects of Il-6 were found in human umbilical artery VSMCs in non-osteogenic medium (44), others found these effects only in co-stimulation with the soluble Il-6 receptor in osteogenic medium in human VSMCs (45). At least one explanation might be the different origin of VSMCs that differ in protein expression, as

demonstrated by proteomic analysis (46). Like Il-1β, processes of cellular senescence are not affected by Il-6 in our model (**Supplementary Material**), whereas an Il-6 production itself is a component of the SASP and therefore a sign of VSMCs senescence (32).

This study has some limitations that might hamper the direct translational aspects of the results: It was performed only in *in vitro* and *ex vivo* settings using cells and thoracic aortas from rats and mice. Further *in vivo* studies verifying the major role of Nlrp3 and Il-1β as a potential therapeutic target for the treatment of vessel "inflammaging" are necessary. In addition, the transferability in the current study is not shown for human aortic or other vessel beds.

In conclusion, the inhibition of PRRs could represent an essential approach for the therapy of systemic vascular diseases. The CANTOS study demonstrated for the first time in humans the importance of chronic vascular inflammation for CVD and the association of cardiovascular mortality with signs of systemic inflammation (47). The current study results provide further indications of a potential benefit of an interruption of the Nlrp3-associated auto-inflammatory loop.

DATA AVAILABILITY STATEMENT

The original contributions presented in the study are included in the article/**Supplementary Material**, further inquiries can be directed to the corresponding author/s.

ETHICS STATEMENT

The animal study was reviewed and approved by Landesamt für Gesundheit und Soziales Berlin, Germany.

AUTHOR CONTRIBUTIONS

MS, MT, and MvdG: conceptualization, supervision, and project administration. JH, MS, and MT: methodology, writing—original draft preparation, and visualization. JH, MS, MX, MG, AG, MS, and AS: investigation. JH, MS, MT, and MvdG: data curation. JH, MT, MG, MX, AG, AS, and MvdG: writing—review and editing. MT, JH, MX, and MS: funding acquisition. All authors contributed to the article and approved the submitted version.

FUNDING

This research was funded by a grant from the Bundesministerium für Bildung und Forschung (MT, MS), the Sonnenfeld Stiftung (MS, MT, JH) and the Berlin Institute of Health (MS). MX received a research scholarship of the Nanchong school science and technology strategic cooperation project (grant number: 20SXQT0117).

ACKNOWLEDGMENTS

The authors thank Katharina Kuschfeldt, Brigitte Egbers and Nadine Neitzel for excellent technical assistance and Raissa Stayzyk for her excellent work in the animal facility. We thank Marcus Maurer (Charité – Universitätsmedizin Berlin) for the release of the Nlrp3 knockout mice for breeding.

SUPPLEMENTARY MATERIAL

The Supplementary Material for this article can be found online at: https://www.frontiersin.org/articles/10.3389/fcvm.2021.752305/full#supplementary-material

REFERENCES

1. Virani SS, Alonso A, Aparicio HJ, Benjamin EJ, Bittencourt MS, Callaway CW, et al. Heart disease and stroke statistics-2021 update: a report from the American heart association. *Circulation.* (2021) 143:e254–743. doi: 10.1161/CIR0000000000000950
2. Tolle M, Reshetnik A, Schuchardt M, Hohne M, Van Der Giet M. Arteriosclerosis and vascular calcification: causes, clinical assessment and therapy. *Eur J Clin Invest.* (2015) 45:976–85. doi: 10.1111/eci.12493
3. Lanzer P, Hannan FM, Lanzer JD, Janzen J, Raggi P, Furniss D, et al. Medial arterial calcification: JACC state-of-the-art review. *J Am Coll Cardiol.* (2021) 78:1145–65. doi: 10.1016/j.jacc.2021.06.049
4. Iribarren C, Sidney S, Sternfeld B, Browner WS. Calcification of the aortic arch: risk factors and association with coronary heart disease, stroke, and peripheral vascular disease. *JAMA.* (2000) 283:2810–5. doi: 10.1001/jama.283.21.2810
5. Raggi P. Cardiovascular disease: coronary artery calcification predicts risk of CVD in patients with CKD. *Nat Rev Nephrol.* (2017) 13:324–6. doi: 10.1038/nrneph.2017.61
6. Childs BG, Durik M, Baker DJ, Van Deursen JM. Cellular senescence in aging and age-related disease: from mechanisms to therapy. *Nat Med.* (2015) 21:1424–35. doi: 10.1038/nm.4000
7. Kooman JP, Kotanko P, Schols AM, Shiels PG, Stenvinkel P. Chronic kidney disease and premature ageing. *Nat Rev Nephrol.* (2014) 10:732–42. doi: 10.1038/nrneph.2014.185
8. Munoz-Espin D, Serrano M. Cellular senescence: from physiology to pathology. *Nat Rev Mol Cell Biol.* (2014) 15:482–96. doi: 10.1038/nrm3823
9. Sanchis P, Ho CY, Liu Y, Beltran LE, Ahmad S, Jacob AP, et al. Arterial "inflammaging" drives vascular calcification in children on dialysis. *Kidney Int.* (2019) 95:958–72. doi: 10.1016/j.kint.2018.12.014
10. Herrmann J, Babic M, Tolle M, Van Der Giet M, Schuchardt M. Research models for studying vascular calcification. *Int J Mol Sci.* (2020) 21:2204. doi: 10.3390/ijms21062204
11. Cobb AM, Yusoff S, Hayward R, Ahmad S, Sun M, Verhulst A, et al. Runx2 (Runt-Related Transcription Factor 2) links the DNA damage response to osteogenic reprogramming and apoptosis of vascular smooth muscle cells. *Arterioscler Thromb Vasc Biol.* (2021) 41:1339–57. doi: 10.1161/ATVBAHA.120.315206
12. Childs BG, Li H, Van Deursen. J.M. Senescent cells: a therapeutic target for cardiovascular disease. *J Clin Invest.* (2018) 128:1217–28. doi: 10.1172/JCI95146
13. Krainer J, Siebenhandl S, Weinhausel A. Systemic autoinflammatory diseases. *J Autoimmun.* (2020) 109:102421. doi: 10.1016/j.jaut.2020.102421
14. Cao X. Self-regulation and cross-regulation of pattern-recognition receptor signalling in health and disease. *Nat Rev Immunol.* (2016) 16:35–50. doi: 10.1038/nri.2015.8
15. Sun HJ, Ren XS, Xiong XQ, Chen YZ, Zhao MX, Wang JJ, et al. NLRP3 inflammasome activation contributes to VSMC phenotypic transformation and proliferation in hypertension. *Cell Death Dis.* (2017) 8:e3074. doi: 10.1038/cddis.2017.470

16. Tangi TN, Elmabsout AA, Bengtsson T, Sirsjo A, Fransen K. Role of NLRP3 and CARD8 in the regulation of TNF-alpha induced IL-1beta release in vascular smooth muscle cells. *Int J Mol Med.* (2012) 30:697–702. doi: 10.3892/ijmm.2012.1026
17. Weber A, Wasiliew P, Kracht M. Interleukin-1 (IL-1) pathway. *Sci Signal.* (2010) 3:cm1. doi: 10.1126/scisignal.3105cm1
18. Kim DH, Bang E, Arulkumar R, Ha S, Chung KW, Park MH, et al. Senoinflammation: a major mediator underlying age-related metabolic dysregulation. *Exp Gerontol.* (2020) 134:110891. doi: 10.1016/j.exger.2020.110891
19. Cagel M, Grotz E, Bernabeu E, Moretton MA, Chiappetta DA. Doxorubicin: nanotechnological overviews from bench to bedside. *Drug Discov Today.* (2017) 22:270–81. doi: 10.1016/j.drudis.2016.11.005
20. Bielak-Zmijewska A, Wnuk M, Przybylska D, Grabowska W, Lewinska A, Alster O, et al. A comparison of replicative senescence and doxorubicin-induced premature senescence of vascular smooth muscle cells isolated from human aorta. *Biogerontology.* (2014) 15:47–64. doi: 10.1007/s10522-013-9477-9
21. Schuchardt M, Tolle M, Prufer J, Prufer N, Huang T, Jankowski V, et al. Uridine adenosine tetraphosphate activation of the purinergic receptor P2Y enhances in vitro vascular calcification. *Kidney Int.* (2012) 81:256–65. doi: 10.1038/ki.2011.326
22. Herrmann J, Babic M, Tolle M, Eckardt KU, Van Der Giet M, Schuchardt M. A novel protocol for detection of senescence and calcification markers by fluorescence microscopy. *Int J Mol Sci.* (2020) 21:3475. doi: 10.3390/ijms21103475
23. Lopes-Paciencia S, Saint-Germain E, Rowell MC, Ruiz AF, Kalegari P, Ferbeyre G. The senescence-associated secretory phenotype and its regulation. *Cytokine.* (2019) 117:15–22. doi: 10.1016/j.cyto.2019.01.013
24. Niemi K, Teirila L, Lappalainen J, Rajamaki K, Baumann MH, Oorni K, et al. Serum amyloid a activates the NLRP3 inflammasome via P2X7 receptor and a cathepsin B-sensitive pathway. *J Immunol.* (2011) 186:6119–28. doi: 10.4049/jimmunol.1002843
25. De Zoete MR, Palm NW, Zhu S, Flavell RA. Inflammasomes. *Cold Spring Harb Perspect Biol.* (2014) 6:a016287. doi: 10.1101/cshperspect.a016287
26. Schuchardt M, Prufer N, Tu Y, Herrmann J, Hu XP, Chebli S, et al. Dysfunctional high-density lipoprotein activates toll-like receptors via serum amyloid a in vascular smooth muscle cells. *Sci Rep.* (2019) 9:3421. doi: 10.1038/s41598-019-39846-3
27. Burtenshaw D, Hakimjavadi R, Redmond EM, Cahill PA. Nox, reactive oxygen species and regulation of vascular cell fate. *Antioxidants.* (2017) 6:90. doi: 10.3390/antiox6040090
28. Bernadotte A, Mikhelson VM, Spivak IM. Markers of cellular senescence. Telomere shortening as a marker of cellular senescence. *Aging.* (2016) 8:3–11. doi: 10.18632/aging.100871
29. Duer M, Cobb AM, Shanahan CM. DNA damage response: a molecular lynchpin in the pathobiology of arteriosclerotic calcification. *Arterioscler Thromb Vasc Biol.* (2020) 40:e193–202. doi: 10.1161/ATVBAHA.120.313792
30. Mijit M, Caracciolo V, Melillo A, Amicarelli F, Giordano A. Role of p53 in the regulation of cellular senescence. *Biomolecules.* (2020) 10:420. doi: 10.3390/biom10030420
31. Campisi J. Senescent cells, tumor suppression, and organismal aging: good citizens, bad neighbors. *Cell.* (2005) 120:513–22. doi: 10.1016/j.cell.2005.02.003
32. Orjalo AV, Bhaumik D, Gengler BK, Scott GK, Campisi J. Cell surface-bound IL-1alpha is an upstream regulator of the senescence-associated IL-6/IL-8 cytokine network. *Proc Natl Acad Sci USA.* (2009) 106:17031–36. doi: 10.1073/pnas.0905299106
33. Acosta JC, Banito A, Wuestefeld T, Georgilis A, Janich P, Morton JP, et al. A complex secretory program orchestrated by the inflammasome controls paracrine senescence. *Nat Cell Biol.* (2013) 15:978–90. doi: 10.1038/ncb2784
34. Burton DG, Giles PJ, Sheerin AN, Smith SK, Lawton JJ, Ostler EL, et al. Microarray analysis of senescent vascular smooth muscle cells: a link to atherosclerosis and vascular calcification. *Exp Gerontol.* (2009) 44:659–65. doi: 10.1016/j.exger.2009.07.004
35. Schuchardt M, Herrmann J, Henkel C, Babic M, Van Der Giet M, Tolle M. Long-term treatment of azathioprine in rats induces vessel mineralization. *Biomedicines.* (2021) 9:327. doi: 10.3390/biomedicines9030327
36. Chen GY, Nunez G. Sterile inflammation: sensing and reacting to damage. *Nat Rev Immunol.* (2010) 10:826–37. doi: 10.1038/nri2873
37. Roh JS, Sohn DH. Damage-associated molecular patterns in inflammatory diseases. *Immune Netw.* (2018) 18:e27. doi: 10.4110/in.2018.18.e27
38. Wen C, Yang X, Yan Z, Zhao M, Yue X, Cheng X, et al. Nalp3 inflammasome is activated and required for vascular smooth muscle cell calcification. *Int J Cardiol.* (2013) 168:2242–7. doi: 10.1016/j.ijcard.2013.01.211
39. Evavold CL, Ruan J, Tan Y, Xia S, Wu H, Kagan JC. The pore-forming protein gasdermin d regulates interleukin-1 secretion from living macrophages. *Immunity.* (2018) 48:35–44 e36. doi: 10.1016/j.immuni.2017.11.013
40. Rea IM, Gibson DS, Mcgilligan V, Mcnerlan SE, Alexander HD, Ross OA. Age and age-related diseases: role of inflammation triggers and cytokines. *Front Immunol.* (2018) 9:586. doi: 10.3389/fimmu.2018.00586
41. Xu D, Zeng F, Han L, Wang J, Yin Z, Lv L, et al. The synergistic action of phosphate and interleukin-6 enhances senescence-associated calcification in vascular smooth muscle cells depending on p53. *Mech Ageing Dev.* (2019) 182:111124. doi: 10.1016/j.mad.2019.111124
42. Han L, Zhang Y, Zhang M, Guo L, Wang J, Zeng F, et al. Interleukin-1beta-induced senescence promotes osteoblastic transition of vascular smooth muscle cells. *Kidney Blood Press Res.* (2020) 45:314–30. doi: 10.1159/000504298
43. Tsai IC, Pan ZC, Cheng HP, Liu CH, Lin BT, Jiang MJ. Reactive oxygen species derived from NADPH oxidase 1 and mitochondria mediate angiotensin II-induced smooth muscle cell senescence. *J Mol Cell Cardiol.* (2016) 98:18–27. doi: 10.1016/j.yjmcc.2016.07.001
44. Sun M, Chang Q, Xin M, Wang Q, Li H, Qian J. Endogenous bone morphogenetic protein 2 plays a role in vascular smooth muscle cell calcification induced by interleukin 6 in vitro. *Int J Immunopathol Pharmacol.* (2017) 30:227–37. doi: 10.1177/0394632016689571
45. Kurozumi A, Nakano K, Yamagata K, Okada Y, Nakayamada S, Tanaka Y. IL-6 and sIL-6R induces STAT3-dependent differentiation of human VSMCs into osteoblast-like cells through JMJD2B-mediated histone demethylation of RUNX2. *Bone.* (2019) 124:53–61. doi: 10.1016/j.bone.2019.04.006
46. Regent A, Ly KH, Lofek S, Clary G, Tamby M, Tamas N, et al. Proteomic analysis of vascular smooth muscle cells in physiological condition and in pulmonary arterial hypertension: toward contractile versus synthetic phenotypes. *Proteomics.* (2016) 16:2637–49. doi: 10.1002/pmic.201500006
47. Ridker PM, Everett BM, Thuren T, Macfadyen JG, Chang WH, Ballantyne C, et al. Antiinflammatory therapy with canakinumab for atherosclerotic disease. *N Engl J Med.* (2017) 377:1119–31. doi: 10.1056/NEJMoa1707914

Conflict of Interest: The authors declare that the research was conducted in the absence of any commercial or financial relationships that could be construed as a potential conflict of interest.

Publisher's Note: All claims expressed in this article are solely those of the authors and do not necessarily represent those of their affiliated organizations, or those of the publisher, the editors and the reviewers. Any product that may be evaluated in this article, or claim that may be made by its manufacturer, is not guaranteed or endorsed by the publisher.

frontiers in Cardiovascular Medicine

BRIEF RESEARCH REPORT
published: 23 December 2021
doi: 10.3389/fcvm.2021.772912

Aortic Pressure Levels and Waveform Indexes in People Living With Human Immunodeficiency Virus: Impact of Calibration Method on the Differences With Respect to Non-HIV Subjects and Optimal Values

Alejandro Diaz[1†], *Marina Grand*[2,3†], *Juan Torrado*[4], *Federico Salazar*[5], *Yanina Zócalo*[6] *and Daniel Bia*[6*]

[1] Consejo Nacional de Investigaciones Científicas y Técnicas, Instituto de Investigación en Ciencias de la Salud (IICS), Universidad Nacional del Centro de la Provincia de Buenos Aires (UNICEN), Tandil, Argentina, [2] Instituto de Investigación en Ciencias de la Salud, Facultad de Ciencias de la Salud, Universidad Nacional del Centro de la Provincia de Buenos Aires, Tandil, Argentina, [3] Hospital Dr. Héctor M. Cura, Olavarría, Argentina, [4] Department of Internal Medicine, Jacobi Medical Center, Albert Einstein College of Medicine, New York, NY, United States, [5] Servicio de Cardiología, Hospital Privado de Comunidad, Mar del Plata, Argentina, [6] Departamento de Fisiología, Facultad de Medicina, Centro Universitario de Investigación, Innovación y Diagnóstico Arterial, Universidad de la República, Montevideo, Uruguay

Background: There are scarce and controversial data on whether human immunodeficiency virus (HIV) infection is associated with changes in aortic pressure (aoBP) and waveform-derived indexes. Moreover, it remains unknown whether potential differences in aoBP and waveform indexes between people living with HIV (PLWHIV) and subjects without HIV (HIV-) would be affected by the calibration method of the pressure waveform.

Aims: To determine: (i) whether PLWHIV present differences in aoBP and waveform-derived indexes compared to HIV- subjects; (ii) the relative impact of both HIV infection and cardiovascular risk factors (CRFs) on aoBP and waveform-derived indexes; (iii) whether the results of the first and second aims are affected by the calibration method.

Methods: Three groups were included: (i) PLWHIV (n = 86), (ii) HIV- subjects (general population; *n* = 1,000) and (iii) a Reference Group (healthy, non-exposed to CRFs; *n* = 398). Haemodynamic parameters, brachial pressure (baBP; systolic: baSBP; diastolic: baDBP; mean oscillometric: baMBPosc) and aoBP and waveform-derived indexes were obtained. Brachial mean calculated (baMBPcalc=baDBP+[baSBP-baDBP]/3) pressure was quantified. Three waveform calibration schemes were used: systolic-diastolic, calculated (baMBPcalc/baDBP) and oscillometric mean (baMBPosc/baDBP).

Results: Regardless of CRFs and baBP, PLWHIV presented a tendency of having lower aoBP and waveform-derived indexes which clearly reached statistical significance when using the baMBPosc/baDBP or baMBPcalc/baDBP calibration. HIV status exceeded the relative weight of other CRFs as explanatory variables, being

OPEN ACCESS

Edited by:
Joan T. Matamalas,
Brigham and Women's Hospital and Harvard Medical School, United States

Reviewed by:
Sarvesh Chelvanambi,
Brigham and Women's Hospital and Harvard Medical School, United States
Audrey Adji,
Victor Chang Cardiac Research Institute, Australia

***Correspondence:**
Daniel Bia
dbia@fmed.edu.uy

[†]These authors have contributed equally to this work

Specialty section:
This article was submitted to Atherosclerosis and Vascular Medicine, a section of the journal Frontiers in Cardiovascular Medicine

Received: 08 September 2021
Accepted: 30 November 2021
Published: 23 December 2021

Citation:
Diaz A, Grand M, Torrado J, Salazar F, Zócalo Y and Bia D (2021) Aortic Pressure Levels and Waveform Indexes in People Living With Human Immunodeficiency Virus: Impact of Calibration Method on the Differences With Respect to Non-HIV Subjects and Optimal Values. Front. Cardiovasc. Med. 8:772912. doi: 10.3389/fcvm.2021.772912

the main explanatory variable for variations in central hemodynamics when using the baMBPosc/baDBP, followed by the baMBPcalc/baDBP calibration.

Conclusions: The peripheral waveform calibration approach is an important determinant to reveal differences in central hemodynamics in PLWHIV.

Keywords: aortic pressure, calibration, human immunodeficiency virus, pulse wave analysis, wave separation analysis, pulse contour analysis

INTRODUCTION

Global mortality in people living with human immunodeficiency virus (PLWHIV or HIV+) has dramatically decreased over the last years due to significant improvements in both the access to highly active antiretroviral therapy and clinical care (1). However, these achievements were challenged by the higher risk of cardiovascular disease that experience these patients compared to non-HIV subjects (HIV-) (2, 3). HIV-related cardiovascular disease risk is thought to be multifactorial, involving the development of a pro-inflammatory state associated with the chronic infection (4), the use of highly active antiretroviral therapy with an adverse metabolic profile (5), and the HIV-related high prevalence of other cardiovascular risk factors (CRFs) (6). Accordingly, PLWHIV on highly active antiretroviral therapy have shown an elevated prevalence of other CRFs, as well as premature cardiovascular disease reflected by a high prevalence of early arterial alterations (e.g., increased arterial stiffness, impaired vascular reactivity) (7, 8). However, the impact of HIV infection itself on some cardiovascular variables remains controversial. More precisely, there are scarce, and above all, controversial data on whether HIV infection is independently associated with aortic blood pressure (aoBP) levels and waveform-derived indexes. Previous studies have reported that both aoBP and some waveform-derived indexes were either elevated (9, 10), unchanged (9, 11), or even reduced (12–14) in PLWHIV compared to HIV- subjects.

At least three factors could explain these controversies. First, prior studies that have reported aoBP levels and waveform-derived indexes in PLWHIV compared to HIV- subjects either (i) did not adjust for any CRF (9, 15) or (ii) only adjusted for some variables (e.g., age, sex, body mass index) without considering other cofactors such as cholesterol, triglycerides and diabetes (10–14). Thus, it remains to be determined at what extent potential differences in central hemodynamics associated with HIV infection would be directly related to the disease condition and/or would be determined by the presence of concomitant CRFs. Second, certain studies have considered control groups (HIV-) with relatively small sample size (e.g., $n = 26$–37) (9, 10, 15), which significantly reduces the statistical power of the tests to find significant differences between the groups (Type-II error). Last, these studies have not considered the relevance of the calibration of the pressure waveform at the time of assessing non-invasively central hemodynamics (16). Several studies that have compared the aoBP between PLWHIV and HIV- subjects either did not report the calibration method (9, 10, 13, 15) or used currently not recommended schemes (i.e., systolic-diastolic calibration; see below) (11, 14).

Non-invasive estimation of aoBP can be achieved by several devices, which differ in multiple features such as the principle applied to assess the pressure or surrogate signals, the arterial site for pulse waveform recording and/or the model or mathematical analysis considered to obtain central hemodynamic data (16). Most of the devices use oscillometry/plethysmography, applanation tonometry, or ultrasonography to obtain pulse waveforms from radial, brachial or carotid arteries. Then, from the acquired pulse waveform and posterior calibration, the devices quantify aoBP directly (i.e., calibration of carotid waveforms) or indirectly (e.g., applying generalized transfer functions to brachial or radial waveforms) (16–29). In both cases, research and clinical practice have mostly used two different brachial artery blood pressure (baBP)-derived calibration schemes, (i) calibration to brachial systolic (baSBP) and diastolic (baDBP) pressure ("systolic-diastolic calibration") and calibration to baDBP and brachial mean blood pressure (baMBP) ("baMBP/baDBP calibration") (27–29). It is noteworthy, that baMBP levels to be used for calibration could be measured directly by oscillometry (baMBPosc; "baMBPosc/baDBP calibration") or calculated (baMBPcalc; "baMBPcalc/baDBP calibration") from baSBP and baDBP, using different scaling forms (e.g., classically a form factor equal to 0.33) (27–29). Previous studies have strongly recommended to describe in detail the calibration scheme used during the hemodynamic measures, since it is essential when interpreting the results at the time of evaluating for statistical differences and when assessing the potential clinical value of quantifying central over peripheral parameters (16, 19, 21, 22, 25, 27, 28). In previous studies performed on subjects of the general population (children, adolescents and adults) we showed that calibration with the "baMBPosc/baDBP" scheme resulted in higher aoBP values and stronger association between aoBP and cardiac structural properties (27–29). In this context, it remains unknown whether potential differences in aoBP levels and waveform-derived indexes between PLWHIV and HIV- subjects would be significantly affected by the calibration method. At least in theory, the calibration scheme could mask the existence of differences between of central hemodynamic indexes measured in PLWHIV vs. HIV- subjects.

This study sought to determine: (1) whether PLWHIV present differences in aoBP levels and waveform-derived indexes, compared to HIV- subjects, matched by demographic, anthropometric and levels of exposure to CRFs; (2) the impact to which HIV infection itself and its treatment vs. classical CRFs

contribute to the levels of affectation (deviation from the age-related expected [optimal] value) for the different aoBP levels and waveform-derived indexes; (3) to what extent the results of the first and second aims are affected by the calibration method.

MATERIALS AND METHODS

Study Population

This study was carried out in the context of the "Tandil Cardiovascular Project" (30–37), a population-based study developed in Provincia de Buenos Aires, Argentina. From this database, three different groups were assessed: (i) PLWHIV ($n = 86$), (ii) age range-matched non-HIV subjects (general population; $n = 1{,}000$) and (iii) a reference group (healthy subjects non-exposed to CRFs; $n = 398$). The reference group was selected to quantify differences between measured and "expected" values (see below). All procedures were conducted in agreement with the Declaration of Helsinki. The study protocol was approved by the Institution's Ethics Committee. Written informed consent was obtained prior to the evaluation.

PLWHIV Group

In addition to the general variables, the following data were obtained from the PLWHIV' electronic medical record: time since HIV diagnosis, highly active antiretroviral therapy exposure and time under this therapy and/or protease inhibitors, history of opportunistic infection, CDC's HIV category, HIV viral load < 50 copies/ml (%), and CD4+ lymphocytes count (cells/mm^3). Subjects under chronic treatment with steroids or chemotherapy, and pregnant women, were excluded.

Clinical Evaluation

Blood samples were obtained after 9–12 h of fasting. Subject's body height and weight were measured and body mass index was calculated (weight/height^2). Dyslipidemia, diabetes and hypertension were considered present if they had been previously diagnosed by referring physicians or the patient was receiving lipid-lowering, glucose-lowering or antihypertensive drugs (38). Diabetes was diagnosed based on abnormal plasma glucose levels (39). Dyslipidemia was defined as total cholesterol >240 mg/dL, low-density lipoprotein cholesterol >160 mg/dL, high-density lipoprotein cholesterol for men <40 mg/ and for women <50 mg/dL and/or triglycerides >250 mg/dL (40). Smokers (defined as usually smoking at least one cigarette/week) were identified. Obesity was defined as body mass index ≥30 kg/m^2.

Cardiovascular Evaluation

Participants were asked to avoid exercise, tobacco, alcohol, caffeine, and food-intake four hours before the evaluation. All hemodynamic measurements were performed in a temperature-controlled room (21–23°C), with the subject in supine position and after resting for at least 10–15 min.

Peripheral baBP levels [baSBP, baDBP and baMBPosc (lowest cuff pressure at which the oscillations are maximal)] and waveforms were obtained by a brachial cuff based oscillometric device (Mobil-O-Graph system, I.E.M, Stolberg, Germany) (20, 29). The brachial pulse pressure (baPP, baPP=baSBP-baDBP) and baMBPcalc (baMBPcalc=baDBP+[baPP]/3) were obtained. Once baBP is measured, the cuff is instantly inflated, and baBP waveforms are recorded for 10 s. Subsequently, the device determines the aoBP levels and waveforms from peripheral recordings.

By means of pulse wave analysis, wave separation analysis and pulse contour analysis, the following variables were obtained: (i) aortic systolic, diastolic and pulse pressure (aoSBP, aoDBP and aoPP); (ii) heart rate; (iii) maximal amplitude of forward-traveling (Pf) and backward-traveling (Pb) wave components, and Pb/Pf ratio (Reflection Magnitude); (iv) first inflection pressure and time (difference in pressure and time, from the beginning of aoBP systolic phase ["foot wave"] to the first systolic inflection point [shoulder] in the aoBP waveform); (v) systolic time (duration of waveform-derived ejection phase); (vi) time from the "foot wave" to the peak or maximal amplitude of Pf and Pb components (TmaxForward and TmaxBackward); (vii) time of arrival of the backward wave (TstartBackward); (viii) aortic pulse wave velocity (aoPWV; calculated from the reconstructed aoBP waveform); (ix) augmentation index (AIx) and heart rate-adjusted AIx (AIxHR75)l; (x) stroke volume, cardiac output and index, and systemic vascular resistance (41). Definitive values were the average of at least six measures obtained in a single visit. Only high-quality recordings and satisfactory waves (visual inspection) were considered (29).

All values were quantified by using the three different methods of calibration: baSBP/baDBP, baMBPcalc/baDBPand baMBPosc/baDBP (27–29).

Statistical Analysis

Cardiovascular Differences Between PLWHIV and HIV- Subjects

After analyzing the characteristics of the included groups (**Table 1**, **Supplementary Table 1**), we compared (in each subgroup) the central hemodynamic levels obtained with different calibration schemes (**Figure 1**; ANOVA+Bonferroni). After that, the cardiovascular properties of HIV+ and HIV- were compared (ANCOVA) adjusting for cofactors (demographic, anthropometric and CRFs) (**Table 2**, **Supplementary Tables 2–4**).

Explanatory Capacity of HIV Infection of the Differences Between the Measured and Expected (Optimal) Value of Cardiovascular Variables

Cardiovascular variables obtained in PLWHIV and non-HIV subjects were expressed as relative difference (%) with respect to age-matched healthy subjects not exposed to CRFs (reference group). To build the reference group, we identified a healthy sub-population from the project database that included subjects who did not meet any of the following exclusion criteria: history of cardiovascular disease, use of baBP-, lipid- or glucose-lowering drugs, hypertension or high baBP levels during the non-invasive evaluation, smoking, diabetes, dyslipidemia, obesity (29–36, 41–44).

Once the reference group was built, age-related equations were obtained for mean values (**Supplementary Table 5**). To

TABLE 1 | Characteristics of included subjects: PLWHIV, Non-HIV group and Reference group.

	PLWHIV							Non-HIV subjects (HIV -)							Reference group						
Variables	**MV**	**SD**	**Min**	**p25**	**p50**	**p75**	**Max**	**MV**	**SD**	**Min**	**p25**	**p50**	**p75**	**Max**	**MV**	**SD**	**Min**	**p25**	**p50**	**p75**	**Max**
Demographic, anthropometric, and clinical characteristics																					
Female (%)				50.6							49.8							52.7			
Age (years)	44	12	19	36	44	53	75	51	14	19	41	52	62	75	38	13	19	28	38	46	74
Height (m)	1.65	0.10	1.45	1.58	1.65	1.72	1.89	1.68	0.10	1.42	1.61	1.68	1.75	2.00	1.69	0.10	1.42	1.61	1.69	1.75	2.00
Weight (kg)	72.3	17.1	42.6	57.0	71.6	82.0	119.2	79.9	17.6	37.0	68.0	79.0	90.0	159.0	67.9	12.5	37.0	59.0	67.0	75.0	113.0
BMI (kg/m^2)	26.4	5.3	17.2	22.3	25.9	30.4	44.3	28.1	5.2	17.1	24.4	27.6	30.9	55.0	23.7	2.8	17.1	21.6	24.0	25.8	29.8
Htc (%)	40.9	4.9	25.6	38.0	40.9	44.4	53.0	42.0	3.3	26.0	40.0	42.0	44.0	55.0	41.7	2.3	36.0	40.0	42.0	43.0	46.0
Glyc (mg/dl)	101	29	67	90	96	103	298	101	29	55	87	97	107	427	81	10	65	72	78	88	109
Cr (mg/dl)	0.9	0.4	0.6	0.7	0.8	1.0	3.9	0.9	0.2	0.4	0.7	0.9	1.0	2.1	0.9	0.2	0.6	0.8	0.9	1.0	1.4
TC (mg/dl)	174	42	97	149	172	191	380	190	41	40	164	189	217	528	168	22	118	150	169	186	246
LDL (mg/dl)	104	26	45	89	100	123	160	114	34	24	89	116	136	248	106	26	48	86	108	124	166
HDL (mg/dl)	44	14	24	33	39	52	93	54	15	18	43	52	62	160	58	12	40	51	57	66	93
TG (mg/dl)	163	134	42	90	134	185	980	137	106	40	87	111	157	1,737	90	29	40	70	98	111	212
Obesity (%)				27.7							30.3							0.0			
HTN (%)				20.5							56.0							0.0			
Diabetes (%)				8.4							12.2							0.0			
Smoking (%)				38.6							12.8							0.0			
Dyslipidemia				13.3							51.7							0.0			
CVD (%)				2.4							3.4							0.0			
Antihypertensive (%)				14.5							47.6							0.0			
Anti-HLD drug (%)				13.3							28.0							0.0			
Antidiabetic drug (%)				7.3							9.0							0.0			
PLWHIV-Related Clinical Characteristics																					
Time HIV (mo)	50	71	0	6	19	64	303				———							———			
CDC:A1, A2, A3				24.7, 16.5, 10.6							———							———			
CDC: B1, B2, B3				3.5, 9.4, 5.9							———							———			
CDC: C3				29.4							———							———			
Hepatitis B and C				5.0 and 0.0							———							———			
HAART use				87.0							———							———			
NNRTIs				37.0							———							———			
NRTIs				33.0							———							———			
Abacavir				3.0							———							———			
PIs				1.0							———							———			
INSTIs				2.0							———							———			
HAART use (mo)	37	61	0	3	11	40	303				———							———			
Use of PIs (mo)	14	43	0	0	0	0	270				———							———			
PO infection				30.6							———							———			
HIV Viral Load				67.1							———							———			
CD4 count/ mm^3	549	414	19	282	466	769	2,273				———							———			
IgG CMV +				58.8							———							———			

MV, mean value; SD, standard deviation; Min, minimal; Max, maximal; p25, p50, p75, percentile 25, 50 and 75; Mo, months; BMI, body mass index; Hct, hematocrit; TC, LDL, HDL, total, low-density, and high-density lipoprotein cholesterol; TG, triglycerides; HTN, hypertension; CVD, cardiovascular disease; PO infection, previous opportunistic infection; PLWHIV, people living with HIV; Time HIV, time since HIV diagnosis; HAART, highly active antiretroviral therapy; NRTIs, nucleoside/nucleotide reverse transcriptase inhibitors; PIs, protease inhibitors; INSTIs, Integrase strand transfer inhibitors; CMV, cytomegalovirus; Cr, creatinine; Glyc, glycemia; A1, A2, A3, B1, B2, B3 and C3 refers to CDC HIV clinical categories.

this end, we implemented parametric regression methods based on various types of mathematical models (e.g., fractional polynomials) (29–36, 41–44). This procedure provides different equations for each model to calculate age-related mean values, then, the most adjusted model was chosen to calculate individual's relative difference between the expected and the measure value: [(measured-expected)/expected]*100 (**Supplementary Table 6**).

Finally, multiple linear regression (stepwise) models were constructed considering (i) the relative differences between the

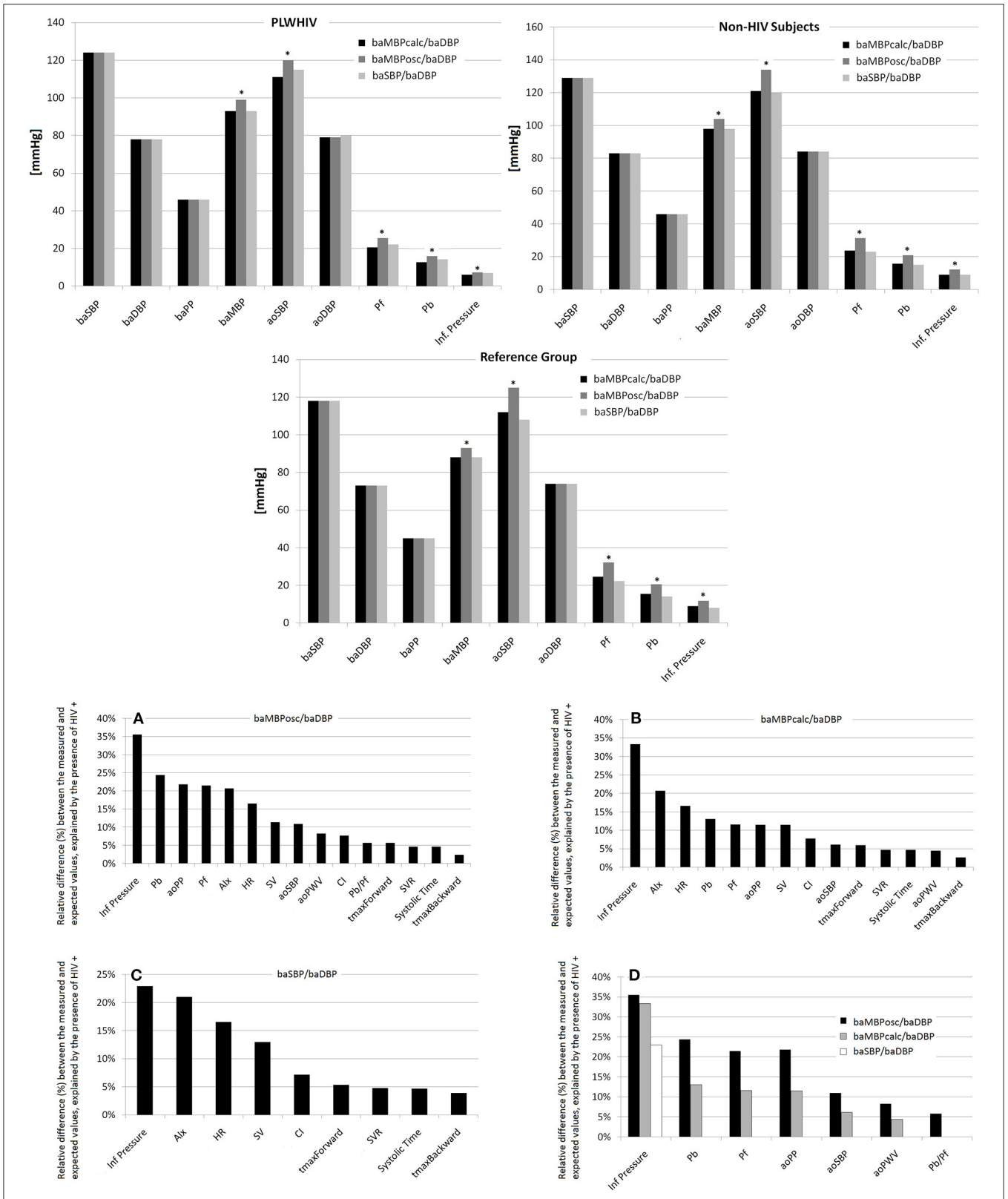

FIGURE 1 | (Top) Comparison of hemodynamic levels obtained with different calibration schemes. *Represents $p < 0.05$ with respect to the same variable quantified using other calibration scheme. **(Bottom)** Percentage of variation between the measured and optimal (expected) value of the cardiovascular variables for each of the calibration schemes that could be explained by the HIV status. **(A–C)** Percentage of variation between the measured and expected ("optimal") value of the cardiovascular variables for each of the calibration schemes that could be explained by the HIV status (values ranked from the highest to the lowest value). **(D)** Presents comparatively the differences depending on the calibration scheme used. Abbreviations in the text.

TABLE 2 | Adjusted pairwise comparisons between PLWHIV and HIV- subjects (ANCOVA).

Analysis of variables that do not depend on the calibration scheme

Variables	Groups	MV	SE	Mean Difference	*p*-value	Variables	Groups	MV	SE	Mean Difference	*P*-value
Brachial pressure, heart rate and hemodynamic parameters						**Aortic wave analysis-derived parameters**					
baSBP (mmHg)	Non-HIV	129.15	0.56	−0.75	0.710	AIx (%)	Non-HIV	23.32	0.54	−3.08	0.117
	PLWHIV	128.40	1.89				PLWHIV	20.24	1.84		
baDBP (mmHg)	Non-HIV	83.38	0.42	−1.94	0.200	AIx@75 (%)	Non-HIV	20.83	0.52	3.31	0.079
	PLWHIV	81.44	1.41				PLWHIV	24.14	1.76		
baPP (mmHg)	Non-HIV	45.77	0.42	1.18	0.432	Inflection Time (s)	Non-HIV	0.129	0.001	0.00	0.283
	PLWHIV	46.95	1.41				PLWHIV	0.125	0.003		
baMBPosc (mmHg)	Non-HIV	104.33	0.44	−1.46	0.359	Systolic Time (s)	Non-HIV	0.200	0.001	−0.008*	0.001
	PLWHIV	102.87	1.49				PLWHIV	0.192	0.002		
baMBPcalc (mmHg)	Non-HIV	98.63	0.43	−1.54	0.318	Tmax Backward (s)	Non-HIV	0.221	0.001	−0.006*	0.018
	PLWHIV	97.09	1.44				PLWHIV	0.215	0.002		
Heart Rate (beats/m)	Non-HIV	70.58	0.48	11.45	0.000	Tmax Forward (s)	Non-HIV	0.186	0.001	−0.010*	0.001
	PLWHIV	82.03	1.64				PLWHIV	0.176	0.003		
Stroke Volume (ml)	Non-HIV	73.88	0.53	−9.009*	0.000	Tstart Backward (s)	Non-HIV	0.055	0.001	−0.004*	0.039
	PLWHIV	64.88	1.81				PLWHIV	0.051	0.002		
Cardiac Output (l/min)	Non-HIV	5.12	0.03	0.11	0.356						
	PLWHIV	5.23	0.11								
Cardiac Index (l/min/m^2)	Non-HIV	2.70	0.02	0.21	0.002						
	PLWHIV	2.90	0.06								
SVR (mmHg/l/min)	Non-HIV	1.25	0.01	−0.05	0.081						
	PLWHIV	1.20	0.03								

Analysis of variables that depend on the calibration scheme

		Calibration scheme											
		baMBPosc/baDBP				baMBPcalc/baDBP				baSBP/baDBP			
Variables	Groups	MV	SE	Mean Difference	*p*-value	MV	SE	Mean Difference	*p*-value	MV	SE	Mean Difference	*P*-value
aoSBP (mmHg)	Non-HIV	135.2	0.64	−12.44	0.000	121.1	0.56	−6.36	0.002	120.3	0.53	−1.75	0.366
	PLWHIV	122.8	2.15			114.7	1.88			118.5	1.80		
aoDBP (mmHg)	Non-HIV	85.0	0.42	−2.53	0.096	84.5	0.42	−2.16	0.152	84.5	0.42	−1.58	0.296
	PLWHIV	82.4	1.42			82.3	1.41			82.9	1.42		
aoPP (mmHg)	Non-HIV	50.2	0.55	−9.87	0.000	36.6	0.44	−4.12	0.010	35.7	0.37	−0.15	0.912
	PLWHIV	40.4	1.87			32.5	1.50			35.6	1.25		
Inflection Pressure (mmHg)	Non-HIV	12.5	0.36	−3.82	0.003	9.2	0.28	−2.34	0.019	8.7	0.23	−0.86	0.308
	PLWHIV	8.7	1.21			6.8	0.93			7.8	0.79		
aoPb (mmHg)	Non-HIV	21.2	0.25	−4.87	0.000	15.3	0.20	−2.23	0.002	14.9	0.16	−0.09	0.877
	PLWHIV	16.3	0.86			13.0	0.68			14.9	0.56		
aoPf (mmHg)	Non-HIV	31.7	0.37	−6.31	0.000	23.3	0.30	−2.77	0.010	22.7	0.21	−0.31	0.686
	PLWHIV	25.4	1.25			20.5	1.01			22.4	0.73		
Pb/Pf (%)	Non-HIV	66.9	0.33	−2.75	0.022	65.7	0.34	−2.48	0.042	65.7	0.32	0.34	0.767
	PLWHIV	64.1	1.12			63.2	1.14			66.1	1.07		
aoPWV (m/s)	Non-HIV	8.3	0.03	−0.55	0.000	7.7	0.03	−0.31	0.002	7.7	0.02	−0.15	0.076
	PLWHIV	7.8	0.10			7.4	0.09			7.5	0.08		

MV, men value; SE, standard error; PLWHIV, people living with HIV; baSBP, baDBP, baPP, brachial artery systolic, diastolic and pulse pressure; baMBPosc and baMBPcalc, brachial artery mean blood pressure directly derived by oscillometry and calculated, respectively; SVR, systemic vascular resistance; PWA, pulse wave analysis; tmax, time to maximal; Aix, augmentation index; aoSBP, aoDBP, aoPP, aortic systolic, diastolic and pulse pressure; Pb and Pf, aortic backward and forward pressure component; aoPWV, aortic pulse wave velocity; Mean Difference refers to, HIV- minus PLWHIV value; Covariates appearing in the modelswere evaluated as follows, age: 51.09 y; sex (1: females; 0: male): 0.49; BMI: 27.98 kg/m^2; obesity (1: yes; 0: no): 1.02; current smoker (1: yes; 0: no): 0.17; CVD (1: yes; 0: no): 0.03; hypertension (1: yes; 0: no): 0.60; anti-hypertensive treatment (1: yes; 0: no): 0.52; dyslipidemia (1: yes; 0: no): 0.61; hyperlipidemia treatment (1: yes; 0: no): 0.26; diabetes (1: yes; 0: no): 0.09; anti-diabetic treatment (1: yes; 0: no): 0.07; hematocrit, 42.02%; glycemia, 98.82 mg/dl; creatinine, 0.8895 mg/dl; total cholesterol, 189.55 mg/dl; LDL-cholesterol, 113.90 mg/dl; HDL-cholesterol, 53.56 mg/dl; triglycerides, 139.84 mg/dl.

measured and expected values for the cardiovascular (dependent) variables and (ii) the presence of HIV infection and CRFs (similar cofactors included in ANCOVA; independent variables) (**Table 3**, **Supplementary Tables 7**, **8**).

Figure 1 highlights the relative difference between the measured and the expected value (ranked from highest to lowest for each calibration scheme) independently explained by the HIV infection.

Sample Size and Bootstrapping

A normal distribution was considered according to the central limit theorem, kurtosis, skewness coefficients distribution and the number of subjects studied (sample size >30) (45). The number of subjects included was higher than the minimum required sample size, both to build the reference group to obtain the mean values equations (included: 398, required size: 377) and to carry out association analyses (included: 1,086, required size: 103). The number of subjects studied was higher than the minimum number calculated for: $\alpha = 0.05$, $\beta = 0.20$, anticipated effect size = 0.15 (medium) and a total number of predictors in the regression models = 7. Even in this adequate and conservative context (e.g., sufficient sample size, adjusted comparisons), when making comparisons and associations we performed Bootstrapping of the samples, as a strategy to evaluate whether potential differences and/or associations observed between cardiovascular variables and subject condition do maintain even after analyzing different random sampling settings (resampling with replacement from the original sample). In other words, with this mechanism, any initial $p<0.05$ may no longer be significant after the "fictional random re-sampling" (i.e., bootstrapping). This type of test obligates the investigators to consider only those significant p values that replicate in both statistical scenarios (the actual sample and bootstrapping sampling). To this end, Bootstrap-derived 95% confidence intervals (1,000 samples) were obtained applying bias-corrected and accelerated methods for computing lower and upper confidence interval limits. The difference between mean values or association was considered significant only if the bootstrapping-derived p value was < 0.05 or 95% confidence interval of regression coefficient, quantified by bootstrapping did not contain the 0 value. It should be taken into account that in all cases, the use of the Bootstrapping technique confirmed the results obtained before it was applied.

All analyses were performed using SPSS Software (v.26, IBM-SPSS Inc., IL, USA), MedCalc (v.14.8.1, MedCalc Inc., Ostend, Belgium) and NCSS 2020 (NCSS, Kaysville, UT). A $p < 0.05$ was considered statistically significant.

RESULTS

Central Hemodynamics: Impact of Different Calibration Schemes

As expected, in all subgroups of subjects, the baMBPosc/baDBP calibration scheme resulted in higher levels of aoBP and waveform-derived parameters (**Figure 1**, **Supplementary Table 1**).

PLWHIV and Central Hemodynamics: Impact of Different Calibration Schemes

Regardless of the exposure to CRFs, PLWHIV presented, compared to non-HIV subjects: (i) similar levels of cardiac output (increased heart rate but reduced stroke volume), (ii) similar baBP levels, (iii) a tendency to lower AIx levels, which dissipated after adjusting for heart rate (AIxHR75), and (iv) similar pressure inflection time (**Table 2**, **Supplementary Tables 2**–**4**).

PLWHIV presented, compared to HIV- subjects, a tendency of having lower levels of aoSBP, aoPP, inflection pressure, Pb, Pf, Pb/Pf ratio and aoPWV, which clearly reached significance ($p < 0.001$, $p < 0.01$, and $p < 0.005$) when using the baMBPosc/baDBP or baMBPcalc/baDBP as the calibration scheme (**Table 2**, **Supplementary Tables 2**–**4**). Conversely, aortic parameters calibrated by baSBP/baDBP did not reach statistical significance between the groups. Consequently, results were highly influenced by the calibration method and dictated whether PLWHIV is associated with lower aoBP levels and differences in wave-derived indexes with respect to HIV- subjects (**Table 2**, **Supplementary Tables 2**–**4**).

HIV+ Status and Central Hemodynamics: Deviation From the Optimal Level in the Context of CRFs

Differences between the expected and measured values for all the baBP levels (baSBP, baDBP, baPP, baMBPcalc, baMBPosc) were not associated with the HIV infection (**Table 3**, **Supplementary Tables 7**–**8**). In contrast, differences between the measured and expected values of global hemodynamic parameters were positively (heart rate and cardiac index) and negatively (stroke volume and systemic vascular resistance) associated with the HIV infection, regardless of the exposure to CRFs. HIV infection was also negatively associated with systolic time, Tmax Backward and Forward and AIx, independently of CRFs (**Table 3**, **Supplementary Tables 7**–**8**).

When analyzing the explanatory capacity (β standardized coefficients) of HIV infection as independent variable in the context of other CRFs, "HIV+" variable becomes (i) the first position, when considering heart rate, Systolic Time and Tmax Forward (e.g., surpassing age and sex), (ii) second position, after sex, when considering stroke volume (e.g., exceeding age and smoking), and (iii) third position when analyzing cardiac index and AIx. In each scenario, HIV infection status exceeded the ability of other CRFs, such as hypertension or obesity, to explain the changes in the hemodynamic parameters (**Table 3**, **Supplementary Tables 7**, **8**).

Table 3, **Supplementary Tables 7**, **8** present the regression models for those variables whose values depend on the calibration scheme. When baMBPosc/baDBP and baMBPcalc/baDBP schemes were used, HIV was negatively associated with relative differences in aoSBP, aoPP, Inflection Pressure, Pb, Pf and aoPWV. The presence of HIV was only associated with the relative differences in the Pb/Pf ratio when the baMBPcalc/baDBP was the calibration scheme. With the sole exception of "Inflection Pressure," HIV was not

TABLE 3 | Multiple linear regression models between (i) relative differences between measured and expected cardiovascular level [(%), dependent variable] and cardiovascular risk factors and HIV status (independent variables).

Analysis of variables that do not depend on the calibration scheme

Brachial blood pressure, heart rate and PCA–derived parameters						Aortic wave analysis-derived parameterss					
Dep. V	**Indep. V**	**Bu**	**Bs**	***p*-value**	**aR²**	**Dep. V**	**Indep. V**	**Bu**	**Bs**	***P*-value**	**aR²**
Heart Rate	Constant	−0.279		0.014	0.18	Systolic Time	Constant	0.120		0.002	0.06
	HIV+	0.166	0.259	0.000			HIV+	−0.046	−0.165	0.000	
	Age	−0.003	−0.199	0.000			Htc	−0.003	−0.120	0.002	
	Glyc	0.001	0.143	0.000			Smoking	−0.021	−0.092	0.017	
	Sex	0.088	0.228	0.000			CVD	0.043	0.084	0.025	
	Obesity	0.022	0.088	0.022		Tmax Backward	Constant	0.135		0.001	0.03
	HDL	−0.001	−0.118	0.004			Htc	−0.002	−0.102	0.008	
	Htc	0.005	0.090	0.024			CVD	0.048	0.099	0.010	
	TC	0.000	0.075	0.041			Age	−0.001	−0.106	0.007	
Stroke Volume	Constant	0.085		0.009	0.16		HIV+	−0.026	−0.099	0.011	
	Sex	−0.115	−0.307	0.000		Tmax Forward	Constant	0.144		0.002	0.05
	HIV+	−0.130	−0.208	0.000			HIV+	−0.059	−0.176	0.000	
	Age	0.002	0.157	0.000			Htc	−0.004	−0.123	0.001	
	Smoking	−0.045	−0.091	0.012			Smoking	−0.022	−0.083	0.032	
	Dyslip	−0.031	−0.080	0.049		AIx	Constant	0.585		0.086	0.08
Cardiac Index	Constant	0.144		0.003	0.19		Sex	0.210	0.178	0.000	
	BMI	−0.013	−0.364	0.000			TG	0.000	−0.089	0.017	
	Sex	0.065	0.182	0.000			HIV+	−0.207	−0.106	0.005	
	HIV+	0.072	0.122	0.001			Htc	−0.020	−0.118	0.005	
	Glyc	0.001	0.094	0.015							
	Anti–dyslip	−0.030	−0.074	0.045							
	HTN	0.076	0.212	0.003							
	Anti–HTN	−0.053	−0.149	0.033							
Systemic Vascular Resistance	Constant	0.273		0.001							
	HTN	0.046	0.132	0.001							
	Glyc	−0.001	−0.106	0.008							
	Htc	−0.004	−0.086	0.025							
	HIV+	−0.047	−0.082	0.037							

Analysis of variables that depend on the calibration scheme

	Calibration scheme													
	baMBPcalc/baDBP					**baMBPosc/baDBP**					**baSBP/baDBP**				
Dep. V	**Indep. V**	**Bu**	**Bs**	***p*-value**	**aR²**	**Indep. V**	**Bu**	**Bs**	***p*-value**	**aR²**	**Indep. V**	**Bu**	**Bs**	***p*-value**	**aR²**
aoSBP	Constant	0.037		0.262	0.21	Constant	0.065		0.056	0.23	Constant	−0.005		0.902	0.23
	HTN	0.140	0.510	0.000		HTN	0.141	0.487	0.000		HTN	0.159	0.590	0.000	
	Sex	−0.054	−0.199	0.000		Sex	−0.053	−0.188	0.000		Anti–HTN	−0.081	−0.307	0.000	
	Anti–HTN	−0.077	−0.284	0.000		HIV+	−0.109	−0.232	0.000		BMI	0.005	0.172	0.000	
	HIV+	−0.061	−0.136	0.000		Anti–HTN	−0.080	−0.283	0.000		Age	−0.001	−0.151	0.000	
	BMI	0.003	0.103	0.005		BMI	0.002	0.080	0.027		Sex	−0.033	−0.123	0.000	
	------	------	------	------		------	------	------	------		Anti–dyslip	−0.034	−0.111	0.003	
	------	------	------	------		------	------	------	------		TC	0.000	0.070	0.046	
aoPP	Constant	−0.142		0.011	0.07	Constant	−0.049		0.353	0.10	Constant	−0.101		0.079	0.03
	Age	0.005	0.223	0.000		HIV+	−0.218	−0.220	0.000		BMI	0.005	0.092	0.021	
	HIV+	−0.115	−0.111	0.003		Age	0.004	0.180	0.000		Anti–dyslip	−0.051	−0.085	0.031	
	Sex	−0.058	−0.094	0.012		Sex	−0.054	−0.090	0.014		HTN	0.127	0.236	0.002	
	------	------	------	------		------	------	------	------		Anti–HTN	−0.092	−0.175	0.020	
Inflection Pressure	Constant	1.352		0.001	0.09	Constant	0.988		0.013	0.08	Constant	0.681		0.095	0.06

(Continued)

TABLE 3 | Continued

Analysis of variables that depend on the calibration scheme

	Calibration scheme													
	baMBPcalc/baDBP					baMBPosc/baDBP					baSBP/baDBP				
Dep. V	**Indep. V**	**Bu**	**Bs**	***p*-value**	**aR²**	**Indep. V**	**Bu**	**Bs**	***p*-value**	**aR²**	**Indep. V**	**Bu**	**Bs**	***p*-value**	**aR²**
	Age	0.012	0.202	0.000		HIV+	−0.356	−0.143	0.000		Sex	0.215	0.154	0.000	
	Hyc	−0.038	−0.162	0.000		Htc	−0.029	−0.132	0.000		HIV+	−0.229	−0.099	0.009	
	HIV+	−0.334	−0.125	0.001		HDL	0.004	0.089	0.022		Htc	−0.021	−0.106	0.012	
	Glyc	−0.003	−0.094	0.013		Age	0.007	0.119	0.002		TG	0.000	−0.076	0.045	
	------	------	------	------		Glyc	−0.003	−0.101	0.009		------	------	------	------	
Pb	Constant	−0.143		0.020	0.08	Constant	0.101		0.203	0.11	Constant	−0.087		0.150	0.03
	Age	0.006	0.221	0.000		HIV+	−0.244	−0.225	0.000		BMI	0.004	0.075	0.060	
	HIV+	−0.131	−0.115	0.003		Age	0.005	0.198	0.000		Anti−dyslip	−0.054	−0.085	0.030	
	Sex	−0.063	−0.093	0.012		Sex	−0.061	−0.094	0.010		HTN	0.143	0.251	0.001	
	Smoking	−0.074	−0.081	0.031		Glyc	−0.002	−0.136	0.002		Anti−HTN	−0.111	−0.200	0.008	
	------	------	------	------		Diabetes	0.114	0.100	0.020		------	------	------	------	
Pf	Constant	−0.145		0.013	0.08	Constant	−0.057		0.294	0.11	Constant	−0.153		0.016	0.03
	Age	0.005	0.228	0.000		HIV+	−0.215	−0.207	0.000		HTN	0.121	0.240	0.002	
	Sex	−0.072	−0.110	0.003		Age	0.005	0.208	0.000		BMI	0.004	0.085	0.032	
	HIV+	−0.116	−0.106	0.005		Sex	−0.072	−0.115	0.002		Anti−HTN	−0.087	−0.175	0.020	
	Anti−DM	0.095	0.075	0.042							Age	0.001	0.082	0.046	
Pb/Pf	Constant	0.023		0.255	0.01	Constant	0.119		0.032	0.02	Constant	−0.009		0.679	0.03
	Smoking	−0.031	−0.095	0.014		HIV+	−0.057	−0.147	0.000		Sex	0.028	0.125	0.001	
	Glyc	0.000	−0.079	0.041		Dyslip	−0.023	−0.097	0.017		Age	−0.001	−0.125	0.001	
	------	------	------	------		Htc	−0.003	−0.083	0.031		Smoking	−0.026	−0.086	0.023	
aoPWV	Constant	0.031		0.139	0.18	Constant	0.125		0.000	0.18	Constant	0.017		0.440	0.23
	HTN	0.065	0.374	0.000		HIV+	−0.083	−0.260	0.000		BMI	0.003	0.188	0.000	
	Sex	−0.039	−0.226	0.000		Sex	−0.043	−0.222	0.000		HTN	0.083	0.525	0.000	
	HIV+	−0.044	−0.154	0.000		HTN	0.074	0.377	0.000		Age	−0.002	−0.264	0.000	
	Anti−HTN	−0.034	−0.200	0.004		Anti−HTN	−0.040	−0.211	0.002		Anti−HTN	−0.041	−0.266	0.000	
	BMI	0.002	0.103	0.005		Age	−0.001	−0.098	0.010		Sex	−0.021	−0.133	0.000	
	------	------	------	------		------	------	------	------		TC	0.000	0.079	0.023	

*Glyc, Glycaemia (1: yes, 0: no); Sex, 1 (female), 0 (male); Obesity, 1 (yes), 0 (no); TC, total cholesterol; HDL, high-density lipoprotein cholesterol; Htc, hematocrit; Smoking, current smoking (1: yes, 0: no); CVD, cardiovascular disease (1: yes, 0: no). Dyslip, dyslipidemia (1: yes, 0: no); BMI, body mass index; TG, triglycerides; HTN, hypertension (1: yes, 0: no); Anti-dyslip, Anti-dyslipidemia treatment (1: yes, 0: no); Anti-HTN, Anti-hypertension treatment (1: yes, 0: no). Anti-DM, anti-diabetic mellitus treatment (1: yes, 0: no); Dep. V, dependent variable; Indep. V, independent or explanatory variable. Bu and Bs, un- and standardized beta coefficient; aR^2, adjusted R^2 p value; Aix, aortic augmentation index; aoSBP and aoPP, aortic systolic and pulse pressure; Pb and Pf, backward and forward aortic component. Units of independent variables are the same than in **Table 1**. Only variables in which HIV infection (HIV+) was statistically significant as an explanatory variable are shown. A variance inflation factor <5 was selected to evaluate (discard) significant multicollinearity.*

associated with the differences in the variables derived from the aoBP waveform analysis when baBSP/baDBP was used. Consequently, calibration by the baSBP/baDBP method was unable to reveal any cardiovascular variation associated with HIV infection.

When analyzing the position compared to other explanatory variables (e.g., CRFs) of the central hemodynamic variations (β standardized coefficients), while HIV infection positioned in the first place for the following variables: aoPP, Inflection Pressure, Pb, Pf, Pb/Pf and aoPWV (e.g., exceeding age and smoking) when considering baMBPosc/baDBP as the calibration method, it positioned in the third place when considering aoSBP. In each mentioned model, HIV+ status exceeded the relative weight of other CRFs, such as hypertension and obesity (**Table 3**, **Supplementary Table 8**).

When considering baMBPcalc/baDBP calibration scheme, the presence of HIV infection continued to surpass important CRFs in the explanatory ability, but it was no longer the main explanatory variable for any of the dependent variables analyzed (**Table 3**, **Supplementary Table 8**).

Finally, baSBP/baDBP calibration method only retains the presence of HIV infection as an explanatory variable of the Inflection Pressure behind other variables (**Table 3**, **Supplementary Table 8**). Interestingly, although HIV infection was not the main explanatory variable for aoSBP levels (regardless of the calibration scheme used), it was only exceeded by the presence of arterial hypertension, sex, or anti-hypertensive treatment, and in every case, its explanatory ability exceeded important CRFs (e.g., obesity, diabetes, dyslipidemia, smoking) (**Table 3**, **Supplementary Table 8**).

HIV+ Status and Central Hemodynamics: Comparative Analysis of Calibration Schemes

Figure 1 shows the percentage of variation between the measured and optimal value of the cardiovascular variables for each of the calibration schemes that could be explained by the HIV status (values ranked from the highest to the lowest value). Additionally, **Figure 1** presents comparatively the differences depending on the calibration scheme used. Regardless of other CRFs the presence of HIV infection explained up to 35.6% of the differences between the measured and the expected value of the cardiovascular variables.

In general, when baMBPosc/baDBP was the calibration scheme, the HIV infection was able to explain a greater percentage of the differences of the cardiovascular variables compared to other calibration methods, regardless of the variable analyzed (**Figure 1**). However, deviations from the expected value of certain variables were explained by HIV infection for (i) Inflection Pressure regardless of the calibration method, (ii) Pb, Pf, aoPP, aoSBP, aoPWV when calibrating by baMBPosc/baDBP or baMBPcalc/baDBP, and (iii) Pb/Pf when baMBPosc/baDBP was the selected calibration scheme (**Figure 1**).

Table 3, **Figure 1** show a hierarchical order between the calibration schemes, since the differences explained by HIV status begin to decrease in magnitude until they are no longer significant when calibrating sequentially by baMBPosc/baDBP, baMBPcalc/baDBP and baSBP/baDBP.

DISCUSSION

The Main Findings of Our Study can be Summarized as Follows:

First, despite presenting similar levels of baBP than CRFs-matched non-HIV subjects, PLWHIV presented significantly lower levels of aoSBP and aoPP. The lower levels of aoSBP and aoPP would be determined by lower magnitudes of Pf and Pb, as well as by lower reflection magnitude (Pb/Pf) and aoPWV. These results were specifically noted when using the calibration approaches recommended in the current literature (baMBP/baDBP) (16) and were not observed when calibrating by the baSBP/baDBP approach. As was hypothesized, the peripheral signal calibration scheme is a determining factor when assessing central hemodynamic variables in PLWHIV.

Second, HIV infection was an important explanatory factor of the differences of the levels of central hemodynamic variables, with respect to the expected value in healthy subjects not exposed to CRFs, exceeding in relative importance to classical CRFs (e.g., obesity, diabetes, dyslipidemia, smoking). Moreover, the presence of HIV infection was the main explanatory variable for variations in central hemodynamics when using the baMBPosc/baDBP calibration (followed by the baMBPcalc/baDBP scheme), exceeding CRFs such as age, sex, and hypertension. Consequently, the HIV status would be able to better explain variations in cardiovascular characteristics than classic CRFs. However, the relative importance of HIV status as an explanatory variable is highly dependent on the calibration scheme used, at the time that its explanatory capacity is reduced or even lost when calibrating by baSBP/baMBP. Therefore, the calibration scheme not only affects the absolute differences in the aortic cardiovascular variables measured in PLWHIV vs. non-HIV subjects, but also the relationship between these variables and the different (potential) explanatory variables of their values.

Third, within the central hemodynamic variables, HIV infection is more associated with variations in waveform-derived indexes (e.g., inflection pressure, AIx) than aoBP levels. In addition, regardless of the cardiovascular variable analyzed, baMBPosc/baDBP calibration determined that the presence of HIV infection explains a greater percentage of the differences of the cardiovascular variables.

These observations stressed out the relevance of reaching a consensus and systematization on the methodology used for the non-invasive assessment of central hemodynamics, since otherwise "different results" can be obtained despite analyzing the same patient. Consequently, it is not surprising, that controversial results have been reported on central hemodynamics between subjects with and without HIV infection (9–15). However, some considerations need to be pointed out. We found that regardless of exposure to CRFs, PLWHIV showed a tendency to present lower levels of stroke volume and cardiac index, higher heart rate, all of which led them to present unchanged cardiac output. The high heart rate observed in PLWHIV is consistent with previous reports (9, 13, 14). Ngatchou et al. (13) and Vlachopoulos et al. (14) reported that heart rate was higher in PLWHIV compared to non-HIV subjects, by an absolute mean value of 10 and 6.4 beats/min, respectively, results that are in line with our study in where the heart rate of PLWHIV was 11 beats/min more in average than the heart rate of HIV- subjects (**Table 2**).

Although it might be unexpected that HIV infection is associated with a "better hemodynamic profile," lower levels of aoBP and wave reflection indexes have already been reported in previous studies (9, 13, 14). Ngatchou et al. (13) in Cameroon, measured waveform-derived parameters (e.g., AIx) in apparently healthy subjects ($n = 96$, 41 ± 12 years) and untreated PLWHIV ($n = 108$, 39 ± 10 years). Authors reported that age- and sex-adjusted AIx was significantly lower in PLWHIV compared to non-HIV subjects (6 ± 4 vs. $8 \pm 7\%$, $p = 0.01$). Vlachopoulos et al. (14) in Greece studied PLWHIV ($n = 51$) with a recent HIV infection, free of antiretroviral treatment, and non-HIV subjects ($n = 35$), matched for age, sex, and smoking. The authors reported that while aortic stiffness was similar in the two groups ($p = 0.74$), aoSBP (by 4.6 mmHg, $p = 0.059$), aoDBP (by 5.7 mmHg, $p = 0.017$), Tr (the time the pulse wave needs to travel to the periphery and return to meet the incident wave), AIx (by 6.4%, $p = 0.048$) and augmentation pressure (by 3.3 mmHg, $p = 0.010$) were lower in PLWHIV. Consequently, these authors provided further evidence of PLWHIV having reduced aoBP and wave reflections, but similar aortic stiffness, at least in the early stages of the disease. Importantly, these authors calibrated the pressure waveform using the baSBP/baDBP scheme, so it would be expected that potential aoBP differences in PLWHIV

vs. non-HIV subjects could have been greater (in the early stages) and/or notoriously significant if another calibration scheme were used (14).

Taken together, reduced aoBP levels in the setting of similar baBP in PLWHIV would suggest that both HIV infection and/or highly active antiretroviral therapy play a role in hemodynamics, with differential effects on different locations of the vasculature (central vs. peripheral vessels). As was discussed by Martínez-Ayala et al. (12) lower aoBP levels may be caused by a peripheral vasodilation of small and medium-sized arteries, possibly induced by prostaglandins and other inflammatory cytokines associated with the chronic HIV infection. The vasodilation effect on peripheral reflection sites (e.g., arterial bifurcations) might cause a reduced Pb and Pb/Pf, and a reduced contribution to aoSBP.

In previous works performed on healthy subjects of the general population we showed that peripheral waveform calibration with the "baMBPosc/baDBP" scheme resulted in higher aoBP values (27–29). In this work we confirm these results. In fact, in all subgroups, the baMBPosc/baDBP calibration scheme resulted in higher levels of aoBP and waveform-derived indexes (**Figure 1**, **Supplementary Table 1**).

Clinical Importance

By using an automated oscillometric device and performing rigorous analyses of different groups, our study revealed that despite similar levels of brachial pressure, PLWHIV presented lower aoBP levels, explained by lower wave reflections and arterial stiffness. Additionally, compared to other CRFs, HIV infection demonstrated the highest explanatory capacity for variations in central hemodynamics.

Taking into account that the baMBP/baDBP method is currently the most recommended calibration scheme, PLWHIV would have a condition of equal or even lower ventricular afterload compared to non-HIV subjects.

Additionally, these results evidenced that the calibration approach is an important determinant of the results non-invasively obtained in central hemodynamics in PLWHIV. Our study strongly emphasizes the need for methodological transparency and consensus for the non-invasive assessment of central hemodynamic parameters in PLWHIV, and possibly in the general population.

Strengths and Limitations

First, our non-invasive approach is unable to identify the "ideal" calibration strategy, since it requires invasive (catheterism) vs. non-invasive agreement analysis. By performing agreement analyses, we would be able to reveal which calibration method is the one that achieves a more accurate and reliable quantification of the blood pressure values existing in the aortic root. However, invasive aoBP measurements are commonly not performed in subjects for obvious ethical reasons (when not performed due to other strict clinical indications). Second, our results are derived from cross-sectional studies, and therefore our observations do not allow us to know which calibration method has the greatest predictive ability of future cardiovascular events and/or disease. Additionally, it provides no data on longitudinal HIV-related temporal variations in variables of interest. Third, in contrast to other studies (9), we have not divided the subjects according to whether they were or were not under pharmacologic treatment, or to the time of being exposed to it. However, previous studies showed that HIV treatment does not contribute significantly to changes in the aoBP associated with HIV infection (10). Fourth, we have not considered the HIV duration as possible determinant variable of the central hemodynamic parameters, given that different studies showed that there were no significant differences in baBP, aoBP, aoPWV or AIx between patients with shorter vs. longer duration of HIV infection (13).

Finally, our population of PLWHIV can be considered characteristic of a population of subjects in outpatient care. Our cohort has an acceptable rate of antiretroviral treatment (46, 47). Moreover, in our cohort, the coinfection rate with cytomegalovirus (48) and hepatitis B (49) was lower than that in other cohorts, possibly because of differences in HIV transmission routes, age, or geographical differences.

CONCLUSIONS

In PLWHIV and non-HIV subjects, the baMBPosc/baDBP calibration scheme resulted in higher levels of aoBP and waveform-derived parameters. Despite similar levels of baBP, PLWHIV presented lower levels of aoSBP and aoPP compared to non-HIV subjects. Lower aoSBP and aoPP would be determined by both lower Pf and Pb, as well as by the lower levels of Pb/Pf and aoPWV. These results were only observed when using the calibration approach currently recommended (baMBP/baDBP), while these differences were not revealed by the baSBP/baDBP calibration scheme. PLWHIV showed a tendency to present lower levels of stroke volume and cardiac index, higher heart rate, and unchanged cardiac output.

The presence of HIV infection was shown to be an important determinant of the differences in the levels of the central hemodynamic variables, with respect to the expected value in healthy subjects not exposed to CRFs, exceeding important classical CRFs. The presence of HIV infection was the main explanatory variable for variations in central hemodynamics when using the baMBPosc/baDBP calibration, followed by the baMBPcalc/baDBP approach.

The calibration approach is an important determinant of the results obtained in central hemodynamics in PLWHIV. Our study strongly emphasizes the need for transparency and consensus in the methodologies employed for the non-invasive assessment of aoBP levels and waveform-derived indexes in PLWHIV and possibly in the general population.

DATA AVAILABILITY STATEMENT

The original contributions presented in the study are included in the article/**Supplementary Material**, further inquiries can be directed to the corresponding authors.

ETHICS STATEMENT

The studies involving human participants were reviewed and approved by Comité de Ética de Investigación. Hospital Dr. Héctor M. Cura, Olavarría, Provincia de Buenos Aires, Argentina. The patients/participants provided their written informed consent to participate in this study.

AUTHOR CONTRIBUTIONS

AD, MG, YZ, and DB contributed to conception and design of the study. AD, FS, and MG performed the cardiovascular non-invasive recordings and constructed, and organized the database. YZ and DB performed the statistical analysis. AD, MG, and DB wrote the first draft of the manuscript. AD, MG, JT, YZ, FS, and DB performed revisions and critically discussed the complete manuscript. All authors, read, and approved the submitted version.

FUNDING

This research was partially funded by extra-budgetary funds provided by the CUiiDARTE Center (YZ and DB).

ACKNOWLEDGMENTS

The authors thank to all the subjects who participated in the study, with special attention to the subjects of the PLWHIV group. MG is a graduate student in the Environment and Health Applied Sciences Doctoral Program (DCAAS) at UNICEN, Argentina.

SUPPLEMENTARY MATERIAL

The Supplementary Material for this article can be found online at: https://www.frontiersin.org/articles/10.3389/fcvm.2021.772912/full#supplementary-material

REFERENCES

1. Patel V, Chisholm D, Dua T, Laxminarayan R, Medina-Mora ME. Global mortality and morbidity of HIV/AIDS: mental, neurological, and substance use disorders. *Disease Control Priorities World Bank.* (2015) 3:4. doi: 10.1596/978-1-4648-0426-7_ch1
2. Shah ASV, Stelzle D, Lee KK, Beck EJ, Alam S, Clifford S, et al. Global burden of atherosclerotic cardiovascular disease in people living with HIV: systematic review and meta-analysis. *Circulation.* (2018) 138:1100–12. doi: 10.1161/CIRCULATIONAHA.117.033369
3. Rosenson RS, Hubbard D, Monda KL, Reading SR, Chen L, Dluzniewski PJ, et al. Excess risk for atherosclerotic cardiovascular outcomes among US adults with HIV in the current era. *J Am Heart Assoc.* (2020) 9:e013744. doi: 10.1161/JAHA.119.013744
4. Neuhaus J, Jacobs DR, Baker JV, Calmy A, Duprez D, La Rosa A, et al. Markers of inflammation, coagulation, and renal function are elevated in adults with HIV infection. *J Infect Dis.* (2010) 201:1788–95. doi: 10.1086/652749
5. Islam FM, Wu J, Jansson J, Wilson DP. Relative risk of cardiovascular disease among people living with HIV: a systematic review and meta-analysis. *HIV Med.* (2012) 13:453–68. doi: 10.1111/j.1468-1293.2012.00996.x
6. Grand M, Bia D, Diaz A. Cardiovascular risk assessment in people living with HIV: a systematic review and meta-analysis of real- life data. *Curr HIV Res.* (2020) 18:1–14. doi: 10.2174/1570162X17666191212091618
7. Stein JH, Kime N, Korcarz CE, Ribaudo H, Currier JS, Delaney JC. Effects of HIV infection on arterial endothelial function: results from a large pooled cohort analysis. *Arterioscler Thromb Vasc Biol.* (2021) 41:512–22. doi: 10.1161/ATVBAHA.120.315435
8. Kuate Defo A, Chalati MD, Labos C, Fellows LK, Mayo NE, Daskalopoulou SS. Association of HIV infection and antiretroviral therapy with arterial stiffness: a systematic review and meta-analysis. *Hypertension.* (2021) 78:320–32. doi: 10.1161/HYPERTENSIONAHA.121.17093
9. Gleason RL, Caulk AW, Seifu D, Parker I, Vidakovic B, Getenet H, et al. Current efavirenz (EFV) or ritonavir-boosted lopinavir (LPV/r) use correlates with elevate markers of atherosclerosis in HIV-infected subjects in Addis Ababa, Ethiopia. *PLoS ONE.* (2015) 10:e0117125. doi: 10.1371/journal.pone.0117125
10. Maloberti A, Dozio D, Betelli M, Bandera A, Squillace N, Gori A, et al. Brachial and central blood pressure in HIV-infected subjects. *Hypertens Res.* (2015) 38:405–12. doi: 10.1038/hr.2015.25
11. Lazar JM, Wu X, Shi Q, Kagame A, Cohen M, Binagwaho A, et al. Arterial wave reflection in HIV-infected and HIV-uninfected Rwandan women. *AIDS Res Hum Retroviruses.* (2009) 25:877–82. doi: 10.1089/aid.2008.0269
12. Martínez-Ayala P, Alanis-Sánchez GA, González-Hernández LA, Álvarez-Zavala M, Cabrera-Silva RI, Andrade-Villanueva JF, et al. Aortic stiffness and central hemodynamics in treatment-naïve HIV infection: a cross-sectional study. *BMC Cardiovasc Disord.* (2020) 20:440. doi: 10.1186/s12872-020-01722-8
13. Ngatchou W, Lemogoum D, Ndobo P, Yagnigni E, Tiogou E, Nga E, et al. Increased burden and severity of metabolic syndrome and arterial stiffness in treatment-naïve HIV+ patients from Cameroon. *Vasc Health Risk Manag.* (2013) 9:509–16. doi: 10.2147/VHRM.S42350
14. Vlachopoulos C, Sambatakou H, Tsiachris D, Mariolis I, Aznaouridis K, Ioakeimidis N, et al. Impact of human immunodeficiency virus infection on arterial stiffness and wave reflections in the early disease stages. *Artery Res.* (2009) 3:104–10. doi: 10.1016/j.artres.2009.08.001
15. Kaluba L, Goma F, Guure C, Munsaka S, Mutale W, Heimburger DC, et al. Immune activation and arterial stiffness in lean adults with HIV on antiretroviral therapy. *South Afr J HIV Med.* (2021) 22:1190. doi: 10.4102/sajhivmed.v22i1.1190
16. Papaioannou TG, Karageorgopoulou TD, Sergentanis TN, Protogerou AD, Psaltopoulou T, Sharman JE, et al. Accuracy of commercial devices and methods for noninvasive estimation of aortic systolic blood pressure a systematic review and meta-analysis of invasive validation studies. *J Hypertens.* (2016) 34:1237–48. doi: 10.1097/HJH.0000000000000921
17. Hope SA, Meredith IT, Cameron JD. Effect of non-invasive calibration of radial waveforms on error in transfer-function-derived central aortic waveform characteristics. *Clin Sci.* (2004) 107:205–11. doi: 10.1042/CS20030294
18. Papaioannou TG, Lekakis JP, Karatzis EN, Papamichael CM, Stamatelopoulos KS, Protogerou AD, et al. Transmission of calibration errors (input) by generalized transfer functions to the aortic pressures (output) at different hemodynamic states. *Int J Cardiol.* (2006) 110:46–52. doi: 10.1016/j.ijcard.2005.07.014
19. Nakagomi A, Okada S, Shoji T, Kobayashi Y. Crucial effect of calibration methods on the association between central pulsatile indices and coronary atherosclerosis. *Am J Hypertens.* (2017) 30:24–7. doi: 10.1093/ajh/hpw118

20. Weber T, Wassertheurer S, Rammer M, Maurer E, Hametner B, Mayer CC, et al. Validation of a brachial cuff-based method for estimating central systolic blood pressure. *Hypertension.* (2011) 58:825–32. doi: 10.1161/HYPERTENSIONAHA.111.176313
21. Wassertheurer S, Hametner B, Mayer CC, Hafez A, Negishi K, Papaioannou TG, et al. Aortic systolic pressure derived with different calibration methods: associations to brachial systolic pressure in the general population. *Blood Press Monit.* (2018) 23:134–40. doi: 10.1097/MBP.0000000000000319
22. Negishi K, Yang H, Wang Y, Nolan MT, Negishi T, Pathan F, et al. Importance of calibration method in central blood pressure for cardiac structural abnormalities. *Am J Hypertens.* (2016) 29:1070–6. doi: 10.1093/ajh/hpw039
23. Weber T, Wassertheurer S, Rammer M, Haiden A, Hametner B, Eber B. Wave reflections, assessed with a novel method for pulse wave separation, are associated with end-organ damage and clinical outcomes. *J Hypertens.* (2012) 60:534–41. doi: 10.1161/HYPERTENSIONAHA.112.194571
24. Protogerou AD, Argyris AA, Papaioannou TG, Kollias GE, Konstantonis GD, Nasothimiou E, et al. Left-ventricular hypertrophy is associated better with 24-h aortic pressure than 24-h brachial pressure in hypertensive patients: the SAFAR study. *J Hypertens.* (2014) 32:1805–14. doi: 10.1097/HJH.0000000000000263
25. Wassertheurer S, Baumann M. Assessment of systolic aortic pressure and its association to all cause mortality critically depends on waveform calibration. *J Hypertens.* (2015) 33:1884–8. doi: 10.1097/HJH.0000000000000633
26. Wassertheurer S, Hametner B, Sharman J, Weber T. Systolic blood pressure amplification and waveform calibration. *Hypertens Res.* (2017) 40:518. doi: 10.1038/hr.2016.181
27. Díaz A, Bia D, Zócalo Y. Impact of methodological and calibration approach on the association of central and peripheral systolic blood pressure with cardiac structure and function in children, adolescents and adults. *High Blood Press Cardiovasc Prev.* (2019). doi: 10.1007/s40292-019-00346-0
28. Díaz A, Bia D. Association between central-peripheral blood pressure amplification and structural and functional cardiac properties in children, adolescents, and adults: impact of the amplification parameter, recording system and calibration scheme. *High Blood Press Cardiovasc Prev.* (2021) 28:185–249. doi: 10.1007/s40292-021-00440-2
29. Zinoveev A, Castro JM, García-Espinosa V, Marin M, Chiesa P, Bia D, et al. Aortic pressure and forward and backward wave components in children, adolescents and young-adults: agreement between brachial oscillometry, radial and carotid tonometry data and analysis of factors associated with their differences. *PLoS ONE.* (2019) 14:e0226709. doi: 10.1371/journal.pone.0226709
30. Díaz A, Zócalo Y, Bia D. Percentile curves for left ventricle structural, functional and haemodynamic parameters obtained in healthy children and adolescents from echocardiography-derived data. *J Echocardiogr.* (2020) 18:16–43. doi: 10.1007/s12574-019-00425-0
31. Díaz A, Zócalo Y, Bia D. Normal percentile curves for left atrial size in healthy children and adolescents. *Echocardiography.* (2019) 36:770–82. doi: 10.1111/echo.14286
32. Díaz A, Zócalo Y, Cabrera-Fischer E, Bia D. Reference intervals and percentile curve for left ventricular outflow tract (LVOT), velocity time integral (VTI), and LVOT-VTI-derived hemodynamic parameters in healthy children and adolescents: Analysis of echocardiographic methods association and agreement. *Echocardiography.* (2018) 35:2014–34. doi: 10.1111/echo.14176
33. Díaz A, Zócalo Y, Bia D. Reference intervals and percentile curves of echocardiographic left ventricular mass, relative wall thickness and ejection fraction in healthy children and adolescents. *Pediatr Cardiol.* (2019) 40:283–301. doi: 10.1007/s00246-018-2000-y
34. Diaz A, Bia D, Zócalo Y, Manterola H, Larrabide I, Lo Vercio L, et al. Carotid intima media thickness reference intervals for a healthy argentinean population aged 11-81 years. *Int J Hypertens.* (2018) 2018:8086714. doi: 10.1155/2018/8086714
35. Diaz A, Zócalo Y, Bia D, Cabrera Fischer E. Reference intervals of central aortic blood pressure and augmentation index assessed with an oscillometric device in healthy children, adolescents, and young adults from Argentina. *Int J Hypertens.* (2018) 2018:1469651. doi: 10.1155/2018/1469651
36. Diaz A, Zócalo Y, Bia D, Wray S, Fischer EC. Reference intervals and percentiles for carotid-femoral pulse wave velocity in a healthy population aged between 9 and 87 years. *J Clin Hypertens.* (2018) 20:659–71. doi: 10.1111/jch.13251
37. Díaz A, Zócalo Y, Bia D, Sabino F, Rodríguez V, Cabrera FIscher EI. Reference intervals of aortic pulse wave velocity assessed with an oscillometric device in healthy children and adolescents from Argentina. *Clin Exp Hypertens.* (2019) 41:101–12. doi: 10.1080/10641963.2018.1445754
38. Whelton PK, Carey RM, Aronow WS, Casey DE, Collins KJ, Dennison Himmelfarb C, et al. 2017 ACC/AHA/AAPA/ABC/ACPM/AGS/APhA/ASH/ASPC/NMA/PCNA guideline for the prevention, detection, evaluation, and management of high blood pressure in adults: a report of the American college of cardiology/American heart association task force on clinical practice guidelines. *Hypertension.* (2018) 71:e13–e115. doi: 10.1161/HYP.0000000000000065
39. Chamberlain JJ, Johnson EL, Leal S, Rhinehart AS, Shubrook JH, Peterson L. Cardiovascular disease and risk management: review of the American diabetes association standards of medical care in diabetes 2018. *Ann Intern Med.* (2018) 168:640–50. doi: 10.7326/M18-0222
40. Authors/Task Force Members, Catapano AL, Graham I, De Backer G, Wiklund O, Chapman MJ, et al. 2016 ESC/EAS Guidelines for the management of dyslipidaemias: the task force for the management of dyslipidaemias of the European society of cardiology (ESC) and European atherosclerosis society (EAS) developed with the special contribution of the European assocciation for cardiovascular prevention & rehabilitation (EACPR). *Atherosclerosis.* (2016) 253:281–344. doi: 10.1016/j.atherosclerosis.2016.08.018
41. Zócalo Y, García-Espinosa V, Castro JM, Zinoveev A, Marin M, Chiesa P, et al. Stroke volume and cardiac output non-invasive monitoring based on brachial oscillometry-derived pulse contour analysis: explanatory variables and reference intervals throughout life (3-88 years). *Cardiol J.* (2020). doi: 10.5603/CJ.a2020.0031. [Epub ahead of print].
42. Zócalo Y, Bia D. Age- and sex-related profiles for macro, macro/micro and microvascular reactivity indexes: association between indexes and normative data from 2609 healthy subjects (3-85 years). *PLoS ONE.* (2021) 16:e0254869. doi: 10.1371/journal.pone.0254869
43. Bia D, Zócalo Y. Physiological age- and sex-related profiles for local (Aortic) and regional (carotid-femoral, carotid-radial) pulse wave velocity and center-to-periphery stiffness gradient, with and without blood pressure adjustments: reference intervals and agreement between methods in healthy subjects (3-84 Years). *J Cardiovasc Dev Dis.* (2021) 8:3. doi: 10.3390/jcdd8010003
44. Zócalo Y, Bia D. Sex-and age-related physiological profiles for brachial, vertebral, carotid and femoral arteries blood flow velocity parameters during growth and aging (4-76 y): comparison with clinical cut-off levels. *Front Physiol.* (2021) 12:729309. doi: 10.3389/fphys.2021.729309
45. Lumley T, Diehr P, Emerson S, Chen L. The importance of the normality assumption in large public health data sets. *Annu Rev Public Health.* (2002) 23:151–69. doi: 10.1146/annurev.publhealth.23.100901.140546
46. Piñeirúa A, Sierra-Madero J, Cahn P, Guevara Palmero RN, Martínez Buitrago E, Young B, et al. The HIV care continuum in Latin America: challenges and opportunities. *Lancet Infect Dis.* (2015) 15:833–9. doi: 10.1016/S1473-3099(15)00108-5
47. Crabtree-Ramírez BE, Caro-Vega Y, Belaunzarán-Zamudio PF, Shepherd BE, Rebeiro PF, Veloso V, et al. Temporal changes in ART initiation in adults with high CD4 counts in Latin America: a cohort study. *J Int AIDS Soc.* (2019) 22:e25413. doi: 10.1002/jia2.25413
48. Lichtner M, Cicconi P, Vita S, Cozzi-Lepri A, Galli M, Lo Caputo S, et al. Cytomegalovirus coinfection is associated with an increased risk of severe non-AIDS-defining events in a large cohort of HIV-infected patients. *J Infect Dis.* (2015) 211:178–86. doi: 10.1093/infdis/jiu417
49. Tengan FM, Abdala E, Nascimento M, Bernardo WM, Barone AA. Prevalence of hepatitis B in people living with HIV/AIDS in Latin America and the

caribbean: a systematic review and meta-analysis. *BMC Infect Dis.* (2017) 17:587. doi: 10.1186/s12879-017-2695-z

Conflict of Interest: The authors declare that the research was conducted in the absence of any commercial or financial relationships that could be construed as a potential conflict of interest.

Publisher's Note: All claims expressed in this article are solely those of the authors and do not necessarily represent those of their affiliated organizations, or those of the publisher, the editors and the reviewers. Any product that may be evaluated in this article, or claim that may be made by its manufacturer, is not guaranteed or endorsed by the publisher.

GLOSSARY

Aix, Aortic augmentation index; AIxHR75, Heart rate-adjusted aortic augmentation index (for heart rate equal 75 beats/min); aoBP, Aortic blood pressure; aoPWV, Aortic pulse wave velocity; aoSBP, Central aortic systolic blood pressure; aoPP, Central aortic pulse pressure; aoDBP, Central aortic diastolic blood pressure; baBP, Brachial artery blood pressure; baDBP, Brachial artery diastolic blood pressure; baMBP, Brachial artery mean blood pressure; baMBPcalc, Brachial artery mean blood pressure calculated using equations; baMBPcalc/baDBP, Calibration to baDBP and calculated brachial mean blood pressure; baMBPosc, Brachial artery mean blood pressure measured directly by oscillometry; baMBPosc/baDBP, Calibration to baDBP and oscillometry-derived brachial mean blood pressure, baPP, Brachial artery pulse pressure; baSBP, Brachial artery systolic blood pressure; baSBP/baDBP, Calibration to brachial systolic and diastolic pressure (systolic-diastolic calibration); CRFs, Cardiovascular risk factors; HIV, Human immunodeficiency virus; HIV-, Non-HIV subjects or non-HIV infection; HIV+, Subjects with HIV infection; Pb, Peak or maximal amplitude of backward (reflected) wave component; Pf, Peak or maximal amplitude of forward (incident) wave component; PLWHIV, People living with human immunodeficiency virus; Tmax Backward, Time from the "foot wave" to the peak of backward (reflected) wave component; Tmax Forward, Time from the "foot wave" to the peak of forward (incident) wave component; Tstart Backward, Time from the "foot wave" to the initial phase (arrival) of the backward component.

frontiers in Cardiovascular Medicine

ORIGINAL RESEARCH
published: 03 January 2022
doi: 10.3389/fcvm.2021.763351

A Multicenter Assessment of Anatomic Suitability for Iliac Branched Devices in Eastern Asian Patients With Unilateral and Bilateral Aortoiliac Aneurysms

Zheyun Li[1,2†], Min Zhou[3†], Guili Wang[4], Tong Yuan[1,2], Enci Wang[1,2], Yufei Zhao[1,2], Xiaolong Shu[1,2], Yuchong Zhang[1,2], Peng Lin[1,2], Weiguo Fu[1,2,5] and Lixin Wang[1,2,5*]*

[1] Department of Vascular Surgery, Zhongshan Hospital, Fudan University, Shanghai, China, [2] Vascular Surgery Institute of Fudan University, Shanghai, China, [3] Department of Vascular Surgery, Nanjing Drum Tower Hospital, Nanjing University Medical School, Nanjing, China, [4] Department of Vascular Surgery, Affiliated Jinan Central Hospital of Shandong First Medical University, Jinan, China, [5] Department of Vascular Surgery, Xiamen Branch, Zhongshan Hospital, Fudan University, Xiamen, China

OPEN ACCESS

Edited by:
Pasqualino Sirignano,
Sapienza University of Rome, Italy

Reviewed by:
Gioele Simonte,
Hospital of Santa Maria della Misericordia in Perugia, Italy
Wassim Mansour,
Sapienza University of Rome, Italy

***Correspondence:**
Weiguo Fu
fu.weiguo@zs-hospital.sh.cn
Lixin Wang
wang.lixin@zs-hospital.sh.cn

[†] These authors have contributed equally to this work

Specialty section:
This article was submitted to Atherosclerosis and Vascular Medicine, a section of the journal Frontiers in Cardiovascular Medicine

Received: 23 August 2021
Accepted: 07 December 2021
Published: 03 January 2022

Citation:
Li Z, Zhou M, Wang G, Yuan T, Wang E, Zhao Y, Shu X, Zhang Y, Lin P, Fu W and Wang L (2022) A Multicenter Assessment of Anatomic Suitability for Iliac Branched Devices in Eastern Asian Patients With Unilateral and Bilateral Aortoiliac Aneurysms. Front. Cardiovasc. Med. 8:763351. doi: 10.3389/fcvm.2021.763351

Objective: This study aims to assess the suitability of four types of commercial iliac branch device systems to treat Eastern Asian abdominal aortic aneurysm (AAA) patients with bilateral or unilateral common iliac artery aneurysms (CIAAs).

Methods: Patients with a coexisting AAA and a unilateral or bilateral CIAAs who underwent endovascular aneurysm repair (EVAR) at two tertiary centers in China from 2015 to 2017 were reviewed. Morphology of lesions was measured and the anatomic suitability for Cook iliac branch device (IBD), Gore iliac branch endoprosthesis (IBE), Lifetech iliac branch stent graft (IBSG), and Jotec IBD was evaluated according to the latest instructions for use.

Results: Seventy-six patients with AAA were enrolled, including 35 bilateral CIAAs, 41 unilateral CIAAs. A hundred and eleven lesions were investigated aggregately: 16.2, 28.8, 21.6, and 19.8% met the criteria for Cook IBD, Gore IBE, Lifetech IBSG, and Jotec IBD, respectively. A total of 34 (44.7%) patients could be treated for at least one lateral lesion. The diameter of the internal iliac artery (IIA) was the most common restriction for IBD application. Additionally, the IIA diameter of lesions in the bilateral group was significantly larger compared with the unilateral group ($P < 0.001$). Based on the anatomical characteristics alone, it is likely that IBDs will be more suitable for unilateral lesions than bilateral ones ($P < 0.05$). However, there was no difference between the suitability for patients with unilateral or bilateral CIAAs ($P > 0.05$).

Conclusions: Less than half of Eastern Asian patients with aortoiliac aneurysms were eligible for IBD application. This was primarily due to the IIA diameter failing to meet the

criteria. And thus, the suitability of lesions in bilateral group was significantly lower than that in the unilateral group. Aiming to expand the indications and optimize the design of the iliac branch devices, IIA diameter and the anatomical characteristics of the bilateral lesions should be considered deliberately.

Keywords: abdominal aortic aneurysm (AAA), aortoiliac aneurysm (AIA), iliac branch device (IBD), bilateral lesions, Eastern Asian patients

INTRODUCTION

Aneurysmal degeneration of the iliac arteries can occur alone or in association with other large vessel aneurysms. Approximately 15-40% of patients presenting with an abdominal aortic aneurysm (AAA) also have a concomitant unilateral or bilateral common iliac artery aneurysm (CIAA) (1–3). For patients with a coexisting CIAA and AAA undergoing endovascular aneurysm repair (EVAR), it is essential to provide adequate distal fixation of the iliac limb into the iliac artery. Nevertheless, the complex anatomical characteristics of the CIAA pose a challenge for device implantation, distal anchoring, and complete aneurysm exclusion. There is evidence indicating that not all patients fit the instructions for use (IFUs) of standard bifurcated endografts (4). A common approach is to extend the limb directly into the external iliac artery (EIA), with or without concomitant internal iliac artery (IIA) embolization (5–7). However, sacrificing both IIAs may result in buttock claudication, erectile dysfunction, colonic ischemia, and spinal cord ischemia (8–10). Moreover, ischemic complications are observed in 30-55% of the patients even after unilateral IIA occlusion (11).

In order to prevent these potential complications, iliac branch devices (IBD) have been developed to preserve perfusion through unilateral or bilateral hypogastric arteries when excluding CIAA. Three commercial IBD configurations by respective manufacturers, namely, Cook Medical, W. L. Gore & Associates, and Jotec have been developed so far in Western countries, and one designed by Lifetech for Asian patients (6, 12–14). Among those, Lifetech iliac branch stent graft (IBSG) is the only device obtained the China National Medical Products Administration (NMPA) approval. Anatomical characteristics of aortoiliac aneurysm (AIA) have been regarded as a major factor affecting the application of IBDs (4, 5). Therefore, in this study, four types of IBDs were assessed for their suitability of Eastern Asian patients with AIA according to their instruction for use (IFU). Moreover, since bilateral implantation of IBDs is considered to be a safe and effective technique to preserve antegrade IIA flow and help decrease potential ischemic complications further (15), the suitability of unilateral and bilateral lesions was also taken into account. An appropriate choice of IBDs to treat Eastern Asian patients is intended to be provided to vascular surgeons through this study, as well as suggestions to improve future generations of iliac branch technologies.

MATERIALS AND METHODS

Study Design and Population

This retrospective, multicenter study was performed in accordance with the principles of the Declaration of Helsinki and approved by the Institutional Review Board of Zhongshan Hospital, Shanghai (approval no. B2018-045) and Drum Tower Hospital, Nanjing (approval no. 2017-015-05). The retrospective data were anonymous, and the requirement for informed consent was therefore waived. Both of these international vascular centers receive patients predominantly from China and East Asia. A total of 1,049 patients received EVAR and 119 underwent open repair in the two institutions between 2015 and 2017. We totally reviewed 76 patients with an infrarenal AAA and coexisting CIAA (35 patients with bilateral CIAAs, 41 patients with a unilateral CIAA) who underwent EVAR from 2015 to 2017. A common iliac artery aneurysm $\geq$ 2.5 cm concomitant with AAA would be treated simultaneously during EVAR. The threshold to include patients in this study cohort was the presence of a unilateral or bilateral CIA of at least 25 mm in diameter associated with a concomitant AAA. All patients who underwent repair for aneurysm rupture, pseudoaneurysm, solitary CIA aneurysm, or mycotic aneurysm were excluded from this study.

Anatomic Measurement

Preoperative computed tomography angiography (CTA) images of the aortoiliac from the enrolled patients were obtained. All imaging data were reviewed on a three-dimensional workstation using Vitrea fX software (Vital Images, Minnetonka, MN, USA). Briefly, a centerline was generated in the aorta from the infrarenal aorta to the bilateral EIAs and IIAs, and aortoiliac lengths and diameters were measured based on centerline images. The maximum diameter of the artery was measured from the adventitia and the mural thrombus was considered as well. We compared the length of EIA with relative IBD criteria rather than presenting the exact measured value directly. We also added annotations on those with poor vascular condition such as severe occlusion, stenosis, calcification, and inappropriate bifurcation angle of iliac artery. A vascular surgeon with at least 3 years of experience and a radiology attending physician performed all measurements independently.

Iliac Branch Device Systems

Currently, there are only four types of iliac branch device systems off the shelf worldwide, which were designed by Cook Medical (Bloomington, IN, USA), W. L. Gore & Associates (Flagstaff, AZ, USA), Lifetech (Shenzhen, Guangdong, China), and Jotec (Hechingen, BW, Germany). The components of respective IBD systems were taken into consideration as well. Among all IBDs, only Lifetech IBSG is approved in China. The exclusion criteria of these devices are described in **Table 1** according to the latest IFUs.

Statistical Analysis

Based on the IFU requirements, we evaluated the anatomical features of lesions to determine if each device was suitable. Accordingly, IBD applicability for patients was assessed in terms of lesion suitability. Descriptive statistics were presented as mean with standard deviation or median with range. The Chi-square test was used to compare the applicability of four IBDs. A *P*-value < 0.05 was considered statistically significant. Calculation and comparison of all data were performed in Excel (Microsoft, Redmond, WA, USA) and SPSS 25.0 (IBM Corp., Armonk, NY, USA).

RESULTS

From 2015 to 2017, 76 AAA patients with 41 unilateral and 35 bilateral CIAAs were identified in Zhongshan Hospital and Nanjing Drum Tower Hospital. The IIA maximum diameters were measured at 18.3 ± 5.1 and 15.3 ± 7.9 mm on the left and right side, while the EIA max diameters were 11.2 ± 2.2 and 11.3 ± 2.9 mm, respectively. The average IIA max diameter in patients with bilateral lesions (18.6 ± 8.9 mm) was larger than those with unilateral lesions (12.9 ± 6.4 mm, $P < 0.001$). The anatomical characteristics of lesions are summarized in **Table 2**. Lesions in the unilateral group exhibited a significant anatomical difference from lesions in the bilateral group (**Table 3**).

Based on the anatomical characteristics, the suitability of the 111 unilateral and bilateral pathological CIAs for the four types of IBDs are depicted in **Table 4**. By strictly evaluating the applicability to each lesion, 74 (66.7%) lesions failed to meet the required criteria of any IBD. Specifically, 93 lesions (83.8%) were excluded based on Cook's criteria, which was significantly higher than the number excluded by Gore's (79, 71.2%, **Figure 1A**). As for Lifetech and Jotec, 87 (78.4%) and 89 (80.2%) did not meet the criteria, respectively. IIA diameter was the most common reason for the exclusion of all four IBDs. Nearly three-quarters of the lesions (81, 73.0%) were excluded by Cook criteria due to IIA diameter, 72 (64.9%) by Gore, 76 (68.5%) by Lifetech and, 81 (73.0%) by Jotec. Another major criterion for exclusion was CIA length. Thirty-three (29.7%) lesions were excluded by Cook and 20 (18.0%) by the other three IBDs. Nevertheless, there is no statistical difference in CIA length or IIA diameter exclusion rate among the four IBDs (**Figures 1B,D**). However, IBDs showed significant differences in the exclusion rate caused by the EIA diameter (**Figure 1C**). In addition, IBD applicability of lesions in the unilateral group was significantly higher than that in the bilateral group ($P < 0.05$, **Figure 1E**), which is mainly because of the difference in IIA diameter (**Table 4**).

We next sought to assess the suitability per patient. The applicability of all types of iliac branch devices for 76 patients is shown in **Table 5**. Approximately half of the patients (34, 44.7%)

TABLE 1 | Summary of exclusions for the four IBDs based on anatomical characteristics.

	Cook IBD	Gore IBE	Lifetech IBSG	Jotec IBD
CIA length (mm)	<50	<40 or Aortoiliac length < 165	<40	<40
CIA diameter (mm)	<16	<17	<18	<18
EIA length (mm)	<20	<10	<15	<15
EIA diameter (mm)	<8 or >11	<6.5 or >25	<8.4 or >14.5	<8 or >13
IIA length (mm)	<10	<10	< 10	<15
IIA diameter (mm)	<6 or >11.4	<6.5 or >13.5	<5 or >11.4	<6 or >11.4

TABLE 3 | Comparison of anatomical characteristics for unilateral and bilateral lesions (mm).

	Unilateral (*n* = 41)	Bilateral (*n* = 35)	*P*-value
CIA max. diameter	30.7 ± 5.3	34.3 ± 10.3	0.016
CIA length	54.0 ± 14.9	61.6 ± 20.6	0.029
IIA max. diameter	12.9 ± 6.4	18.6 ± 8.9	<0.001
IIA length	52.4 ± 10.5	50.9 ± 11.4	0.477
EIA max. diameter	10.6 ± 1.6	11.6 ± 3.0	0.022

TABLE 2 | Anatomical characteristics of aortoiliac aneurysms of Eastern Asian patients (mm).

	Zhongshan cohort (*n* = 56)			Nanjing cohort (*n* = 55)			All (*n* = 111)		
	Mean	SD	Median (range)	Mean	SD	Median (range)	Mean	SD	Median (range)
Left CIA max. diameter	30.0	5.2	28.7 (25.0–45.8)	34.6	8.8	32.3 (25.1–51.9)	32.6	7.7	30.7 (25.0–51.9)
Right CIA max. diameter	32.3	8.4	31.0 (25.0–66.0)	34.3	11.2	30.8 (25.1–67.2)	33.2	9.7	30.9 (25.0–67.2)
Left CIA length	55.1	16.3	52.5 (30.0–88.0)	61.3	20.8	63.7 (24.5–94.5)	58.6	19.0	56.6 (24.5–94.5)
Right CIA length	56.7	16.2	58.3 (23.0–92.0)	61.6	22.1	61.5 (22.2–111.4)	58.9	19.1	59.0 (22.2–111.4)
Left IIA max. diameter	16.6	9.1	16.4 (5.1–35.9)	19.5	8.8	18.6 (8.4–45.1)	18.3	5.1	18.3 (5.1–45.1)
Right IIA max. diameter	13.0	8.5	10.5 (4.9–41.0)	18.1	6.2	17.4 (7.8–31.4)	15.3	7.9	13.9 (4.9–41.0)
Left IIA length	51.3	10.1	50.1 (33.9–74.3)	49.0	14.3	45.4 (28.6–76.7)	50.0	12.6	47.0 (28.6–76.7)
Right IIA length	53.5	8.6	52.6 (39.6–73.3)	51.1	11.3	49.2 (27.3–77.7)	52.4	9.9	52.0 (27.3–77.7)
Left EIA max. diameter	9.9	1.4	9.9 (7.5–13.4)	12.2	2.2	12.2 (9.1–19.3)	11.2	2.2	10.7 (7.5–19.3)
Right EIA max. diameter	10.2	1.6	10.0 (7.7–14.0)	12.7	3.4	11.8 (8.8–25.1)	11.3	2.9	10.8 (7.7–25.1)

TABLE 4 | Anatomic reasons for exclusion and comparison for unilateral and bilateral lesions.

Exclusion criteria	Lesion excluded			
	Unilateral ($n = 41$)	Bilateral ($n = 70$)	*P*-value	All ($n = 111$)
ALL	21 (51.2%)	53 (75.7%)	0.008	74 (66.7%)
Cook IBD	30 (73.2%)	62 (88.6%)	0.036	93 (83.8%)
CIA length < 50 mm	14 (34.1%)	19 (27.1%)	0.285	33 (29.7%)
CIA diameter < 16 mm	0 (0%)	0 (0%)	–	0 (0%)
EIA length < 20 mm	0 (0%)	0 (0%)	–	0 (0%)
EIA diameter < 8 or > 11 mm	17 (41.5%)	34 (48.6%)	0.299	51 (45.9%)
IIA length < 10 mm	0 (0%)	0 (0%)	–	0 (0%)
IIA diameter < 6 or > 11.4 mm	22 (53.7%)	59 (84.3%)	0.001	81 (73.0%)
Gore IBE	23 (56.1%)	56 (80.0%)	0.007	79 (71.2%)
Aortoiliac length < 165 or CIA length < 40 mm	7 (17.1%)	13 (18.6%)	0.529	20 (18.0%)
CIA diameter < 17 mm	0 (0%)	0 (0%)	–	0 (0%)
EIA length < 10 mm	0 (0%)	0 (0%)	–	0 (0%)
EIA diameter < 6.5 or > 25 mm	0 (0%)	1 (1.4%)	0.631	1 (.9%)
IIA length < 10 mm	0 (0%)	0 (0%)	–	0 (0%)
IIA diameter < 6.5 or > 13.5 mm	20 (48.8%)	52 (74.3%)	0.006	72 (64.9%)
Lifetech IBSG	27 (65.9%)	60 (85.7%)	0.014	87 (78.4%)
CIA length < 40 mm	7 (17.1%)	13 (18.6%)	0.529	20 (18.0%)
CIA diameter < 18 mm	0 (0%)	0 (0%)	–	0 (0%)
EIA length < 15 mm	0 (0%)	0 (0%)	–	0 (0%)
EIA diameter < 8.4 or > 14.5 mm	3 (7.3%)	9 (12.9%)	0.283	12 (10.8%)
IIA length < 10 mm	0 (0%)	0 (0%)	–	0 (0%)
IIA diameter < 5 or > 11.4 mm	20 (48.8%)	56 (80.0%)	0.001	76 (68.5%)
Jotec IBD	27 (65.9%)	62 (88.6%)	0.004	89 (80.2%)
CIA length < 40 mm	7 (17.1%)	13 (18.6%)	0.529	20 (18.0%)
CIA diameter < 18 mm	0 (0%)	0 (0%)	–	0 (0%)
EIA length < 15 mm	0 (0%)	0 (0%)	–	0 (0%)
EIA diameter < 8 or > 13 mm	4 (9.8%)	18 (25.7%)	0.033	22 (19.8%)
IIA length < 15 mm	0 (0%)	0 (0%)	–	0 (0%)
IIA diameter < 6 or > 11.4 mm	22 (53.7%)	59 (84.3%)	0.001	81 (73.0%)

could be treated with preserving at least one IIA. There were 30 (39.3%) patients eligible for Gore IBE, and its applicability is significantly higher than Cook IBD (18, 23.7%, **Figure 2A**). As for the other two IBDs, 24 (21.6%) patients were eligible for Lifetech and 22 (19.8%) for Jotec devices. Suitability per patient with unilateral aortoiliac aneurysm for all IBDs was found to have no statistical discrepancy compared with those who have bilateral lesions ($P > 0.05$, **Figure 2B**). Of note, only three patients (3.9%) in the bilateral group could be treated on both sides. One of them met the criteria of Gore IBE for the left lesion and the three other IBDs for the right, while the other two patients were eligible for all IBDs for both sides.

The difference among the four types of IBDs is further analyzed in **Figure 3**. The diameter of IIA played an essential role in restricting the use of Cook (49%), Gore (77%), Lifetech (70%), and Jotec devices (66%, **Figure 3A**). The suitability of all the lesions for four IBDs was summarized by a Venn diagram (**Figure 3B**). Only 15 lesions were eligible for all four types of IBDs. Fourteen lesions met the criteria of merely one device, of which Gore accounted for 11 lesions (**Figure 3C**). Overall, 32 aortoiliac aneurysms were eligible for Gore IBE which was higher than any other devices (**Figure 3D**).

DISCUSSION

Iliac branch devices have been reported as a safe, feasible, and effective solution to preserve IIA blood flow in select patients with suitable anatomy (16, 17). Currently, there are several designs of IBD on clinical trials or commercially available all over the world (18, 19). The devices of Cook and Jotec are undergoing clinical trials in the United States, while Gore IBD has already received Food and Drug Administration approval. IBSG, designed by Lifetech, obtained the market registration approval in China recently. However, the usage of IBDs is limited by anatomical characteristics. Several published literature have analyzed the applicability of Cook and Gore device for AAA patients requiring extension into EIA during EVAR (4, 5). Itoga et al. demonstrated that the anatomic suitability of Japanese patients with aortoiliac aneurysm for those two IBDs was limited by smaller CIA diameter and shorter CIA length (20). Our

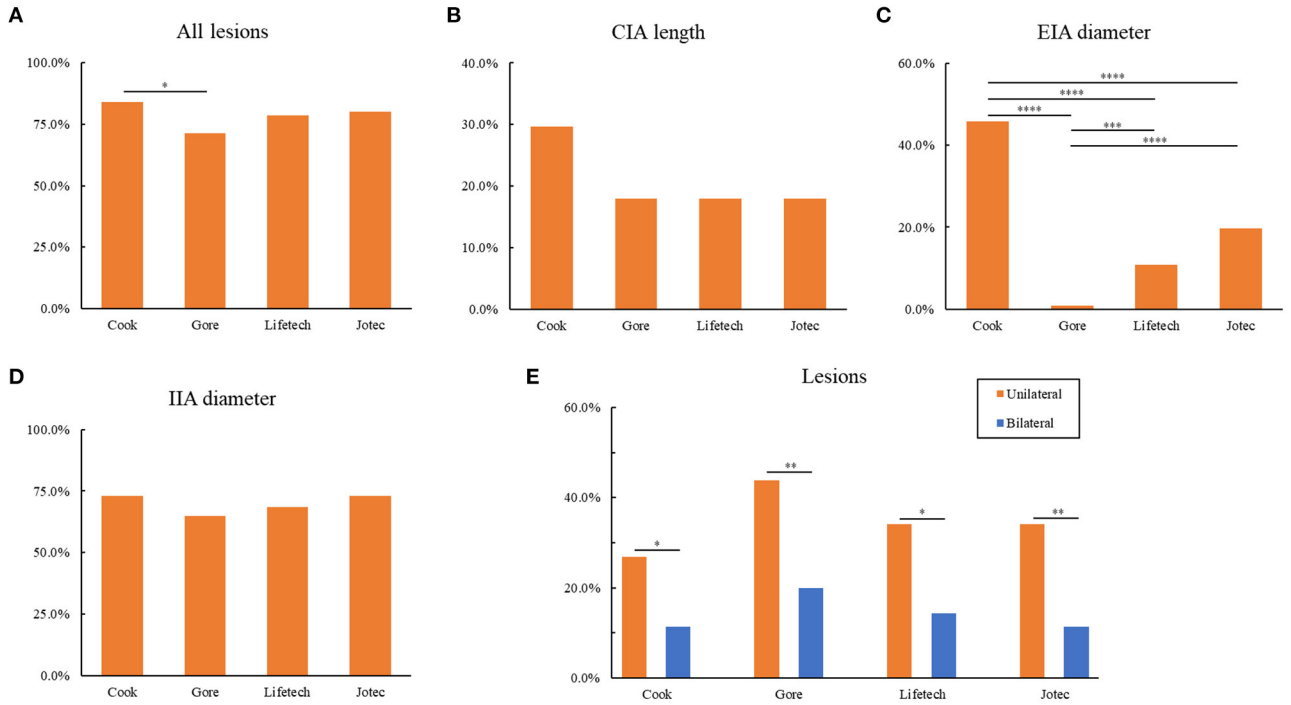

FIGURE 1 | Exclusion for IBDs based on anatomical characteristics. **(A)** Exclusion of all lesions for four IBDs. **(B)** Exclusion of CIA length for four IBDs. **(C)** Exclusion of EIA diameter for four IBDs. **(D)** Exclusion of IIA diameter for four IBDs. **(E)** Comparison of the exclusion of unilateral and bilateral lesions for four IBDs. *$P < 0.05$; **$P < 0.01$; ***$P < 0.001$; ****$P < 0.0001$; as determined by Chi-square test. IBD, iliac branch device; CIA, common iliac artery; EIA, external iliac artery; IIA, internal iliac artery.

TABLE 5 | Exclusion for patients with unilateral and bilateral lesions.

	Unilateral ($n = 41$)	Bilateral ($n = 35$)			All ($n = 76$)
		1	2	all	
Cook IBD	11 (26.8%)	6 (17.1%)	1 (2.9%)	7 (20.0%)	18 (23.7%)
Gore IBE	18 (43.9%)	10 (28.6%)	2 (5.7%)	12 (34.3%)	30 (39.5%)
Lifetech IBSG	14 (34.1%)	8 (22.9%)	1 (2.9%)	9 (25.7%)	23 (30.3%)
Jotec IBD	14 (34.1%)	6 (17.1%)	1 (2.9%)	7 (20.0%)	21 (27.6%)
Total	20 (48.8%)	11 (31.4%)	3 (8.6%)	14 (40.0%)	34 (44.7%)

study analyzes the suitability of four IBDs for Eastern Asian AAA patients with a coexisting CIAA and provides a selecting guidance for physicians who are considering to use any of these IBDs in preservations of IAA for this group of patients.

Seventy-six patients who underwent EVAR were reviewed and all of them present with a unilateral or bilateral CIA of at least 25 mm in diameter associated with a concomitant AAA. We retrospectively measured their morphological features. According to the centerline measurement CTA scans, the average left and right CIA lengths were 56.6 and 59.0 mm, respectively. It was similar to Japanese patients (56.5 mm) reported by Itoga et al. (20), but was significantly shorter than that in American patients (70.8–72 mm) and German patients (68 mm) (5, 21). In addition, Wang et al. measured infrarenal aorta and common iliac artery in Chinese population and found that the normal CIA was approximately 9.7 mm in males and 8.5 mm in females (22). However, the average CIA diameter was 1.2 cm in men and 1.0 cm in women in the United States (23). As with any vessel, a true common iliac artery aneurysm is defined as a focal dilation of the artery with more than 50% in comparison with the normal one (24). Based upon these values, a CIAA is generally present if the artery measures >1.85 cm in males and >1.5 cm in females according to a Western study (24). It indicates that more accurate diagnostic criteria are needed for Asian CIAA patients. Therefore, the standard of Asian CIAA treatment may also change due to the adjustment of diagnostic criteria.

Based on the anatomical characteristics, we assessed the suitability for four types of IBD systems. Unlike the previous studies, it was the first time that the domestic IBSG by Lifetech and newly appeared Jotec devices have been added for evaluation. Moreover, the exclusion criteria were updated in accordance with the latest IFUs. One-third of the lesions (37, 33.3%) would have been eligible for at least one device by pure anatomical criteria. In our study, Gore IBE was found to have a significantly higher applicability than Cook IBD ($P < 0.05$) but no difference with Lifetech or Jotec devices.

Since IAAs often involve the internal and external iliac arteries simultaneously, the dilated arteries might lack a distal sealing zone for IBDs. IIA diameter was found to be the most common exclusion factor for all IBDs in our study. Although Gore IBE

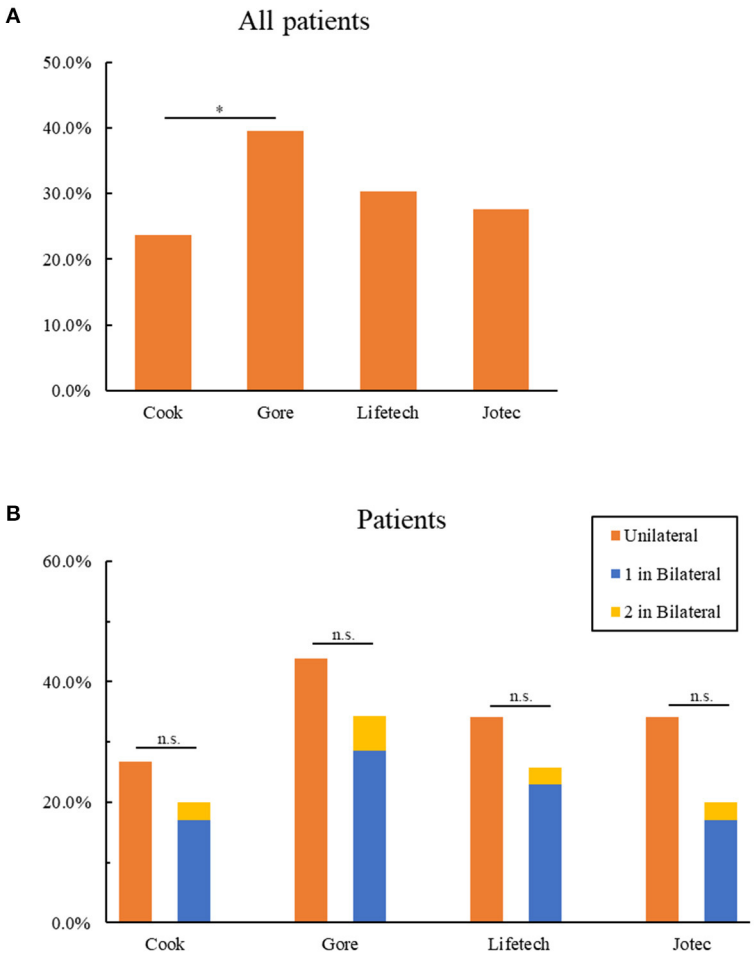

FIGURE 2 | Anatomic suitability of patients for IBDs. **(A)** Exclusion of all patients for four IBDs. **(B)** Comparison of the exclusion of patients with unilateral and bilateral lesions for four IBDs. 1 in bilateral represent patients with bilateral lesions who could be only treated one side by IBDs; 2 in bilateral represent patients with bilateral lesions who could be treated both sides by IBDs *$P < 0.05$; n.s. $P > 0.05$ (no significance); as determined by Chi-square test. IBD, iliac branch device.

had a wide IIA applicability (6.5-13.5 mm), this still resulted in an exclusion rate of 64.9% per lesion. Donas et al. reported that about 34% internal iliac arteries were larger than 12 mm among over 900 IBD implants (25). Simonte et al. also demonstrated a low rate of hypogastric aneurysms in their IBD practice (26). Our study excluded about 70% patients for an IBD implant because of the IIA diameter. Except for those excluded for thin IIAs, there were still roughly 50% of patients ineligible for IBDs owing to a large diameter of IIAs. This may be due to the differences in ethnicity and measurement methods. The devices by different manufacturers showed a difference to some extent in IIA diameter exclusion criteria. It might be due to an internal iliac component contained in Gore and Lifetech IBD systems while Cook and Jotec choose commercial bridging stent such as Advanta V12 (Atrium Medical, Hudson, NH, USA), Viabahn (W.L. Gore &Associates, Flagstaff, AZ, USA) and Lifestream (Bard Peripheral Vascular, Tempe, AZ, USA) (18, 27). Although the internal iliac component might match better for its tapered structure, the result suggests no difference between IBDs with commercial stent or IBDs with its own bridging component in IIA exclusion. It may be due to the same distal size of these two types of bridging stent. Actually, no matter the initially devices have their own internal iliac components or require commercial stents, various bridging combinations can be used in real clinical practice to improve the applicability. In some cases, the distal landing zone can be extended into a larger IIA branch with coiling of the smaller branch simultaneously if necessary. Consequently, a short or ectatic main IIA that does not meet the anatomic criteria could be cured by IBDs in clinical practice.

The external iliac artery is considered as another essential sealing artery for iliac branch devices. As for the EIA diameter, nevertheless, the exclusion rate showed a significant difference among four IBD systems. Only one lesion was excluded by Gore for the less stringent criteria on EIA diameter (<6.5 or >25 mm). This is attributed to the GORE excluder iliac limb which could extend the Gore IBE distally into the external iliac artery. The iliac branch component alone of the IBE system can treat EIA diameters up to 13.5 mm. The external iliac artery

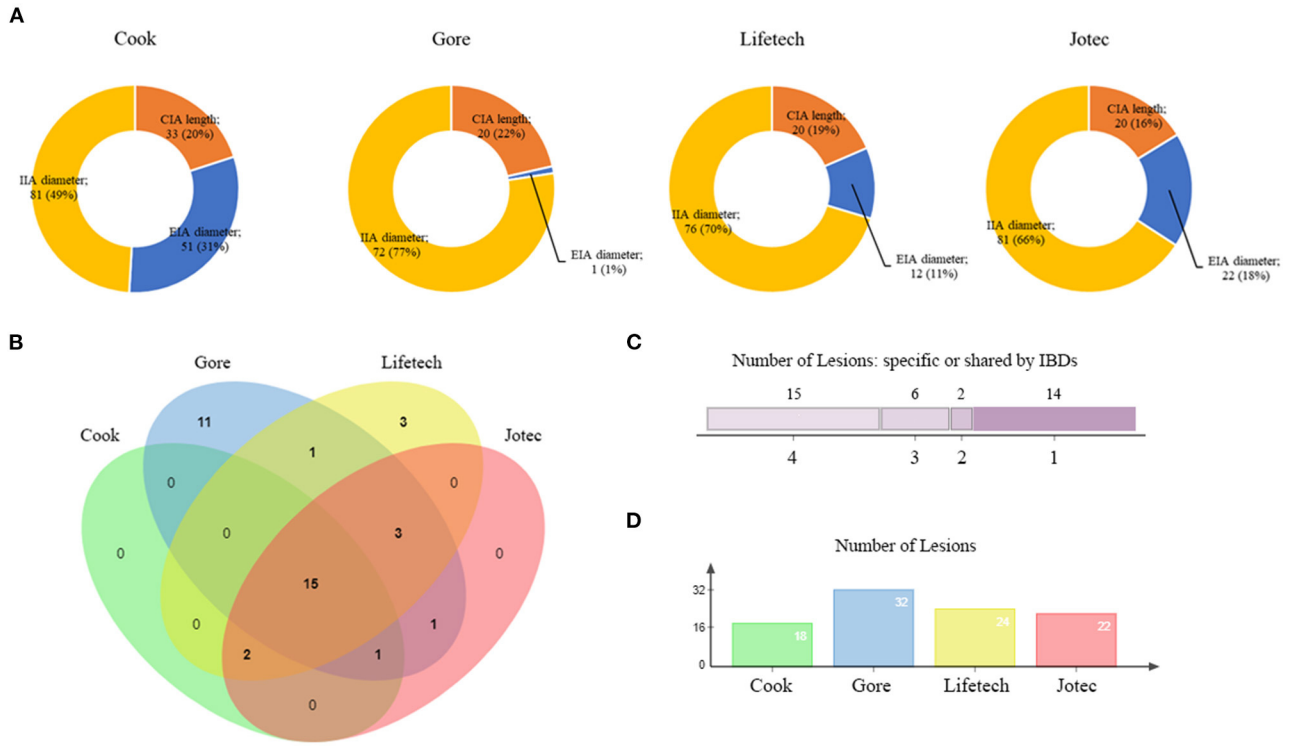

FIGURE 3 | Overview of IBD applicability. **(A)** The proportion of exclusion reasons for four IBDs. **(B)** A four-set Venn diagram showing the numbers of lesions meeting the criteria of IBDs. **(C)** The number of lesions meeting different IBD criteria. **(D)** The number of lesions included by each device. IBD, iliac branch device.

treatment range expands to 25 mm if using one iliac extension component with a large distal size. The other three devices, however, do not contain this component in their IBD system. As a matter of fact, these three IBDs can also repair AIA with large EIA diameter by bridging commercial extension components in clinical applications. Furthermore, despite the fact that Lifetech IBSG considered the anatomical characteristics, especially CIA length and IIA diameter of the Asian population, there is no statistical significance in suitability among Lifetech and the other three devices.

Of note, our study also demonstrated a significant difference in anatomic features of patients with unilateral and bilateral lesions, especially in the diameter of dilated arteries. The average diameters of CIAs, EIAs, and IIAs, along with CIA lengths, were all unanimously larger in the bilateral group. As a result, the morphological difference excluded more bilateral lesions from the all kinds of iliac branch devices. And IIA diameter was the major reason for exclusion of bilateral lesions as well. This indicates that the affected area becomes more diffuse and extends to the IIA and EIA when bilateral CIA aneurysms are present. Concomitant bilateral CIAAs were therefore considered to be more severe, complexed anatomical and thus more difficult for treatment.

If strictly follow the IFU, the majority of the aortoiliac aneurysms are not suitable for IBD application. Pearce et al. reported that only 35% of the aneurysm repairs involving common iliac arteries would have been candidates for the Gore and Cook IBDs in western countries (5). Itoga et al. reported 17% met the criteria for Cook and 25% for Gore in Japanese (20). The inclusion percentages in our study were similar compared with the studies of Pearce et al. and Itoga et al. (5, 20). Additionally, there was no difference in suitability per patient with unilateral and bilateral lesions. This was because patients in the bilateral group were eligible for IBD on condition that one lateral lesion met the criteria. However, only 3.9% of Eastern Asian patients could be treated on both sides. Most authors advocate for the preservation of one IIA with an IBD and embolization of the contralateral IIA. However, risks of ischemic complications seem to appear in 30-55% of the patients after unilateral IIA occlusion (11). Mansour et al. reported a higher complication rate in patients with both IIA excluded compared with those preserving the contralateral one and suggested to revascularize at least one IIA in case of bilateral iliac aneurysmal involvement (28). Under this circumstance, IBDs may provide more clinical benefits for patients with bilateral iliac aneurysms. Published researches have demonstrated similar technical success and mid-term outcomes for using bilateral IBD in patients with suitable anatomical characteristics compared with unilateral iliac branched grafting (15). Few ischemic complications were reported as well in bilateral IBD implantation (29). It indicates that new generation IBDs should take bilateral lesions into consideration.

Overall, 14 lesions were barely eligible for only one IBD while 15 could be treated by all four IBDs. There were 11 lesions that only met the criteria of Gore. And overall, 32 aortoiliac aneurysms were eligible for Gore IBE which was higher than any other devices. This suggests that the Gore IBE system may be a potentially better choice for Eastern Asian patients. Nevertheless, more than half of the patients were ineligible for any iliac branch devices in this study. The IBD technology and design still require advancements, and alternative techniques for IIA preservation such as bell-bottom, sandwich and chimney techniques are continuously needed to play their role when IBDs are unsuitable in clinical practice.

There are some limitations to our study. Above all, the number of patients enrolled was still limited despite the fact that this study was based on two large tertiary centers in China, and it would be advantageous to include more patients from more centers to achieve a more solid conclusion. Besides, the evaluation of IBD suitability in these patients is purely based on anatomic criteria of the CTA results. Multiple confounding factors, such as patient general condition and medication could lead to a higher exclusion rate of IBDs.

CONCLUSION

IIA preservation with any IBD was applicable for 44.7% of Eastern Asian AIA patients. IIA diameter was the main reason for failure to meet the criteria. The suitability of bilateral lesions was significantly lower than unilateral. For clinical applications on Eastern Asian patients, it is imperative to expand the IBD indications in clinical applications and evaluate the effect and efficacy in the meantime. Moreover, the design and development of next-generation IBDs should focus on internal iliac diameter suitability. In addition, the IBD system also needs to be adapted to accommodate patients with bilateral lesions in order to ensure the preservation of IIA for both sides of the patients.

DATA AVAILABILITY STATEMENT

The original contributions presented in the study are included in the article/supplementary material, further inquiries can be directed to the corresponding author/s.

ETHICS STATEMENT

The studies involving human participants were reviewed and approved by the Institutional Review Board of Zhongshan Hospital, Shanghai (approval no. B2018-045) and Drum Tower Hospital, Nanjing (approval no. 2017-015-05). The retrospective data were anonymous, and the requirement for informed consent was therefore waived.

AUTHOR CONTRIBUTIONS

MZ, GW, and TY performed the measurements. EW and YFZ were involved in planning and supervised the work. ZL and LW processed the experimental data, performed the analysis, drafted the manuscript, and designed the figures. XS, YCZ, and PL performed the calculations. ZL and WF aided in interpreting the results and worked on the manuscript. All authors discussed the results and commented on the manuscript.

FUNDING

This work was supported by the National Natural Science Foundation of China (grant number: 81970412), Shanghai Municipal Science and Technology Commission Innovation Fund (grant number: 18441902400), Xiamen Municipal Health Science and Technology Program Fund (grant number: 3502Z20194034), Zhongshan Hospital's Talents Supporting Plan (grant number: 2019ZSGG11), and Shanghai Engineering Research Center of Interventional Medicine (grant number: 19DZ2250300).

REFERENCES

1. Cheng SW, Ting AC, Ho P, Poon JT. Aortic aneurysm morphology in Asians: features affecting stent-graft application and design. *J Endovasc Ther.* (2004) 11:605-12. doi: 10.1583/04-1268R.1
2. Henretta JP, Karch LA, Hodgson KJ, Mattos MA, Ramsey DE, McLafferty R, et al. Special iliac artery considerations during aneurysm endografting. *Am J Surg.* (1999) 178:212-8. doi: 10.1016/S0002-9610(99)00156-7
3. Park KH, Lim C, Lee JH, Yoo JS. Suitability of endovascular repair with current stent grafts for abdominal aortic aneurysm in Korean patients. *J Korean Med Sci.* (2011) 26:1047-51. doi: 10.3346/jkms.2011.26.8.1047
4. Muzepper M, Zhou M. Anatomic suitability of iliac branched devices for Chinese patients with abdominal-iliac aortic aneurysm. *Ann Vasc Surg.* (2020) 67:178-84. doi: 10.1016/j.avsg.2020.03.010
5. Pearce BJ, Varu VN, Glocker R, Novak Z, Jordan WD, Lee JT. Anatomic suitability of aortoiliac aneurysms for next generation branched systems. *Ann Vasc Surg.* (2015) 29:69-75. doi: 10.1016/j.avsg.2014.08.003
6. Serracino-Inglott F, Bray AE, Myers P. Endovascular abdominal aortic aneurysm repair in patients with common iliac artery aneurysms–initial experience with the Zenith bifurcated iliac side branch device. *J Vasc Surg.* (2007) 46:211-7. doi: 10.1016/j.jvs.2007.03.040
7. Papazoglou KO, Sfyroeras GS, Zambas N, Konstantinidis K, Kakkos SK, Mitka M. Outcomes of endovascular aneurysm repair with selective internal iliac artery coverage without coil embolization. *J Vasc Surg.* (2012) 56:298-303. doi: 10.1016/j.jvs.2011.08.063
8. Angiletta D, Marinazzo D, Guido G, Greco L, Regina G. Spinal cord, bowel, and buttock ischemia after endovascular aneurysm repair. *Ann Vasc Surg.* (2011) 25:980.e15-9. doi: 10.1016/j.avsg.2010.12.044
9. Freyrie A, Testi G, Gargiulo M, Faggioli G, Mauro R, Stella A. Spinal cord ischemia after endovascular treatment of infrarenal aortic aneurysm. Case report and literature review. *J Cardiovasc Surg.* (2011) 52:731-4.
10. Lin PH, Chen AY, Vij A. Hypogastric artery preservation during endovascular aortic aneurysm repair: is it important? *Semin Vasc Surg.* (2009) 22:193-200. doi: 10.1053/j.semvascsurg.2009.07.012
11. Rayt HS, Bown MJ, Lambert KV, Fishwick NG, McCarthy MJ, London NJ, et al. Buttock claudication and erectile dysfunction after internal iliac artery embolization in patients prior to endovascular aortic aneurysm repair. *Cardiovasc Intervent Radiol.* (2008) 31:728-34. doi: 10.1007/s00270-008-9319-3

12. van Sterkenburg SM, Heyligers JM, van Bladel M, Verhagen HJ, Eefting D, van Sambeek MR, et al. Experience with the GORE EXCLUDER iliac branch endoprosthesis for common iliac artery aneurysms. *J Vasc Surg.* (2016) 63:1451-7. doi: 10.1016/j.jvs.2016.01.021
13. Anton S, Wiedner M, Stahlberg E, Jacob F, Barkhausen J, Goltz JP. Initial experience with the E-liac(®) Iliac Branch Device for the endovascular aortic repair of aorto-iliac aneurysm. *Cardiovasc Intervent Radiol.* (2018) 41:683-91. doi: 10.1007/s00270-017-1868-x
14. Zhang H, Zhang H, Dai X, Chen Z, Zhang X, Fu W, et al. Endovascular repair of aortoiliac or common iliac artery aneurysm using the lifetech iliac bifurcation stent graft system: a Prospective Multicenter Clinical Study. *Ann Vasc Surg.* (2020) 63:136-44. doi: 10.1016/j.avsg.2019.06.048
15. Marques de Marino P, Botos B, Kouvelos G, Verhoeven ELG, Katsargyris A. Use of bilateral cook zenith iliac branch devices to preserve internal iliac artery flow during endovascular aneurysm repair. *Eur J Vasc Endovasc Surg.* (2019) 57:213-9. doi: 10.1016/j.ejvs.2018.08.002
16. Giosdekos A, Antonopoulos CN, Sfyroeras GS, Moulakakis KG, Tsilimparis N, Kakisis JD, et al. The use of iliac branch devices for preservation of flow in internal iliac artery during endovascular aortic aneurysm repair. *J Vasc Surg.* (2020) 71:2133-44. doi: 10.1016/j.jvs.2019.10.087
17. Kouvelos GN, Katsargyris A, Antoniou GA, Oikonomou K, Verhoeven EL. Outcome after interruption or preservation of internal iliac artery flow during endovascular repair of abdominal aorto-iliac aneurysms. *Eur J Vasc Endovasc Surg.* (2016) 52:621-34. doi: 10.1016/j.ejvs.2016.07.081
18. Loth AG, Rouhani G, Gafoor SA, Sievert H, Stelter WJ. Treatment of iliac artery bifurcation aneurysms with the second-generation straight iliac bifurcated device. *J Vasc Surg.* (2015) 62:1168-75. doi: 10.1016/j.jvs.2015.06.135
19. Wong S, Greenberg RK, Brown CR, Mastracci TM, Bena J, Eagleton MJ. Endovascular repair of aortoiliac aneurysmal disease with the helical iliac bifurcation device and the bifurcated-bifurcated iliac bifurcation device. *J Vasc Surg.* (2013) 58:861-9. doi: 10.1016/j.jvs.2013.02.033
20. Itoga NK, Fujimura N, Hayashi K, Obara H, Shimizu H, Lee JT. Outcomes of endovascular repair of aortoiliac aneurysms and analyses of anatomic suitability for internal iliac artery preserving devices in Japanese patients. *Circ J.* (2017) 81:682-8. doi: 10.1253/circj.CJ-16-1109
21. Gray D, Shahverdyan R, Jakobs C, Brunkwall J, Gawenda M. Endovascular aneurysm repair of aortoiliac aneurysms with an iliac side-branched stent graft: studying the morphological applicability of the Cook device. *Eur J Vasc Endovasc Surg.* (2015) 49:283-8. doi: 10.1016/j.ejvs.2014.12.021
22. Wang X, Zhao WJ, Shen Y, Zhang RL. Normal diameter and growth rate of infrarenal aorta and common iliac artery in Chinese population measured by contrast-enhanced computed tomography. *Ann Vasc Surg.* (2020) 62:238-47. doi: 10.1016/j.avsg.2019.05.030
23. Horejs D, Gilbert PM, Burstein S, Vogelzang RL. Normal aortoiliac diameters by CT. *J Comput Assist Tomogr.* (1988) 12:602-3. doi: 10.1097/00004728-198807000-00011
24. Johnston KW, Rutherford RB, Tilson MD, Shah DM, Hollier L, Stanley JC. Suggested standards for reporting on arterial aneurysms. Subcommittee on Reporting Standards for Arterial Aneurysms, Ad Hoc Committee on Reporting Standards, Society for Vascular Surgery and North American Chapter, International Society for Cardiovascular Surgery. *J Vasc Surg.* (1991) 13:452-8. doi: 10.1067/mva.1991.26737
25. Donas KP, Taneva GT, Pitoulias GA, Torsello G, Veith FJ. Coexisting hypogastric aneurysms worsen the outcomes of endovascular treatment by the iliac branch devices within the pELVIS Registry. *J Vasc Surg.* (2019) 69:1072-9.e1. doi: 10.1016/j.jvs.2018.07.036
26. Simonte G, Parlani G, Farchioni L, Isernia G, Cieri E, Lenti M, et al. Lesson learned with the use of iliac branch devices: single centre 10 year experience in 157 consecutive procedures. *Eur J Vasc Endovasc Surg.* (2017) 54:95-103. doi: 10.1016/j.ejvs.2017.03.026
27. Mylonas SN, Rümenapf G, Schelzig H, Heckenkamp J, Youssef M, Schäfer JP, et al. A multicenter 12-month experience with a new iliac side-branched device for revascularization of hypogastric arteries. *J Vasc Surg.* (2016) 64:1652-9.e1. doi: 10.1016/j.jvs.2016.04.065
28. Mansour W, Capoccia L, Sirignano P, Montelione N, Pranteda C, Formiconi M, et al. Clinical and functional impact of hypogastric artery exclusion during EVAR. *Vasc Endovasc Surg.* (2016) 50:484-90. doi: 10.1177/1538574416665968
29. Illuminati G, D'Urso A, Ceccanei G, Pacilè MA. Iliac side branch device for bilateral endovascular exclusion of isolated common iliac artery aneurysms without brachial access. *J Vasc Surg.* (2009) 49:225. doi: 10.1016/j.jvs.2008.05.071

Conflict of Interest: The authors declare that the research was conducted in the absence of any commercial or financial relationships that could be construed as a potential conflict of interest.

frontiers in Cardiovascular Medicine

ORIGINAL RESEARCH
published: 03 January 2022
doi: 10.3389/fcvm.2021.811431

The Functional Polymorphism of *DDAH2* rs9267551 Is an Independent Determinant of Arterial Stiffness

Carolina Averta[1†], *Elettra Mancuso*[1†], *Rosangela Spiga*[1], *Sofia Miceli*[1], *Elena Succurro*[1,2], *Teresa Vanessa Fiorentino*[1], *Maria Perticone*[1], *Gaia Chiara Mannino*[1*], *Prapaporn Jungtrakoon Thamtarana*[3], *Angela Sciacqua*[1,2], *Giorgio Sesti*[4] and *Francesco Andreozzi*[1,2]

[1] Department of Medical and Surgical Sciences, University Magna Graecia of Catanzaro, Catanzaro, Italy, [2] Research Center for the Prevention and Treatment of Metabolic Diseases (CR METDIS), University Magna Graecia of Catanzaro, Catanzaro, Italy, [3] Siriraj Center of Research Excellence for Diabetes and Obesity, Division of Molecular Medicine, Department of Research, Faculty of Medicine Siriraj Hospital, Mahidol University, Bangkok, Thailand, [4] Department of Clinical and Molecular Medicine, University of Rome-Sapienza, Rome, Italy

OPEN ACCESS

Edited by:
Manfredi Tesauro,
University of Rome Tor Vergata, Italy

Reviewed by:
Oren Rom,
Louisiana State University Health Shreveport, United States
Alessandro De Stefano,
Catholic University of the Sacred Heart, Italy

***Correspondence:**
Gaia Chiara Mannino
gaiamannino@unicz.it

[†]*These authors have contributed equally to this work and share first authorship*

Specialty section:
This article was submitted to Atherosclerosis and Vascular Medicine, a section of the journal Frontiers in Cardiovascular Medicine

Received: *08 November 2021*
Accepted: *29 November 2021*
Published: *03 January 2022*

Citation:
Averta C, Mancuso E, Spiga R, Miceli S, Succurro E, Fiorentino TV, Perticone M, Mannino GC, Thamtarana PJ, Sciacqua A, Sesti G and Andreozzi F (2022) The Functional Polymorphism of DDAH2 rs9267551 Is an Independent Determinant of Arterial Stiffness. Front. Cardiovasc. Med. 8:811431. doi: 10.3389/fcvm.2021.811431

Background: The association of circulating asymmetric dimethylarginine (ADMA) levels with cardiovascular risk and arterial stiffness has been reportedly demonstrated, although the causal involvement of ADMA in the pathogenesis of these conditions is still debated. Dimethylaminohydrolase 2 (DDAH2) is the enzyme responsible for ADMA hydrolysis in the vasculature, and carriers of the polymorphism rs9267551 C in the 5′-UTR of *DDAH2* have been reported to have higher *DDAH2* expression and reduced levels of serum ADMA.

Approach and Results: We genotyped rs9267551 in 633 adults of European ancestry and measured their carotid–femoral pulse wave velocity (cfPWV), the gold-standard method to estimate arterial stiffness. cfPWV resulted significantly lower in rs9267551 C allele carriers ($\Delta = -1.12$ m/s, $P < 0.01$) after correction for age, sex and BMI, and a univariate regression showed that the presence of rs9267551 C variant was negatively associated with cfPWV ($\beta = -0.110$, $P < 0.01$). In a multivariable regression model, subjects carrying the rs9267551 C allele manifested significantly lower cfPWV than GG carriers ($\beta = -0.098$, $P = 0.01$) independently from several potential confounders. We measured circulating ADMA levels in a subset of 344 subjects. A mediation analysis revealed that the effect of *DDAH2* rs9267551 genotype on cfPWV was mediated by the variation in ADMA levels.

Conclusions: These evidences hint that the presence of rs9267551 C allele may explain, at least in part, a reduction in vessel rigidity as measured by cfPWV, and support the attribution of a causative role to ADMA in the pathogenesis of arterial stiffness.

Keywords: pulse wave velocity, arterial stiffness, dimethylarginine dimethylaminohydrolase, rs9267551, ADMA

INTRODUCTION

The arterial wall is characterized by its high elasticity, which participates to the physiological regulation of this highly pressurized compartment. The stiffness of the arterial wall increases gradually from the central segments to the periphery, determining a gradient of blood pressure, and although brachial blood pressure is commonly measured in clinical practice, aortic blood pressure

correlates more strictly with markers of cardiovascular risk (1). An augmented rigidity of the vessels is associated with increased occurrence of cardiovascular disease (2), stroke (3) and kidney disease (4). Several factors contribute to the stiffening of arterial walls as a normal consequence of aging, but arterial elasticity may also be found reduced in younger subjects who carry cardiovascular risk factors such as hypertension, obesity and dyslipidemia. The latter phenomenon suggests that exposure of the vessels to the milieu determined by those pathologic conditions may interfere with the balance of hemodynamic forces (5).

Pulse wave velocity (PWV) is a simple measurement representing the average stiffness between two sites of the arterial system, with higher values indicating the presence of higher resistance (stiffer vessels), and it is considered as a *bona fide* surrogate early marker of atherosclerosis and cardiovascular morbidity and mortality (6, 7). Indeed, several guidelines propose carotid–femoral PWV (cfPWV), the current gold-standard method used to evaluate arterial stiffness, as a conservative method to determine the presence of aortic function alteration (8–10), and it is an independent predictor of cardiovascular events and all-cause mortality in the general population and in high-risk subjects (2, 11–13).

In the subclinical phases of the atherogenic process the reduced availability of the vasodilator hormone nitric oxide (NO) may foster endothelial dysfunction. The endothelial NO synthase (eNOS) is the enzyme responsible for the synthesis of NO in the vascular district, starting from the substrate L-arginine. Asymmetric dimethylarginine (ADMA) is an endogenous methylated form of arginine able to competing with L-arginine and to inhibit NO production (14, 15). Several research efforts have demonstrated the existence of an association between elevated circulating levels of ADMA and major cardiovascular events or mortality (16–20). In spite of this, the predictive role of ADMA is still subject of debate (21–24). Altogether, there is an evidence gap regarding the causal role of ADMA in the dysregulation of arterial blood pressure and endothelial function. In 2006 a small intervention trial demonstrated that acute exogenous administration of ADMA in healthy male volunteers was able to induce a reduction of cerebral blood flow and arterial compliance due to increased arterial stiffness (25). Very recently, Malle et al. (26) have attempted to resolve this gap and they could not detect the presence in hypertensive patients of a significant association between ADMA and blood pressure or PWV. It is worth noticing, though, that observational studies cannot rule out the masking influence of confounding factors, i.e., due to co-morbidities, or establish whether a marker is the cause or the manifestation of a specific condition, due to their non-interventional nature. Given the contrasting reports, the attribution of a causative role to ADMA in the pathogenesis of arterial hypertension in humans remains difficult.

The enzyme dimethylarginine dimethylaminohydrolase (DDAH) (27, 28) is responsible for the hydrolysis of ADMA to citrulline plus methyl-amine, and is encoded by genes *DDAH1* and *DDAH2*. DDAH1 co-localizes with neuronal NOS, whereas DDAH2 can be found in tissues expressing eNOS, such as the endothelium (29). Mendelian randomization is a method that employs genetic polymorphisms known to be able to modify an exposure of interest to determine the existence of a causal association between this exposure (i.e., a biomarker) and a disease. This approach is arguably less prone to reverse causation than other observational studies, because disease status cannot affect germline DNA sequences (30). Most importantly, since genetic variants persist throughout the lifespan, Mendelian randomization studies provide information on life-long exposition to genetically altered levels of biomarkers (in this case, ADMA). The rs9267551 G/C variant in the 5′-untranslated region (UTR) of *DDAH2* has been reportedly demonstrated to affect the quantitative expression of *DDAH2*, specifically in primary human endothelial cells, and a protective role has been proposed for the C allele due to its association with increased NO production (31). Individuals carrying the rs9267551 C allele were shown to have lower circulating levels of ADMA, better response to insulin, and reduced prevalence of chronic kidney disease (31, 32). In a previous work, we reported a significant association with myocardial infarction in two independent cohorts of subjects with type 2 diabetes mellitus, with the C allele consistently showing a protective effect (33). Therefore, we elected to perform a Mendelian randomization study using the functional rs9267551 polymorphism and to assess its effects on *in vivo* measurements of arterial stiffness (by cfPWV), in a heterogenic cohort of subjects, assuming that carriers of the C allele have a vascular protection (as a consequence of higher NO availability).

MATERIALS AND METHODS

Study Subjects

For this study we consecutively recruited 633 adults of European ancestry referred to the Department of Medical and Surgical Sciences of the University "Magna Graecia" of Catanzaro (34). The inclusion criteria were: age $\geq$ 19 years, and presence of one or more cardio-metabolic risk factors including elevated fasting glucose levels, hypertension, dyslipidemia, overweight/obesity, and family history for diabetes. Exclusion criteria were: end-stage renal disease, chronic gastrointestinal diseases or pancreatitis, history of any malignant disease or of alcohol/drug abuse, hepatic failure or positivity for antibodies to hepatitis C virus (HCV) or hepatitis B surface antigen (HBsAg). Venous blood samples were obtained after a 12-h overnight fast. Body mass index (BMI) was calculated as body weight in kilograms divided by the square of height in meters. Readings of blood pressure (BP) were performed in the non-dominant arm with the patient in supine position, after 5 min of rest, with a sphygmomanometer. Type 2 diabetes was defined according to the American Diabetes Association (ADA) criteria (35). Subjects were classified as hypertensive if they had systolic blood pressure $\geq$ 130 and/or diastolic $\geq$ 85 mmHg or in presence of antihypertensive treatment and history of hypertension.

As previously reported (36), we adopted a validated system (Sphygmocor^{TM}; AtCor Medical, Sydney, Australia), that utilizes high-fidelity applanation tonometry (Millar) and appropriate software for the analysis of pressure waves (Sphygmocor^{TM}). Pressure calibration was obtained with patients lying supine,

through automatic recording of brachial BP at the dominant arm, after resting for 30 min (Dinamap Compact T; Johnson & Johnson Medical Ltd, Newport, UK). Measurement of BP was repeated five times, and the average of the final three recordings was used for calibration. Pulse wave was measured at the radial artery of the dominant arm with the wrist softly hyperextended, as the average of single pressure waves during eight consecutive seconds. Pulse wave recordings were admitted if peak and bottom values of single waves showed <5% variability. Aortic pulse wave velocity (PWV) was derived from carotid and femoral pressure waveforms. Carotid to femoral transit time (ΔT) was calculated from the foot-to-foot time difference between carotid and femoral waveforms. The distance between the landmark of the sternal notch and femoral artery was used to estimate the path length between the carotid and femoral arteries (L), and PWV was measured as $L/\Delta T$.

The study was approved by the Local Institutional Ethics Committee of the University "Magna Graecia" of Catanzaro (approval code: 2012.63). Written informed consent was obtained from each subject in accordance with the principles of the Declaration of Helsinki.

Analytical Determinations

Glucose, triglyceride, total cholesterol and HDL particles concentration was determined by enzymatic methods (Roche, Basel, Switzerland). Plasma insulin concentration was assessed with a chemiluminescence-based assay (Immulite®, Siemens, Italy). High performance liquid chromatography with a National Glycohemoglobin Standardization Program certified automated analyzer (Adams HA-8160 HbA1C analyzer, Menarini, Italy) was used to measure HbA1c levels. High sensitivity C reactive protein (hsCRP) levels were determined by an automated instrument (CardioPhase® hsCRP, Milan, Italy). Serum ADMA concentration was measured with Human Asymmetric dimethylarginine (ADMA) ELISA Kit (MBS264847, My BioSource, San Diego, CA, USA). The detection range was 5 μmol/L-0.078 μmol/L, with sensitivity up to 0.01 μmol/L, Intra-assay CV $\leq$ 8% and inter-assay CV $\leq$ 12%.

Genotyping of *DDAH2* Gene Polymorphism

DNA was extracted from whole blood using commercial DNA isolation kits (Promega, Madison, WI and Roche, Mannheim, Germany). rs9267551 *DDAH2* genotype calls were assigned by TaqMan allelic discrimination assay (C__27848488_10; Applied Biosystems, Foster City, CA), after amplification on an iCycler Thermal Cycler with iQ5 Multicolor Real-Time PCR Detection System (Bio-Rad Laboratories, Inc., Hercules, CA). 0.05 ng of custom oligo strings (GeneArt® Strings™ DNA Fragments, Invitrogen, Thermo Fisher Scientific) corresponding to ~200 bp around the context sequence of the genotyping assay, differing only for the rs9267551 allele C or G were loaded onto each plate run to represent one heterozygous C/G and two sets of homozygous C/C and G/G controls. Genotyping concordance of the oligo strings was 100%.

Statistical Analysis

The estimation of sample size requirements was performed with the program Quanto (version 1.2) and based upon previously reported data obtained in populations similar to ours. To compute our model we assumed an average cfPWV between 6.7 and 7.5 m/s, with a standard deviation (SD) ranging between 1.8 and 2.5 m/s (37, 38), and a minimum minor allele frequency = 4.5% (31–33). In order to be able to detect a clinically relevant difference in cfPWV between genotypes according to a dominant model [at least 1 m/s (13, 39)], with two-sided $\alpha = 0.05$ and $\beta = 0.80$, the recommended sample size was equal to 607 subjects. Each SNP was coded as 0, 1, or 2 depending on the number of C alleles. Therapies were coded as binary variables, 0 indicated absence of treatment, 1, respectively, meant use of anti-hypertensive, glucose lowering agents, or statins as anti-dyslipidemic therapy. Log transformation was employed when analyzing insulin, triglycerides and hsCRP levels because their distribution did not respect the assumption of normality. Comparison of differences between continuous variables in genotype groups were tested by ANCOVA (general linear model) after adjusting for age, sex, and BMI. Categorical variables were compared by χ^2 test. The Hardy–Weinberg equilibrium between genotypes was evaluated by χ^2 test. The existing relationships between cfPWV and all collected clinical, biochemical and anthropometrical parameters were explored by univariate regression analysis, with cfPWV as dependent variable. To assess which variables were independently associated with cfPWV we built an exploratory stepwise multivariable linear regression model. The resulting predictive variables were used to compile a predictor factor through principal component analysis. The quality of the reduced-dimension factor was determined through the Bartlett's test for sphercity. The Mediation analysis was conducted through a series of linear regression analyses to calculate the indirect and direct effects and test them for significance (40); we adopted the product of coefficients approach to test the mediating effect of ADMA on the variability of cfPWV, and we tested the significance of the mediation through the Sobel test (41). The significance of indirect and total effects was estimated *via* bootstrapping (40). A two-sided p-value < 0.05 was considered statistically significant. All calculations were done with SPSS software program Version 22.0 for Windows.

RESULTS

A summary of the clinical and anthropometric characteristics of the population, stratified by rs9267551 polymorphism, is reported in **Table 1**. The study population consisted of 633 unrelated Caucasian subjects (425 men and 208 women with mean age 52 ± 12 years), who were enrolled in the CATAMERI study (42). The genotype distribution of rs9267551 polymorphism was in Hardy–Weinberg equilibrium ($p > 0.10$). GC and CC individuals were collectively considered and analyzed as C carriers, according to a dominant genetic model, because we detected only three individuals with rs9267551 CC homozygous genotype, and because previous functional studies performed in

TABLE 1 | Clinical features of 633 study subjects according to the rs9267551 polymorphism of DDAH2.

Variables	Whole cohort	GG	GC + CC	*P*
N	633	579	54	
Sex (F/M)	208/425	192/387	16/38	0.597
Age (years)	52 (±12)	52 (±13)	50 (±9)	0.299
BMI (Kg/m^2)	29.34 (±5.1)	29.36 (±5.1)	29.15 (±5.0)	0.764$^{\#}$
SBP (mmHg)	137.6 (±16.6)	137.6 (±16.7)	138.3 (±16.1)	0.665*
DBP (mmHg)	84.0 (±11.5)	83.7 (±11.6)	86.1 (±10.5)	0.218*
Total cholesterol (mg/dl)	199.8 (±38.3)	199.1 (± 38.5)	207.6 (±36.5)	0.132*
HDL (mg/dl)	49.0 (±13.6)	49.1 (±13.4)	48.7 (±16.1)	0.932*
LDL (mg/dl)	124.0 (±34.1)	123.5 (±34.3)	130.1 (±31.3)	0.209*
Triglycerides (mg/dl)	136.7 (±75.1)	136.1 (±75.4)	142.8 (±72.1)	0.508*
Fasting glucose (mg/dl)	107.6 (±41.9)	108.4 (±43.2)	99.6 (±24.2)	0.233*
Fasting insulin (U/l)	14.2 (±9.7)	14.2 (±9.5)	14.1 (±11.5)	0.944*
cfPWv (m/s)	7.88 (±2.79)	7.98 (±2.86)	6.86 (±1.61)	**<0.01***
hsCRP (mg/L)	3.7 (±4.4)	3.8 (±4.5)	3.4 (±4.1)	0.794*
Smoking habit (N/Ex/Y)	353/158/122	324/143/112	29/15/10	0.886
Hypolipidemic therapy (N/Y)	532/101	480/99	52/2	**0.010**
Hypertension therapy (N/Y)	322/311	293/286	29/25	0.663
Diabetes prevalence (N/Y)	497/136	448/131	49/5	**0.022**
Hypoglycemic therapy (N/Y)	555/78	503/76	52/2	**0.049**

*Continuous variables are summarized as means ± SD. Differences of continuous variables between groups were tested after adjusting for age, sex, and BMI by ANCOVA (general linear model). Categorical variables are summarized as absolute number of subjects per category, and compared by $\chi 2$ test. A P-value < 0.05 was considered statistically significant and highlighted in bold. $^{\#}$P-values refer to results after adjustment for age and sex; *P-values refer to results after adjustment for age, sex, and BMI. BMI, body mass index; cfPWV, carotid-femoral pulse wave velocity; DBP, diastolic blood pressure; HDL, high density lipoprotein; hsCRP, high sensitivity C-reactive protein; LDL, low density lipoprotein; SBP, systolic blood pressure.*

TABLE 2 | Univariate regression analysis with cfPWv as dependent variable.

Independent contributors	β	*P*
Age (years)	0.230	**<0.001**
Sex (F/M)	0.077	**0.053**
BMI (Kg/m^2)	0.062	0.122
SBP (mmHg)	0.152	**<0.001**
DBP (mmHg)	0.026	0.511
Total cholesterol (mg/dl)	−0.007	0.856
HDL (mg/dl)	−0.091	**0.024**
LDL (mg/dl)	0.002	0.967
Triglycerides (mg/dl)	0.061	0.128
Fasting glucose (mg/dl)	0.133	**<0.001**
Fasting insulin (U/l)	0.142	**<0.001**
hsCRP (mg/L)	0.116	**<0.01**
Smoking habit (N/Ex/Y)	0.016	0.680
Hypolipidemic therapy (N/Y)	0.067	0.090
Hypertension therapy (N/Y)	0.048	0.229
Diabetes prevalence (N/Y)	0.157	**<0.001**
Diabetes therapy (N/Y)	0.138	**<0.001**
DDAH2 rs9267551 (GG/GC + CC)	−0.110	**<0.01**

A P-value < 0.05 was considered statistically significant and highlighted in bold. BMI, body mass index; cfPWV, carotid-femoral pulse wave velocity; DBP, diastolic blood pressure; DDAH2, dimethylarginine dimethylaminohydrolase 2; HDL, high density lipoprotein; hsCRP, high sensitivity C-reactive protein; LDL, low density lipoprotein; SBP, systolic blood pressure.

endothelial cells (31) had demonstrated a dominant effect of the C allele. When comparing the two groups (GG vs. GC + CC) the rs9267551 polymorphism did not show any significant association with age, sex, BMI, systolic, and diastolic blood pressure, circulating levels of hsCRP, smoking status, and therapy for hypertension (**Table 1**). After correction for age, sex and BMI, cfPWV was significantly lower in carriers of the C allele as compared with subjects carrying the GG genotype (6.86 vs. 7.98 m/s, respectively; $P < 0.01$), supporting the hypothesis that constant exposure to higher ADMA levels might lead to reduced vascular elasticity. No differences in lipid profile were observed between groups, despite the higher prevalence of hypolipidemic therapies in the GG group (20.6 vs. 3.8% in the GC + CC group, $P = 0.01$). Similarly, no differences were reported in fasting plasma glucose and insulin levels, although it is worth noticing that the GC + CC group harbored a significantly lower proportion of diabetic subjects (10.3 vs. 29.2% in the GG group, $P = 0.022$) and of subjects undergoing a hypoglycemic regimen (3.8 vs. 15.1% in the GG group, $P = 0.049$).

The association of cfPWV with clinical, biochemical and anthropometrical parameters is reported in **Table 2**. cfPWV resulted positively and significantly associated with age ($\beta = 0.230$, $P < 0.001$), systolic blood pressure ($\beta = 0.152$, $P < 0.001$), hsCRP ($\beta = 0.116$, $P < 0.01$), fasting plasma glucose ($\beta = 0.133$, $P < 0.001$), fasting plasma insulin ($\beta = 0.142$, $P = 0.001$), prevalence of diabetes ($\beta = 0.157$, $P < 0.001$), and prevalence of treatment with hypoglycemic agents ($\beta = -0.138$, $P < 0.001$). On the other hand, circulating HDL levels ($\beta = -0.091$, $P = 0.024$) and *DDAH2* rs9267551 C allele ($\beta = -0.110$, $P < 0.01$) showed a negative effect on cfPWV, consistent with their protective role exerted on the vasculature. Sex is notoriously associated with cardiovascular risk, but in our population we found that male subjects had only a fringe association with higher cfPWV ($\beta = 0.077$, $P = 0.053$). No significant associations were detected between values of cfPWV in our population and BMI, diastolic blood pressure, total cholesterol, LDL particles, circulating triglycerides, prevalence of treatment for hypertension or dyslipidemia, and smoking habit (**Table 2**).

To estimate the independent contribution of rs9267551 polymorphism to arterial stiffness evaluated through cfPWV, we carried out a multivariable linear regression analysis. The covariates were selected as follows: traditional confounder factors affecting PWV (age, sex, BMI, and smoking habit), variables that resulted significantly associated to cfPWV in our population in the univariate regression analysis mentioned above (SBP, HDL,

TABLE 3 | Stepwise multiple regression analysis with cfPWv as dependent variable.

	β	*P*
Multivariable regression model A		
Age (years)	0.201	<0.001
Fasting insulin (mU/ml)	0.134	<0.001
SBP (mmHg)	0.111	<0.01
DDAH2 rs9267551 (GG/GC + CC)	−0.098	0.01
HDL (mg/dl)	0.137	0.939
Smoking habit (N/Ex/Y)	0.985	0.989
BMI (Kg/m^2)	0.727	0.876
Fasting glucose (mg/dl)	0.307	0.883
Sex (F/M)	0.147	0.982
hsCRP (mg/L)	0.050	0.975
Multivariable regression model B		
Age (years)	0.199	<0.001
SBP (mmHg)	0.105	<0.01
DDAH2 rs9267551 (GG/GC + CC)	−0.100	<0.01
hsCRP (mg/L)	0.078	0.044
HDL (mg/dl)	−0.076	0.049
Smoking habit (N/Ex/Y)	0.780	0.975
BMI (Kg/m^2)	0.552	0.883
Sex (F/M)	0.186	0.856
Diabetes prevalence (N/Y)	0.118	0.840

Model A includes as covariates: age, fasting insulin, SBP, DDAH2 rs9267551 genotype, HDL, fasting glucose, sex, BMI, smoking habit, and hsCRP. In Model B fasting glucose and insulin levels have been replaced by diabetes prevalence. BMI, body mass index; cfPWV, carotid-femoral pulse wave velocity; DDAH2, dimethylarginine dimethylaminohydrolase 2; HDL, high density lipoprotein; hsCRP, high sensitivity C-reactive protein; SBP, systolic blood pressure.

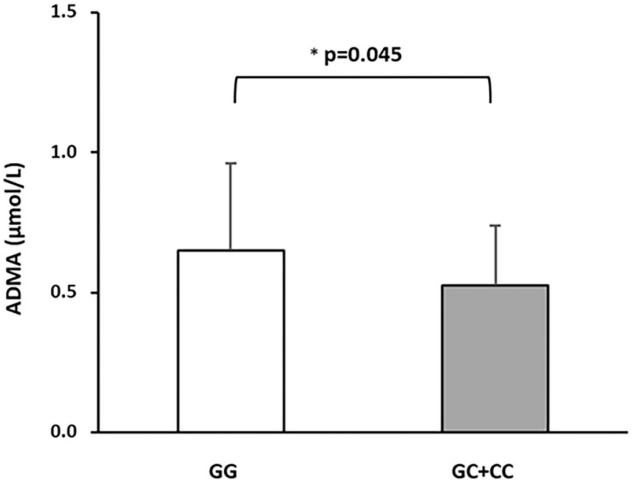

FIGURE 1 | Differences in circulating ADMA concentrations in a subset of 344 subjects stratified based on DDAH2 rs9267551 genotypes. The white bar represents the rs9267551 GG genotype ($n = 321$) and the grey bar represents the rs9267551 GC + CC genotype (21 subjects with GC genotype and 2 with CC homozygous). **p*-value after correction of age, sex, and BMI. Data are means ± Standard Deviation.

fasting plasma glucose and insulin, hsCRP, diabetes prevalence and hypoglycemic therapy, **Table 2**). In order to avoid conflict due to the fact that fasting glucose and insulin levels are strongly correlated to diabetes diagnosis, we built two independent statistical models featuring, respectively, fasting glucose and fasting insulin in Model A and diabetes prevalence in Model B (**Table 3**). Additionally, when we assessed a third Model, in which treatment with hypoglycemic agents was used as a possible confounding variable in the stead of diabetes prevalence or fasting glucose and insulin levels, we observed no significant influence exerted by the pharmacological treatment on cfPWV (data not shown). The major independent determinants of cfPWV according to Model A were (listed from strongest to weakest): age ($\beta = 0.201$, $P < 0.001$), fasting insulin ($\beta = 0.134$, $P < 0.001$), systolic blood pressure ($\beta = 0.111$, $P < 0.01$) and the rs9267551 polymorphism, with carriers of the C allele having significantly lower vessel rigidity as compared with GG individuals ($\beta = -0.098$, $P = 0.01$) (**Table 3**). Model B revealed a similar pattern of association, with age ($\beta = 0.199$, $P < 0.001$), systolic blood pressure ($\beta = 0.105$, $P < 0.01$), *DDAH2* rs9267551 genotype ($\beta = -0.100$, $P < 0.01$), plus hsCRP ($\beta = 0.078$, $P = 0.044$), and HDL ($\beta = -0.076$, $P = 0.049$) (**Table 3**). As a dependent variable, cfPWV did not show any significant association with sex, BMI or smoking habit in neither Model A or B (**Table 3**).

In order to exclude any confounding influence deriving from other factors associated with *DDAH2* rs9267551 genotype (by chance, or pleiotropy), we constructed a final multivariable regression model (**Supplementary Table**) encompassing traditional risk factors for arterial stiffness and covariates which resulted associated either with cfPWV, as in Model B, plus the remaining variables associated to rs9267551 in our population (hypolypidemic therapy, **Table 1**). The independent contribution of each trait to the variability of cfPWV resulting from this supplementary model was almost superimposable to the results obtained from Model B. Serum ADMA concentrations were assessed for a subset of 344 subjects whose biological specimen were available. In this subset there were 321 GG genotypes, and 23 carriers of the C allele (21 subjects with GC genotype and 2 CC homozygous). Consistent with previous data, circulating ADMA was higher in GG individuals than in C allele carriers (0.65 ± 0.31 vs. 0.52 ± 0.21 µmol/l, respectively; $P = 0.045$ after correction for age, sex, and BMI, **Figure 1**). At first, we elected to replicate the analysis as in multivariable regression Model B in order to ensure that the subset was a *bona fide* representative of the full cohort, and we confirmed that the observed genetic effect was preserved (Model C, **Table 4**) with *DDAH2* rs9267551 C allele exerting a comparable protective action ($\beta = -0.102$, $P = 0.04$) over cfPWV. When we added the measurement of serum ADMA levels to the statistical model (Model D, **Table 4**), it manifested a stronger independent effect on cfPWV ($\beta = 0.139$, $P = 0.006$), and the contribution of *DDAH2* rs9267551 genotype became non-significant ($\beta = 0.088$, $P = 0.969$).

This observation prompted us to the performance of a mediation analysis, graphically summarized in **Figure 2**. As predictor variable we adopted a factor produced by principal component analysis encompassing age, hsCRP, SBP, diagnosis

TABLE 4 | Stepwise multiple regression analysis in the subset sample, with cfPWv as dependent variable.

	β	*P*
Subset analysis model C		
hsCRP (mg/L)	0.189	<0.0001
Age (years)	0.183	<0.001
SBP (mmHg)	0.175	<0.01
Diabetes prevalence (N/Y)	0.155	<0.01
DDAH2 rs9267551 (GG/GC + CC)	−0.102	<0.04
Sex (F/M)	0.171	0.159
HDL (mg/dl)	−0.070	0.164
Smoking habit (N/Ex/Y)	0.027	0.600
BMI (Kg/m^2)	0.001	0.986
Subset analysis Model D		
Age (years)	0.172	0.02
hsCRP (mg/L)	0.167	0.001
SBP (mmHg)	0.166	0.001
Diabetes prevalence (N/Y)	0.164	0.003
ADMA (μmol/L)	0.139	0.006
DDAH2 rs9267551 (GG/GC+CC)	−0.088	0.969
Sex (F/M)	0.075	0.131
HDL (mg/dl)	−0.062	0.076
Smoking habit (N/Ex/Y)	0.019	0.712
BMI (Kg/m2)	0.001	0.978

Model C includes as covariates: age, SBP, diabetes prevalence, DDAH2 rs9267551 genotype, HDL, sex, BMI, smoking habit, and hsCRP. In Model D serum ADMA levels are added to the covariates in Model C. BMI, body mass index; cfPWV, carotid-femoral pulse wave velocity; DDAH2, dimethylarginine dimethylaminohydrolase 2; HDL, high density lipoprotein; hsCRP, high sensitivity C-reactive protein; SBP, systolic blood pressure.

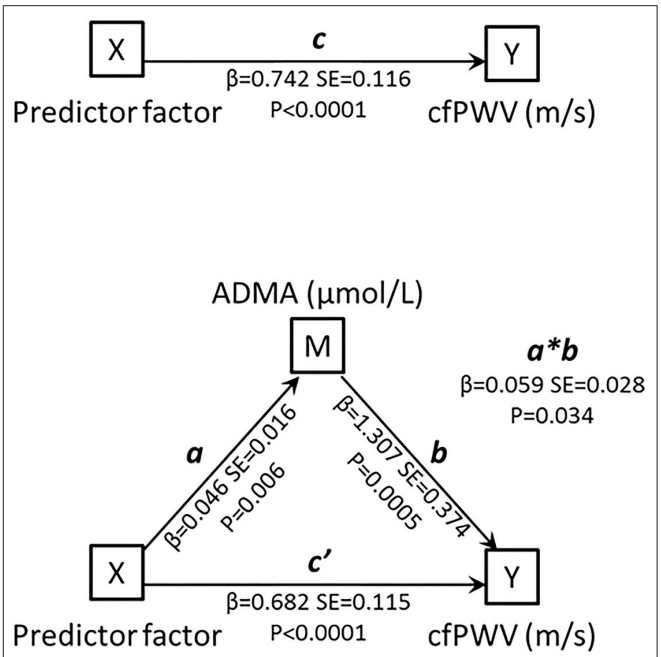

FIGURE 2 | Schematic representation of the mediation model. The mediation analyses were conducted using a series of linear regression models to estimate the total effect of X on Y *(c)*, the indirect effect of X on Y *(a*b),* and the direct effect of X on Y with removal of the effect of the mediator (c'). M, mediating variable; X, independent variable; Y, dependent variable.

of diabetes and *DDAH2* rs9267551 genotype ($\chi^2 = 90.8$, $P < 0.0001$). This predictor factor had eigenvalue = 1.490 and explained 29.806% of total variance. The total effect of the predictor factor on cfPWV, including the indirect and direct effect, is represented by the coefficient *c* (β = 0.742, SE = 0.116, $P < 0.00001$). The coefficient *a* (β = 0.046, SE = 0.016, $P = 0.006$) represents the effect of the predictor factor on ADMA, and the coefficient *b* (β = 1.307, SE = 0.374, $P = 0.0005$) represents the effect of ADMA on cfPWV. The coefficient *c'* (β = 0.682, SE = 0.115, $P < 0.00001$) represents the direct effect of the predictor factor on cfPWV, after correcting for the effect of ADMA. Finally, the mediated (or indirect) effect of the predictor factor on cfPWV through ADMA is represented as *a*b* (β = 0.059, SE = 0.028), and it was statistically significant *via* the bootstrapped estimation approach of the Sobel test, ($P = 0.034$). Thus, as both the direct and the mediated effects between the predictor factor and cfPWV were statistically significant, it may be suggested that a partial mediation exists, and this hypothesis is further supported by the fact that the direct effect *c'* has a smaller magnitude than the total effect *c*. Because *DDAH2* polymorphism rs9267551 was the only parameter included in the predictor factor to lose its association with cfPWV when circulating ADMA levels were added in the multivariable regression Model D, it is possible to infer that the effect of rs9267551 genotype on cfPWV is mediated by ADMA.

DISCUSSION

In the current study, we report, for the first time, evidences hinting that the presence of rs9267551 C allele may protect, at least in part, from an increase in arterial stiffness as measured by cfPWV, independently from the presence of traditional cardiovascular risk factors including age, sex, BMI, smoking habit and type 2 diabetes. Furthermore, our observations support the attribution of a causative role to ADMA in the pathogenesis of arterial rigidity, in line with evidences that long-term ADMA infusion is able to induce arteriosclerotic damage in an animal model of eNOS deficient mice (43), and that the acute infusion of subpressor doses of ADMA (0.10 mg/kg/min) increases vascular stiffness and decreases cerebral perfusion in healthy humans, independently from changes in blood pressure (25).

The measurement of PWV is a simple, non-invasive, and trustworthy method to evaluate the rigidity of a segment in the arterial system, and its use is advised by several guidelines (8, 10). More specifically, cfPWV is considered the gold-standard method for the measurement of aortic stiffness in a simple and non-invasive way (44). Several studies have shown that high cfPWV predict the occurrence of cardiovascular diseases even more than other traditional major risk factors (2, 6, 11, 12, 45, 46). Our population showed a difference in cfPWV of more than 1 m/s when the groups based on rs9267551 polymorphism were compared (**Table 1**). This difference is clinically relevant, as discussed in 2010 by the meta-analysis authored by Vlachopoulos et al. (13) that evaluated 15,877 ethnically etherogenous subjects

with variable high baseline risk (populations with hypertension, diabetes, end-stage renal disease, coronary artery disease, and subjects from the general population). The results of the meta-analysis revealed that the relative risk associated with an increase of 1 m/s in aortic PWV was 1.14 (95% CI: 1.09-1.20) for total CV events, 1.15 (95% CI: 1.09-1.21) for cardiovascular mortality, and 1.15 (95% CI: 1.09-1.21) for all-cause mortality.

ADMA is an endogenous inhibitor of eNOS activity, it competes for the binding of eNOS active site with L-Arginine, which is the substrate for the synthesis of NO. There is substantial evidence that NO bioavailability is associated with the levels of various components of the L-arginine/NO pathway (47), and several studies have documented a significant association between ADMA and hypertension (48–50). Furthermore, increased levels of ADMA are considered predictors of cardiovascular morbidity and mortality (18) and have been proposed as an explanation for the reduced production of NO typically observed in insulin resistance (50–52). Hence, serum ADMA levels have the potential to serve as diagnostic markers and therapeutic targets, however, animal and human studies have supplied conflicting results, and could not ultimately determine whether ADMA has a causal role in the pathogenesis of arterial stiffness and hypertension (26, 53, 54).

The hydrolysis of ADMA catalyzed by the DDAH enzyme is a major determinant of plasma ADMA concentration (27). Notably, animal models in which the modulation of ADMA had been constricted through overexpression or knockout of *DDAH* have provided support to the hypothesis that ADMA might play a pathogenic role (53–55), whereas other models have failed to report consistent evidences (56–58). This discrepancy suggests that pharmacological lowering of ADMA by targeting DDAH could be the key to understand whether ADMA directly plays a role in human cardiovascular pathology.

Demonstrating the existence of a causal role for ADMA in vessel dysfunction has the potential to determine meaningful changes in the clinical practice, and few therapeutic approaches specifically targeting ADMA pathways have already been proposed (59, 60). Among them, there is one experimental molecule with DDAH properties (M-DDAH) that resulted effective at lowering ADMA in preclinical models (61). Therefore, it is important to clarify the pathological role of ADMA in humans, in order to set the foundation in support of future studies. To achieve this objective we applied a Mendelian randomization study design, with the final goal of understanding if ADMA levels are associated with higher vascular stiffness, measured through cfPWV. This approach requires that the selected instrument (in this case SNP rs9267551) associates with the exposure. In our study, ADMA is the exposure and, although previous researches evaluating the impact of genetic variation of the *DDAH2* locus with cardiovascular risk have not supplied consistent results (62–64), the rs9267551 variant in the 5′-UTR of *DDAH2* has been proven to have a robust functional impact: primary human endothelial cells obtained from donors carrying the C allele showed increased transcription of *DDAH2*; and circulating ADMA levels were reduced in adult human subjects carrying the C allele when compared to the rs9267551 GG homozygous group (31). These evidences suggest that the rs9267551 C polymorphism in the locus of *DDAH2* may protect eNOS activity and NO production through its effects on ADMA levels. Indeed, in a previous published paper, we reported a role for our instrument, the functional polymorphism rs9267551, in modulating the risk of myocardial infarction even among diabetic patients (33). To date, no data are available in the literature about the impact of polymorphism rs9267551 on arterial stiffness.

Our results support the hypothesis that rs9267551 genotype may affect cfPWV, and suggest that this effect is mediated by circulating ADMA levels. In addition to this, it is worth noticing that the association between rs9267551 and cfPWV was independent from blood pressure, an observation that, if confirmed, might help elucidate, at least partially, the discrepancies in the literature about the causal role of ADMA in the pathogenesis of arterial stiffness and hypertension. Indeed, our data hint that long-term exposure to higher ADMA levels determines a specific vascular risk *via* the alteration of vessel elasticity (as measured by cfPWV) without affecting arterial hypertension.

The present study has some strengths including the exclusion of possible biases deriving from the presence of infectious or malignant conditions by study design, the accurate characterization of all enrolled subjects (no self-reported data were used) that permitted to encompass multiple recognized cardio-metabolic risk factors in the analyses, and the compliance with the assumptions of Mendelian randomization. Moreover, the homogeneity of the ethnicity of the population (all Italians of European descent), the accuracy of data collection via standardized protocol, and the centralized laboratory determinations, represent other points of strength of our analysis.

Notwithstanding this, several limitations are also present. First, the cross-sectional nature of the design does not permit to evaluate incident vascular dysfunction; therefore the present results require replication in prospective studies for validation. Furthermore, unfortunately, due to the low minor allele frequency, we were not able to establish the effect relative to allelic dosage ("per allele" effect), and biological specimen for laboratory determination of circulating ADMA levels were only available for a subset of our population. However, we have been able to confirm our previous report that ADMA levels were significantly higher in individuals with rs9267551 GG genotype than in C allele carriers (31). Although the robustness of our main claim (the association between rs9267551 genotype and cfPWV) is significantly reinforced by the positive independent linear relationship between circulating ADMA levels and cfPWV, we cannot completely exclude the influence of residual confounding. Additionally, caution should be exerted in extending the present findings to the general population, because they were based upon observational data collected from Caucasian subjects of European ancestry with mild to high cardiometabolic risk.

In conclusion, to the best of our knowledge, we are supplying the first evidences in support of the hypothesis that the variant rs9267551 in the *DDAH2* gene can modulate cfPWV in Italian adult subjects, and we have been able to demonstrate the existence of an interaction between rs9267551 genotype and circulating ADMA levels, able to affect arterial stiffness.

Hopefully, replication of these results in future studies will allow their extension to other populations of different ethnic background, with the final goal of definitively unraveling the role of ADMA in the pathogenesis of vascular risk and if intervening on *DDAH2* may turn out to be a fruitful therapeutic/preventive strategy.

DATA AVAILABILITY STATEMENT

The original contributions presented in the study are included in the article/**Supplementary Material**, further inquiries can be directed to the corresponding author/s.

ETHICS STATEMENT

The study was approved by the Institutional Ethics Committee of the University Magna Graecia of Catanzaro (Approval Code: 2012.63). Written informed consent was obtained from each subject in accordance with the principles of the Declaration of Helsinki.

AUTHOR CONTRIBUTIONS

GM, CA, and EM researched data, reviewed, and edited the article. EM, RS, SM, TF, GM, ES, and AS researched data. GM, PJ, and GS contributed to the discussion and reviewed the article. GM and GS analyzed the data and reviewed the article. FA designed the study, analyzed the data, and wrote the article. All authors contributed to the article and approved the submitted version.

FUNDING

GM was supported by funds from the EU project AIM1829805-3.

SUPPLEMENTARY MATERIAL

The Supplementary Material for this article can be found online at: https://www.frontiersin.org/articles/10.3389/fcvm.2021.811431/full#supplementary-material

REFERENCES

1. Avolio AP, Van Bortel LM, Boutouyrie P, Cockcroft JR, McEniery CM, Protogerou AD, et al. Role of pulse pressure amplification in arterial hypertension: experts' opinion and review of the data. *Hypertension.* (2009) 54:375–83. doi: 10.1161/HYPERTENSIONAHA.109.134379
2. Willum-Hansen T, Staessen JA, Torp-Pedersen C, Rasmussen S, Thijs L, Ibsen H, et al. Prognostic value of aortic pulse wave velocity as index of arterial stiffness in the general population. *Circulation.* (2006) 113:664–70. doi: 10.1161/CIRCULATIONAHA.105.579342
3. Mattace-Raso FUS, van der Cammen TJM, Hofman A, van Popele NM, Bos ML, Schalekamp MADH, et al. Arterial stiffness and risk of coronary heart disease and stroke: the Rotterdam Study. *Circulation.* (2006) 113:657–63. doi: 10.1161/CIRCULATIONAHA.105.555235
4. Safar ME, London GM, Plante GE. Arterial stiffness and kidney function. *Hypertension.* (2004) 43:163–8. doi: 10.1161/01.HYP.0000114571.75762.b0
5. Mitchell GF, Parise H, Benjamin EJ, Larson MG, Keyes MJ, Vita JA, et al. Changes in arterial stiffness and wave reflection with advancing age in healthy men and women: the Framingham Heart Study. *Hypertension.* (2004) 43:1239–45. doi: 10.1161/01.HYP.0000128420.01881.aa
6. Boutouyrie P, Tropeano AI, Asmar R, Gautier I, Benetos A, Lacolley P, et al. Aortic stiffness is an independent predictor of primary coronary events in hypertensive patients: a longitudinal study. *Hypertension.* (2002) 39:10–5. doi: 10.1161/hy0102.099031
7. Vlachopoulos C, Aznaouridis K, Terentes-Printzios D, Ioakeimidis N, Stefanadis C. Prediction of cardiovascular events and all-cause mortality with brachial-ankle elasticity index: a systematic review and meta-analysis. *Hypertension.* (2012) 60:556–62. doi: 10.1161/HYPERTENSIONAHA.112.194779
8. Ogihara T, Kikuchi K, Matsuoka H, Fujita T, Higaki J, Horiuchi M, et al. The Japanese Society of Hypertension Guidelines for the Management of Hypertension (JSH 2009). *Hypertens Res.* (2009) 32:3–107. doi: 10.1038/hr.2009.34
9. Covic A, Siriopol D. Pulse wave velocity ratio: the new "gold standard" for measuring arterial stiffness. *Hypertension.* (2015) 65:289–90. doi: 10.1161/HYPERTENSIONAHA.114.04678
10. Williams B, Mancia G, Spiering W, Agabiti Rosei E, Azizi M, Burnier M, et al. 2018 ESC/ESH Guidelines for the management of arterial hypertension: the task force for the management of arterial hypertension of the European Society of Cardiology and the European Society of Hypertension: the task force for the management of arterial hypertension of the European Society of Cardiology and the European Society of Hypertension. *J Hypertens.* (2018) 36:1953–2041. doi: 10.1097/HJH.0000000000001940
11. Laurent S, Boutouyrie P, Asmar R, Gautier I, Laloux B, Guize L, et al. Aortic stiffness is an independent predictor of all-cause and cardiovascular mortality in hypertensive patients. *Hypertension.* (2001) 37:1236–41. doi: 10.1161/01.HYP.37.5.1236
12. Laurent S, Katsahian S, Fassot C, Tropeano A-I, Gautier I, Laloux B, et al. Aortic stiffness is an independent predictor of fatal stroke in essential hypertension. *Stroke.* (2003) 34:1203–6. doi: 10.1161/01.STR.0000065428.03209.64
13. Vlachopoulos C, Aznaouridis K, Stefanadis C. Prediction of cardiovascular events and all-cause mortality with arterial stiffness: a systematic review and meta-analysis. *J Am Coll Cardiol.* (2010) 55:1318–27. doi: 10.1016/j.jacc.2009.10.061
14. Cooke JP. Does ADMA cause endothelial dysfunction? *Arterioscler Thromb Vasc Biol.* (2000) 20:2032–7. doi: 10.1161/01.ATV.20.9.2032
15. Perticone F, Sciacqua A, Maio R, Perticone M, Maas R, Boger RH, et al. Asymmetric dimethylarginine, L-arginine, and endothelial dysfunction in essential hypertension. *J Am Coll Cardiol.* (2005) 46:518–23. doi: 10.1016/j.jacc.2005.04.040
16. Böger RH, Maas R, Schulze F, Schwedhelm E. Asymmetric dimethylarginine (ADMA) as a prospective marker of cardiovascular disease and mortality–an update on patient populations with a wide range of cardiovascular risk. *Pharmacol Res.* (2009) 60:481–7. doi: 10.1016/j.phrs.2009.07.001
17. Willeit P, Freitag DF, Laukkanen JA, Chowdhury S, Gobin R, Mayr M, et al. Asymmetric dimethylarginine and cardiovascular risk: systematic review and meta-analysis of 22 prospective studies. *J Am Heart Assoc.* (2015) 4:e001833. doi: 10.1161/JAHA.115.001833
18. Schlesinger S, Sonntag SR, Lieb W, Maas R. Asymmetric and symmetric dimethylarginine as risk markers for total mortality and cardiovascular outcomes: a systematic review and meta-analysis of prospective studies. *PLoS ONE.* (2016) 11:e0165811. doi: 10.1371/journal.pone.0165811
19. Zhou S, Zhu Q, Li X, Chen C, Liu J, Ye Y, et al. Asymmetric dimethylarginine and all-cause mortality: a systematic review and meta-analysis. *Sci Rep.* (2017) 7:44692. doi: 10.1038/srep44692
20. Xuan C, Tian Q-W, Li H, Zhang B-B, He G-W, Lun L-M. Levels of asymmetric dimethylarginine (ADMA), an endogenous nitric oxide synthase inhibitor, and risk of coronary artery disease: a meta-analysis based on 4713 participants. *Eur J Prev Cardiol.* (2016) 23:502–10. doi: 10.1177/2047487315586094

21. Krzyzanowska K, Mittermayer F, Wolzt M, Schernthaner G. Asymmetric dimethylarginine predicts cardiovascular events in patients with type 2 diabetes. *Diabetes Care.* (2007) 30:1834–9. doi: 10.2337/dc07-0019
22. Lu T-M, Chung M-Y, Lin M-W, Hsu C-P, Lin S-J. Plasma asymmetric dimethylarginine predicts death and major adverse cardiovascular events in individuals referred for coronary angiography. *Int J Cardiol.* (2011) 153:135–40. doi: 10.1016/j.ijcard.2011.06.120
23. Tarnow L, Hovind P, Teerlink T, Stehouwer CDA, Parving H-H. Elevated plasma asymmetric dimethylarginine as a marker of cardiovascular morbidity in early diabetic nephropathy in type 1 diabetes. *Diabetes Care.* (2004) 27:765–9. doi: 10.2337/diacare.27.3.765
24. Zobel EH, von Scholten BJ, Reinhard H, Persson F, Teerlink T, Hansen TW, et al. Symmetric and asymmetric dimethylarginine as risk markers of cardiovascular disease, all-cause mortality and deterioration in kidney function in persons with type 2 diabetes and microalbuminuria. *Cardiovasc Diabetol.* (2017) 16:88. doi: 10.1186/s12933-017-0569-8
25. Kielstein JT, Donnerstag F, Gasper S, Menne J, Kielstein A, Martens-Lobenhoffer J, et al. ADMA increases arterial stiffness and decreases cerebral blood flow in humans. *Stroke.* (2006) 37:2024–9. doi: 10.1161/01.STR.0000231640.32543.11
26. Malle O, Trummer C, Theiler-Schwetz V, Meinitzer A, Keppel MH, Grübler MR, et al. NO synthesis markers are not significantly associated with blood pressure and endothelial dysfunction in patients with arterial hypertension: a cross-sectional study. *J Clin Med.* (2020) 9:3895. doi: 10.3390/jcm9123895
27. Ogawa T, Kimoto M, Watanabe H, Sasaoka K. Metabolism of NG,NG-and NG,N'G-dimethylarginine in rats. *Arch Biochem Biophys.* (1987) 252:526–37. doi: 10.1016/0003-9861(87)90060-9
28. Ogawa T, Kimoto M, Sasaoka K. Purification and properties of a new enzyme, NG,NG-dimethylarginine dimethylaminohydrolase, from rat kidney. *J Biol Chem.* (1989) 264:10205–9. doi: 10.1016/S0021-9258(18)81786-0
29. Leiper JM, Santa Maria J, Chubb A, MacAllister RJ, Charles IG, Whitley GS, et al. Identification of two human dimethylarginine dimethylaminohydrolases with distinct tissue distributions and homology with microbial arginine deiminases. *Biochem J.* (1999) 343:209–14. doi: 10.1042/bj3430209
30. Thanassoulis G. Mendelian randomization: how genetics is pushing the boundaries of epidemiology to identify new causes of heart disease. *Can J Cardiol.* (2013) 29:30–6. doi: 10.1016/j.cjca.2012.09.014
31. Andreozzi F, Presta I, Mannino GC, Scarpelli D, Di Silvestre S, Di Pietro N, et al. A functional variant of the dimethylarginine dimethylaminohydrolase-2 gene is associated with insulin sensitivity. *PLoS ONE.* (2012) 7:e36224. doi: 10.1371/journal.pone.0036224
32. Sesti G, Mannino GC, De Lorenzo C, Greco A, Sciacqua A, Marini MA, et al. A functional variant of the dimethylarginine dimethylaminohydrolase-2 gene is associated with chronic kidney disease. *Atherosclerosis.* (2013) 231:141–4. doi: 10.1016/j.atherosclerosis.2013.08.041
33. Mannino GC, Pezzilli S, Averta C, Fuoco A, Spiga R, Mancuso E, et al. A functional variant of the dimethylarginine dimethylaminohydrolase-2 gene is associated with myocardial infarction in type 2 diabetic patients. *Cardiovasc Diabetol.* (2019) 18:102. doi: 10.1186/s12933-019-0906-1
34. Scarpelli D, Cardellini M, Andreozzi F, Laratta E, Hribal ML, Marini MA, et al. Variants of the interleukin-10 promoter gene are associated with obesity and insulin resistance but not type 2 diabetes in caucasian italian subjects. *Diabetes.* (2006) 55:1529–33. doi: 10.2337/db06-0047
35. American Diabetes Association. 2. Classification and Diagnosis of Diabetes: Standards of Medical Care in Diabetes-2019. *Diabetes Care.* (2019) 42(Suppl 1):S13–28. doi: 10.2337/dc19-S002
36. Perticone M, Maio R, Tassone EJ, Tripepi G, Di Cello S, Miceli S, et al. Insulin-resistance HCV infection-related affects vascular stiffness in normotensives. *Atherosclerosis.* (2015) 238:108–12. doi: 10.1016/j.atherosclerosis.2014.11.025
37. Sciacqua A, Maio R, Miceli S, Pascale A, Carullo G, Grillo N, et al. Association between one-hour post-load plasma glucose levels and vascular stiffness in essential hypertension. *PLoS ONE.* (2012) 7:e44470. doi: 10.1371/journal.pone.0044470
38. Cassano V, Crescibene D, Hribal ML, Pelaia C, Armentaro G, Magurno M, et al. Uric acid and vascular damage in essential hypertension: role of insulin resistance. *Nutrients.* (2020) 12:E2509. doi: 10.3390/nu12092509
39. Kousios A, Kouis P, Hadjivasilis A, Panayiotou A. Cardiovascular risk assessment using ultrasonographic surrogate markers of atherosclerosis and arterial stiffness in patients with chronic renal impairment: a narrative review of the evidence and a critical view of their utility in clinical practice. *Can J Kidney Health Dis.* (2020) 7:2054358120954939. doi: 10.1177/2054358120954939
40. Preacher KJ, Hayes AF. SPSS and SAS procedures for estimating indirect effects in simple mediation models. *Behav Res Methods Instrum Comput.* (2004) 36:717–31. doi: 10.3758/BF03206553
41. MacKinnon DP, Lockwood CM, Hoffman JM, West SG, Sheets V. A comparison of methods to test mediation and other intervening variable effects. *Psychol Methods.* (2002) 7:83–104. doi: 10.1037/1082-989X.7.1.83
42. Andreozzi F, Succurro E, Mancuso MR, Perticone M, Sciacqua A, Perticone F, et al. Metabolic and cardiovascular risk factors in subjects with impaired fasting glucose: the 100 versus 110 mg/dL threshold. *Diabetes Metab Res Rev.* (2007) 23:547–50. doi: 10.1002/dmrr.724
43. Suda O, Tsutsui M, Morishita T, Tasaki H, Ueno S, Nakata S, et al. Asymmetric dimethylarginine produces vascular lesions in endothelial nitric oxide synthase-deficient mice: involvement of renin-angiotensin system and oxidative stress. *Arterioscler Thromb Vasc Biol.* (2004) 24:1682–8. doi: 10.1161/01.ATV.0000136656.26019.6e
44. Laurent S, Cockcroft J, Van Bortel L, Boutouyrie P, Giannattasio C, Hayoz D, et al. Expert consensus document on arterial stiffness: methodological issues and clinical applications. *Eur Heart J.* (2006) 27:2588–605. doi: 10.1093/eurheartj/ehl254
45. Ben-Shlomo Y, Spears M, Boustred C, May M, Anderson SG, Benjamin EJ, et al. Aortic pulse wave velocity improves cardiovascular event prediction: an individual participant meta-analysis of prospective observational data from 17,635 subjects. *J Am Coll Cardiol.* (2014) 63:636–46. doi: 10.1016/j.jacc.2013.09.063
46. Mitchell GF, Hwang S-J, Vasan RS, Larson MG, Pencina MJ, Hamburg NM, et al. Arterial stiffness and cardiovascular events: the Framingham Heart Study. *Circulation.* (2010) 121:505–11. doi: 10.1161/CIRCULATIONAHA.109.886655
47. Mels CMC, Huisman HW, Smith W, Schutte R, Schwedhelm E, Atzler D, et al. The relationship of nitric oxide synthesis capacity, oxidative stress, and albumin-to-creatinine ratio in black and white men: the SABPA study. *Age.* (2016) 38:9. doi: 10.1007/s11357-016-9873-6
48. Surdacki A, Nowicki M, Sandmann J, Tsikas D, Boeger RH, Bode-Boeger SM, et al. Reduced urinary excretion of nitric oxide metabolites and increased plasma levels of asymmetric dimethylarginine in men with essential hypertension. *J Cardiovasc Pharmacol.* (1999) 33:652–8. doi: 10.1097/00005344-199904000-00020
49. Achan V, Broadhead M, Malaki M, Whitley G, Leiper J, MacAllister R, et al. Asymmetric dimethylarginine causes hypertension and cardiac dysfunction in humans and is actively metabolized by dimethylarginine dimethylaminohydrolase. *Arterioscler Thromb Vasc Biol.* (2003) 23:1455–9. doi: 10.1161/01.ATV.0000081742.92006.59
50. Perticone F, Sciacqua A, Maio R, Perticone M, Galiano Leone G, Bruni R, et al. Endothelial dysfunction, ADMA and insulin resistance in essential hypertension. *Int J Cardiol.* (2010) 142:236–41. doi: 10.1016/j.ijcard.2008.12.131
51. Stühlinger MC, Abbasi F, Chu JW, Lamendola C, McLaughlin TL, Cooke JP, et al. Relationship between insulin resistance and an endogenous nitric oxide synthase inhibitor. *JAMA.* (2002) 287:1420–6. doi: 10.1001/jama.287.11.1420
52. McLaughlin T, Stühlinger M, Lamendola C, Abbasi F, Bialek J, Reaven GM, et al. Plasma asymmetric dimethylarginine concentrations are elevated in obese insulin-resistant women and fall with weight loss. *J Clin Endocrinol Metab.* (2006) 91:1896–900. doi: 10.1210/jc.2005-1441
53. Leiper J, Nandi M, Torondel B, Murray-Rust J, Malaki M, O'Hara B, et al. Disruption of methylarginine metabolism impairs vascular homeostasis. *Nat Med.* (2007) 13:198–203. doi: 10.1038/nm1543
54. Hasegawa K, Wakino S, Tatematsu S, Yoshioka K, Homma K, Sugano N, et al. Role of asymmetric dimethylarginine in vascular injury in transgenic mice overexpressing dimethylarginie dimethylaminohydrolase 2. *Circ Res.* (2007) 101:e2-10. doi: 10.1161/CIRCRESAHA.107.156901
55. Xu X, Zhang P, Kwak D, Fassett J, Yue W, Atzler D, et al. Cardiomyocyte dimethylarginine dimethylaminohydrolase-1 (DDAH1) plays an important

role in attenuating ventricular hypertrophy and dysfunction. *Basic Res Cardiol.* (2017) 112:55. doi: 10.1007/s00395-017-0644-z
56. Nakayama Y, Ueda S, Yamagishi S, Obara N, Taguchi K, Ando R, et al. Asymmetric dimethylarginine accumulates in the kidney during ischemia/reperfusion injury. *Kidney Int.* (2014) 85:570–8. doi: 10.1038/ki.2013.398
57. Rodionov RN, Martens-Lobenhoffer J, Brilloff S, Hohenstein B, Jarzebska N, Jabs N, et al. Role of alanine:glyoxylate aminotransferase 2 in metabolism of asymmetric dimethylarginine in the settings of asymmetric dimethylarginine overload and bilateral nephrectomy. *Nephrol Dial Transplant.* (2014) 29:2035–42. doi: 10.1093/ndt/gfu236
58. Jacobi J, Maas R, Cordasic N, Koch K, Schmieder RE, Böger RH, et al. Role of asymmetric dimethylarginine for angiotensin II-induced target organ damage in mice. *Am J Physiol Heart Circ Physiol.* (2008) 294:H1058-66. doi: 10.1152/ajpheart.01103.2007
59. Xuan C, Lun L-M, Zhao J-X, Wang H-W, Wang J, Ning C-P, et al. L-citrulline for protection of endothelial function from ADMA-induced injury in porcine coronary artery. *Sci Rep.* (2015) 5:10987. doi: 10.1038/srep10987
60. Reule CA, Goyvaerts B, Schoen C. Effects of an L-arginine-based multi ingredient product on endothelial function in subjects with mild to moderate hypertension and hyperhomocysteinemia - a randomized, double-blind, placebo-controlled, cross-over trial. *BMC Complement Altern Med.* (2017) 17:92. doi: 10.1186/s12906-017-1603-9
61. Lee Y, Mehrotra P, Basile D, Ullah M, Singh A, Skill N, et al. Specific lowering of asymmetric dimethylarginine by pharmacological dimethylarginine dimethylaminohydrolase improves endothelial function, reduces blood pressure and ischemia-reperfusion injury. *J Pharmacol Exp Ther.* (2021) 376:181–9. doi: 10.1124/jpet.120.000212
62. Anderssohn M, McLachlan S, Lüneburg N, Robertson C, Schwedhelm E, Williamson RM, et al. Genetic and environmental determinants of dimethylarginines and association with cardiovascular disease in patients with type 2 diabetes. *Diabetes Care.* (2014) 37:846–54. doi: 10.2337/dc13-0546
63. Xuan C, Xu L-Q, Tian Q-W, Li H, Wang Q, He G-W, et al. Dimethylarginine dimethylaminohydrolase 2 (DDAH 2) gene polymorphism, asymmetric dimethylarginine (ADMA) concentrations, and risk of coronary artery disease: a case-control study. *Sci Rep.* (2016) 6:33934. doi: 10.1038/srep33934
64. Pérez-Hernández N, Vargas-Alarcón G, Arellano-Zapoteco R, Martínez-Rodríguez N, Fragoso JM, Aptilon-Duque G, et al. Protective role of DDAH2 (rs805304) gene polymorphism in patients with myocardial infarction. *Exp Mol Pathol.* (2014) 97:393–8. doi: 10.1016/j.yexmp.2014.09.015

Conflict of Interest: The authors declare that the research was conducted in the absence of any commercial or financial relationships that could be construed as a potential conflict of interest.

Publisher's Note: All claims expressed in this article are solely those of the authors and do not necessarily represent those of their affiliated organizations, or those of the publisher, the editors and the reviewers. Any product that may be evaluated in this article, or claim that may be made by its manufacturer, is not guaranteed or endorsed by the publisher.

frontiers in Cardiovascular Medicine

ORIGINAL RESEARCH
published: 25 January 2022
doi: 10.3389/fcvm.2021.741221

Monocyte-Platelet Aggregates Triggered by CD31 Molecule in Non-ST Elevation Myocardial Infarction: Clinical Implications in Plaque Rupture

Ramona Vinci[1,2†], Daniela Pedicino[1,2†], Alice Bonanni[1,2], Alessia d'Aiello[1,2], Eugenia Pisano[2], Myriana Ponzo[1], Anna Severino[1,2], Pellegrino Ciampi[1], Francesco Canonico[2], Giulio Russo[2], Marianna Di Sario[1], Rocco Vergallo[2], Simone Filomia[1], Rocco Antonio Montone[2], Davide Flego[3], Lucia Stefanini[3], Roberto Piacentini[4,5], Cristina Conte[1], Francesco Cribari[1], Massimo Massetti[1,2], Filippo Crea[1,2‡] and Giovanna Liuzzo[1,2‡]*

[1] Department of Cardiovascular and Pulmonary Sciences, Università Cattolica del Sacro Cuore, Rome, Italy, [2] Department of Cardiovascular Sciences, Fondazione Policlinico Universitario A. Gemelli IRCCS, Rome, Italy, [3] Department of Internal Medicine and Medical Specialties, Sapienza University of Rome, Rome, Italy, [4] Department of Neuroscience, Università Cattolica del Sacro Cuore, Rome, Italy, [5] Fondazione Policlinico Universitario A. Gemelli IRCCS, Rome, Italy

Despite the recent innovations in cardiovascular care, atherothrombosis is still a major complication of acute coronary syndromes (ACS). We evaluated the involvement of the CD31 molecule in thrombotic risk through the formation of monocyte-platelet (Mo-Plt) aggregates in patients with ACS with no-ST-segment elevation myocardial infarction (NSTEMI) on top of dual anti-platelet therapy (DAPT). We enrolled 19 control (CTRL) subjects, 46 stable angina (SA), and 86 patients with NSTEMI, of which, 16 with Intact Fibrous Cap (IFC) and 19 with Ruptured Fibrous Cap (RFC) as assessed by the Optical Coherence Tomography (OCT). The expression of CD31 on monocytes and platelets was measured. Following the coronary angiography, 52 NSTEMIs were further stratified according to thrombus grade (TG) evaluation. Finally, a series of *ex vivo* experiments verified whether the CD31 participates in Mo-Plt aggregate formation. In patients with NSTEMI, CD31 was reduced on monocytes and was increased on platelets, especially in NSTEMI presented with RFC plaques compared to those with IFC lesions, and in patients with high TG compared to those with zero/low TG. *Ex vivo* experiments documented an increase in Mo-Plt aggregates among NSTEMI, which significantly decreased after the CD31 ligation, particularly in patients with RFC plaques. In NSTEMI, CD31 participates in Mo-Plt aggregate formation in spite of optimal therapy and DAPT, suggesting the existence of alternative thrombotic pathways, as predominantly displayed in patients with RFC.

Keywords: acute coronary syndromes, thrombus burden, unstable plaque, plaque rupture, monocyte-platelet aggregates, CD31, precision medicine

OPEN ACCESS

Edited by:
Daiju Fukuda,
Tokushima University, Japan

Reviewed by:
Kenichiro Otsuka,
Massachusetts General Hospital, United States
Junnan Tang,
First Affiliated Hospital of Zhengzhou University, China

****Correspondence:***
Daniela Pedicino
daniela.pedicino@policlinicogemelli.it

[†] These authors have contributed equally to this work and share first authorship
[‡] These authors have contributed equally to this work and share last authorship

Specialty section:
This article was submitted to Atherosclerosis and Vascular Medicine, a section of the journal Frontiers in Cardiovascular Medicine

Received: *14 July 2021*
Accepted: *20 December 2021*
Published: *25 January 2022*

Citation:
Vinci R, Pedicino D, Bonanni A, d'Aiello A, Pisano E, Ponzo M, Severino A, Ciampi P, Canonico F, Russo G, Di Sario M, Vergallo R, Filomia S, Montone RA, Flego D, Stefanini L, Piacentini R, Conte C, Cribari F, Massetti M, Crea F and Liuzzo G (2022) Monocyte-Platelet Aggregates Triggered by CD31 Molecule in Non-ST Elevation Myocardial Infarction: Clinical Implications in Plaque Rupture. Front. Cardiovasc. Med. 8:741221. doi: 10.3389/fcvm.2021.741221

INTRODUCTION

Despite the advances in medical treatments and interventional innovations, the prevalence of acute coronary syndromes (ACS) is still high (1). Anti-thrombotic drugs represent the first-line of therapeutic choice; however, recurrences and bleeding risk (2) remain two of the main concerns in the management of the patient (3–7).

The rupture of a lipid-rich plaque, with the consequent release of highly thrombotic elements, characterizes at least 50% of patients with ACS (8). Furthermore, atherosclerotic lesions with superimposed thrombus show increased levels of platelet-leucocyte aggregates that could contribute to the generation of further adverse events (9–11).

Each plaque phenotype may be associated with a different thrombotic burden and this may be due to alternative pathogenic mechanisms (12–17). Intracoronary imaging using optical coherence tomography (OCT) allows us to distinguish between a ruptured fibrous cap (RFC) and an intact fibrous cap (IFC) lesion. Histological analysis of thrombus aspirates from patients with ACS revealed a reduced thrombotic burden in patients with IFC, compared with those with RFC, which was enriched by inflammatory infiltrates (18).

The platelet endothelial cell adhesion molecule CD31 is a transmembrane immunoglobulin-like glycoprotein of about 130 kilodaltons (kDa) expressed on the surface of leukocytes, endothelial cells, and platelets (19–21); it exerts multiple functions using six Ig-like domains, building homophilic and/or heterophilic bindings (22–24), although mechanisms under these interactions are mostly unknown. Aside from these Ig-like extracellular domains, CD31 consists of a transmembrane region and a cytoplasmatic tail, whereby the molecule triggers co-inhibitory, pro-survival, and downstream pathways (25). The role of CD31 is recognized in immune cell transmigration; indeed, cellular trafficking across vascular endothelium can be inhibited, both *in vitro* and *in vivo*, by anti-CD31 antibodies (26, 27).

Alongside, CD31 carries out an immunomodulatory role limiting the activation of T- and B-cells (28–31), as well as it exerts a regulatory role on platelet activation (32).

In patients presenting with ACS, the reduction of CD31 in leukocytes is associated with increased inflammation (33).

Furthermore, exposure to CD31 at the site of the vascular injury could amplify platelet adhesion and could lead to the formation of plugs. This could promote a further expansion of inflammatory signaling by initiating a homing activity through the recruitment of other cells expressing CD31 on their surface, such as monocytes and granulocytes (19).

However, the contribution of CD31 in platelet activation is largely unknown and requires further evaluation. Few results have shown that the antibodies directed against CD31 can reduce platelet aggregation (34–36), suggesting a role of this molecule in platelet aggregation and thrombus formation.

This study investigates the following: (1) the expression of CD31 on monocytes and platelets in ACS patients, patients with stable angina (SA), and control (CTRL) subjects; (2) the different role of CD31 in patients with ACS presented with RFC and IFC at the site of the culprit stenosis, according to OCT assessment; and (3) the involvement of CD31 in monocyte-platelet cross-talk and the coronary thrombus burden severity.

MATERIALS AND METHODS

Study Population

Our population included a total of 151 individuals: (1) 86 patients with Acute Coronary Syndrome (ACS) admitted to our Coronary Care Unit (CCU) with a diagnosis of Non-ST Elevation Myocardial Infarction (NSTEMI) confirmed at coronary angiography (37); (2) 46 patients with Stable Angina (SA) with symptoms of stable effort angina lasting more than 1 year, angiographically confirmed coronary artery disease, with any precedent acute coronary events, and any evident ischemic episodes during the last 48 h (38); (3) 19 Control (CTRL) subjects without apparent clinical sign of coronary artery disease screened during their cardiovascular prevention medical examination. In addition, we analyzed a group of ST-Elevation Myocardial Infarction (STEMI, $n = 16$) patients enrolled in the Cath Lab, at the time of primary percutaneous coronary intervention (refer to **Supplementary Table 1** for characteristics of the patient group).

Exclusion criteria were: (1) age <18 or >80 years; (2) severe chronic heart failure, i.e., New York Heart Association (NYHA) functional classes III and IV with Left Ventricular Ejection Fraction (LVEF) <35%; (3) severe heart valve disease; (4) recent (<3 months) major surgical procedures or trauma; (4) in-stent restenosis, stent thrombosis, and culprit lesion in a saphenous vein graft; (3) autoimmune diseases, evidence of immunologic disorders, or chronic infectious disease; (4) liver diseases; (5) use of anti-inflammatory or immunosuppressive drugs other than low-dose aspirin; (6) malignancies; and (7) chronic kidney disease stage 4 (GFR < 30 ml/min).

Clinical features were carefully recorded at the time of patient admission and enrollment. Patients were all matched for age ($p = 0.826$).

The main population characteristics are listed in **Table 1**. All individuals gave their informed consent. Our local Ethics Committee approved the study (Protocol No 36077/19 ID 2747).

Hematological Routine Tests

Venous blood samples were collected at the time of hospital admission for hematological routine tests. Total and differential white blood cell counts were analyzed on fresh blood samples with a Bayer H*3-hematology analyzer (Leverkusen, Germany), using automated flow cytochemistry. Serum cardiac troponin I (cTnI) was determined at the time of hospital admission as routine measurement by high-sensitivity Single Molecule Counting technology (ADVIA Centaur immunoassay system, Siemens, Erlangen, Germany Roche Diagnostics, Mannheim, Germany). The minimum detectable concentration was 0.04 ng/ml (99th percentile in healthy individuals). Moreover, high-sensitive-CRP (hs-CRP) was measured using a high-sensitivity latex-enhanced immunonephelometric assay (Latex/BN II, Dade Behring, Marburg, Germany).

TABLE 1 | Baseline characteristics of the study population.

	CTRL $n = 19$	SA $n = 46$	NSTEMI $n = 86$	*P*-value
Age, mean ± SD	64 ± 9.7	66 ± 9.9	65 ± 13.5	0.826
Gender, M/F	9/10	38/8	58/28	0.016
CV risk factors				
Smoking, (%)	3 (16)	26 (57)	43 (50)	0.009
Diabetes, (%)	0 (0)	18 (39)	27 (33)	0.006
Hypertension, (%)	9 (47)	40 (87)	65 (78)	0.002
Dyslipidemia, (%)	4 (21)	30 (65)	45 (54)	0.005
Obesity, (%)	3 (16)	3 (7)	20 (24)	0.042
Family history, (%)	2 (11)	15 (33)	32 (39)	0.064
Recurrence, (%)	–	–	13 (15)	–
Medical therapy				
[0.3pt] DAPT, (%)[#]	–	17 (37)	40 (47)	0.001
ASA, (%)	2 (14)	37 (80)	55 (65)	<0.001
Clopidogrel, (%)	–	18 (19)	19 (23)	0.03
Prasugrel, (%)	–	0	0	–
Ticagrelor, (%)	–	2 (4)	24 (34)	< 0.001
Anticoagulants, (%)	2 (14)	2 (4)	7 (8)	0.455
Beta-Blockers, (%)	7 (37)	29 (63)	40 (47)	0.088
Diuretics, (%)	2 (11)	10 (22)	22 (23)	0.360
ACE-I, (%)	2 (11)	13 (28)	33 (38)	0.051
ARBs, (%)	5 (26)	22 (48)	25 (29)	0.07
Statins, (%)	6 (32)	32 (70)	41 (48)	0.009
Ca-antagonists, (%)	0	12 (26)	15 (17)	0.044
Nitrates, (%)	0	3 (7)	1 (1)	0.140
Insulin, (%)	0	5 (11)	4 (5)	0.179
Oral antidiabetic, (%)	0	11 (24)	19 (22)	0.066
Laboratory Values, mean ± SD				
CK, μg/l	75 ± 19	135 ± 139	169 ± 128	0.273
CKMB, μg/l	1 ± 0.3	4 ± 2.7	25 ± 51	0.768
Tn I, ng/ml	–	0.01 ± 0.1	6.7 ± 12.1	0.017
Hb, g/dl	14.9 ± 0.7	13.3 ± 2.3	13.3 ± 2.1	0.447
WBC, $x10^3$/ml	7.2 ± 1.6	9.2 ± 2.1	9.6 ± 2.8	0.326
Platelets, $x10^3$/ml	220 ± 28	217 ± 52	244 ± 58	0.030
Lymphocytes, $x10^9$/l	2.1 ± 0.7	2.4 ± 1	2.2 ± 1.1	0.846
Lymphocytes, %	29 ± 7	27 ± 9	24 ± 9	0.493
Glycemia, mg/dl	100 ± 24	109 ± 35	120 ± 52	0.318
Creatinine, mg/dl	0.8 ± 0.2	1.0 ± 0.4	0.9 ± 0.5	0.54
Cholesterol, mg/dl	219 ± 50	154 ± 44	164 ± 45	0.02
LDL-cholesterol, mg/dl	129 ± 22	86 ± 37	100 ± 35	0.04
HDL-cholesterol, mg/dl	65 ± 12	44 ± 10	51 ± 11	0.468
Triglycerides, mg/dl	128 ± 37	109 ± 42	139 ± 51	0.030
ESR, mm/h	13 ± 4	12 ± 15	26 ± 25	0.537
hs-CRP, mg/l	2.1 ± 0.7	3.0 ± 4.1	11.9 ± 18.2	0.09

[#]*These data refer to the time of the enrollment of the patient and blood withdrawal. At the time of coronary angiography, all the patients with NSTEMI were on DAPT according to current guidelines (4). ACE-I, ACE inhibitors; ARBs, angiotensin II receptor blockers; ASA, aspirin; Ca, calcium; CTRL, control individuals; CV, cardiovascular; CK, creatine kinase; DAPT, dual antiplatelet therapy; ESR, erythrocyte sedimentation rate; Hb, hemoglobin; HDL, high-density lipoprotein; hsCRP, high sensitive C-reactive protein; LDL, low-density lipoprotein; M/F, male/female; SA, stable angina; NSTEMI, Non ST-segment elevation myocardial infarction; SD, standard deviation; Tn, troponin; and WBC, white blood cells.*

Optical Coherence Tomography (OCT)

Optical coherence tomography (OCT) interrogation was performed before the stent implantation for clinical reasons, by using the OCT system C7-XR (St. Jude Medical, St. Paul, MN). Therefore, not all patients underwent an OCT interrogation. Moreover, for further analysis, we considered only those patients in whom it was technically possible to clearly identify the feature of the culprit plaques. We classified as plaques with Intact Fibrous Cap all lesions with thrombus overlying a plaque characterized by an intact fibrous cap, or with the presence of irregularities of the luminal surface at the culprit site in the absence of thrombus. On the other hand, we classified as Rupture Fibrous Cap (RFC) all the lesions characterized by a discontinuity of the fibrous cap that presents a cavity formed inside the plaque or with direct communication between the lumen and inner core of the lesion (39–41).

Two experienced investigators, who were blinded about the clinical information, performed the OCT analyses using the established criteria (refer to above), with an inter-observer agreement of 86.4% ($K = 0.7$; $p < 0.001$), and with intra-observer reliability of the two investigators between 95% ($K = 0.8$; $p < 0.0001$) and 100% ($K = 1$; $p < 0.0001$). To assess the OCT intra-observer reliability, the investigators reapplied the same criteria for OCT analysis at least 1 month after the first reading. In case of discordance, a consensus was obtained involving a third investigator.

The 35 patients with NSTEMI, who underwent OCT analysis of culprit coronary lesions, were sub-grouped in RFC ($n = 19$) and IFC ($n = 16$), beyond the unknown plaque phenotypes that were excluded ($n = 5$).

Angiographic and OCT findings are shown in **Supplementary Table 2**.

Thrombus Grade Evaluation

Angiographic thrombus burden was categorized into 5 grades, as described in a previous study (42, 43), providing high intra- and inter-observer agreements. In particular, thrombus grade 0 (zero) defines the absence of angiographic characteristics of thrombus; thrombus grade 1 defines the possible presence of thrombus (i.e., reduced contrast density, haziness, and irregular lesion contour); thrombus grade 2 corresponds to definite thrombus, with greatest linear dimension $\leq$1/2 vessel diameter; thrombus grade 3 corresponds to definite thrombus, with greatest linear dimension >1/2 but < 2 vessel diameters; thrombus grade 4 corresponds to definite thrombus, with greatest linear dimension $\geq$2 vessel diameters; and thrombus grade 5 corresponds to total coronary occlusion. Lesions with a thrombus grade from 0 to 2 were classified as having a zero/low thrombus burden, while those with a thrombus grade from 3 to 5 were classified as having a high thrombus burden.

Two blinded investigators performed a thrombus grade analysis, with an inter-observer agreement of 80.5% ($K = 0.7$; $p < 0.0001$), and an intra-observer reliability of the two investigators between 87% ($K = 0.8$; $p < 0.0001$) and 94.8% ($K = 0.9$; $p < 0.0001$). To assess the thrombus grade intra-observer reliability, the investigators reapplied the same criteria

for thrombus grade analysis at least 1 month after the first reading. In case of discordance, a consensus was obtained involving a third investigator.

Blood Sampling and Isolation of Human Peripheral Mononuclear Cells

At the time of study enrollment, 30 cc of venous blood samples were collected, within 24 h from the onset of symptoms (9 ± 3 h). Peripheral blood mononuclear cells (PBMCs) were isolated from whole blood EthyleneDiamineTetraacetic Acid (EDTA) samples by density gradient centrifugation method at 1,200 x g for 25 min at room temperature (RT) (with no brake applied) (Lympholyte®-H Cell Separation Media, CEDARLANE, Burlington, Canada). The pellets of PBMC were washed and were resuspended in Dulbecco's phosphate-buffered saline (DPBS) (GIBCO, Invitrogen, Carlsband, CA, USA), and were aliquoted according to the final analyses. Cell concentration was determined by using an automated cell counter (Nucleocounter, ChemoMetec, Allerod, Denmark).

Isolation of Human Platelets

Whole blood citrate dextrose samples were centrifuged at 200 x g for 15 min at RT (with no brake applied). The top 3/4 of the platelet-rich plasma (PRP) was transferred into a new plastic tube, without disturbing the buffy coat layer, and was centrifuged as above for 5 min to remove by pelleting the residual erythrocytes/white blood cells. The 2/3 of supernatant was withdrawn and centrifuged in Acid-Citrate-Dextrose (ACD) solution (1-part ACD solution to 9 parts blood) (Sigma-Aldrich, S. Louis, MO, USA) at 800 x g for 20 min (with no brake applied). Platelet pellets were gently washed and resuspended in Hepes-Tyrode buffer pH 7.4 and aliquoted according to the final analyses. Before the flow cytometry analyses, to ensure that platelets cannot be induced to a new functional state, we used ThromboFix Platelet stabilizer (Beckman Coulter, Brea, CA); moreover, during all the procedures, strong mechanical forces (i.e., fast pipetting or vigorous shaking) have been avoided, while blood and reagents were always kept and handled at RT or 37°C.

Flow Cytometry Immunophenotyping and Analysis of Basal Monocytes and Platelets

All the acquisitions on the fresh starting materials were made possible by the close proximity of the clinic and the laboratory areas, which are both situated in the Department of Cardiovascular and Pulmonary Sciences at Fondazione Policlinico Universitario A. Gemelli IRCCS. CD31 expression on basal PBMCs and platelets was assessed by flow cytometry after staining with monoclonal (m) antibody (Ab) anti-CD31-Phycoerytrin (PE) (clone 1F11, IM2409; Beckman Coulter, Brea, CA, USA). We used an anti-CD14-Electron Coupled Dye (ECD) (clone RM052, B92391; Beckman Coulter, Brea, CA, USA) and a CD42b-fluorescein isothiocyanate (FITC) (clone SZ2, IM0648U; Beckman Coulter, Brea, CA, USA) as monocyte and platelet markers, respectively. We used anti-CD45-PE (clone J33, Beckman Coulter, Brea, CA, USA) for verifying the purity of our platelet samples and a mAb anti-CD62 P-selectin (P) (clone Psel.KO2.3, 12-0626-82; eBioscience, INC., San Diego, CA, USA) to determine the platelet activation. All the antibody staining were performed for 15 min at RT and under a dark condition. The expression of each Median Fluorescence Intensity (MFI) was assessed by subtracting the negative peak-MFI from the positive peak-MFI. After the incubation, cells were washed with 0.5 ml of 1X DPBS (Gibco, Thermo-Fisher, Waltham, MA, USA) and were pelleted by centrifugation (250 × g for 5 min); the supernatant was discarded. Finally, cells were resuspended in 1 ml of 1X DPBS (Gibco, Thermo-Fisher, Waltham, MA, USA) for flow cytometry analysis. For each acquisition, a total of 50,000 events were captured. Flow cytometry analyses were conducted with Cytomics FC500 Analyzer (lasers: blue 488 nm, red 631 nm; serial number AH20082) (Beckman Coulter, Brea, CA, USA) and data were analyzed with Kaluza software (Beckman Coulter, Brea, CA, USA) (44) (**Supplementary Figures 1**, **2**).

Ex vivo Co-culture Experiments for Evaluating Monocyte-Platelet Aggregates and Effect of CD31 Ligation

Freshly isolated PBMCs of 2 × 10^6/ml were co-cultured in 12-well plates with freshly isolated platelets in a ratio of 1:1 for 16 h at 37°C under 5% carbon dioxide (CO_2) and 20% Oxigen (O_2), in Roswell Park Memorial Institute (RPMI) 1640 medium (LONZA, Verviers, Belgium) supplemented with 100 U penicillin, 0.1 mg/ml streptomycin, 2 mmol glutamine, and 10% Fetal Bovine Serum (FBS) (Thermo-Fisher, Waltham, MA, USA). The mAb anti-CD31 was added to the culture medium (1 μg/ml, clone WM59, 16-0319-82, Functional Grade; eBioscience, San Diego CA, USA) for CD31 ligation experiments. Furthermore, we performed the above-described experiments in presence of adenosine 5′-diphosphate (ADP) (2 μmol/L; Thermo-Fisher, Waltham, MA, USA).

Ex-vivo Co-culture Experiments With Collagen and Evaluation of Monocyte-Platelet Aggregates Before and After CD31 Ligation

The PBMCs at 0.5 × 10^6/ml (0.1 × 10^6/0.2 ml) were co-cultured *ex vivo* with platelets in a ratio of 1:1 in 96-well plates and were incubated at 37°C under 5% CO_2 and 20% O_2, in RPMI 1640 medium (LONZA, Verviers, Belgium), supplemented with 100 U penicillin, 0.1 mg/ml streptomycin, 2 mmol glutamine, and 10% FBS (Thermo-Fisher, Waltham, MA, USA). The mAb anti-CD31were added to each culture medium (1 μg/ml, clone WM59, 16-0319-82, Functional Grade; eBioscience, San Diego CA, USA) for CD31 ligation experiments. After 4 h of incubation, cells were fixed with fixation buffer (eBioscience™, San Diego, CA, USA) and were washed with sterile 1X DPBS (GIBCO, Invitrogen, Carlsband, CA, USA). Cells were then stained with an anti-CD14-ECD (clone RM052; B92391) and a CD42b-FITC (clone SZ2, IM0648U) (both Beckman Coulter, Brea, CA, USA) as monocyte and platelet markers, an anti-CD69-Allophycocyanin (APC) (clone TP1.55.3, A80711; Beckman Coulter, Brea, CA, USA) and an anti-CD62P-PE (clone Psel.KO2.3, 12-0626-82; eBioscience, INC., San Diego, CA, USA) to determine the monocyte and platelet activation.

After the incubation, cells were washed with 0.5 ml of 1X DPBS (Gibco, Thermo-Fisher, Waltham, MA, USA) and were pelleted by centrifugation (250 X g for 5 min), the supernatant was discarded. Finally, cells were resuspended in 1 ml of 1X DPBS (Gibco, Thermo-Fisher, Waltham, MA, USA) for flow cytometry analysis. For each acquisition, a total of 50,000 events were captured. Flow cytometry analyses were conducted with Cytomics FC500 Analyzer (lasers: blue 488 nm, red 631 nm; serial number AH20082) (Beckman Coulter, Brea, CA, USA) and data were analyzed with Kaluza software (Beckman Coulter, Brea, CA, USA).

Moreover, to evaluate the effect of CD31 ligation on isolated monocytes and platelets, we incubated individual cell cultures in the presence or absence of *Escherichia coli*-lipopolysaccharide (1 μg/ml; LPS; Sigma-Aldrich, S. Louis, MO, USA) and collagen (1 μg/ml; Mascia-Brunelli, Milan, IT) before and after mAb anti-CD31 (1 μg/ml, clone WM59, 16-0319-82, Functional Grade; eBioscience, San Diego CA, USA). Anti-CD69-APC (clone TP1.55.3, A80711; Beckman Coulter, Brea, CA, USA) and anti-CD62P-PE (clone Psel.KO2.3; 12-0626-82, eBioscience, INC., San Diego, CA, USA) were used for checking, respectively, the monocyte and platelet activation before and after each treatment. After the incubation, cells in 96-well plates were washed with 0.2 ml of 1X DPBS (Gibco, Thermo-Fisher, Waltham, MA, USA) and were pelleted by centrifugation (250 × g for 5 min); the supernatants were discarded. Finally, cells were resuspended in 0.2 ml of 1X DPBS (Gibco, Thermo-Fisher, Waltham, MA, USA) for flow cytometry analysis using the plate injection mode.

This last flow-cytometry analysis was conducted with CyoFlex S B2-R3-V4-Y0 (serial number AD15040; Beckman Coulter, Brea, CA, USA) and the acquired data were analyzed with CytExpert software (Beckman Coulter, Brea, CA, USA).

Note that all the flow cytometry analyses were performed within 30–60 min after the blood draw for basal samples, and immediately after 16 h for *in vitro* studies of monocyte-platelet aggregates.

Confocal Microscopy on Co-culture of Monocytes and Platelets

We performed a series of confocal microscopy image acquisition on 16-h co-cultured cells. Cells were fixed with a 10% formalin solution neutrally buffered (Sigma-Aldrich, St. Louis, MO, USA) at RT for 15 min and were permeabilized with 0.1% Triton X-100 in PBS for 15 min. Cells were then washed two times with PBS and were blocked in 0.5% bovine serum albumin (BSA) in PBS for 20 min before incubating overnight with the primary mouse monoclonal anti-CD31 antibody (1:500 clone JC/70A, AbCam, Cambridge, UK) and a mouse monoclonal anti-CD42b-FITC antibody (1:500; eBioscience, San Diego, CA, USA). The secondary antibody for the anti-CD31 was Alexa Fluor 546-conjugated goat anti-mouse IgG (1:1,000; Thermo Fisher Scientific, Waltham, MA, USA). About 4′,6-diaminophenylindole (DAPI) in ProLong® Gold Antifade Mountant (Thermo-Fisher, Waltham, MA, USA) was used for nucleic acid staining. Confocal images were obtained with a Nikon A1 MP confocal scanning system connected to an Eclipse T-i microscope, with an ×40 objective plus further 1 and ×3 magnification, acquired by Nis-Elements imaging software, and were analyzed by the processing Image-J/Fiji software (LOCI, University of Wisconsin-Madison, USA). The degree of co-localization was quantified using Mander's overlap coefficient (MOC). Data are presented as mean ± SEM with respect to untreated samples, from a minimum of 50 cells.

Statistical Analysis

Variables were assessed by the Shapiro Wilk test. For normally distributed data, Student's *t*-test was performed for statistics between two groups, or a 1-way ANOVA and 1-ANOVA for repeated measures, with Bonferroni correction, were used for multiple comparisons; in presence of unequal variance, the Welch's *t*-test was used. Non-parametric data were analyzed using nonparametric tests: the Mann-Whitney U test for comparison between two groups, and the Kruskal-Wallis test followed by Dunn's multiple tests for between-group comparisons. For all the experimental assays performed, a two-tailed value of $p \leq 0.05$ was considered statistically significant. Statistical analyses were performed with GraphPad Prism version 8.02 for Windows (GraphPad Software, La Jolla, San Diego, CA, USA) and with an SPSS software v22.0 (IBM Corporation, Armonk, New York, USA). For flow-cytometry analyses, Kaluza and CytExpert softwares (Beckman Coulter, USA) were used.

RESULTS

Study Population

The main characteristics of the whole population are listed in **Table 1**. A flow chart describes the distribution of the enrolled population within the main experimental settings (**Figure 1**).

CD31 Protein Surface Expression on Basal Monocytes and Platelets Displays a Cell-Dependent Behavior

To evaluate the expression of CD31 molecules on the surface of $CD14^+$ monocytes and $CD42b^+$ platelets, we performed multicolor flow-cytometry analyses on isolated PBMCs and platelets. We assessed the expression of CD31 on PBMCs of 80 NSTEMI, 27 SA, and 19 CTRL; meanwhile, we evaluated CD31 on platelets on 53 NSTEMI, 36 SA, and 8 CTRL subjects. The CD31 protein surface expression was significantly lower on monocytes from patients with NSTEMI (mean ± SD: 31.90 ± 10.81) compared to those from CTRL individuals (mean ± SD: 43.12 ± 12.43; $p = 0.001$) and patients with SA (mean ± SD: 37.31 ± 11.32; $p = 0.036$), respectively. No differences were observed between CTRL and SA groups ($p = 0.114$) (ANOVA for trend: $p = 0.001$) (**Figure 2**).

In contrast, as shown in **Figure 3**, CD31 surface expression on basal $CD42b^+$ platelets was significantly higher in NSTEMI (Mean ± SD: 1.93 ± 0.86), as compared with CTRL individuals (Mean ± SD: 1.31 ± 0.38; $p = 0.002$) and patients with SA (Mean ± SD: 1.54 ± 0.65; $p = 0.011$). No differences were observed between CTRL and SA groups ($p = 0.209$) (ANOVA for trend: $p = 0.001$). We used the P-Selectin (CD62P) as a marker of platelet activation. No difference was observed between the patients with SA and patients with NSTEMI for the CD62P expression levels (*p*

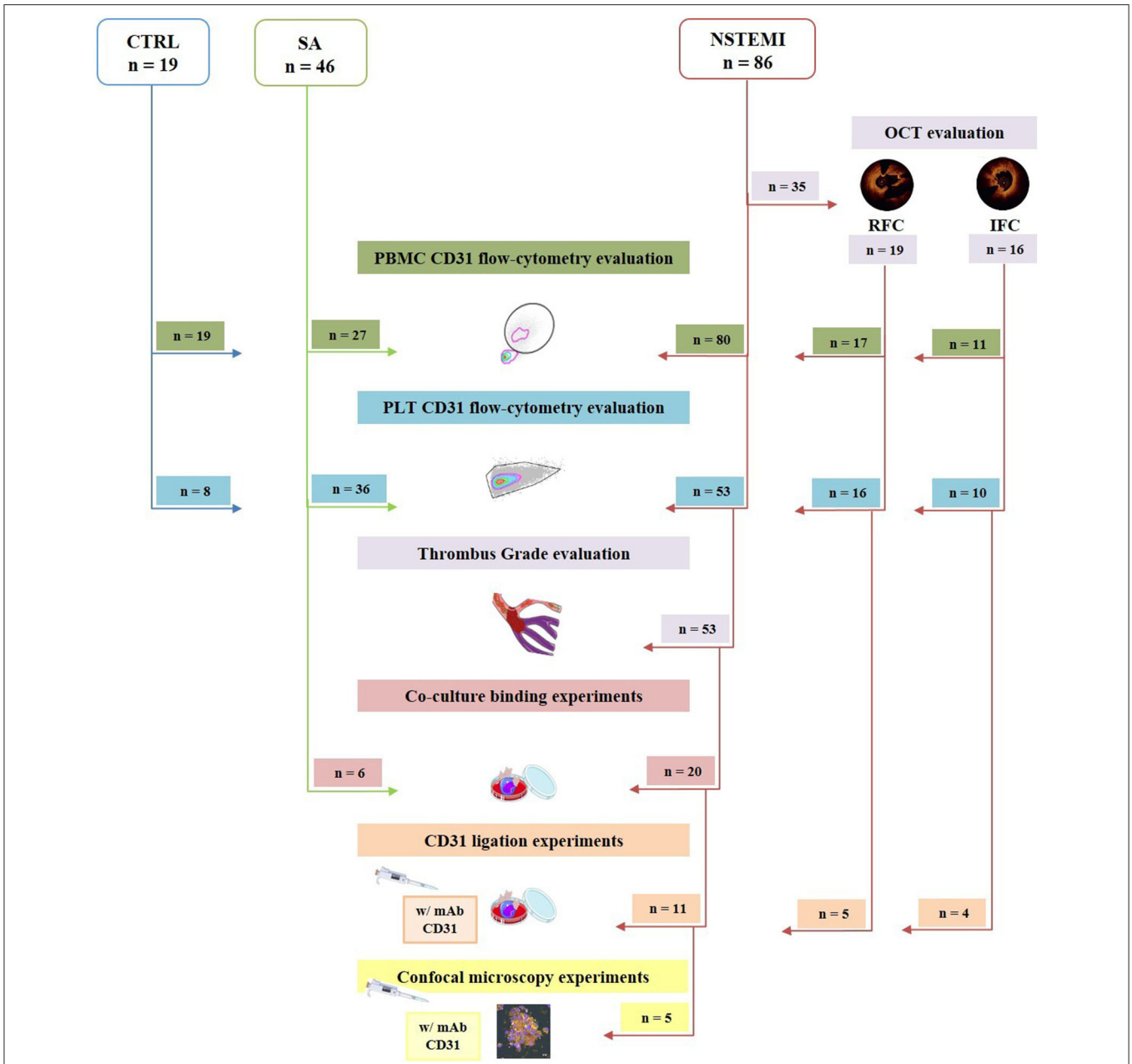

FIGURE 1 | Flow chart showing the enrolled study population and its allocation within the main experimental procedures. Of 86 patients with NSTEMI, 35 underwent OCT investigation, defining $n = 16$ IFC, and $n = 19$ RFC. Obtained PBMC from 80 NSTEMI, 27 patients with SA and 19 CTRL subjects enrolled were evaluated for CD31 expression by flow cytometry. Platelet CD31 was assessed by flow-cytometry on 53 NSTEMI, 36 patients with SA, and 8 CTRL subjects. Thrombus grade analysis was performed on the latter 53 patients with NSTEMI. For co-culture binding experiments, 20 NSTEMI and 6 SA were employed. Finally, 11 were engaged for CD31 ligation experiments; of those patients, 5 were investigated through confocal microscopy. CTRL, control subjects; IFC, intact fibrous cap; NSTEMI, non-ST-elevation myocardial infarction; PBMCs, peripheral blood mononuclear cells; PLTs, platelets; RFC, ruptured fibrous cap; and SA, stable angina patients (art images from http://smart.servier.com/ site).

$= 0.942$), thus, suggesting equal levels of activation of platelets in each population (**Supplementary Figure 3**).

Platelet CD31 Expression Reflects a Specific Plaque Phenotype

From the analysis of all patients with NSTEMI who underwent intracoronary imaging, according to plaque morphology at OCT interrogation, we further sub-grouped the population of NSTEMI in RFC and IFC groups (RFC, $n = 19$; IFC, $n = 16$). Details of angiographic and OCT measurements are listed in **Supplementary Table 2**. The main clinical characteristics of patients with RFC and patients with IFC are presented in **Table 2**. No significant differences were recorded between RFC and IFC groups regarding therapies, type of dual antiplatelet therapy

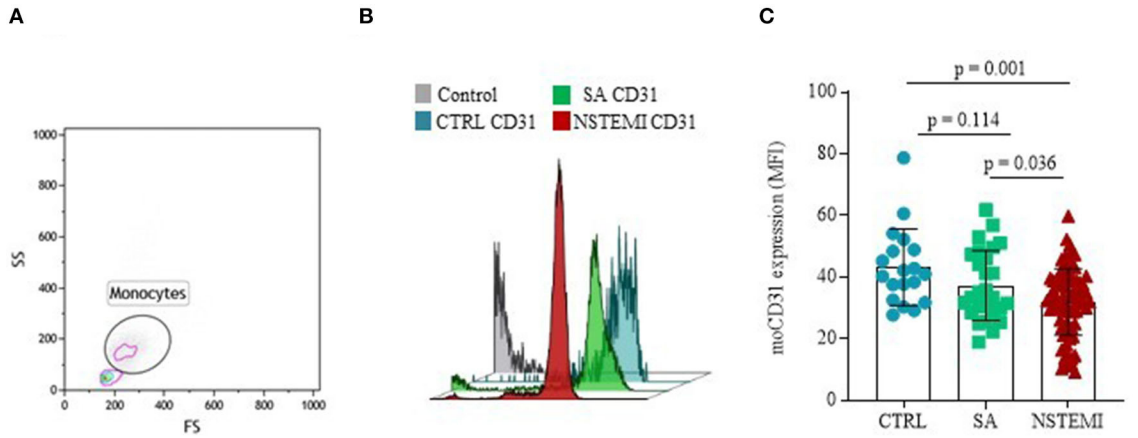

FIGURE 2 | CD31 expression on monocytes. Graphs showing the surface protein expression of CD31 on $CD14^+$ monocytes assessed by flow-cytometry (mean ± SD) in basal conditions. **(A)** Representative flow cytometry forward vs. side scatter plot of monocyte subset; **(B)** Representative flow cytometry overlay plot; **(C)** Data analysis of $_{mo}$CD31 surface protein expression between the three groups (CTRL, Control individuals; FS, Forward Scatter; MFI, Median Fluorescence Intensity; $_{mo}$CD31, monocyte CD31; NSTEMI, Non-ST-Elevation Myocardial Infarction; SA, Patients with Stable Angina; SD, Standard Deviation; and SS, Side Scatter).

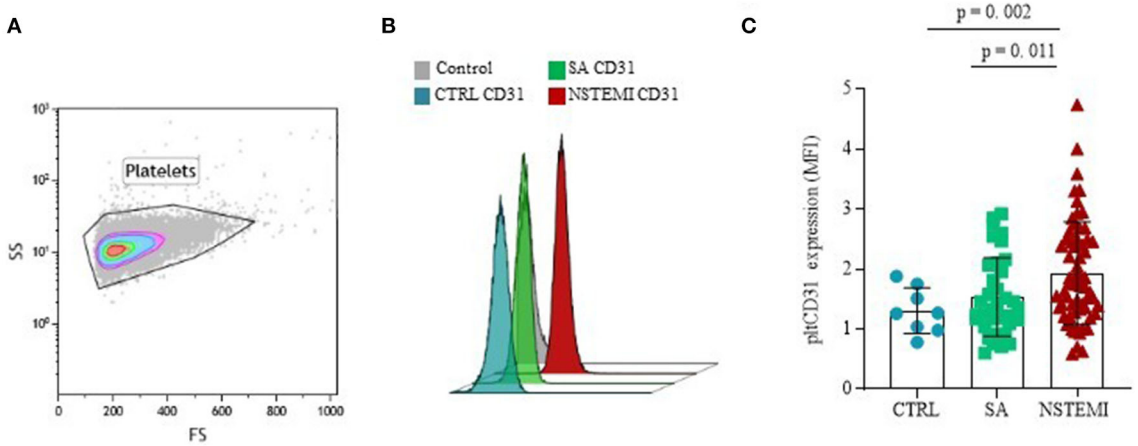

FIGURE 3 | CD31 expression on platelets. Graphs showing the surface protein expression of CD31 on $CD42b^+$ platelets assessed by flow-cytometry (mean ± SD), in basal conditions. **(A)** Representative flow cytometry forward *vs* side scatter plot of platelets; **(B)** Representative flow cytometry overlay plot; **(C)** Data analysis of pltCD31 surface protein expression between the three groups (CTRL, Control individuals; FS, Forward Scatter; MFI, Median Fluorescence Intensity; NSTEMI, Non-ST-Elevation Myocardial Infarction; pltCD31, platelet CD31; SA, Patients with Stable Angina; SD, Standard Deviation; and SS, Side Scatter).

(DAPT), age, sex, and risk factors, except for familial history of cardiovascular disease, which is significantly higher in RFC ($p = 0.03$, see **Table 2**). Data revealed a decreased, although not statistically significant, expression of CD31 on $CD14^+$ monocytes from patients with an RFC plaque ($n = 17$; Mean ± SD: 31.43 ± 10.15) compared to those with an IFC plaque ($n = 11$; Mean ± SD: 39.04 ± 10.04) ($p = 0.064$) (**Figure 4A**). In contrast, $CD42b^+$ platelets from patients with an RFC plaque ($n = 16$) displayed a significant higher expression of CD31 compared to those with an IFC plaque ($n = 10$) (Mean ± SD: 2.23 ± 0.98 and 1.52 ± 0.51, respectively; $p = 0.023$) (**Figure 4B**). No differences were recorded between patients with NSTEMI with RFC and IFC plaques in circulating platelet numbers ($p = 0.647$) (**Supplementary Figure 4**).

We further analyzed CD31 expression on monocytes and platelets from a small group of patients with STEMI, as compared to those with NSTEMI. We found no differences in CD31 expression on monocytes in the two groups ($p = 0.118$) while the CD31 expression on platelets of patients with STEMI was significantly lower as compared to those with NSTEMI ($p = 0.0006$). A gradient of CD31 expression on platelets was observed, while patients with RFC-NSTEMI showed the highest levels and patients with STEMI the lowest. These data are shown in **Supplementary Figure 5**.

Platelet CD31 Expression Levels Relate to High Thrombus Burden in Patients With NSTEMI

To understand whether platelet CD31 levels are related or not to thrombus burden severity at the site of the culprit stenosis, we differentiated the patients with NSTEMI ($n = 53$) according to a previously published angiographic classification, also referred to

TABLE 2 | Main clinical characteristics of patients with RFC and with IFC.

	RFC $n = 19$	IFC $n = 16$	P-value
Age, mean ± SD	62 ± 13	63 ± 11	0.89
Gender, M/F	13/6	10/7	0.73
CV risk factors			
Smoke, (%)	7 (41)	10 (62)	0.20
Diabetes, (%)	5 (26)	2 (12)	0.41
Hypertension, (%)	14 (74)	11 (69)	1.00
Dyslipidemia, (%)	10 (53)	6 (37)	0.50
Obesity, (%)	4 (21)	4 (25)	1.00
Family history, (%)	10 (53)	2 (12)	**0.03**
Medical therapy			
DAPT, (%)#	6 (32)	9 (56)	0.18
ASA, (%)	12 (63)	12 (75)	0.50
Clopidogrel, (%)	3 (15)	3 (19)	0.32
Prasugrel, (%)	0 (0)	0 (0)	–
Ticagrelor, (%)	5 (26)	7 (31)	0.53
Anticoagulants, (%)	2 (10)	2 (12)	0.52
Beta-Blockers, (%)	6 (32)	9 (56)	0.24
Diuretics, (%)	4 (21)	4 (25)	0.45
ACE-I, (%)	6 (32)	4 (25)	0.33
ARBs, (%)	9 (47)	6 (38)	0.31
Statins, (%)	6 (32)	7 (43)	0.47
Ca-antagonists, (%)	2 (10)	5 (31)	0.21
Nitrates, (%)	0 (0)	1 (6)	0.46
Insulin, (%)	0 (0)	1 (6)	0.46
Oral antidiabetic, (%)	3 (16)	2 (12)	0.39

#These data refer to the time of the enrollment of the patient and blood withdrawal. At the time of coronary angiography, all the patients with NSTEMI were on DAPT according to current guidelines. Bold values denote statistical significance. ACE-I, ACE-inhibitors; ARBs, angiotensin II receptor blockers; ASA, Aspirin; CV, cardiovascular; DAPT, dual antiplatelet therapy; IFC, intact fibrous cap; and RFC, ruptured fibrous cap.

as thrombus grade score. We distinguished two groups: zero/low ($n = 32$, TG from 0 to 2) and high ($n = 21$, TG from 3 to 5) thrombus grade (**Figure 5A**) (42, 43). At the time of the coronary angiography, all patients were in DAPT, with no significant differences in P2Y12 inhibitor agent used as part of DAPT between zero/low and high patients with TG (clopidogrel 41.3 vs. 40%; ticagrelor 58.7 vs. 60%; prasugrel 0 vs. 0%). Results showed that the CD31 expression levels were significantly higher in platelets of patients with high TG compared to those with zero/low TG (mean ± SD: 2.27 ± 0.97 and 1.67 ± 0.71, respectively; $p = 0.021$) (**Figure 5B**).

CD31 Involvement on Monocyte-Platelet Binding in Patients With NSTEMI With RFC Plaque

To unravel the relationship between platelets and monocytes, we performed a series of *ex vivo* experiments by culturing them in a monolayer co-culture setting. In details, we performed 16-h co-culture experiments on cells from SA ($n = 6$) and on patients with NSTEMI ($n = 20$). As shown in **Figure 6A**, monocyte-platelet (Mo-Plt) binding, expressed as % of CD14-CD42b ($CD14^+CD42b^+$) positive cells, was higher in NSTEMI compared to patients with SA (mean ± SD: 40.8 ± 19.3 and 10.2 ± 11.3, respectively; $p = 0.016$). Furthermore, to test the involvement of CD31 on Mo-Plt binding, we performed the same experiment on cells isolated from patients with NSTEMI ($n = 11$) by adding mAb anti-CD31 (CD31 ligation performed with functional grade anti-Hu-CD31, clone WM59) in the co-culture medium. We observed a decreased % of $CD14^+CD42b^+$ after the CD31 ligation compared to those who were not subjected to CD31 engagement (mean ± SD: 40 ± 24 and 26.1 ± 1, respectively; $p = 0.004$) (**Figure 6B**). According to OCT investigation, only patients with RFC ($n = 5$) plaques displayed a decreased % of $CD14^+CD42b^+$ after the CD31 ligation compared to those who were not subjected to CD31 ligation (Mean ± SD: 38.8 ± 8.1 and 25.2 ± 12, respectively; $p = 0.04$). No effect of CD31 ligation was observed in patients with IFC ($n = 4$) (**Figure 6C**).

Immunofluorescence confocal microscopy images and analyses within the NSTEMI group ($n = 5$) (**Figures 7A,B**; **Supplementary Figure 6**) showed a significantly reduced co-localization of mononuclear cells and platelets after the CD31 ligation (**Figure 7C**), confirming a flow-cytometry data ($p = 0.022$).

Additionally, to explore the involvement of platelet activation, we assessed the Mo-Plt response to adenosine diphosphate (ADP) stimulation within the NSTEMI group ($n = 5$) before and after the CD31 ligation. Data showed that CD31 ligation did not affect Mo-Plt binding of ADP treated co-cultures ($p = 0.700$) (**Supplementary Figure 7**).

Therefore, we set up a series of *ex vivo* co-culture experiments using samples from the newly enrolled patients with NSTEMI ($n = 6$), always before and after the CD31 ligation, in the presence or not of collagen and *Escherichia Coli*-lipopolysaccharide (LPS) for testing the effect of pro-thrombotic and pro-inflammatory stimuli on Mo-Plt aggregate formation. The CD31 ligation affects the Mo-Plt aggregate formation decreasing the % of $CD14^+CD42b^+$ on not treated ($p = 0.003$) and LPS- treated co-cultures ($p < 0.0001$) (**Supplementary Figure 8A**). The CD31 ligation did not affect Mo-Plt binding of collagen treated co-cultures ($p = 0.139$). We performed the same evaluation on individual cells committed in Mo-Plt binding and no differences were recorded for both CD69 and CD62P expressions, respectively, used as a marker of monocytes and platelet activation (**Supplementary Figure 8B**).

DISCUSSION

According to *post-mortem* studies, two-thirds of patients presenting with ACS show an RFC culprit plaque, rich in lipids, and inflammatory cells, as the mechanisms underpinning plaque instability, predisposing these patients to worse clinical outcomes (45). Growing evidence demonstrates that different plaque phenotypes may be the result of diverse pathogenetic mechanisms, which deserve specific therapeutic approaches (12–17). In this perspective, unusual molecular pathways at the site of

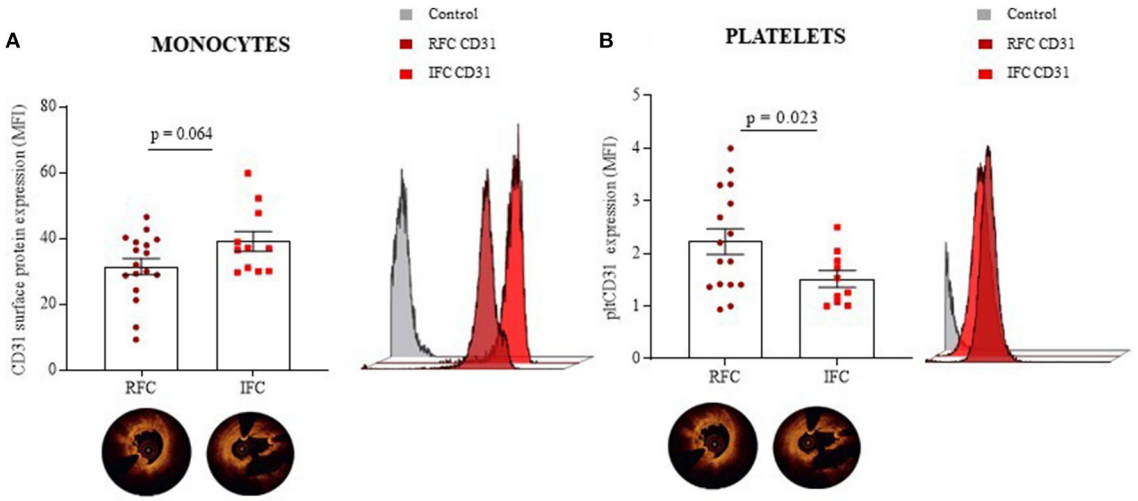

FIGURE 4 | CD31 expression on monocytes and platelets according to OCT investigation. Dot plots (mean ± SD) and related representative overlay histograms showing the surface protein expression of CD31 within the NSTEMI group that underwent an OCT investigation on $CD14^+$ monocytes **(A)**, and $CD42b^+$ platelets assessed by flow cytometry **(B)**, in basal conditions. (NSTEMI, Non-ST-Elevation Myocardial Infarction; $_{mo}$CD31, monocyte CD31; $_{plt}$CD31, platelet; RFC, Ruptured Fibrous Cap; IFC, Intact Fibrous Cap; and MFI, Median Fluorescence Intensity.

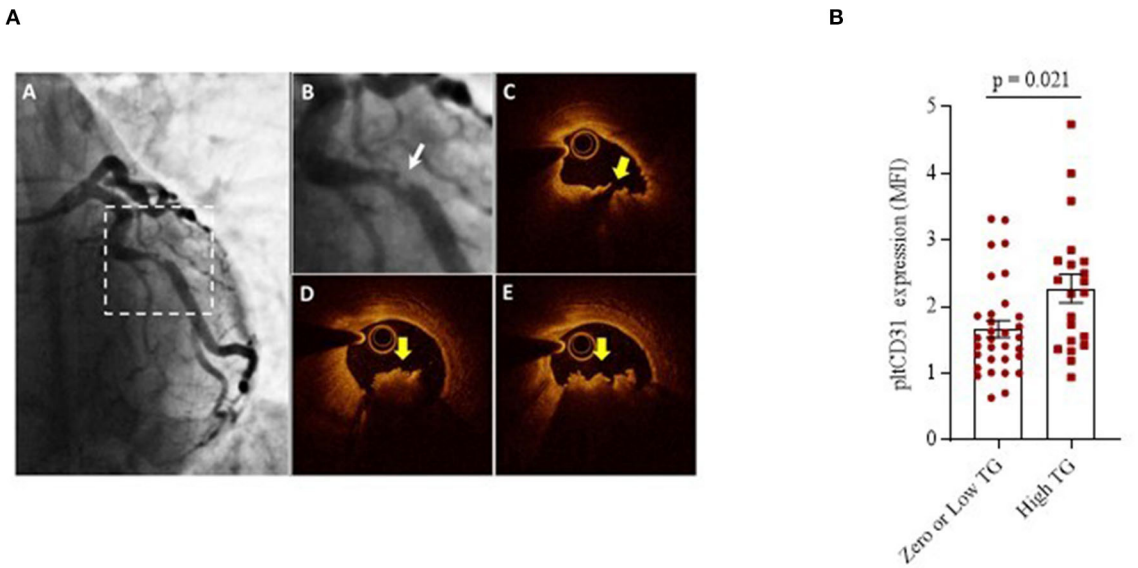

FIGURE 5 | Platelet CD31 expression and Thrombus-Grade evaluation. **(A)** Representative angiographic and OCT images of a plaque. **(A)** Coronary angiogram of the left coronary artery showing a culprit lesion on the left circumflex (dotted squared selection); **(B)** Magnification of the angiogram showing a complex culprit lesion with a thrombus grade 3 and a scalloped profile (Ambrose type II eccentric); **(C)** Corresponding OCT cross-sectional image showing a lipid-rich plaque with a disrupted fibrous cap (yellow arrow); **(D,E)** Adjacent OCT cross-sections showing a large thrombus (yellow arrows). **(B)** pltCD31 surface protein expression within NSTEMI group showing the differences between patients with zero/low and high thrombus grade at the site of culprit stenosis. Data were assessed by flow-cytometry (mean ± SD), in basal conditions (MFI, Median Fluorescence Intensity; $_{plt}$CD31, platelet CD31; SD, Standard Deviation; and TG, Thrombus Grade).

the culprit plaque might beget a distinctive thrombotic burden and the antiplatelet therapy in our armamentarium might be insufficient to prevent an athero-thrombotic risk.

Our study demonstrates that circulating $CD14^+$ monocytes isolated from patients with NSTEMI express lower levels of CD31 compared to patients with SA and CTRL subjects, and more interestingly, that this result is limited to patients with RFC plaques. These findings confirm the immunomodulatory role of CD31 seen in previous studies (33). Indeed, under inflammatory conditions, subsequently to the proteolytic cleavage of the N-terminal domain, leukocytes fail to express the CD31 acquiring a hyper-reactive pro-inflammatory phenotype (46).

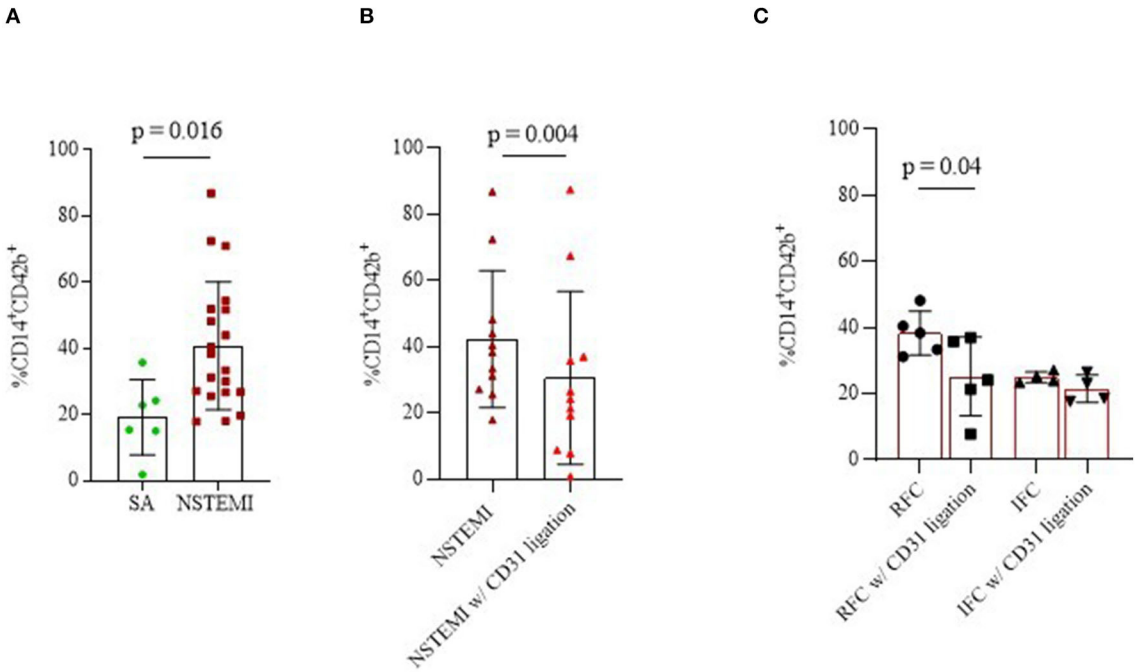

FIGURE 6 | Monocyte-platelet binding. Graphs showing monocyte-platelet (Mo-Plt) binding assessed by flow-cytometry in patients with NSTEMI as compared with patients with SA **(A)**; in patients with NSTEMI before and during the CD31 ligation **(B)**, also according to an OCT investigation **(C)**. Data are presented as % of CD14/CD42b-positive cells (mean ± SD). (NSTEMI, Non-ST-Elevation Myocardial Infarction; SA, Stable Angina; SD, Standard Deviation; and w/, with).

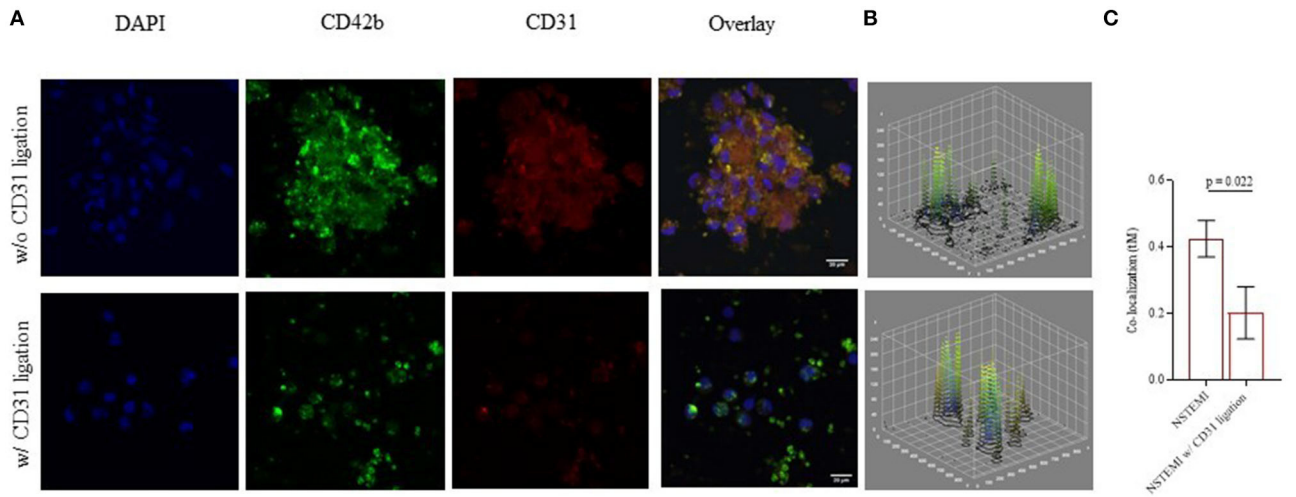

FIGURE 7 | Monocyte-platelet binding at confocal microscopy. Immunofluorescence confocal microscopy images (512 × 512 pixels of resolution, scale bar 20 μm) showing monocyte-platelet (Mo-Plt) binding before and after the CD31 ligation. **(A)** A representative patient with NSTEMI; **(B)** 3D plots showing display the changing in Mo-Plt binding after the CD31 ligation; **(C)** Mo-Plt co-localization within NSTEMI group ($n = 5$). The degree of co-localization was quantified by using a Mander's overlap coefficient (MOC) (μm = micrometer; NSTEMI, Non-ST-Elevation Myocardial Infarction; w/, with, w/o, without).

It has been widely demonstrated that the CD31-targeting antibodies block the lymphocyte transmigration restoring the immunomodulatory effects (26, 34–36). Intriguingly, in the presence of pathological wall shear stress, which is one of the eligible triggers underneath plaque rupture (47, 48), CD31 acts as a mechanosensor on endothelial cells (49–52) and might mediate a platelet adhesion on the endothelial layer and thrombosis (53).

On one hand, if the immunomodulatory role of CD31 has been established in ACS, its effects on platelet function have been poorly investigated. Platelets incubated with anti-CD31 before

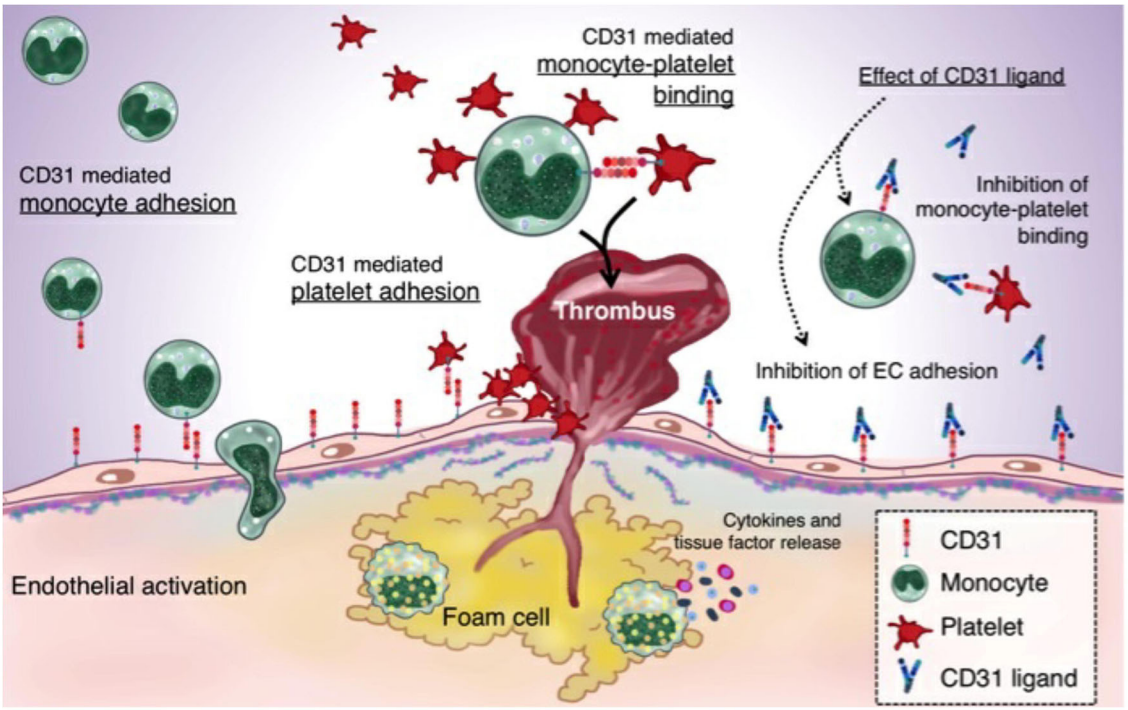

FIGURE 8 | CD31 and the thromboinflammatory response of the unstable plaque: A plaque rupture paradigm. The figure summarizes the driving hypothesis that derives from both the existing evidence on plaque rupture and the data that emerged from the present study. In ACS, CD31 is involved in leukocytes and platelets adhesion on ECs. The increased monocyte-platelet (Mo-Plt) binding in the RFC *milieu* might account for an increased athero-thrombotic burden driven by the inflammation and involving, at least in part, CD31 molecule, as demonstrated by the significant reduction of Mo-Plt aggregate formation following the CD31 ligation (ACS, acute coronary syndromes; and endothelial cells, ECs).

treatment with convulxin, a GPVI agonist, or with thrombin, have significantly decreased the intracellular Ca^{2+} mobilization levels suggesting an effect of CD31 on thrombus size and formation through platelet inactivation (32). For the first time, in our study, we noted that patients with NSTEMI under an optimal antiplatelet therapy, in particular those with RFC plaques at OCT investigation, displayed increased levels of CD31 on circulating platelets, possibly affecting the clinical outcome, as shown by the relation between the platelet CD31 expression and the angiographic thrombotic burden.

Our hypothesis has been further confirmed in mechanistic experiments showing a high Mo-Plt binding in patients with NSTEMI and with RFC, and its significant reduction after CD31-ligation. Moreover, these results seem to be independent of the exogenous over-stimulation of Mo-Plt co-cultures with common platelet activators, such as ADP and collagen. Intriguingly, CD31-ligation affects the Mo-Plt aggregate formation in LPS-treated co-cultures. These findings revealed a different mechanism of platelet activation and thrombus formation that is strongly related to the activation of inflammatory pathways, as well as to the abrupt impairment of the immunomodulatory effect of CD31 in ACS (33).

In the setting of RFC plaque, the discrepancy of CD31 expression levels between monocytes and platelets may rely on the down-regulatory activity that the CD31 exerts when it is expressed on leukocytes (33). On the other hand, on the activating role that CD31 seems to carry out on platelets (32, 36), hinting a double nature of this molecule (31). Indeed, our novel information about the *Janus*-faced CD31 expression on monocytes and platelets may suggest a differential commitment of this molecule for the different actors involved in the pathogenesis of ACS.

Our results obtained from a group of patients with STEMI confirm the multi-faced behavior and complex biology of the CD31 molecule. Although our patients in both STEMI and NSTEMI were different for the clinical settings and use of prasugrel at the time of blood withdrawal, our data are in line with the existing evidence documenting the differences in culprit plaques, the thrombus type, and the composition between patients with NSTEMI and with STEMI (54, 55).

In the era of tailored medicine, we are facing the need for further personalized therapeutic strategies (56). To this purpose, CD31 might represent a promising target (57) in the treatment of thrombotic burden (**Figure 8**).

Limitations of the Study

First, population enrollment and their experimental allocation were arbitrary and mainly driven by the amount of biological material available. The OCT interrogation was performed based on clinical needs and, therefore, not all patients were included in the OCT analysis. Our study was a prospective observational analysis that included a limited number of patients. We did

not include follow-up analyzes to investigate the role of the CD31 molecule during the long-term outcome. Our results obtained from a group of patients with STEMI are strongly limited by the differences in clinical management at the time of blood withdrawal and, therefore, cannot be fully compared with those obtained in patients with NSTEMI. No power calculation could be performed regarding CD31 expression on monocytes and platelets according to plaque morphology at OCT investigation because of lack of previous studies in this setting; these limitations imply that several variables other than the coronary plaque morphology might explain the observed differences across these two populations of patients with RFC and with IFC. However, no differences were found regarding clinical characteristics, therapeutic strategies including DAPT, and angiographic and OCT findings other than the type of coronary plaque morphology (i.e., RFC and IFC). Thus, CD31 might be a player in Mo-Plt aggregate formation despite the optimal therapy and DAPT, suggesting the existence of alternative thrombotic pathways, predominantly displayed in patients with NSTEMI-RFC.

Second, the use of flow cytometry as the main investigative tool should be recognized as a potential limitation of our work. Due to the limited number of cells processed, we could not proceed with parallel *ex vivo* ligation experiments using more than one anti-CD31 clone or anti-IgG1 as a reference control test. Although CD31 expression on peripheral cells has been related to local clinical features such as high thrombus grade, its involvement in the onset and progression of plaque instability relies only on its systemic assessment. In addition, the influence of DAPT therapy on thrombus grade cannot be ruled out. The presence of different pathways underpinning intracoronary thrombosis can still be argued by the observation that despite the lower CD31 platelet expression and more intensive antiplatelet regimes, patients with STEMI still display a higher TG compared with both RFC- and IFC-NSTEMI groups.

Finally, since CD31 possesses multiple glycosylation sites and multiple splicing variant sites, we should consider the resulting isoforms to reveal its cell-dependent behavior. Moreover, it is obviously essential to unravel whether the CD31-ligation in the context of Mo-Plt aggregates induces an activation or an inhibition of an intracellular-signaling dependent on pltCD31.

Therefore, further experiments are needed to the candidate the CD31 as a new therapeutic target.

CONCLUSIONS

Our findings indicate the existence of a pro-thrombotic target that may not be related to the pathways that are usually inhibited by current antiplatelet drugs and which may have relevant clinical implications in the future management of patients with ACS with plaque rupture.

DATA AVAILABILITY STATEMENT

The original contributions presented in the study are included in the article/**Supplementary Material**, further inquiries can be directed to the corresponding author.

ETHICS STATEMENT

The studies involving human participants were reviewed and approved by Ethics Committee of the Fondazione Policlinico Universitario Agostino Gemelli IRCCS—Università Cattolica del Sacro Cuore. The patients/participants provided their written informed consent to participate in this study.

AUTHOR CONTRIBUTIONS

RV, DP, and GL: contributed to conceptualization. RV, Ad'A, AB, EP, MP, AS, PC, FCa, GR, MD, SF, DF, LS, RP, CC, and FCri: contributed to methodology. RV, DP, GL, Ad'A, GR, RV, and RM: contributed to the investigation. GL: contributed to funding acquisition and contributed to project administration. GL, FCre, and MM: contributed to supervision. RV, DP, and GL: contributed to writing the original draft. RV, DP, GL, and FCre: contributed to writing review and editing. All authors contributed to the article and approved the submitted version.

FUNDING

The present study was supported by the Italian National Project Grant PRIN 2017, Protocol 2017WJBKKW_001.

ACKNOWLEDGMENTS

We thank Dr. Alice Zampetti and Dr. Tommaso Rondelli (Beckman Coulter) for their kind assistance during the revision process.

SUPPLEMENTARY MATERIAL

The Supplementary Material for this article can be found online at: https://www.frontiersin.org/articles/10.3389/fcvm.2021.741221/full#supplementary-material

REFERENCES

1. Roth GA, Mensah GA, Johnson CO, Addolorato G, Ammirati E, Baddour LM, et al. Global burden of cardiovascular diseases and risk factors, 1990–2019: update from the GBD 2019 study. *J Am Coll Cardiol.* (2020) 76:2982–21. doi: 10.1016/j.jacc.2020.11.010
2. Costa F, Van Klaveren D, Feres F, James S, Räber L, Pilgrim T. Dual antiplatelet therapy duration based on ischemic and bleeding risks after coronary stenting. *J Am Coll Cardiol.* (2019) 73:741–54. doi: 10.1016/j.jacc.2018.11.048
3. Collet JP, Thiele H, Barbato E, Barthélémy O, Bauersachs J, Bhatt DL, et al. ESC scientific document group. 2020 ESC Guidelines for the management of acute

coronary syndromes in patients presenting without persistent ST-segment elevation. *Eur Heart J*. (2021) 42:1289–367. doi: 10.1093/eurheartj/ehab088
4. Valgimigli M, Bueno H, Byrne RA, Collet JP, Costa F, Jeppsson A, et al. ESC Scientific Document Group; ESC Committee for Practice Guidelines (CPG); ESC National Cardiac Societies. 2017 ESC focused update on dual antiplatelet therapy in coronary artery disease developed in collaboration with EACTS: The Task Force for dual antiplatelet therapy in coronary artery disease of the European Society of Cardiology (ESC) and of the European Association for Cardio-Thoracic Surgery (EACTS). *Eur Heart J*. (2018) 39:213–60. doi: 10.1093/eurheartj/ehx638
5. Benenati S, Galli M, Marzo V, Pescetelli F, Toma M, Andreotti F. et al. Very short vs. long dual antiplatelet therapy after second generation drug-eluting stents in 35 785 patients undergoing percutaneous coronary interventions: a meta-analysis of randomized controlled trials. *Eur Heart J Cardiovasc Pharmacother*. (2021) 7:86–93. doi: 10.1093/ehjcvp/pvaa001
6. Mitra AK, Agrawal DK. In stent restenosis: bane of the stent era. *J Clin Pathol*. (2006) 59:232–9. doi: 10.1136/jcp.2005.025742
7. Gawaz M. Role of platelets in coronary thrombosis and reperfusion of ischemic myocardium. *Cardiovasc Res*. (2004) 61:498–511. doi: 10.1016/j.cardiores.2003.11.036
8. Sakhuja R, Suh WM, Jaffer FA, Jang IK. Residual thrombogenic substrate after rupture of a lipid-rich plaque: possible mechanism of acute stent thrombosis? *Circulation*. (2010) 122:2349–50. doi: 10.1161/CIRCULATIONAHA.110.970079
9. Michelson AD, Barnard MR, Krueger LA, Valeri CR, Furman MI. Circulating monocyte-platelet aggregates are a more sensitive marker of in vivo platelet activation than platelet surface P-selectin: studies in baboons, human coronary intervention, and human acute myocardial infarction. *Circulation*. (2001) 104:1533–7. doi: 10.1161/hc3801.095588
10. Liu C, Yang Y, Du L, Chen S, Zhang J, Zhang C, et al. Platelet-leukocyte aggregate is associated with adverse events after surgical intervention for rheumatic heart disease. *Sci Rep*. (2019) 9:13069. doi: 10.1038/s41598-019-49253-3
11. Mezger M, Nording H, Sauter R, Graf T, Heim C, von Bubnoff N, et al. Platelets and immune responses during thromboinflammation. *Front Immunol*. (2019) 10:1731. doi: 10.3389/fimmu.2019.01731
12. Pedicino D, Vinci R, Giglio AF, Pisano E, Porto I, Vergallo R, et al. Alterations of hyaluronan metabolism in acute coronary syndrome: implications for plaque erosion. *J Am Coll Cardiol*. (2018) 72:1490–503. doi: 10.1016/j.jacc.2018.06.072
13. Ruggio A, Pedicino D, Flego D, Vergallo R, Severino A, Lucci C, et al. Correlation between CD4+CD28null T lymphocytes, regulatory T cells and plaque rupture: an optical coherence tomography study in acute coronary syndromes. *Int J Cardiol*. (2019) 276:289–92. doi: 10.1016/j.ijcard.2018.08.101
14. Leistner DM, Kränkel N, Meteva D, Abdelwahed YS, Seppelt C, Stähli BE, et al. Differential immunological signature at the culprit site distinguishes acute coronary syndrome with intact from acute coronary syndrome with ruptured fibrous cap: results from the prospective translational OPTICO-ACS study. *Eur Heart J*. (2020) 41:3549–60. doi: 10.1093/eurheartj/ehaa703
15. Liuzzo G, Pedicino D, Vinci R, Crea F. CD8 lymphocytes and plaque erosion: a new piece in the jigsaw. *Eur Heart J*. (2020) 41:3561–3. doi: 10.1093/eurheartj/ehaa721
16. Vinci R, Pedicino D, D'Aiello A, Ciampi P, Ponzo M, Bonanni A, et al. Platelet hyaluronidase 2 enrichment in acute coronary syndromes: a conceivable role in monocyte-platelet aggregate formation. *J Enzyme Inhib Med Chem*. (2021) 36:785–9. doi: 10.1080/14756366.2021.1900159
17. Vinci R, Pedicino D, Bonanni A, D'Aiello A, Severino A, Pisano E, et al. A novel monocyte subset as a unique signature of atherosclerotic plaque rupture. *Front Cell Dev Biol*. (2021) 9:753223. doi: 10.3389/fcell.2021.753223
18. Saia F, Komukai K, Capodanno D, Sirbu V, Musumeci G, Boccuzzi G, et al. Eroded versus ruptured plaques at the culprit site of stemi: *in vivo* pathophysiological features and response to primary PCI. *JACC Cardiovasc Imaging*. (2015) 8:566–75. doi: 10.1016/j.jcmg.2015.01.018
19. Newman PJ, Berndt MC, Gorski J, White GC. 2nd, Lyman S, Paddock C, et al. PECAM-1 (CD31) cloning and relation to adhesion molecules of the immunoglobulin gene superfamily. *Science*. (1990) 247:1219–22. doi: 10.1126/science.1690453
20. Newman PJ. The biology of PECAM-1. *J Clin Invest*. (1997) 99:3–8. doi: 10.1172/JCI119129
21. Metzelaar MJ, Korteweg J, Sixma JJ, Nieuwenhuis HK. Biochemical characterization of PECAM-1 (CD31 antigen) on human platelets. *Thromb Haemost*. (1991) 66:700–7. doi: 10.1055/s-0038-1646488
22. Kitazume S, Imamaki R, Ogawa K, Komi Y, Futakawa S, Kojima S. et al. Alpha2,6-sialic acid on platelet endothelial cell adhesion molecule (PECAM) regulates its homophilic interactions and downstream antiapoptotic signaling. *J Biol Chem*. (2010) 285:6515–2. doi: 10.1074/jbc.M109.073106
23. Zhao T. Newman PJ. Integrin activation by regulated dimerization and oligomerization of platelet endothelial cell adhesion molecule (PECAM)-1 from within the cell. *J Cell Biol*. (2001) 152:65–73. doi: 10.1083/jcb.152.1.65
24. Nakada MT, Amin K, Christofidou-Solomidou MD, O'Brien CD, Sun J, Gurubhagavatula I, et al. Antibodies against the first Ig-like domain of human platelet endothelial cell adhesion molecule-1 (PECAM-1) that inhibit PECAM-1-dependent homophilic adhesion block in vivo neutrophil recruitment. *J Immunol*. (2000) 164:452–62. doi: 10.4049/jimmunol.164.1.452
25. Cheung K, Ma L, Wang G, Coe D, Ferro R, Falasca M, et al. CD31 signals confer immune privilege to the vascular endothelium. *Proc Natl Acad Sci USA*. (2015) 112:E5815–24. doi: 10.1073/pnas.1509627112
26. Rival Y, Del Maschio A, Rabiet MJ, Dejana E, Duperray A. Inhibition of platelet endothelial cell adhesion molecule-1 synthesis and leukocyte transmigration in endothelial cells by the combined action of TNF-alpha and IFN-gamma. *J Immunol*. (1996) 157:1233–41.
27. Muller WA, Weigl SA, Deng X, Phillips DM. PECAM-1 is required for transendothelial migration of leukocytes. *J Exp Med*. (1993) 178:449–60. doi: 10.1084/jem.178.2.449
28. Prager E, Sunder-Plassmann R, Hansmann C, Koch C, Holter W, Knapp W, et al. Interaction of CD31 with a heterophilic counterreceptor involved in downregulation of human T cell responses. *J Exp Med*. (1996) 184:41–50. doi: 10.1084/jem.184.1.41
29. Ma L, Mauro C, Cornish GH, Chai JG, Coe D, Fu H, et al. Ig gene-like molecule CD31 plays a nonredundant role in the regulation of T-cell immunity and tolerance. *Proc Natl Acad Sci USA*. (2010) 107:19461–6. doi: 10.1073/pnas.1011748107
30. Wilkinson R, Lyons AB, Roberts D, Wong MX, Bartley PA, Jackson DE. Platelet endothelial cell adhesion molecule-1 (PECAM-1/CD31) acts as a regulator of B-cell development, B-cell antigen receptor (BCR)-mediated activation, and autoimmune disease. *Blood*. (2002) 100:184–93. doi: 10.1182/blood-2002-01-0027
31. Woodfin A, Voisin MB, Nourshargh S. PECAM-1: a multi-functional molecule in inflammation and vascular biology. *Arterioscler Thromb Vasc Biol*. (2007) 27:2514–23. doi: 10.1161/ATVBAHA.107.151456
32. Cicmil M, Thomas JM, Leduc M, Bon C, Gibbins JM. Platelet endothelial cell adhesion molecule-1 signaling inhibits the activation of human platelets. *Blood*. (2002) 99:137–44. doi: 10.1182/blood.V99.1.137
33. Flego D, Severino A, Trotta F, Previtero M, Ucci S, Zara C, et al. Altered CD31 expression and activity in helper T cells of acute coronary syndrome patients. *Basic Res Cardiol*. (2014) 109:448. doi: 10.1007/s00395-014-0448-3
34. Rosenblum WI, Murata S, Nelson GH, Werner PK, Ranken R, Harmon RC. Anti-CD31 delays platelet adhesion/aggregation at sites of endothelial injury in mouse cerebral arterioles. *Am J Pathol*. (1994) 145:33–6.
35. Rosenblum WI, Nelson GH, Wormley B, Werner P, Wang J, Shih CC. Role of platelet-endothelial cell adhesion molecule (PECAM) in platelet adhesion/aggregation over injured but not denuded endothelium in vivo and ex vivo. *Stroke*. (1996) 27:709–11. doi: 10.1161/01.STR.27.4.709
36. Wu XW, Lian EC. Binding properties and inhibition of platelet aggregation by a monoclonal antibody to CD31 (PECAM-1). *Arterioscler Thromb Vasc Biol*. (1997) 17:3154–8. doi: 10.1161/01.ATV.17.11.3154
37. Amsterdam EA, Wenger NK, Brindis RG, Casey DE, Ganiats TG, Holmes DR, et al. 2014 AHA/ACC Guideline for the management of patients with non-ST-elevation acute coronary syndromes: a report of the American College of Cardiology/American Heart Association Task Force on Practice Guidelines. *J Am Coll Cardiol*. (2014) 64:e139–228. doi: 10.1016/j.jacc.2014.09.017
38. Knuuti J, Wijns W, Saraste A, Capodanno D, Barbato E, Funck-Brentano C, et al. 2019 ESC Guidelines for the diagnosis and management of chronic coronary syndromes. *Eur Heart J*. (2020) 41:407–77. doi: 10.1093/eurheartj/ehz425

39. Prati F, Regar E. Mintz, GS, Arbustini E, Di Mario C, Jang IK, et al. Expert review document on methodology, terminology, and clinical applications of optical coherence tomography: physical principles, methodology of image acquisition, and clinical application for assessment of coronary arteries and atherosclerosis. *Eur Heart J.* (2010) 31:401–15. doi: 10.1093/eurheartj/ehp433
40. Tearney GJ, Regar E, Akasaka T, Adriaenssens T, Barlis P, Bezerra HG, et al. Consensus standards for acquisition, measurement, and reporting of intravascular optical coherence tomography studies: a report from the International working group for intravascular optical coherence tomography standardization and validation. *J Am Coll Cardiol.* (2012) 59:1662. Dudeck, Darius [corrected to Dudek, Darius]; Falk, Erlin [corrected to Falk, Erling]; Garcia, Hector [corrected to Garcia-Garcia, Hector M]; Sonada, Shinjo [corrected to Sonoda, Shinjo]; Troels, Thim [corrected to Th4im, Troels]; van Es, Gerrit-Ann [correct]. J. Am. Coll. Cardiol. 59, 1058–72. doi: 10.1016/j.jacc.2011.09.079
41. Johnson TW, Räber L, Di Mario C, Bourantas CV, Jia H, Mattesini A, et al. Clinical use of intracoronary imaging. Part 2: acute coronary syndromes, ambiguous coronary angiography findings, and guiding interventional decision-making: an expert consensus document of the European association of percutaneous cardiovascular interventions. *EuroIntervention.* (2019) 15:434–45. doi: 10.4244/EIJY19M06_02
42. Vergallo R, Porto I, De Maria GL, Trani C, Banning AP, Crea F. Dual quantitative coronary angiography accurately quantifies intracoronary thrombotic burden in patients with acute coronary syndrome: comparison with optical coherence tomography imaging. *Int J Cardiol.* (2019) 292:25–31. doi: 10.1016/j.ijcard.2019.04.060
43. Sianos G, Papafaklis MI, Serruys PW. Angiographic thrombus burden classification in patients with ST-segment elevation myocardial infarction treated with percutaneous coronary intervention. *J Invasive Cardiol.* (2010) 22:6B−14B. Available online at: http://hmpsup.epubxpress.com
44. Lee JA, Spidlen J, Boyce K, Cai J, Crosbie N, Dalphin M, et al. MIFlowCyt: the minimum information about a flow cytometry experiment. *Cytometry A.* (2008) 73:926–30. doi: 10.1002/cyto.a.20623
45. Niccoli G, Montone RA, Di Vito L, Gramegna M, Refaat H, Scalone G, et al. Plaque rupture and intact fibrous cap assessed by optical coherence tomography portend different outcomes in patients with acute coronary syndrome. *Eur Heart J.* (2015) 36:1377–84. doi: 10.1093/eurheartj/ehv029
46. Angelini G, Flego D, Vinci R, Pedicino D, Trotta F, Ruggio A, et al. Matrix metalloproteinase-9 might affect adaptive immunity in non-ST segment elevation acute coronary syndromes by increasing CD31 cleavage on CD4+ T-cells. *Eur Heart J.* (2018) 39:1089–97. doi: 10.1093/eurheartj/ehx684
47. Fukumoto Y, Hiro T, Fujii T, Hashimoto G, Fujimura T, Yamada J, et al. Localized elevation of shear stress is related to coronary plaque rupture: a 3-dimensional intravascular ultrasound study with *in-vivo* color mapping of shear stress distribution. *J Am Coll Cardiol.* (2008) 51:645–50. doi: 10.1016/j.jacc.2007.10.030
48. Groen HC, Gijsen FJ, van der Lugt A, Ferguson MS, Hatsukami TS, van der Steen AF, et al. Plaque rupture in the carotid artery is localized at the high shear stress region: a case report. *Stroke.* (2007) 38:2379–81. doi: 10.1161/STROKEAHA.107.484766
49. Osawa M, Masuda M, Kusano K, Fujiwara K. Evidence for a role of platelet endothelial cell adhesion molecule-1 in endothelial cell mechanosignal transduction: is it a mechanoresponsive molecule? *J Cell Biol.* (2002)158:773–85. doi: 10.1083/jcb.200205049
50. Caligiuri G. Mechanotransduction, immunoregulation, and metabolic functions of CD31 in cardiovascular pathophysiology. *Cardiovasc Res.* (2019) 115:1425–34. doi: 10.1093/cvr/cvz132
51. Harrison M, Smith E, Ross E, Krams R, Segers D, Buckley CD, et al. The role of platelet-endothelial cell adhesion molecule-1 in atheroma formation varies depending on the site-specific hemodynamic environment. *Arterioscler Thromb Vasc Biol.* (2013) 33:694–701. doi: 10.1161/ATVBAHA.112.300379
52. Bartosch AMW, Mathews R, Mahmoud MM, Cancel LM, Haq ZS, Tarbell JM. Heparan sulfate proteoglycan glypican-1 and PECAM-1 cooperate in shear-induced endothelial nitric oxide production. *Sci Rep.* (2021) 11:11386. doi: 10.1038/s41598-021-90941-w
53. Meza D, Shanmugavelayudam SK, Mendoza A, Sanchez C, Rubenstein DA, Yin W. Platelets modulate endothelial cell response to dynamic shear stress through PECAM-1. *Thromb Res.* (2017) 150:44–50. doi: 10.1016/j.thromres.2016.12.003
54. Pasterkamp G, den Ruijter HM, Libby P. Temporal shifts in clinical presentation and underlying mechanisms of atherosclerotic disease. *Nat Rev Cardiol.* (2017) 14:21–9. doi: 10.1038/nrcardio.2016.166
55. Libby P, Pasterkamp G, Crea F, Jang IK. Reassessing the Mechanisms of Acute Coronary Syndromes. *Circ Res.* (2019) 124:150–60. doi: 10.1161/CIRCRESAHA.118.311098
56. Bona RD, Liuzzo G, Pedicino D, Crea F. Anti-inflammatory treatment of acute coronary syndromes. *Curr Pharm Des.* (2011) 17:4172–89. doi: 10.2174/138161211798764771
57. Caligiuri G. CD31 as a therapeutic target in atherosclerosis. *Circ Res.* (2020) 126:1178–89. doi: 10.1161/CIRCRESAHA.120.315935

Conflict of Interest: The authors declare that the research was conducted in the absence of any commercial or financial relationships that could be construed as a potential conflict of interest.

frontiers in Cardiovascular Medicine

ORIGINAL RESEARCH
published: 16 February 2022
doi: 10.3389/fcvm.2022.746888

Differential Expression Profile of microRNAs and Tight Junction in the Lung Tissues of Rat With Mitomycin-C-Induced Pulmonary Veno-Occlusive Disease

Qing Song[1,2,3], *Ping Chen*[1,2,3], *Shang-Jie Wu*[1,2,3], *Yan Chen*[1,2,3] *and Yan Zhang*[1,2,3]*

[1] Department of Respiratory and Critical Care Medicine, The Second Xiangya Hospital, Central South University, Changsha, China, [2] Research Unit of Respiratory Disease, Central South University, Changsha, China, [3] Diagnosis and Treatment Center of Respiratory Disease, Central South University, Changsha, China

OPEN ACCESS

Edited by:
Masanori Aikawa,
Brigham and Women's Hospital and Harvard Medical School, United States

Reviewed by:
Aiko Ogawa,
National Hospital Organization Okayama Medical Center, Japan
Charles Colin Thomas Hindmarch,
Queen's University, Canada

***Correspondence:**
Yan Zhang
zhangyanhx2@csu.edu.cn

Specialty section:
This article was submitted to Atherosclerosis and Vascular Medicine, a section of the journal Frontiers in Cardiovascular Medicine

Received: *25 July 2021*
Accepted: *05 January 2022*
Published: *16 February 2022*

Citation:
Song Q, Chen P, Wu S-J, Chen Y and Zhang Y (2022) Differential Expression Profile of microRNAs and Tight Junction in the Lung Tissues of Rat With Mitomycin-C-Induced Pulmonary Veno-Occlusive Disease. Front. Cardiovasc. Med. 9:746888. doi: 10.3389/fcvm.2022.746888

Background: Pulmonary veno-occlusive disease (PVOD) is characterized by increased pulmonary vascular resistance. Currently, there is a lack of effective treatment. It is of great significance to explore molecular targets for treatment. This study investigated the differential expression profile of miRNAs and tight junction in the lung tissues of rats with mitomycin-C (MMC)-induced PVOD.

Methods: A total of 14 rats were divided into the control group and he PVOD group. We measured mean pulmonary arterial pressure (mPAP) and right ventricular hypertrophy index (RVHI). Pathological changes including those in lung tissues, pulmonary venules, and capillary were detected by H&E and orcein staining. Western blot was used to detect GCN2, ZO-1, occludin, and claudin-5 expression. We analyzed the miRNAs profile in the rat lung tissues by high-throughput sequencing. The top differentially expressed miRNAs were validated by using real-time polymerase chain reaction (RT-PCR).

Results: There were severe pulmonary artery hypertrophy/hyperplasia, thickening, and occlusion in the small pulmonary veins, pulmonary edema, and dilated capillaries in MMC-induced rats with PVOD. In addition, mPAP and RVHI were significantly increased ($P < 0.05$). The expression of GCN2 was significantly decreased ($P < 0.05$). A total of 106 differentially expressed miRNAs were identified. According to the fold changes, the top ten upregulated miRNAs were miRNA-543-3p, miRNA-802-5p, miRNA-493-3p, miRNA-539-3p, miRNA-495, miRNA-380-5p, miRNA-214-5p, miRNA-539-5p, miRNA-190a-3p, and miRNA-431. The top 10 downregulated miRNAs were miRNA-201-3p, miRNA-141-3p, miRNA-1912-3p, miRNA-500-5p, miRNA-3585-5p, miRNA-448-3p, miRNA-509-5p, miRNA-3585-3p, miRNA-449c-5p, and miRNA-509-3p. RT-PCR confirmed that miRNA-214-5p was upregulated, while miRNA-141-3p was downregulated ($P < 0.05$). Functional analysis showed various signaling pathways and metabolic processes, such as fatty acid biosynthesis, tight junction, and the mTOR signaling pathway. In addition,

the expression of the tight junction-related protein of ZO-1, occludin, and claudin-5 was significantly decreased in rats with PVOD ($P < 0.05$).

Conclusion: miRNAs may be involved in the pathogenesis of PVOD. Furthermore, ZO-1, occludin, and claudin-5 verification confirmed that the tight junction may be involved in the development of the disease.

Keywords: pulmonary veno-occlusive disease, mitomycin-C, high-throughput sequencing, miRNA, tight junction (TJ)

INTRODUCTION

Pulmonary veno-occlusive disease (PVOD) is sometimes misdiagnosed with idiopathic pulmonary arterial hypertension (PAH) in the clinic and at least 3–12% of patients with PAH should be diagnosed as PVOD. In addition, PVOD is a highly fatal disease with a mortality rate of 72% within 1 year of diagnosis. Currently, there is a lack of effective treatment except for lung transplantation (1, 2). PVOD is related to a variety of risk factors, such as genetics, smoking, infection, and drugs [mitomycin-C (MMC)], but its pathogenesis is less studied (3). Therefore, in view of its high-fatality rate and lack of effective therapeutic drugs, it is very important to determine the pathogenesis and therapeutic targets.

Perros et al. (4) analyzed the clinical characteristics in seven patients of MMC-induced PVOD and found that all patients had severe hypoxemia and a low-diffusing capacity of the lung for carbon monoxide. Furthermore, right-sided heart catheterization confirmed that the mean pulmonary artery pressure (mPAP) was significantly increased, while a decreased of cardiac index. In addition, high-resolution CT of the chest identified septal lines, centrilobular ground-glass opacities, and lymph enlargement in all patients. What is more, a rat model of MMC-induced PVOD was successfully established by Perros et al. and found that the mPAP, total pulmonary resistance, and the fulton index were increased, and also the severe pulmonary vascular remodeling including smooth muscle cell hypertrophy/hyperplasia in pulmonary arteries, vasculitis of the pulmonary arteries and veins, foci of pulmonary edema and capillaritis, and foci of alveolar wall thickening. In addition, the expression of general control non-derepressible 2 kinase (GCN2) protein was decreased, whose gene is the major one linked to PVOD development and associated with heritability of PVOD.

microRNA (miRNA, miR) is a type of non-coding RNA with regulatory functions and a length of about 22–25 nucleotides. miRNA can regulate genes expression by incomplete or complete direct binding to the mRNA 3'-untranslated region to participate in genes regulation. It plays an important role in regulating genes expression, growth, proliferation and differentiation of cells, and participating in disease development (5, 6). miRNAs have been confirmed as being related to PAH. A study showed that miRNA-124 is down-regulated in a hypoxic PAH mouse model. However, miRNA-21 is upregulated in pulmonary artery smooth muscle cells, which leads to abnormal proliferation and pulmonary vascular remodeling (7–9). However, it is unclear whether miRNA is involved in the development of PVOD.

The tight junction is an important structure through which interactions between multiple-related proteins, maintains endothelial barrier function, and vascular permeability (10). Occludin, claudins, and zonula occludens (ZO) are key members of tight junction proteins. The ZO is an important component of the tight junction which includes ZO-1, ZO-2, and ZO-3 proteins. As a protein complex, the tight junction connects with F-actin through the ZO-1 protein (11). Pulmonary edema is a typical pathological change of PVOD. Studies have shown that the expression of occludin and ZO-1 is significantly decreased in lipopolysaccharide (LPS)-induced mouse, while piceatannol can recover the expression of occludin and ZO-1 and alleviate LPS-induced damage of the air–blood barrier and pulmonary edema (12). In PAH, tight junction destruction can lead to barrier dysfunction of pulmonary artery endothelial cells and promote the progression of the disease (13–15). So, based on the pathological changes of PVOD, we speculated that tight junction might be involved in the pathogenesis of PVOD.

Therefore, the purpose of this study is to investigate the differential expression profile of miRNAs and tight junction in the lung tissues of rats with MMC-induced PVOD.

MATERIALS AND METHODS

Animals

A total of 14 8-week-old male rats with SD were purchased from the SJA Lab Animals Corporation (Hunan, China) and were divided into two groups: the control group ($N = 4$ rats) and the PVOD group ($N = 10$ rats). They were fed in a clean room in the experimental animal center of the second Xiangya Hospital of Central South University (Hunan, China), with the temperature maintained between 20 and 26°C and the humidity at 50–70%. Free access to water and food was provided, with 12 h cycles of light and dark.

This study was approved by the Qinghai Red Cross hospital, Xining, China, 2016, clinical trial number 72, registered on the Chinese Clinical Trial Registry (ChiCTR-TRC-16003142). We declare that all experimental design and analysis involving animal, animal tissues are in comply with the ARRIVE guidelines (16).

Animal Models

The rats in the PVOD group were injected intraperitoneally with mitomycin-C (GC12353, GLPBIO, USA) on the first day (2 mg/kg) and eighth days (2 mg/kg), while the rats in the

control group were injected intraperitoneally with phosphate-buffered saline at the same doses and times. The experimental period for all groups was 30 days after the animal model was established (**Figure 1**). First, we measured mPAP by a right heart catheter and used the heart to detect the right ventricular hypertrophy index (RVHI). Then, we removed the bronchi, pulmonary arteriovenous and enclosed lung tissues near the right hilum, and tried to take the lung tissues near the periphery for detection under a dissecting microscope (**Figure 2**). Finally, the right pulmonary veins along with lung tissues were collected and placed in liquid nitrogen tanks for storage before RNA extraction and western blot, while the left lung tissues were fixed with formalin to observe the structure.

Measurement of mPAP

Mean pulmonary artery pressure was measured as previously described (17). Briefly, rats were injected intraperitoneally with 1% sodium pentobarbital (40 mg/kg). Then, a PE-50 polyvinyl chloride catheter was slowly inserted through the right external jugular vein and connected with a BL-420 Biological Function Experiment System (AD-Instruments, Oxford, UK). After the catheter was inserted into the pulmonary artery, the position of the catheter was determined by detecting the change of the pressure curve, and the pulmonary artery pressure was recorded.

Determination of RVHI

After the rats were sacrificed, the whole heart was taken out. The interventricular septum (S), right ventricle (RV), and left ventricle (LV) were separated and the blood was sucked up by filter paper. The weight of the RV and LV + S was weighed. RVHI = RV / (LV + S).

Histomorphology of Lung Tissue

After rats were dissected, the left lung tissues were inflated with 4% paraformaldehyde at a constant pressure of 25 cm H_2O and then fixed with 4% paraformaldehyde for 24 h. The lung tissues were embedded in paraffin to fix it, and then sectioned into 4 μm sections. The slices were stained with H&E (Solarbio, China) and orcein (Solarbio, China). Finally, lung tissues histomorphology was observed under an electron microscope.

Profile of miRNAs by High-Throughput Sequencing

The main steps for the preparation of miRNA libraries as follows. At first, the right lung tissues total RNA was isolated using Trizol reagent (CW0580S, CWBIO, China) and RNA quality was determined by using a Qubit RNA kit (Life Technologies Corporation, CA, USA). Second, the 3' end of RNA was spliced using T4 RNA ligase 2 (0511412, NEB, Herts, UK). Third, RT primer was added to the 3' end ligands for reverse transcription primer hybridization. Fourth, the 5' end of RNA was spliced using T4 RNA ligase 1 (0011309, NEB, Herts, UK). Then, the cDNA strand of the linker was obtained by reverse transcription. Next, the reverse transcription was amplified by PCR. Finally, the cDNA purity was verified with 12% PAGE gelelectrophoresis, and PCR product bands of about 140–150 bp were recovered. We used a Qubit DNA kit to quantify DNA, and then used for library preparation and Illumina sequencing.

Sequencing and analysis of the transcriptome of the samples were performed at Sangon Biotechnology Corporation Ltd. (Shanghai, China). Briefly, in this study, Nextseq 550, SE75 was used to conduct high-throughput sequencing. There were three samples in control group and the raw data of reads count was 9,435,980, 10,052,754, and 12,553,433, respectively. In addition, there were three samples in the PVOD group and the raw data of reads count was 11,540,621, 11,284,053, and 11,420,588, respectively (**Supplementary Table 1**). For the raw data, we used cutadapt software (version 1.14) to remove the 3'-end connector (sequence: TGGAATTCTCGGGTGCCAAGGAACTC) and set reads after removal of connector length range within 17–35 bp. Reads after removal of connector were processed with trimmomatic software (version 0.36) to delete bases with quality lower than 20 at 5'-end and 3'-ends, and filter out four consecutive bases with average quality lower than 20 and reads with length lower than 17 to obtain clean data (**Supplementary Table 2**). The comparison of clean reads and rRNA, tRNA, snRNA, and snoRNA in RFAM database were analyzed using blast software (version 2.6.0), and the comparison conditions were set as follows: the value of gapopen is 0, the value of evalue is <0.01, and the value of mismatch is ≤ 1. The species were rat. For the count and normalize reads, the R package was used to process mature miRNA and the number of counts was quantified, and counts were normalized to reads per million. The detailed steps were shown in **Supplementary Table 3**.

miRNA Validation

Total RNA was extracted from the right lung tissues using Trizol reagent (CW0580S, CWBIO, China). RNA was reverse transcribed using RevertAid^{TM} First Strand cDNA Synthesis Kit (CW2141, CWBIO, China). Then, the real-time polymerase chain reaction (RT-PCR) was performed with UltraSYBR Mixture (CW2601, CWBIO, China) following the introduction of the manufacturer. The sequences of miRNA-214-5p former primer: 5'-AGAGTTGTCATGTGTCTAAAAA-3' and reverse primer: 5'-GCTGTCAACGATACGCTACGTAA-3'. The miRNA-141-3p former primer: 5'-TCCATCTTCCAGTGCAGTGTTG-3' and reverse primer: 5'-GCTGTCAACGATACGCTACGTAA-3'. The 5S was used as the internal loading control and the former primer: 5'-GCCTACAGCCATACCACCCGGAA-3', reverse primer: 5'-CCTACAGCACCCGGTATCCCA-3'. Each PCR analysis was done in triplicate.

Then, we performed a comprehensive literature search using the online databases PubMed and Embase up to October 2021 to determine whether multiple genes are regulated by miRNA-214-5p and miRNA-141-3p. The terms "miRNA-214-5p" or "miR-214-5p" or "microRNA-214-5p," and "miRNA-141-3p" or "miR-141-3p" or "microRNA-141-3p" were used to identify the relevant literature. Studies were included if they fulfill these following criteria: (1) English publication; (2) A-identified target genes were validated by dual-luciferase assays.

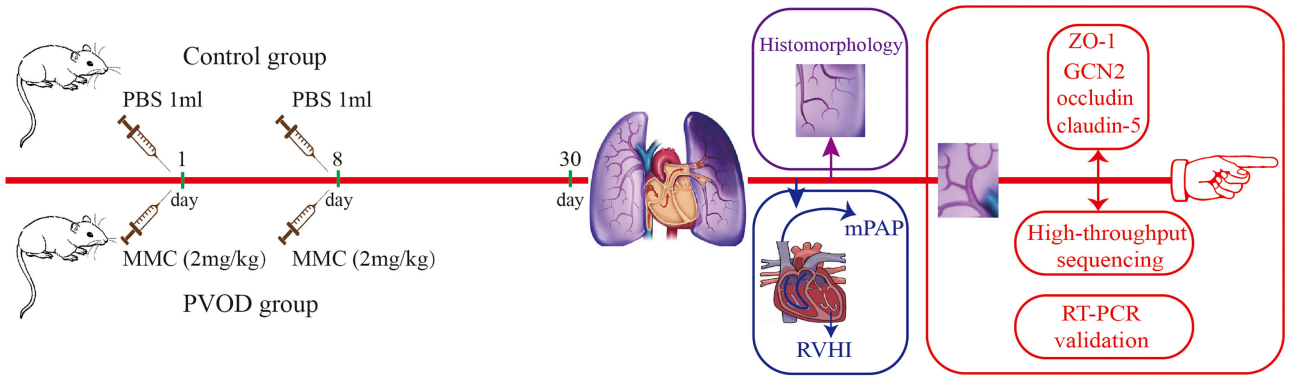

FIGURE 1 | Flowchart of study. The control group ($n = 4$ rats) and the PVOD group ($n = 10$ rats). PVOD, pulmonary veno-occlusive disease; GCN2, General control non-derepressible 2; mPAP, mean pulmonary arterial pressure; MMC, mitomycin-C; PBS, phosphate buffered solution; RVHI, right ventricular hypertrophy index; RT-PCR, real-time polymerase chain reaction; ZO-1, zonula occludens-1.

FIGURE 2 | The whole lung tissues in control and MMC-induced rat with PVOD. The lung tissue was significantly swollen, and also severe hyperemia and edema in the PVOD group compared with the control group. The control group ($n = 4$ rats) and the PVOD group ($n = 10$ rats). PVOD, pulmonary veno-occlusive disease.

Target Gene Prediction

In this study, we used the miRanda algorithm to predict miRNA target genes. miRNA-3'UTR sequence matching and energy stability evaluation were used to comprehensively predict miRNA target genes, and dynamic programming algorithms were used to search for miRNA and 3'UTR complementary and stable

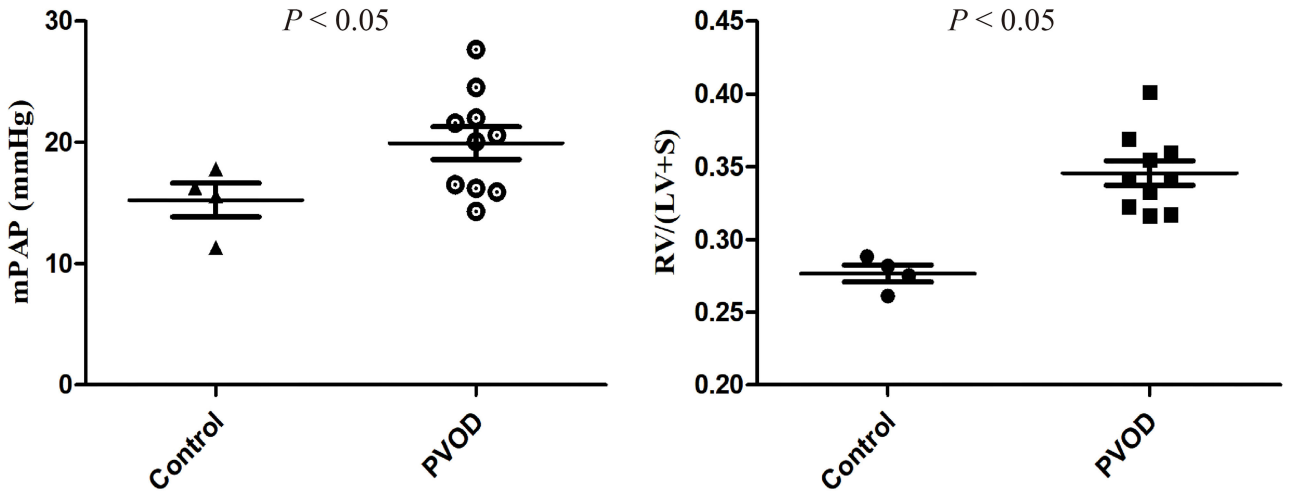

FIGURE 3 | The mPAP and RVHI in control and MMC-induced PVOD rat. The control group ($n = 4$ rats) and the PVOD group ($n = 10$ rats). LV, left ventricular; mPAP, mean pulmonary arterial pressure; MMC, mitomycin-C; PVOD, pulmonary veno-occlusive disease; RVHI, right ventricular hypertrophy index; S, interventricular septum; RVHI = RV/(LV+S).

double-stranded regions. The threshold for candidate target sites was $S \geq 150$, $\Delta G \leq -30$ kcal/mol and demand strict 5'-seed pairing, where S is the sum of single-residue-pair match scores over the alignment trace and ΔG is the free energy of duplex formation (18).

Functional Analysis

The Gene Ontology (GO) project provides information on whether the functions of differential genes are significantly enriched in certain functional annotations or pathways (http://www.geneontology.org). The ontology domains analyzed were biological processes, cellular components, and molecular functions. In this study, the purpose genes including differential expression of miRNA and their target mRNA were selected to perform the enrichment analysis of the GO. Pathway analysis is a functional analysis of mapping genes to the Kyoto Encyclopedia of Genes and Genomes (KEGG) pathways. This study selected differentially expressed miRNAs and their target mRNA to perform the GO analysis and the KEGG pathway analysis by using Cluster Profiler software which is an R package for comparing biological themes among gene clusters offers a gene classification method to classify genes based on their projection at a specific level of the GO corpus, and provides functions, enrich GO and enrich KEGG, to calculate enrichment test for the GO terms and the KEGG pathways based on hypergeometric distribution (19).

Western Blot Analysis

An appropriate size of lung tissue was selected and then the total protein was extracted and measured. The samples were incubated with the primary antibodies for GCN2 (3302S, CST, USA, 1:1000), ZO-1 (21773-1-AP, Proteintech Group, Rosemont, Illinois, USA, 1:5,000), occludin (27260-1-AP, Proteintech Group, Rosemont, Illinois, USA, 1:3000), claudin-5 (35-2,500, Invitrogen, Waltham, Massachusetts, USA, 1:3,000), β-actin (66009-1-Ig, Proteintech Group, Rosemont, Illinois, USA, 1:5,000), and GAPDH (10494-1-AP, Proteintech Group, Rosemont, Illinois, USA, 1:3,000) at 4°C for 24 h. Then, incubated with the secondary antibodies of antirabbit IgG horseradish peroxidase (HRP)-conjugated (SA00001-2, Proteintech Group, Rosemont, Illinois, USA, 1:6,000) for 1 h at normal temperature. Antibody labeling was detected using enhanced chemiluminescence (ECL) (Santa Cruz Biotechnology, Santa Cruz, California, USA).

Statistical Analysis

Statistical analysis was performed using a software package (SPSS version 26.0, SPSS Incorporation, Chicago, Illinois, USA). Continuous variables were performed using independent sample *t*-test. The data with non-normal distribution or uneven variance were used non-parametric test. A value of $P < 0.05$ was considered to be statistically significant.

RESULTS

RVHI, mPAP, and Histomorphology of Lung Tissues

Compared with the control group, the mPAP and RVHI were significantly increased in rats with PVOD ($P < 0.05$) (**Figure 3**). In addition, marked pulmonary artery hypertrophy/hyperplasia, thickening and occlusion in small pulmonary veins, pulmonary edema, dilated capillaries, and inflammatory cell infiltrate were observed in rats with PVOD when compared with the control group (**Figures 4**, **5**).

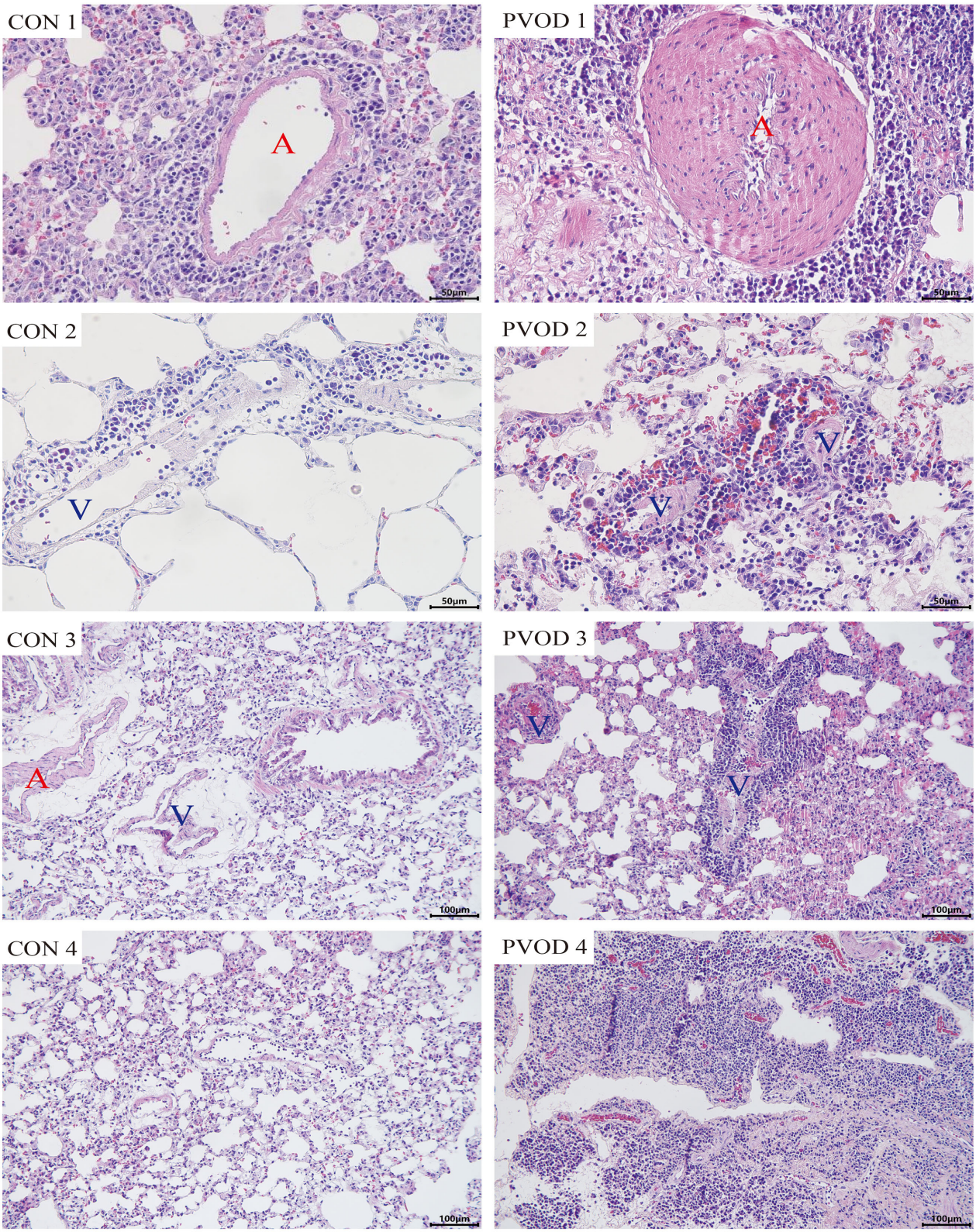

FIGURE 4 | The pathological of lung tissues in control and MMC-induced rat with PVOD with H&E stained. PVOD 1, pulmonary artery with medial hypertrophy/hyperplasia; PVOD 2, vasculitis of pulmonary capillary; PVOD 3, foci of pulmonary edema and capillaritis hemangiomatosis; PVOD 4, alveolar wall thickening. CON 1–4, control lungs; PVOD 1–4, MMC-induced lungs. CON 1–2 and PVOD 1–2: scale bar, 50 μm; CON 3–4 and PVOD 3–4: scale bar, 100 μm. The control group ($n = 4$ rats) and the PVOD group ($n = 10$ rats). A, artery; V, vein; MMC, mitomycin-C; PVOD, pulmonary veno-occlusive disease.

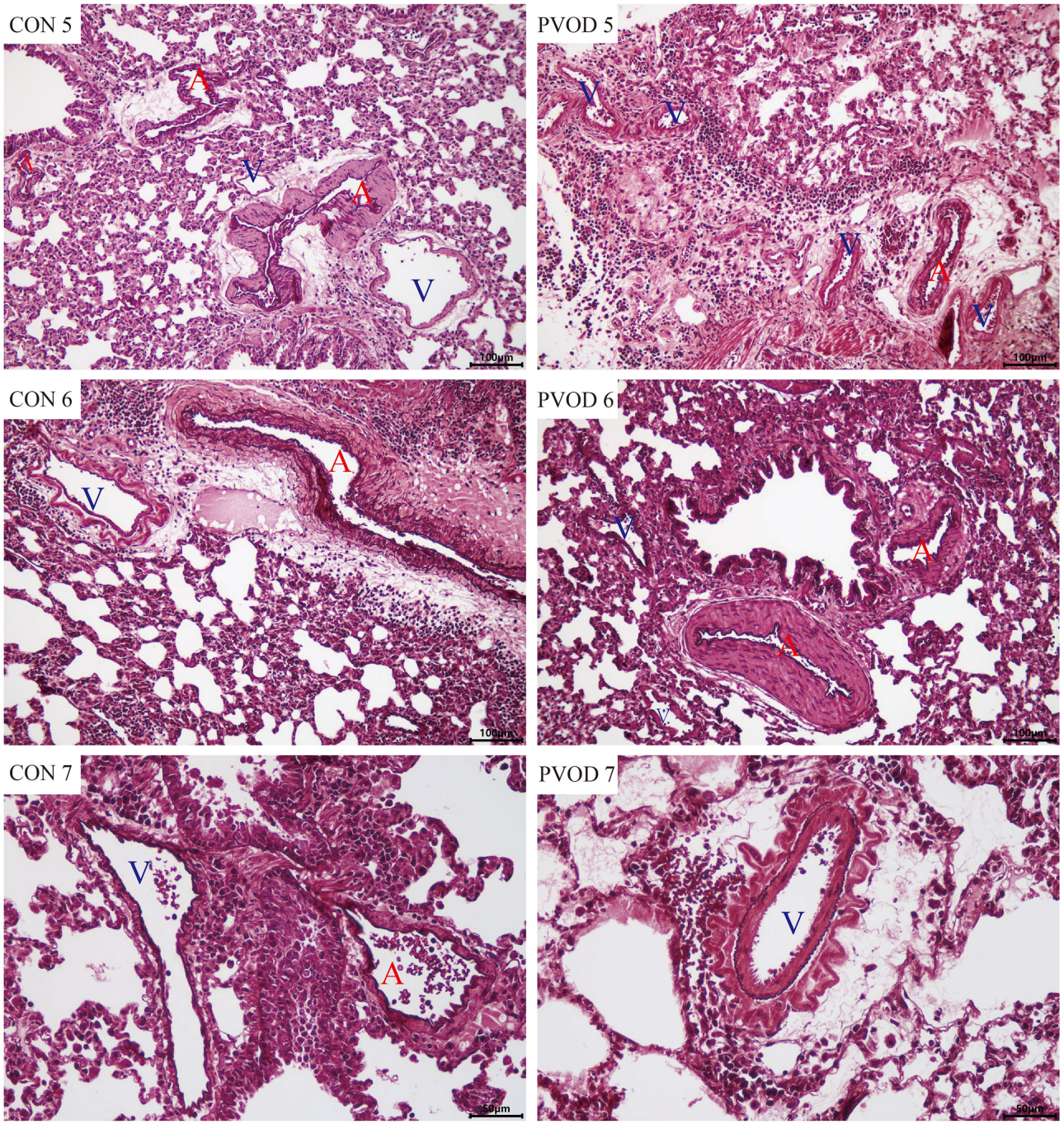

FIGURE 5 | The pulmonary vascular changes in control and MMC-induced rat with PVOD with orcein stained. The pulmonary artery with medial hypertrophy/hyperplasia, thickening, and occlusion in the small pulmonary veins were observed in PVOD group compared with control group. CON 5-7, control lungs; PVOD 5-7, MMC-induced lungs. CON 5-6 and PVOD 5-6: scale bar, 100 μm; CON 7 and PVOD7: scale bar, 50 μm. The control group ($n = 4$ rats) and the PVOD group ($n = 10$ rats). A, artery; V, vein; MMC, mitomycin-C; PVOD, pulmonary veno-occlusive disease.

Expression of GCN2

Furthermore, we detected the protein expression of GCN2 using western blot analysis. Compared with the control group, the expression of GCN2 was significantly decreased in rats with PVOD ($P < 0.05$) (**Figure 6**).

Overview of the miRNA Profiles

A total of 1,030 distinct miRNA transcripts were detected. In rats with PVOD, 64 miRNAs were significantly upregulated and 42 were downregulated (≥ 2-fold change and $P < 0.05$) when compared with the control group (**Figure 7A**).

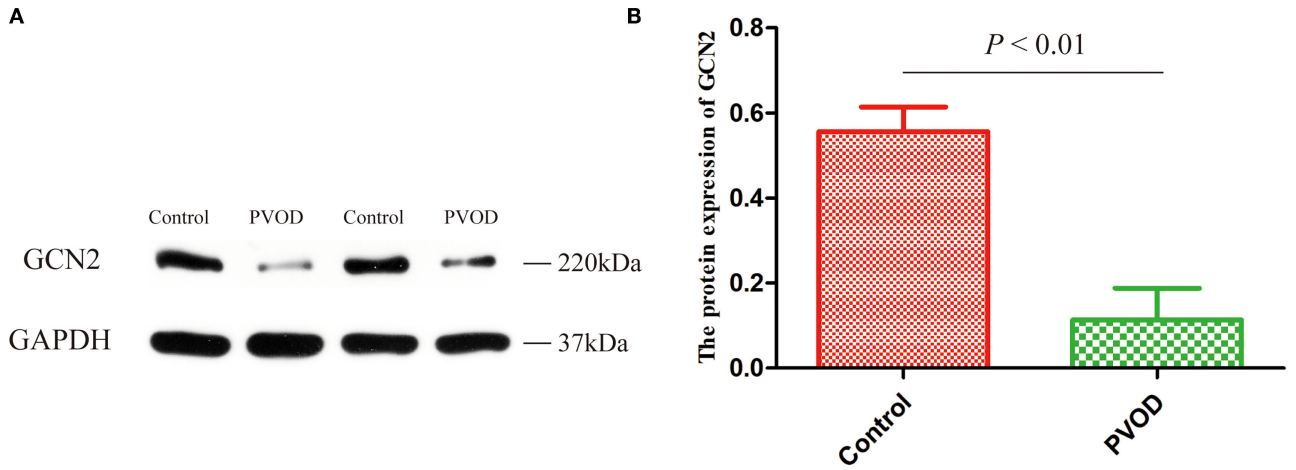

FIGURE 6 | The protein expression of GCN2 in rat. **(A)** Western blot band of proteins expression. **(B)** Relative quantitative of GCN2 expression in the control group and the PVOD group. Values are expressed as means ± SD. GCN2, general control non-derepressible 2; PVOD, pulmonary veno-occlusive disease. The control group ($n = 4$ rats) and the PVOD group ($n = 10$ rats).

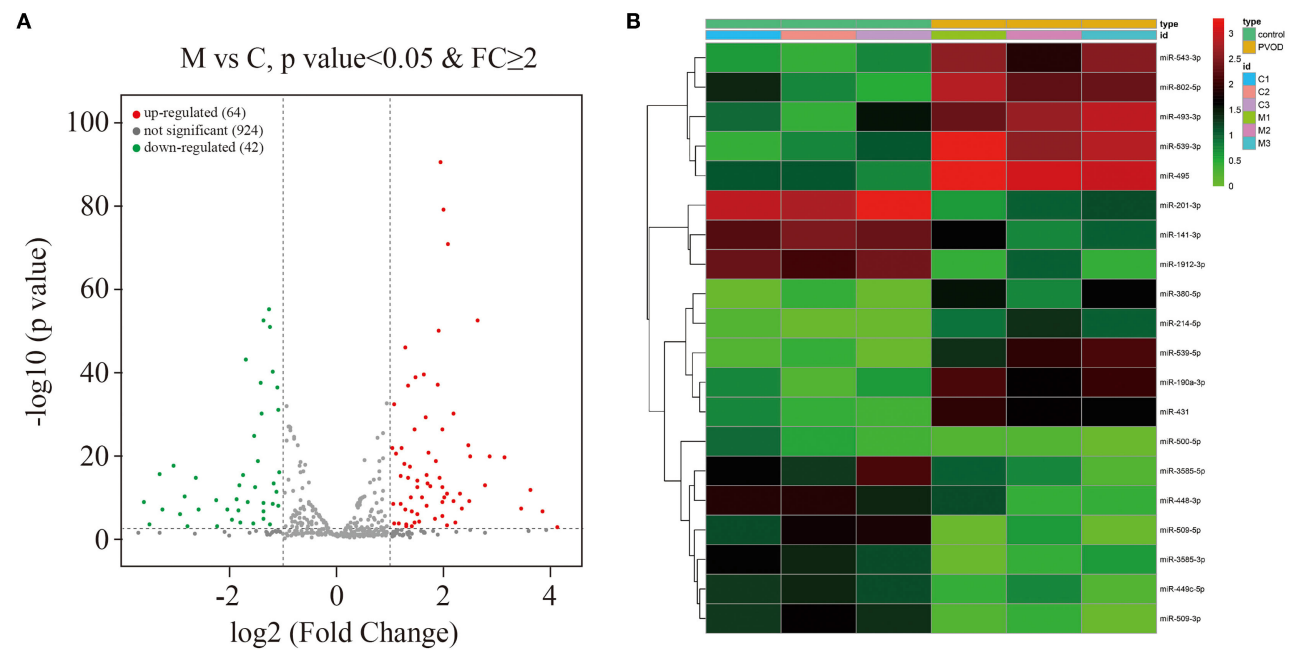

FIGURE 7 | Overview of the miRNA profiles. **(A)** The volcano plot of differential expressed miRNAs in PVOD compared with control group. The upregulated expressed miRNAs were presented in red (≥2-fold change and $P < 0.05$), the downregulated expressed miRNAs were presented in green (≥2-fold change and $P < 0.05$), while no differentially expressed miRNAs were presented in gray ($P \geq 0.05$). **(B)** Hierarchical clustering showed the top ten upregulated miRNAs and top ten downregulated miRNAs in PVOD group (yellow bar) compared with control group (green bar). The expression was displayed on a scale from light to deep. C, C1–C3 were the control group; M, M1–M3 were the PVOD group. FC, fold change; PVOD, pulmonary veno-occlusive disease.

The top ten upregulated miRNAs were miRNA-543-3p, miRNA-802-5p, miRNA-493-3p, miRNA-539-3p, miRNA-495, miRNA-380-5p, miRNA-214-5p, miRNA-539-5p, miRNA-190a-3p and miRNA-431, while the top 10 downregulated miRNAs were miRNA-201-3p, miRNA-141-3p, miRNA-1912-3p, miRNA-500-5p, miRNA-3585-5p, miRNA-448-3p, miRNA-509-5p, miRNA-3585-3p, miRNA-449c-5p, and miRNA-509-3p (**Figure 7B**).

miRNAs Validation

According to the results of high-throughput sequencing, the top differentially expressed miRNA-214-5p and miRNA-141-3p that

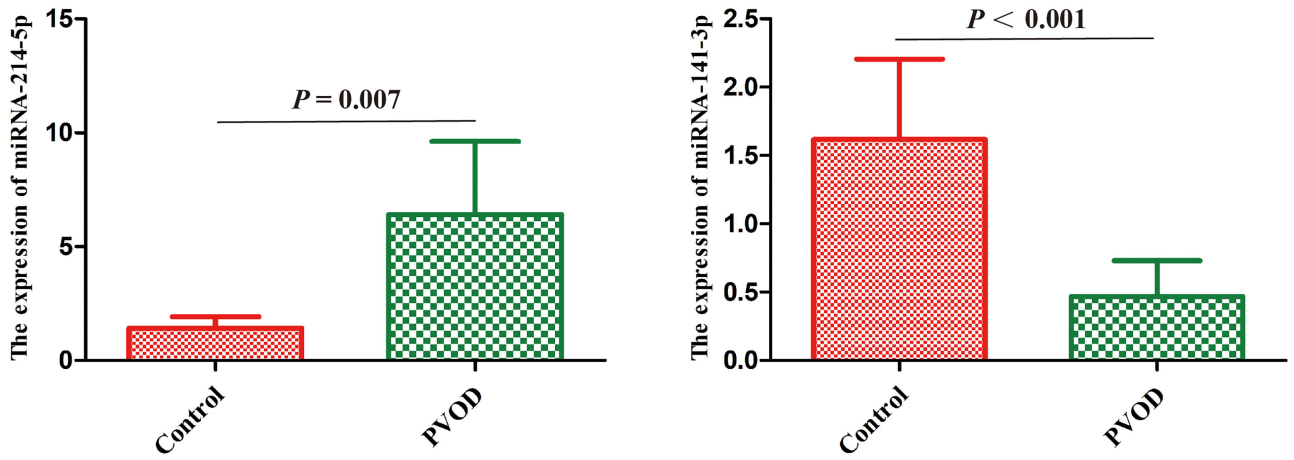

FIGURE 8 | Real-time polymerase chain reaction validated the differential expression of miRNA-214-5p and miRNA-141-3p in rat. Values are expressed as means ± SD. PVOD, pulmonary veno-occlusive disease. The control group ($n = 4$ rats) and the PVOD group ($n = 10$ rats).

have been shown to be involved in the development of PAH were selected for the validation by using RT-PCT. The result showed that miRNA-214-5p was significantly upregulated, while miRNA-141-3p was downregulated in group with PVOD compared with the control group ($P < 0.05$) (**Figure 8**).

Target Gene Prediction

According to the miRanda algorithm, there were 64 upregulated miRNAs with 2,470 target genes, while 42 downregulated miRNAs with 1,098 target genes (**Table 1**). The detail target genes were showed in **Supplementary Tables 4**, **5**.

Gene Ontology Enrichment Analysis

The GO analysis was performed to determine gene product enrichment. For the three ontology domains of biological processes, cellular components and molecular function, the classification of the GO count was showed in **Figure 9A**. They were enriched in the biological processes including the collagen-activated tyrosine kinase receptor signaling pathway, intracellular signal transduction, and protein phosphorylation. Collagen trimer, nucleoplasm, and axon were enriched in cellular components. In addition, extracellular matrix structural constituent, ATP binding, and protein binding were enriched in the molecular functions (**Figures 9B,C**).

Kyoto Encyclopedia of Genes and Genomes Pathway Analysis

Pathway analysis demonstrated that there were several enrichment-related pathways. The KEGG pathway analysis involved PVOD-related pathways including focal adhesion, ECM-receptor interaction, notch-signaling pathway, lysosome, tight junction, hedgehog-signaling pathway, aminoacyl-tRNA biosynthesis, fatty acid biosynthesis, other types of O-glycan biosynthesis, and the mTOR-signaling pathway (**Figures 10A–C**).

TABLE 1 | Prediction of number of differential expression miRNAs and their target genes.

Comparison group	Up-regulated miRNAs	Target genes	Down-regulated miRNAs	Target genes
PVOD vs. Control	64	2,470	42	1,098

According to the miRanda algorithm to predict the target genes of differential expression miRNAs. PVOD, pulmonary veno-occlusive disease.

Expression of ZO-1, Occludin, and Claudin-5

In order to explore the possible mechanisms of PVOD, we detected expression of the tight junction-related proteins of ZO-1, occludin, and claudin-5 according to the results of pathway analysis and our inference. The proteins expression of ZO-1, occludin, and claudin-5 was significantly decreased in rats with PVOD when compared with the control group ($P < 0.05$) (**Figure 11**).

DISCUSSION

Pulmonary veno-occlusive disease is disease with difficult to diagnosis and treatment, of the pathogenesis remains unclear. In this study, we found that the levels of mPAP and RVHI were increased, and there were severe pathological changes including pulmonary artery hypertrophy/hyperplasia, thickening, and occlusion in small pulmonary veins, pulmonary edema, dilated capillaries, and inflammatory cell infiltrate in MMC-induced rat. This was consistent with the study of Perros et al. (4). Therefore, the rat PVOD model was successfully established according to the typical pathological changes, mPAP and RVHI.

GCN2 is a serine-threonine kinase responsible for the phosphorylation of eukaryotic translation initiation factor to regulate the cell cycle and participate in the

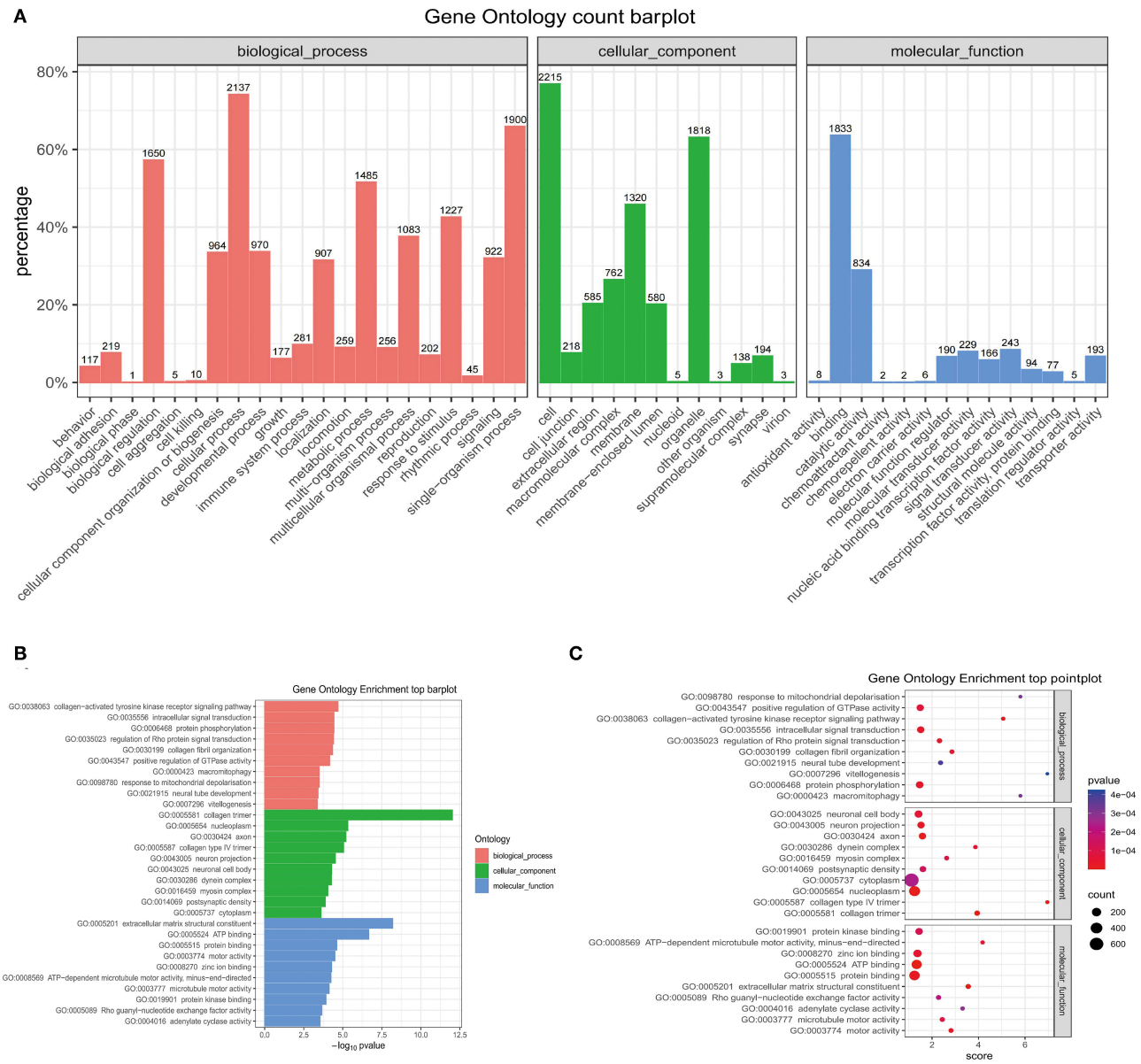

FIGURE 9 | The GO enrichment analysis. **(A)** The barplot of the GO count. **(B)** The barplot of top enrichment in the biological process, cellular component, and molecular function. **(C)** The pointplot of top enrichment in biological process, cellular component, and molecular function. GO, Gene Ontology.

development of disease. Studies have shown that the mutation of GCN2 is linked to the development of PVOD and the expression of GCN2 is significantly decreased in patients with PVOD and MMC-induced rat pulmonary microvascular endothelial cells (20–22). In addition, Chen et al. (23) found that GCN2 deficiency decreased ATF3-dependent p38 phosphorylation inhibition in development of PVOD. This implies that GCN2 plays an important role in the pathogenesis of PVOD. We also found the same result, that the expression of GCN2 was decreased in rats with PVOD.

miRNA is a type of non-coding RNA with regulatory functions and plays an important role in regulating genes expression and disease development. In addition, miRNA is involved in the regulation of vascular proliferation and remodeling, as well as vascular endothelial cells apoptosis (24). However, whether miRNA is involved in the development of PVOD has not been studied. In this study, we used high-throughput sequencing which is an efficient, rapid method to analyze the differential expression profile of miRNAs between PVOD and normal rats, and screened out a total of 106 miRNAs among 1,030 transcripts that are differentially expressed in the lung tissues.

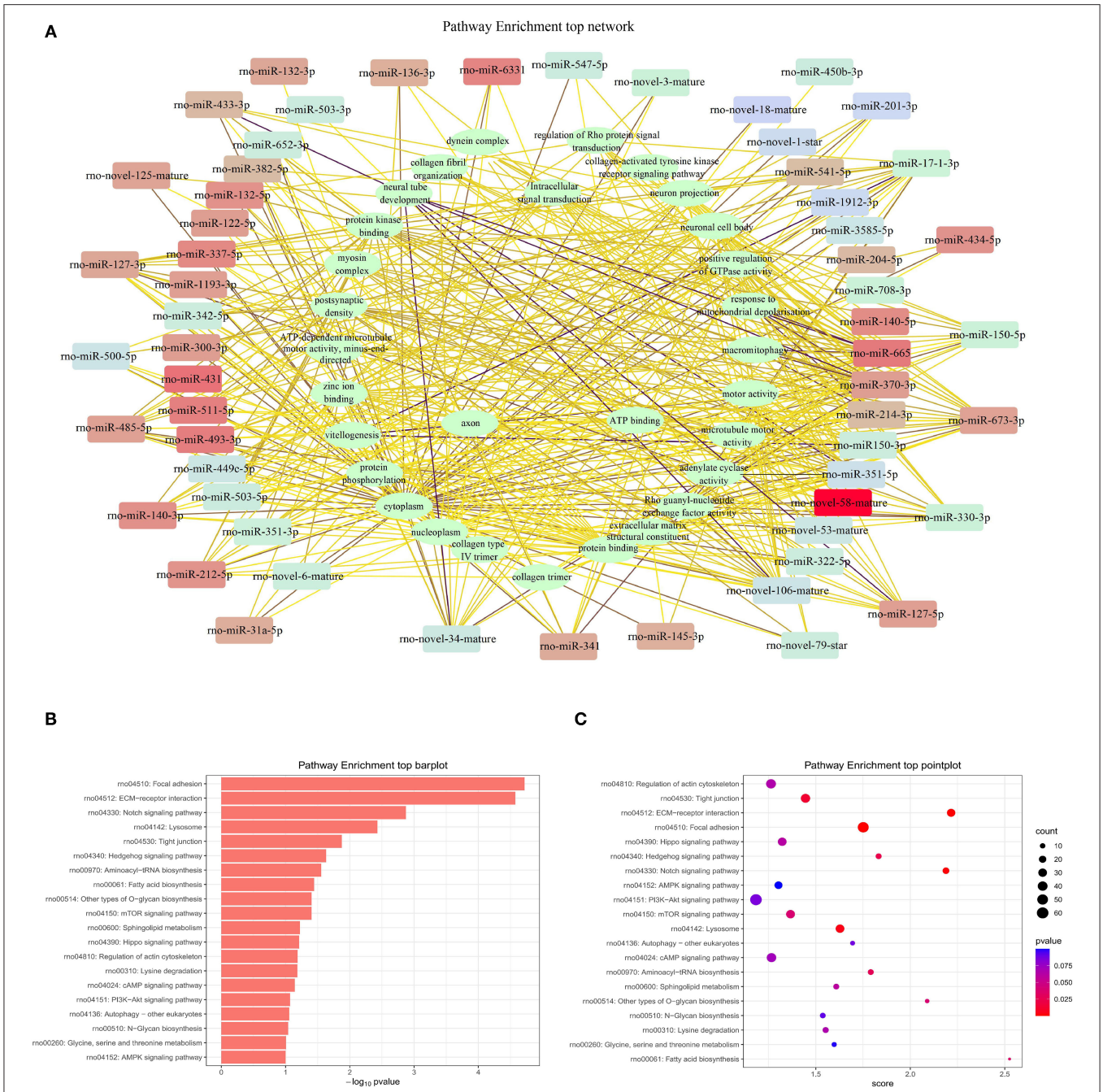

FIGURE 10 | The top pathway enrichment analysis. **(A)** Network of top pathway enrichment. **(B)** Barplot of top pathway enrichment. **(C)** Pointplot of top pathway enrichment.

This implies that the profile of these significantly differentially expressed miRNAs might be involved in the development of PVOD. As described in the results, the top upregulated including miRNA-495, miRNA-214-5p, and miRNA-190a-3p and the downregulated miRNAs including miRNA-141-3p, miRNA-509-5p, and miRNA-509-3p. In addition, RT-PCR confirmed that miRNA-214-5p was upregulated, while miRNA-141-3p was downregulated that were consistent with our results of high-throughput sequencing. PVOD is a rare form of PAH. Studies have shown that participates of miRNA in the development of PAH. Stevens et al. (25) found that miRNA-214 is shown to be significantly upregulated in rat models of PAH. In addition, miRNA-214 can promote smooth muscle cell phenotype changes and proliferation and participate in PAH vascular dysfunction (26). This is consistent with our results of sequencing analysis and validation. Fu et al. (27) found that

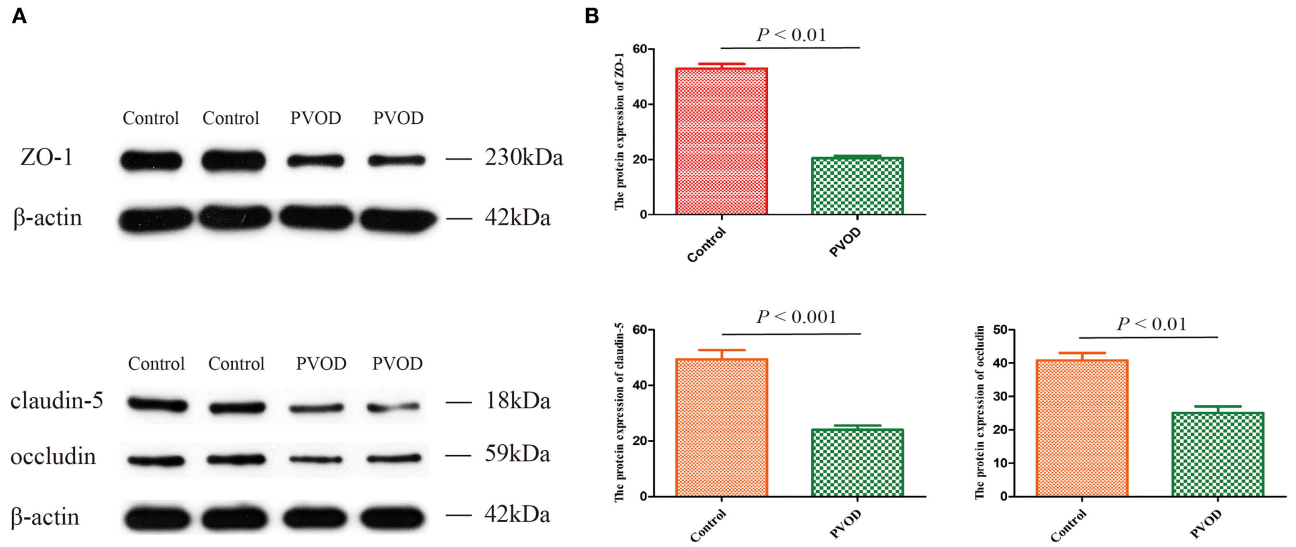

FIGURE 11 | The protein expression of ZO-1, occludin, and claudin-5 in rat. **(A)** Western blot band of proteins expression. **(B)** Relative quantitative of ZO-1, claudin-5, and occludin expression in control group and PVOD group. Values are expressed as means ± SD. ZO-1, zonula occludens-1; PVOD, pulmonary veno-occlusive disease. The control group ($n = 4$ rats) and the PVOD group ($n = 10$ rats).

attenuation of miRNA-495 derepresses phosphatase and tensin homolog to effectively protect right ventricular hypertrophy in rats with PAH. Another study showed that miRNA-190 plays an important role in hypoxic pulmonary vascular constriction which participates in the development of PAH (28). Lei et al. (29) found that the expression of miRNA-141 is downregulated in patients with PAH, while enhanced miRNA-141 expression can suppress the RhoA/ROCK pathway to regulate vascular remodeling of PAH. Tang (30) found that the expression of miRNA-509-3p expression decreases in the serum of patients with PAH. This is consistent with our results of high-throughput sequencing. However, the mechanisms by which these differentially expressed miRNAs participated in the development of PVOD need to be further researched.

Studies have shown that miRNAs are involved in the regulation of multiple-signaling pathways and functional analysis of the target genes is helpful for understanding the functional mechanisms of miRNAs (31). In this study, the GO and the KEGG pathway analyses showed that miRNAs are involved in various signaling pathways and metabolic processes, such as the fatty acid biosynthesis, tight junctions, mammalian target of rapamycin (mTOR) signaling pathway, PI3K-AKT signaling pathway, notch signaling pathway, hedgehog signaling pathway, AMPK signaling pathway, and cAMP signaling pathway. Therefore, we have performed a comprehensive literature search using the online databases PubMed and Embase up to October 2021 to determine whether multiple genes are regulated by miRNA-214-5p (**Supplementary Table 6**) and miRNA-141-3p (**Supplementary Table 7**).

Studies have shown that tight junctions are involved in the development of PAH (32). The study of Dalvi et al. (33) showed that Tat/cocaine-mediated production of reactive oxygen species activates the Ras/Raf/ERK1/2 pathway that contributes to disruption of the tight junction-related protein ZO-1, leading to pulmonary vascular remodeling and promoting the development of PAH. In our study, we also found significantly decreased expression of the tight junction-related protein of ZO-1, occludin and claudin-5 which might be involved in the development of PVOD. In addition, Lv et al. (34) study showed that miRNA-214 linked with ZO-1 to promote epithelial-mesenchymal transition process that was consistent with our finding.

Early studies have shown that fatty acid biosynthesis plays an important role in PVOD. Ogawa et al. (35) found that epoprostenol, as a metabolite of fatty acids, can be considered as a therapeutic option in patients with PVOD. Another study showed that a remarkable improvement of hemodynamics and of the clinical course of PVOD was produced by adjunctive use of oral sildenafil in association with intravenous high-dose epoprostenol (36). Brittain et al. (37) also found that abnormalities in fatty acid metabolism can be detected in the blood and myocardium in patients with PAH. This is consistent with our pathway prediction analysis results that it is indeed involved in the development of PVOD.

Although these pathways have not been studied in PVOD, they have been shown to be involved in the development of PAH. mTOR is a member of the serine/threonine protein kinase family that regulates cell proliferation, protein synthesis, and actin cytoskeleton; it is the catalytic subunit of two structurally distinct kinase complexes termed TOR complex 1 (TORC1) and TORC2 (38). Studies have shown that mTOR is involved in the occurrence and development of PAH. Inhibition of mTOR can reduce hypoxia-induced right ventricular hypertrophy and remodeling in animals (39) and improve PAH in patients (40). In addition, AKT as the substrate of mTORC2, can

activate mTORC1 to involve in the development of disease (41). Jia et al. (42) found that osteoprotegerin induces pulmonary arterial smooth muscle cell proliferation by interacting with integrin αvβ3 to elicit downstream focal adhesion kinase and AKT pathway activation to facilitate PAH pathogenesis. Notch signaling is critically involved in the vascular morphogenesis and function including Notch 1–4. It has been determined that Notch 3 is associated with PAH. The expression of Notch 3 is increased in the lung tissues of patients with PAH and hypoxia-induced mouse with PAH (43). mTOR has previously been identified as a positive regulator of Notch 3 (44).

Hedgehog is a proangiogenic factor involved in the regulation of endothelial cell proliferation. Ghouleh et al. (45) found that the expression of hedgehog is increased in hypoxia-induced pulmonary artery endothelial cells and involved in the progression of PAH. Adenosine monophosphate-activated protein kinase (AMPK), a sensor of cellular energy, has been found to regulate cell proliferation (46). Studies have suggested that activation of AMPK by metformin prevents the development of PAH in animal models and activation of AMPK prevents the development of PAH by targeting nuclear factor-kappa B (NF-κB) to suppress autophagy and vascular remodeling (47, 48). cAMP signaling is involved in extracellular matrix metabolism as well as in proliferation control. The expression of p21(Waf1/Cip1) is regulated by C/EBP-α, which in turn is controlled by cAMP. Similarly, treprostinil, through cAMP-C/EBP-α p42-p21 (WAf1/Cip1) signaling, reduces arterial wall remodeling which benefits patients with PAH (49–51). So, the molecular mechanisms in PVOD are worth further exploration.

This study still has potential limitations. First, all the RNA and protein were extracted using the lung tissues, not pulmonary veins. In fact, it is also very difficult to separate small pulmonary veins and the capillaries also had serious pathological changes in rats with PVOD. In addition, in this study, we used lung tissues to perform high-throughput sequencing and validate the differentially expressed miRNAs so that it is unclear whether the results were from endothelial cells or smooth muscle cells. Then, not all of the differentially expressed miRNAs in rat with PVOD were validated by RT-PCR that might decrease the accuracy. Finally, we found that various signaling pathways might be involved in the development of PVOD by enrichment analysis, but we just detected the expression of tight junction protein of ZO-1, occludin, and claudin-5 which is consistent with the result of pathways enrichment analysis. Surely, we will further validate other differentially expressed miRNAs and molecular pathways to reveal their specific mechanisms of PVOD in the future.

In summary, we screened the expression profile of miRNAs closely related to PVOD by using high-throughput sequencing. In addition, the GO and the KEGG pathway analyses could help us to explored and predicted the function of certain miRNAs, which would provide a new experimental basis and ideas for further research on the effect of miRNAs on the occurrence and development of PVOD in future. In addition, the tight junction protein ZO-1, occludin, and claudin-5 might be related to be PVOD, which confirmed the GO and KEGG pathway analyses, but the underlying mechanisms need to be explored further.

DATA AVAILABILITY STATEMENT

The datasets presented in this study can be found in online repositories. The names of the repository/repositories and accession number(s) can be found at: https://www.ncbi.nlm.nih.gov/geo/query/acc.cgi?acc=GSE189080.

ETHICS STATEMENT

The animal study was reviewed and approved by Qinghai Red Cross Hospital. Written informed consent was obtained from the owners for the participation of their animals in this study.

AUTHOR CONTRIBUTIONS

QS performed the data analysis, drafted manuscript, and drew the figures. PC, YC, and S-JW coordinated the study and performed the experiment. YZ conceived the study, performed the experiment, and revised the manuscript. All the authors read and approved the final version of the manuscript.

FUNDING

This study was supported by the Major Scientific and Technological Achievement Transformation Project of Qinghai Province, China [2017-SF-122].

SUPPLEMENTARY MATERIAL

The Supplementary Material for this article can be found online at: https://www.frontiersin.org/articles/10.3389/fcvm.2022.746888/full#supplementary-material

REFERENCES

1. Montani D, Lau EM, Dorfmüller P, Girerd B, Jaïs X, Savale L, et al. Pulmonary veno-occlusive disease. *Eur Respir J.* (2016) 47:1518–34. doi: 10.1183/13993003.00026-2016
2. Holcomb BW Jr, Loyd JE, Ely EW, Johnson J, Robbins IM. Pulmonary veno-occlusive disease: a case series and new observations. *Chest.* (2020) 118:1671–9. doi: 10.1378/chest.67.4.487
3. Certain MC, Chaumais MC, Jaïs X, Savale L, Seferian A, Parent F, et al. Characteristics and long-term outcomes of pulmonary venoocclusive disease induced by mitomycin C. *Chest.* (2021) 159:1197–207. doi: 10.1016/j.chest.2020.09.238
4. Perros F, Günther S, Ranchoux B, Godinas L, Antigny F, Chaumais MC, et al. Mitomycin-induced pulmonary veno-occlusive disease: evidence from human disease and animal models. *Circulation.* (2015) 132:834–47. doi: 10.1161/CIRCULATIONAHA.115.014207
5. O'Brien J, Hayder H, Zayed Y, Peng C. Overview of microRNA biogenesis, mechanisms of actions, and circulation. *Front Endocrinol.* (2015) 9:402. doi: 10.3389/fendo.2018.00402

6. Yan S, Shi J, Sun D, Lyu L. Current insight into the roles of microRNA in vitiligo. *Mol Biol Rep.* (2020) 47:3211–9. doi: 10.1007/s11033-020-05336-3
7. Li Q, Qian Z, Wang L. Pri-microRNA-124 rs531564 polymorphism minor allele increases the risk of pulmonary arteryhypertension by abnormally enhancing proliferation of pulmonary artery smooth muscle cells. *Int J Chron Obstruct Pulmon Dis.* (2017) 12:1351–61. doi: 10.2147/COPD.S99318
8. Green DE, Murphy TC, Kang BY, Searles CD, Hart CM. PPARγ ligands attenuate hypoxia-induced proliferation in human pulmonary artery smooth muscle cells through modulation of microRNA-21. *PLoS ONE.* (2015) 10:e0133391. doi: 10.1371/journal.pone.0133391
9. Green DE, Murphy TC, Kang BY, Bedi B, Yuan Z, Sadikot RT, et al. Peroxisome proliferator-activated receptor-γ enhances human pulmonary artery smooth muscle cell apoptosis through microRNA-21 and programmed cell death 4. *Am J Physiol Lung Cell Mol Physiol.* (2017) 313:L371–83. doi: 10.1152/ajplung.00532.2016
10. Kakogiannos N, Ferrari L, Giampietro C, Scalise AA, Maderna C, Ravà M, et al. JAM-A acts *via* C/EBP-α to promote claudin-5 expression and enhance endothelial barrier function. *Circ Res.* (2020) 127:1056–73. doi: 10.1161/CIRCRESAHA.120.316742
11. Feng S, Zou L, Wang H, He R, Liu K, Zhu H. RhoA/ROCK-2 pathway inhibition and tight junction protein upregulation by catalpol suppresses lipopolysaccaride-induced disruption of blood-brain barrier permeability. *Molecules.* (2018) 23:2371. doi: 10.3390/molecules23092371
12. Peng LY, Yuan M, Shi HT, Li JH, Song K, Huang JN, et al. Protective effect of piceatannol against acute lung injury through protecting the integrity of air-blood barrier and modulating the TLR4/NF-κB signaling pathway activation. *Front Pharmacol.* (2020) 10:1613. doi: 10.3389/fphar.2019.01613
13. Good RB, Gilbane AJ, Trinder SL, Denton CP, Coghlan G, Abraham DJ, et al. Endothelial to mesenchymal transition contributes to endothelial dysfunction in pulmonary arterial hypertension. *Am J Pathol.* (2015) 185:1850–8. doi: 10.1016/j.ajpath.2015.03.019
14. Fazakas C, Nagaraj C, Zabini D, Végh AG, Marsh LM, Wilhelm I, et al. Rho-kinase inhibition ameliorates dasatinib-induced endothelial dysfunction and pulmonary hypertension. *Front Physiol.* (2018) 9:537. doi: 10.3389/fphys.2018.00537
15. Dasgupta SK, Le A, Vijayan KV, Thiagarajan P. Dasatinib inhibits actin fiber reorganization and promotes endothelial cell permeability through RhoA-ROCK pathway. *Cancer Med.* (2017) 6:809–18. doi: 10.1002/cam4.1019
16. Percie du Sert N, Hurst V, Ahluwalia A, Alam S, Avey MT, Baker M, et al. The ARRIVE guidelines 2.0: updated guidelines for reporting animal research. *PLoS Biol.* (2020) 18:e3000410. doi: 10.1371/journal.pbio.3000410
17. Deng C, Zhong Z, Wu D, Chen Y, Lian N, Ding H, et al. Role of FoxO1 and apoptosis in pulmonary vascular remolding in a rat model of chronic thromboembolic pulmonary hypertension. *Sci Rep.* (2017) 7:2270. doi: 10.1038/s41598-017-02007-5
18. Enright AJ, John B, Gaul U, Tuschl T, Sander C, Marks DS. MicroRNA targets in Drosophila. *Genome Biol.* (2003) 5:R1. doi: 10.1186/gb-2003-5-1-r1
19. Yu G, Wang LG, Han Y, He QY. ClusterProfiler: an R package for comparing biological themes among gene clusters. *OMICS.* (2012) 16:284–7. doi: 10.1089/omi.2011.0118
20. Zhang C, Lu W, Luo X, Liu S, Li Y, Zheng Q, et al. Mitomycin C induces pulmonary vascular endothelial-to-mesenchymal transition and pulmonary veno-occlusive disease via Smad3-dependent pathway in rats. *Br J Pharmacol.* (2021) 178:217–35. doi: 10.1111/bph.15314
21. Lai YJ, Chen PR, Huang YL, Hsu HH. Unique wreath-like smooth muscle proliferation of the pulmonary vasculature in pulmonary veno-occlusive disease versus pulmonary arterial hypertension. *J Formos Med Assoc.* (2020) 119:300–9. doi: 10.1016/j.jfma.2019.05.019
22. Nossent EJ, Antigny F, Montani D, Bogaard HJ, Ghigna MR, Lambert M, et al. Pulmonary vascular remodeling patterns and expression of general control nonderepressible 2 (GCN2) in pulmonary veno-occlusive disease. *J Heart Lung Transplant.* (2018) 37:647–55. doi: 10.1016/j.healun.2017.09.022
23. Chen Z, Zhang J, Wei D, Chen J, Yang J. GCN2 regulates ATF3-p38 MAPK signaling transduction in pulmonary veno-occlusive disease. *J Cardiovasc Pharmacol Ther.* (2021) 26:677–89. doi: 10.1177/10742484211015535
24. Song Q, Chen P, Liu XM. The role of cigarette smoke-induced pulmonary vascular endothelial cell apoptosis in COPD. *Respir Res.* (2021) 22:39. doi: 10.1186/s12931-021-01630-1
25. Stevens HC, Deng L, Grant JS, Pinel K, Thomas M, Morrell NW, et al. Regulation and function of miR-214 in pulmonary arterial hypertension. *Pulm Circ.* (2016) 6:109–17. doi: 10.1086/685079
26. Sahoo S, Meijles DN, Al Ghouleh I, Tandon M, Cifuentes-Pagano E, Sembrat J, et al. MEF2C-MYOCD and leiomodin1 suppression by miRNA-214 promotes smooth muscle cell phenotype switching in pulmonary arterial hypertension. *PLoS ONE.* (2016) 11:e0153780. doi: 10.1371/journal.pone.0153780
27. Fu J, Chen Y, Li F. Attenuation of microRNA-495 derepressed PTEN to effectively protect rat cardiomyocytes from hypertrophy. *Cardiology.* (2018) 139:245–54. doi: 10.1159/000487044
28. Li SS, Ran YJ, Zhang DD, Li SZ, Zhu D. MicroRNA-190 regulates hypoxic pulmonary vasoconstriction by targeting a voltage-gated K channel in arterial smooth muscle cells. *J Cell Biochem.* (2014) 115:1196–205. doi: 10.1002/jcb.24771
29. Lei S, Peng F, Li ML, Duan WB, Peng CQ, Wu SJ. LncRNA-SMILR modulates RhoA/ROCK signaling by targeting miR-141 to regulate vascular remodeling in pulmonary arterial hypertension. *Am J Physiol Heart Circ Physiol.* (2020) 319:H377–91. doi: 10.1152/ajpheart.00717.2019
30. Tang P. Clinical diagnostic value of circulating serum miR-509-3p in pulmonary arterial hypertension with congenital heart disease. *Hellenic J Cardiol.* (2020) 61:26–30. doi: 10.1016/j.hjc.2018.06.004
31. Bartel DP. MicroRNAs: genomics, biogenesis, mechanism, and function. *Cell.* (2004) 116:281–97. doi: 10.1016/S0092-8674(04)00045-5
32. Dhillon NK, Li F, Xue B, Tawfik O, Morgello S, Buch S, et al. Effect of cocaine on human immunodeficiency virus-mediated pulmonary endothelial and smooth muscle dysfunction. *Am J Respir Cell Mol Biol.* (2011) 45:40–52. doi: 10.1165/rcmb.2010-0097OC
33. Dalvi P, Wang K, Mermis J, Zeng R, Sanderson M, Johnson S, et al. HIV-1/cocaine induced oxidative stress disrupts tight junction protein-1 in human pulmonary microvascular endothelial cells: role of Ras/ERK1/2 pathway. *PLoS ONE.* (2014) 9:e85246. doi: 10.1371/journal.pone.0085246
34. Lv JW, Wen W, Jiang C, Fu QB, Gu YJ, Lv TT, et al. Inhibition of microRNA-214 promotes epithelial-mesenchymal transition process and induces interstitial cystitis in postmenopausal women by upregulating Mfn2. *Exp Mol Med.* (2017) 49:e357. doi: 10.1038/emm.2017.98
35. Ogawa A, Miyaji K, Yamadori I, Shinno Y, Miura A, Kusano KF, et al. Safety and efficacy of epoprostenol therapy in pulmonary veno-occlusive disease and pulmonary capillary hemangiomatosis. *Circ J.* (2012) 76:1729–36. doi: 10.1253/circj.CJ-11-0973
36. Kuroda T, Hirota H, Masaki M, Sugiyama S, Oshima Y, Terai K, et al. Sildenafil as adjunct therapy to high-dose epoprostenol in a patient with pulmonary veno-occlusive disease. *Heart Lung Circ.* (2006) 15:139–42. doi: 10.1016/j.hlc.2005.07.002
37. Brittain EL, Talati M, Fessel JP, Zhu H, Penner N, Calcutt MW, et al. Fatty acid metabolic defects and right ventricular lipotoxicity in human pulmonary arterial hypertension. *Circulation.* (2016) 133:1936–44. doi: 10.1161/CIRCULATIONAHA.115.019351
38. Betz C, Hall MN. Where is mTOR and what is it doing there? *J Cell Biol.* (2013) 203:563–74. doi: 10.1083/jcb.201306041
39. Pena A, Kobir A, Goncharov D, Goda A, Kudryashova TV, Ray A, et al. Pharmacological inhibition of mTOR kinase reverses right ventricle remodeling and improves right ventricle structure and function in rats. *Am J Respir Cell Mol Biol.* (2017) 57:615–25. doi: 10.1165/rcmb.2016-0364OC
40. Wessler JD, Steingart RM, Schwartz GK. Dramatic improvement in pulmonary hypertension with rapamycin. *Chest.* (2010) 138:991–3. doi: 10.1378/chest.09-2435
41. Memmott RM, Dennis PA. Akt-dependent and -independent mechanisms of mTOR regulation in cancer. *Cell Signal.* (2009) 21:656–64. doi: 10.1016/j.cellsig.2009.01.004
42. Jia D, Zhu Q, Liu H, Zuo C, He Y, Chen G, et al. Osteoprotegerin disruption attenuates HySu-induced pulmonary hypertension through integrin αvβ3/FAK/AKT pathway suppression. *Circ Cardiovasc Genet.* (2017) 10:e001591. doi: 10.1161/CIRCGENETICS.116.001591
43. Morris HE, Neves KB, Montezano AC, MacLean MR, Touyz RM. Notch3 signalling and vascular remodelling in pulmonary arterial hypertension. *Clin Sci.* (2019) 133:2481–98. doi: 10.1042/CS20190835
44. Ma J, Meng Y, Kwiatkowski DJ, Chen X, Peng H, Sun Q, et al. Mammalian target of rapamycin regulates murine and human cell differentiation

through STAT3/p63/Jagged/Notch cascade. *J Clin Invest.* (2010) 120:103–14. doi: 10.1172/JCI37964
45. Ghouleh IA, Sahoo S, Meijles DN, Amaral JH, de Jesus DS, Sembrat J, et al. Endothelial Nox1 oxidase assembly in human pulmonary arterial hypertension; driver of Gremlin1-mediated proliferation. *Clin Sci.* (2017) 131:2019–35. doi: 10.1042/CS20160812
46. Grahame Hardie D. AMP-activated protein kinase: a key regulator of energy balance with many roles in human disease. *J Intern Med.* (2014) 276:543–59. doi: 10.1111/joim.12268
47. Li S, Han D, Zhang Y, Xie X, Ke R, Zhu Y, et al. Activation of AMPK prevents monocrotaline-induced extracellular matrix remodeling of pulmonary artery. *Med Sci Monit Basic Res.* (2016) 22:27–33. doi: 10.12659/MSMBR.897505
48. Zhai C, Shi W, Feng W, Zhu Y, Wang J, Li S, et al. Activation of AMPK prevents monocrotaline-induced pulmonary arterial hypertension by suppression of NF-κB-mediated autophagy activation. *Life Sci.* (2018) 208:87–95. doi: 10.1016/j.lfs.2018.07.018
49. Lambers C, Qi Y, Eleni P, Costa L, Zhong J, Tamm M, et al. Extracellular matrix composition is modified by β_2-agonists through cAMP in COPD. *Biochem Pharmacol.* (2014) 91:400–8. doi: 10.1016/j.bcp.2014.07.026
50. Lambers C, Costa L, Ying Q, Zhong J, Lardinois D, Dekan G, et al. Aclidinium bromide combined with formoterol inhibits remodeling parameters in lung epithelial cells through cAMP. *Pharmacol Res.* (2015) 102:310–8. doi: 10.1016/j.phrs.2015.09.010
51. Lambers C, Kornauth C, Oberndorfer F, Boehm PM, Tamm M, Klepetko W, et al. Mechanism of anti-remodelling action of treprostinil in human pulmonary arterial smooth muscle cells. *PLoS ONE.* (2018) 13:e0205195. doi: 10.1371/journal.pone.0205195

Conflict of Interest: The authors declare that the research was conducted in the absence of any commercial or financial relationships that could be construed as a potential conflict of interest.

Publisher's Note: All claims expressed in this article are solely those of the authors and do not necessarily represent those of their affiliated organizations, or those of the publisher, the editors and the reviewers. Any product that may be evaluated in this article, or claim that may be made by its manufacturer, is not guaranteed or endorsed by the publisher.

frontiers in Cardiovascular Medicine

ORIGINAL RESEARCH
published: 08 March 2022
doi: 10.3389/fcvm.2022.813215

Novel Nongenetic Murine Model of Hyperglycemia and Hyperlipidemia-Associated Aggravated Atherosclerosis

Susanne Gaul[1†], Khurrum Shahzad[2†], Rebekka Medert[3,4†], Ihsan Gadi[2], Christina Mäder[1], Dagmar Schumacher[3,4], Angela Wirth[3], Saira Ambreen[2], Sameen Fatima[2], Jes-Niels Boeckel[1], Hamzah Khawaja[2], Jan Haas[4,5], Maik Brune[6], Peter P. Nawroth[6], Berend Isermann[2‡], Ulrich Laufs[1‡] and Marc Freichel[3,4*‡]*

[1] Klinik und Poliklinik für Kardiologie, Universitätsklinikum Leipzig, Leipzig, Germany, [2] Department of Diagnostics, Laboratory Medicine, Clinical Chemistry and Molecular Diagnostic, University Hospital Leipzig, Leipzig, Germany, [3] Institute of Pharmacology, Heidelberg University, Heidelberg, Germany, [4] DZHK (German Centre for Cardiovascular Research), partner site Heidelberg/Mannheim, Germany, [5] Department of Internal Medicine III, Heidelberg University, Heidelberg, Germany, [6] Internal Medicine I and Clinical Chemistry, German Diabetes Center (DZD), Heidelberg University, Heidelberg, Germany

Objective: Atherosclerosis, the main pathology underlying cardiovascular diseases is accelerated in diabetic patients. Genetic mouse models require breeding efforts which are time-consuming and costly. Our aim was to establish a new nongenetic model of inducible metabolic risk factors that mimics hyperlipidemia, hyperglycemia, or both and allows the detection of phenotypic differences dependent on the metabolic stressor(s).

Methods and Results: Wild-type mice were injected with gain-of-function PCSK9^{D377Y} (proprotein convertase subtilisin/kexin type 9) mutant adeno-associated viral particles (AAV) and streptozotocin and fed either a high-fat diet (HFD) for 12 or 20 weeks or a high-cholesterol/high-fat diet (Paigen diet, PD) for 8 weeks. To evaluate atherosclerosis, two different vascular sites (aortic sinus and the truncus of the brachiocephalic artery) were examined in the mice. Combined hyperlipidemic and hyperglycemic (HGHCi) mice fed a HFD or PD displayed characteristic features of aggravated atherosclerosis when compared to hyperlipidemia (HCi HFD or PD) mice alone. Atherosclerotic plaques of HGHCi HFD animals were larger, showed a less stable phenotype (measured by the increased necrotic core area, reduced fibrous cap thickness, and less α-SMA-positive area) and had more inflammation (increased plasma IL-1β level, aortic pro-inflammatory gene expression, and MOMA-2-positive cells in the BCA) after 20 weeks of HFD. Differences between the HGHCi and HCi HFD models were confirmed using RNA-seq analysis of aortic tissue, revealing that significantly more genes were dysregulated in mice with combined hyperlipidemia and hyperglycemia than in the hyperlipidemia-only group. The HGHCi-associated genes were related to pathways regulating inflammation (increased *Cd68*, *iNos*, and *Tnfa* expression) and extracellular matrix degradation (*Adamts4* and *Mmp14*). When comparing HFD with PD, the PD aggravated atherosclerosis to a greater extent in mice and showed

OPEN ACCESS

Edited by:
Yanqiao Zhang,
Northeast Ohio Medical University, United States

Reviewed by:
Delphine Gomez,
University of Pittsburgh, United States
Heidi Noels,
Institute for Molecular Cardiovascular Research (IMCAR), Germany

***Correspondence:**
Khurrum Shahzad
khurrum.shahzad@medizin.uni-leipzig.de
Marc Freichel
Marc.freichel@pharma.uni-heidelberg.de

†These authors have contributed equally to this work and share first authorship

‡These authors have contributed equally to this work and share last authorship

Specialty section:
This article was submitted to Atherosclerosis and Vascular Medicine, a section of the journal Frontiers in Cardiovascular Medicine

Received: *11 November 2021*
Accepted: *02 February 2022*
Published: *08 March 2022*

Citation:
Gaul S, Shahzad K, Medert R, Gadi I, Mäder C, Schumacher D, Wirth A, Ambreen S, Fatima S, Boeckel J-N, Khawaja H, Haas J, Brune M, Nawroth PP, Isermann B, Laufs U and Freichel M (2022) Novel Nongenetic Murine Model of Hyperglycemia and Hyperlipidemia-Associated Aggravated Atherosclerosis. Front. Cardiovasc. Med. 9:813215. doi: 10.3389/fcvm.2022.813215

plaque formation after 8 weeks. Hyperlipidemic and hyperglycemic mice fed a PD (HGHCi PD) showed less collagen (Sirius red) and increased inflammation (CD68-positive cells) within aortic plaques than hyperlipidemic mice (HCi PD). HGHCi-PD mice represent a directly inducible hyperglycemic atherosclerosis model compared with HFD-fed mice, in which atherosclerosis is severe by 8 weeks.

Conclusion: We established a nongenetically inducible mouse model allowing comparative analyses of atherosclerosis in HCi and HGHCi conditions and its modification by diet, allowing analyses of multiple metabolic hits in mice.

Keywords: animal model of disease, atherosclerosis, diabetes, hyperglycemia, hyperlipidemia, PCSK9, streptozotocin

INTRODUCTION

Atherosclerotic cardiovascular diseases, including coronary artery disease (CAD) and its complications, are a leading cause of mortality and morbidity globally (1). The risk of CAD is markedly increased in patients with both type 1 and type 2 diabetes mellitus (DM), with CAD events occurring earlier in patients with diabetes mellitus (2). Approximately 10% of total vascular deaths have been attributed to diabetes mellitus and its complications (2). Despite recent studies showing cardioprotective effects of new antidiabetic agents (3), there is a high need to understand how diabetes-associated alterations, particularly the evoked chronic hyperglycemia and metabolic alterations, aggravate atherosclerosis in CAD patients as a basis for the development of more effective treatments for these high-risk patients.

Currently used mouse models of hyperglycemia-associated atherosclerosis require a combination of streptozotocin (STZ) and crossbreeding with either apolipoprotein E ($ApoE^{-/-}$) or low-density lipoprotein receptor ($LDLR^{-/-}$) genetic KO mice, or alternatively, a double crossbreeding of $ApoE^{-/-}$ or $LDLR^{-/-}$ with insulin receptor ($Ins2^{+}$, Akita) mutant mice (4). Some murine models, such as STZ-injected human apoB-expressing transgenic mice (5) or nonobese diabetic (NOD) mice (6), are resistant to the development of atherosclerosis. In addition, crossing mouse lines is time-consuming and costly. In particular, if mouse models harboring other genetic manipulations are to be used, backcrossing becomes a major issue. Thus, there is a high demand to generate an inducible mouse model of multiple metabolic hits, e.g., hyperlipidemia and hyperglycemia, which can be used alone or in combination with other genetic modifications. Bjorklund et al. developed a nongenetic mouse model of atherosclerosis induced by a single injection of recombinant adeno-associated virus (rAAV) encoding a hyperactive proprotein convertase subtilisin/kexin type 9 $(PCSK9)^{D377Y}$ mutant followed by high-fat diet (HFD) feeding that has been used in nondiabetic settings (7, 8) as well as in mature diabetic Akita mice, where they showed diabetic-associated accelerated atherosclerosis (7). Here, we combined injections of rAAV8-$PCSK9^{D377Y}$ and STZ with HFD feeding to generate a rapid and versatile method to induce hyperglycemia-induced aggravation of atherosclerosis in mice.

MATERIALS AND METHODS

All information regarding the materials and reagents is listed in the **Supplementary Major Resources Table**.

Reagents

The following antibodies were used in the current study: rabbit anti-LDLR (R&D Systems, United States); mouse anti-β-actin (Abcepta Inc. United States); goat anti-rabbit IgG HRP (Cell Signaling Technology, Germany); rat anti-MOMA-2, rabbit anti-CD68 and rabbit anti-alpha smooth muscle actin (α-SMA) (Abcam, Germany); and rabbit anti-GAPDH (Sigma–Aldrich, Germany). The following secondary antibodies for immunofluorescence were used: Texas red rabbit anti-mouse IgG (Vector Laboratories, United States) and goat anti-rat IgG (H+L) cross-adsorbed secondary antibody, Alexa Fluor 568 (Thermo Fisher, United States). Other reagents were as follows: BCA reagent (Perbio Science, Germany); vectashield mounting medium with DAPI (Vector Laboratories, United States); nitrocellulose membrane (Bio–Rad, USA) and immobilon^{TM} western chemiluminescent HRP substrate (Merck, Millipore, United States); streptozotocin (Enzo Life Sciences, Germany); Oil-Red O (Sigma–Aldrich, Germany); Accu-Chek test strips, Accu-Check glucometer, and protease inhibitor cocktail (Roche Diagnostics, Germany); albumin fraction V, hematoxylin Gill II, acrylamide, and agarose (Carl ROTH, Germany); aqueous mounting medium (ZYTOMED, Germany); "high-fat diet" (HFD) experimental food (Western-type diet containing 21% fat and 0.21% cholesterol or Paigen diet containing 16% fat, 1.25% cholesterol (TD88137, Ssniff, Germany), and 0.5% sodium cholate, (D12336, Ssniff, Germany); PBS (Life Technologies, Germany); rompun 2% (Bayer, Germany); and ketamine 10% (beta-pharm, Germany).

Mice

Eight-week-old male $LDLR^{-/-}$ (002207) mice were obtained from the Jackson Laboratory (Bar Harbor, ME, USA). Male wild-type C57BL/6N mice were obtained from Charles River Laboratories (Wilmington, MA, USA). Only age-matched male mice were used throughout the study (6–7 mice per group). All animal experiments complied with the ARRIVE guidelines and were carried out in accordance with the

Directive 2010/63/EU guidelines. They were conducted following standards and procedures approved by the local Animal Care and Use Committee (35-9185.81/G-185/19, Regierungspräsidium Karlsruhe, Germany).

Generation and Quantification of rAAV8 Viral Particles

Recombinant rAAV8 vector particles were generated and purified using the iodixanol gradient ultracentrifugation method (9, 10). rAAV8 production was carried out using HEK293T cells. First, 1.8×10^8 HEK293T cells were seeded in a ten-chamber CellStack (Corning, USA) and cultured in DMEM+ Glutamax (Gibco, Thermo Fisher Scientific, USA) supplemented with 10% fetal bovine serum (FBS) and 1% penicillin G/streptomycin. After 48 h, a 1:1:1 molar ratio of pAAV-D377YmPCSK9-bGHpA plasmid (7), the rep-cap AAV8 helper plasmid and an adenoviral helper plasmid was mixed and transfected using polyethylenimine (PEI) (Polyscience, USA). The cells were harvested in 3 ml of lysis buffer and lysed by four freeze–thaw cycles 72 h after transfection. The vector particles were purified using an iodixanol (Progen, Germany) gradient consisting of four phases with decreasing density (60%, 40%, 25%, and 15%) and ultracentrifugation at 50,000 × g for 135 min at 4°C. Approximately 3 ml of the 40% phase, in which predominantly full virus particles accumulated, was recovered with a 27G needle. Finally, the vector solution was buffered into PBS using dialysis tubes (Zeba Spin Desalting Columns 7K MWCO, Thermo Scientific, USA) and concentrated (VivaSpin 10K MWCO, Sartorius, Germany). The vector titer was quantified as genome copy numbers per milliliter using a qPCR SYBR-Green assay (Bio–Rad) and primer sequences specific for the bGHpA sequence (bGHpA-fw 5′ACCTAACTCACTGATCCGAAATTA 3′, bGHpA-rev 5′ATTTCGGATCAGTGAGTTAGG 3′) (11).

Induction of Atherosclerosis by Hypercholesterolemia (HCi) and Hypercholesterolemia and Hyperglycemia (HGHCi) in Mice

Adeno-associated viral vectors encoding the gain-of-function variant D377Y of murine PCSK9 (rAAV8-PCSK9^{D377Y}) under the control of a liver-specific promoter were delivered via a single retro-orbital sinus injection (1.0×10^{11} viral genomes/mouse), and treated animals were fed either a high-fat Western-type diet (HFD, containing 21% fat and 0.21% cholesterol) or a high-cholesterol/high-fat Paigen diet (PD, containing 16% fat, 1.25% cholesterol, and 0.5% sodium cholate) to induce chronic hypercholesterolemia (HCi). Control animals not treated with rAAV8-PCSK9^{D377Y} were fed a high-fat diet (graphic abstract).

To induce chronic hyperglycemia and hypercholesterolemia (HGHCi), mice were injected with streptozotocin (STZ, 60 mg/kg, intraperitoneally, once daily for 5 consecutive days, freshly dissolved in 0.05 M sterile sodium citrate, pH 4.5) 1 week after rAAV8-PCSK9^{D377Y} application. As a control for STZ injections, mice received injections with an equal volume of 0.05 M sodium citrate, pH 4.5, for 5 days. As PCSK9 expression leads to the degradation of low-density lipoprotein (LDL) receptors, we quantitatively compared the development of atherosclerotic plaque formation in the inducible HCi and HGHCi models with that in LDLR$^{-/-}$ mice fed a HFD or PD. LDLR$^{-/-}$ mice served as the established control model for hypercholesterolemia-evoked atherosclerosis (12). Blood glucose levels were monitored twice a week using the Accu-Chek Aviva system (Roche, USA) and maintained in the range of 300–500 mg/dl. Body weight was measured once weekly. HFD and/or hyperglycemia (minimum 300 mg/dl) was maintained for up to 12 or 20 weeks. In the first 4 weeks of the study, some mice in the PD and HFD groups did not tolerate the food. These animals showed a strong reduction in body weight, which was defined as a termination criterion. Consequently, these mice were removed from the study. Mice fed the PD were analyzed after 8–9 weeks due to early mortality in the hyperglycemic group (**Supplementary Figure I**). At the respective study endpoints, mice were sacrificed, and atherosclerotic plaque morphology was analyzed as previously described (13–15).

Analysis of Mice

At the end of the study period (12 or 20 weeks for HFD or 8 weeks for PD), body weight was measured, and the mice were sacrificed (14–16). Blood samples were obtained from the inferior vena cava of anticoagulated mice (500 U of unfractionated heparin, intraperitoneally). Blood was centrifuged at 2,000 × g for 20 min at 4°C, and plasma was snap frozen in liquid nitrogen. Mice were perfused with ice-cold PBS for 10 min, and the heart and aortic arches, including the brachiocephalic arteries, were embedded in O.C.T. compound and snap frozen. Brachiocephalic arteries (from distal to proximal) and upper hearts (aortic sinus) were sectioned at 5- and 10-μm thickness, respectively.

Plasma Analysis

Heparin plasma was prepared for the measurement of plasma lipids. A total of 500–700 μl of blood per mouse was collected in heparin tubes and centrifuged at 3,500 × g for 10 min at room temperature. Plasma was transferred to a 1.5-ml tube and stored at −80°C. Plasma samples of HFD- and PD-fed mice were diluted 1:5 with 0.9% NaCl before cholesterol and triglyceride measurements. Plasma samples were analyzed in the accredited central laboratory of Heidelberg University Hospital using standard operating procedures according to the manufacturers' instructions. Cholesterol and triglycerides were analyzed on a Siemens ADVIA Chemistry XPT System (reagent kits 04993681 and 10697575, respectively). We measured the concentrations of mouse IL-1β by ELISA (R&D Systems) according to the manufacturer's instructions.

Histology

Oil-Red O staining was conducted on frozen cross-sections of the aortic sinus and the truncus of the brachiocephalic artery (BCA) (14, 17). Cryopreserved cross-sections of the brachiocephalic arteries and aortic sinus (5 and 10 μm, respectively) were fixed in ice-cold acetone for 2 min, rinsed twice in ice-cold 1x PBS, and stained with Oil-Red O for 10 min. Sections were rinsed twice with distilled water for 20 seconds and once in running tap water for 10 min. Sections were then counterstained with hematoxylin

for 40 seconds, rinsed in tap water, and mounted with aqueous mounting medium. Movat staining was performed on frozen sections of the aortic sinus and brachiocephalic arteries. Frozen sections (5 μm) were fixed in Bouin's solution at 50°C for 10 min and stained with 5% sodium thiosulfate for 5 min, 1% alcian blue for 15 min, alkaline alcohol for 10 min, Movat's Weigert's solution for 20 min, crocein scarlet acid/fuchsin solution for 1 min, 5% phosphotungstic acid for 5 min and 1% acetic acid for 5 min. Between every staining step, the tissue sections were washed with tap water and distilled water. Sections were then covered with cytoseal mounting medium. Every 15th section (∼90 μm) of the brachiocephalic arteries and aortic sinus were analyzed to quantify the plaque area. The following parameters were determined. (1) The vessel lumen, where the vessel lumen is the area within the blood vessel, consisting of both the remaining open lumen and the plaque area, that does not include the vessel wall itself. (2) Total plaque size, where the size of the plaque comprises all parts of the atherosclerema (fibrous cap, necrotic tissue, fibrous tissue, etc.) within the vessel lumen. (3) The necrotic core (as a percentage) is defined as the area stained blue upon Movat's pentachrome staining and is presented as the percentage of the total plaque size. (4) The fibrous cap, which is the minimal thickness of the fibrous tissue overlaying the necrotic core. If multiple necrotic cores were present within one plaque, the thickness of all fibrous caps was determined, and the average was used for further analyses. (5) the EEL, IEL and media, where the area surrounded by the external elastic lamina (EEL) and the internal elastic lamina (IEL) were measured using bright field images of Oil-Red O-stained BCA images as described previously (18) (**Supplementary Figure II**). The EEL and IEL were encircled (**Supplementary Figure II**), and their areas were measured using Image-Pro Plus software. The media area was calculated by subtracting the IEL area from the EEL area. The lumen area was calculated by subtracting the plaque area from the IEL area. Thickness was measured using ImageJ software using a free-hand tool (13, 14). Cryosections of PD-fed mice were used for picrosirius red staining (Sigma–Aldrich, Germany) according to the manufacturer's instructions. Tissue sections were then stained with picrosirius red solution for 1 h at room temperature. The sections were washed 2 times in acidified water (5 ml of glacial acetic acid to 1 liter of water) and mounted. For histological analysis, images were captured with a Keyence BZ-X810 fluorescence microscope (aortic sinus) and an Olympus Bx43 microscope (brachiocephalic arteries). Image-Pro Plus software (version 6.0) and ImageJ software were used for image analysis (14, 15, 17).

Immunohistochemistry and Immunofluorescence Staining

For immunohistochemistry and immunofluorescence staining, frozen sections of brachiocephalic arteries (BCA) and aortic roots were fixed in ice-cold acetone for 8 min, washed twice with ice-cold PBS and incubated in 2% BSA in PBST for 1 h. Sections were then incubated overnight at 4°C with primary antibodies against α-SMA (1:250) and CD68 (1:1000). Sections incubated without primary antibodies were used as negative controls for background correction. After overnight incubation, the sections were washed three times with PBS followed by incubation with corresponding horseradish peroxidase (HRP)-labeled secondary antibodies. After washing, tissues were counterstained using 3,3′-diaminobenzidine (DAB)/hematoxylin. Primary antibody against MOMA-2 (1:100) was incubated overnight at 4°C, followed by washing three times with PBS and incubation with fluorescently labeled corresponding secondary antibody. Sections incubated without secondary antibody were used as negative controls and for background correction. After washing, nuclear counterstaining was conducted using mounting medium with DAPI. Images were captured and analyzed using a Keyence BZ-X810 all-in-one fluorescence microscope and an Olympus Bx43 microscope (Olympus, Hamburg, Germany) using the same settings in the experimental and control groups. Analyses were performed by two independent blinded investigators. ImageJ software (Version 1.8.0) was used for image analysis.

Immunoblotting

Proteins were isolated, and immunoblotting was performed as previously described (19). Mouse livers were weighed, and an adjusted volume of RIPA buffer containing protease inhibitor cocktail (100 μl/10 mg) was added. Tissue was homogenized mechanically using 20G and 25G needles followed by a 30-min incubation on ice with sequential vortexing. Samples were centrifuged at 12,000 × g for 20 min at 4°C. The supernatant was transferred to a fresh tube, and the protein concentration was determined using the Pierce™ BCA Protein Assay Kit following the manufacturer's instructions and a Varioskan Lux plate reader (Thermo Fisher Scientific, Waltham, MA, USA). Samples were separated using the Mini-PROTEAN® TGX™ Precast Gel 4–15% (Bio–Rad Laboratories, Inc., Hercules CA, USA) and transferred to a nitrocellulose membrane. Membranes were incubated with Invitrogen No-Stain solution for 10 min and blocked for 1 h in 5% low-fat milk dissolved in TBS-T. Incubation with primary anti-mLDLR antibody and anti-β-actin was performed overnight at 4°C. Membranes were incubated with the corresponding secondary rabbit anti-goat immunoglobulin/HRP and goat anti-mouse immunoglobulin/HRP for 1 h at room temperature. Millipore Immobilon Classico Western HRP Substrate was applied to detect the signal using iBright 1500 (Thermo Fisher Scientific, Waltham, MA, USA). Densiometric analysis was performed using ImageJ software.

RNA-Seq, Functional Annotation and Pathway Analysis

RNA was extracted from aortic tissues (comprising the plaque and surrounding tissue) using an RNeasy mini kit (QIAGEN, Germany), and the RNA concentration was measured using a Nanodrop (2000C, Peq lab, Germany). The quality and integrity of RNA were controlled with an Agilent Technologies 2100 Bioanalyzer (Agilent Technologies, Waldbronn, Germany). Expression profiling was performed using RNA sequencing (RNA-seq). An RNA sequencing library was generated from 500 ng of total RNA using a Dynabeads® mRNA DIRECT(tm) Micro Purification Kit (Thermo Fisher) for mRNA purification followed by a NEBNext® Ultra(tm) II Directional RNA Library

Prep Kit (New England BioLabs) according to the manufacturer's protocols. The libraries were sequenced on an Illumina NovaSeq 6000 using a NovaSeq 6000 S2 Reagent Kit (100 cycles, paired-end run) with an average of 3×10^7 reads per RNA sample. A quality report was generated by the FASTQC (version 0.11.8) tool for each FASTQ file. Before alignment to the reference genome, each sequence in the raw FASTQ files was trimmed on base call quality and sequencing adapter contamination using the Trim Galore! wrapper tool (version 0.4.4). Reads shorter than 20 bp were removed from the FASTQ file. Trimmed reads were aligned to the reference genome using the open source short read aligner STAR (version 2.5.2b, https://code.google.com/archive/p/rna-star/) with settings according to the log file. Feature counts were determined using the R package Rsubread (version 1.32.4). Only genes showing counts >5 at least two times across all samples were considered for further analysis (data cleansing). Gene annotation was performed using the R package bioMaRt (version 2.38.0). Before starting the statistical analysis steps, expression data were log2 transformed and normalized according to the 50th percentile (quartile normalization using edgeR, version 3.24.3). Differential gene expression was calculated by the R package edgeR. Statistically significant DEGs ($p < 0.05$ and FDR < 0.05) were sorted and categorized after correcting for multiple hypothesis testing by the Benjamini–Hochberg method. The threshold to identify differentially expressed genes (DEGs) was set to a logFc value of $\pm$ 0.58 (IRI group), resulting in a 1.5-fold expression change. To identify genes differentially regulated by either hyperlipidemia (HCi) or combined hyperglycemia and hyperlipidemia (HGHCi), DEGs between the HFD (control) group and either group were identified based on a minimum logFc difference value of $\pm$0.58. Heatmapper (http://www.heatmapper.ca/) was used to generate heatmaps of gene expression data. Genes shown in the heatmap were sorted based on DEGs in the control group (HFD without PCSK9 injections) based on their log Fc values. For representation purposes, no clustering method was applied, and the z score was used. Venny (version 2.1), an online interactive tool, was used for comparison and identification of overlapping DEGs between different groups. Gene ontology was performed using the online tool Database for Annotation, Visualization and Integrated Discovery (DAVID) version 6.8 bioinformatics package, and Benjamini Hochberg adjustment was applied to all enriched p values to control for multiple testing. All RNA-seq analyses were performed by an independent blinded investigator.

qPCR Analysis

RNA was isolated using an RNeasy Mini kit from Qiagen, and reverse transcription was performed with iScript (Bio–Rad) Mastermix. Primer sequences and probes are listed in the Major Resources Table in the **Supplemental Material**. qPCR analyses were performed with PowerUp SYBR Green Mastermix (Thermo Fisher). All samples were run in duplicate, and relative gene expression was converted using the 2-ΔΔCT method against the mean of two internal control housekeeping genes, namely, hypoxanthine-guanine phosphoribosyl transferase (*Hprt*) and β-2 Microglobulin (*B2m*) for mice. ΔΔCT = (CTexperiment gene–CTmean experiment housekeeping)–(CTcontrol gene–CTmean control housekeeping). The relative gene expression in the control HFD group was set at 1.

Statistical Analysis

Statistical analyses were performed with GraphPad Prism (version 7; GraphPad Software Inc., La Jolla, CA, USA). The significance level was set at $p < 0.05$ for all comparisons. The data are summarized as the mean $\pm$ standard error of the mean (SEM). Comparisons of two groups were analyzed with unpaired Student's T test. Statistical analyses of more than two groups were performed with analysis of variance (ANOVA) and Sidak's *post hoc* comparisons. Differences between groups of a single independent variable were determined using one-way ANOVA, and between two independent variables using two-way ANOVA. The Kolmogorov–Smirnov test or D'Agostino-Pearson normality test was used to determine whether the data were consistent with a Gaussian distribution.

RESULTS

The Combination of Hyperglycemia and Hyperlipidemia Exacerbates Atherosclerosis in PCSK9^{D377Y}-Expressing Mice Fed a High-Fat Diet

To induce hypercholesterolemia (HCi), 8-week-old C57BL/6N mice were administered a single dose of rAAV8-PCSK9^{D377Y} (1.0×10^{11} adeno-associated viral particles, intravenously) 1 week before feeding a high-fat diet (HFD, Western-type diet). Saline-injected mice fed a HFD served as a control for rAAV8-PCSK9^{D377Y} intervention (control HFD). Saline-injected mice with genetic deficiency of low-density lipoprotein receptor (LDLR knockout (KO) on a HFD served as controls for rAAV8-PCSK9^{D377Y} treatment (**Figure 1A**). The mouse group in which hypercholesterolemia evoked by PCSK9 expression and HFD (HCi, single hit) was combined with induction of chronic hyperglycemia using STZ injection (double hit) is hereafter termed HGHCi (high glucose high cholesterol–inducible) throughout the manuscript. For quantification of atherosclerotic plaque formation, mice were euthanized 12 (early time point) or 20 (late time point) weeks after rAAV8-PCSK9^{D377Y} injection and the start of HFD feeding.

As anticipated, rAAV8-PCSK9^{D377Y} administration resulted in a strong reduction in hepatic LDL receptor protein levels compared with saline-injected mice after both 12 and 20 weeks of intervention (**Figures 1B,C**). All mice thrived well, and body weight (**Supplementary Table 1**), blood lipids and glucose levels differed among treatment groups (**Figures 1D,E**). Plasma cholesterol levels were higher in the HGHCi HFD group than in the HCi HFD animals both at the early and late time points (**Figure 1D**); however, plasma triglyceride levels were higher in the HGHCi HFD vs. HCi HFD group only after 20 weeks (**Figure 1F**). Plasma triglyceride, cholesterol and glucose levels were comparable between rAAV8-PCSK9^{D377Y} (HCi HFD group) and LDLR KO mice on a HFD (**Figures 1D–F**).

Analyses of hematoxylin and eosin (H&E)- and Oil-Red O-stained aortic root sections as well as the assessment of the

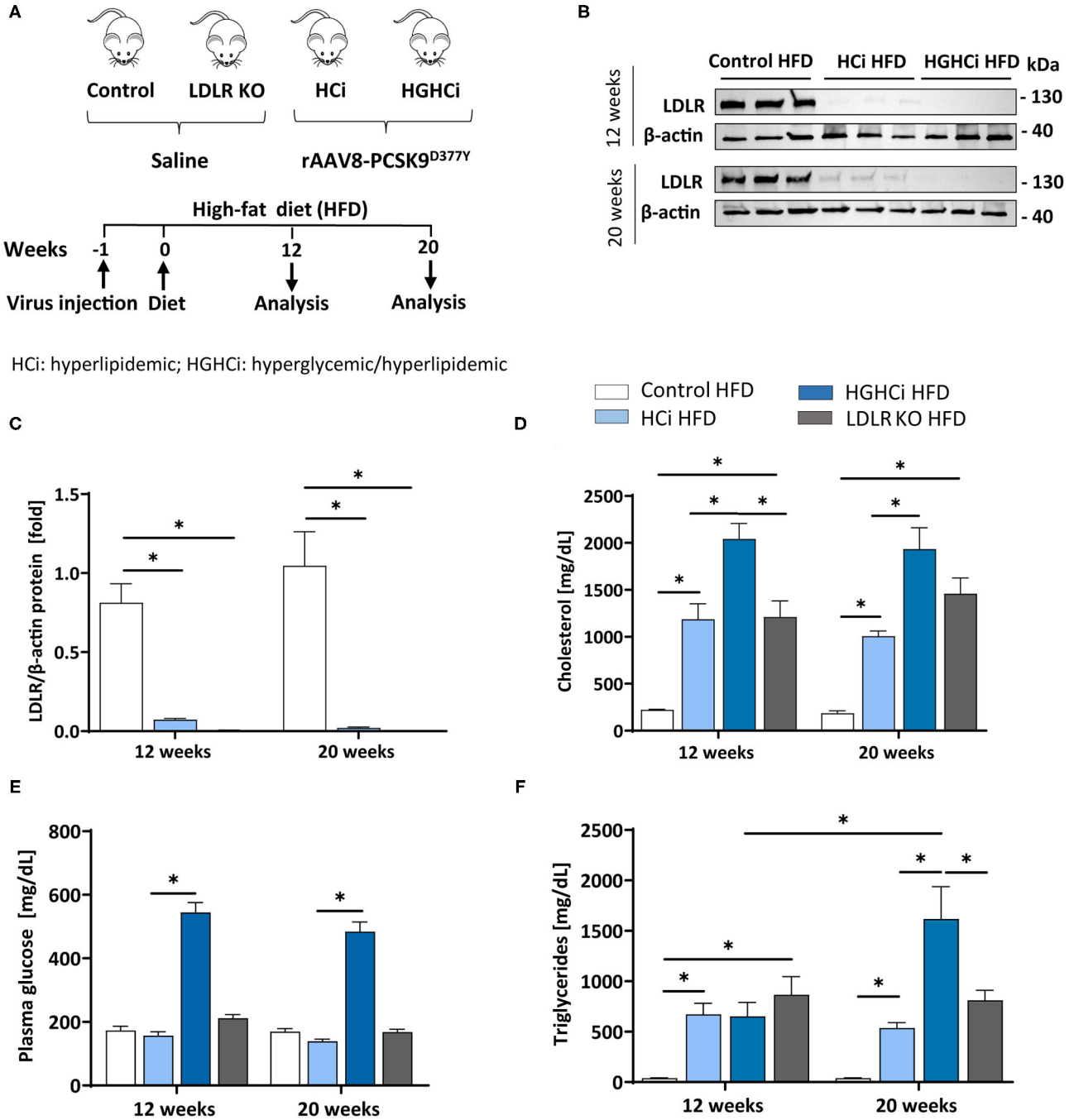

FIGURE 1 | Simultaneous treatment of rAAV8-PCSK9 virus and Streptozotocin induces a hyperlipidemic and hyperglycemic mouse phenotype. **(A)** Schematic summary of the experimental setup. Mice were analyzed after 12 or 20 weeks of interventions initiation. Wild type mice without rAAV8-PCSK9^{D377Y} injection on high-fat diet (HFD, 21% fat, 0.21% cholesterol) was used as control. Mice injected with rAAV8-PCSK9^{D377Y} and fed a HFD are termed HCi HFD (hyperlipidemic), or injected with both rAAV8-PCSK9^{D377Y} and streptozotocin and fed a HFD are termed HGHCi HFD (hyperlipidemic and hyperglycemic). LDLR KO mice on HFD served as atherosclerosis reference control. **(B)** Representative immunoblot of liver lysate showing hepatic protein levels of low-density lipoprotein receptor (LDLR). β-actin was used as loading control. **(C)** Densitometric analysis of LDLR immunoblot was normalized on β-actin and referred to control HFD group which is set at 1. Bar graphs are showing level of **(D)** plasma cholesterol level [mg/dL], **(E)** blood glucose levels [mg/dL] and **(F)** Triglycerides [mg/dL]. Data are presented as mean ± SEM and two-way ANOVA was performed with Sidak's multiple comparison *post-hoc* test (*$p < 0.05$). $N = 6$ for each group.

aortic plaque score (**Supplementary Figure IIIA**) showed larger atherosclerotic plaques at both vascular sites (aortic sinus and BCA) in HGHCi HFD mice than in HCi HFD mice, both at early and late time points (aortic sinus at 12 weeks: HCi HFD 16% vs. HGHCi HFD 37% plaque area; 20 weeks: HCi HFD 29% vs. HGHCi HFD 43% plaque area) (**Figures 2A–D**). Control HFD

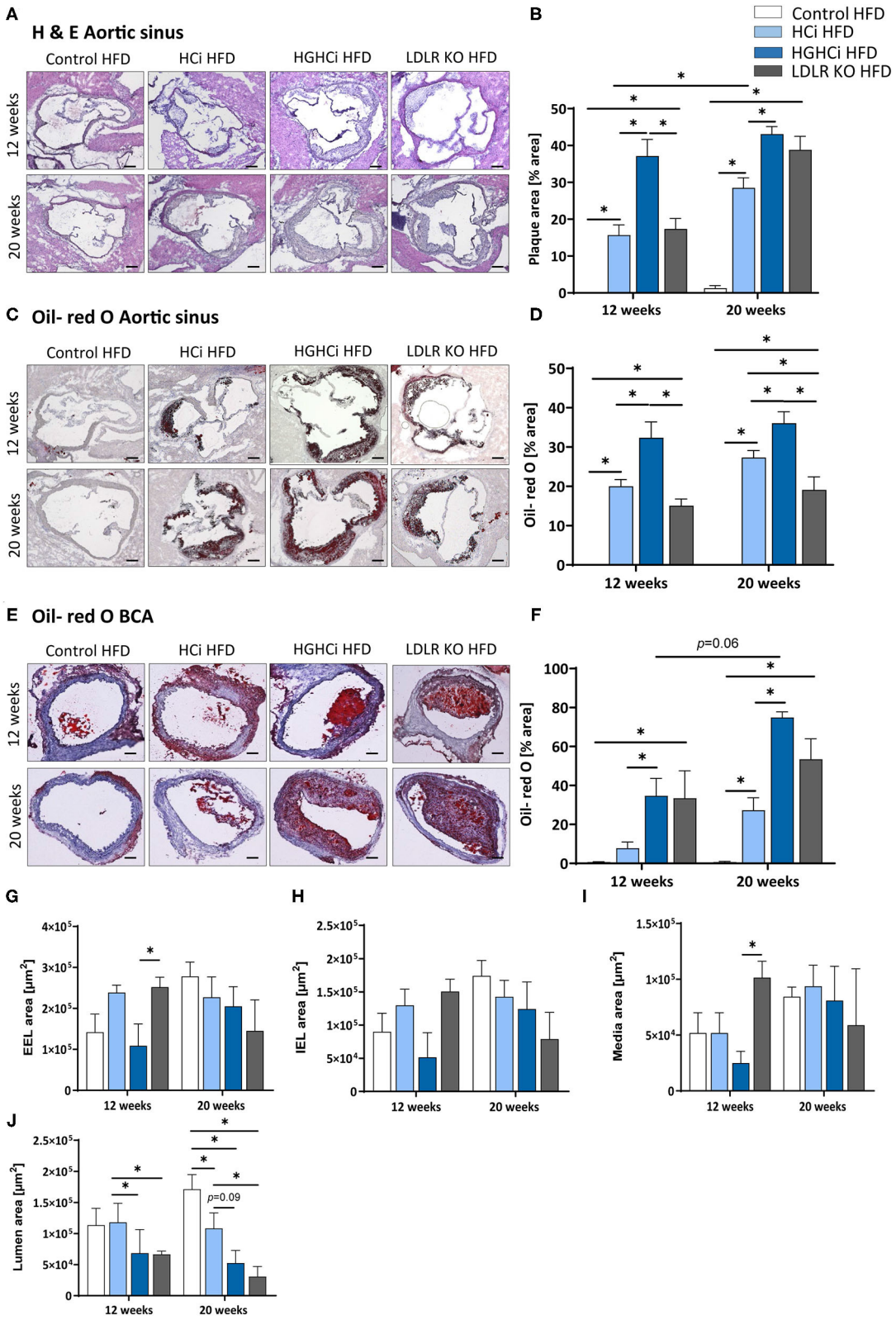

FIGURE 2 | Mice with combined hyperlipidemia and hyperglycemia show larger plaques than hyperlipidemic mice. **(A–D)** Representative histological images showing cross-sections of aortic sinus stained with Hematoxylin/ Eosin [H & E, **(A)**] and bar graphs summarizing data **(B)**. Representative histological images showing aortic

(Continued)

FIGURE 2 | sinus sections stained with Oil-red O **(C)** and bar graphs summarizing data **(D)**. **(E–H)** Representative histological images showing truncus brachiocephalic arteries (BCA) sections stained with Oil-red O **(E)** and bar graphs summarizing data **(F)**. Stainings were imaged at 4 × magnification (scale bar 100 μm) **(A,C,E)**. HFD control 12 and 20 weeks ($N = 7$), HCi HFD 12 and 20 weeks ($N = 5$), and HGHCi HFD 12 and 20 weeks ($N = 6$). Determination of the external elastic lamina (EEL) **(G)**, internal elastic lamina (IEL) **(H)**, media area **(I)** and the lumen area **(J)** from Oil-red O stained cross-sections of the BCA (see **Supplementary Figure II**). Data presented as mean ± SEM and two-way ANOVA were performed with Sidak's multiple comparison *post-hoc* test (*$p < 0.05$). Control HFD: Wild type mice without rAAV8-PCSK9^{D377Y} injection on high fat diet (HFD); HCi HFD: rAAV8-PCSK9^{D377Y} injection plus HFD (hyperlipidemic); HGHCi HFD: rAAV8-PCSK9^{D377Y} and streptozotocin injection and HFD (hyperlipidemic and hyperglycemic).

mice had no lesions, whereas all rAAV8-PCSK9^{D377Y}-injected mice on HFD (HCi HFD group) developed atherosclerosis to a similar extent as LDLR KO mice on HFD after 12 weeks and with no significant difference after 20 weeks (**Figures 2A–I**). In addition, HGHCi mice on a HFD had larger Oil-Red O-stained plaques in the aortic sinus than LDLR KO HFD mice at both time points (**Figures 2C,D**). There was no significant difference in atherosclerotic plaque size between HGHCi HFD and LDLR KO HFD (**Figures 2E,F**) in the truncus brachiocephalic artery (BCA). In contrast to the aortic sinus, we found no significantly increased lesion area in the truncus brachiocephalic artery at 12 weeks, suggesting that the lesion develops earlier in the aortic sinus than in the brachiocephalic artery (**Figures 2E,F**). Image analysis of cross sections of BCA revealed a comparable EEL and IEL-area in HCi HFD and LDLR HFD mice, but thicker media and reduced lumen area in LDLR HFD mice (**Figures 2G–J**), the latter in line with increased plaque size in BCA of the LDLR HFD group (**Figures 2E,F**). In HGHCi HFD mice, EEL, IEL, media, and lumen area were reduced at 12 weeks compared with the HCi-HFD group. After 20 weeks, a reduction in lumen area persisted in HGHCi HFD mice compared with HCi HFD mice (**Figure 2J**), whereas EEL, IEL and media were comparable between the two groups (**Figures 2G–I**).

Less Stable Plaque Phenotypes in Hyperglycemia and Hyperlipidemia (HGHCi) vs. Hyperlipidemic (HCi) Mice

In addition to plaque size, plaque stability is an important determinant of clinical outcome. We therefore evaluated indirect parameters of plaque stability in HCi, HGHCi and LDLR KO mice. Indeed, signs of plaque instability were more pronounced in HGHCi HFD mice than in HCi HFD mice, as evidenced from an increased necrotic core area, thinner fibrous caps, and reduced intraplaque α-SMA-positive cells, while no changes in the total vessel lumen were observed (**Figures 3A–J**, **Supplementary Figure IIIB**). Measurement of indirect markers of plaque stability was analyzed in Movat pentachrome-stained cross-sections of the aortic sinus (**Figures 3A–C**) and truncus brachiocephalic artery (**Figures 3D–F**). While HCi HFD and LDLR KO HFD mice developed few atherosclerotic lesions with increased necrotic core areas in the aortic sinus at 12 weeks (**Figure 3A**), diabetic HGHCi HFD mice showed increased necrotic core areas at this early time point. At 20 weeks, diabetic HGHCi HFD mice had significantly increased necrotic core areas and thinner fibrous caps at both vascular sites (aortic sinus and truncus brachiocephalic artery) compared to HCi HFD and LDLR KO HFD mice (**Figures 3A–F**). Plaque morphology and stability depend in part on the cellular composition of plaques. After 20 weeks, the number of α-SMA-positive cells within plaques of the aortic sinus and truncus brachiocephalic artery of HGHCi HFD mice was significantly decreased compared to that of nondiabetic HCi HFD mice but not of LDLR KO HFD mice (**Figures 3H,J**). There was no difference in α-SMA in the aortic sinus between HGHCi HFD and HCi HFD and LDLR KO mice after 12 weeks (**Figures 3G,H**). In the truncus brachiocephalic artery, HCi HFD mice showed no increased plaque development at 12 weeks, and accordingly, the number of α-SMA-positive cells was very low in this group (**Figures 3I,J**). However, in all other groups (HGHCi and LDLR KO at 12 weeks and HCi, HGHCi, and LDLR KO at 20 weeks), the number of α-SMA-positive cells within plaques was significantly increased compared to the control group in BCA (**Figures 3I,J**). Furthermore, we investigated intraplaque hemorrhage (by the erythrocyte marker protein Ter-119) in HGHCi HFD mice and found no significant differences between the HCi HFD and HGHCi HFD groups (**Supplementary Figure IV**).

Increased IL-1β Plasma Levels and Expression of Proinflammatory Markers in Hyperlipidemic and Hyperglycemic Mice Compared to Hyperlipidemic Mice

As atherosclerosis is a chronic inflammatory disease and cytokines strongly influence disease development, we measured the plasma level of IL-1β and found significantly increased IL-1β levels in the diabetic HGHCi HFD group (5.8 pg/mL at 12 weeks; 5.6 pg/mL at 20 weeks) compared to the HCi HFD (1.9 pg/mL at 12 weeks; 1.8 pg/mL at 20 weeks) and LDLR KO HFD mice (3.5 pg/mL at 12 weeks; 2.6 pg/mL at 20 weeks) at both study time points (**Figure 4A**), indicating that systemic inflammation is already increased during early plaque development. As IL-1β was already increased after 12 weeks in the HGHCi HFD group, we analyzed the expression of marker genes of macrophage polarization (*Cd68* and *iNos* as M1 macrophage polarization marker genes; *Arg1* and *Fizz* as M2 marker genes) in the aorta of 12-week-old mice and found increased expression of M1 macrophage markers (*Cd68* and *iNos*) (**Figures 4B,C**) and correspondingly lower gene expression of M2 macrophage markers (*Arg1* and *Fizz*) (**Figures 4D,E**). In line with these results, the content of MOMA-2-positive cells was increased in plaques of the truncus brachiocephalic artery (BCA) (**Figures 4F,G**) of HGHCi HFD mice. In the aortic sinus, the number of MOMA-2-positive cells was elevated in all groups exhibiting atherosclerosis (HCi, HGHCi, and LDLR KO at 12 and 20 weeks) (**Figures 4H,I**).

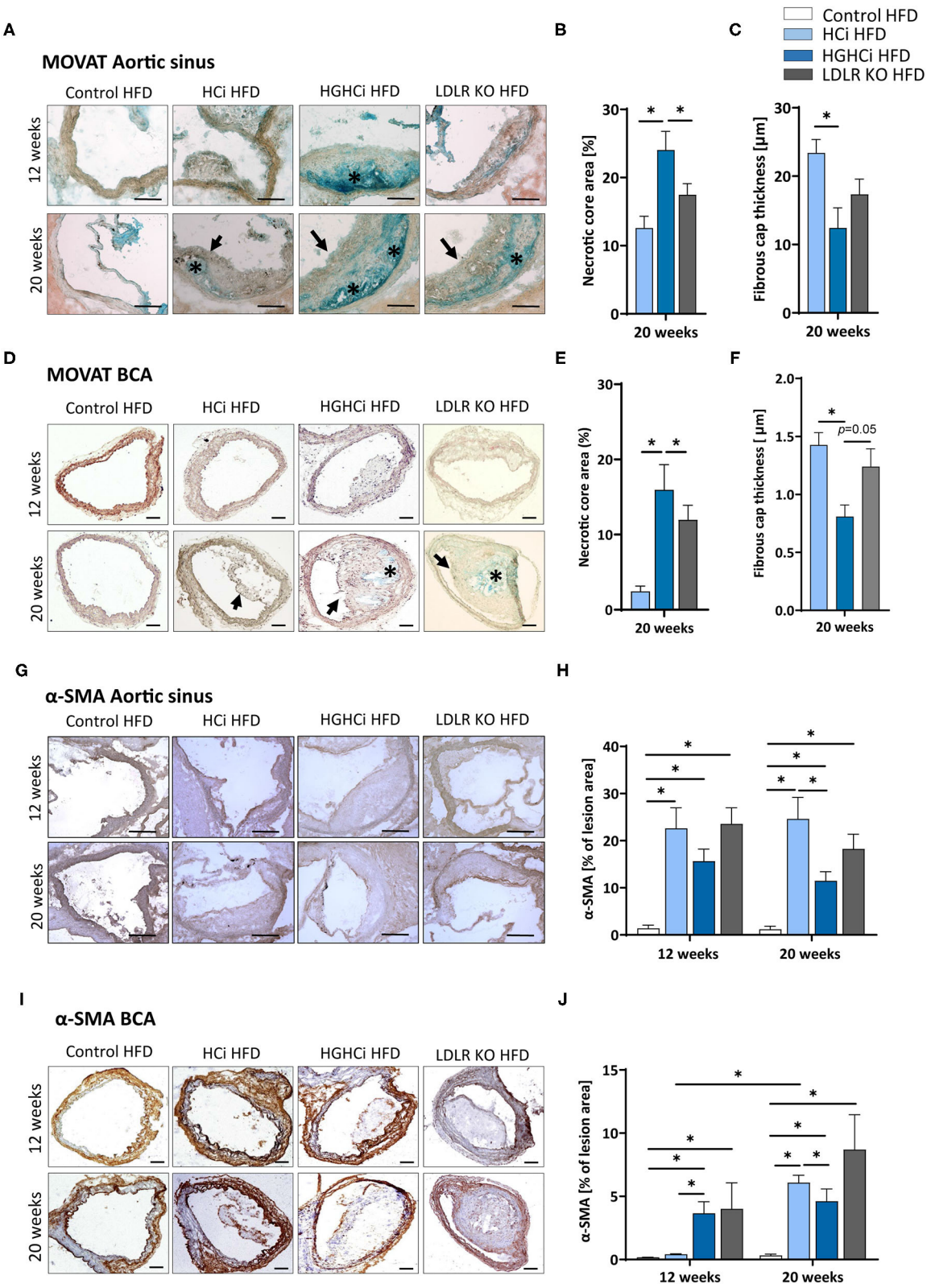

FIGURE 3 | Increased necrotic core, reduced fibrous cap thickness, and α-SMA positive cells within plaques of hyperlipidemic and hyperglycemic mice as compared to hyperlipidemic mice. **(A–C)** Representative images showing MOVATs pentachrome staining of cross-sections of the aortic sinus (**A**, scale bar 100 µm, 10x

(Continued)

FIGURE 3 | magnification). Bar graphs summarizing morphometric analyses of MOVATs stained images for necrotic core area (indicated by *) **(B)** and fibrous cap thickness (indicated by a black arrow) **(C)**. Necrotic core area is depicted as % of total lesion area. **(D–F)** Representative images showing MOVATs pentachrome staining of cross-sections of truncus brachiocephalic arteries (BCA) (**D**, scale bar 200 μm, 4x magnification). Bar graphs summarizing morphometric analyses of MOVATs stained images for necrotic core area (indicated by *) **(E)** and fibrous cap thickness thickness (indicated by a black arrow) **(F)**. Data presented as mean + SEM and one-way ANOVA was performed with Sidak's multiple comparison *post-hoc* test (*$p < 0.05$). **(G,H)** Representative images showing immunohistochemical staining for α-SMA positive cells detected by HRP-DAB reaction (brown) on cross-sections of aortic sinus **(G,H)** (scale bar 100 μm, 10x magnification) and truncus brachiocephalic arteries **(I,J)** (scale bar 200 μm, 4x magnification). Corresponding bar graphs summarizing data **(H,J)**. Data presented as mean + SEM and two-way ANOVA were performed with Sidak's multiple comparison *post-hoc* test (*$p < 0.05$). HFD control 12 and 20 weeks ($N = 7$), HCi HFD 12 and 20 weeks ($N = 5$), and HGHCi HFD 12 and 20 weeks ($N = 6$). Control HFD: Wild type mice without rAAV8-PCSK9^{D377Y} injection on high fat diet (HFD); HCi HFD: rAAV8-PCSK9^{D377Y} injection plus HFD (hyperlipidemic); HGHCi HFD: rAAV8-PCSK9^{D377Y} and streptozotocin injection and HFD (hyperlipidemic and hyperglycemic).

Taken together, the observed shift toward increased lesion area, inflammation and necrotic core area and reduced fibrous cap thickness and α-SMA content suggests that plaque stability is reduced in HGHCi HFD mice compared to HCi HFD mice (20, 21).

Identification of HGHCi-Specific Transcriptional Responses in the Aorta

We next aimed to identify transcriptional signatures that are engaged in the vasculature by combining chronic hyperlipidemia and hyperglycemia to generate hypotheses about signaling pathways contributing to larger but unstable plaques in HGHCi HFD mice. To this end, we conducted unbiased gene expression analyses (RNAseq) in the cohorts of control HFD, HCi HFD and HGHCi HFD mice at 12 weeks. In aortic tissue of HCi HFD mice, the expression of 942 genes was induced compared to the control mice solely on a HFD (**Figure 5A**). Conversely, gene expression in the aorta of HGHCi HFD mice was strikingly different from that of HCi HFD mice. Gene expression of a large set of genes was dysregulated in HGHCi HFD mice. Thus, in aortic tissue of HGHCi HFD mice, the expression of 2759 genes was induced compared to aortic samples of saline-treated HFD-fed mice (control HFD) (**Figure 5A**). A total of 418 genes showed similar expression in both HGHCi HFD and HCi HFD mice, and differential regulation of 2341 genes could be specifically assigned to combined hyperglycemia and hyperlipidemia.

We next performed functional annotation analysis to study the gene pathways that are specifically engaged in the vessels of the HGHCi HFD group and observed that combined hyperglycemia plus hyperlipidemia led to significant changes in the expression of genes encoding signaling molecules involved in inflammation, intracellular lipid transport, cholesterol metabolic processes, extracellular matrix (ECM) degradation, and cellular metabolism (**Figure 5B**). We further performed gene ontology analysis on genes that were induced in aortic tissue of HCi HFD and HGHCi HFD mice. Gene ontology analysis of differentially expressed genes revealed that combined hyperglycemia and hyperlipidemia led to the upregulation of genes involved in the inflammatory response (GO: 0006954) (**Figure 5C**) and ECM degradation (GO: 0030198) (**Figure 5F**). We further investigated the expression of TNFa, which is a central mediator of inflammatory reactions and plays an important role in atherogenesis, and found that it was significantly upregulated in the HGHCi HFD mice compared to HCi HFD mice at both study time points (**Figures 5D,E**). Moreover, we analyzed additional matrix metalloproteinases, such as Mmp14 and Adamts4 (A Disintegrin and Metalloproteinase with Thrombospondin motifs 4), in the RNA-seq data and corroborated their dysregulation by qPCR analysis (**Figures 5G–J**). Both marker genes were upregulated in HGHCi HFD mice compared to HCi HFD mice after both 12 and 20 weeks (**Figures 5G–J**).

The Paigen Diet Accentuates Atherosclerosis and Promotes Plaque Instability in Mice With Combined Hyperglycemia and Hyperlipidemia

We next tested the atherosclerosis model following induction of combined hyperglycemia and hyperlipidemia (HGHCi) in mice fed a Paigen diet (PD), which leads to higher plasma cholesterol levels (7) and might thus further exacerbate the formation of atherosclerotic plaques. PD-fed mice were treated with the same batch and dose of rAAV8-PCSK9^{D377Y}, and LDLR KO mice on the PD served as a reference for comparison. Saline-injected mice fed the PD served as a control for rAAV8-PCSK9^{D377Y} intervention. Hyperlipidemic and hyperlipidemic plus hyperglycemic mice on the PD are hereafter called HCi PD and HGHCi PD mice, respectively, for simplicity. In HGHCi PD mice, we observed an increased mortality (25% in week 8, i.e., 5 out of 20 mice died in this group (**Supplementary Figure IA**). Based on these incidences, it was decided that the remaining animals in this group should be sacrificed and analyzed 8–9 weeks after induction of combined hypercholesterolemia and hyperglycemia, since the 12- and 20-week time points chosen for the HGHCi group on HFD might not have been reached. Thus, mice from all groups on the PD diet were euthanized 8–9 weeks after rAAV8-PCSK9^{D377Y} injection to quantify atherosclerosis (**Figure 6A**). Hepatic LDL receptor protein expression was already abrogated at this time point compared with saline-injected mice (control PD) (**Figures 6B,C**). As expected, body weight (**Supplementary Table 1**), plasma cholesterol levels and blood glucose levels differed among the HCi and HGHCi PD groups (**Figures 6D–F),** while HCi PD mice and LDLR KO PD mice did not differ regarding cholesterol, triglyceride and glucose levels (**Figures 6D–F**). In a preliminary pilot study, we compared the plasma cholesterol levels of the HGHCi PD group with STZ-treated mice (STZ PD) and citrate-treated controls (citrate PD) fed a Paigen diet (**Supplementary Figure V**). Notably, mice with STZ-evoked hyperglycemia and on a high-cholesterol, high-fat Paigen diet (without AAV-mPCSK9 treatment) did not exhibit an increase in plasma cholesterol (**Supplementary Figure V).**

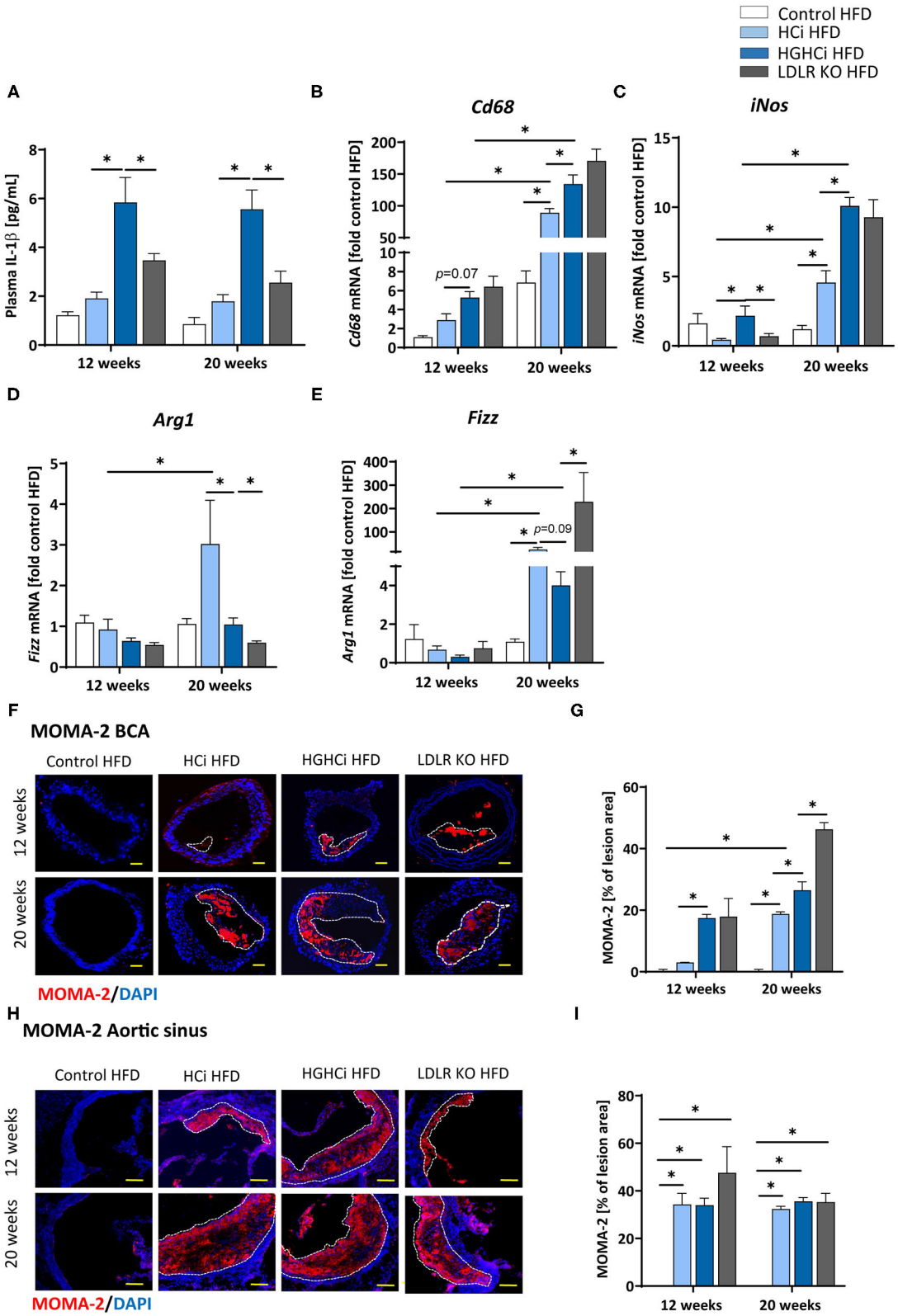

FIGURE 4 | Increased IL-1β plasma level and expression of pro-inflammatory markers in hyperlipidemic and hyperglycemic mice as compared to hyperlipidemic mice. **(A)** Plasma IL-1β [pg/mL] level at 12 and 20 weeks. **(B–E)** mRNA expression of macrophage polarization markers. M1 macrophage polarization is depicted by *CD68*

(Continued)

FIGURE 4 | (B) and *iNos* **(C)** mRNA expression. *Arg1* **(D)** and *Fizz* **(E)** mRNA expression levels are shown as M2 polarization marker. The data are presented as mean ± SEM and were normalized on the mean of two housekeeping genes (*Hprt* and *B2m*). HFD control served as reference and was set at 1. **(F,G)** Representative images showing immunofluorescence staining of truncus brachiocephalic arteries (BCA) sections for macrophage marker MOMA-2 (**F**, MOMA-2 = red; DAPI nuclear counterstain = blue; plaque region is circled with a white dashed line, scale bar 200 μm, 4 × magnification) and bar graphs summarizing data **(G)**. Representative images showing immunofluorescence staining of cross-sections of aortic sinus for MOMA-2 (**H**, MOMA-2 = red; DAPI nuclear counterstain = blue; plaque region is circled with a white dashed line, scale bar 100 μm, 10 × magnification) and bar graphs summarizing data **(I)**. Data presented as mean ± SEM and two-way ANOVA were performed with Sidak's multiple comparison *post-hoc* test (*$p < 0.05$). HFD control 12 and 20 weeks ($N = 7$), HCi HFD 12 and 20 weeks ($N = 5$), and HGHCi HFD 12 and 20 weeks ($N = 6$). Control HFD: Wild type mice without rAAV8-PCSK9^{D377Y} injection on high fat diet (HFD); HCi HFD: rAAV8-PCSK9^{D377Y} injection plus HFD (hyperlipidemic); HGHCi HFD: rAAV8-PCSK9^{D377Y} and streptozotocin injection and HFD (hyperlipidemic and hyperglycemic).

Application of the Paigen diet exacerbated atherosclerosis in both HGHCi PD and HCi PD mice compared to the corresponding groups on the HFD diet ($p < 0.05$). Interestingly, the aortic root plaque sizes of HGHCi PD and HCi PD mice at 8 weeks (**Figures 6G–J**) were comparable to those of HGHCi and HCi mice on a HFD at 20 weeks (**Figure 2A**). Consistent with data from the HFD groups, signs of plaque instability were more pronounced in HGHCi PD mice than in HCi-PD mice as measured by decreased collagen deposition (picrosirius red staining) and increased plaque CD68-positive cells in HGHCi PD mice in comparison with HCi PD mice (**Figures 7A–D**). Taken together, these data suggest that the PD aggravates atherosclerosis in mice and shows plaque formation after 8 weeks, therefore representing a direct inducible diabetic atherosclerosis model with more aggravated atherosclerosis than HGHCi HFD.

DISCUSSION

The most frequently used models to study diabetes mellitus-associated atherosclerosis in mice rely on genetically modified models. Thus, mouse studies evaluating diabetes-associated atherosclerosis rely on ApoE$^{-/-}$ or LDLR$^{-/-}$ mice, where hypercholesterolemia is combined with chronic hyperglycemia following beta-cell destruction by injection of streptozotocin (STZ) or viral infection (22) or by crossbreeding with mouse strains carrying a point mutation in the gene encoding insulin leading to a misfolding of the proinsulin 2 protein (Ins2^{+}/Akita) (4, 23). Induction of hyperglycemia with STZ led to higher plasma cholesterol levels and showed significant acceleration of atherosclerotic lesion formation in ApoE$^{-/-}$ and LDLR$^{-/-}$ mice compared to nondiabetic ApoE$^{-/-}$ and LDLR$^{-/-}$ controls (6, 24–30). Additionally, the severe hyperglycemia in Ins2^{+}/Akita mice crossbred with ApoE$^{-/-}$ and LDLR$^{-/-}$ leads to a pronounced increase in atherosclerosis and non-HDL cholesterol and triglyceride levels compared to those of nonhyperglycemic control mice (4, 31, 32). Although these genetic models are useful tools for studying diabetic complications, intensive crossbreeding of these mouse lines is required. This becomes even more laborious and time-consuming when diabetic long-term complications are to be induced in knockout mouse lines for evaluation of the causal role of the gene of interest under certain metabolic conditions. Concomitant induction of both hypercholesterolemia and hyperglycemia at discrete time points in a given mouse line has not been reported.

Here, we describe a novel strategy to induce an atherosclerosis model aggravated by concomitant induction of hyperglycemia without the necessity of genetic germline engineering but via rAAV8-mediated gene transfer of mutant PCSK9^{D377Y} in hepatocytes in combination with STZ-evoked beta-cell destruction (HGHCi). Comparison of plasma cholesterol levels shows increased cholesterol levels in the HCi model, which increase further by additional induction of hyperglycemia in the HGHCi model. The additional increase in cholesterol levels is a consequence of the two-hit model because induction of hyperglycemia alone does not increase plasma cholesterol levels. The increased plasma cholesterol levels in the diabetic mice (HGHCi group) are part of the phenotype of our model and resemble findings in previous studies (7, 26, 28, 29). Dyslipidemia aggravated by hyperglycemia is independent of whether the diabetes was induced by STZ injection or genetically (e.g., InsAkita mutant mice). Increased cholesterol levels in the diabetic mice most likely reflect decreased lipoprotein clearance, and as such, they may reflect an important feature of diabetes-associated dyslipidemia. Thus, Goldberg et al. demonstrated that the plasma cholesterol levels of STZ-induced diabetic LDLR$^{-/-}$ mice were twice those of nondiabetic control mice. The authors observed an increase in both VLDL and LDL. VLDL in plasma was more enriched in cholesterol, and both VLDL and LDL had high levels of ApoE (30). Further lipidomics analyses are required to define the lipid profile in diabetic and nondiabetic mice with PCSK9^{D377Y}-induced dyslipidemia. We cannot differentiate whether the increased cholesterol level or other factors (e.g., the elevated systemic inflammation) or their combination is responsible for the increased plaque progression in HGHCi mice compared to HCi mice. However, STZ treatment alone did not lead to elevated LDL cholesterol in our study (**Supplementary Figure V**) or in previous studies (6), where it was shown that diabetic mice are resistant to atherosclerosis even in the presence of a high-fat diet. To address the question of whether the additional increase in LDL cholesterol (evoked by hyperglycemia in PCSK9^{D377Y}-treated mice) is indeed responsible for increased plaque progression, one might design a study using a selective LDL-lowering therapy without an effect on hyperglycemia (e.g., by HMG-CoA reductase inhibitors) in the HGHCi model. The influence of systemic inflammation on increased plaque progression in the HGHCi group compared to the HCi group could be investigated with an anti-inflammatory therapy (e.g., by the anti-IL-1β antibody canakinumab). Studies addressing such mechanistic links will be required in the future.

Furthermore, we show that combined hyperlipidemia and hyperglycemia led to a significant enhancement of atherosclerotic plaque formation compared to mice in which

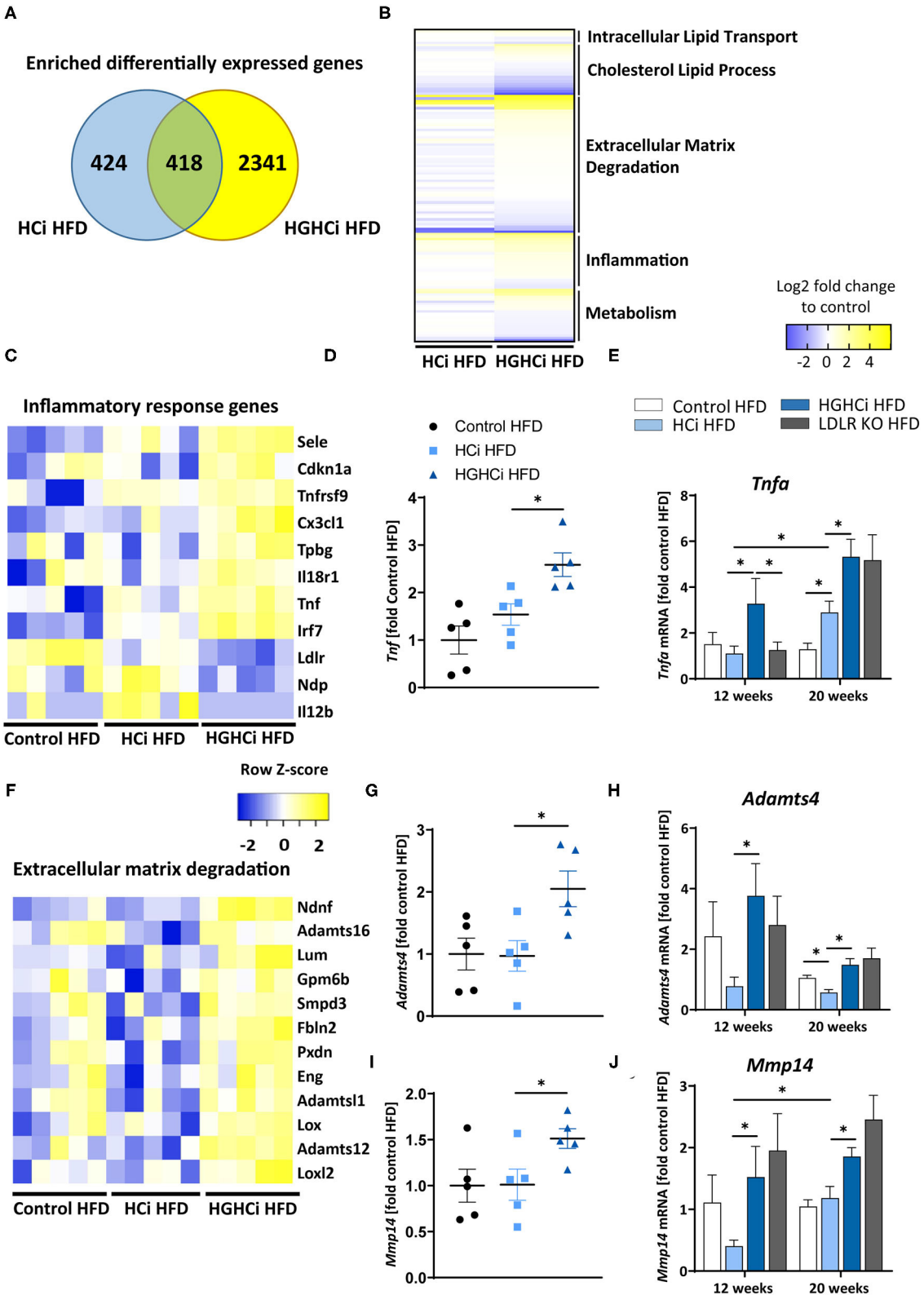

FIGURE 5 | Combined hyperglycemia and hyperlipidemia induce large set of differentially expressed genes and activates inflammatory response and extracellular matrix degradation pathways. RNA sequencing in aortic tissue of control HFD, HCi HFD and HGHCi HFD mice after 12 weeks. Wild type mice without

(Continued)

FIGURE 5 | AAV8-PCSK9^{D377Y} injection on high fat diet (control HFD) or injected with rAAV8-PCSK9^{D377Y} and on HFD (hyperlipidemic, HCi HFD) or injected with both rAAV8-PCSK9^{D377Y} and streptozotocin and fed HFD (hyperlipidemic and hyperglycemic, HGHCi HFD). **(A)** Venn diagram showing overlap of genes significantly changed in HGHCi HFD or HCi HFD mice in relation to gene expression in control HFD mice. **(B)** Heat map summarizing differentially expressed gene (DEGs) identified by RNA sequencing and DEGs related biological processes using Gene Ontology and EnrichR analysis. **(C)** Heat map showing list of DEGs related to inflammatory response (GO: 0006954) using Gene Ontology and EnrichR analysis. **(D)** *Tnf* expression level (FPKM normalized on Control HFD) from RNASeq at 12 weeks ($N = 5$/ group) and its **(E)** qPCR validation in all groups at both time points (12 and 20 weeks). **(F)** Heat map showing list of DEGs related to extracellular matrix degradation pathways (GO: 0030198) using Gene Ontology and EnrichR analysis. RNA expression levels of selected ECM degradation genes *Adamts4* **(G,H)** and *Mmp14* **(I,J)** (FPKM normalized on Control HFD) from RNASeq at 12 weeks ($N = 5$/ group) **(G,I)** and its qPCR validation **(H,J)** in all groups at both time points (12 and 20 weeks). Gene count values larger than the average control are represented in yellow, while lower counts than the average control are represented in blue. Whenever transcript values are close to the control value, samples are colored in white. The data are presented as mean ± SEM and qPCR data were normalized on the mean of two housekeeping genes (*Hprt* and *B2m*). HFD control served as reference control. Two-way ANOVA was performed with Sidak's multiple comparison *post-hoc* test ($^*p < 0.05$).

hypercholesterolemia was induced without hyperglycemia (HCi). The HCi model in rAAV8-mediated mutant PCSK9^{D377Y}-expressing mice leads to downregulation of hepatic LDL receptor expression and the development of atherosclerotic lesions. The lesion phenotypes closely resemble those in the established LDL-receptor knockout mouse model. Mice in the HGHCi treatment group displayed larger plaques than norrmoglycemic HCi mice on the same diet and LDLR knockout mice (after 12 weeks). Treatment-induced systemic atherosclerosis (e.g., in the aortic sinus and in the brachiocephalic artery) and inflammation were measured by increased plasma levels of IL-1β. The plaque phenotypes induced by HGHCi compared to HCi mice are characterized by increased necrotic core area and decreased fibrous cap thickness. Plaques are characterized by increased gene expression of M1 macrophage markers and MOMA-2-positive cells as well as a reduced number of α-SMA-positive cells (at 20 weeks). A comparably increased amount of α-SMA-positive cells was observed in HGHCi HFD and LDLR KO HFD mice at 12 weeks in the aortic sinus and BCA, which is characteristic of early lesion development (33, 34). In HCi HFD mice, the number of α-SMA-positive cells was also increased in the aortic sinus after 12 weeks but not in the BCA, where a small plaque size was observed at that time point. The reason for these differences in plaque size and α-SMA-positive cell content between the aortic sinus and BCA in HCi mice after 12 weeks can be explained by an earlier development of lesions at the aortic sinus, which has been described in other studies (35–37). Whether the earlier onset of α-SMA-positive cell proliferation and migration in the BCA of HGHCi HFD and LDLR KO mice is due to stronger systemic inflammation indicated by the higher increase in IL-1β levels compared with HCi HFD mice at 12 weeks needs to be investigated in future studies. Taken together, these data show that the novel HGHCi model provides an overview of plaque development and progression at two locations in the aorta to study interventions aiming to improve plaque size and, importantly, plaque stability.

A similar severity of atherosclerosis was observed with the Paigen diet, albeit much earlier, at 8 weeks Post-intervention initiation, compared to 20 weeks with the HFD. It has been reported that the addition of cholate in combination with a high cholesterol and high fat content in the Paigen diet boosts hypercholesterolemia by facilitating fat and cholesterol absorption, resulting in very early fatty streak lesions in the aortic root and proximal aorta in C57BL/6 mice (38). Thus, our findings are in line with previous work in genetic models, demonstrating that hyperglycemia promotes unstable plaques in both ApoE$^{-/-}$ and LDLR$^{-/-}$ mice (14, 39–41). Our results identify the HGHCi PD model using a Paigen diet as a novel option for specific experimental setups where strong plaque formation and progression are needed at an early time point.

Our unbiased gene expression analysis revealed that combined hyperlipidemia and hyperglycemia (HGHCi) dysregulates a large set of genes (i.e., 2341 genes) in the atherosclerotic aorta compared to hyperlipidemia alone (HCi). The aortic tissue gene expression profile of HGHCi mice fed a HFD differed markedly from HCi HFD mice. Among the pathways that were most prominently affected were the inflammatory response, ECM degradation and metabolism. Upregulated proinflammatory genes, such as *Cx3cl1* (or fractalkine) and *Il18r1*, have been shown to be involved in atherogenesis. *Cx3cl1* is a chemokine and exerts cytotoxic effects on the endothelium. Its membrane-bound form promotes adhesion of rolling leukocytes onto the vessel wall, while in its soluble form, it serves as a potent chemoattractant for CX3CR1-expressing cells. Therefore, it affects the context and stability of the atherosclerotic plaque. Blocking the CX3CL1/CX3CR1 pathway in *in vivo* studies ameliorated the severity of atherosclerosis (42). Il18r1 is a member of the interleukin receptor family and is expressed on T-lymphocytes but also on cell types associated with atherogenesis, such as macrophages, endothelial cells, and smooth muscle cells (43). After binding its ligand IL-18, it leads to the expression of IFNγ via the NF-kB-mediated signaling pathway (44). High expression of IL18R is found in plaque-resident macrophages and endothelial cells in humans (45).

The increased expression of genes related to ECM degradation (e.g., *Mmp14* and *Adamts4*) is consistent with previous findings showing that glucose-induced advanced glycation end products (RAGE) mediate modification of the components of the ECM and accelerate atherosclerosis under diabetic conditions (46–49). The ECM degradation genes *Mmp14* and *Adamts4* were shown to play key roles in plaque stability. Loss of *Adamts4* in ApoE KO mice increased plaque stability (50), and ADAMTS4 expression in humans was upregulated during carotid atherosclerotic plaque development. Furthermore, ADAMTS4 serum levels were associated with increased plaque vulnerability (51). Metalloproteinases (MMPs), such as *Mmp14*, play an important role in the pathogenesis of atherosclerosis by participating in vascular remodeling, smooth muscle cell migration, and plaque

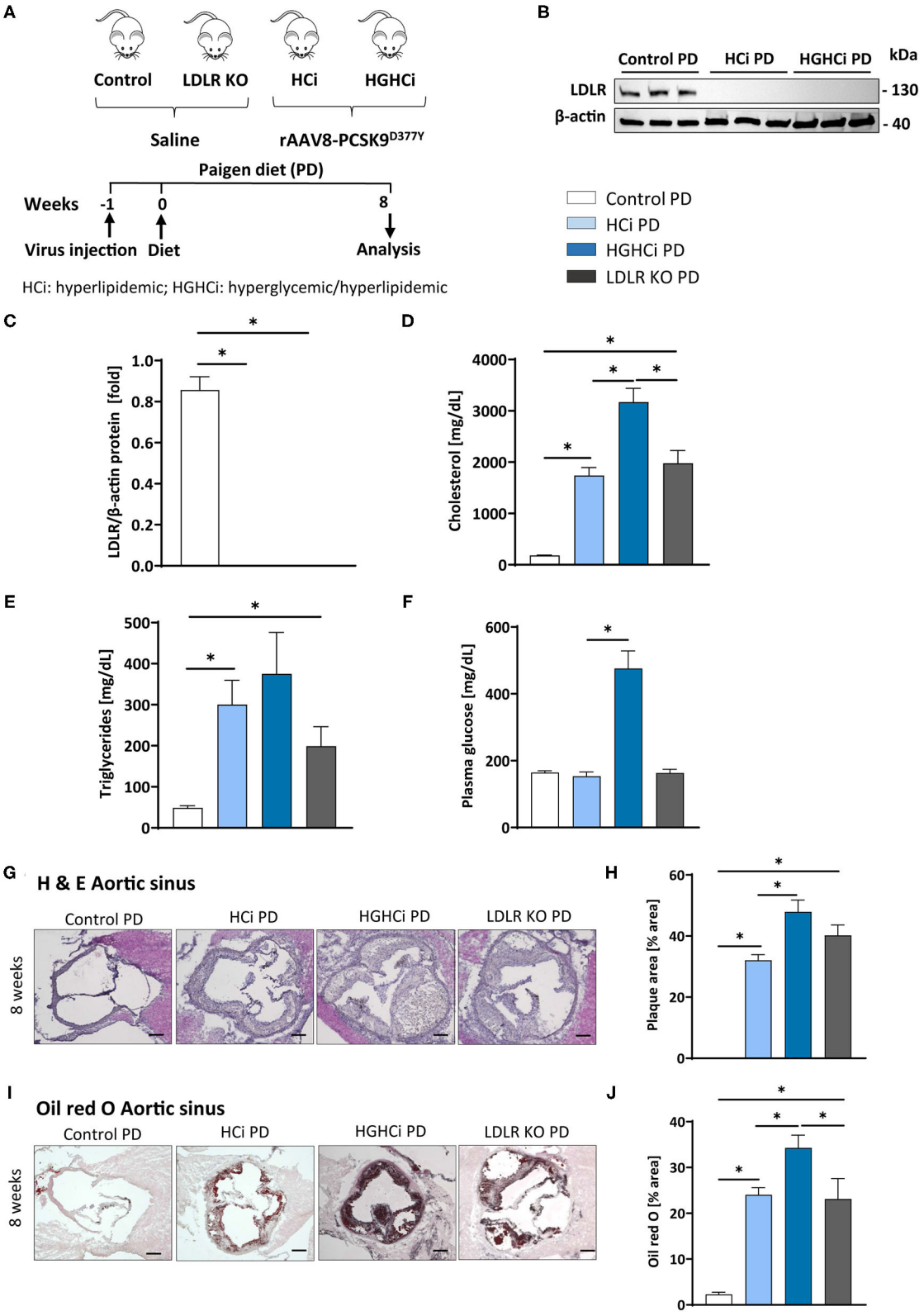

FIGURE 6 | Paigen diet accelerates plaque formation after 8 weeks in the rAAV8-PCSK9 streptozotocin induced hyperglycemic atherosclerosis mouse model. **(A)** Schematic summary of the experimental setup. Mice were analyzed after 8 weeks of interventions initiation. **(B)** Representative immunoblot showing hepatic protein

(Continued)

FIGURE 6 | levels of low-density lipoprotein receptor (LDLR). β-actin was used as loading control and bar graphs summarizing data. Data were normalized on β-actin and control PD mice were set at 1 **(C)**. Bar graphs summarizing data of plasma cholesterol level [mg/dL, **D**], triglycerides [mg/dL, **E**), and blood glucose levels [mg/dL, **F**]. **(G–J)** Representative histological images showing aortic sinus sections stained with Hematoxylin Eosin [H & E, **(G)**] and bar graphs summarizing data **(H)**. Representative histological images showing aortic sinus sections stained with Oil-red-O **(I)** and bar graphs summarizing data **(J)**. Data presented as mean ± SEM and one-way ANOVA was performed with Sidak's multiple comparison *post-hoc* test (*$p < 0.05$). Scale bar 200 μm. Control paigen diet (PD) ($N = 6$), HCi PD ($N = 6$), HGHCi PD ($N = 6$), LDLR KO PD ($N = 5$). Control PD: Wild type mice without rAAV8-PCSK9^{D377Y} injection on PD; HCi PD: mice injected with rAAV8-PCSK9^{D377Y} and fed PD (hyperlipidemic); HGHCi PD: mice injected with both rAAV8-PCSK9^{D377Y} and streptozotocin and fed PD (hyperlipidemic and hyperglycemic); LDLR KO PD: LDLR KO mice fed PD.

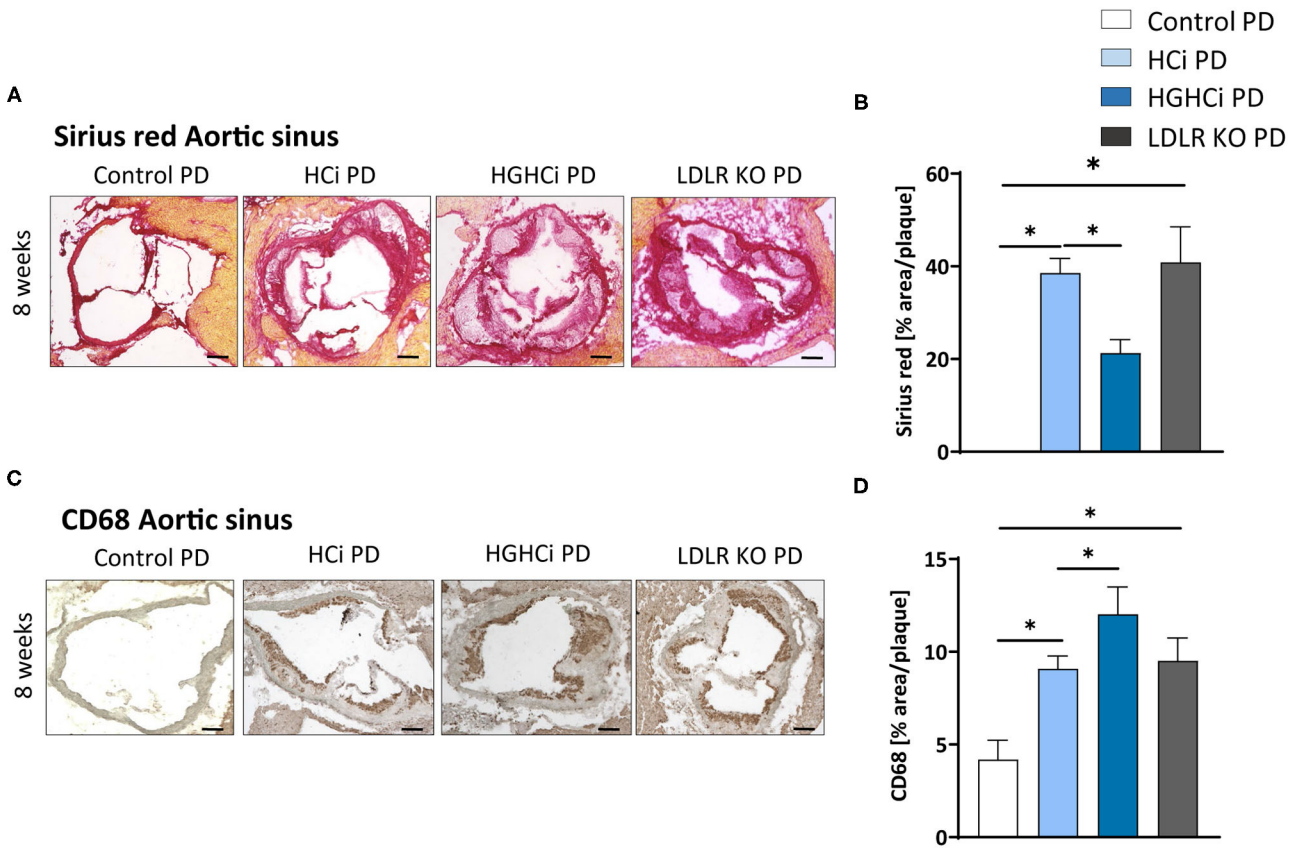

FIGURE 7 | Hyperlipidemic and hyperglycemic mice fed a Paigen diet (PD) show less collagen and increased inflammation within aortic plaques compared to hyperlipidemic mice. **(A)** Representative images showing picrosirius red staining for collagen in aortic sinus sections and bar graphs summarizing data **(B)**. Scale bar 200 μm. **(C)** Representative images showing immunohistochemical staining of aortic sinus sections for macrophages marker CD68 (positive cells detected by HRP-DAB reaction, brown) and bar graphs summarizing data **(D)**. Data presented as mean ± SEM and one-way ANOVA was performed with Sidak's multiple comparison *post-hoc* test (*$p < 0.05$). Scale bar 100 μm. Control paigen diet (PD) ($N = 7$), HCi PD ($N = 4$), HGHCi PD ($N = 4$), LDLR KO PD ($N = 5$). Control PD: Wild type mice without rAAV8-PCSK9^{D377Y} injection on PD; HCi PD: mice injected with rAAV8-PCSK9^{D377Y} and fed PD (hyperlipidemic); HGHCi PD: mice injected with both rAAV8-PCSK9^{D377Y} and streptozotocin and fed PD (hyperlipidemic and hyperglycemic); LDLR KO PD: LDLR KO mice fed PD.

disruption. Mmp14 is recognized as a prominent member of this family, causes pericellular degradation and has the ability to activate other matrix metalloproteinases. It is further detected at high levels in atherosclerotic plaques (52).

Genes involved in inflammation, such as *Tnfa*, *Cd68,* and *iNos,* were shown to be upregulated in HGHCi HFD mice compared to HCi HFD mice, which has been described in previous studies where their expression is one of the key drivers in atherosclerosis-associated chronic inflammation in arterial blood vessels (48). The progression of atherosclerosis correlates directly with a local increase in TNF-α production in atherosclerotic plaques and blood (53). The expression data may provide a helpful resource for researchers using this model and suggest that this nongenetic model will be suitable for studying important aspects of the emerging crosstalk between inflammatory signaling, glucose metabolism and lipoprotein metabolism (23, 54–56).

Limitations of the Study

In this study, only male mice were analyzed. As reported previously, rAAV8-PCSK9^{D377Y}-evoked hypercholesterolemia was 3-fold lower in females than in males (57), and consequently, the extent of atherosclerosis development can be expected

to be lower or delayed. To characterize the development of atherosclerosis in our HGHCi model in females, new studies will be required in the future to elucidate sex-specific effects in this model. The aim of the study was to develop and characterize novel models of hyperlipidemia and hyperglycemic-associated atherosclerosis. Plasma lipid levels were not identical between groups. Due to the study design, a cohort with only STZ injection was not included, as hyperglycemia induced by STZ treatment or lymphocytic choriomeningitis virus (LCMV) infection alone is not sufficient to induce atherosclerosis development in mice (29, 39). Hence, conclusions about the impact of isolated hyperglycemia on the atherosclerotic plaque phenotype cannot be drawn from the current study.

Atherosclerosis development in mice and humans differs in several parameters, including lipoprotein metabolism. In mice, cholesterol is transported mainly in HDL particles due to a lack of cholesteryl ester transfer protein (CETP) expression, whereas humans show high CETP expression, which results in high LDL cholesterol levels (23). Furthermore, wild-type mice have significantly lower total cholesterol levels than humans, which may explain why they do not develop atherosclerosis under natural conditions. In recent years, atherosclerosis-associated genes have been identified and used to generate genetically modified mouse models that are used in atherosclerosis research. The two most commonly used genetic models in atherosclerosis research are the Apoe$^{-/-}$ and Ldlr$^{-/-}$ models (58, 59). Among other parameters, the models exhibit critical differences in cholesterol and lipid metabolism, which makes their use highly dependent on the scientific question. Apolipoprotein E (apoE) binds to chylomicrons and VLDL in plasma and acts as a ligand that initiates uptake of the remnants via the LDL receptor, thereby removing them from the circulation. Deletion of apoE in Apoe$^{-/-}$ mice results in an increase in cholesterol levels by the accumulation of chylomicrons and VLDL (58). In contrast, in the Ldlr$^{-/-}$ model, deletion of LDLR results in an increase in cholesterol levels by the accumulation of plasma LDL, which is much more comparable to the human situation than the elevation of plasma VLDL in Apoe$^{-/-}$ mice (23). Expression of the rAAV-PCSK9^{D377Y} (7) used in this study leads to increased degradation of LDLR, which is comparable to the deletion of LDLR in the Ldlr$^{-/-}$ model. Additionally, in this inducible model, there is an increase in total cholesterol due to the accumulation of LDL particles, and it was shown by Roche-Molina et al. (60) that the lipoprotein profiles of Ldlr$^{-/-}$ mice and rAAV-PCSK9^{D377Y}-treated animals fed a HFD are very similar. Therefore, both the Ldlr$^{-/-}$ and the inducible rAAV-PCSK9^{D377Y} models are currently most suitable for cholesterol and lipid metabolism studies investigating processes in human atherosclerosis development (23). In addition to their lipoprotein profile, the models also differ from the human disease pattern with respect to the sites at which lesions develop. In humans, disease-relevant plaques develop preferentially in the coronary arteries, carotid arteries and peripheral arteries of the legs and arms, whereas in mouse models, lesions are mainly found in the aortic sinus, aortic arch and brachiocephalic artery (23). In addition, the extent of plaque development in mice is reduced, and large vulnerable plaques are often absent compared to humans; thus, plaque ruptures are rarely observed in genetic mouse models, which in turn occur in humans at advanced stages of atherosclerosis and lead to atherothrombotic vessel occlusions (23, 58, 59).

In the future, it may be possible to use the HGHCi model in preclinical animal models that more accurately reflect human lipoprotein metabolism and the development and progression of atherosclerotic lesions in coronary arteries than the already established genetic mouse models. Both STZ-mediated hyperglycemia in pigs and rabbits (61, 62) and PCSK9 gain-of-function overexpression-induced hypercholesterolemia in pigs (63) have been demonstrated to date and, in combination, may achieve further important disease-relevant findings about diabetes-accelerated atherosclerosis and inflammation in humans.

CONCLUSION

We describe a novel nongenetically inducible mouse model using a defined treatment with gain-of-function PCSK9 viral particles, streptozotocin and high-fat diets. The detailed characterization of the plaque phenotypes and the expression analysis indicate that this new experimental approach can be used to study the clinically important pathogenesis of atherosclerosis in hyperglycemia and hyperlipidemia and can be induced at any given time point to prevent or therapeutically interfere with the development of atherosclerosis under diabetic conditions.

DATA AVAILABILITY STATEMENT

RNA-seq raw data have been deposited to the NCBI BioSample database under accessions SAMN23410354, SAMN23410355, and SAMN23410356. Datasets can be explored interactively at: https://www.ncbi.nlm.nih.gov/biosample/23410354; https://www.ncbi.nlm.nih.gov/biosample/23410355; https://www.ncbi.nlm.nih.gov/biosample/23410356.

ETHICS STATEMENT

The animal study was reviewed and approved by Regierungspräsidium Karlsruhe, Germany. Approval number: 35-9185.81/G-185/19.

AUTHOR CONTRIBUTIONS

SG, KS, and RM interpreted the experimental work and prepared the manuscript. AW, RM, SG, IG, and DS performed and conducted the *in vivo* experiments. SG, IG, and CM performed histological analyses and figure preparation. JH, J-NB, and HK performed RNAseq analysis. SA and SF assisted in histology. BI and UL interpreted the data and assisted in manuscript preparation. MF designed the study and assisted in manuscript preparation. All authors contributed to the article and approved the submitted version.

FUNDING

This work was supported by grants of the Deutsche Forschungsgemeinschaft (including project S03 of the Collaborative Research Centers (SFB) SFB1118 (MF), and IS-67/5-3, IS-67/8-1, IS-67/11-1, and CRC854/B26 to BI, SH 849/4-1 to KS, and DFG grant 361210922/GRK2408 to BI and KS.

ACKNOWLEDGMENTS

We thank Sonja Talmon, Beate Hilbert, Christin Richter, Manuela Ritzal, Anja Barnikol-Oettler, and Kathrin Deneser for excellent technical support. We certify that all persons who have made substantial contributions to the manuscript, but who do not fulfill authorship criteria, are named in the acknowledgments section and have provided the corresponding author with written permission to be named in the manuscript.

SUPPLEMENTARY MATERIAL

The Supplementary Material for this article can be found online at: https://www.frontiersin.org/articles/10.3389/fcvm.2022.813215/full#supplementary-material

REFERENCES

1. Benjamin EJ, Muntner P, Alonso A, Bittencourt MS, Callaway CW, Carson AP et al. Correction to: Heart disease and stroke statistics-2019 update: a report from the American heart association. *Circulation*. (2020) 141:e33. doi: 10.1161/CIR.0000000000000746
2. Raghavan S, Vassy JL, Ho Y-L, Song RJ, Gagnon DR, Cho K, et al. Diabetes mellitus-related all-cause and cardiovascular mortality in a national cohort of adults. *J Am Heart Assoc*. (2019) 8:e011295. doi: 10.1161/JAHA.118.011295
3. Fang M, Wang D, Coresh J, Selvin E. Trends in diabetes treatment and control in U.S. adults, 1999–2018. *N Engl J Med*. (2021) 384:2219–28. doi: 10.1056/NEJMsa2032271
4. Jun JY, Ma Z, Segar L. Spontaneously diabetic Ins2+/Akita:apoE-deficient mice exhibit exaggerated hypercholesterolemia and atherosclerosis. *Am J Physiol Endocrinol Metab*. (2011) 301:E145-E154. doi: 10.1152/ajpendo.00034.2011
5. Voyiaziakis E, Goldberg IJ, Plump AS, Rubin EM, Breslow JL, Huang LS. ApoA-I deficiency causes both hypertriglyceridemia and increased atherosclerosis in human apoB transgenic mice. *J Lipid Res*. (1998) 39:313–21. doi: 10.1016/S0022-2275(20)33893-1
6. Keren P, George J, Keren G, Harats D. Non-obese diabetic (NOD) mice exhibit an increased cellular immune response to glycated-LDL but are resistant to high fat diet induced atherosclerosis. *Atherosclerosis*. (2001) 157:285–92. doi: 10.1016/S0021-9150(00)00685-7
7. Bjorklund MM, Hollensen AK, Hagensen MK, Dagnaes-Hansen F, Christoffersen C, Mikkelsen JG, et al. Induction of atherosclerosis in mice and hamsters without germline genetic engineering. *Circ Res*. (2014) 114:1684–9. doi: 10.1161/CIRCRESAHA.114.302937
8. Goettsch C, Hutcheson JD, Hagita S, Rogers MA, Creager MD, Pham T, et al. A single injection of gain-of-function mutant PCSK9 adeno-associated virus vector induces cardiovascular calcification in mice with no genetic modification. *Atherosclerosis*. (2016) 251:109–18. doi: 10.1016/j.atherosclerosis.2016.06.011
9. Grieger JC, Choi VW, Samulski RJ. Production and characterization of adeno-associated viral vectors. *Nat Protoc*. (2006) 1:1412–28. doi: 10.1038/nprot.2006.207
10. Zolotukhin S, Byrne BJ, Mason E, Zolotukhin I, Potter M, Chesnut K, et al. Recombinant adeno-associated virus purification using novel methods improves infectious titer and yield. *Gene Ther*. (1999) 6:973–85. doi: 10.1038/sj.gt.3300938
11. Jungmann A, Leuchs B, Rommelaere J, Katus HA, Müller OJ. Protocol for efficient generation and characterization of adeno-associated viral vectors. *Hum Gene Ther Methods*. (2017) 28:235–46. doi: 10.1089/hgtb.2017.192
12. Ishibashi S, Goldstein JL, Brown MS, Herz J, Burns DK. Massive xanthomatosis and atherosclerosis in cholesterol-fed low density lipoprotein receptor-negative mice. *J Clin Invest*. (1994) 93:1885–93. doi: 10.1172/JCI117179
13. Zhou Q, Bea F, Preusch M, Wang H, Isermann B, Shahzad K, et al. Evaluation of plaque stability of advanced atherosclerotic lesions in Apo E-deficient mice after treatment with the oral factor Xa inhibitor rivaroxaban. *Mediators Inflamm*. (2011) 2011:432080. doi: 10.1155/2011/432080
14. Shahzad K, Gadi I, Nazir S, Al-Dabet M'dM, Kohli S, Bock F, et al. Activated protein C reverses epigenetically sustained $p66^{Shc}$ expression in plaque-associated macrophages in diabetes. *Commun Biol*. (2018) 1:104. doi: 10.1038/s42003-018-0108-5
15. Seehaus S, Shahzad K, Kashif M, Vinnikov IA, Schiller M, Wang H, et al. Hypercoagulability inhibits monocyte transendothelial migration through protease-activated receptor-1-, phospholipase-Cbeta-, phosphoinositide 3-kinase-, and nitric oxide-dependent signaling in monocytes and promotes plaque stability. *Circulation*. (2009) 120:774–84. doi: 10.1161/CIRCULATIONAHA.109.849539
16. Shahzad K, Thati M, Wang H, Kashif M, Wolter J, Ranjan S, et al. Minocycline reduces plaque size in diet induced atherosclerosis via p27(Kip1). *Atherosclerosis*. (2011) 219:74–83. doi: 10.1016/j.atherosclerosis.2011.05.041
17. Schuster S, Rubil S, Endres M, Princen HM, Boeckel J-N, Winter K, et al. Anti-PCSK9 antibodies inhibit pro-atherogenic mechanisms in APOE*3Leiden.CETP mice. *Sci Rep*. (2019) 9:11079. doi: 10.1038/s41598-019-47242-0
18. Mohanta S, Yin C, Weber C, Hu D, Habenicht A JR. Aorta atherosclerosis lesion analysis in hyperlipidemic mice. *Bio-protocol*. (2016) 6. doi: 10.21769/BioProtoc.1833
19. Gaul S, Leszczynska A, Alegre F, Kaufmann B, Johnson CD, Adams LA, et al. Hepatocyte pyroptosis and release of inflammasome particles induce stellate cell activation and liver fibrosis. *J Hepatol*. (2021) 74:156–67. doi: 10.1016/j.jhep.2020.07.041
20. Harman JL, Jørgensen HF. The role of smooth muscle cells in plaque stability: therapeutic targeting potential. *Br J Pharmacol*. (2019) 176:3741–53. doi: 10.1111/bph.14779
21. Doran AC, Meller N, McNamara CA. Role of smooth muscle cells in the initiation and early progression of atherosclerosis. *Arterioscler Thromb Vasc Biol*. (2008) 28:812–9. doi: 10.1161/ATVBAHA.107.159327
22. Shen X, Bornfeldt KE. Mouse models for studies of cardiovascular complications of type 1 diabetes. *Ann N Y Acad Sci*. (2007) 1103:202–17. doi: 10.1196/annals.1394.004
23. Oppi S, Lüscher TF, Stein S. Mouse models for atherosclerosis research—which is my line? *Front Cardiovasc Med*. (2019) 6:46. doi: 10.3389/fcvm.2019.00046
24. Tse J, Martin-McNaulty B, Halks-Miller M, Kauser K, DelVecchio V, Vergona R, et al. Accelerated atherosclerosis and premature calcified cartilaginous metaplasia in the aorta of diabetic male Apo E knockout mice can be prevented by chronic treatment with 17β-estradiol. *Atherosclerosis*. (1999) 144:303–13. doi: 10.1016/S0021-9150(98)00325-6
25. Vikramadithyan RK, Hu Y, Noh H-L, Liang C-P, Hallam K, Tall AR, et al. Human aldose reductase expression accelerates diabetic atherosclerosis in transgenic mice. *J Clin Invest*. (2005) 115:2434–43. doi: 10.1172/JCI24819
26. Lewis P, Stefanovic N, Pete J, Calkin AC, Giunti S, Thallas-Bonke V, et al. Lack of the antioxidant enzyme glutathione peroxidase-1 accelerates atherosclerosis in diabetic apolipoprotein E–deficient mice. *Circulation*. (2007) 115:2178–87. doi: 10.1161/CIRCULATIONAHA.106.664250
27. Vedantham S, Noh H, Ananthakrishnan R, Son N, Hallam K, Hu Y, et al. Human aldose reductase expression accelerates atherosclerosis in diabetic

apolipoprotein E–/– Mice. *Arterioscler Thromb Vasc Biol*. (2011) 31:1805–13. doi: 10.1161/ATVBAHA.111.226902
28. Park L, Raman KG, Lee KJ, Lu Y, Ferran LJ, Chow WS, et al. Suppression of accelerated diabetic atherosclerosis by the soluble receptor for advanced glycation endproducts. *Nat Med*. (1998) 4:1025–31. doi: 10.1038/2012
29. Hammad SM, Hazen-Martin DJ, Sohn M, Eldridge L, Powell-Braxton L, Won W, et al. Nephropathy in a hypercholesterolemic mouse model with streptozotocin-induced diabetes. *Kidney Blood Press Res*. (2003) 26:351–61. doi: 10.1159/000073942
30. Goldberg IJ, Hu Y, Noh H-L, Wei J, Huggins LA, Rackmill MG, et al. Decreased lipoprotein clearance is responsible for increased cholesterol in LDL receptor knockout mice with streptozotocin-induced diabetes. *Diabetes*. (2008) 57:1674–82. doi: 10.2337/db08-0083
31. Zhou C, Pridgen B, King N, Xu J, Breslow JL. Hyperglycemic Ins2AkitaLdlr–/– mice show severely elevated lipid levels and increased atherosclerosis: a model of type 1 diabetic macrovascular disease[S]. *J Lipid Res*. (2011) 52:1483–93. doi: 10.1194/jlr.M014092
32. Engelbertsen D, To F, Dunér P, Kotova O, Söderberg I, Alm R, et al. Increased inflammation in atherosclerotic lesions of diabetic *Akita-LDLr*$^{-/-}$ mice compared to nondiabetic *LDLr*$^{-/-}$ mice. *Exp Diabetes Res*. (2012) 2012:176162. doi: 10.1155/2012/176162
33. Bennett MR, Sinha S, Owens GK. Vascular smooth muscle cells in atherosclerosis. *Circ Res*. (2016) 118:692–702. doi: 10.1161/CIRCRESAHA.115.306361
34. Dzau VJ, Braun-Dullaeus RC, Sedding DG. Vascular proliferation and atherosclerosis: new perspectives and therapeutic strategies. *Nat Med*. (2002) 8:1249–56. doi: 10.1038/nm1102-1249
35. Paigen B, Morrow A, Holmes PA, Mitchell D, Williams RA. Quantitative assessment of atherosclerotic lesions in mice. *Atherosclerosis*. (1987) 68:231–40. doi: 10.1016/0021-9150(87)90202-4
36. Reddick RL, Zhang SH, Maeda N. Atherosclerosis in mice lacking apo E. Evaluation of lesional development and progression. *Arterioscler Thromb J Vasc Biol*. (1994) 14:141–7. doi: 10.1161/01.ATV.14.1.141
37. Tangirala RK, Rubin EM, Palinski W. Quantitation of atherosclerosis in murine models: correlation between lesions in the aortic origin and in the entire aorta, and differences in the extent of lesions between sexes in LDL receptor-deficient and apolipoprotein E-deficient mice. *J Lipid Res*. (1995) 36:2320–8. doi: 10.1016/S0022-2275(20)39713-3
38. Getz GS, Reardon CA. Diet and murine atherosclerosis. *Arterioscler Thromb Vasc Biol*. (2006) 26:242–9. doi: 10.1161/01.ATV.0000201071.49029.17
39. Johansson F, Kramer F, Barnhart S, Kanter JE, Vaisar T, Merrill RD, et al. Type 1 diabetes promotes disruption of advanced atherosclerotic lesions in LDL receptor-deficient mice. *Proc Natl Acad Sci USA*. (2008) 105:2082–7. doi: 10.1073/pnas.0709958105
40. Bornfeldt KE. Uncomplicating the macrovascular complications of diabetes: the 2014 Edwin Bierman Award Lecture. *Diabetes*. (2015) 64:2689–97. doi: 10.2337/db14-1963
41. Renard CB, Kramer F, Johansson F, Lamharzi N, Tannock LR, Herrath MG von, et al. Diabetes and diabetes-associated lipid abnormalities have distinct effects on initiation and progression of atherosclerotic lesions. *J Clin Invest*. (2004) 114:659–68. doi: 10.1172/JCI200417867
42. Apostolakis S, Spandidos D. Chemokines and atherosclerosis: focus on the CX3CL1/CX3CR1 pathway. *Acta Pharmacol Sin*. (2013) 34:1251–6. doi: 10.1038/aps.2013.92
43. Gerdes N, Sukhova GK, Libby P, Reynolds RS, Young JL, Schönbeck U. Expression of interleukin (IL)-18 and functional IL-18 receptor on human vascular endothelial cells, smooth muscle cells, and macrophages: implications for atherogenesis. *J Exp Med*. (2002) 195:245–57. doi: 10.1084/jem.20011022
44. Wang J, Sun C, Gerdes N, Liu C, Liao M, Liu J, et al. Interleukin 18 function in atherosclerosis is mediated by the interleukin 18 receptor and the Na-Cl co-transporter. *Nat Med*. (2015) 21:820–6. doi: 10.1038/nm.3890
45. Mallat Z, Corbaz A, Scoazec A, Besnard S, Lesèche G, Chvatchko Y, et al. Expression of interleukin-18 in human atherosclerotic plaques and relation to plaque instability. *Circulation*. (2001) 104:1598–603. doi: 10.1161/hc3901.096721
46. Ihara Y, Egashira K, Nakano K, Ohtani K, Kubo M, Koga J-i, et al. Upregulation of the ligand-RAGE pathway via the angiotensin II type I receptor is essential in the pathogenesis of diabetic atherosclerosis. *J Mol Cell Cardiol*. (2007) 43:455–64. doi: 10.1016/j.yjmcc.2007.07.044
47. Bu D-x, Rai V, Shen X, Rosario R, Lu Y, D'Agati V, et al. Activation of the ROCK1 branch of the transforming growth factor-beta pathway contributes to RAGE-dependent acceleration of atherosclerosis in diabetic ApoE-null mice. *Circ Res*. (2010) 106:1040–51. doi: 10.1161/CIRCRESAHA.109.201103
48. Soro-Paavonen A, Watson AM, Li J, Paavonen K, Koitka A, Calkin AC, et al. Receptor for advanced glycation end products (RAGE) deficiency attenuates the development of atherosclerosis in diabetes. *Diabetes*. (2008) 57:2461–9. doi: 10.2337/db07-1808
49. Wang Z, Jiang Y, Liu N, Ren L, Zhu Y, An Y, et al. Advanced glycation end-product Nε-carboxymethyl-Lysine accelerates progression of atherosclerotic calcification in diabetes. *Atherosclerosis*. (2012) 221:387–96. doi: 10.1016/j.atherosclerosis.2012.01.019
50. Kumar S, Chen M, Li Y, Wong FH, Thiam CW, Hossain MZ, et al. Loss of ADAMTS4 reduces high fat diet-induced atherosclerosis and enhances plaque stability in ApoE–/– mice. *Sci Rep*. (2016) 6:31130. doi: 10.1038/srep31130
51. Dong H, Du T, Premaratne S, Zhao CX, Tian Q, Li Y, et al. Relationship between ADAMTS4 and carotid atherosclerotic plaque vulnerability in humans. *J Vasc Surg*. (2018) 67:1120–6. doi: 10.1016/j.jvs.2017.08.075
52. Ray BK, Shakya A, Turk JR, Apte SS, Ray A. Induction of the MMP-14 gene in macrophages of the atherosclerotic plaque: role of SAF-1 in the induction process. *Circ Res*. (2004) 95:1082–90. doi: 10.1161/01.RES.0000150046.48115.80
53. Canault M, Peiretti F, Poggi M, Mueller C, Kopp F, Bonardo B, et al. Progression of atherosclerosis in ApoE-deficient mice that express distinct molecular forms of TNF-alpha. *J Pathol*. (2008) 214:574–83. doi: 10.1002/path.2305
54. Martins IJ, Hone E, Foster JK, Sünram-Lea SI, Gnjec A, Fuller SJ, et al. Apolipoprotein E, cholesterol metabolism, diabetes, and the convergence of risk factors for Alzheimer's disease and cardiovascular disease. *Mol Psychiatry*. (2006) 11:721–36. doi: 10.1038/sj.mp.4001854
55. Farmer BC, Johnson LA, Hanson AJ. Effects of apolipoprotein E on nutritional metabolism in dementia. *Curr Opin Lipidol*. (2019) 30:10–5. doi: 10.1097/MOL.0000000000000566
56. Hui DY, Basford JE. Distinct signaling mechanisms for apoE inhibition of cell migration and proliferation. *Neurobiol Aging*. (2005) 26:317–23. doi: 10.1016/j.neurobiolaging.2004.02.030
57. Vozenilek AE, Blackburn CM, Schilke RM, Chandran S, Castore R, Klein RL, et al. AAV8-mediated overexpression of mPCSK9 in liver differs between male and female mice. *Atherosclerosis*. (2018) 278:66–72. doi: 10.1016/j.atherosclerosis.2018.09.005
58. Golforoush P, Yellon DM, Davidson SM. Mouse models of atherosclerosis and their suitability for the study of myocardial infarction. *Basic Res Cardiol*. (2020) 115:73. doi: 10.1007/s00395-020-00829-5
59. Getz GS, Reardon CA. Do the Apoe-/- and Ldlr-/- mice yield the same insight on atherogenesis? *Arterioscler Thromb Vasc Biol*. (2016) 36:1734–41. doi: 10.1161/ATVBAHA.116.306874
60. Roche-Molina Marta, Sanz-Rosa David, Cruz Francisco M, García-Prieto Jaime, López Sergio, Abia Rocío, et al. Induction of sustained hypercholesterolemia by single adeno-associated virus–mediated gene transfer of mutant hPCSK9. *Arterioscler Thromb Vasc Biol*. (2015) 35:50–9. doi: 10.1161/ATVBAHA.114.303617
61. Rolandsson O, Haney MF, Hagg E, Biber B, Lernmark A. Streptozotocin induced diabetes in minipig: a case report of a possible model for type 1 diabetes? *Autoimmunity*. (2002) 35:261–4. doi: 10.1080/0891693021000010703
62. Saleem Mir M, Maqbool Darzi M, Khalil Baba O, Khan HM, Kamil SA, Sofi AH, et al. Streptozotocin induced acute clinical effects in rabbits (Oryctolagus cuniculus). *Iran J Pathol*. (2015) 10:206–13.
63. Yuan F, Guo L, Park K-H, Woollard JR, Taek-Geun K, Jiang K, et al. Ossabaw pigs with a PCSK9 gain-of-function mutation develop accelerated coronary atherosclerotic lesions: a novel model for

preclinical studies. *J Am Heart Assoc*. (2018) 7. doi: 10.1161/JAHA.117.006207

Conflict of Interest: The authors declare that the research was conducted in the absence of any commercial or financial relationships that could be construed as a potential conflict of interest.

Publisher's Note: All claims expressed in this article are solely those of the authors and do not necessarily represent those of their affiliated organizations, or those of the publisher, the editors and the reviewers. Any product that may be evaluated in this article, or claim that may be made by its manufacturer, is not guaranteed or endorsed by the publisher.

frontiers in Cardiovascular Medicine

ORIGINAL RESEARCH
published: 10 March 2022
doi: 10.3389/fcvm.2022.778206

Identification of Specific Coronary Artery Disease Phenotypes Implicating Differential Pathophysiologies

*Jona B. Krohn[1,2†], Y Nhi Nguyen[1,2†], Mohammadreza Akhavanpoor[3], Christian Erbel[1,2], Gabriele Domschke[1,2], Fabian Linden[1,2], Marcus E. Kleber[4], Graciela Delgado[4], Winfried März[4,5,6], Hugo A. Katus[1,2] and Christian A. Gleissner[1,2,3]**

[1] Department of Cardiology, Pulmonology and Angiology, University Hospital Heidelberg, Heidelberg, Germany, [2] German Centre for Cardiovascular Research (DZHK) Partner Site Heidelberg/Mannheim, University of Heidelberg, Heidelberg, Germany, [3] Department of Cardiology and Stroke Centre, Rottal-Inn Kliniken, Eggenfelden, Germany, [4] Medical Clinic V, Medical Faculty Mannheim, University of Heidelberg, Mannheim, Germany, [5] Clinical Institute of Medical and Chemical Laboratory Diagnostics, Medical University Graz, Graz, Austria, [6] Synlab Academy, Synlab Holding Deutschland GmbH, Mannheim, Germany

Background and Aims: The roles of multiple risk factors of coronary artery disease (CAD) are well established. Commonly, CAD is considered as a single disease entity. We wish to examine whether coronary angiography allows to identify distinct CAD phenotypes associated with major risk factors and differences in prognosis.

Methods: In a cohort of 4,344 patients undergoing coronary angiography at Heidelberg University Hospital between 2014 and 2016, cluster analysis of angiographic reports identified subgroups with similar patterns of spatial distribution of high-grade stenoses. Clusters were independently confirmed in 3,129 patients from the LURIC study.

Results: Four clusters were identified: cluster one lacking critical stenoses comprised the highest percentage of women with the lowest cardiovascular risk. Patients in cluster two exhibiting high-grade stenosis of the proximal RCA had a high prevalence of the metabolic syndrome, and showed the highest levels of inflammatory biomarkers. Cluster three with predominant proximal LAD stenosis frequently presented with acute coronary syndrome and elevated troponin levels. Cluster four with high-grade stenoses throughout had the oldest patients with the highest overall cardiovascular risk. All-cause and cardiovascular mortality differed significantly between the clusters.

Conclusions: We identified four phenotypic subgroups of CAD bearing distinct demographic and biochemical characteristics with differences in prognosis, which may indicate multiple disease entities currently summarized as CAD.

Keywords: coronary artery disease, cardiovascular outcome, cardiovascular mortality, cardiovascular risk, coronary angiography

OPEN ACCESS

Edited by:
Masanori Aikawa, Brigham and Women's Hospital and Harvard Medical School, United States

Reviewed by:
Gemma Chiva-Blanch, CIBER Fisiopatología Obesidad y Nutrición (CIBEROBN), Spain
Alexander Akhmedov, University of Zurich, Switzerland

****Correspondence:***
Christian A. Gleissner
gleissner.christian@rottalinnkliniken.de

† These authors have contributed equally to this work and share first authorship

Specialty section:
This article was submitted to Atherosclerosis and Vascular Medicine, a section of the journal Frontiers in Cardiovascular Medicine

Received: *16 September 2021*
Accepted: *14 February 2022*
Published: *10 March 2022*

Citation:
Krohn JB, Nguyen YN, Akhavanpoor M, Erbel C, Domschke G, Linden F, Kleber ME, Delgado G, März W, Katus HA and Gleissner CA (2022) Identification of Specific Coronary Artery Disease Phenotypes Implicating Differential Pathophysiologies. Front. Cardiovasc. Med. 9:778206. doi: 10.3389/fcvm.2022.778206

INTRODUCTION

Coronary artery disease (CAD) is a leading cause of death worldwide (1). While underlying pathophysiological mechanisms of plaque genesis, propagation and rupture have been studied extensively, varying outcomes in individuals with CAD point at underlying pathomechanisms relevant to disease prognosis that still elude our present mechanistic understanding of atherogenesis.

CAD has been recognized as an inflammatory disease of the arterial wall propagated by a large number of cardiovascular risk factors (2). Among these, arterial hypertension, hyperlipidemia, diabetes mellitus, obesity or a history of tobacco consumption are known to effectuate plaque genesis and growth by attracting monocyte-derived cells into the arterial wall and inducing pro-inflammatory processes through chemokine and cytokine secretion. Moreover, additional factors such as chronic kidney disease or chronic inflammatory diseases are linked to CAD progression (3).

Despite extensive knowledge on the systemic risk factors of CAD progression, the vast variety of temporospatial distribution as well as severity of coronary stenoses between or even within individual patients remains inexplicable. Beyond traditional cardiovascular risk factors, numerous hypotheses ascribe a crucial role to factors such as shear stress (4) or inflammatory processes involving the vasa vasorum (5) in atherosclerotic lesion development. Considering the variety of coronary artery disease despite identical risk profile, we hypothesized that specific patterns of coronary atherosclerosis may exist, potentially pointing at different underlying pathophysiological entities.

To test our hypothesis, we performed an unbiased analysis of catheterization reports from the Department of Cardiology at Heidelberg University Hospital. Based on a cluster analysis, we intended to identify specific coronary artery disease patterns. Furthermore, we tested whether the specific patterns could be reproduced and associated to specific cardiovascular risk profiles in an independent cohort (LURIC) and whether these were relevant in terms of overall prognosis.

PATIENTS AND METHODS

Patient Cohorts

Heidelberg Coronary Catheterization Cohort

From the database of the Department of Cardiology at University Hospital Heidelberg, consecutive medical records including complete angiographic data of 4,344 patients undergoing coronary angiography between 2014 and 2016 were used for analysis of spatial distribution of coronary stenoses in the hypothesis-generating step of this study. Patients with chronic non-cardiac diseases, a history of malignancy within the past 5 years or those with previous coronary artery bypass graft procedure were excluded. A sample of 495 patients for whom a complete set of clinical and demographical data could be attained from medical records were used for comparative analysis with the LURIC cohort. An overview of the complete data set from the Heidelberg cohort sample is provided as Online Resource 4 (**Supplementary Material**).

Ludwigshafen Risk and Cardiovascular Health Study

The LURIC study consists of 3,129 patients of German descent hospitalized for coronary angiography between 1997 and 2000 at a tertiary care center in Southwestern Germany (6). To limit clinical heterogeneity, individuals suffering from acute illnesses other than acute coronary syndromes were excluded.

Structural Comparison Between Heidelberg Complete Cohort and LURIC Study Cohort

Compared to the LURIC cohort, patients in the Heidelberg complete cohort were older on average (67.9 ± 11.5 years vs. 62.4 ± 10.6 years) and less likely to be male [67.3 vs. 73.8% male; Online Resource 4 (**Supplementary Material**)]. They were more likely to be hypertensive (77.4 vs. 44.5%), more likely to have a history of nicotine abuse (51.2 vs. 19.6%), and more likely to present with an acute coronary syndrome (31.7 vs. 27.1%). Consecutively, patients in the Heidelberg cohort were more likely to show impaired left ventricular ejection fraction (LV-EF <40% in 26.7 vs. 7.5% of patients) as well as lower renal function (mean eGFR 78 ± 25 ml/min vs. 82 ± 20 ml/min). Mean levels of HsTnT (194 ± 1,214 ng/l vs. 87 ± 375 ng/l) and NT-proBNP (2,902 ± 15,693 ng/ml vs. 871 ± 2,049 ng/ml) were higher compared to patients of the LURIC cohort. Conversely, patients in the Heidelberg cohort were less likely to be obese (38.0 vs. 61.8%) and less likely to suffer from hyperlipidemia (63.8 vs. 68.5%) with an overall more favorable LDL/HDL ratio. No significant difference was observed in the prevalence of diabetes mellitus (37.3 vs. 39.4%) and levels of high-sensitive C-reactive protein (mean hs-CRP 7.4 ± 19.9 μg/ml vs. 8.7 ± 18.0 μg/ml).

Ethics Approval

This study was conducted in accordance with the 1975 Declaration of Helsinki and its later amendments, and analysis of patient data in the Heidelberg cohort was performed following approval by the Ethics Committee of the Faculty of Medicine at University of Heidelberg.

The LURIC study was approved by the Ethics Committee at the "Ärztekammer Rheinland-Pfalz" and was conducted in accordance with the 1975 Declaration of Helsinki and its later amendments.

Clinical Definitions

Coronary artery disease (CAD) was examined angiographically. Routine angiography comprised four to six projections of the left and two to three projections of right coronary artery. For each coronary artery segment, the highest degree of stenosis seen in any projection was reported. Significant coronary stenosis was defined as greater 50% in at least one of the 15 coronary segments according to the American Heart Association. Assessment of stenoses was done independently by two experienced interventional cardiologists, one of whom was not present during angiography. Consensus between independent estimates regarding degree of stenosis was found to be >90% for all angiographic reports.

Diabetes mellitus was defined according to the American Diabetes Association 2010 as increased fasting (>125 mg/dl) and/or post-challenge (2 h after 75 g oral glucose >200 mg/dl)

glucose and/or elevated glycated hemoglobin (>6.4%) and/or history of diabetes mellitus (7). Hypertension was defined as a systolic blood pressure >140 mmHg and/or diastolic blood pressure >90 mmHg or antihypertensive treatment.

Terminology

The term "coronary artery disease phenotype" in the context of this study is defined as the different patterns of spatial distribution of high-grade stenoses across the coronary branches according to the Gensini scheme identified by two-step cluster analysis. For the purpose of simplicity, these patterns are henceforth referred to as "CAD phenotypes," "(phenotypic) clusters," or simply "phenotypes."

Statistical Analysis

Statistical analyses were conducted using SPSS version 22.0 (IBM Corps 2013), figures were prepared using Prism (GraphPad 2017). All values are stated as mean ± standard deviation for normally distributed parameters or median with interquartile range for non-normally distributed parameters, respectively, unless otherwise specified. $p \leq 0.05$ were assumed to be of statistical significance. Descriptive analysis of demographic, laboratory and angiographic data as well as a comparative analysis of female and male patients with respect to all parameters was performed. Normal distribution and deviation thereof were tested for each parameter using the Kolmogorov–Smirnov-Test. Statistical tests included Student's *t*-test for independent variables, non-parametric Mann–Whitney-*U*-Test for non-normally distributed and/or interval-scaled variables or the χ^2-test for nominally scaled variables.

Identification of Clusters

Cluster analysis was performed using the dichotomized stenosis values (>50%) of the 15 coronary segments. To determine the appropriate number of clusters, a random sample of 100 patients was taken for hierarchical agglomerative clustering using the squared Euclidian distance. For stepwise fusion of clusters, Complete Linkage and Ward's method were applied. The number of clusters determined through the Elbow method was used as basis for consecutive *two-step cluster* (*TSC*) *analysis*. TSC was conducted using the dichotomized stenosis values of the 15 coronary segments as categorical cluster variables with the log-likelihood ratio as a measure of distance. In the first step of cluster formation, pre-clusters were formed according to the BIRCH algorithm as described previously (8). In the second step, these pre-clusters were further summarized to form clusters using a hierarchical algorithm. A total of six test runs were performed with varying sequences of patients to ensure maximum consistency within each cluster. All patients recruited from each of the two cohorts were subsequently included in cluster analysis. Furthermore, an analysis of discriminance with formed clusters as categorical variables and dichotomized coronary stenoses as dependent variables were used to determine the likelihood by which an individual patient could be assigned to his/her respective cluster.

Characterization of Clusters

Each cluster underwent descriptive analysis to allow for comparison between the individual clusters using univariate analysis of variance (ANOVA) with *post-hoc* Tukey test for normally distributed parameters, non-parametric Kruskal–Wallis test for non-normally distributed parameters and the χ^2-test, each test using cluster affiliation as a test variable. Associations between cluster affiliation and demographic or laboratory parameters were investigated by ANOVA with *post-hoc* Tukey test in the LURIC cohort. Logistic regression was performed with stepwise inclusion of age, gender, BMI, eGFR, family history, systolic blood pressure, tobacco, diabetes, and LDL. Further, a multivariate Cox regression analysis was performed to determine cardiovascular mortality adjusted for all included demographic and laboratory parameters (age, gender, BMI, diabetes, dyslipidemia, systolic blood pressure, tobacco use, family history, LV function, NT-proBNP, TnT, hs-CRP, and white blood count). Cumulative survival within each cluster was visualized using Kaplan–Meier analysis. Receiver operating characteristic (ROC) analysis was performed using cardiovascular survival as status variable and age <60 years, female sex, no family history for MI, no hypertension or dyslipidemia as well as cluster 1 affiliation as test variables.

RESULTS

Atherosclerotic Plaques Are Not Equally Distributed Among Coronary Arteries

Consecutive coronary angiography reports from the Heidelberg cohort ($n = 4{,}344$) were analyzed for distribution of coronary stenoses within the 15 coronary segments according to the Gensini scheme. Patients were 65.8 ± 13.2 years of age and 58.4% (2,539) were male. Heat mapping of stenosis >50% of vessel diameter revealed unequal distribution of critical stenoses among the coronary segments (**Figure 1A**). Visualization furthermore showed an accumulation of high-grade stenoses in the regions of the proximal right (RCA, segments 1 and 2) and left anterior descending artery (LAD, segments 6–9) (**Figures 1B,C**).

Coronary Artery Disease Can Be Subdivided Into Four Distinct Phenotypic Clusters

To determine whether aforementioned findings could be categorized into distinct groups of CAD patients exhibiting a similar CAD phenotype, we performed a cluster analysis of our patient cohort using the 15 Gensini segments as categorical variables. Using Elbow's method, four clusters were found to show the highest cluster quality as measured by the silhouette value of cohesion and separation. A subsequent two-step cluster analysis identified four distinct phenotypic clusters of coronary artery disease. **Figure 2A** shows the rearrangement of the heat map in **Figure 1A** according to these four clusters revealing a cluster 1 (blue = "irregularities," 58%) with predominantly mild vessel wall irregularities devoid of critical stenoses (**Figures 2B–D**). Cluster 2 [yellow = "RCA," 9%; OR = 5.41 (3.42–8.56), $p < 0.001$] was characterized by high-grade

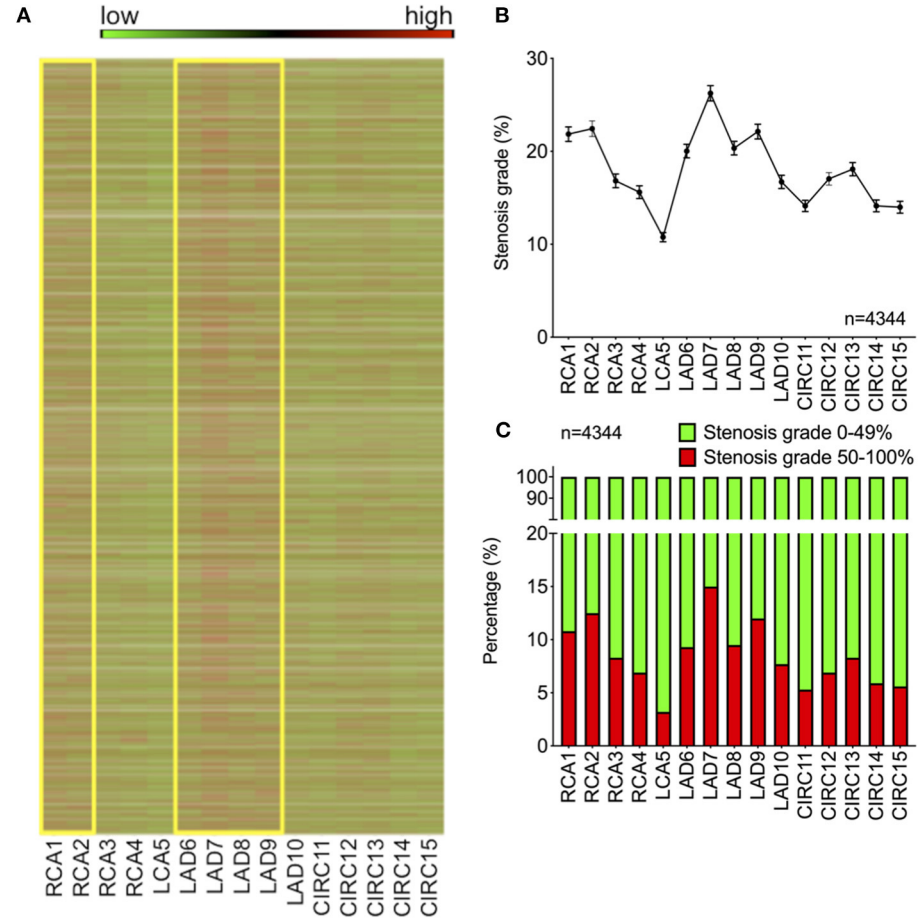

FIGURE 1 | Distribution of plaques among the coronary segments of the Gensini scheme shows specific predilection sites of critical stenosis. **(A)** Heat map color-coded for degree of stenosis for each patient in the cohort (green = 0%, red = 100%). Yellow boxes indicate proximal LAD and RCA regions. **(B)** Average stenosis grade across the 15 Gensini segments (shown as mean ± SEM). **(C)** Percentage of high-grade stenoses >50% (shown in red) across the 15 Gensini segments (LAD, left anterior descending artery; RCA, right coronary artery).

stenosis of the proximal right coronary artery (segments 1–2), whereas cluster 3 [orange = "LAD," 22%; OR = 13.31 (7.80–22.74), $p < 0.001$] showed high-grade stenosis of the proximal LAD (segments 7–9). Patients in cluster 4 [red = "diffuse," 11%; OR for at least one stenosis >50% in all three coronary branches 23.53 (9.72–56.94), $p < 0.001$] exhibited diffuse high-grade stenoses of all three coronary branches (**Figures 2B–D**). Coronary angiograms representative of each cluster are shown in Online Resource 1 (**Supplementary Material**).

CAD Clusters Can Independently Be Reproduced in the LURIC Cohort

As validation of our results, comparative analysis of the spatial distribution of critical stenoses across the 15 Gensini segments in the LURIC cohort revealed similar results to those obtained in the Heidelberg cohort, with prominent peaks in the area of the proximal RCA and the proximal LAD [Online Resource 2A/B/C (**Supplementary Material**)]. Furthermore, all four clusters could be identified in this cohort, with similar prevalence rates and strong association with high-grade stenosis in their respective coronary branches [cluster 1 (blue = "irregularities," 50%), cluster 2 [yellow = "RCA," 22%; OR = 4.64 (3.84–5.60), $p < 0.001$], cluster 3 [orange = "LAD," 20%; OR = 6.58 (5.25–8.24), $p < 0.001$], cluster 4 [red = "diffuse," 9%; OR for at least one stenosis >50% in all three coronary branches 35.31 (17.10–72.88), $p < 0.001$]. These results confirm the concept of specific coronary artery disease patterns as a common phenomenon in two independent Central European coronary artery disease cohorts.

The Four Clusters Exhibit Distinct Demographic and Biochemical Properties

Comparative analysis of demographic and biochemical data within the individual clusters in the LURIC cohort identified a set of characteristic traits unique to each cluster [Online Resource 3 (**Supplementary Material**)]. **Figure 3** shows ANOVA results characterizing the four clusters. Results of logistic regression to

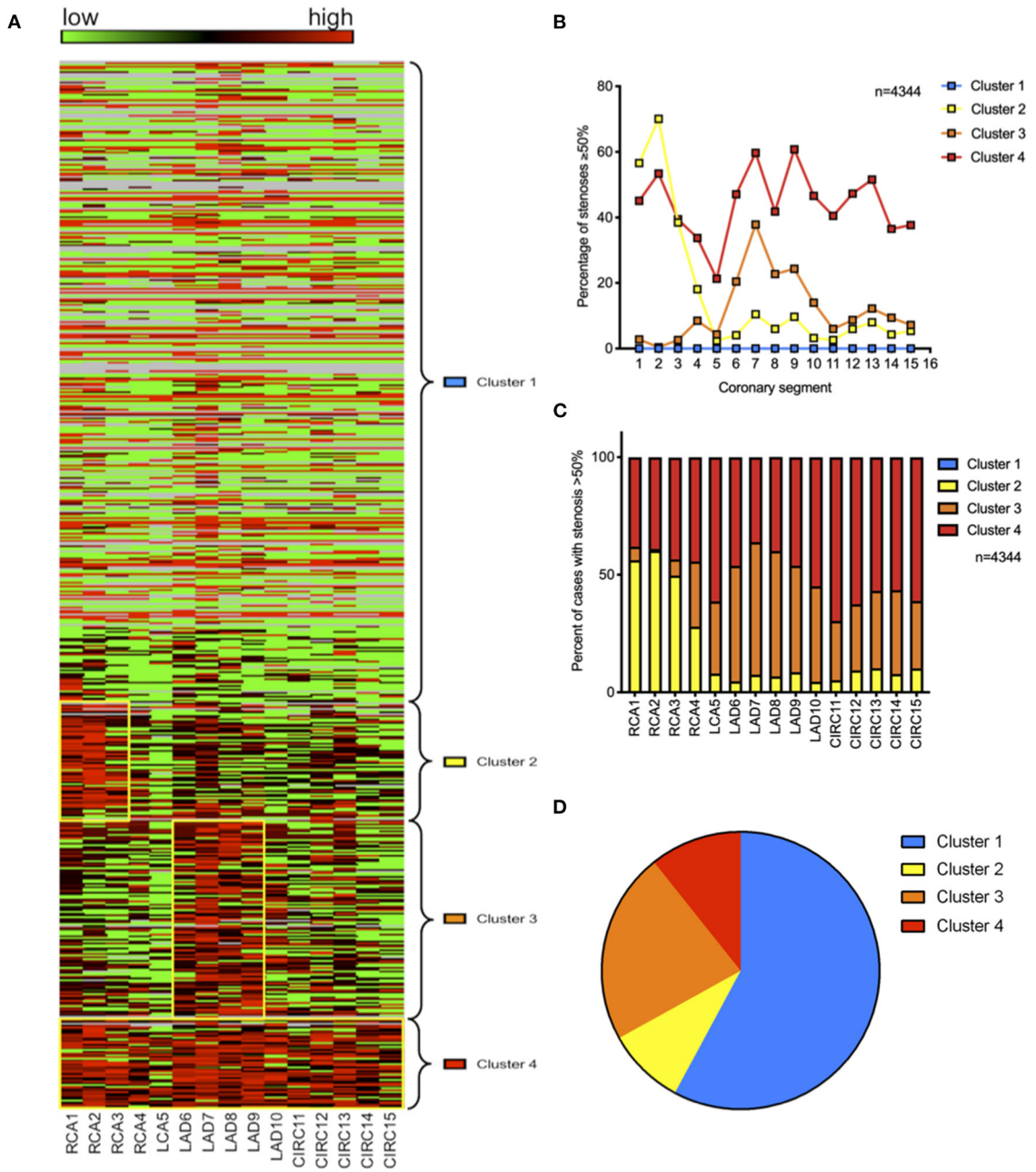

FIGURE 2 | Cluster analysis reveals four distinct phenotypes of coronary artery disease. **(A)** Heat map indicating the degree of stenosis by coronary segment (green = 0%, red = 100%) with free clustering of coronary segments to allow for best fit; yellow boxes indicate high grade stenoses in clusters 2, 3, and 4. **(B)** Average stenosis grade across the 15 Gensini segments within each cluster. **(C)** Percentage of stenoses >50% per coronary segment and cluster of all stenoses >50%. (**D**) Prevalence of the four phenotypic clusters within the cohort.

determine specific characteristics of each cluster are shown in Online Resource 5 (**Supplementary Material**).

In brief, patients in cluster 1 (blue = "irregularities") were young [HR for age 0.142 (0.088–0.228), $p < 0.001$] and female [HR = 3.367 (2.847–3.981), $p < 0.001$], they display a normal renal function [HR for eGFR 1.464 (1.108–1.933), $p < 0.01$], absence of diabetes [HR for diabetes mellitus 0.620 (0.530–0.725), $p < 0.001$] and low inflammatory activity as seen by low hs-CRP [HR for hs-CRP 0.857 (0.808–0.908), $p < 0.001$] and low LDL levels [HR for LDL 0.410 (0.327–0.516), $p < 0.001$]. Cluster 2 (yellow = "RCA") had a higher percentage of male individuals [HR = 1.783 (1.486–2.141), $p < 0.001$], patients were older [HR = 4.136 (2.555–6.697), $p < 0.001$], and more likely to be diabetic [HR for diabetes mellitus 1.297 (1.104–1.523), $p < 0.01$]. Cluster

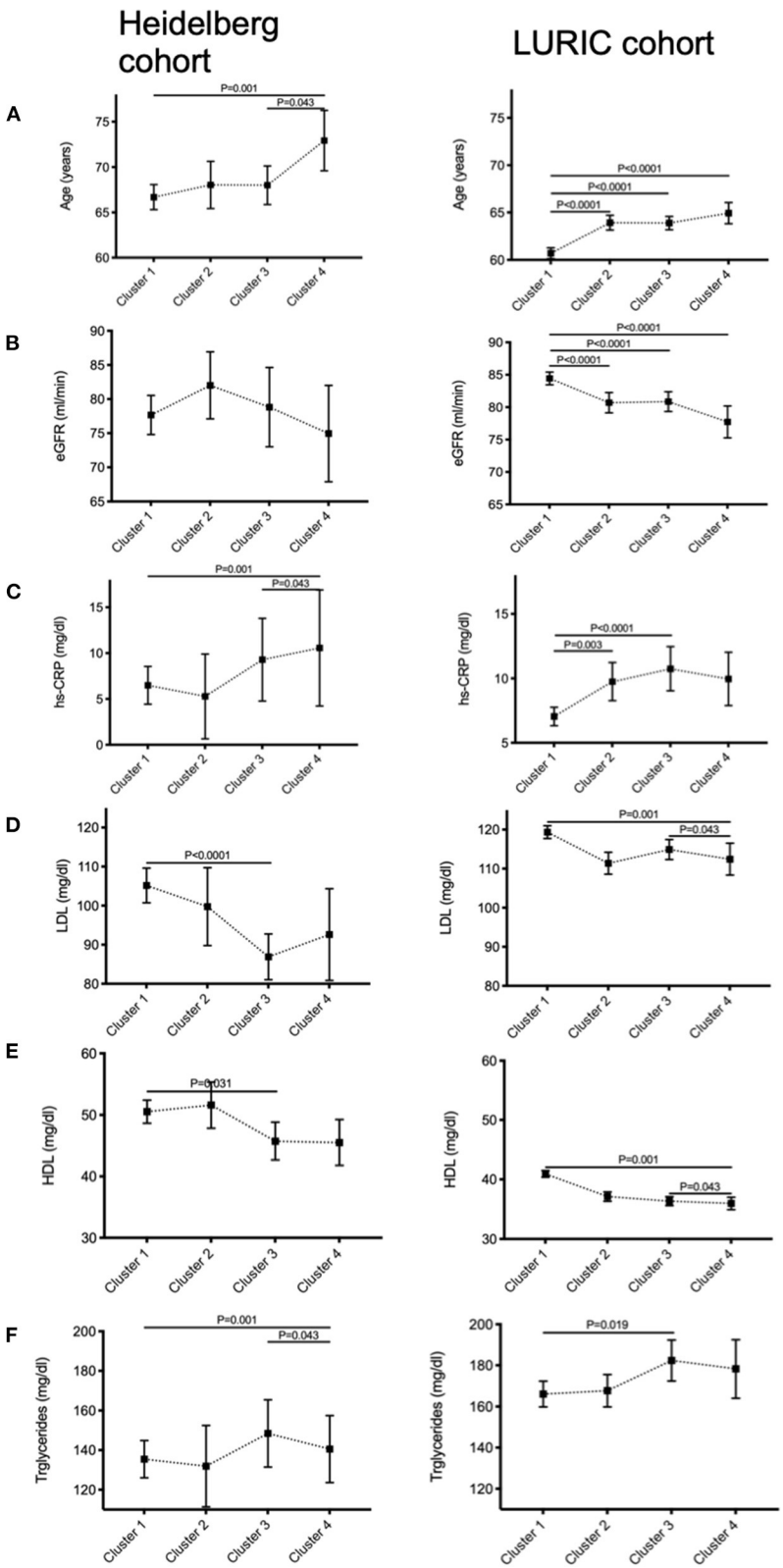

FIGURE 3 | Demographic characterization of each cluster reveals significant differences in cardiovascular risk profile. Comparison between the four phenotypic clusters of the Heidelberg "complete cohort" and the LURIC cohort with respect to **(A)** age, **(B)** renal function, **(C)** residual inflammation quantified by high-sensitive C-reactive protein levels (hs-CRP), **(D)** LDL-, **(E)** HDL-cholesterol, and **(F)** triglyceride levels using analysis of variance (ANOVA).

3 (orange = "LAD") displayed the highest percentage of patients who initially presented with an acute coronary syndrome [HR = 2.208 (1.786–2.732), $p < 0.001$], which is reflected by the highest average high-sensitive troponin T levels of all clusters [HR = 1.357 (1.167–1.579), $p < 0.001$]. Also, hs-CRP levels were higher than in clusters 1 and 2 [HR = 1.206 (1.125–1.292), $p < 0.001$]. Patients in cluster 4 (red = "diffuse") were the oldest on average [HR = 8.146 (3.465–19.151), $p < 0.001$] and most likely male [HR = 3.378 (2.433–4.695), $p < 0.001$]. Patients in this cluster were found to have the highest overall cardiovascular risk profile including family history [HR = 1.530 (1.199–1.952), $p = 0.001$], high triglycerides, hs-CRP [HR = 1.015 (1.004–1.026), $p < 0.01$] as well as diabetes [HR = 1.390 (1.093–1.768), $p < 0.01$].

Coronary Artery Disease Phenotype Affects Short-Term Cardiovascular Survival

To investigate whether CAD phenotype holds a prognostic value in terms of cardiovascular mortality, Kaplan–Meier analyses were performed in the LURIC cohort (**Figure 4A**). Even after adjustment for age, gender, body mass index, diabetes mellitus, dyslipidemia, hypertension, tobacco use, family history, LV-function, NT-proBNP, hs-TnT, and hs-CRP levels, CAD phenotype significantly predicted cardiovascular mortality [**Figure 4B**; Online Resource 6 (**Supplementary Material**)]. Cluster 1 with only mild CAD showed the highest survival, whereas patients in cluster 4 with diffuse high-grade coronary stenoses had the poorest overall survival over the 12-month observation period (median survival 8.9–9.9 years), with a significant increase in mortality both before and after multivariable adjustment [HR unadjusted 2.710 (2.107–3.485), $p < 0.001$; HR adjusted 1.784 (1.350–2.358), $p < 0.001$]. Of note, patients in cluster 3 with prominent stenosis of the left anterior descending (LAD) artery had a poorer 12-month survival [HR unadjusted 2.204 (1.653–2.478), $p < 0.001$; HR adjusted 1.607 (1.282–2.015), $p < 0.001$] compared to those of cluster 2 with predominantly high-grade stenosis of the proximal to mid right coronary artery (RCA) [HR unadjusted 1.620 (1.297–2.025), $p < 0.001$; HR adjusted 1.225 (0.956–1.569, $p = 0.09$)].

Likewise, receiver operating characteristic (ROC) analysis of survival prognosis using either a favorable cardiovascular risk profile alone (age < 60 years, female sex, no family history for MI, no hypertension or dyslipidemia) or in combination with cluster 1 affiliation in the LURIC cohort showed a significant increase in the area under the ROC curve [ROC AUC = 0.681 (0.659–0.703), $p < 0.001$ vs. 0.657 (0.635–0.679), $p < 0.0001$; difference in AUC = 0.024 (0.012–0.037), $p < 0.001$], indicating an additional benefit of cluster 1 affiliation for survival prediction (**Figure 4C**).

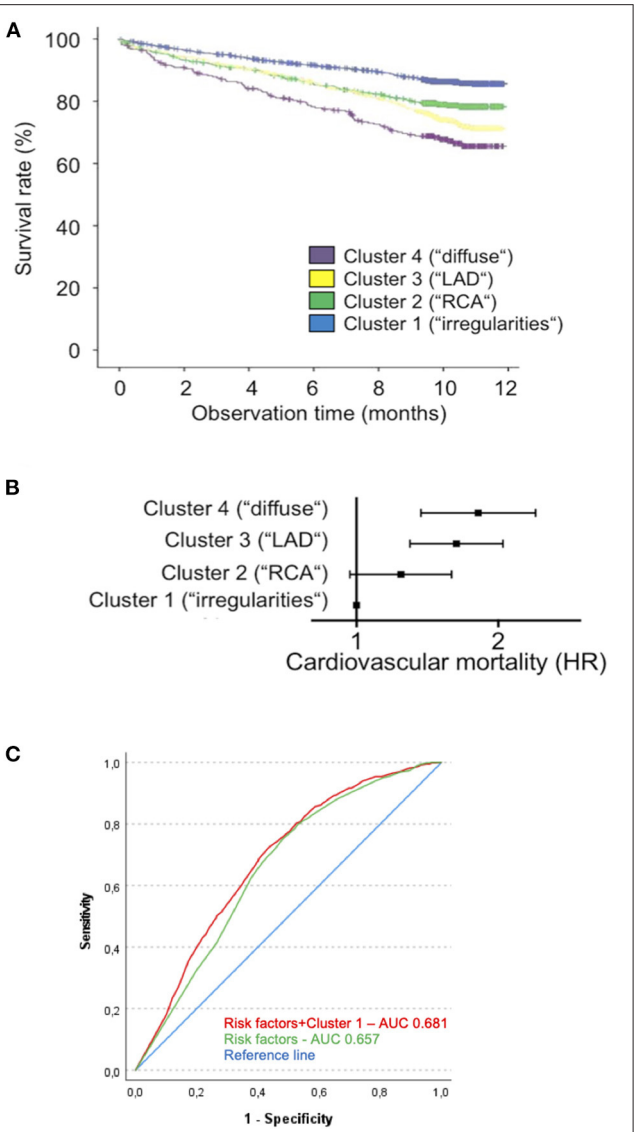

FIGURE 4 | Cluster affiliation is associated with differences in prognosis. **(A)** Kaplan–Meier curve for cardiovascular survival over a 12-month time period for clusters 1 (blue), 2 (green), 3 (yellow), and 4 (purple) in the LURIC cohort. **(B)** Forest plot indicating hazard ratios for cardiovascular death in each cluster (using cluster 1 as reference) as determined by multivariate analysis adjusted for age, gender, BMI, Diabetes, dyslipidemia, systolic blood pressure, tobacco use, family history, LV function, NT-proBNP, hs-TnT, hs-CRP, and white blood count. Cluster 2: HR = 1.242, 0.986–1.592, n.s.; cluster 3: HR = 1.630, 1.298–2.047, $P < 0.0001$; cluster 4: HR = 1.814, 1.371–2.400, $P < 0.0001$. **(C)** ROC curve demonstrating predictive ability of a favorable cardiovascular risk profile (age < 60 years, female sex, no family history for MI, no hypertension or dyslipidemia) alone or in combination with cluster 1 affiliation with regard to cardiovascular survival (BMI, body mass index; NT-proBNP, n-terminal pro-brain natriuretic protein; hs-TnT, high-sensitive troponin T; hs-CRP, high-sensitive C-reactive protein).

DISCUSSION

The molecular mechanisms underlying atherogenesis have been extensively studied over the past decades. Despite our knowledge how the systemic risk factors affect CAD progression, the fact that coronary atherosclerosis can differ significantly between patients with similar risk profile remains enigmatic. Moreover, it is anything but clear why even in a single individual atherosclerotic plaque burden may substantially differ between coronary segments. The explanation that this heterogeneity is entirely due to shear stress remains unsatisfactory.

Our attempt to shed light on this obscurity is an unbiased approach analyzing lesion distribution throughout the coronary artery tree in a cohort of >4,000 consecutive patients at Heidelberg University Hospital. We thereby—for the first time—reveal four distinct patterns of coronary atherosclerotic plaque distribution, which could subsequently be independently confirmed in >3,000 patients of the LURIC study. In the LURIC cohort, these clusters correlate with specific demographic and clinical parameters, and are furthermore associated independently with cardiovascular mortality. Patients in cluster 1 ("irregularities") with a relatively young age and low cardiovascular risk exhibiting diffuse vessel wall irregularities devoid of critical stenoses may represent a form of "baseline CAD" expressed in every individual with increasing age, the extent of which may be modified as the consequence of cardiovascular risk factors. In this respect, the CAD phenotype seen in cluster 1 may represent the incipient plaque formation in coronary arteries of children and young adults observed in a previous study (9). By contrast, patients belonging to cluster 2 ("RCA") showed signs of an elevated metabolic risk, associated with a CAD phenotype predominantly affecting the proximal right coronary artery. While the pathomechanisms resulting in this particular and prognostically relevant distribution of coronary atherosclerosis are unclear, a possible link may be the marked presence of chronic low-grade inflammation present in individuals with metabolic syndrome (10) that was observed in our cohort. An elevated inflammatory response was found to be a prominent hallmark of both clusters 3 ("LAD") and 4 ("diffuse"), the latter being associated with the most unfavorable cardiovascular risk profile of all clusters as well as a strong family history of CAD, resulting in diffuse high-grade stenoses of all coronary branches with the poorest short-term survival. Notably, patients in cluster 3 who most often presented with an acute coronary syndrome and were found to exhibit critical stenosis of the proximal left anterior descending artery may point toward a propensity of unstable plaque formation in these coronary segments. This is in line with proximal LAD stenosis being a prognostically relevant target for coronary intervention or bypass surgery (11).

Analogous to myocardial infarction, previously believed to be one homogenous entity with linear pathophysiology that has now been recognized as the common pathway of a number of pathologies reaching from superficial plaque erosion to plaque rupture (12), CAD itself may similarly be the end product of a number of pathophysiologically distinct disease mechanisms. In our study, we are first to associate commonly known risk factors of cardiovascular disease such as age, male gender or the metabolic syndrome as well as emerging risk factors such as systemic inflammation (13) with a specific spatial pattern of coronary artery disease, supporting this hypothesis of differential pathomechanisms in coronary atherosclerosis with potential prognostic as well as therapeutic value. Previous work such as the APPROACH trial has provided extensive evidence on the impact of coronary plaque burden on long-term survival (14), and few assumptions on the relevance of location of critical stenosis for overall survival have been made previously (15). Overall, however, current knowledge on an association of spatial distribution of CAD with specific cardiovascular risk factors is scarce.

Limitations to our study are grounded on the mode of data collection and availability of data in our study cohort. The degree of stenosis for each segment of the Gensini scheme is usually documented based on the interventionalist's estimate and is therefore prone to some degree of variation due to inter-observer bias (16). However, each angiography was analyzed independently by two experienced interventional cardiologists, one of which was not present during the procedure. Consensus respective to degree of stenosis was >90% between independent reports for all angiographies. Furthermore, our data do not take into account variation of coronary anatomy (i.e., dominant left or right coronary artery, coronary anomalies). However, based on the large number of catheterization reports, this bias should not significantly affect our overall results.

Moreover, we cannot exclude that our findings are at least partly affected by a temporospatial variation of disease progression, although multivariate analysis including patient age as confounder still demonstrates significant association between coronary phenotype and cardiovascular mortality. Nevertheless, as there is no defined incipient point of coronary atherogenesis, and development of coronary atherosclerotic plaques may have started at an earlier age in some individuals, we cannot fully exclude the possibility of some form of temporal variation as a confounding factor.

Furthermore, the lack of intravascular imaging and functional data may affect the quality of analysis, since particularly in intermediate-degree stenoses, further diagnostic assessment of functional relevance of a coronary stenosis is indicated, thus potentially guiding the interventionalist's decision in favor of percutaneous coronary intervention. This additional diagnostic information may help improve the quality of dichotomization of coronary stenoses in our cluster analysis. On that note, evolution of diagnostic standards and non-invasive imaging along with a sharp improvement in the sensitivity of cardiac troponin assays in the last decades may implicate a certain degree of variance in the indication for angiographic testing between the two cohorts, the LURIC cohort recruiting patients as early as 1997. Albeit a recent diagnostic shift away from invasive angiography and toward increased non-invasive imaging as a confounding factor in this study, all patients included herein underwent guideline-conform diagnostic steps, and all troponin tests used in our study cohorts were performed using state-of-the-art high sensitivity assays. Lastly, due to the predominantly Caucasian cohorts used for this analysis, genetic heterogeneity may pose a confounding factor in the translation of the results obtained herein to an ethnically different or more diverse population.

In conclusion, our study sets a precedent in identifying four specific coronary artery disease phenotypes, which are correlated with a specific cardiovascular risk profile, thus pointing at the possible existence of different disease entities within the pathology presently known as coronary artery disease. These different CAD entities may reflect different underlying pathomechanisms dictating spatial distribution of atherosclerotic lesion formation beyond the current holistic assumption that plaque location is largely dependent on hemodynamics (17)

and otherwise somewhat arbitrary. Furthermore, the evidence provided herein may indicate a difference in disease prognosis dependent on CAD phenotype. Further studies are needed to investigate the existence of distinct pathomechanisms associated with the phenotypes identified herein that may advance our understanding of the pathophysiological nuances of coronary artery disease, potentially providing novel targets for individualized preventative therapies.

DATA AVAILABILITY STATEMENT

The raw data supporting the conclusions of this article will be made available by the authors upon reasonable request, without undue reservation.

ETHICS STATEMENT

The studies involving human participants were reviewed and approved by Ethics Committee at the Faculty of Medicine at University of Heidelberg. The patients/participants provided their written informed consent to participate in this study. The LURIC study was approved by the Ethics Committee at the "Ärztekammer Rheinland-Pfalz" and was conducted in accordance with the 1975 Declaration of Helsinki and its later amendments.

AUTHOR CONTRIBUTIONS

JK, YN, and CG postulated the hypothesis and designed the framework of this study. YN and JK did the majority of data collection and processing. JK and CG were in charge of drafting the manuscript. WM and HK held advisory functions throughout the conceptualization and realization of this study. WM contributed to cluster analysis using the LURIC database. MA, CE, GaD, FL, MK, and GrD contributed to data collection and processing. All authors contributed to the article and approved the submitted version.

FUNDING

This study was funded by the Faculty of Medicine at Heidelberg University. Partial financial support was received from the Cardiology Career Program (CCP) of the University Hospital Heidelberg (to YN).

SUPPLEMENTARY MATERIAL

The Supplementary Material for this article can be found online at: https://www.frontiersin.org/articles/10.3389/fcvm.2022.778206/full#supplementary-material

REFERENCES

1. Go AS, Mozaffarian D, Roger VL, Benjamin EJ, Berry JD, Blaha MJ, et al. Heart disease and stroke statistics—2014 update: a report from the American Heart Association. *Circulation.* (2014) 129:e28–e292. doi: 10.1161/01.cir.0000441139.02102.80
2. Patel SA, Winkel M, Ali MK, Narayan KM, Mehta NK. Cardiovascular mortality associated with 5 leading risk factors: national and state preventable fractions estimated from survey data. *Ann Intern Med.* (2015) 163:245–53. doi: 10.7326/M14-1753
3. Emerging Risk Factors Collaboration, Kaptoge S, Di Angelantonio E, Lowe G, Pepys MB, Thompson SG, et al. C-reactive protein concentration and risk of coronary heart disease, stroke, and mortality: an individual participant meta-analysis. *Lancet.* (2010) 375:132–40. doi: 10.1016/S0140-6736(09)61717-7
4. Won D, Zhu SN, Chen M, Teichert AM, Fish JE, Matouk CC, et al. Relative reduction of endothelial nitric-oxide synthase expression and transcription in atherosclerosis-prone regions of the mouse aorta and in an *in vitro* model of disturbed flow. *Am J Pathol.* (2007) 171:1691–704. doi: 10.2353/ajpath.2007.060860
5. Boyle EC, Sedding DG, Haverich A. Targeting vasa vasorum dysfunction to prevent atherosclerosis. *Vascul Pharmacol.* (2017) 96–8:5–10. doi: 10.1016/j.vph.2017.08.003
6. Winkelmann BR, März W, Boehm BO, Zotz R, Hager J, Hellstern P, et al. Rationale and design of the LURIC study - a resource for functional genomics, pharmacogenomics and long-term prognosis of cardiovascular disease. *Pharmacogenomics.* (2001) 2:S1–S73. doi: 10.1517/14622416.2.1.S1
7. Sacks DB, Arnold M, Bakris GL, Bruns DE, Horvath AR, Kirkman MS, et al. Position statement executive summary: guidelines and recommendations for laboratory analysis in the diagnosis and management of diabetes mellitus. *Diabetes Care.* (2011) 34:1419–23. doi: 10.2337/dc11-9997
8. Zhang T, Ramakrishnan R, Livny M. BIRCH: an efficient data clustering method for very large databases. *SIGMOD Rec.* (1996) 25:103–14. doi: 10.1145/235968.233324
9. Berenson GS, Srinivasan SR, Bao W, Newman WP 3rd, Tracy RE, Wattigney WA. Association between multiple cardiovascular risk factors and atherosclerosis in children and young adults. The Bogalusa Heart Study. *N Engl J Med.* (1998) 338:1650–6. doi: 10.1056/NEJM199806043382302
10. Al Rifai M, Silverman MG, Nasir K, Budoff MJ, Blankstein R, Szklo M, et al. The association of nonalcoholic fatty liver disease, obesity, and metabolic syndrome, with systemic inflammation and subclinical atherosclerosis: the Multi-Ethnic Study of Atherosclerosis (MESA). *Atherosclerosis.* (2015) 239:629–33. doi: 10.1016/j.atherosclerosis.2015.02.011
11. Neumann FJ, Sousa-Uva M, Ahlsson A, Alfonso F, Banning AP, Benedetto U, et al. 2018 ESC/EACTS Guidelines on myocardial revascularization. *EuroIntervention*. (2019) 14:1435–534. doi: 10.4244/EIJY19M01_01
12. Quillard T, Franck G, Mawson T, Folco E, Libby P. Mechanisms of erosion of atherosclerotic plaques. *Curr Opin Lipidol.* (2017) 28:434–41. doi: 10.1097/MOL.0000000000000440
13. Ridker PM, Libby P, MacFadyen JG, Thuren T, Ballantyne C, Fonseca F, et al. Modulation of the interleukin-6 signalling pathway and incidence rates of atherosclerotic events and all-cause mortality: analyses from the Canakinumab Anti-Inflammatory Thrombosis Outcomes Study (CANTOS). *Eur Heart J.* (2018) 39:3499–507. doi: 10.1093/eurheartj/ehy310
14. Kissel CK, Chen G, Southern DA, Galbraith PD, Anderson TJ, investigators A. Impact of clinical presentation and presence of coronary sclerosis on long-term outcome of patients with non-obstructive coronary artery disease. *BMC Cardiovasc Disord.* (2018) 18:173. doi: 10.1186/s12872-018-0908-z
15. Harris PJ, Harrell FE, Jr., Lee KL, Behar VS, Rosati RA. Survival in medically treated coronary artery disease. *Circulation.* (1979) 60:1259–69. doi: 10.1161/01.CIR.60.6.1259
16. Fleming RM, Kirkeeide RL, Smalling RW, Gould KL. Patterns in visual interpretation of coronary arteriograms as detected by quantitative coronary arteriography. *J Am Coll Cardiol.* (1991) 18:945–51. doi: 10.1016/0735-1097(91)90752-U
17. Kwak BR, Back M, Bochaton-Piallat ML, Caligiuri G, Daemen MJ, Davies PF, et al. Biomechanical factors in atherosclerosis: mechanisms and clinical implications. *Eur Heart J.* (2014) 35:3013–20, 3020a–d. doi: 10.1093/eurheartj/ehu353

Conflict of Interest: JK, YN, and CG: pending patent, CoroScore—ein automatisiert bestimmbarer Angiographie-basierter Score zur Verbesserung der kardiovaskulären Risikoprädiktion. MK: personal fees from Bayer. WM: grants from Siemens Healthineers, Aegerion Pharmaceuticals, AMGEN, AstraZeneca, Sanofi, Alexion Pharmaceuticals, BASF, Abbott Diagnostics, Numares AG, Berlin-Chemie, Akzea Therapeutics, Bayer Vital, bestbion dx, Boehringer Ingelheim, Immundiagnostik, Merck Chemicals, MSD Sharp and Dohme, Novartis, Olink Proteomics. Personal fees from Aegerion Pharmaceuticals, AMGEN, Sanofi, Alexion Pharmaceuticals, BASF, Abbott Diagnostics, Numares AG, Berlin-Chemie, Akzea Therapeutics. HK: personal fees from AstraZeneca, Bayer Vital, Daiichi Sankyo, Boehringer Ingelheim, Roche Diagnostics. WM is employed by Synlab GmbH.

The remaining authors declare that the research was conducted in the absence of any commercial or financial relationships that could be construed as a potential conflict of interest.

Publisher's Note: All claims expressed in this article are solely those of the authors and do not necessarily represent those of their affiliated organizations, or those of the publisher, the editors and the reviewers. Any product that may be evaluated in this article, or claim that may be made by its manufacturer, is not guaranteed or endorsed by the publisher.

frontiers | Frontiers in Cardiovascular Medicine

ORIGINAL RESEARCH
published: 11 April 2022
doi: 10.3389/fcvm.2022.809007

Antibodies Against Phosphorylcholine Among 60-Year-Olds: Clinical Role and Simulated Interactions

*Shailesh Kumar Samal[1], Pritam Kumar Panda[2], Max Vikström[3], Karin Leander[3], Ulf de Faire[3], Rajeev Ahuja[2,4] and Johan Frostegård[1]**

[1] Section of Immunology and Chronic Disease, Institute of Environmental Medicine, Karolinska Institutet, Solna, Sweden, [2] Condensed Matter Theory Group, Materials Theory Division, Department of Physics and Astronomy, Uppsala University, Uppsala, Sweden, [3] Unit of Cardiovascular and Nutritional Epidemiology, Institute of Environmental Medicine, Karolinska Institutet, Solna, Sweden, [4] Department of Physics, Indian Institute of Technology Ropar, Rupnagar, India

OPEN ACCESS

Edited by:
Dennis W. T. Nilsen, Stavanger University Hospital, Norway

Reviewed by:
Paul H. A. Quax, Leiden University, Netherlands
Valery Bochkov, University of Graz, Austria
Yang Shi, Augusta University, United States

***Correspondence:**
Johan Frostegård
johan.frostegard@ki.se

Specialty section:
This article was submitted to Atherosclerosis and Vascular Medicine, a section of the journal Frontiers in Cardiovascular Medicine

Received: *04 November 2021*
Accepted: *25 February 2022*
Published: *11 April 2022*

Citation:
Samal SK, Panda PK, Vikström M, Leander K, de Faire U, Ahuja R and Frostegård J (2022) Antibodies Against Phosphorylcholine Among 60-Year-Olds: Clinical Role and Simulated Interactions. Front. Cardiovasc. Med. 9:809007. doi: 10.3389/fcvm.2022.809007

Aims: Antibodies against phosphorylcholine (anti-PC) are implicated as protection markers in atherosclerosis, cardiovascular disease (CVD), and other chronic inflammatory conditions. Mostly, these studies have been focused on IgM. In this study, we determined IgG, IgG1, and IgG2 anti-PC among 60-year-olds.

Methods: Based on a 7-year follow-up of 60-year-olds (2,039 men and 2,193 women) from Stockholm County, we performed a nested case-control study of 209 incident CVD cases with 620 age- and sex-matched controls. Anti-PC was determined using ELISA. We predicted the binding affinity of PC with our fully human, in-house-produced IgG1 anti-PC clones (i.e., A01, D05, and E01) using the molecular docking and molecular dynamics simulation approach, to retrieve information regarding binding properties to PC.

Results: After adjustment for confounders, IgG and IgG2 anti-PC showed some significant associations, but IgG1 anti-PC was much stronger as a protection marker. IgG1 anti-PC was associated with an increased risk of CVD below 33rd, 25th, and 10th percentile and of stroke below 33rd and 25th, and of myocardial infarction (MI) below 10th percentile. Among men, a strong association with stroke was determined below the 33rd percentile [HR 9.20, CI (2.22–38.12); $p = 0.0022$]. D05 clone has higher binding affinity followed by E01 and A01 using molecular docking and further have been confirmed during the course of 100 ns simulation. The stability of the D05 clone with PC was substantially higher.

Conclusion: IgG1 anti-PC was a stronger protection marker than IgG anti-PC and IgG2 anti-PC and also separately for men. The molecular modeling approach helps in identifying the intrinsic properties of anti-PC clones and atomistic interactions with PC.

Keywords: antibodies, phosphorylcholine (PC), stroke, myocardial infarction, immune system, molecular docking and dynamics, SAbPred

INTRODUCTION

Phosphorylcholine (PC) is a danger-associated molecular pattern (DAMP), exposed on oxidized phospholipids as in oxidized low-density lipoprotein (OxLDL) and on apoptotic cells (1). In addition, PC is a pathogen-associated molecular pattern (PAMP) and an important antigen on bacteria, for example, *Streptococcus pneumoniae* and parasites and nematodes (**Figure 1**). PC is only recognized by the immune system and antibodies when exposed, bound to carriers, which can be lipids, proteins, or carbohydrates (1). IgG and IgM antibodies against PC (anti-PC) are present in healthy adults, at relatively high levels (1).

We have reported that IgM anti-PC is a protection marker for several chronic inflammatory disease conditions, including atherosclerosis and cardiovascular disease (CVD), rheumatic diseases, especially systemic lupus erythematosus (SLE), and mortality in chronic kidney disease (1–5). These findings have been largely confirmed by other groups (6–9). We recently reported that IgG1, but not IgG2, has similar associations with protection as IgM, in atherosclerosis (10), SLE (11), and chronic kidney disease (CKD) (12). Several potential underlying mechanisms have been reported (4, 5, 10, 11, 13–15).

We recently investigated the human anti-PC repertoire and generated fully human monoclonal anti-PC. In contrast to previous reports on laboratory mice, humans had somatically mutated anti-PC using a wide variety of Ig genes (16). We reported that these clones vary in binding capacity to PC and, in some cases, promote phagocytosis of dead cells (11).

To elucidate the mechanism of affinity and binding of PC to anti-PC clones, molecular modeling approaches, e.g., molecular docking and molecular dynamics simulations studies, help understand the functional profile of individual anti-PCs and their intrinsic atomistic interactions with PC. We thus investigated information about metabolic pathways, crystal structures, binding to proteins and other compounds, and relationships of drug targets by the use of these methods (17, 18). Through phenotypic studies of text mining and chemical structure, links between different compounds can be determined. In this study, we reported that anti-PC, especially IgG1 anti-PC, is a protection marker for CVD among 60-year-olds and determined the interaction of IgG1 anti-PC clones with PC using bioinformatics approaches.

MATERIALS AND METHODS

Subjects

The 60-year-old cohort is a large group study of cardiovascular outcomes as described (5). In 1997/1998, every third individual living in Stockholm County at the age of 60 was asked to participate in a screening accessing their cardiovascular health. A total of 4,228 participants (2,036 men and 2,192 women) were investigated for anthropometric, metabolic, and lifestyle factors. Serum and blood samples were collected (stored at –80°C). Until 2005, 211 new incidences of CVD were recorded in this cohort by matching with national registries. These include fatal and non-fatal myocardial infarction (MI), stroke, and angina pectoris. For each case, three healthy controls matched for age, sex, and other risk factors were selected randomly for a nested case-control design (5). The study was approved by the Karolinska Institutet research ethics committee and is in accordance with the Declaration of Helsinki. All subjects gave informed consent before entering the study.

To record incident cases of first CVD, new events of coronary heart disease, including fatal and non-fatal MI and ischemic stroke and hospitalization for angina pectoris, were registered. The study based on 4,232 subjects was matched with the national cause-of-death registry (fatal events until December 31, 2003) and the national in-hospital registry (non-fatal events until December 31, 2005). Through these matching procedures, 211 incident cases of CVD were recorded. Only living subjects without a history of CVD prior to recruitment were included in the matching procedures. The International Classification of Diseases (ICD-10) was used to register coronary heart disease deaths (i.e., I 20, I 21, and I 46), MI (i.e., I 21), angina pectoris including percutaneous coronary interventions and coronary artery bypass grafts (i.e., I 20, Z 95.5, and Z 95.1), and ischemic stroke (i.e., I 63–I 66). For each case, 3 controls were randomly selected, matched for sex and age (60 days). Thus, a nested case-control design (with 211 cases and 633 controls) was applied for the epidemiological and statistical analyses, and 209 cases and 620 controls were available for testing of the IgG, IgG1, and IgG2 anti-PC levels.

Antibody Determination

IgG, IgG1, and IgG2 anti-PC were determined using ELISA essentially as described previously (11). Pooled serum from Sigma Aldrich (St Louis, MO, United States) was used as a standard control for each plate. Another sample from a control group was used as an internal control for each plate. The ratio of internal control and standard control was used to determine the coefficient of variation (CV) between the plates. The CV between the plates was kept below 10%. The concentration of the antigen used in each well was 10 μg/ml. Nunc Immuno microwell plates (Thermo Labsystems, Franklin Lakes, MA, United States) were coated with PC-bovine serum albumin (BSA). Coated plates were incubated overnight at 4°C. After washing four times with wash buffer [1 × phosphate-buffered saline with Tween® 20 (PBST)], the plates were blocked with 2% BSA-phosphate-buffered saline (PBS) for 1 h at room temperature. We followed the same washing steps, and then serum samples were diluted for IgG, IgG1, and IgG2 (1:200, 1:100, and 1:100, respectively) in 0.2% BSA-PBS and added at 100 μl/well. Plates were incubated at room temperature for 2 h and washed as described above. Biotin-conjugated mouse anti-human IgG, mouse anti-human IgG1, mouse anti-human, IgG2 (diluted 1:25,000, 1:800, 1:25,000, respectively, in 1% BSA-PBS) were added at 100 μl/well and incubated at room temperature for 2 h. After four washings, the plates were incubated with incubated with horseradish peroxidase-conjugated streptavidin (1:6,000, 1:3,000, and 1:5,000, respectively, in 0.2% BSA-PBS) (Thermo Fisher Scientific, Roskilde, Denmark) at 100 μl/well for 20 min. The color was developed by adding the horseradish peroxidase substrate, 3,3′,5,5′-tetramethylbenzidine (TMB) (3.30,

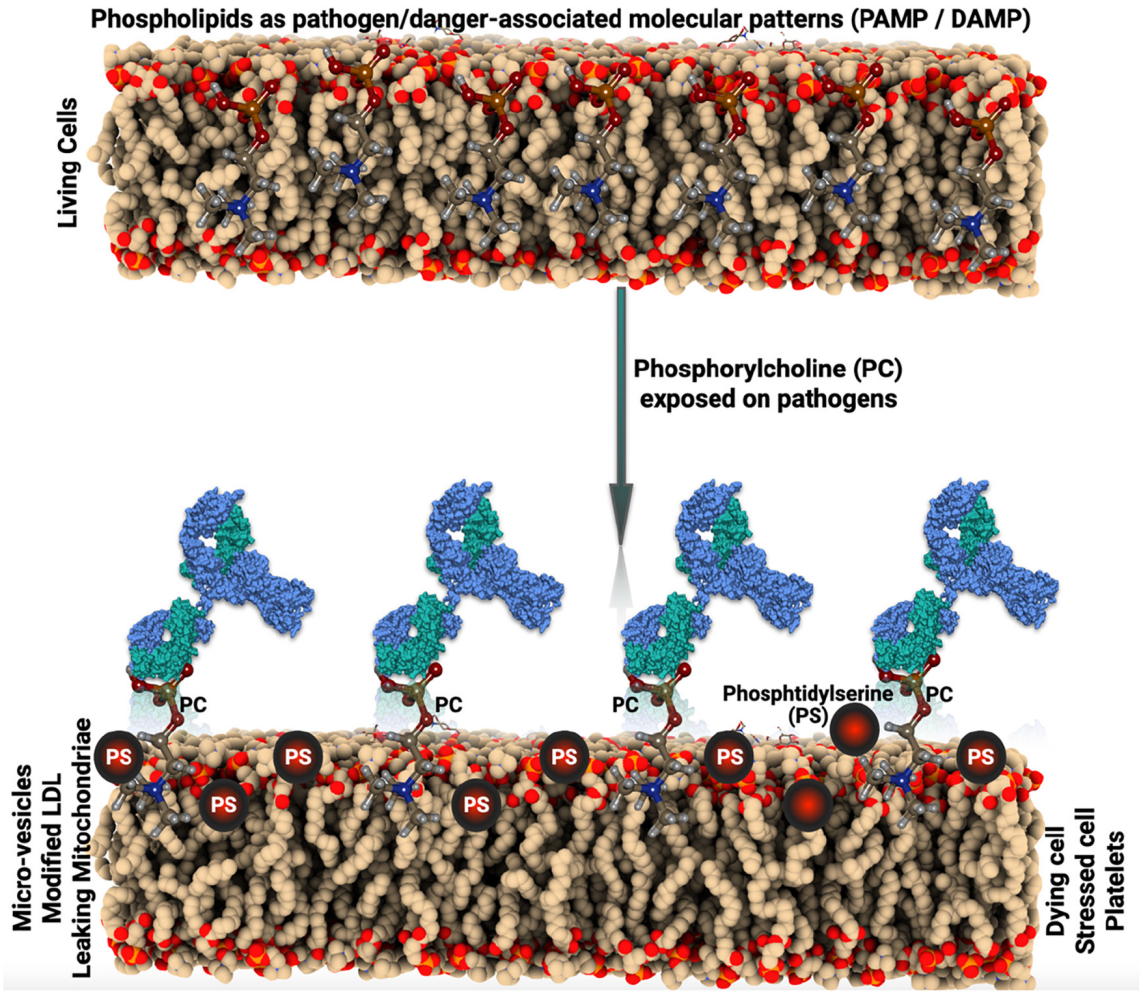

FIGURE 1 | Schematic illustration of the pathogen-associated molecular pattern (PAMP) and danger-associated molecular pattern (DAMP) mechanism.

5.50; Sigma Aldrich) at 100 μl/well and incubating the plates for 10, 10, and 15 min, respectively, at room temperature in the dark. The further reaction was stopped with stop solution 1 N H_2SO_4 at 50 μl/well. Finally, plates were read on an ELISA Multiscan Plus spectrophotometer (Spectra Max 250; Molecular Devices, San Jose, CA, United States) at 450 and 540 nm for IgG, and IgG1, IgG2, with the Biotek 800 TS absorbance reader at 450 and 630 nm. The delta value was determined *via* the subtraction of the blanked OD at 630 nm from the blanked optical density (OD) at 450 nm. The delta value of the respective sample was then divided by the delta value of the standard to reach a relative unit value of the abundance of antibodies in this sample. All samples were measured in duplicate within a single assay, and the CV between the duplicates was below 15% for all the antibodies.

In House Generated IgG1 Anti-phosphorylcholine Clones

We used our monoclonal antibodies (mAbs), which we produced, as described (16). As in our recent publication, we used three mAbs, namely, A01, D05, and E01, which were isolated from single PC-reactive B cells from healthy human donors and which differed in binding properties to PC (11). In brief, we synthesized and cloned the cDNAs expression vectors containing human Igγ, Igλ, or Igκ. Antibodies were then produced by co-transfection of exponentially growing human embryonic kidney (HEK) cells, and then the proteins were purified using the Protein G chromatography column. Antibody protein purity and the expression of heavy (H) and light (L) chains were then confirmed by sodium dodecyl sulfate-polyacrylamide gel electrophoresis (SDS-PAGE), and affinity to PC was measured by surface plasmon resonance on Biacore X-100 (GE Healthcare, Uppsala, Sweden) with isotype control as described (16).

Computational Methods

We have performed IgBLAST against the heavy (H) and light (L) chain sequences, e.g., E01, A01, and D05 clones derived from healthy subjects. The sequences of the clones were described in our previous work (11, 16). The hits were aligned based on the International ImMunoGeneTics information system human

(IMGT), V, D, and J genes (F + ORF). The protein sequences of the H chain and L chains derived from the alignments were subjected to the antibody structure prediction using the SAbPred tool (19). Antibody informatics tools, e.g., SAbPred, helps in improving our understanding of immune responses to disease and aid in the design and engineering of therapeutic molecules. Furthermore, we have retrieved the structure of the PC molecule from PubChem database (20) and refined using Marvin Sketch for the molecular docking analysis. The docking has been performed using the AutoDock Vina tool (21) where the intrinsic atomistic interactions and binding orientations of PC with antibodies have been deciphered. Furthermore, to validate the binding conformation of PC with the clone antibody structure, we have selected the best binding conformation of PC (antigen) with a high binding affinity score and subjected it to molecular dynamics simulation using Gromacs version 2020 (22). We obtained topologies from the CGenFF database (23) for the PC molecule. The CHARMM36 force field has been used to optimize the parameters of the target receptors (i.e., E01, A01, and D05 anti-PC clones). The complex systems have been mounted on a standard, solvent-molecular cubic frame. The Ewald (PME) particle mesh method was employed to compensate for the long range of electrostatic interactions under periodic boundary conditions with the 15 Å cutoff for non-bonded contacts. A total of 0.05 ns were simulated with a time step of 1 fs. Neighbor searching was performed every 1 step. The PME algorithm was used for electrostatic interactions with a cutoff value of 1.2 nm. A reciprocal grid of 72 × 72 × 72 cells was used with fourth-order B-spline interpolation. A single cutoff value of 1.2 nm was used for Van der Waals interactions. To achieve equilibrium, the system has been neutralized with Na^+ and Cl^- ions equivalents. Energy minimization and equilibration were performed by three steps as follows: (i) the entire system of ions, solvents, antibody, and PC was minimized for up to 50,000 steps using a steep algorithm, (ii) constraints were added to the antibody, and the conjugate for 100 ps during heating using a number of atoms, volume, and temperature (NVT), and (iii) at constant pressure (1 bar) and temperature (300 K) for 100 ps, with a time step of 2 fs in the equilibrium phase, a number of atoms, pressure, or temperature (NPT) ensemble were used. The algorithm SHAKE was used to restrict hydrogen to heavy atomic contacts. A total of 100 ns were simulated with a time step of 2 fs. Neighbor searching was performed every 20 steps. The PME algorithm was used for electrostatic interactions with a cutoff value of 1.2 nm. A single cutoff value of 1.223 nm was used for Van der Waals interactions. Temperature coupling was carried out with the V-rescale algorithm. Pressure coupling was carried out with the Parrinello-Rahman algorithm. In addition, the protein-linking energy was evaluated after 100 ns simulation to measure non-bonding energy interaction and short-range on-associated energy that was quantifiably reproduced in Gromacs energy profiles. Furthermore, the BSA conjugated with PC bearing PDB ID: 2BIB has been taken to study the antibody-antigen interaction to understand the mechanism of PC binding to clone antibodies in the presence of BSA. The antibody-antigen interactions were carried out using the Cluspro2.0 tool (24). The Cluspro 2.0 tool rotates the ligand with 70,000 rotations. For each rotation, it translates the ligand in x, y, and z relative to the receptor on a grid. Then, it chooses the translation with the best score from each rotation. Of the 70,000 rotations, the 1,000 rotation/translation combinations that have the lowest score were chosen. The algorithm is based on the greedy clustering of these 1,000 ligand positions with a 9-angstrom C-alpha root mean square deviation (RMSD) radius. The energy is based on repulsive, attractive, electrostatics, and Decoys as the Reference State (DARS) forces combined to give a negative score with high binding affinity. The more the negative score, the better the binding and involvement of cluster members.

Statistical Analysis

Various data analyses, including demographic biochemistry and anthropometry related, were performed for cases and controls, respectively, with values expressed as mean (SD) for normally distributed parameters and medians (ranges) for parameters that were not normally distributed after logarithmic transformation. Statistical differences between cases and controls were evaluated through parametric tests. Odds ratios (OR) with 95% CI were calculated applying conditional logistic regression with anti-PC levels divided into percentiles as indicated. For the analyses of specific percentiles, the remaining values formed the reference. Analyses were run crude or adjusted for traditional risk factors as indicated. These analyses were performed using the SAS 9.4 release (SAS Institute, Cary, NC). For all statistical analyses, a $p < 0.05$ was considered significant.

RESULTS

Clinical Associations

We identified 211 incident cases (i.e., 77 with MI, 85 with angina pectoris, and 49 with ischemic stroke) of first CVD events throughout the follow-up period. For each incident case, 3 age- and sex-matched controls were selected (i.e., 633 controls in total). Serum samples were missing for 2 cases and 13 controls, leaving 209 cases and 620 controls for analyses. As previously reported in a similar dataset, there were more hypertensives and smokers among the cases than controls and a trend-wise higher body mass index. Blood pressure level, high-density lipoprotein, and high-sensitivity C-reactive protein were associated with risk among cases as compared with those in controls. Among anti-PC determinations, only IgG1 anti-PC among men and IgG2 anti-PC among women were higher among cases than controls ($p = 0.046$ and $p = 0.019$, respectively) (**Table 1**). We then focused on comparisons between percentiles of anti-PC determinations.

IgG levels were divided into percentiles, and low or high levels were compared with the rest, as indicated (**Table 2** and **Supplementary Figure 1A**). After adjustment for smoking, body mass index, type 2 diabetes mellitus, hypercholesterolemia, and hypertension, decreased risk of stroke was observed in the higher percentiles of IgG anti-PC, which was significant at the 90th percentile: OR 0.19, CI (0.04–0.98); and the *p*-value is 0.0468. We could not find significant differences in the low or high levels when compared with whole CVD events or MI/angina pectoris.

TABLE 1 | Baseline characteristics among incident cardiovascular disease (CVD) cases and matched controls.

	Incident cases	Controls	*P*-value
Number	209	620	NA
Age, years	60	60	NA
Male gender, %	66	66	NA
Smokers, %	32	19.7	0.0002
Diabetes %	24.4	15.6	0.005
BMI kg/m^2	27.8 ± 4.6	26.7 ± 3.8	0.0031
Hypertension (>140/90 mm Hg), %	42.6	25.7	<0.0001
Glucose mmol/L	6.1 ± 2.5	5.6 ± 1.5	0.0004
Insulin μ mol/L	11.4 ± 7.1	10.1 ± 5.87	0.0067
Systolic blood pressure, mm Hg	148 ± 21.8	139 ± 21.2	<0.0001
Diastolic blood pressure, mm Hg	89 ± 10.6	85 ± 10.4	<0.0001
Cholesterol, mMol/l	6.1 ± 1.0	6.0 ± 1.2	0.1366
HDL, mMol/l	1.3 ± 0.4	1.4 ± 0.4	0.0005
LDL, mMol/l	4.07 ± 0.93	3.8 ± 0.94	0.04
Triglycerides, mMol/l	1.6 ± 1.0	1.4 ± 0.8	0.0005
hsCRP, mg/l	3.47 ± 10.03	2.88 ± 0.84	0.003
Anti-PC IgG unit values all	301.1 (171.1–470.2)	288.2 (161.5–458.3)	0.84
Anti-PC IgG unit values men	299.3 (160.5–454.5)	274.9 (158.7–431.9)	0.80
Anti-PC IgG unit values women	320.9 (175.8–557.1)	318 (169.5–532.5)	0.99
Anti-PC IgG1 unit values all	166.5 (97.5–283.3)	174 (112.4–282.9)	0.20
Anti-PC IgG1 unit values men	133.8 (82.6–208.6)	158 (103.7–227.4)	0.046
Anti-PC IgG 1 unit values women	264.9 (143.4–425.5)	279.5 (148.3–390.2)	0.70
Anti-PC IgG2 unit values all	203 (123.3–397.1)	213 (134.5–389.8)	0.35
Anti-PC IgG2 unit values men	255.7 (99,8–483.7)	234.7 (124.1–462.7)	0.99
Anti-PC IgG2 unit values women	159.8 (137.7–277.6)	201 (152.9–282.2)	0.019

IgG levels on the basis of gender were compared with similar percentiles, and for men, these associations were even more pronounced. At low levels, we observed an increased risk of CVD events: below 10th percentile: OR 1.92, CI (1.03–3.60), and *p*-value is 0.0410, and in relation to stroke, a decreased risk was observed above 75th percentile: OR 0.07, CI (0.01–0.59), and *p*-value is 0.0144, while no association was observed in women.

IgG1 levels were divided into percentiles, and low or high levels were compared with the rest, as indicated (**Table 3** and **Supplementary Figure 1B**). After adjustment for smoking, body mass index, type 2 diabetes mellitus, hypercholesterolemia, and hypertension, an increased risk of CVD was observed in the low percentiles of IgG1 anti-PC, at 10th: OR 1.80, CI (1.07–3.04), and *p*-value is 0.0272; at 25th: OR 1.62, CI (1.10–2.37), *p*-value is 0.0143, and at 33rd: OR 1.51, CI (1.05–2.15), and *p*-value is 0.0244. For stroke, the higher risk was observed at 25th: OR 2.62, CI (1.17–5.91), and *p*-value is 0.0199 and at 33rd: OR 2.97, CI (1.36–6.51), and *p*-value is 0.0065. The significant risk was observed in low levels of IgG1 anti-PC for MI/angina pectoris, the association at 10th: OR 2.20, CI (1.19–4.06), and *p*-value is 0.0116.

IgG1 levels on the basis of genders were compared with similar percentiles, and for men, these associations were even more pronounced for CVD, stroke, and MI/angina. The stronger significant association for CVD was at 10th: OR 2.05, CI (1.12–3.75), and *p*-value is 0.0196; at 25th: OR 1.72, CI (1.11–2.67), and *p*-value is 0.0159; and at 33rd: OR 1.69, CI (1.11–2.56), and *p*-value is 0.0140. For stroke, the higher risk was observed at 25th: OR 4.76, CI (1.26–17.91), and *p*-value is 0.0211, and at 33rd: OR 9.20, CI (2.22–38.12), and *p*-value is 0.0022. For MI/angina, also higher risk was found at 10th: OR 2.18, CI (1.10–4.33), and *p*-value is 0.0254, while no association was observed in women.

IgG2 levels were divided into percentiles, and low or high levels were compared with the rest, as indicated (**Table 4** and **Supplementary Figure 1C**). After adjustment for smoking, body mass index, type 2 diabetes mellitus, hypercholesterolemia, and hypertension, an increased risk of CVD was observed at 33rd: OR 1.47, CI (1.04–2.07), and *p*-value is 0.0285, and for stroke, the higher risk was observed in the low percentiles of IgG2 anti-PC, at 33rd: OR 2.26, CI (1.01–5.04), and *p*-value is 0.0473. There was no association for MI/angina pectoris. IgG2 levels on the basis of genders were compared with similar percentiles, and for men and women, some significant associations were seen. Among men, we observed an increased risk of stroke: at percentile 50th: OR 0.36, CI (0.14–0.91), and *p*-value is 0.0452. When divided into CVD, stroke, or MI/angina, associations did not reach statistical significance for CVD and MI/angina in men, it was interesting to see some associations were present in women for CVD below 33rd: OR 2.67, CI (1.46–4.87), and *p*-value is 0.0014; above 50th: OR 0.43, CI (0.22–0.83), and *p*-value is 0.0122, and similar for MI/angina in women below 33rd: OR 3.65, CI (1.67–8.0), and *p*-value is 0.0012; and above 50th percentile was protection with OR 0.41, CI (0.18–0.94), and *p*-value is 0.0352.

TABLE 2 | Association between levels of IgG anti-phosphorylcholine (PC) and risk for cardiovascular disease (CVD), stroke, and myocardial infarction (MI) among all participants and men and women.

All outcomes												
Anti-PC IgG	**ALL**				**Males**				**Females**			
	Crude	***P*-values**	**Adjusted***	***P*-values**	**Crude**	***P*-values**	**Adjusted***	***P*-values**	**Crude**	***P*-values**	**Adjusted***	***P*-values**
	OR (95% CI)				**OR (95% CI)**				**OR (95% CI)**			
≤10%	1.32 (0.80–2.19)	0.2744	1.47 (0.87–2.48)	0.1539	1.50 (0.83–2.69)	0.1772	**1.92 (1.03–3.60)**	**0.0410**	0.96 (0.36–2.56)	0.9346	0.77 (0.28–2.13)	0.6176
≤25%	0.99 (0.69–1.42)	0.9508	1.09 (0.75–1.60)	0.6441	1.00 (0.64–1.57)	0.9848	1.16 (0.72–1.87)	0.5333	0.96 (0.51–1.79)	0.8954	0.97 (0.50–1.88)	0.9270
≤33%	0.94 (0.67–1.32)	0.7097	1.00 (0.71–1.43)	0.9816	0.90 (0.60–1.37)	0.6354	1.03 (00.67–1.60)	0.8801	1.01 (0.56–1.82)	0.9800	0.91 (0.48–1.70)	0.7566
>50%	1.12 (0.82–1.53)	0.4729	1.04 (0.75–1.44)	0.8343	1.22 (0.83–1.78)	0.3083	1.06 (0.71–1.59)	0.7762	0.94 (0.55–1.63)	0.8339	1.02 (0.56–1.83)	0.9518
>66%	1.09 (0.78–1.51)	0.6306	0.92 (0.64–1.31)	0.6312	1.12 (0.74–1.69)	0.5852	0.86 (0.54–1.34)	0.4975	1.02 (0.58–1.78)	0.9432	1.05 (0.58–1.90)	0.8746
>75%	1.04 (0.71–1.52)	0.8212	0.91 (0.61–1.37)	0.6561	1.07 (0.66–1.74)	0.7730	0.83 (0.48–1.42)	0.4933	1.00 (0.55–1.83)	1.0000	1.05 (0.55–1.99)	0.8880
>90%	1.03 (0.60–1.78)	0.9067	0.80 (0.45–1.44)	0.4646	1.00 (0.47–2.13)	1.0000	0.68 (0.29–1.57)	0.3633	1.07 (0.49–2.36)	0.8653	0.96 (0.41–2.23)	0.9192
Stroke as an outcome												
Anti-PC IgG	**ALL**				**Males**				**Females**			
	Crude	***P*-values**	**Adjusted***	***P*-values**	**Crude**	***P*-values**	**Adjusted***	***P*-values**	**Crude**	***P*-values**	**Adjusted***	***P*-values**
	OR (95% CI)				**OR (95% CI)**				**OR (95% CI)**			
≤10%	1.79 (0.71–4.53)	0.2197	1.80 (0.67–4.82)	0.2450	2.43 (0.69–8.64)	0.1692	2.91 (0.66–12.87)	0.1588	1.25 (0.31–5.11)	0.7556	0.86 (0.19–3.87)	0.7556
≤25%	1.09 (0.52–2.26)	0.8253	1.00 (046–2.19)	0.9981	1.20 (0.41–3.51)	0.7430	1.14 (0.35–3.74)	0.8265	1.00 (0.37–2.73)	1.0000	0.86 (0.29–2.54)	1.0000
≤33%	1.01 (0.50–2.03)	0.9763	0.98 (0.47–2.06)	0.9663	0.94 (0.35–2.51)	0.9010	1.28 (0.40–4.07)	0.6732	1.09 (0.40–2.95)	0.8651	0.80 (0.27–2.38)	0.8651
>50%	0.89 (0.46–1.71)	0.7179	0.89 (0.44–1.82)	0.7478	0.80 (0.31–2.03)	0.6355	0.52 (0.15–1.74)	0.2862	0.98 (0.39–2.46)	0.9688	1.27 (0.46–3.53)	0.9688
>66%	0.54 (0.26–1.13)	0.1034	0.47 (0.21–1.07)	0.0710	0.51 (0.17–1.53)	0.2325	0.30 (0.07–1.26)	0.0993	0.57 (0.2 1–1.53)	0.2667	00.58 (0.20–1.66)	0.2667
>75%	0.45 (0.18–1.11)	0.0825	0.38 (0.14–1.02)	0.0547	0.25 (0.05–1.26)	0.0937	**0.07 (0.01–0.59)**	**0.0144**	0.63 (0.21–1.90)	0.4108	0.67 (0.21–2.14)	0.4108
>90%	0.26 (0.06–1.21)	0.0855	**0.19 (0.04–0.98)**	**0.0468**	**N/A**	**N/A**	**N/A**	**N/A**	0.65 (0.14–3.13)	0.5926	0.54 (0.10–2.87)	0.5926
Angina/MI as an outcome												
Anti-PC IgG	**ALL**				**Males**				**Females**			
	Crude	***P*-values**	**Adjusted***	***P*-values**	**Crude**	***P*-values**	**Adjusted***	***P*-values**	**Crude**	***P*-values**	**Adjusted***	***P*-values**
	OR (95% CI)				**OR (95% CI)**				**OR (95% CI)**			
≤10%	1.17 (0.64–2.14)	0.6002	1.32 (0.69–2.51)	0.3983	1.31 (0.67–2.57)	0.4220	1.67 (0.80–3.47)	0.1735	0.77 (0.20–2.99)	0.7003	0.59 (0.14–2.50)	0.4710
≤25%	0.96 (0.63–1.46)	0.8462	1.09 (0.70–1.71)	0.7019	097 (0.59–1.59)	0.9008	1.12 (0.65–1.90)	0.6887	0.93 (0.42–2.07)	0.8664	1.04 (0.44–2.45)	0.9373
≤33%	0.92 (0.62–1.35)	0.6574	0.98 (0.65–1.47)	0.9080	0.90 (0.57–1.42)	0.6420	0.98 (0.60–1.61)	0.9439	0.97 (0.47–2.0)	0.9262	0.88 (0.39–1.98)	0.7592
> 50%	1.20 (0.84–1.72)	0.3107	1.12 (0.77–1.63)	0.5567	1.33 (0.87–2.01)	0.1842	1.20 (0.77–1.86)	0.4281	0.92 (0.47–1.82)	0.8166	0.98 (0.47–2.08)	0.9665
>66%	1.32 (0.91–1.93)	0.1405	1.14 (0.76–1.71)	0.5211	1.31 (0.83–2.04)	0.2445	1.04 (0.64–1.69)	0.8821	1.38 (0.69–2.77)	0.3618	1.47 (0.69–3.13)	0.3126
> 75%	1.30 (0.85–1.99)	0.2196	1.14 (0.72–1.80)	0.5892	1.33 (0.79–2.22)	0.2818	1.05 (0.59–1.87)	0.8649	1.26 (0.60–2.64)	0.5458	1.29 (0.58–2.90)	0.5334
>90%	1.44 (0.79–2.62)	0.2385	1.08 (0.56–2.08)	0.8172	1.53 (0.70–3.35)	0.2893	1.04 (0.43–2.51)	0.9259	1.32 (0.52–3.36)	0.5653	1.08 (0.38–3.07)	0.8850

**Adjusted for confounders (e.g., smoking, blood pressure, and diabetes).*
Bold values mean significant.

TABLE 3 | Association between levels of IgG1 anti-PC and risk for CVD, stroke, and MI among all participants and men and women.

Anti-PC IgG1	All outcomes											
	ALL				Males				Females			
	Crude	*P*-values	Adjusted*	*P*-values	Crude	*P*-values	Adjusted*	*P*-values	Crude	*P*-values	Adjusted*	*P*-values
	OR (95% CI)				OR (95% CI)				OR (95% CI)			
≤10%	**1.73 (1.06–2.84)**	**0.0291**	**1.80 (1.07–3.04)**	**0.0272**	**1.87 (1.07–3.29)**	**0.0286**	**2.05 (1.12–3.75)**	**0.0196**	1.33 (0.46–3.83)	0.5999	1.22 (0.40–3.68)	0.7285
≤25%	**1.51 (1.05–2.18)**	**0.0265**	**1.62 (1.10–2.37)**	**0.0143**	**1.53 (1.01–2.31)**	**0.0433**	**1.72 (1.11–2.67)**	**0.0159**	1.44 (0.66–3.14)	0.3556	1.33 (0.59–2.99)	0.4886
≤33%	**1.49 (1.06–2.09)**	**0.0209**	**1.51 (1.05–2.15)**	**0.0244**	**1.55 (1.05–2.28)**	**0.0287**	**1.69 (1.11–2.56)**	**0.0140**	1.33 (0.67–2.66)	0.4165	1.08 (0.52–2.25)	0.8356
>50%	0.87 (0.63–1.21)	0.3989	0.80 (0.57–1.13)	0.2008	0.81 (0.54–1.20)	0.2901	0.70 (0.45–1.07)	0.0960	1.02 (0.57–1.85)	0.9398	1.07 (0.57–1.98)	0.8413
>66%	0.92 (0.65–1.32)	0.6605	0.87 (0.60–1.27)	0.4747	0.80 (0.50–1.29)	0.3637	0.69 (0.42–1.13)	0.1436	1.14 (0.64–2.02)	0.6616	1.27 (0.69–2.36)	0.4406
>75%	0.93 (0.63–1.38)	0.7297	0.89 (0.60–1.33)	0.5651	0.90 (0.52–1.57)	0.7127	0.79 (0.45–1.40)	0.4160	0.97 (0.56–1.68)	0.9064	1.01 (0.56–1.81)	0.9832
>90%	1.41 (0.85–2.33)	0.1791	1.39 (0.82–2.33)	0.2189	1.50 (0.64–3.51)	0.3488	1.45 (0.60–3.51)	0.4059	1.37 (0.73–2.55)	0.3251	1.36 (0.71–2.60)	0.3528
	Stroke as an outcome											
Anti-PC IgG1	**ALL**				**Males**				**Females**			
	Crude	***P*-values**	**Adjusted***	***P*-values**	**Crude**	***P*-values**	**Adjusted***	***P*-values**	**Crude**	***P*-values**	**Adjusted***	***P*-values**
	OR (95% CI)				**OR (95% CI)**				**OR (95% CI)**			
≤10%	1.17 (0.40–3.42)	0.7775	1.08 (0.34–3.40)	0.8967	1.88 (0.49–7.24)	0.3597	1.72 (0.35–8.44)	0.5037	0.50 (0.06–4.15)	0.5211	0.44 (0.05–4.00)	0.4634
≤25%	**2.41 (1.12–5.19)**	**0.0251**	**2.62 (1.17–5.91)**	**0.0199**	**2.96 (1.04–8.43)**	**0.0424**	**4.76 (1.26–17.91)**	**0.0211**	1.87 (0.60–5.85)	0.2831	1.84 (0.55–6.16)	0.3229
≤33%	**2.55 (1.23–5.28)**	**0.0117**	**2.97 (1.36–6.51)**	**0.0065**	**4.65 (1.62–13.31)**	**0.0042**	**9.20 (2.22–38.12)**	**0.0022**	1.21 (0.40–3.68)	0.7379	1.04 (0.31–3.53)	0.9473
>50%	0.66 (0.34–1.30)	0.2304	0.62 (0.30–1.27)	0.1882	0.46 (0.17–1.25)	0.1268	0.44 (0.14–1.37)	0.1554	0.94 (0.37–2.43)	0.9034	0.88 (0.33–2.38)	0.8057
>66%	0.70 (0.33–1.48)	0.3526	0.64 (0.29–1.41)	0.2680	0.49(0.15–1.62)	0.2432	0.29 (0.06–1.34)	0.1128	0.92 (0.34–2.48)	0.8647	1.02 (0.35–2.96)	0.9736
>75%	0.88 (0.42–1.84)	0.7315	0.81 (0.37–1.78)	0.5992	0.68 (0.21–2.28)	0.5359	0.49 (0.11–2.16)	0.3439	1.04 (0.40–2.74)	0.9344	1.14 (0.41–3.17)	0.8048
>90%	0.85 (0.30–2.42)	0.7645	0.82 (0.28–2.45)	0.7242	1.20 (0.23–6.19)	0.8275	0.95 (0.16–5.72)	0.9510	0.70 (0.18–2.66)	0.5979	0.76 (0.19–3.11)	0.7077
	Angina/MI as an outcome											
Anti-PC IgG1	**ALL**				**Males**				**Females**			
	Crude	***P*-values**	**Adjusted***	***P*-values**	**Crude**	***P*-values**	**Adjusted***	***P*-values**	**Crude**	***P*-values**	**Adjusted***	***P*-values**
	OR (95% CI)				**OR (95% CI)**				**OR (95% CI)**			
≤10%	**1.94 (1.11–3.40)**	**0.0204**	**2.20 (1.19–4.06)**	**0.0116**	**1.87 (1.01–3.47)**	**0.0469**	**2.18 (1.10–4.33)**	**0.0254**	2.29 (0.61–8.56)	0.2170	2.23 (0.54–9.18)	0.2651
≤25%	1.31 (0.87–1.99)	0.2007	1.45 (0.92–2.26)	0.1071	1.35 (0.86–2.12)	0.1991	1.55 (0.95–2.53)	0.0816	1.14 (0.38–3.44)	0.8111	0.93 (0.29–3.03)	0.9066
≤33%	1.27 (0.87–1.88)	0.2191	1.31 (0.87–1.98)	0.1927	1.24 (0.81–1.91)	0.3209	1.36 (0.85–2.16)	0.1970	1.41 (0.59–3.40)	0.4388	1.08 (042–2.77)	0.8718
>50%	0.95 (0.65–1.38)	0.7749	0.84 (0.56–1.25)	0.3803	0.91 (0.59–1.40)	0.6607	0.75 (0.47–1.22)	0.2450	1.08 (0.50–2.32)	0.8465	1.17 (0.52–2.66)	0.7060
>66%	1.00 (0.67–1.51)	0.9862	0.92 (0.60–1.41)	0.7076	0.89 (0.53–1.49)	0.6535	0.75 (0.43–1.28)	0.2899	1.27 (0.62–2.57)	0.5145	1.54 (0.70–3.41)	0.2870
>75%	0.96 (0.61–1.51)	0.8473	0.88 (0.55–1.42)	0.6031	0.98 (0.52–1.82)	0.9375	0.81 (0.42–1.56)	0.5232	0.93 (0.48–1.83)	0.8411	1.02 (0.49–2.12)	0.9664
>90%	1.68 (0.94–3.02)	0.0795	1.64 (0.89–3.01)	0.1145	1.64 (0,61–4.43)	0.3314	1.64 (0.57–4.73)	0.3609	1.71 (0.83–3.51)	0.1443	1.70 (0.80–3.64)	0.1694

**Adjusted for confounders (e.g., smoking, blood pressure, and diabetes).*
Bold values mean significant.

TABLE 4 | Association between levels of IgG2 anti-PC and risk for CVD, stroke, and MI among all participants and men and women.

All outcomes												
Anti-PC IgG2	**All**				**Males**				**Females**			
	Crude	***P*-values**	**Adjusted***	***P*-values**	**Crude**	***P*-values**	**Adjusted***	***P*-values**	**Crude**	***P*-values**	**Adjusted***	***P*-values**
	OR (95% CI)				**OR (95% CI)**				**OR (95% CI)**			
≤10%	1.54 (0.93–2.55)	0.0934	1.51 (0.90–2.55)	0.1196	1.60 (0.91–2.79)	0.1015	1.56 (0.87–2.80)	0.1376	1.32 (0.41–4.29)	0.6402	1.47 (0.45–4.85)	0.5268
≤25%	1.15 (0.81–1.65)	0.4411	1.23 (0.85–1.78)	0.2790	1.14 (0.75–1.74)	0.5287	1.25 (0.80–1.93)	0.3252	1.17 (0.59–2.33)	0.6549	1.19 (0.59–2.43)	0.6246
≤33%	1.34 (0.97–1.87)	0.0772	**1.47 (1.04–2.07)**	**0.0285**	0.99 (0.66–1.48)	0.9448	1.08 (0.70–1.66)	0.7285	**2.49 (1.40–4.44)**	**0.0020**	**2.67 (1.46–4.87)**	**0.0014**
>50%	0.81 (0.58–1.12)	0.2034	0.75 (0.53–1.06)	0.1052	1.03 (0.69–1.54)	0.8916	0.95 (0.62–1.44)	0.7978	**0.47 (0.25–0.87)**	**0.0169**	**0.43 (022–0.83)**	**0.0122**
>66%	1.04 (0.73–1.48)	0.8215	0.97 (0.67–1.42)	0.8871	1.15 (0.78–1.70)	0.4903	1.06 (0.70–1.62)	0.7754	0.70 (0.31–1.58)	0.3904	0.70 (0.30–1.61)	0.3959
>75%	1.10 (0.76–1.60)	0.5996	1.01 (0.68–1.50)	0.9659	1.18 (0.78–1.78)	0.4427	1.06 (0.68–1.64)	0.8064	0.86 (0.37–1.99)	0.7264	0.84 (0.35–2.03)	0.7041
>90%	0.95 (0.55–1.63)	0.8374	0.93 (0.53–1.64)	0.8035	1.04 (0.56–1.94)	0.8933	0.99 (0.52–1.89)	0.9763	0.70 (0.23–2.17)	0.5390	0.69 (0.21–2.34)	0.5534
Stroke as an outcome												
Anti-PC IgG2	**All**				**Males**				**Females**			
	Crude	***P*-values**	**Adjusted***	***P*-values**	**Crude**	***P*-values**	**Adjusted***	***P*-values**	**Crude**	***P*-values**	**Adjusted***	***P*-values**
	OR (95% CI)				**OR (95% CI)**				**OR (95% CI)**			
≤10%	1.75 (0.63–4.89)	0.2858	1.77 (0.59–5.27)	0.3075	2.03 (0.54–7.72)	0.2979	2.05 (0.42–10.04)	0.3778	1.42 (0.28–7.07)	0.6708	1.75 (0.33–9.19)	0.5069
≤25%	1.31 (0.60–2.83)	0.5005	1.58 (0.69–3.63)	0.2794	1.67 (0.58–4.83)	0.3475	1.97 (0.56–6.97)	0.2951	1.00 (0.32–3.10)	1.0000	1.13 (0.34–3.72)	0.8449
≤33%	1.64 (0.80–3.34)	0.1752	**2.26 (1.01–5.04)**	**0.0473**	2.06 (0.75–5.65)	0.1587	2.93 (0.85–10.13)	0.0894	1.30 (0.48–3.55)	0.6062	1.62 (0.53–4.91)	0.3976
>50%	**0.42 (0.21–0.87)**	**0.0187**	**0.38 (0.18–0.81)**	**0.0128**	**0.36 (0.14–0.91)**	**0.0298**	**0.32 (0.11–0.98)**	**0.0452**	0.54 (0.18–1.67)	0.2864	0.43 (0.13–1.40)	0.1618
>66%	0.66 (0.31–1.40)	0.2803	0.62 (0.27–1.41)	0.2515	0.57 (0.22–1.45)	0.2338	0.52 (0.17–1.56)	0.2395	0.88 (0.26–3.03)	0.8362	0.71 (0.19–2.65)	0.6057
>75%	0.72 (0.32–1.63)	0.4269	0.69 (0.28–1.71)	0.4231	0.60 (0.22–1.62)	0.3147	0.57 (0.18–1.82)	0.3385	1.10 (0.25–4.82)	0.8990	0.95 (0.20–4.56)	0.9464
>90%	0.73 (0.23–2.37)	0.6058	0.89 (0.25–3.23)	0.8610	0.85 (0.21–3.41)	0.8181	0.98 (0.21–4.50)	0.9776	0.53 (0.06–4.90)	0.5723	0.57 (0.04–8.26)	0.6806
Angina/MI as an outcome												
Anti-PC IgG2	**All**				**Males**				**Females**			
	Crude	***P*-values**	**Adjusted***	***P*-values**	**Crude**	***P*-values**	**Adjusted***	***P*-values**	**Crude**	***P*-values**	**Adjusted***	***P*-values**
	OR (95% CI)				**OR (95% CI)**				**OR (95% CI)**			
≤10%	1.48 (0.83–2.65)	0.1852	1.39 (0.75–2.58)	0.2928	1.52 (0.82–2.81)	0.1849	1.49 (0.77–2.89)	0.2383	1.23 (0.22–6.94)	0.8188	0.90 (0.15–5.66)	0.9142
≤25%	1.11 (0.74–1.66)	0.6033	1.19 (0.78–1.82)	0.4280	1.07 (0.68–1.69)	0.7702	1.17 (0.72–1.91)	0.5274	1.28 (0.54–3.04)	0.5696	1.17 (0.46–2.99)	0.7425
≤33%	1.28 (0.88–1.85)	0.1976	1.39 (0.94–2.05)	0.1027	0.86 (0.55–1.34)	0.4986	0.92 (0.57–1.49)	0.7360	**3.43 (1.67–7.06)**	**0.0008**	**3.65 (1.67–8.00)**	**0.0012**
>50%	0.97 (0.67–1.42)	0.8860	0.91 (0.61–1.35)	0.6217	1.31 (0.84–2.08)	0.2109	1.21 (0.75–1.96)	0.4302	**0.44 (0.21–0.93)**	**0.0310**	**0.41 (0.18–0.94)**	**0.0352**
>66%	1.19 (0.80–1.78)	0.3914	1.06 (0.69–1.62)	0.7935	1.35 (0.87–2.08)	0.1793	1.16 (0.73–1.86)	0.5286	0.60 (0.21–1.74)	0.3450	0.67 (0.22–1.99)	0.4655
>75%	1.25 (0.82–1.89)	0.3021	1.05 (0.67–1.64)	0.8443	1.38 (0.87–2.19)	0.1667	1.13 (0.69–1.86)	0.6329	0.77 (0.28–2.12)	0.6152	0.80 (0.28–2.31)	0.6773
>90%	1.02 (0.55–1.87)	0.9583	0.90 (0.47–1.70)	0.7369	1.10(0.55–2.21)	0.7868	0.90 (0.43–1.85)	0.7680	0.78 (0.21–2.89)	0.7147	0.82 (0.21–3.26)	0.7778

**Adjusted for confounders (e.g., smoking, blood pressure, and diabetes).*
Bold values mean significant.

Structural Modeling of Clone Antibodies

Taking into account the association results observed, we decided to proceed with in-depth analyses using our sequences and IgG1 anti-PC clones by *in silico* methods.

SAbPred analysis resulted in three structural antibody models based on VH and VL sequences from respective clones, namely, E01, A01, and D05 (**Figure 2A**). The resultant structural models comprise variable complementary-determining regions (CDRs), of which the CDR3 region is considered to be the most crucial part in binding specific antigens. The diversity of CDR3 amino acid sequences provides a measure of B-cell diversity in an antigen-selected B-cell repertoire. The sequence variability of the CDR3 region in all three clones was retrieved using the IgBLAST alignment. The alignment summary has been depicted in **Figure 2B**. From structural modeling of antibodies, we have also illustrated sequence liabilities that depict the amino acid level modifications. Among the three clones, asparagine isomerization has been observed in a high frequency. Apart from asparagine isomerization, several other modifications have been illustrated in **Figures 3A–C**.

One of the most prominent differences between the three clones is the lysine glycation observed only in the D05 clone, which makes it a standout. Most of the amino acid modifications were observed in H chain regions in comparison to light chain sequences. Furthermore, IgBLAST also resulted in the amino acid substitution landscape, where we observed both light and H chain sequence variability in comparison to IMGT germline genes (**Figures 4A–C**). D05 turns out to be different in the amino acid substitution pattern, where we have observed substitution in the H chain region. E01 and A05 do not have any substitution in the H chain region. In light chain sequence, the observed amino-acid substitution resemblance to the IMGT germline genes, i.e., IGKV3-20*01 and IGKV4-1*01, turns out to be the same in the substitution pattern, whereas D05 differs in both H and L chain cases.

Binding Affinity of Phosphorylcholine With E01, A01, and D05 Clone Antibodies

Molecular docking of single-molecule PC with the clone antibodies reveals intrinsic atomic insights and binding orientation of PC with different CDR3 regions of clone antibodies. When the PC molecule was subjected to the molecular docking analysis with clone antibodies, the difference in binding energies has been observed (**Figure 5A**).

In most cases, the PC seems to interact with the CDR3 region and its vicinity. Among all the clone antibodies, the binding energies of PC with D05 clone have the highest range of binding energies, whereas the lowest have been observed in the case of the A01 clone. The nine binding modes of PC with all the clone antibodies have a range of binding energies, i.e., -3.9 to -4.5 kcal/mol. The first binding mode of PC with E01, A01, and D05 has a binding energy of -4.5 kcal/mol as the sequence variability of the clone antibodies does not differ in terms of amino acid compositions. However, when different binding modes of PC have been considered, the binding energies of PC substantially differ in all the cases. Furthermore, we have also performed the antibody-antigen interaction analysis of the PC complex conjugated with choline-binding protein E (CbpE) of *Streptococcus pneumoniae* (PDB ID: 2BIB) with the E01, A01, and D05 clone antibodies. The analysis revealed that the D05 clone has the highest binding affinity (lowest energy, i.e., -385.8 kcal/mol) toward the complex PC conjugate in comparison to other clones (**Figure 5B**). The interaction analyses revealed that the D05 clone has the highest binding affinity toward the single-molecule PC as well as the PC conjugate.

The intrinsic atomic interaction of single-molecule PC binding to the E01, A01, and D05 clone antibodies has been illustrated in **Figures 6A–C**.

The interaction analyses showed the hydrophobicity mapping, hydrogen-bonding patterns, and 2D interaction map. The CDR3 region has been mapped to all the clone antibodies where PC was expected to interact. The hydrophobicity map of E01, A01, and D05 has been depicted in **Figures 6A–C** (right), respectively. When we compared the hydrophobicity map, the D05 clone had the highest possible hydrophobic amino acids interacting with PC as compared with E01 and A01 clones. Moreover, the hydrogen-bonding pattern of the D05 clone has a greater number of PC interacting partners among all the interactions.

Molecule Dynamics Simulation of Phosphorylcholine With Clone Antibodies

With hindsight, the D05 clone stands out to be the best among all the clone antibodies in terms of molecular interactions, hydrophobicity level, and binding affinity. To further confirm the PC affinity toward the anti-PC clones, the complex has been subjected to all-atom molecular dynamics simulation using Gromacs for 100 ns (**Figures 7A–C** and **Supplementary Video 1**).

To test the binding affinity and conformation of PC, the binding mode of PC with the lowest binding energy has been considered. The root-mean-square deviation of the cloned antibody was observed to be constant throughout the simulation in the case of the D05 clone (**Figure 7D**). However, the solvent accessibility surface area and free energy of solvation tend to decrease as the binding affinity of PC increases. When simulated for 100 ns within the solvent environment, the PC tends to swap its position toward the CDR3 region, as shown in **Figures 7A–C**. As observed from the aforementioned findings, the hydrogen bonding of the PC with the D05 clone antibody increased during the 100 ns simulation followed by E01 (29.331 Å) and A01 (48.817 Å). When the hydrophobicity scale was mapped during the simulation, the final confirmation of PC tends to bind to hydrophobic amino acids as compared with the initial conformation. The analysis correlates with the 2D interaction mapping, where the PC tends to interact more with hydrophobic amino acid residues. We have also investigated the root mean square fluctuations from the perspective of the PC (**Figure 7E**) and the complex (**Figure 7F**).

In all the anti-PC clones, we found a substantial difference in terms of PC binding to the receptors. When comparing the PC binding to the anti-PC clones with respect to its stability, E01 and A01 have more deviations and thus confirm the affinity of the PC molecule toward the D05 clone.

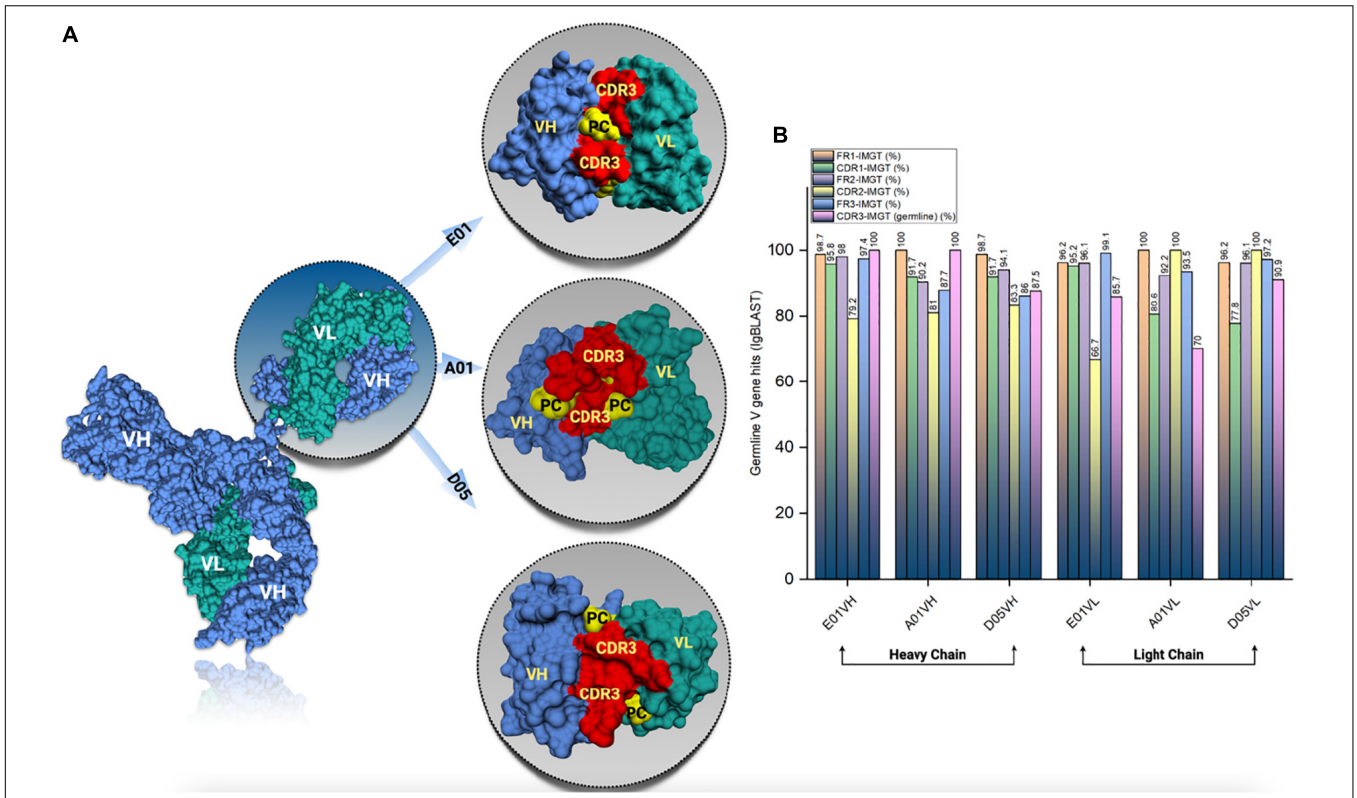

FIGURE 2 | Antibody structural modeling. **(A)** The structural representation of the modelled cloned antibodies from E01, A01 and D05 clones using SAbPred. **(B)** The frequency of germline V gene hits resulted from IgBLAST analysis.

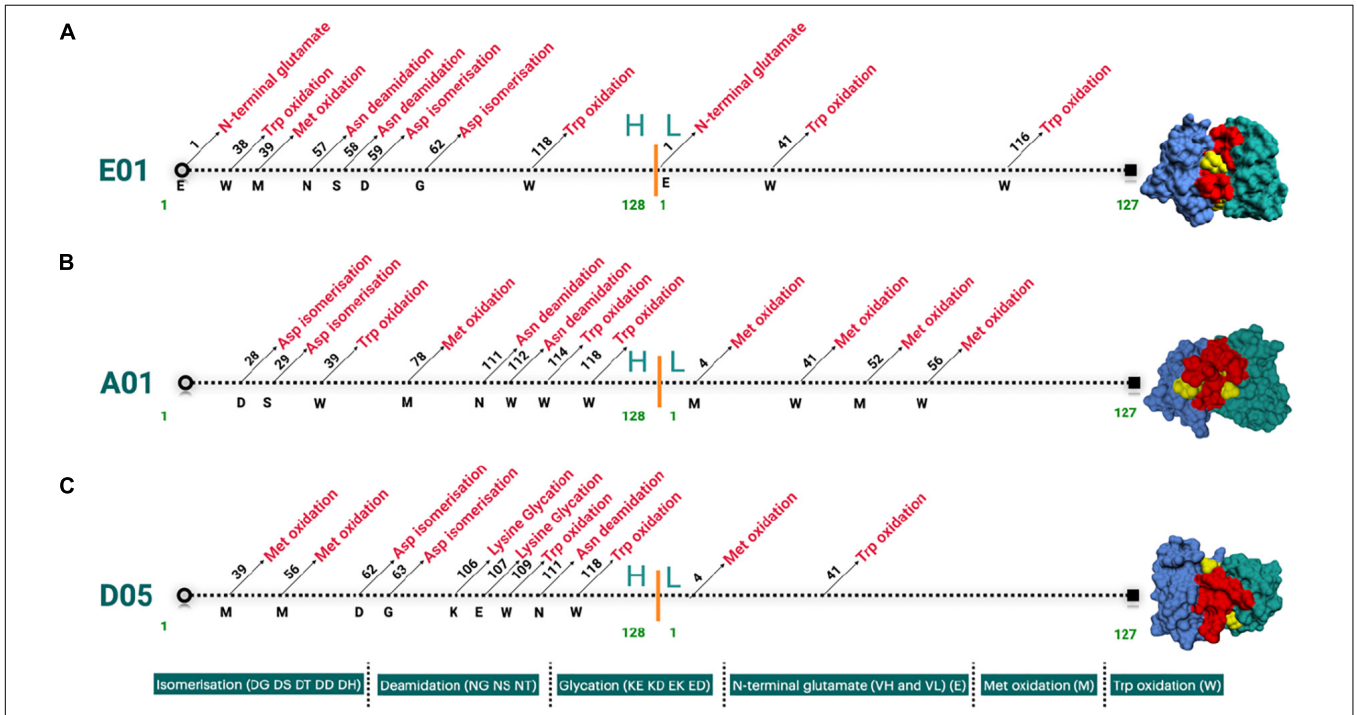

FIGURE 3 | (A–C) Landscape of cloned antibodies sequence liabilities depicted structurally for both heavy and light chain sequences. The figure represents the sequence liabilities of various clones considered in this work, i.e., E01, A01, and D05 clones, respectively.

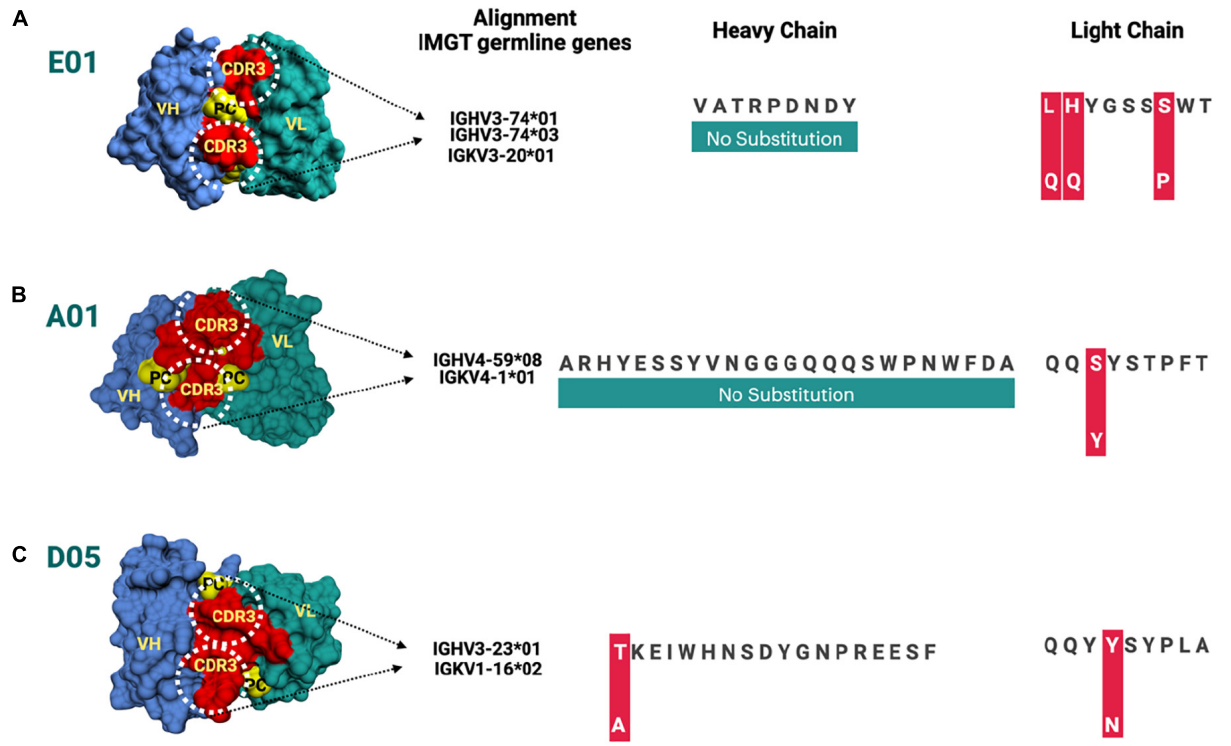

FIGURE 4 | (A–C) Amino acid substitution map for heavy and light chain sequences compared to ImMunoGeneTics information system human (IMGT) germline genes. The amino acid substitutions are depicted for different clones, i.e., E01, A01, and D05, respectively. The red bar represents the substitution of amino acid.

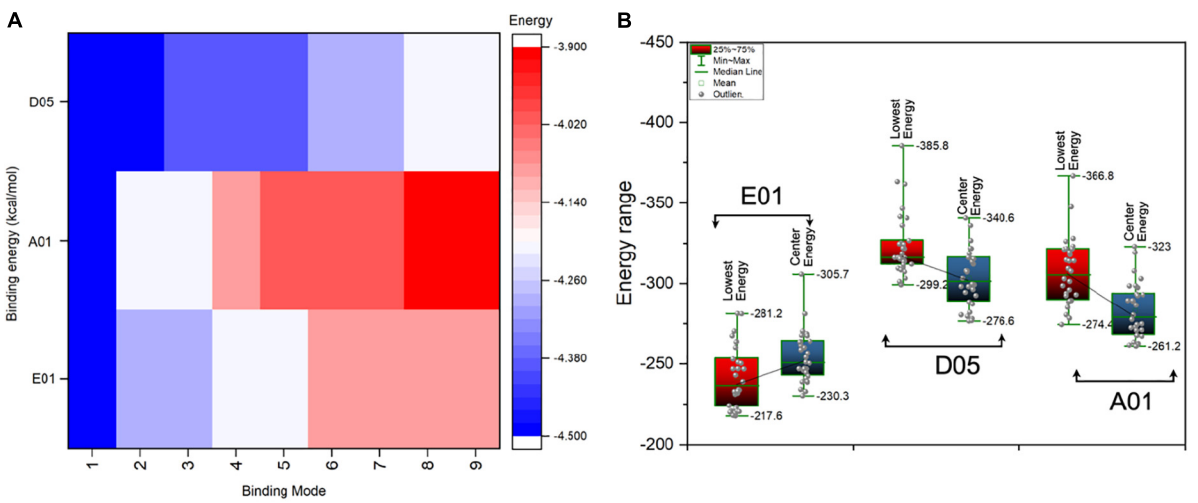

FIGURE 5 | Binding energies (kcal/mol) of single molecule phosphorylcholine (PC) and PC conjugate with cloned antibodies, i.e., E01, A01, and D05. **(A)** The AutoDock Vina binding energies score of single molecule PC in kcal/mol with various clones (heatmap). The scale bar indicates the highest (indicated in blue) and lowest (indicated in red) in terms of negative score. The negative score indicated the highest binding affinity. **(B)** The box plot represents the antibody (clone antibodies)-antigen (PC conjugate) binding energies (lowest energies) for various clones.

DISCUSSION

We reported that low levels of anti-PC IgG1, below the 33rd percentile, are significantly associated with increased risk of CVD, including MI and stroke, where the associations for stroke were especially strong. Being a 60-year-old man and having low IgG1 anti-PC was associated with a significant and more than the ninefold increased risk of stroke within 5 years. At high levels (above 90th percentile), IgG1 anti-PC was significantly associated with protection against stroke. Associations for IgG did not reach

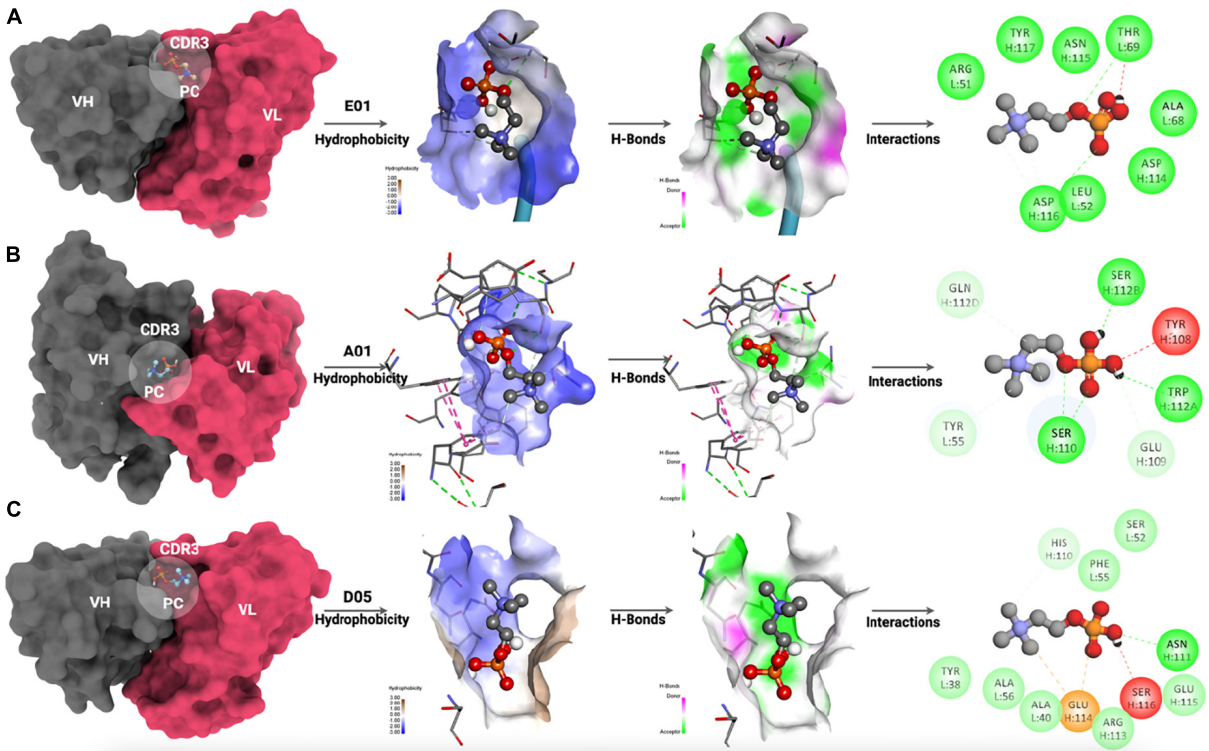

FIGURE 6 | Molecular interaction of PC with **(A)** E01 clone, **(B)** A01 clone, and **(C)** D05 clone antibodies. The hydrophobicity mapping, hydrogen bonding patterns, and 2D interaction map have been illustrated.

significance, except among men, where this was only apparent at the very highest or lowest percentiles. Anti-PC IgG2 was associated with protection, among men, but also among women, reaching significance at some levels, but not as clear as IgG1 anti-PC. There were few women in this study, which was explained by the fact that the mean age for CVD is higher among women than men, about 10 years in some studies. Interestingly, anti-PC is lower among men than women in all our published studies, including among individuals from Kitava, New Guinea, living a traditional life as hunters, gatherers, and horticulturalists at the time of the investigation (1, 25–27). We have hypothesized that anti-PC, being lower in men, may contribute to the increased risk of CVD among men as compared with women at the same age (1).

As with previous studies, associations between anti-PC and various outcomes were not observed at mean levels, but rather at low levels, and in general, these findings could be interpreted as indicating that having low anti-PC levels, particularly IgM and IgG1, indicates an immune-deficient state with insufficient activity in what is typically described as natural immunity, in this case, anti-PC. We previously observed that IgM anti-PC is related to protection in this cohort (5), and the current investigation found that IgG1 anti-PC is predictive of outcome in a manner similar to IgM.

Less is known about other isotypes and subclasses of anti-PC. Our findings are in line with our previous reports, where IgG1 anti-PC were associated with protection in atherosclerosis progress (10), with the prevalence of atherosclerotic plaques, and potentially vulnerable echolucent plaques in SLE (11) and with mortality in uremia (12). We have also recently reported about the protection mechanism of anti-PC as a natural immunization against atherosclerosis in hibernating bears (28).

Animal experiments also support a protective role of anti-PC in atherosclerosis development (29), SLE (30), and RA (31). This is also supported by potential mechanisms in experimental studies, mostly performed on IgM anti-PC. These include an anti-inflammatory effect for IgG anti-PC inhibiting inflammatory lipids like platelet-activating factor (PAF) with PC as a major epitope (4), inhibition of OxLDL uptake by macrophages (5), inhibition of cell death (10), increased clearance of dead cells (13), which is also a property of anti-PC IgG1, especially, the D05 clone (11), and promotion of polarization of T regulatory cells (14). PC is playing an important role in OxLDL-induced immune activation in atherosclerosis and thus CVD (1, 10, 32). Anti-PC, especially IgM and IgG1, could thus be protective in several different chronic inflammatory diseases. We proposed development of the Hygiene/Old Friends hypothesis: lack of exposure to PC-bearing microorganisms, including nematodes, parasites, and also bacteria (including Treponema), causes low levels of anti-PC and increased risk of chronic inflammatory conditions, including atherosclerosis, CVD, and other diseases including autoimmune (1, 25–27). Low levels of anti-PC could be described as an immune-deficient state, predisposing to these conditions.

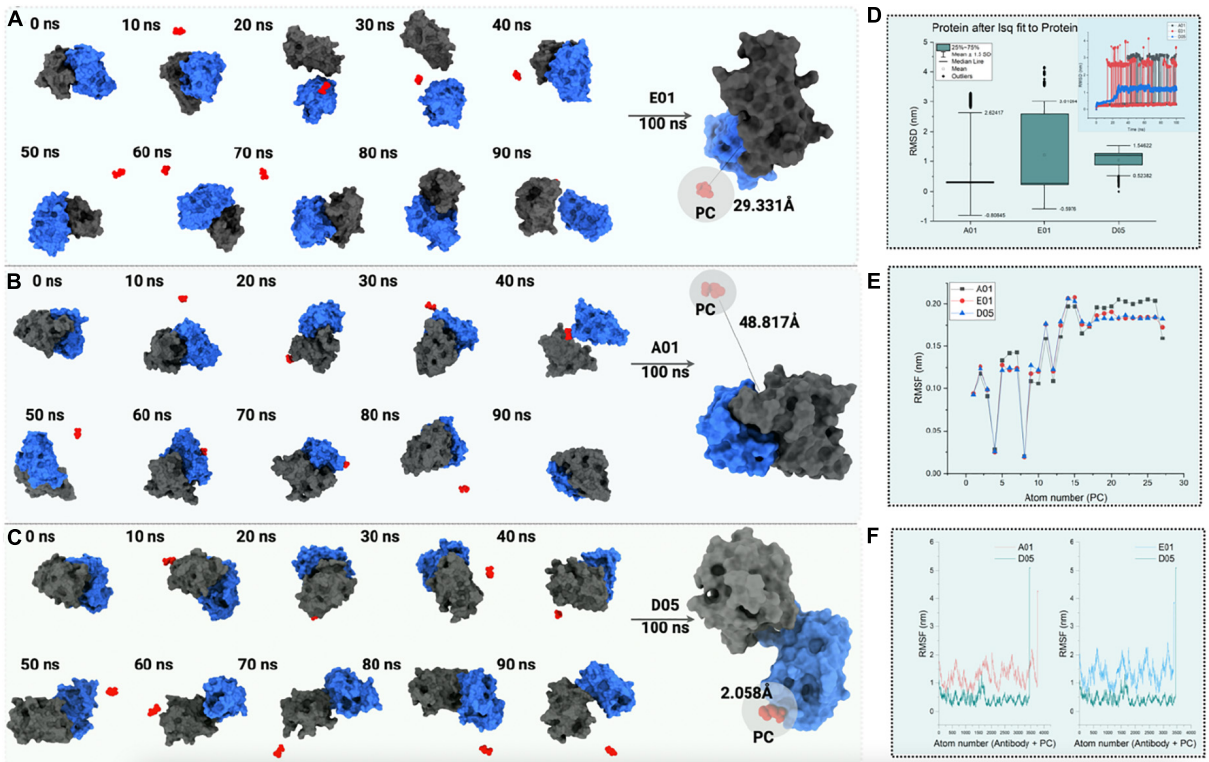

FIGURE 7 | The 100 ns all-atom molecular dynamics simulation of PC with **(A)** E01, **(B)** A01, and **(C)** D05 clone antibodies. The conformations of PC binding to clone antibodies during the course of the 100 ns simulation **(D)** root mean square deviation (RMSD) analysis (nm). The box plot represents the deviation in RMSD with standard deviation depicted as mean ± 1.5 SD. **(E)** Line plot illustrating root mean square fluctuation (RMSF in nm) for PC molecule. **(F)** RMSF (in nm) for complex anti-PC clones with a comparison of D05 anti-PC clone with other clones.

The finding in this and previous studies that IgG1 anti-PC is more associated with protection than IgG2 anti-PC is of interest and could also have implications for therapy, in addition to prediction. In general, PC can be presented as p-nitrophenyl phosphorylcholine (NPPC) (10), and human anti-PC can be divided into group I (IgM and IgG1) and group II (IgG2) (10). Interestingly, while group I anti-PC recognizes both forms of PC, group II antibodies only recognize NPCC, and the phenyl-ring attached to PC is antigenic. IgG2 anti-PC is directed against capsulated bacteria, recognizes carbohydrate antigens, and has bactericidal properties (10, 33, 34). In periodontitis, the risk of CVD is increased (35), while IgG2 anti-PC also is raised (36, 37). If our hypothesis that IgG2 anti-PC is much less of a protection marker than IgG1, this could at least partly explain why IgG2 anti-PC is mainly against PC exposed to bacterial carbohydrates.

Since anti-PC IgG1 also in this study was demonstrated to be associated with protection much more than IgG2 anti-PC, we decided to make further studies focused on this subclass, with our fully human in-house produced monoclonal anti-PC IgG1 as one basis of the studies, together with bioinformatics approaches. We recently reported that these IgG1 anti-PC clones bind differently to PC to a varying degree, increase the uptake of dead cells by efferocytosis, and inhibit proinflammatory effects of endotoxin (11, 16). In peptide analysis using a proteomics *de novo* sequencing approach, we reported differences in the CDR3 region of anti-PC IgG1 clones, which are crucial for recognition of PC on the apoptotic cell surface and other neo-epitopes (11). We currently develop these IgG1 anti-PC studies on these clones, by further analysis, with bioinformatics tools, using molecular modeling analyses of these three clones. We used the genetic sequences of their CDR region and VH and VL sequences as a basis of the analyses, which focused on structural modeling through SAbPred analysis. This resulted in three structural antibody models of CDR of which the CDR3 region is considered to be the most crucial part in binding specific antigens. The diversity of CDR3 amino acid sequences provides a measure of B-cell diversity in an antigen-selected B-cell repertoire. The sequence variability of the CDR3 region in all three clones was retrieved from IgBLAST alignment.

The diversity of CDR3 amino acid sequences provides a measure of B-cell diversity in an antigen-selected B-cell repertoire. We determined sequence liabilities and amino acid level modifications. There were several such modifications, for example, asparagine isomerization in high frequency, and there was also another modification including lysine glycation observed only in the D05 clone, which has a high-affinity binding to PC. Lysine is interesting because, in age-related disorders, glycation of macromolecules plays a vital role, especially proteins leading to their oxidation. The immunological epitopes that are impaired by the development of autoantibodies are proteins

changed with glycation and glycoxidation. Protein glycation mainly leads to a stable and precocious Amadori-lysine substance to form advanced glycation end products (AGE) and is subjected to more irreversible chemical reactions (38). Most of the amino acid modifications were observed in H chain regions in comparison to light chain sequences, in the D05 clone, which thus stands out. Our previous observation that D05 is a high binder in experimental systems is in line with the observations herein.

Our findings are in line with our previous observation that in humans, anti-PC is not germline-encoded and thus in principle, not natural antibodies. In mouse models, anti-PC is germline-encoded, dominated by the one clone, T15 (39), and in line with this, knocking out this antibody is deleterious for the immune response against bacteria, which expose PC (40). Further, a mAb E06 from apolipoprotein E-knockout mouse, which is formed from OxLDL, was identical to T15 (39). We were not able to demonstrate a T15 equivalent in humans where instead anti-PC is produced by multiple B-cell subsets, with somatically mutated antibodies utilizing a wide variety of Ig-genes.

Posttranslational modifications (PTMs) of an antibody can affect an antibody's affinity, stability, potency, and homogeneity, resulting in complicated downstream processing. The bioactivity and production of various isoforms of the product will be impacted. PTMs normally include deamidation, isomerization, oxidation, glycosylation, free thiol, pyro-glutamate, C-terminal lysine, etc. Immunogenicity, inconsistency, self-association, high viscosity, polyspecificity, or poor expression can prevent an antibody from becoming therapeutic. Early detection of these characteristics may play a pivotal role in improving the therapeutic nature of an antibody. Improved understanding of the factors regulating these biophysical properties has allowed the production of quicker *in silico* assays than their experimental counterparts (41–43).

LIMITATIONS

The *in silico* methods used are simulations, and further experimental studies are needed to establish a clinical role of anti-PC in humans. Taken together, our findings indicate that IgG1 anti-PC is a protection marker for CVD among 60-year-olds, especially for stroke in men. We determined variations in different properties of IgG1 anti-PC clones. In the future, raising levels of anti-PC through immunization could be a promising therapeutic possibility.

DATA AVAILABILITY STATEMENT

All data needed to evaluate the conclusions in the article are present in the article and/or the **Supplementary Material**. The raw data supporting the conclusions of this article will be made available by the authors, without undue reservation.

ETHICS STATEMENT

The studies involving human participants were reviewed and approved by the Karolinska Institutet research ethics committee. The patients/participants provided their written informed consent to participate in this study.

AUTHOR CONTRIBUTIONS

JF: conceptualization. SKS: experiments. PKP: computational analyses. MV (input from KL and UF): statistics. JF: writing (original draft preparation). SKS and PKP: co-writing. MV, KL, UF, and RA: review and editing. JF: supervision. All authors approved the submitted version of the manuscript.

FUNDING

This study was supported by the INTRICARE Marie Skłodowska Curie Grant No. 722609 (www.intricare.eu). Swedish Heart Lung Foundation, the Swedish Research Council (VR Grant No. 2016-06014), the Stockholm County (ALF), the King Gustav V 80th Birthday Fund, and the Swedish Association against Rheumatism.

ACKNOWLEDGMENTS

SNIC and HPC2N have been acknowledged for providing computational resources.

SUPPLEMENTARY MATERIAL

The Supplementary Material for this article can be found online at: https://www.frontiersin.org/articles/10.3389/fcvm.2022.809007/full#supplementary-material

REFERENCES

1. Frostegård J. Immunity, atherosclerosis and cardiovascular disease. *BMC Med.* (2013) 11:117.doi: 10.1186/1741-7015-11-117
2. Su J, Georgiades A, Wu R, Thulin T, de Faire U, Frostegård J. Antibodies of IgM subclass to phosphorylcholine and oxidized LDL are protective factors for atherosclerosis in patients with hypertension. *Atherosclerosis.* (2006) 188:160–6. doi: 10.1016/j.atherosclerosis.2005.10.017
3. Anania C, Gustafsson T, Hua X, Su J, Vikstrom M, de Faire U, et al. Increased prevalence of vulnerable atherosclerotic plaques and low levels of natural IgM antibodies against phosphorylcholine in patients with systemic lupus erythematosus. *Arthritis Res Ther.* (2010) 12:R214. doi: 10.1186/ar3193
4. Su J, Hua X, Concha H, Svenungsson E, Cederholm A, Frostegård J. Natural antibodies against phosphorylcholine as potential protective factors in SLE. *Rheumatology (Oxford).* (2008) 47:1144–50. doi: 10.1093/rheumatology/ken120
5. de Faire U, Su J, Hua X, Frostegård A, Halldin M, Hellenius ML, et al. Low levels of IgM antibodies to phosphorylcholine predict cardiovascular disease

in 60-year old men: effects on uptake of oxidized LDL in macrophages as a potential mechanism. *J Autoimmun.* (2010) 34:73–9. doi: 10.1016/j.jaut.2009.05.003
6. Vas J, Gronwall C, Marshak-Rothstein A, Silverman GJ. Natural antibody to apoptotic cell membranes inhibits the proinflammatory properties of lupus autoantibody immune complexes. *Arthritis Rheum.* (2012) 64:3388–98. doi: 10.1002/art.34537
7. Wilde B, Slot M, van Paassen P, Theunissen R, Kemna M, Witzke O, et al. Phosphorylcholine antibodies are diminished in ANCA-associated vasculitis. *Eur J Clin Invest.* (2015) 45:686–91. doi: 10.1111/eci.12457
8. Imhof A, Koenig W, Jaensch A, Mons U, Brenner H, Rothenbacher D. Long-term prognostic value of IgM antibodies against phosphorylcholine for adverse cardiovascular events in patients with stable coronary heart disease. *Atherosclerosis.* (2015) 243:414–20. doi: 10.1016/j.atherosclerosis.2015.10.024
9. Nguyen TG, McKelvey KJ, March LM, Hunter DJ, Xue M, Jackson CJ, et al. Aberrant levels of natural IgM antibodies in osteoarthritis and rheumatoid arthritis patients in comparison to healthy controls. *Immunol Lett.* (2016) 170:27–36. doi: 10.1016/j.imlet.2015.12.009
10. Fiskesund R, Su J, Bulatovic I, Vikstrom M, de Faire U, Frostegård J. IgM phosphorylcholine antibodies inhibit cell death and constitute a strong protection marker for atherosclerosis development, particularly in combination with other auto-antibodies against modified LDL. *Results Immunol.* (2012) 2:13–8. doi: 10.1016/j.rinim.2012.01.001
11. Thiagarajan D, Fiskesund R, Frostegård A, Steen J, Rahman M, Vikström M, et al. Immunoglobulin G1 Antibodies against phosphorylcholine are associated with protection in systemic lupus erythematosus and atherosclerosis: potential underlying mechanisms. *ACR Open Rheumatol.* (2020) 2:344–56. doi: 10.1002/acr2.11127
12. Samal SK, Qureshi AR, Rahman M, Stenvinkel P, Frostegård J. Different subclasses and isotypes of antibodies against phosphorylcholine in haemodialysis patients: association with mortality. *Clin Exp Immunol.* (2020) 201:94–104. doi: 10.1111/cei.13441
13. Rahman M, Sing S, Golabkesh Z, Fiskesund R, Gustafsson T, Jogestrand T, et al. IgM antibodies against malondialdehyde and phosphorylcholine are together strong protection markers for atherosclerosis in systemic lupus erythematosus: regulation and underlying mechanisms. *Clin Immunol.* (2016) 166–7:27–37. doi: 10.1016/j.clim.2016.04.007
14. Sun J, Lundstrom SL, Zhang B, Zubarev RA, Steuer J, Gillgren P, et al. IgM antibodies against phosphorylcholine promote polarization of T regulatory cells from patients with atherosclerotic plaques, systemic lupus erythematosus and healthy donors. *Atherosclerosis.* (2018) 268:36–48. doi: 10.1016/j.atherosclerosis.2017.11.010
15. Samal SK, Qureshi AR, Rahman M, Stenvinkel P, Frostegård J. Antibodies against malondialdehyde in haemodialysis patients and its association with clinical outcomes: differences between subclasses and isotypes. *J Clin Med.* (2020) 9:753. doi: 10.3390/jcm9030753
16. Fiskesund R, Steen J, Amara K, Murray F, Szwajda A, Liu A, et al. Naturally occurring human phosphorylcholine antibodies are predominantly products of affinity-matured B cells in the adult. *J Immunol.* (2014) 192:4551–9. doi: 10.4049/jimmunol.1303035
17. Szklarczyk D, Santos A, von Mering C, Jensen LJ, Bork P, Kuhn M. STITCH 5: augmenting protein-chemical interaction networks with tissue and affinity data. *Nucleic Acids Res.* (2016) 44:D380–4. doi: 10.1093/nar/gkv1277
18. Kuhn M, von Mering C, Campillos M, Jensen LJ, Bork P. STITCH: interaction networks of chemicals and proteins. *Nucleic Acids Res.* (2008) 36:D684–8. doi: 10.1093/nar/gkm795
19. Dunbar J, Krawczyk K, Leem J, Marks C, Nowak J, Regep C, et al. SAbPred: a structure-based antibody prediction server. *Nucleic Acids Res.* (2016) 44:W474–8. doi: 10.1093/nar/gkw361
20. Kim S, Thiessen PA, Bolton EE, Chen J, Fu G, Gindulyte A, et al. PubChem substance and compound databases. *Nucleic Acids Res.* (2016) 44:D1202–13.
21. Trott O, Olson AJ. AutoDock Vina: improving the speed and accuracy of docking with a new scoring function, efficient optimization, and multithreading. *J Comput Chem.* (2010) 31:455–61. doi: 10.1002/jcc.21334
22. Van Der Spoel D, Lindahl E, Hess B, Groenhof G, Mark AE, Berendsen HJC. GROMACS: fast, flexible, and free. *J Comput Chem.* (2005) 26:1701–18. doi: 10.1002/jcc.20291
23. Vanommeslaeghe K, MacKerell AD. Automation of the CHARMM general force field (CGenFF) I: bond perception and atom typing. *J Chem Inf Model.* (2012) 52:3144–54. doi: 10.1021/ci300363c
24. Kozakov D, Hall DR, Xia B, Porter KA, Padhorny D, Yueh C, et al. The ClusPro web server for protein–protein docking. *Nat Protoc.* (2017) 12:255–78. doi: 10.1038/nprot.2016.169
25. Frostegård J, Tao W, Råstam L, Lindblad U, Lindeberg S. Antibodies against phosphorylcholine among new guineans compared to Swedes: an aspect of the hygiene/missing old friends hypothesis. *Immunol Invest.* (2017) 46:59–69. doi: 10.1080/08820139.2016.1213279
26. Agmon-Levin N, Bat-sheva PK, Barzilai O, Ram M, Lindeberg S, Frostegård J, et al. Antitreponemal antibodies leading to autoantibody production and protection from atherosclerosis in Kitavans from Papua New Guinea. *Ann N Y Acad Sci.* (2009) 1173:675–82. doi: 10.1111/j.1749-6632.2009.04671.x
27. Frostegård J, Tao W, Georgiades A, Rastam L, Lindblad U, Lindeberg S. Atheroprotective natural anti-phosphorylcholine antibodies of IgM subclass are decreased in Swedish controls as compared to non-westernized individuals from New Guinea. *Nutr Metab (Lond).* (2007) 4:7. doi: 10.1186/1743-7075-4-7
28. Samal SK, Fröbert O, Kindberg J, Stenvinkel P, Frostegård J. Potential natural immunization against atherosclerosis in hibernating bears. *Sci Rep.* (2021) 11:12120. doi: 10.1038/s41598-021-91679-1
29. Caligiuri G, Khallou-Laschet J, Vandaele M, Gaston AT, Delignat S, Mandet C, et al. Phosphorylcholine-targeting immunization reduces atherosclerosis. *J Am Coll Cardiol.* (2007) 50:540–6. doi: 10.1016/j.jacc.2006.11.054
30. Aprahamian TR, Zhong X, Amir S, Binder CJ, Chiang LK, Al-Riyami L, et al. The immunomodulatory parasitic worm product ES-62 reduces lupus-associated accelerated atherosclerosis in a mouse model. *Int J Parasitol.* (2015) 45:203–7. doi: 10.1016/j.ijpara.2014.12.006
31. Chen Y, Khanna S, Goodyear CS, Park YB, Raz E, Thiel S, et al. Regulation of dendritic cells and macrophages by an anti-apoptotic cell natural antibody that suppresses TLR responses and inhibits inflammatory arthritis. *J Immunol.* (2009) 183:1346–59. doi: 10.4049/jimmunol.0900948
32. Frostegård J, Huang YH, Ronnelid J, Schafer-Elinder L. Platelet-activating factor and oxidized LDL induce immune activation by a common mechanism. *Arterioscler Thromb Vasc Biol.* (1997) 17:963–8. doi: 10.1161/01.atv.17.5.963
33. Scott MG, Shackelford PG, Briles DE, Nahm MH. Human-Igg subclasses and their relation to carbohydrate antigen immunocompetence. *Diagn Clin Immunol.* (1988) 5:241–8.
34. Goldenberg HB, McCool TL, Weiser JN. Cross-reactivity of human immunoglobulin G2 recognizing phosphorylcholine and evidence for protection against major bacterial pathogens of the human respiratory tract. *J Infect Dis.* (2004) 190:1254–63. doi: 10.1086/424517
35. Buhlin K, Gustafsson A, Pockley AG, Frostegård J, Klinge B. Risk factors for cardiovascular disease in patients with periodontitis. *Eur Heart J.* (2003) 24:2099–107. doi: 10.1016/j.ehj.2003.09.016
36. Blaizot A, Vergnes JN, Nuwwareh S, Amar J, Sixou M. Periodontal diseases and cardiovascular events: meta-analysis of observational studies. *Int Dent J.* (2009) 59:197–209.
37. Schenkein HA, Gunsolley JC, Best AM, Harrison MT, Hahn CL, Wu JH, et al. Antiphosphorylcholine antibody levels are elevated in humans with periodontal diseases. *Infect Immun.* (1999) 67:4814–8. doi: 10.1128/IAI.67.9.4814-4818.1999
38. Ansari NA, Moinuddin, Ali R. Glycated lysine residues: a marker for non-enzymatic protein glycation in age-related diseases. *Dis Markers.* (2011) 30:317–24. doi: 10.3233/DMA-2011-0791

39. Shaw PX, Horkko S, Chang MK, Curtiss LK, Palinski W, Silverman GJ, et al. Natural antibodies with the T15 idiotype may act in atherosclerosis, apoptotic clearance, and protective immunity. *J Clin Invest.* (2000) 105:1731–40. doi: 10.1172/JCI8472
40. Mi QS, Zhou L, Schulze DH, Fischer RT, Lustig A, Rezanka LJ, et al. Highly reduced protection against *Streptococcus pneumoniae* after deletion of a single heavy chain gene in mouse. *Proc Natl Acad Sci USA.* (2000) 97:6031–6. doi: 10.1073/pnas.110039497
41. Raybould MIJ, Marks C, Krawczyk K, Taddese B, Nowak J, Lewis AP, et al. Five computational developability guidelines for therapeutic antibody profiling. *Proc Natl Acad Sci USA.* (2019) 116:4025–30. doi: 10.1073/pnas.1810576116
42. Smakaj E, Babrak L, Ohlin M, Shugay M, Briney B, Tosoni D, et al. Benchmarking immunoinformatic tools for the analysis of antibody repertoire sequences. *Bioinformatics.* (2020) 36:1731–9. doi: 10.1093/bioinformatics/btz845
43. Lu X, Nobrega RP, Lynaugh H, Jain T, Barlow K, Boland T, et al. Deamidation and isomerization liability analysis of 131 clinical-stage antibodies. *MAbs.* (2019) 11:45–57. doi: 10.1080/19420862.2018.1548233

Conflict of Interest: JF was named as inventor on patents related to Phosphorylcholine.

The remaining authors declare that the research was conducted in the absence of any commercial or financial relationships that could be construed as a potential conflict of interest.

frontiers | Frontiers in Cardiovascular Medicine

ORIGINAL RESEARCH
published: 25 April 2022
doi: 10.3389/fcvm.2022.824561

Relationships of Serum Bone Turnover Markers With Metabolic Syndrome Components and Carotid Atherosclerosis in Patients With Type 2 Diabetes Mellitus

Wei Li[1], *Xiaojun Liu*[1], *Lijun Liu*[1], *Lei Zhang*[1], *Mengdi Li*[1], *Rui Liu*[1], *Tianfang Li*[1], *En Chen*[2]* *and Shengyun Liu*[1]*

[1] Department of Rheumatology, The First Affiliated Hospital of Zhengzhou University, Zhengzhou, China, [2] Department of Laboratory Medicine, The First Affiliated Hospital, Hengyang Medical School, University of South China, Hengyang, China

OPEN ACCESS

Edited by:
Michelangela Barbieri, University of Campania Luigi Vanvitelli, Italy

Reviewed by:
Maaike Schilperoort, Columbia University Irving Medical Center, United States
Pasquale Paolisso, University of Naples Federico II, Italy

***Correspondence:**
En Chen
cheneng3821@sina.com
Shengyun Liu
fccliusy2@zzu.edu.cn

Specialty section:
This article was submitted to Atherosclerosis and Vascular Medicine, a section of the journal Frontiers in Cardiovascular Medicine

Received: 07 December 2021
Accepted: 31 March 2022
Published: 25 April 2022

Citation:
Li W, Liu X, Liu L, Zhang L, Li M, Liu R, Li T, Chen E and Liu S (2022) Relationships of Serum Bone Turnover Markers With Metabolic Syndrome Components and Carotid Atherosclerosis in Patients With Type 2 Diabetes Mellitus. Front. Cardiovasc. Med. 9:824561. doi: 10.3389/fcvm.2022.824561

Objective: This study aimed to investigate the association of serum bone turnover markers (BTMs) with metabolic syndrome components and carotid atherosclerosis in patients with type 2 diabetes mellitus (T2DM).

Methods: We performed a cross-sectional based study in T2DM populations. Serum BTMs including N-terminal osteocalcin (N-MID), β-cross-linked C-telopeptide of type I collagen (β-CTX), and procollagen type I N-terminal propeptide (PINP) were measured by immunoassay method. Carotid artery intima-media thickness and carotid artery plaque (CAP) were measured by B-mode ultrasound.

Results: The serum N-MID, PINP, and β-CTX levels significantly lower in the CAP group compared with the non-CAP group. N-MID and PINP levels were inversely associated with fasting blood glucose, HOMA-IR, CRP, eGFR, and triglycerides (all $P < 0.05$), whereas β-CTX levels were negatively associated with triglycerides ($P < 0.05$). After multiple adjustment, the odds ratios (ORs) were substantially higher for CAP with decreased N-MID level (OR = 0.958; 95% CI = 0.926–0.991; P = 0.013). However, serum levels of PINP and β-CTX were not associated with the presence of CAP. Multivariate logistic regression analysis further revealed that serum N-MID, PINP, and β-CTX levels were significantly associated with hypertriglyceridemia, whereas serum N-MID and β-CTX levels were associated with overweight/obesity risk.

Conclusions: These findings indicated that serum N-MID level was an independent risk factor for carotid atherosclerosis, whereas BTM levels were associated with other metabolic syndrome components in a T2DM population.

Keywords: bone turnover biomarkers, metabolic syndrome, carotid artery plaques, carotid atherosclerosis, type 2 diabetes mellitus

BACKGROUND

Bone turnover is a dynamic process that comprises the formation of new bone by osteoblasts and the resorption of old bone by osteoclasts. This process generates many bone turnover markers (BTMs) from bone cells and the bone matrix, which provide a noninvasive evaluation of bone remodeling status (1, 2). BTMs comprises bone formation markers, namely, N-terminal osteocalcin (N-MID), procollagen type I N-terminal propeptide (PINP), and bone resorption markers, such as β-cross-linked C-telopeptide of type I collagen (β-CTX). All these molecules are key markers of bone metabolism (3, 4). In addition to the use of BTMs as indicators of bone formation and resorption, as well as markers for the assessment, diagnosis, and treatment of osteoporosis, BTMs have been shown to be associated with energy metabolism in recent studies (5, 6).

Previous studies have shown that bone metabolism is affected by the risk factors of atherosclerosis, such as obesity, hypertension, dyslipidemia, and diabetes (7–9). Patients with diabetes are at two-to fourfold increased risk of cardiovascular disease (CVD), which is reflected by atherosclerosis (10). BTMs are highly associated with diabetes, insulin sensitivity, and beta cell function, and serum osteocalcin plays an important role in the association of bone metabolism with glucose metabolism (11, 12). A cross-sectional based study has demonstrated that serum osteocalcin level is an independent risk factor for carotid atherosclerosis in patients with T2DM (13). In addition, previous observational and indirect interventional studies suggested a relationship between serum osteocalcin level with metabolic homeostasis and CVD (14). However, the relationship of other BTMs with metabolic syndrome and carotid atherosclerosis risk is substantially unknown. Recently, a case-control study has shown that higher osteopontin concentrations are associated with increased CVD risk in T2DM patients, but no association is found for the osteocalcin level and risk of CVD (15). Furthermore, a longitudinal follow-up study demonstrated that the serum total osteocalcin level was not associated with the development of CVD after adjusting for other risk factors (16).

Clinical studies have revealed that the association between different BTMs and cardiometabolic risk is controversial, and most studies have focused on osteocalcin (15, 16). Accordingly, the present study aimed to determine whether serum N-MID levels and other BTMs were independently associated with carotid atherosclerosis and other cardiometabolic risk factors, such as obesity, hypertension, dyslipidemia, and metabolic syndrome (MetS) in patients with T2DM.

Abbreviations: β-CTX, β-cross-linked C-telopeptide of type I collagen; BMI, Body mass index; BTM, bone turnover markers; CAP, Carotid artery plaque; CI, Confidence interval; CIMT, Carotid intima-media thickness; CVD, Cardiovascular disease; CRP, C-reactive protein; DBP, Diastolic blood pressure; eGFR, Estimated glomerular filtration rate; FBG, Fasting plasma glucose; HbA1c, Glycosylated hemoglobin; HDL-C, High-density lipoprotein cholesterol; LDL-C, Low-density lipoprotein cholesterol; MetS, metabolic syndrome; N-MID, N-terminal osteocalcin; OR, Odds ratio; PINP, procollagen type I N-terminal propeptide; SBP, Systolic blood pressure; TC, Total cholesterol; TG, Triglyceride; T2DM, Type 2 diabetes mellitus; SUA, Serum uric acid.

METHODS

Study Populations

Cross-sectional study populations were recruited from the First Affiliated Hospital of Zhengzhou University between 2018 and 2020. Diabetes was defined as fasting blood glucose ≥7.0 mmol/l, HbA1c≥ 6.5% or the use of any antidiabetic medication or self-reported history of diabetes based on the American Diabetes Association. Subjects were excluded if they had any known infection, malignant tumors, or were taking medicine that may influence the level of serum BTMs. Finally, a total of 1520 patients with T2DM were enrolled. Questionnaires were used to identify history of medical conditions, family history of disease, current medication use, and other lifestyle factors. Body weight and height were measured at baseline, and body mass index (BMI) was calculated by body weight (kg) divided by height square (m^2). Blood pressure was measured using an automatic blood-pressure meter after seating for at least 10 min. The average of three measurements was recorded for further analysis. This study was approved by the Institutional Review Broad of the First Affiliated Hospital of Zhengzhou University.

Biochemical Measurements

Venous blood samples were collected in the morning followed by overnight fasting. An auto-biochemical analyzer was used to determine the fasting blood glucose (FBG), serum concentrations of total cholesterol (TC), triglycerides (TG), low-density lipoprotein cholesterol (LDL-C), high-density lipoprotein cholesterol (HDL-C), uric acid (UA), fasting plasma insulin, creatinine, and C-reactive protein (CRP) as previously described. Glycated hemoglobin (HbA1c) concentrations were quantified using high-performance liquid chromatography. The estimated glomerular filtration rate (eGFR) was calculated according to the CKD-EPI equation. Insulin resistance was estimated using homeostasis model assessment index-insulin resistance (HOMA-IR). BTMs associated with bone metabolism including N-MID, PINP, and β-CTX were measured by electrical chemiluminescent immunoassay.

Carotid Ultrasonography

Trained technicians performed B mode ultrasonography using an Acuson Sequoia. A lateral view of bilateral images of common carotid arteries (1 cm proximal to the dilatation of the carotid bulb), carotid bulb, and internal carotid artery was obtained. Carotid artery intima-media thickness (CIMT) was defined as the mean of the maximum thickness in both right and left sides of the common carotid artery, and IMT is the distance between the lumen-intima interface and the media adventitia interface. The carotid artery plaque (CAP) was defined as either a focal structure that encroaches into the arterial lumen by at least 50% of the surrounding IMT value or a thickness of > 1.5 mm. CAP presence was defined as ≥1 plaque in any of the carotid arteries.

Definition of MetS

We used the definition of MetS according to the NCEPATP III criteria (17). Subjects were classified as having MetS when ≥3 of the following criteria were present: FBG level ≥5.6 mmol/L, blood pressure ≥130/85 mmHg, TG ≥1.7 mmol/L, HDL-C <1.03

TABLE 1 | Baseline characteristics for participants.

	Non-CAP	CAP	*P*-value
N (%)	825 (54.3%)	695 (45.7%)	
Male, *n* (%)	535 (64.8%)	466 (67.1%)	**<0.0001**
Age (years)	45 (34–54)	56 (48–62)	**<0.0001**
Diabetes duration (years)	2 (0.17–6)	5 (1–12)	**<0.0001**
History of CVD, *n* (%)	46 (5.6%)	93 (13.4%)	**<0.0001**
Hypertension, *n* (%)	293 (35.5%)	368 (52.9%)	**<0.0001**
Smoking, *n* (%)	199 (24.1%)	185 (26.6%)	0.624
Drinking, *n* (%)	162 (19.6%)	161 (23.2%)	0.094
BMI (kg/m^2)	26.2 (23.7–29.9)	25 (23–27)	**<0.0001**
CRP (mg/L)	1.29 (0.62–3.26)	1.22 (0.56–2.64)	0.157
HbA1C (%)	8.3 (6.7–10.4)	8.5 (7.2, 10.0)	0.858
FBG (mmol/L)	7.3 (6.0–10.3)	7.6 (6.2–10.0)	0.84
Insulin (μU/mL)	5.9 (2.8–10.5)	5.0 (2.3–9.4)	**0.019**
HOMA-IR	2.06 (1.01–3.47)	1.70 (0.77–3.14)	**0.015**
UA (μmol/L)	304 (247–378)	286 (247–347)	**0.023**
eGFR	111.1 (101.5–120.4)	102.9 (94.3–109.9)	**<0.0001**
TC (mmol/L)	4.54 (3.9–5.3)	4.45 (3.7–5.2)	**0.003**
TG (mmol/L)	1.9 (1.1–3.1)	1.8 (1.2–2.5)	**<0.0001**
HDL-C (mmol/L)	1.01 (0.81–1.24)	1.05 (0.89–1.25)	0.07
LDL-C (mmol/L)	2.75 (2.12–3.36)	2.65 (1.94–3.24)	0.058
N-MID (ng/mL)	12.6 (10.4–16.0)	11.8 (9.1–15.5)	**0.019**
β-CTX (ng/mL)	0.4 (0.29–0.55)	0.35 (0.25–0.51)	**0.001**
PINP (ng/mL)	37.1 (29.3–49.9)	35.1 (25.3–45.4)	**0.021**
SBP (mmHg)	133 (125–141)	132 (124–145)	**0.004**
DBP (mmHg)	84 (77–90)	83 (76–90)	**0.004**
Antidiabetic, *n* (%)	201 (24.4%)	279 (40.1%)	**<0.0001**
Antihypertensive, *n*(%)	501 (60.7%)	505 (72.7%)	**<0.0001**
Lipid lowering, *n* (%)	45 (5.5%)	83 (11.9%)	**<0.0001**

β-CTX, β-cross-linked C-telopeptide of type I collagen; BMI, Body mass index; CAP, Carotid artery plaques; CVD, Cardiovascular disease; CRP, C-reactive protein; DBP, Diastolic blood pressure; eGFR, Estimated glomerular filtration rate; FBG, Fasting plasma glucose; HbA1c, Glycosylated hemoglobin; HDL-C, High-density lipoprotein cholesterol; LDL-C, Low-density lipoprotein cholesterol; N-MID, N-terminal osteocalcin; PINP, procollagen type I N-terminal propeptide; SBP, Systolic blood pressure; TC, Total cholesterol; TG, Triglyceride. The bold values indicated that difference is statistically significant.

mmol/L for men and <1.29 mmol/L for women, and waist circumference >102 cm for men and >88 cm for women.

Statistical Analysis

Normally distributed data were expressed as the mean ±SD, whereas variables with a skewed distribution were reported as median (interquartile range). Categorical variables were represented by percentage. Mann–Whitney *U*-test was used to compare the mean ranks between the CAP and non-CAP groups. Correlation coefficients between BTMs and metabolic features were calculated by partial correlation analysis. Multivariate logistic regression models were used to estimate the association of CAP with BTMs. Potential confounding variables including age, gender, smoking, alcohol drinking, self-reported CVD, hypertension, CRP, BMI, FBG, HbA1c, HOMA-IR, TG, TC, HDL-C, and LDL-C were controlled in the regression models. Statistical analyses were performed using SPSS version 26.0 (Chicago, IL, USA). Results were considered statistically significant at $P < 0.05$.

RESULTS

Study Population and Characteristics

The baseline clinical characteristics of the participants are shown in **Table 1**. A total of 1520 subjects were enrolled in the present study, among which 695 (45.7%) had CAP. Participants were classified according to the presence of carotid plaques as CAP and non-CAP groups. The CAP group had significantly lower systolic blood pressure (SBP), diastolic blood pressure (DBP), BMI, TC, TG, and UA levels, as well as eGFR, HOMA-IR, this group also had a higher frequency of hypertension and self-reported CVD (all $P < 0.05$). The CAP group had higher HDL-C levels and longer diabetes duration. Furthermore, serum N-MID, PINP, and β-CTX levels significantly lower in the CAP group compared with the non-CAP group (all $P < 0.05$).

Correlation Analysis of the Relationship Between BTMs and Biochemical Parameters

Spearman analysis showed that serum N-MID level was correlated with CRP ($r = -0.127$; $P = 0.009$), FBG ($r = -0.235$; $P < 0.001$), HbA1C ($r = -0.224$; $P < 0.001$), HDL-C ($r = 0.105$; $P = 0.033$), TG ($r = -0.1$; $P = 0.041$), eGFR ($r = -0.19$; $P < 0.001$), and SBP ($r = 0.134$; $P = 0.006$) after adjusting for age and sex. However, serum β-CTX was associated only with TG ($r = -0.105$; $P = 0.032$) and was not significantly associated with other parameters. Furthermore, serum PINP level was correlated with BMI ($r = 0.149$; $P = 0.002$), CRP ($r = -0.103$; $P = 0.035$), FBG ($r = -0.233$; $P < 0.001$), HbA1C ($r = -0.187$; $P < 0.001$), fasting plasma insulin ($r = 0.193$; $P < 0.001$), HOMA-IR ($r = 0.098$; $P = 0.045$), eGFR ($r = -0.162$; $P = 0.001$), and TG ($r = -0.13$; $P = 0.007$) after adjusting for age and sex (**Table 2**). However, the serum BTM levels was not independently associated with CIMT in all study populations.

Association Between Serum BTM Levels and CAP

Given that the BTM levels were significantly in inverse association with CRP, we adjusted for CRP in the multivariable logistic regression analysis. **Table 3** shows that after adjusting for age, sex, BMI, and CRP, only reduced serum N-MID level were revealed to be significantly associated with increased risk of CAP (odds ratios (OR) 0.957; 95% CI = 0.927–0.988; $P = 0.006$). We obtained similar associations when the multivariable logistic regression analysis was further adjusted for smoking, alcohol drinking, duration of diabetes, hypertension, and history of CVD (OR = 0.958; 95% CI = 0.928–0.989; $P = 0.008$). Low serum N-MID indicated a high risk for CAP (OR = 0.958; 95% CI = 0.926–0.991; $P = 0.013$) after further adjusting for FBG, HbA1C, serum TC, TG, HDL-C, and LDL-C. However, the PINP and β-CTX levels were not significantly associated with the risk of CAP in all multivariable logistic regression models.

TABLE 2 | Correlation between BTMs and other parameters in patients with T2DM.

Variables	N-MID		β-CTX		PINP	
	r	*P*-value	r	*P*-value	r	*P*-value
BMI	−0.002	0.967	0.047	0.333	0.149	**0.002**
CRP	−0.127	**0.009**	−0.042	0.392	−0.103	**0.035**
HbA1C	−0.224	**<0.0001**	−0.026	0.598	−0.187	**<0.0001**
FBG	−0.235	**<0.0001**	−0.089	0.069	−0.233	**<0.0001**
HOMA-IR	−0.011	0.819	0.016	0.742	0.098	**0.045**
Insulin	0.071	0.15	0.029	0.559	0.193	**<0.0001**
eGFR	−0.19	**<0.0001**	−0.067	0.17	−0.162	**0.001**
UA	−0.006	0.903	−0.041	0.397	0.011	0.824
TC	0.021	0.676	−0.011	0.815	−0.031	0.52
TG	−0.1	**0.041**	−0.105	**0.032**	−0.13	**0.007**
HDL-C	0.105	**0.033**	0.066	0.179	0.051	0.296
LDL-C	0.075	0.124	0.05	0.306	0.056	0.255
SBP	0.134	0.006	0.02	0.689	0.042	0.385
DBP	0.08	0.105	−0.008	0.867	0.018	0.719
CIMT	0.084	0.286	0.118	0.131	0.06	0.452

All correlation coefficients were calculated after adjustment for age, gender. The bold values indicated that difference is statistically significant.

TABLE 3 | Association of serum BTMs with CAP in T2DM populations.

	OR (95% CI)	*P*-value
N-MID		
Model 1	0.957 (0.927–0.988)	**0.006**
Model 2	0.958 (0.928–0.989)	**0.008**
Model 3	0.958 (0.926–0.991)	**0.013**
β-CTX		
Model 1	0.631 (0.313–1.273)	0.198
Model 2	0.686 (0.334–1.407)	0.304
Model 3	0.672 (0.315–1.435)	0.304
PINP		
Model 1	0.995 (0.987–1.004)	0.283
Model 2	0.995 (0.987–1.004)	0.281
Model 3	0.995 (0.986–1.004)	0.287

Model 1 adjusted for age, gender, BMI and CRP.
Model 2 further adjusted for alcohol drinking, smoking, duration of diabetes, hypertension, and history of CVD.
Model 3 further adjusted for FBG, HbA1C, TG, TC, HDL-C, and LDL-C.
The bold values indicated that difference is statistically significant.

Association Between Serum BTMs and MetS Components

Among MetS components, after adjusting for age, sex, BMI, CRP, smoking, alcohol drinking, duration of diabetes, hypertension, and history of CVD (model 2), overweight/obesity (BMI $\geq$ 25 kg/m^2) were found to be negatively associated with N-MID (OR = 0.96; 95% CI = 0.94–0.99; P = 0.015) and β-CTX (OR = 0.446; 95% CI = 0.24–0.85; P = 0.014). Similarly, hypertriglyceridemia was negatively associated with N-MID (OR = 0.96; 95% CI = 0.93–0.99; P = 0.004) and β-CTX (OR = 0.34; 95% CI = 0.18–0.67; P = 0.002). Significant associations were also observed between the presence of hypertriglyceridemia and PINP after adjusting for potential confounders (OR = 0.99; 95% CI = 0.98–1.00; P = 0.003; model 2). However, no significant association was found between serum BTMs and the presence of MetS, hypertension, and HDL-C dyslipidemia in T2DM populations (**Table 4**).

DISCUSSION

In the present study, we found an association between serum N-MID and the risk of carotid atherosclerosis in T2DM populations. These associations were independent of lifestyle factors, duration of diabetes, history of CVD, CRP, HbA1c, FBG, lipid parameters, and BMI. Multivariate logistic regression analysis revealed that serum N-MID, PINP, and β-CTX levels were significantly associated with hypertriglyceridemia, whereas serum N-MID and β-CTX levels were associated with overweight/obesity risk. These findings indicated the association between serum N-MID and metabolic syndrome components, as well as carotid atherosclerosis, independent of other known CVD risk factors in patients with T2DM, thus suggesting that BTMs (especially N-MID) were important for glucose and lipid metabolism, and atherosclerosis.

Several studies have shown that serum BTMs may be a predictor of CVD risk in patients with T2DM (15, 18). In a previous study, serum osteocalcin was negatively associated with parameters of atherosclerosis in T2DM patients (19). In another study, serum levels of osteocalcin were inversely associated with the metabolic syndrome and the severity of coronary artery disease in Chinese populations (20). Interestingly, consistent with previous studies, we observed that serum N-MID levels were an independent risk factor for carotid atherosclerosis in patients with T2DM. Endothelial dysfunction is considered as an early step in atherosclerosis development as it contributes to the

TABLE 4 | Association of serum BTMs with metabolic syndrome components.

Variables	N-MID		β-CTX		PINP	
	OR (95% CI)	*P*-value	OR (95% CI)	*P*-value	OR (95% CI)	*P*-value
MetS	0.99 (0.95–1.03)	0.601	0.54 (0.24–1.21)	0.135	0.99 (0.98–1.00)	0.195
Overweight/Obesity	0.96 (0.94–0.99)	**0.015**	0.45 (0.24–0.85)	**0.014**	1.00 (0.99–1.01)	0.651
Hypertension	1.01 (0.98–1.04)	0.369	1.22 (0.63–2.34)	0.555	1.00 (0.99–1.01)	0.896
Dyslipidemia (TG)	0.96 (0.93–0.99)	**0.004**	0.34 (0.18–0.67)	**0.002**	0.99 (0.98–1.00)	**0.003**
Dyslipidemia (HDL-C)	1.00 (0.97–1.03)	0.736	0.85 (0.44–1.66)	0.637	1.00 (0.99–1.01)	0.708

All variables adjusted for age-gender, BMI, CRP, alcohol drinking, smoking, duration of diabetes, hypertension, and history of CVD. The bold values indicated that difference is statistically significant.

initiation and early progression of atherosclerosis (21, 22). Some studies suggested that high serum osteocalcin level contributes to vascular calcification and atherosclerosis. However, different population lead to inconclusive results (23). Large longitudinal studies are needed to further explore the clinical relevance of serum osteocalcin in vascular calcification and atherosclerosis (24). In a mouse model of atherosclerosis, daily injections of osteocalcin reduced the risk of CVD, which showed an endothelial-protective effect because it improves glucose and lipid metabolism by activating the PI3K-Akt-eNOS signaling pathway (25). However, prospective studies are needed to clarify whether low osteocalcin level plays a causal role in atherosclerosis development.

The current study revealed that another bone formation marker, PINP level, was significantly associated with HOMA-IR, FBG, fasting insulin levels, CRP, and TG. These associations were reported in a previous study in which PINP was positively correlated with insulin sensitivity and negatively correlated with glucose and triglycerides (26). Significant associations were also observed between BTM levels and the presence of hypertriglyceridemia after adjustment for potential confounders. However, we did not find an association of serum PINP and β-CTX levels with CAP risk in T2DM populations. In view of the high correlation between PINP, β-CTX, and N-MID, the effects of PINP and β-CTX on carotid atherosclerosis were most likely to be attributable to the function of N-MID (11). Thus, the interactions among different BTMs require further investigations.

Vascular endothelial inflammation was considered to play a vital role in the mechanism of CVD development (27, 28). CRP is an acute-phase reactant and a well-known serum marker of chronic low-grade inflammation. It is associated with diabetes, hypertension, obesity, and CVDs (29, 30). In the present study, serum N-MID and PINP levels were negatively correlated with CRP. Accordingly, the results of current study may be partially attributed to the mechanism of chronic low-grade inflammation. Furthermore, elevated serum TG was an independent risk factor for CVD development (31). Consistent with previous studies, serum N-MID and PINP levels were negatively correlated with TG in our study (32). Meanwhile, after adjustment for potential confounders, all BMTs (including N-MID, β-CTX, and PINP) were negatively associated with hypertriglyceridemia. Therefore, given that serum N-MID levels were significantly associated with CRP and TG levels and the strong relationship of serum N-MID with carotid atherosclerosis risk, N-MID can be considered as a promising candidate for risk assessment and a potential intervention target for CVD.

A previous study has shown no significant correlation between CIMT and serum osteocalcin (33). In accordance with these findings, the present study demonstrated that the three BTMs were not significantly associated with CIMT in T2DM patients. Furthermore, clinical studies investigating the association of serum osteocalcin and CVD risk are controversial, and the lack of consistency may be due to different study populations or different degrees of confounding factors associated with serum osteocalcin level, such as metabolic factors and chronic low-grade inflammation, and these metabolic dysfunctions are related to the progression of atherosclerosis (34–36). In humans, bone turnover rate varies obviously according to individual variables, age and sex are the most important variables determining bone remodeling. Given that the serum levels of osteocalcin differ between sexes and alter with age, the relationship of serum osteocalcin levels with CVD risk may also differ according to these variables (37). Studies have demonstrated that close correlations of serum osteocalcin level with glucose and lipid metabolic disorders, obesity, and MetS (8, 38). Herein, the serum N-MID level was correlated with CRP, FBG, HbA1C, HDL-C, and TG after adjusting for age and sex. Similar associations were found in PINP, indicating that serum BTMs may play a key role in glucose and lipid metabolism. Thus, given the strong association between metabolic risk and atherosclerosis, our findings suggested that the association of BTMs with atherosclerosis may be influenced by metabolic variables.

CONCLUSION

Our cross-section study suggested that serum N-MID levels were significantly associated with carotid atherosclerosis in patients with T2DM even after adjusting for potential confounders. Serum BTMs level were associated with other metabolic syndrome components, which may reflect the role of BTMs as a circulating endocrine markers regulating glucose and lipid metabolism, thereby posing a cardiovascular risk to T2DM patients.

DATA AVAILABILITY STATEMENT

The original contributions presented in the study are included in the article/supplementary material, further inquiries can be directed to the corresponding author/s.

ETHICS STATEMENT

The studies involving human participants were reviewed and approved by Ethical Committee of the First Affiliated Hospital of Zhengzhou University. The Ethics Committee waived the requirement of written informed consent for participation.

AUTHOR CONTRIBUTIONS

WL, EC, XL, LZ, LL, TL, and SL contributed to the conception and design of the study. WL, SL, ML, and RL recruited the subjects and supervised the study. WL, EC, LZ, LL, and XL analyzed the data. WL, EC, and SL wrote the initial draft of the article. WL, EC, LZ, TL, XL, and SL contributed to the writing, reviewing, and revising of the manuscript. All authors contributed to the article and approved the submitted version.

FUNDING

WL is funded by the National Natural Science Foundation of China (82000831).

ACKNOWLEDGMENTS

We would like to thank the participants in this study.

REFERENCES

1. Eastell R, Szulc P. Use of bone turnover markers in postmenopausal osteoporosis. *Lancet Diabetes Endocrinol.* (2017) 5:908–23. doi: 10.1016/S2213-8587(17)30184-5
2. Fontalis A, Eastell R. The challenge of long-term adherence: The role of bone turnover markers in monitoring bisphosphonate treatment of osteoporosis. *Bone.* (2020) 136:115336. doi: 10.1016/j.bone.2020.115336
3. Greenblatt MB, Tsai JN, Wein MN. Bone turnover markers in the diagnosis and monitoring of metabolic bone disease. *Clin Chem.* (2017) 63:464–74. doi: 10.1373/clinchem.2016.259085
4. Naylor K, Eastell R. Bone turnover markers: use in osteoporosis. *Nat Rev Rheumatol.* (2012) 8:379–89. doi: 10.1038/nrrheum.2012.86
5. Hygum K, Starup-Linde J, Harslof T, Vestergaard P, Langdahl BL. Mechanisms In Endocrinology: diabetes mellitus, a state of low bone turnover - a systematic review and meta-analysis. *Eur J Endocrinol.* (2017) 176:R137–57. doi: 10.1530/EJE-16-0652
6. Bellissimo MP, Roberts JL, Jones, KH. Liu, KR. Taibl, K. Uppal, et al. Metabolomic Associations with Serum Bone Turnover Markers. *Nutrients.* (2020) 12:3161. doi: 10.3390/nu12103161
7. Reiss AB, Miyawaki N, Moon J, Kasselman LJ, Voloshyna IRD'Avino, Jr, J De Leon. CKD, arterial calcification, atherosclerosis and bone health: inter-relationships and controversies. *Atherosclerosis.* (2018) 278:49–59. doi: 10.1016/j.atherosclerosis.2018.08.046
8. Kanazawa I, Yamaguchi T, Sugimoto T. Relationship between bone biochemical markers versus glucose/lipid metabolism and atherosclerosis; a longitudinal study in type 2 diabetes mellitus. *Diabetes Res Clin Pract.* (2011) 92:393–9. doi: 10.1016/j.diabres.2011.03.015
9. Florez H, Hernandez-Rodriguez J, Carrasco JL, Filella X, Prieto-Gonzalez S, Monegal A, et al. Low serum osteocalcin levels are associated with diabetes mellitus in glucocorticoid treated patients. *Osteoporos Int.* (2021) 33:745-50. doi: 10.1007/s00198-021-06167-z
10. La Sala L, Prattichizzo F, Ceriello A. The link between diabetes and atherosclerosis. *Eur J Prev Cardiol.* (2019) 26:15–24. doi: 10.1177/2047487319878373
11. Wang J, Yan DD, Hou XH, Bao YQ, Hu C, Zhang ZL, et al. Association of bone turnover markers with glucose metabolism in Chinese population. *Acta Pharmacol Sin.* (2017) 38:1611–7. doi: 10.1038/aps.2017.23
12. Cipriani C, Colangelo L, Santori R, Renella M, Mastrantonio M, Minisola S, et al. The interplay between bone and glucose metabolism. *Front Endocrinol (Lausanne).* (2020) 11:122. doi: 10.3389/fendo.2020.00122
13. Sheng L, Cao W, Cha B, Chen Z, Wang F, Liu J. Serum osteocalcin level and its association with carotid atherosclerosis in patients with type 2 diabetes. *Cardiovasc Diabetol.* (2013) 12:22. doi: 10.1186/1475-2840-12-22
14. Levinger I, Brennan-Speranza TC, Zulli A, Parker L, Lin X, Lewis JR, et al. Multifaceted interaction of bone, muscle, lifestyle interventions and metabolic and cardiovascular disease: role of osteocalcin. *Osteoporos Int.* (2017) 28:2265–73. doi: 10.1007/s00198-017-3994-3
15. Zwakenberg SR, van der Schouw YT, Schalkwijk CG, Spijkerman AMW, Beulens JWJ. Bone markers and cardiovascular risk in type 2 diabetes patients. *Cardiovasc Diabetol.* (2018) 17:45. doi: 10.1186/s12933-018-0691-2
16. Hwang YC, Kang M, Cho IJ, Jeong IK, Ahn KJ, Chung HY, et al. Association between the circulating total osteocalcin level and the development of cardiovascular disease in middle-aged men: a mean 8.7-year longitudinal follow-up study. *J Atheroscler Thromb.* (2015) 22:136–43. doi: 10.5551/jat.25718
17. Grundy SM, Cleeman JI, Merz CN, Brewer HB, Jr., Clark LT, Hunninghake DB, et al. American College of Cardiology, American Heart. Implications of recent clinical trials for the National Cholesterol Education Program Adult Treatment Panel III guidelines. *Circulation.* (2004) 110:227–39. doi: 10.1161/01.CIR.0000133317.49796.0E
18. Holvik K, van Schoor NM, Eekhoff EM, Heijer Mden, Deeg DJ, Lips P, et al. Plasma osteocalcin levels as a predictor of cardiovascular disease in older men and women: a population-based cohort study. *Eur J Endocrinol.* (2014) 171:161–70. doi: 10.1530/EJE-13-1044
19. Reyes-Garcia R, Rozas-Moreno P, Jimenez-Moleon JJ, Villoslada MJ, Garcia-Salcedo JA, Santana-Morales S, et al. Relationship between serum levels of osteocalcin and atherosclerotic disease in type 2 diabetes. *Diabetes Metab.* (2012) 38:76–81. doi: 10.1016/j.diabet.2011.07.008
20. Bao Y, Zhou M, Lu Z, Li H, Wang Y, Sun L, et al. Serum levels of osteocalcin are inversely associated with the metabolic syndrome and the severity of coronary artery disease in Chinese men. *Clin Endocrinol.* (2011) 75:196–201. doi: 10.1111/j.1365-2265.2011.04065.x
21. Gimbrone MA Jr, Garcia-Cardena G. Endothelial cell dysfunction and the pathobiology of atherosclerosis. *Circ Res.* (2016) 118:620–36. doi: 10.1161/CIRCRESAHA.115.306301
22. Xu S. Therapeutic potential of blood flow mimetic compounds in preventing endothelial dysfunction and atherosclerosis. *Pharmacol Res.* (2020) 155:104737. doi: 10.1016/j.phrs.2020.104737
23. Skenteris NT, Seime T, Witasp A, Karlof E, Wasilewski GB, Heuschkel MA, et al. Osteomodulin attenuates smooth muscle cell osteogenic transition in vascular calcification. *Clin Transl Med.* (2022) 12:e682. doi: 10.1002/ctm2.682
24. Millar SA, Patel H, Anderson SI, England TJ, O'Sullivan SE. Osteocalcin, vascular calcification, and atherosclerosis: a systematic review and meta-analysis. *Front Endocrinol.* (2017) 8:183. doi: 10.3389/fendo.2017.00183
25. Dou J, Li H, Ma X, Zhang M, Fang Q, Nie M, et al. Osteocalcin attenuates high fat diet-induced impairment of endothelium-dependent relaxation through Akt/eNOS-dependent pathway. *Cardiovasc Diabetol.* (2014) 13:74. doi: 10.1186/1475-2840-13-74
26. Laurent MR, Cook MJ, Gielen E, Ward KA, Antonio L, Adams JE, et al. Lower bone turnover and relative bone deficits in men with metabolic syndrome: a matter of insulin sensitivity? The European male ageing study. *Osteoporos Int.* (2016) 27:3227–37. doi: 10.1007/s00198-016-3656-x
27. Serino A, and Salazar G. Protective role of polyphenols against vascular inflammation, aging and cardiovascular disease. *Nutrients.* (2018) 11:53 doi: 10.3390/nu11010053

28. Marchio P, Guerra-Ojeda S, Vila JM, Aldasoro M, Victor VM, Mauricio MD. Targeting early atherosclerosis: a focus on oxidative stress and inflammation. *Oxid Med Cell Longev.* (2019) 2019:8563845. doi: 10.1155/2019/8563845
29. Zanoli L, Pino ADi, Terranova V, Marca SDi, Pisano M, Quattro RD, et al. Inflammation and ventricular-vascular coupling in hypertensive patients with metabolic syndrome. *Nutr Metab Cardiovasc Dis.* (2018) 28:1222–9. doi: 10.1016/j.numecd.2018.08.003
30. Yoon K, Ryu S, Lee J, Park JD. Higher and increased concentration of hs-CRP within normal range can predict the incidence of metabolic syndrome in healthy men. *Diabetes Metab Syndr.* (2018) 12:977–83. doi: 10.1016/j.dsx.2018.06.008
31. Simha V. Management of hypertriglyceridemia. *BMJ.* (2020) 371:m3109. doi: 10.1136/bmj.m3109
32. Liu XX, Jiang L, Liu Q, Zhang J, Niu W, Liu J, et al. Low bone turnover markers in young and middle-aged male patients with type 2 diabetes mellitus. *J Diabetes Res.* (2020) 2020:6191468. doi: 10.1155/2020/6191468
33. Luo Y, Ma X, Hao Y, Xiong Q, Xu Y, Pan X, et al. Relationship between serum osteocalcin level and carotid intima-media thickness in a metabolically healthy Chinese population. *Cardiovasc Diabetol.* (2015) 14:82. doi: 10.1186/s12933-015-0245-9
34. Poznyak A, Grechko AV, Poggio P, Myasoedova VA, Alfieri V, Orekhov AN. The diabetes mellitus-atherosclerosis connection: the role of lipid and glucose metabolism and chronic inflammation. *Int J Mol Sci.* (2020) 21:1835 doi: 10.3390/ijms21051835
35. Aboonabi A, Meyer RR, Singh I. The association between metabolic syndrome components and the development of atherosclerosis. *J Hum Hypertens.* (2019) 33:844–55. doi: 10.1038/s41371-019-0273-0
36. Mehu M, Narasimhulu CA, Singla DK. Inflammatory cells in atherosclerosis. *Antioxidants (Basel).* (2022) 11:233. doi: 10.3390/antiox11020233
37. Jung KY, Kim KM, Ku EJ, Kim YJ, Lee DH, Choi SH, et al. Age- and sex-specific association of circulating osteocalcin with dynamic measures of glucose homeostasis. *Osteoporos Int.* (2016) 27:1021–9. doi: 10.1007/s00198-015-3315-7
38. Onyenekwu CP, Azinge EC, Egbuagha EU, Okpara HC. Relationship between plasma osteocalcin, glycaemic control and components of metabolic syndrome in adult Nigerians with type 2 diabetes mellitus. *Diabetes Metab Syndr.* (2017) 11:281–6. doi: 10.1016/j.dsx.2016.12.013

Conflict of Interest: The authors declare that the research was conducted in the absence of any commercial or financial relationships that could be construed as a potential conflict of interest.

frontiers | Frontiers in Cardiovascular Medicine

ORIGINAL RESEARCH
published: 29 April 2022
doi: 10.3389/fcvm.2022.755619

Adenosine A2a Receptor Regulates Autophagy Flux and Apoptosis to Alleviate Ischemia-Reperfusion Injury *via* the cAMP/PKA Signaling Pathway

Yun Xia†, Feng He†, Mohamed Bassirou Moukeila Yacouba, Huimin Zhou, Jingfan Li, Ying Xiong, Jingjing Zhang, Hui Li, Yanlin Wang and Jianjuan Ke**

Department of Anesthesiology, Zhongnan Hospital of Wuhan University, Wuhan, China

OPEN ACCESS

Edited by:
Masanori Aikawa, Brigham and Women's Hospital and Harvard Medical School, United States

Reviewed by:
Katsuya Hirano, Kagawa University, Japan
BoZhi Ye, Wenzhou Medical University, China

***Correspondence:**
Yanlin Wang
wyl0342@sina.com
Jianjuan Ke
1219628972@qq.com

†These authors have contributed equally to this work

Specialty section:
This article was submitted to Atherosclerosis and Vascular Medicine, a section of the journal Frontiers in Cardiovascular Medicine

Received: *09 August 2021*
Accepted: *23 March 2022*
Published: *29 April 2022*

Citation:
Xia Y, He F, Moukeila Yacouba MB, Zhou H, Li J, Xiong Y, Zhang J, Li H, Wang Y and Ke J (2022) Adenosine A2a Receptor Regulates Autophagy Flux and Apoptosis to Alleviate Ischemia-Reperfusion Injury via the cAMP/PKA Signaling Pathway. Front. Cardiovasc. Med. 9:755619. doi: 10.3389/fcvm.2022.755619

Exploring effective methods to lessen myocardial ischemia-reperfusion injury still has positive significance. The adenosine A2a receptor (A2aR) has played a crucial part in cardiac ischemia-reperfusion injury. Previous studies revealed that the adenosine A2a receptor regulated autophagy, but the specific mechanism in myocardial ischemia-reperfusion injury was still unclear. We established an ischemia-reperfusion model (30 min of ischemia and 2 h of reperfusion) *in vivo* and a model with oxygen-glucose deprivation for 6 h and reoxygenation for 18 h (OGDR) *in vitro*. The ischemia-reperfusion injury resulted in prolonged QTc interval, left ventricular systolic dysfunction, and myocardial infarction. *In vitro* model, we found that the OGDR-induced autophagosomes and apoptosis caused myocardial cell death, as evidenced by a significant increase in the generation of lactate dehydrogenase and creatine kinase-MB. Furthermore, overactivated autophagy with rapamycin showed an anti-apoptotic effect. The interaction between autophagy and apoptosis in myocardial ischemia-reperfusion injury was complex and variable. We discovered that the activation of adenosine A2a receptor could promote the expression of Bcl-2 to inhibit the levels of Beclin-1 and LC3II. The number of autophagosomes exceeded that of autolysosomes under OGDR, but the result reversed after A2aR activation. Activated A2aR with its agonist CGS21680 before reperfusion saved cellular survival through anti-apoptosis and anti-autophagy effect, thus improving ventricular contraction disorders, and visibly reducing myocardial infarction size. The myocardial protection of adenosine A2a receptor after ischemia may involve the cAMP-PKA signaling pathway and the interaction of Bcl-2-Beclin-1.

Keywords: adenosine A2A receptor, autophagy, autophagosomes, myocardial ischemia-reperfusion injury, apoptosis

INTRODUCTION

The pathological basis of coronary heart disease (CHD) is myocardial ischemia, hypoxia, and necrosis caused by coronary artery occlusion and stenosis. It remains higher global morbidity and mortality. For acute myocardial infarction (AMI), as a kind of CHD, reperfusion and revascularization are the conventional treatments used in clinical. However, vascular reperfusion will inevitably lead to myocardial ischemia-reperfusion injury (MIRI) complications involving a

sequence of pathophysiological and metabolic alterations. Severe MIRI will result in myocardial failure, arrhythmia, and death of myocardial cells, mainly caused by hypoxia, changes in cytoplasmic pH, calcium overload, ATP deficiency, and immune cell aggregation (1). The occurrence of MIRI will change the disease outcome and treatment of some patients with AMI (2). Therefore, some approaches are needed to reduce the incidence of MIRI or its extent of damage.

Adenosine receptor (AR), a type of glycoprotein, exists on the membrane of most cells of the body. It has a critical effect on the cardiovascular system by cascading with numerous effectors such as enzymes, channels, transporters, and cytoskeleton (3). Multiple angiocardiopathy, for instance, hypertension, atherosclerosis, diabetic cardiomyopathy, and ischemic heart disease have been related to changes in adenosine-adenosine receptor signaling in coronary microcirculation (4). There are three types of AR: A1R, A2R, and A3R, of which A2R has two subtypes, A2aR and A2bR. Adenosine A2a receptor (A2aR) most widely distributes in coronary vessels (5). It exerts a positive significance in adjusting MIRI. Previous studies showed that A2aR's activation could alleviate MIRI in normal hearts (6, 7) or sepsis ones (8), in stunned myocardium (1), and reduce mitochondrial oxidative stress after reperfusion (9). The cardioprotective effects of A2aR in MIRI also include the inhibition of the inflammatory response (10) [$CD4^+$ T lymphocytes (11) and mast cells (12)] and apoptotic cell death (13). Moreover, the combination of activators with A2aR can activate adenosine cyclase (AC) and increase the formation of cyclic adenosine monophosphate (cAMP) (14). As a second messenger, cAMP promotes the generation of protein kinase A (PKA), which makes downstream proteins phosphorylation to form the cAMP-PKA signaling pathway (15). The cAMP-PKA signaling pathway also relates to inhibition of myocardial fibrosis (16) and limitation of MIRI (17).

Autophagy is an important mechanism for preserving the dynamic balance of the intracellular environment (18–20). It undertakes the degradation and recycling of intracellular organelles and proteins, as well as the secretion and transportation of intracellular substances (21). Current researches have shown that autophagy appears to play markedly different roles during ischemia and reperfusion period. It is unanimously considered that autophagy in ischemia is pivotal to maintain the stability of cardiac function and lessen myocardial damage. During the ischemic period, autophagy, activated in response to a lack of oxygen and nutrients, can promptly resolve harmful substances and damaged organelles (22). The startup of this self-preservation program not only reduces the cardiomyocytes' damage but also provides amino acids, fatty acids, ATP regenerative substrates as supplements to protein synthesis and ATP generation for cell survival (19, 22). However, the role of autophagy in reperfusion seems to be a debate (23, 24). Unlike the effect of energy recovery, over-activated autophagy may cause cell death and further increase the damage. Thus, that is considered harmful. In the case of using Atg7 knockout mice to impair autophagy function, the production of ROS decreased, and the activity of myocardial cells enhanced after reperfusion (25). But contrary views (26, 27) claimed that the increase of autophagy during reperfusion had a previously undescribed and formidable protective response on MIRI. In addition, autophagy in MIRI has a complex relationship with apoptosis, and their interplay and balance also provide a new treatment concept for coronary heart disease (24).

Our earlier research (7) suggests that A2R activation can suppress autophagy during reperfusion, which dues to the A2bR subtype. A2aR activation alone, however, seemed cannot decrease the infarcted area of heart. Considering the beneficial expression of A2aR in other reports, we reconsider whether its potential is underestimated in autophagy of MIRI. Due to the limited research on A2aR regulating autophagy in MIRI, we designed this experiment.

MATERIALS AND METHODS

Detailed information about related compounds, reagents, antibodies were provided in the attached table (**Supplementary Tables 1, 2**).

Animals

All Sprague Dawley adult rats (250 g−280 g) and neonates (1–3 days) were offered by Hubei Experimental Animal Research Center. Animal management and experimental protocols following the Guide for the Care and Use of Laboratory Animals (National Institutes of Health) were approved by the Animal Experimentation Committee of Wuhan University (approval number WP2020-01108).

Extraction and Purification of Myocardial Cells

Neonatal rat cardiomyocytes (NRCMs) were extracted from the neonates of 1–3 days, according to the improved method based on the classic protocol (28). Ventricles were separated from large vessels, atria, and pericardium in a 10 cm petri dish with DMEM/F12 medium at 4°C, and subsequently transferred into a 20 ml beaker, containing the digestive juices of PBS, 0.125% trypsin, and 0.08% type II collagenase for tissue digestion. We added a 1 cm stir bar in beaker and put the beaker on a magnetic blender, which was set at 220 rotations per min (rpm) to facilitate the digestion. And the beaker and magnetic blender were all put in the digital biochemical incubator at 37°C. Each digestion lasted 10 min, with a total of 12-14 times. After each digestion, the digestive juice was transferred to a 15 ml test tube to terminate digestion with DMEM/F12 supplemented with 10% fetal bovine serum (FBS), 1% penicillin-streptomycin and 1:1000 5-Bromo-2′-deoxyuridine (BrdU). Next, the cell deposition was re-suspended with the fresh medium after 5 min centrifugation at 4000 rpm. Then the cell suspension was filtrated with a sterile 70 um filter into the 10 cm cell culture dishes for 1 h incubation to remove the adherent fibroblasts. Eventually, the cell suspension was filtrated again and 2×10∧6 cells was planted into each 6 cm dish after cell counting (Countstar® BioMed, Shanghai). In addition, immunofluorescence identification was performed to evaluate the purification of cardiomyocytes.

Establishment of OGDR Model *in vitro*

NRCMs cultured *in vitro* were treated with oxygen-glucose deprivation and reoxygenation (OGDR) to simulate ischemia-reperfusion injury *in vivo*. Cardiomyocytes were cultivated in a glucose-free, serum-free medium with 95% N_2 and 5% CO_2 for 6 h. Then, the fresh DMEM/F12 supplemented with 10% FBS, 1% penicillin-streptomycin, and 1‰ BrdU was used again and reoxygenated for 18 h incubating at 37°C and 5% CO_2 (29).

Cardiomyocytes' Identification

When myocardial cells were grown for 24 h, immunofluorescence was performed with cardiac troponin I (TNNI3) (30) as the primary antibody and FITC goat anti-rabbit IgG as secondary antibodies to distinguish them from non-myocytes. The coverslips were washed with PBS, fixed with 4% paraformaldehyde for 5 min, and infiltrated with 0.5% Triton X-100-PBS for 5 min at room temperature. Next, slips were rinsed 3 times with PBS for 3 min each and blocked with 1% BSA-PBST (PBS with 1‰ Tween-20) for 30 min at room temperature. Then NRCMs were incubated with rabbit polyclonal antibody of TNNI3 (1:500; Abclonal, A6995) at 4°C overnight. On the second day, coverslips were rinsed 3 times with PBS again and incubated with FITC goat anti-rabbit IgG (1:500, Abclonal, AS011) for 1 h. The cell nuclei were stained with DAPI for 5 min after the third time of washing with PBST. And the number of DAPI stained nuclei represented the total number of cells in the same field of microscope. Begin with the use of secondary antibodies, all subsequent operations were performed in the dark. Finally, three images were randomly captured by laser confocal microscopy for counting. And Image J was performed to count the number of myocardial cells and nuclei. The purification rate of cardiomyocytes (%) = the sum of cells labeled by fluorescence in the three visual fields ÷ the total number of cell nuclei ×100%.

Autophagic Flux Measurement

The day before OGDR, NRCMs were transfected with Ad-mCherry-GFP-LC3 (MOI 1) for 24 h. At the end of reoxygenation, the cells were fixed with 4% paraformaldehyde, and nuclei were stained with DAPI. The fluorescence signal was observed by a confocal microscope (LEICA TCS SP8, Germany). Yellow spots (autophagosomes) and red spots (autolysosomes) under multiple visions were analyzed and counted by image J.

siRNA-Mediated Knockdown of A2aR

To verify the role of A2aR, we used siRNA-A2aR adenovirus. siRNA sequences synthesized at Hanbio Co., LTD (Shanghai, China) were cited from the reference (31) (5′-GCUACAUCGCCAUCCGAAU-3′). Adenovirus (MOI 15) and its control vehicle were severally co-incubated with cardiomyocytes in a serum-free medium for 8 h of transfection. Next, sucking and discarding the serum-free medium, and the cardiomyocytes were continually incubated with fresh DMEM/F12 supplemented with 10% FBS, 1% penicillin-streptomycin, and 1‰ BrdU for 48 h (32). Then, immunoblot was performed to confirmed the final effect of A2aR knockdown.

The Myocardial Ischemia-Reperfusion Injury Model

Each rat has received the anesthesia of 2% sodium pentobarbital 35 mg/kg by intraperitoneal injection (33, 34). Mechanical ventilation (Rodent Ventilator, Beijing ZSDichuang Technology Co., Ltd., China) was performed after tracheotomy. The parameters of the ventilator were adjusted as RR 60-80 beats per min, tidal volume 2 ml/100 g, the ratio of inspiration to expiration was 1:1. Open the left thorax to expose the heart. The left anterior descending coronary artery (LAD) was ligated with a 5-0 suture approximately 2 mm below the junction of the left atrial appendage and the pulmonary artery cone. Before tightening the knot, a polyethylene tube was passed through it to form an openable knot for reversible LAD occlusion. In the sham operation group, sutures only passed through the corresponding positions, and no ligation was performed. Ischemia can be affirmed by a transient drop in blood pressure and the appearance of cyanosis on the surface of myocardium. An epicardial hyperemic response and the speedy extinction of cyanosis demonstrated the recovery of reperfusion (35). After 30 min of coronary occlusion and 120 min of reperfusion (36), the rats were euthanized by injection of an overdose of anesthetic.

Hemodynamic Measurements

After anesthesia, an electrocardiogram was connected and the right internal carotid artery (RICA) was punctured in the supine position of rats. A catheter was placed into RICA to monitor the arterial blood pressure after the anticoagulation of 100 U/kg heparin. Changes in the electrocardiogram and arterial blood pressure of rats were monitored by the BL-420 system (TaiMeng Informatization Biological Signal Acquisition and Analysis System, China). The QT interval is corrected (QTc) using Bazzet's formula to exclude the influence of heart rate (37).

Echocardiography

Cardiac function was assessed by transthoracic echocardiography using an 11 MHz imaging transducer from GE Vivid 7 (GE Health Medical, USA). All procedures were implemented by the same researcher unknown to the experimental scheme. Parameters related to left ventricular structure: diastolic ventricular septal thickness (IVSd), systolic ventricular septal thickness (IVSs), left ventricular end-diastolic diameter (LVIDd), left ventricular end-systolic diameter (LVIDs), left ventricular diastolic posterior wall thickness (LVPWd), left ventricular systolic posterior wall thickness (LVPWs) were all obtained by M-mode ultrasound. Left ventricular end-diastolic volume (LVEDV), left ventricular end-systolic volume (LVESV), left ventricular ejection fraction (LVEF), stroke volume (SV), and left ventricular fractional shortening (FS) were automatically generated by computer algorithms.

Measurement of Myocardial Infarction Area

After the reperfusion, the reversible LAD occlusion was completely ligated again, and 1% Evans blue dye was injected into the femoral vein. And the isolated hearts were washed three times with physiological saline, then rapidly frozen in a refrigerator at−80°C for 10 min. These isolated hearts were sliced into

coronal 1-mm-thick sections by the rat heart slicer matrix (JNT-XZM, Beijing). Heart sections were soaked in 1% 2,3,5-triphenyl tetrazolium chloride (TTC) at 37°C for 15 min, and the tissues were gradually stained. The area of left ventricular area (LV) and proportions of myocardial infarction area (pale), ischemia risk area (red), and non-infarct area (blue) were measured by Image-Pro Plus 6.0 software. Ischemic area (%) = ischemia risk area (red) ÷ left ventricular size (LV) ×100%. Infarction area (%) = infarction area (pale) ÷ ischemia risk area (red) ×100%.

Experimental Protocols

In vitro, each group repeated independently for 3 times ($n = 3$). And all experimental groups received 6 h of oxygen-glucose deprivation and 18 h of reoxygenation (29). CGS-21680 (A2aR specific agonist, 30μM, Tocris Bioscience, 1036) and dbcAMP (selective PKA activator, 5μM, MedChemExpress, HY-B0764) were added 1 h before reoxygenation. H89 (the PKA selective inhibitor, 10 μM, MedChemExpress, HY-15979) was used 5 min before CGS21680. To verify the effect of autophagy on cell survival, autophagy agonist Rapamycin (100 nM, MedChemExpress, HY-10219) and antagonist 3-Methyladenine (3-MA, 10 mM, MedChemExpress, HY-19312) were used 1 h before reoxygenation (38, 39).

In vivo study, 36 adult male rats were randomized into six groups ($n = 6$): Sham group, IR group (30 min LAD occlusion and 120 min reperfusion, 1% DMSO in 1 ml saline, iv), IR+CGS21680 group (30 μg/kg 5min before reperfusion and 30 μg/(kg·min) for 1 h, i.v.), and IR+ZM241385 group (A2aR antagonist, 0.2 mg/kg 5 min before reperfusion, i.v.), IR+dbcAMP group (5 mg/kg, 5 min before reperfusion, i.v.) (40), and IR+CGS21680+H89 group (20 mg/kg, 5 min before CGS21680, i.v.) (41).

Protein Extraction and Western Blot

Cell and tissue samples were lysed with a RIPA lysis buffer containing protease and phosphatase inhibitory ingredients. The final protein sample was obtained after quantification by bicinchoninic acid (BCA) protein assay. Then 10% and 12% SDS PAGE gels were prepared for electrophoresis, and proteins were transferred to PVDF membranes. Finally, visualization of the target's bands was achieved using ECL-Plus detection reagents (Beyotime Biotechnology, China) and an imaging system (model 5200, Tianneng, China). The antibodies used were listed in **Supplementary Table 2**.

Cell Survival Rate Detected by CCK-8 and LDH Assays

Cells were seeded in 48-well plates at a density of $9.5\times10\wedge5/cm^2$. After 16 h of reoxygenation, 10% CCK-8 solution was added into the medium and allowed to act for 2 h to detect the absorbance at 450 nm (PerkinElmer EnSpire Microplate Reader, USA). In the blank control group, CCK-8 solution was dissolved in the cell-free medium. Given the interference of drugs and adenovirus, their control group was set as follows: adding agonist, antagonist, or adenovirus to cell-free medium respectively, and then adding CCK-8 solution. According to the instruction, the OD value was calculated as the cellular viability. The level of LDH (lactate dehydrogenase), an indicator of cell necrosis, was measured using the kit following its operating instructions (Elabscience, E-EL-R0338c). The final absorbance was scaled at 450 nm.

The Concentration Measurement of CK-MB and cTnI

When ending reperfusion, the medium samples of each group were collected, centrifuged at 12,000 rpm for 1 min, and the supernatant was sucked out to detect the concentration of CK-MB and cTnI. Indicators of cardiomyocyte injury, CK-MB (creatine kinase-MB, Elabscience, E-EL-R1327c) and cTnI (cardiac troponin I, Elabscience, E-EL-R1253c), were detected by the corresponding kits followed its instruction. The final absorbance was scaled at 450 nm.

Hematoxylin-Eosin Staining

The hearts were harvested rapidly after reperfusion and washed by sterile normal saline 3 times. Next the hearts were fixed by paraformaldehyde for 24 h. And the fixed heart was successively treated with ethanol dehydration (the concentration gradient of 70%, 80%, 90%, 95%, and 100%), xylene transparency and paraffin embedding. Then, the paraffin tissue blocks were prepared as 5 μm sections. Tissue sections were progressively subjected to xylene dewaxing, ethanol hydration (the concentration gradient of 100%, 95%, 80%, and 75%), and hematoxylin-eosin staining. Last, all tissue slices were dehydrated, transparentized, and sealed with neutral resins. The myocardial pathological alterations of the slices were assessed by the optical microscope.

Transmission Electron Microscopy

After reoxygenation, myocardial cells were collected and fixed with 2.5% glutaraldehyde at 4°C for 4 h. Next, cells were rinsed 3 times with 0.1M phosphoric acid buffer, and fixed with 1% osmic acid for 2 h. The samples were dehydrated in gradient ethanol (50%, 70%, 90%, 100%), permeated, and embedded in epoxy resin at 60°C for 48 h. Then the embedded samples were sliced into 80 nm by ultrathin slicer (Leica, EM UC7, German) and stained with 2% uranyl acetate and lead citrate. The morphological structure and autophagy flux of cells was observed by the transmission electron microscope (Hitachi TEM system, HT7800, Japan). *In vitro* experiment, random observation was performed on three cardiomyocytes in each group and the images were taken in a clockwise direction around the nucleus. The number of autophagosomes and autolysosomes was counted at 10000 magnification times. In animal experiments, a field of view was stochastically chosen from each rat's sample to count the quantity of autophagosomes and autolysosomes.

Statistical Analysis

All data were expressed as mean ± standard error of the mean unless otherwise specified, and statistical differences between groups were analyzed by GraphPad Prism 8.0 (GraphPad Software, Inc., La Jolla, CA). And the differences between multiple groups were verified through the one-way ANOVA with Bonferroni or Dunnett *post-hoc* test unless otherwise stated. Data, passed the normality and equal variance tests, were normalized to

the control or sham groups. A p-value of <0.05 was considered statistically significant.

RESULTS

A2aR's Activation Reduced QTc Prolongation and Facilitated the Recovery of Ventricular Systolic Function After Ischemia

To reassess the effect of A2aR on cardiac function in MIRI, we established the model of rats i*n vivo*. The ST-segment elevation of ECG indicated a successful establishment of the ischemic model. MIRI caused the QTc prolongation of the ECG. From the point of 30 min' reperfusion to the end, the ECG of the A2aR antagonist group appeared inverted Q waves with larger amplitude (as showed by arrow) and had a longer QTc interval. On the contrary, the prolongation of QTc interval was significantly improved after A2aR activation (**Figures 1A**,**B**). Moreover, we monitored the carotid artery pressure of each rat in real time after anesthesia. In order to explore the impact of drug treatments on the hemodynamics of rats in each group, we selected 5 time points (**Figure 1C**). The mean arterial pressure (MAP) of the Sham group always remained stable at about 100 mmHg. The ischemic treatment of the three experimental groups significantly decreased the MAP, and after 30 min of reperfusion, the decline became more visible. But the MAP among the three experimental groups were not statistically significant at the point of reperfusion 30 min. At 60 min of reperfusion, rats in the IR group and IR+ZM241385 group had adapted to reperfusion. And their MAP returned to a level of about 100 mmHg back. Oppositely, the MAP of the A2aR agonist group decreased further than before at 60 min of reperfusion, and it kept the low level until the end of reperfusion.

Five min before the end of reperfusion, we performed a cardiac ultrasound on each rat to investigate if its cardiac function had changed (**Figure 1D**). And echocardiography showed that ischemia-reperfusion injury impaired left ventricular ejection function (LVEF) and fractional shortening (LVFS) (**Figures 1E**,**F**). LVEF and LVFS in the IR+CGS21680 group improved evidently, while those in the antagonist ZM241385 group decreased further. The traditional Evans Blue-TTC staining method was performed to calculate the size of myocardial infarction. Based on the IR group, the infarct area of the IR+CGS21680 group decreased by 41%, while that of the ZM241385 group was conversely increased (**Figures 1G**,**I**). The ischemic areas among the groups were not statistically significant, indicating that the LAD ligated sites were consistent in the model (**Figure 1H**). These demonstrated that A2aR activation before reperfusion contributed to ameliorate ventricular systolic function and lessen the area of myocardial infarction.

A2aR's Activation Inhibited Autophagy and Apoptosis Produced by MIRI and Diminished Myocardial Cell Death

To explore the change brought by ischemia-reperfusion injury (IR), we performed immunoblotting. The results manifested that IR could induce the high level of autophagy and apoptosis as the increased LC3II/I, P62, Beclin-1, and Bax, while the antiapoptotic protein Bcl-2 and lysosome membrane protein LAMP2 oppositely decreased (**Figures 2A,B**). Although A2aR showed an increasing trend in the IR group, that was not statistically significant compared with the Sham group. When A2aR was significantly enhanced with CGS21680, the expression of LC3II/I, P62, Beclin-1, and Bax was decreased, whereas Bcl-2 and LAMP2 increased. On the contrary, autophagy and apoptotic production in the antagonist ZM241385 group were significantly increased. Furthermore, consistent with the change level of A2aR, the expression of cAMP and p-PKA increased significantly after CGS21680 stimulation but decreased remarkably after ZM241385 stimulation.

Changes in myocardial tissue structure were investigated by HE staining. The myocardial fibers in Sham group were neatly arranged and compact (**Figure 1J**). In the IR group, however, the fibers were broken and wavy, accompanied by inflammatory cell infiltration and erythrocyte exudation. Cardiomyocytes swelling, myofibrillar fracture, and cell nuclei blur were exacerbated in the antagonist ZM241385 group. Inversely, the muscle fiber breakage was significantly decreased and the fiber texture was visible in the A2aR agonist group.

Transmission electron microscopy (TEM) was one of the most convincing methods to observe and evaluate autophagy flow. Myocardial fiber texture and Z-line were clearly visible in the Sham group (**Figure 2E**). Mitochondria with normal morphology and cristae structure were arranged between myocardial fibers. And a small amount of basic autophagy flow was observed under normal physiological conditions (red arrow indicated the autolysosome). In the IR group, mitochondria were swollen, vacuolar degeneration and the crest structure were damaged and blurred. The emergence of autophagosomes and autolysosomes increased, but the amount of autophagosomes was dominant (**Figure 2F**). There are more megamitochondria and vacuoles in the IR+ZM241385 group, accompanied by the rupture and dissolution of muscle fibers and intercalated disk (indicated by blue arrow). Consistent with the severity of tissue injury, more autophagosomes were produced and the autophagy flux was blocked in this group. In contrast, the autophagy flux was apparently restored with increased autophagy-lysosome fusion when A2aR was activated. Meanwhile, the myocardial damage was significantly improved, manifested by reduced vacuolar degeneration and disruption of mitochondrial cristae. These results suggested that A2aR plays a protective part in the myocardium by inhibiting autophagy and apoptosis.

The cAMP-PKA Signaling Pathway Was Participated in the Cardioprotection of A2aR

Western blot revealed the A2aR's downstream signal cAMP and PKA was changed under IR. Hence, the special agonist and antagonist of PKA were chosen to test the function of cAMP-PKA signal pathway in MIRI. The agonist IR+dbcAMP group effectively ameliorated IR-induced QTc prolongation at 30, 60 and 120 min of reperfusion. After using dbcAMP, the

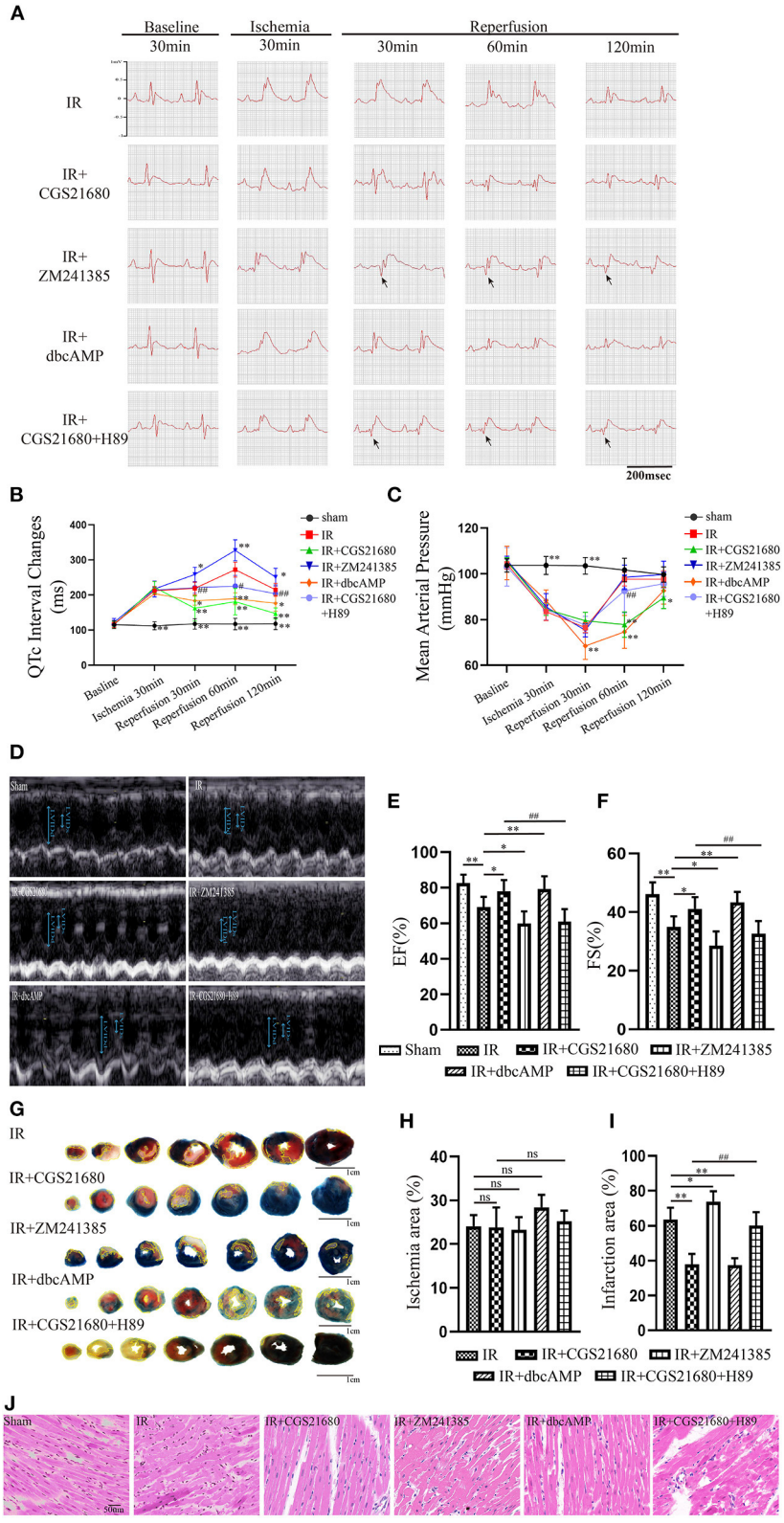

FIGURE 1 | A2aR's activation facilitated the recovery of ventricular systolic function after ischemia. **(A,B)** Real-time ECG and the QTc interval change in different time points. Arrows showed the pathological Q waves. **(C)** Hemodynamic parameters during the experiment. **(D)** Ultrasound M-mode images of the parasternal long axis showed left ventricular motions. The examination was performed on animals with the left lateral decubitus position. **(E,F)** LVEF, and LVFS were calculated by

(Continued)

FIGURE 1 | echocardiography. Data presented as mean ± SD and analyzed by one-way ANOVA with uncorrected Fisher's LSD *post hoc* test. **(G)** Evans blue-TTC staining of cardiac tissue. The infarct area was marked with yellow lines. **(H,I)** Analysis of the ischemic and infarct area of the ventricle. **(J)** HE staining of cardiac tissue. $^{**}P < 0.01$, $^{*}P < 0.05$, and ns means $P > 0.05$ vs. IR group. $^{\#\#}P<0.01$, $^{\#}P<0.05$ vs. IR+CGS21680 group. Unless otherwise noted, all data presented as mean ± SD and analyzed by one-way ANOVA with Bonferroni *post hoc* test ($n = 6$).

MAP in this group showed a significant downward trend. But it began to rise gradually after 30 min of reperfusion, and till the finish of reperfusion, there was no significant difference with the IR group (**Figures 1B**,**C**). Consistent with the ECG performance of the IR+ZM241385 group, the antagonist IR+CGS21680+H89 group also showed inverted Q waves, and the QTc interval was prolonged at 30 min of reperfusion. At 60 min of reperfusion, MAP in the antagonist IR+dbcAMP group was statistically higher than in its control IR+CGS21680 group, but not significantly different at other time points (**Figures 1A–C**). Echocardiography and tissue staining showed that downstream PKA activation with dbcAMP was equally effective in improving IR-induced impairment of EF and FS and reducing myocardial infarct size (**Figures 1D–I**). And HE staining showed a neat arrangement of myocardial fibers with clear nuclei and fewer breakage in this group (**Figure 1J**). However, the antagonist H89 counteracted the cardioprotective effects of CGS21680 during the reperfusion phase, manifested by decreased EF and FS, markedly swollen and ruptured myocardial fibers, and increased myocardial infarct size (**Figures 1D–J**).

Western blot analysis displayed that the addition of cAMP analog, dbcAMP, promoted the phosphorylation of PKA, the expression of LAMP2, and the level of anti-apoptotic protein Bcl-2. In contrast, the production of autophagy and apoptosis-related proteins, Beclin-1, P62, LC3II, and Bax, were significantly inhibited (**Figures 2C,D**). Moreover, using transmission electron microscopy (TEM) to observe autophagic flow found that, the use of dbcAMP promoted autophagosome-lysosome fusion, alleviated mitochondrial edema and cristae damage, and significantly reduced vacuolar degeneration (**Figures 2E,F**). These results suggested that the activation of A2aR's downstream cAMP-PKA had the same inhibitory effect on autophagy and apoptosis as activation of A2aR. When the downstream cAMP-PKA signaling pathway of A2aR was blocked by H89, however, the myocardial protective effect of A2aR was eliminated. Protein synthesis associated with autophagy initiation in the IR+CGS21680+H89 group, such as Beclin-1, P62, LC3II, was significantly increased, while lysosomes process autophagosomes-related LAMP2 was inhibited. The level of pro-apoptotic Bax was also enhanced, but the anti-apoptosis Bcl-2 was conversely decreased (**Figure 2E**). Furthermore, the blockage of autophagic flux caused the accumulation of autophagosomes under TEM (**Figure 2F**). And myocardial muscle fibers showed dissolution and vacuolar degeneration.

Overall, the animal experiment with MIRI manifested that A2aR activation can reduce cell death caused by autophagy and apoptosis, improve left ventricular systolic dysfunction, and diminish myocardial infarction. Moreover, this protective effect of A2aR was related to the cAMP-PKA signaling pathway.

Purification of Cardiomyocytes *in vitro*

To verify whether A2aR had the same effect *in vitro* models, we extracted primary myocardial cells. In cell extraction, the final cell suspension contained vascular endothelial cells, smooth muscle cells, and ventricular muscle cells. Given the non-dividing and proliferative characteristics of cardiomyocytes, we improved their purification rate by the centrifugal selection, differential paces of sticking to the wall, and BrdU drug inhibition. After 24 h of incubation, we observed the rhythmic beating of cardiomyocytes under a microscope. And cardiomyocytes were labeled with a specific antibody of cardiac troponin I (cTnI). Under confocal microscopy (600× and 1200×), the sarcomere of cells appeared as the striations of light and dark (**Figure 3**). Eventually, the purification rate of cardiomyocytes reached 97.8%. Therefore, in the following experiments, the interference of non-muscular cells was no longer considered.

Increased Autophagy Caused Cardiomyocyte Death Under OGDR

An OGDR model *in vitro* was used to simulate ischemia-reperfusion injury *in vivo*. Compared with the control, the cell survival rate was deteriorating rather noticeably in the OGDR group (**Figure 4A**). The level of LDH, CK-MB, and cTnI releasing from dead and damaged cells prominently increased (**Figures 4B–D**). Then western blot showed that OGDR triggered autophagy and apoptosis in cardiomyocytes, as evidenced by a remarkable increase in the level of LC3II/I, P62, and Bax (**Figures 4E,F**). To clarify the relationship between autophagy and apoptosis, we used an autophagy antagonist and agonist before reoxygenation. Rapamycin (100 nM) stimulated the increase of LC3II and the depletion of its substrate P62. Although the anti-apoptotic protein Bcl-2 increased in response to rapamycin, the cell survival rate still declined. And the release of CK-MB, cTnI, and LDH was further increase. In contrast, cell death was improved until autophagy was suppressed by 3-MA (10 mM). And the apoptosis also recovered with the reduction of autophagy. These suggested that over-activated autophagy during reperfusion had an anti-apoptotic effect and was harmful to cell survival.

The Protection of A2aR in Attenuating OGDR-Induced Cell Death Depended on Restraint to Apoptosis and Autophagy

To investigate the role of A2aR in OGDR damage, CGS21680 was used to activate A2aR 1 h before reoxygenation. In the agonist group, cell survival visibly improved (**Figure 5A**), and fewer cytoplasmic components, such as LDH, CK-MB, and cTnI released into the culture medium (**Figures 5B–D**). And CGS21680 inhibited the level of Bax and the conversion of

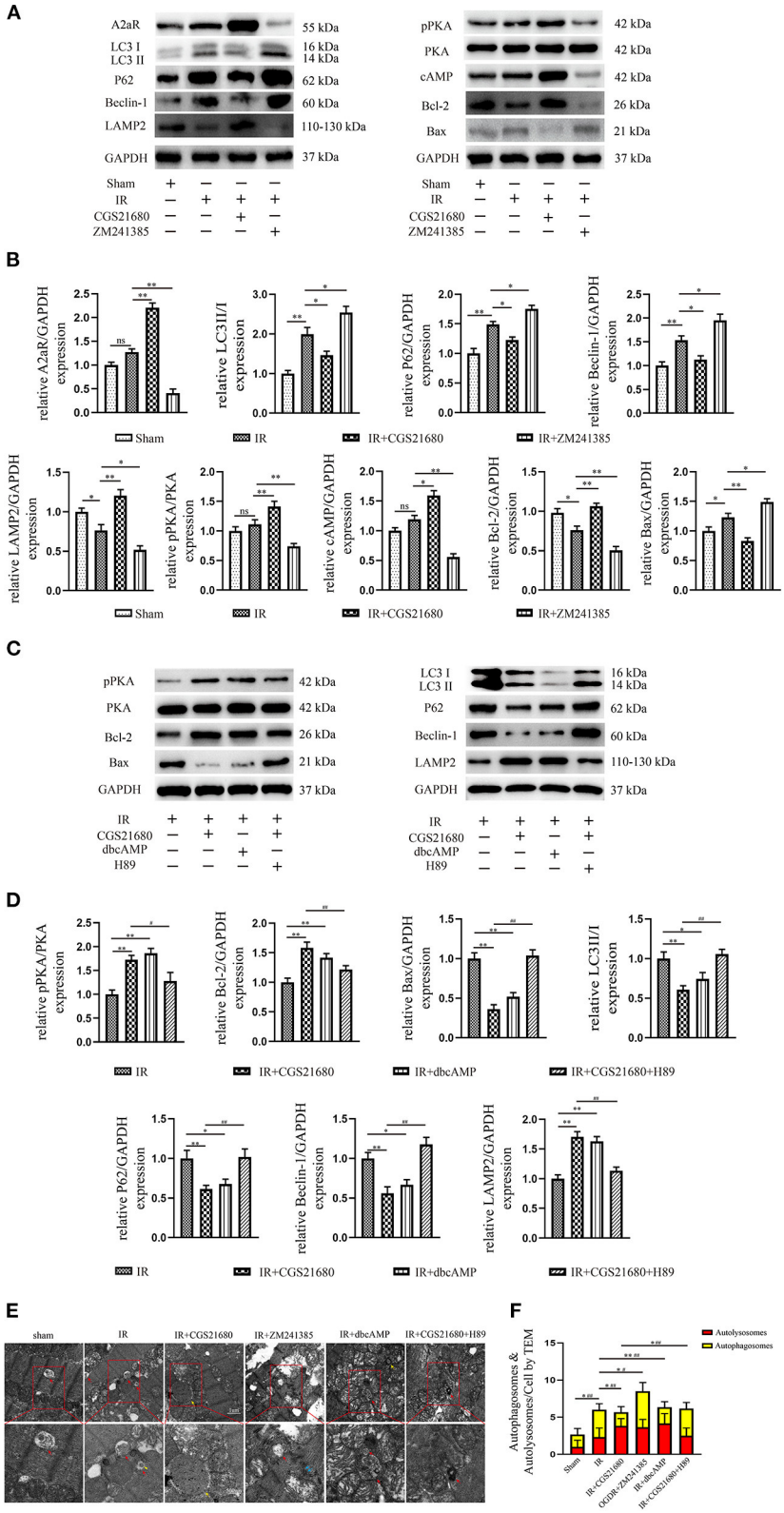

FIGURE 2 | A2aR's activation inhibited autophagy and apoptosis caused by MIRI. **(A,C)** Representative immunoblotting results of autophagy and apoptosis-related protein. **(B,D)** All data of western blot were presented as mean ± SEM and analyzed by one-way ANOVA with Bonferroni *post hoc* test. $^{*}P < 0.05$, $^{**}P < 0.01$, and ns means $P > 0.05$ vs. IR group and $^{\#}P < 0.05$, $^{\#\#}P < 0.01$ vs. IR+CGS21680 group. **(E,F)** The morphological changes of rat hearts were observed under the

(Continued)

FIGURE 2 | transmission electron microscope. $^{\#}P < 0.05$, $^{\#\#}P < 0.01$ represented the statistical significance between two groups in autophagosomes' number. $^{*}P < 0.05$, $^{**}P < 0.01$ represented the difference between two groups in autolysosomes. All data presented as mean ± SD and analyzed by one-way ANOVA with Bonferroni *post hoc* test; $n = 6$.

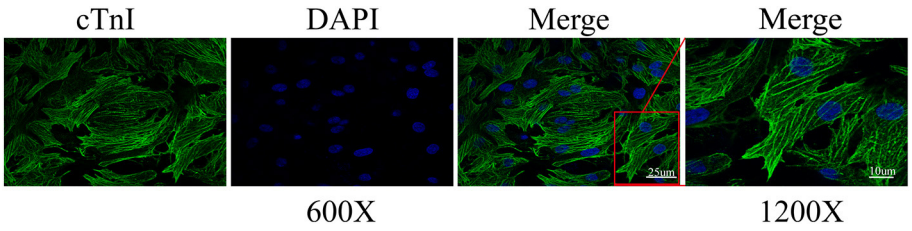

FIGURE 3 | Cardiomyocyte identification by cardiac troponin I (cTnI). The representative immunofluorescence images were captured by confocal microscopy at 600 and 1200× magnification. Calculation by image J, the ratio of the number of cardiomyocytes to total cells of three different sights was 97.8%.

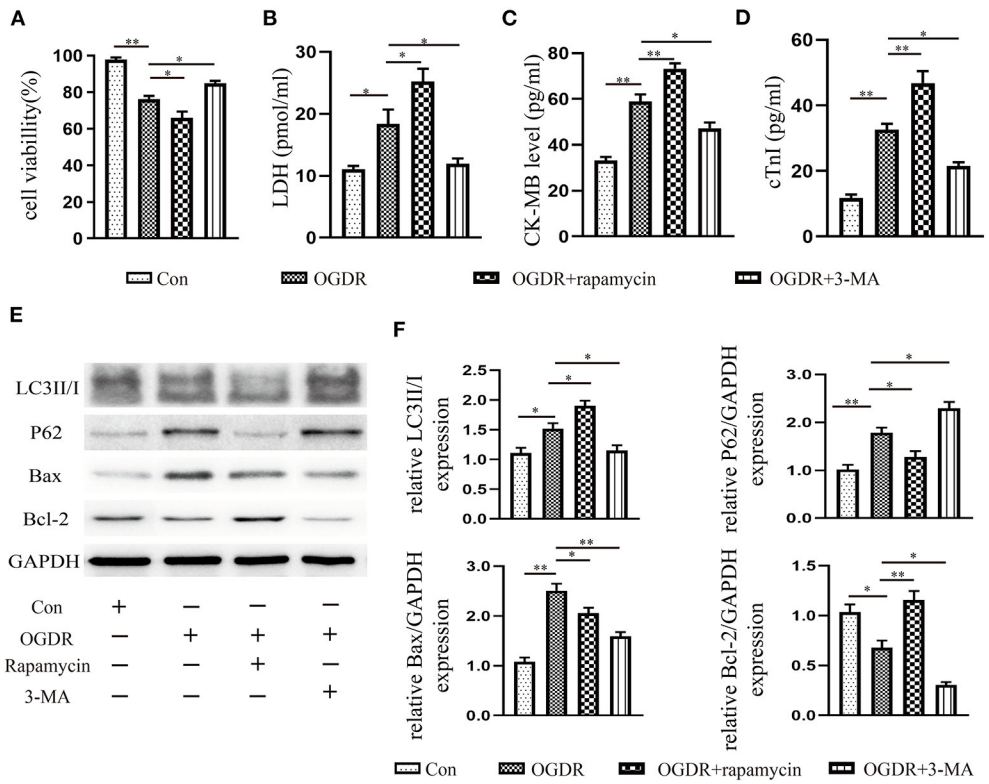

FIGURE 4 | Increased autophagy caused cardiomyocyte death under OGDR. **(A)** Cell viability was assessed by the CCK-8 reagent. **(B–D)** LDH, CK-MB, and cTnI released from cardiomyocytes were detected by the Elisa kit. **(E,F)** Representative western blot results, and image J analysis results of LC3II/I, P62, Bax, and Bcl-2. All data presented as mean ± SEM and analyzed by one-way ANOVA with Dunnett's *post hoc* test; $n = 3$. $^{**}P < 0.01$, $^{*}P < 0.05$ vs. OGDR group.

LC3I to LC3II (**Figures 5E,H,J**). The reduced substrate protein P62 of the autophagosome also confirmed the reduction of autophagy production (**Figures 5E,I**). Besides, A2aR activation increased Bcl-2 expression, decreased the level of Beclin-1, and further promoted the expression of LAMP2 (**Figures 5F,K–M**). To verify that, we knocked down A2aR expression with adenovirus of siRNA-A2aR (**Figures 5E,G**). In the OGDR+si-A2aR group, however, the level of LDH, CK-MB, and cTnI was respectively increased 1.65 times, 2.16 times, and 1.84 times compared with the si-Control group. And accompanied by those increased indexes, the cell viability decreased significantly (**Figures 5A–D**). Gene knockdown of A2aR can increase the expression of Bax, LC3II and Beclin-1 while inhibiting the production of LAMP2. A decline in the expression level of the lysosome membrane protein, LAMP2, represented impaired autophagosome processing. These proved that activation of A2aR can inhibit apoptosis and autophagy, thus saving cardiomyocytes for survival.

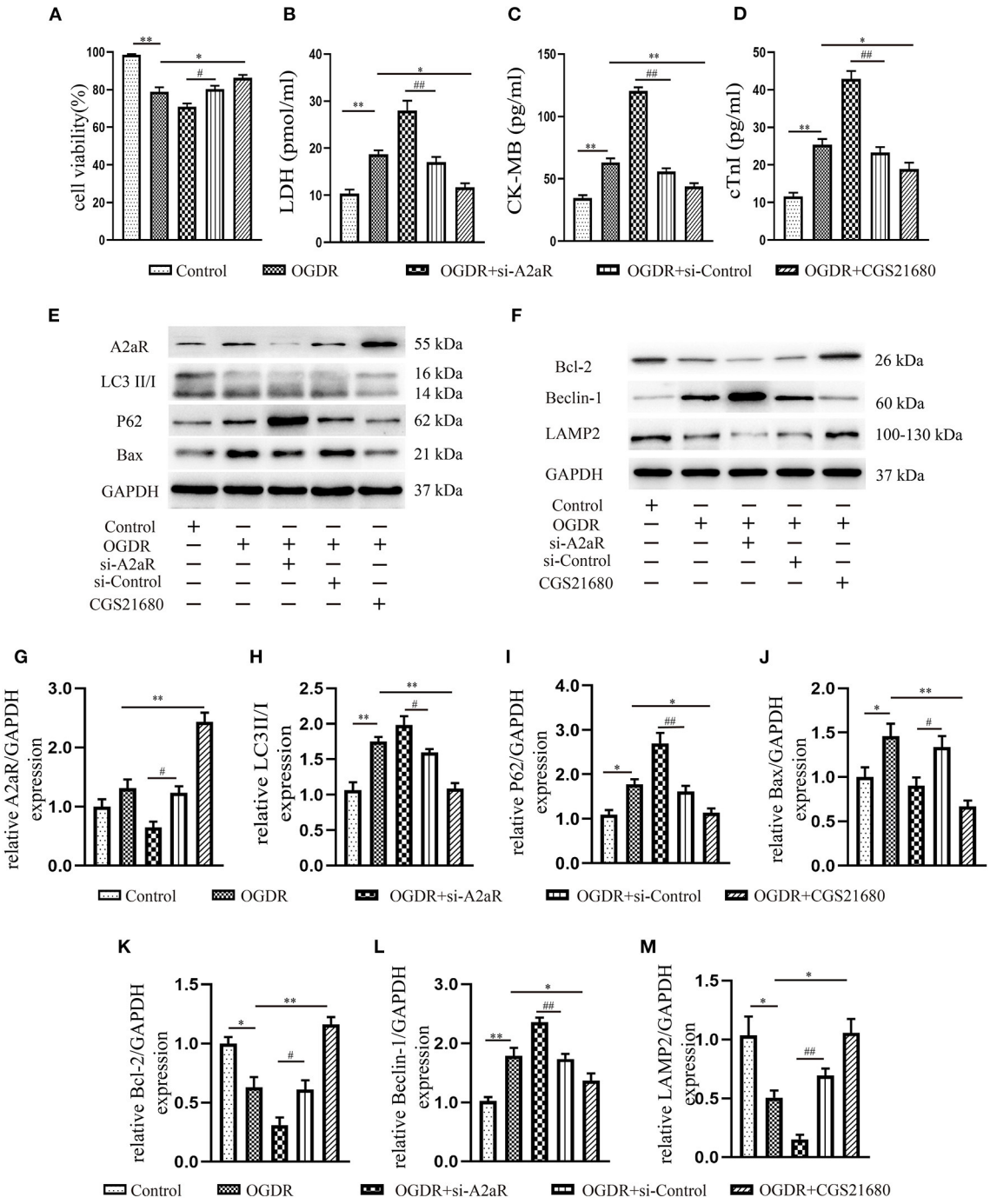

FIGURE 5 | The protection of A2aR in attenuating OGDR-induced cell death depended on inhibition of apoptosis and autophagy. **(A)** Cell viability was detected by CCK-8. **(B–D)** LDH, CK-MB and cTnI in the medium were measured by Elisa kit. **(E–M)** The content of related proteins was evaluated by western blot and then analyzed by image J. $^{*}P<0.05$, $^{**}P < 0.01$ vs. OGDR group and $^{\#}P < 0.05$, $^{\#\#}P < 0.01$ vs. OGDR+si-Control group. All data presented as mean ± SEM and analyzed by one-way ANOVA with Dunnett's *post hoc* test; $n = 3$.

A2aR′s Cardioprotective Effect Was Modulated via the CAMP-PKA Signaling Pathway

Consistent with the results of animal experiment, A2aR and its downstream cAMP and p-PKA showed an increasing trend under OGDR, but there was no statistical significance. When given an additional agonist, the increase of the A2aR level could raise the level of intracellular cAMP and promote the phosphorylation of PKA. si-A2aR, however, diminished intracellular cAMP and p-PKA expression

(**Figures 6A–C**). A selective PKA activator, dbcAMP, was used to test the effect of cAMP-PKA in A2aR-induced protection. It showed dbcAMP did the same as A2aR in the restraint of autophagy generation and anti-apoptosis effect (**Figures 6D–L**). Reversely, the PKA selective inhibitor, H89, can significantly eliminate the myocardial protection of A2aR. Thus, these results concluded that the cAMP-PKA signaling pathway participated in the cytoprotective action of A2aR.

The Protective Effect of A2aR Relied on the Inhibition of Autophagosome Generation

The mCherry-GFP-LC3II adenovirus was transfected NRCMs to study the changes of autophagy flux. Compared with the control group, yellow autophagosomes in the OGDR group were significantly increased and were dominant in terms of number. Red autolysosomes in the OGDR group had an increasing trend, but there was no statistically significant compared with the control group (**Figures 7A,C**). After A2aR or its downstream PKA activation, the formation of autophagosomes was inhibited, and autophagy flux recovered. Thus, autolysosomes were significantly dominant in counting. In contrast, when siA2aR or PKA antagonist H89 was used, the autophagic flow was further impaired, and the autophagosomes accumulated in cells and were difficult to degrade.

The autophagy flux of NRCMs was also observed by TEM (**Figures 7B,D**). In the control group, filamentous myocardial muscle fibers can be observed (as shown by green triangle, **Figure 7B**). There were plenty of normal mitochondria with clear crest structure around the nucleus (blue arrow). And a small amount of autophagic flux (yellow arrow represented autophagosome, red arrow represented autolysosome) was observed under normal physiological conditions. In the OGDR group, the number of autophagy and autolysosome was both increased in puff cytoplasm (42). Autophagosome was a double-membraned vesicle (yellow arrow), and autolysosome was single-membraned vesicle (red arrow) containing ruined organelles, cellular debris, and membrane-like structures (43, 44). The yellow triangle represented the autophagosome surrounded by autolysosome. In addition, OGDR damaged the mitochondrial crest structure, which was fractured and blurry (blue arrow). In si-A2aR group, cells were showing perinuclear cytoplasmic vacuolation and mitochondrial blebbing compared to its si-control group. And the number of its autophagosomes correspondingly increased. Interestingly, the activation of A2aR or its downstream PKA recovered the autophagic flux after OGDR by promoting autophagosome conversion to autolysosome (**Figure 7D**). Cell damage caused by OGDR in those two groups was also reduced, as evidenced by decreased mitochondrial vacuolation and clear crest structure. Notably, megamitochondria with fractured crest structure appeared in the OGDR+CGS21680+H89 group, and autophagy flow was also impaired. These results from the perspective of confocal immunofluorescence and TEM were consistent with the western blot ones.

DISCUSSION

CHD remains the leading mortality among diseases around the world, whose root cause is the death and loss of non-proliferative myocardial cells. And most cell death occurs during ischemia-reperfusion (45). Cell death involved in MIRI manifests in various forms, specifically apoptosis, autophagy, pyroptosis, and ferroptosis (46). Morphologically, pyroptosis has the manifestations as apoptosis (DNA fragmentation, nuclear condensation) and necrosis (cellular swelling, formation of pores in the cytomembrane, and rupture of cells). Mechanistically, pyroptosis is characterized by its dependence on inflammatory caspases (mainly caspase-1, 4, 5, and 11) and along with the release of pro-inflammatory factors (45, 47). Studies have shown that cardiomyocytes under IR showed classic morphological features of pyroptosis: cell swelling, formation of bubble-like protrusions, formation of pores in the cytoplasmic membrane by gasdermin D (GSDMD), rupture of the cell membrane, and the release of inflammatory factors IL-1β and IL-18 (48). There is a positive correlation between pyroptosis and MIRI severity by existing research. Conversely, inhibiting the production of NLRP3 inflammasome or GSDMD induced pyroptosis can reduce MIRI and myocardial infarction size (49, 50).

Ferroptosis, a new type of iron-dependent regulatory cell death, is distinguished from apoptosis, necrosis, pyroptosis, and autophagy in morphology. The distinct feature of ferroptosis is principally represented as mitochondrial variation, covering mitochondrial shrinkage, membrane densification, and cristae damage. Whereas, the morphology of cell nucleus is generally normal (51). Multiple signal pathways and metabolic reactions are involved in the occurrence of ferroptosis, which is a complex mechanism. The primary mechanism of ferroptosis is considered as the system x_c^-/GSH/GPX4 pathway of amino acid metabolism. Furthermore, iron metabolism and lipid metabolism are also the essential formation condition for ferroptosis (52). Ferroptosis has been confirmed to be involved in MIRI and has become a new therapeutic target of MIRI in recent years (53). Inhibiting transferrin function, reducing intracellular Fe^{2+} deposition, and anti-lipid peroxidation are all effective means to reduce ferroptosis and improve MIRI (54–57).

The patterns of cell death in MIRI are diverse and complicated, and each of the programmed cell death is interrelated and interactive to others. This study focused on exploring the mechanism of action of autophagy and apoptosis in MIRI.

Autophagy is an intracellular catabolism process that is a beneficial process of energy recovery and reuse. For non-dividing cells such as myocardium, autophagy activation, which can provide amino acids, fatty acids, ATP, or other energy substrates, is especially essential for cell survival and normal tissue function during ischemia or nutrient deficiency. And, autophagy is a considerable regulator to maintain the stable structure and stable functionality of the heart. Under the stimulation of stress, protein aggregates increase and accumulate in the cytoplasm, which is usually malignant for cell survival. P62 identifies those aggregates and recruits LC3II (58, 59), forming autophagosomes with the phagophore. Then, autophagosomes and lysosomes fuse to form

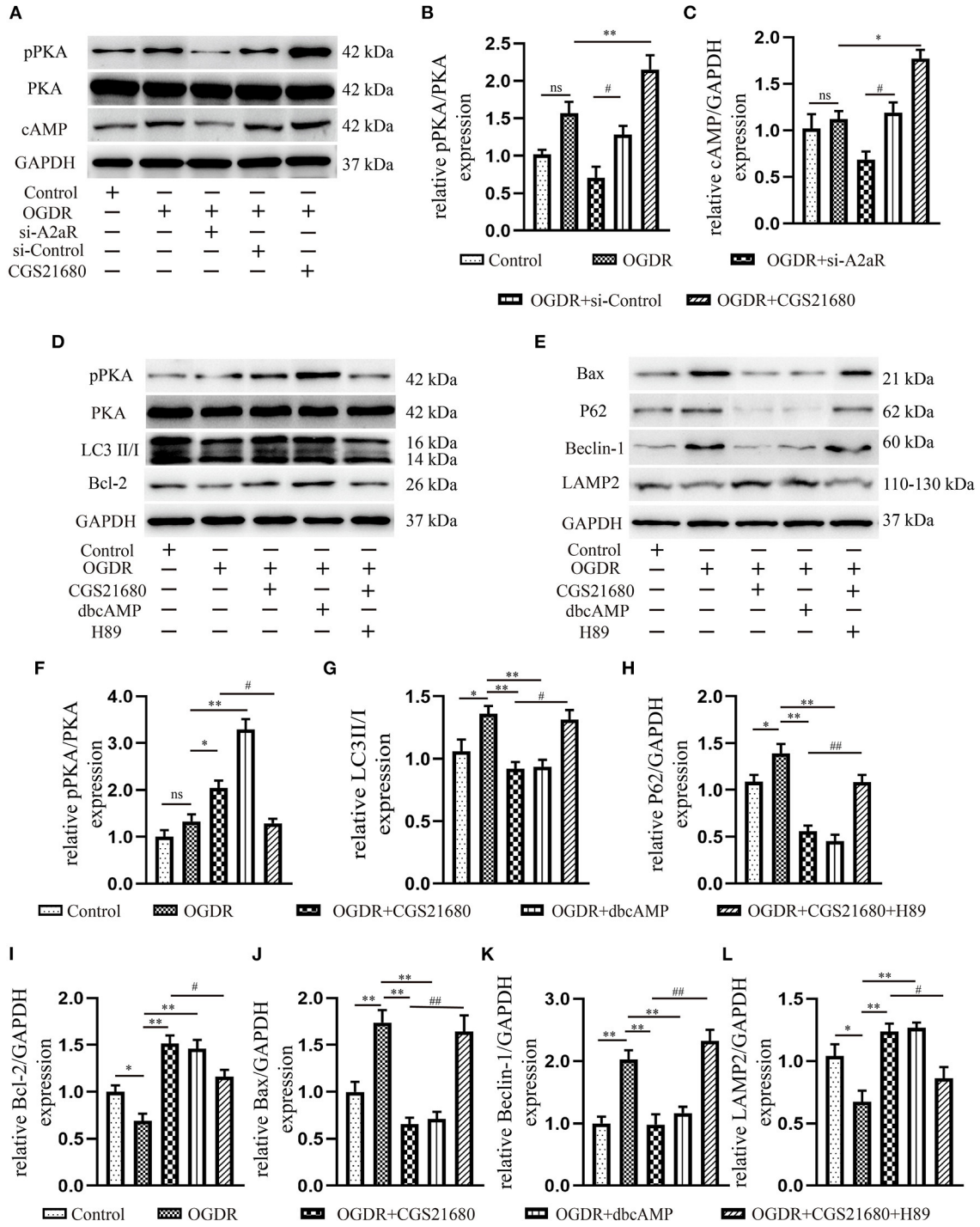

FIGURE 6 | A2aR's cardioprotection was mediated via the cAMP-PKA signaling pathway. **(A–C)** Quantitative analysis of the corresponding protein. $^{*}P < 0.05$, $^{**}P<0.01$ vs. OGDR group and $^{\#}P < 0.05$, $^{\#\#}P < 0.01$ vs. OGDR+si-Control group. **(D–L)** Expression of respective target protein and the quantitative analysis by image J. $^{*}P < 0.05$, $^{**}P < 0.01$ vs. OGDR group and $^{\#}P < 0.05$, $^{\#\#}P < 0.01$ vs. OGDR+CGS21680 group. All data presented as mean ± SEM and analyzed by one-way ANOVA with Bonferroni *post hoc* test; $n = 3$.

autolysosomes with the help of a crucial factor, LAMP2 (60, 61). And autolysosomes break down damaged organelles and harmful proteins, making cells survive.

However, this stress-induced autophagy appears to be beneficial only when activated at the right time and to the appropriate level. Our study found that the OGDR-induced

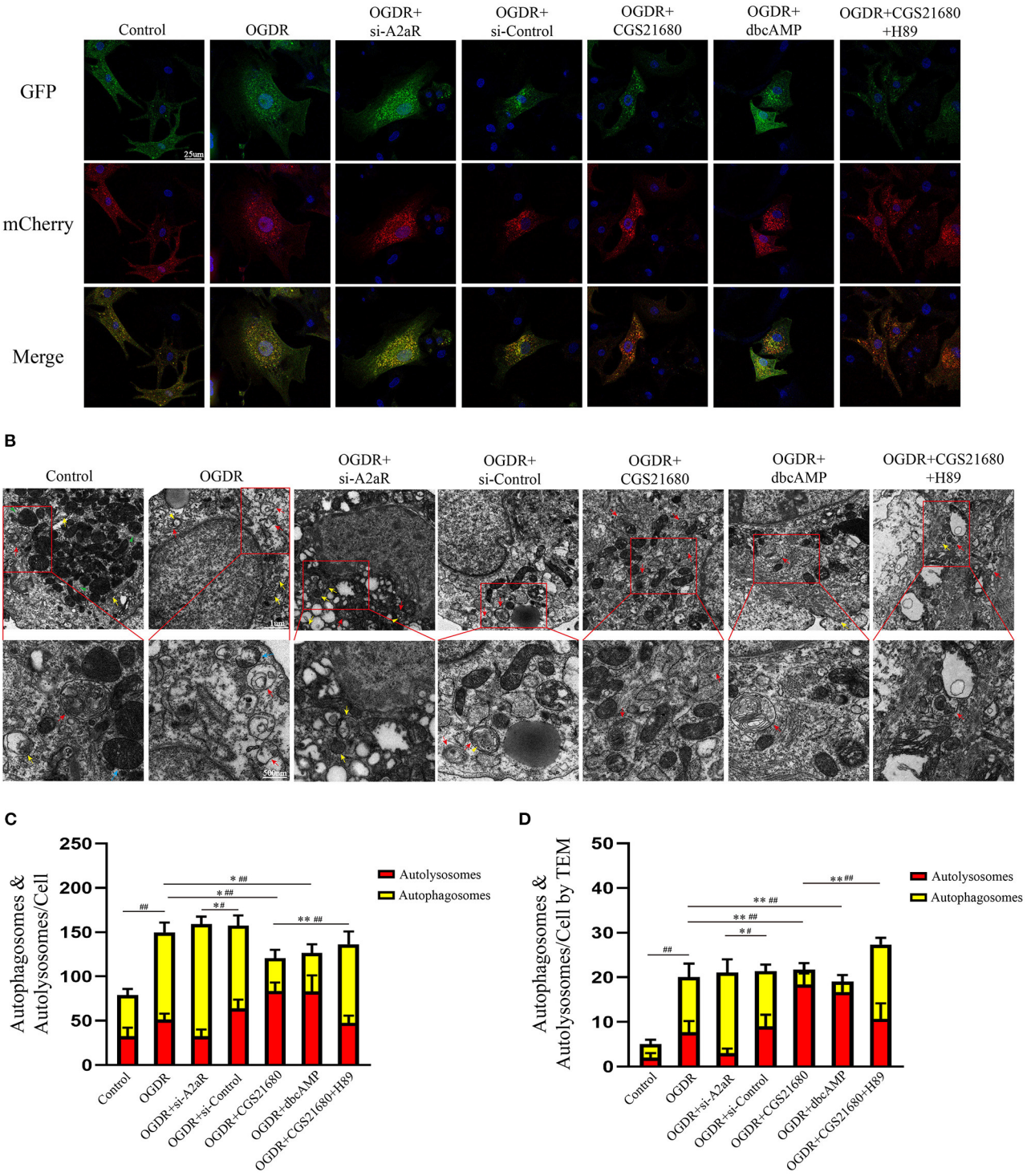

FIGURE 7 | The protective effect of A2aR relied on the inhibition of autophagosome generation. **(A,C)** Autophagy flux detected by Ad-mCherry-GFP-LC3B. Representative graphs (630×) of each group under a confocal microscope and quantitative analysis of red and yellow spots in multiple fields. **(B,D)** Transmission electron micrographs of autophagosomes (indicated by yellow arrows and triangles) and autolysosomes (indicated by red arrows). Blue arrows indicate myocardial fibers, and green arrows indicate mitochondria. $^{\#}P < 0.05$, $^{\#\#}P < 0.01$ represented the statistical significance between two groups in autophagosomes' number. $^{*}P < 0.05$, $^{**}P < 0.01$ represented the difference between two groups in autolysosomes. All data presented as mean ± SD and analyzed by one-way ANOVA with Bonferroni *post hoc* test; $n = 3$.

autophagy resulted in cardiomyocytes' damage and decreased survival rate characterized as the release of LDH, CK-MB, and cTnI. We observed that OGDR caused the cumulation of numerous autophagosomes in cells, while the increase of autolysosomes was not significant through the fluorescent tags of LC3II and TEM. These were because autophagy during reperfusion stimulated by the Beclin-1-dependent mechanism (23) and the rise of Beclin-1 in OGDR suppressed the expression of LAMP2, which caused impaired production of autolysosomes and accumulated autophagosomes. Moreover, the overactive autophagy with rapamycin aggravated cell death, and it also played an anti-apoptosis role. When autophagy was inhibited, however, the cells exhibited apoptosis of Bax depletion. It was consistent with the views (23, 62) that excessive autophagy during the reperfusion was detrimental. Also, it indicated a contradictory relationship between autophagy and apoptosis under the OGDR condition.

Autophagy and apoptosis are two different adaptive responses of cells under stress. The relationship between autophagy and apoptosis is intricate and variable, which ultimately determines cell fate. Some protein interactions bridge the link between autophagy and apoptosis. It has been confirmed that the anti-apoptotic protein Bcl-2/Bcl-X(L) can inhibit autophagy by binding to the Bcl-2 homology-3 (BH3) receptor domain of Beclin-1 (63). The Beclin-1-Bcl-2/Bcl-X(L) complex is critical to MIRI, for its vital role in transforming autophagy and apoptosis in the cell (24). Our results suggested that post-treatment with activation of A2aR may alleviate MIRI through promoting anti-apoptotic Bcl-2 production,inhibiting Beclin-1 expression, and reducing autophagosome formation. It enabled cell survival, promoted the recovery of cardiac contractility, and reduced the area of infarction. Inversely, after knocking down A2aR, cumulate autophagosomes exasperated cell death and myocardial infarction injury. The results differ from previous studies (7), possibly because the duration of the agonist's action varies. However, it is worth noting that continuous pump injection of CGS21680 and the use of dbcAMP may cause a significant drop in blood pressure levels. This hypotension side effect was associated with bradycardia and vasodilation caused by massive activation of A2aR and cAMP (4). Conversely, despite more severe myocardial damage, the compensatory effect of the fast heart rate kept blood pressure stable in the A2aR and PKA antagonist group.

In the classical signal cascade reaction, adenosine or its analogs can activate AC after activating A2aR, causing an increase of cAMP and PKA. The cAMP-PKA pathway has a protective effect on IRI in multiple organs, for instance, the brain (64), intestine (65), liver (66), kidney (67), and heart (7). For MIRI, the participation of cAMP and PKA in OGDR may explain the down-regulation of autophagy. It involves two aspects, one of which is the direct regulation of autophagy by cAMP-PKA. Increased PKA activity will restrict harmful autophagy, whereas the deactivation of PKA will induce a strong autophagy response (68), as evidenced by our use of its activators and inhibitors. The reason is that the Atg1/Atg13 complex, the key to signal integration in the autophagy pathway, is the direct substrate of PKA (69). And cAMP-dependent PKA can regulate Atg1 phosphorylation, thereby regulated the early autophagosome formation (70) and inhibiting the occurrence of autophagy (71). Also, PKA can inhibit autophagy by phosphorylating the Ser12 site of LC3 (58). And the other aspect could be the involvement of Beclin-1-Bcl-2 related mechanisms. The study of Wang et al. (72) showed that the level of Beclin-1 expression determines the detrimental or beneficial action of autophagy activity. Our results indicate that activations of both A2aR and PKA could inhibit the high levels of Beclin-1 and reduce the harm caused by autophagy during MIRI. The A2aR/cAMP-PKA signal pathway and its regulated Bcl-2 were involved in the negative regulation of Beclin-1 in MIRI. Under other experimental conditions or parameters, this may need to discuss separately. For example, cAMP activates autophagy through an original pathway related to Beclin-1 in mesenchymal stem cells (73).

In vivo experiments shown that the area of myocardial infarction decreased and ventricular systolic dysfunction improved after A2aR activation. The contractile function of the left ventricle after myocardial infarction was closely relevant to the infarct size (74). Through cardiac ultrasound, we found that the activation of upstream A2aR and its downstream cAMP-PKA can enhance positive inotropic action. MIRI impaired the LVEF and LVFS, but A2aR activation effectively improved these two indicators of ventricular systolic function. In contrast, left ventricular systolic dysfunction was further deteriorative after using A2aR antagonist. Another study (75) mentioned that A2aR activation could improve myocardial systolic function far from the infarct area, but due to limited experimental equipment, we did not cover this index. The recovery of ventricular systolic function after MIRI depended on the elevation of cAMP and PKA induced by A2aR. The increased intracellular cAMP and PKA can trigger multiple cAMP-PKA-dependent ion channels, which heighten the maximum peak transient outward current and improve ventricular repolarization after ischemia (37, 38, 76). The research of Liang (77) considered that the positive inotropic effect of A2aR attributes to the activation of cAMP-dependent L-type calcium channels, which take a crucial place on CGS21680-induced increase of calcium influx. Kerfant et al. (78)found that regulation of cAMP can induce Ca^{2+} transients and absorb Ca^{2+} through SERCA2 (sarcoplasmic/endoplasmic reticulum Ca2+-ATPase 2) into the SER, thus enhancing the contractility of the myocardium. In conclusion, the cAMP-mediated Ca^{2+} influx contributes to the recovery of myocardial contractility.

Furthermore, MIRI caused ST-segment elevation and prolonged QT interval in Electrocardiogram. The interruption of blood flow and oxygen supply in ischemia and the changes in tissue perfusion during the reperfusion led to an imbalance in the inflow and outflow of intracellular and extracellular Ca^{2+}, K^{+}, H^{+}, and Na^{+}, resulting in changes in repolarization current (77, 79). This change of cell current in the IRI region prolonged the duration of the action potential, resulting in the prolonged QT and ST-segment elevation. Recent studies (62, 80) illustrated that AR activation during ischemic postprocessing had an antiarrhythmic effect, which was associated with action potential

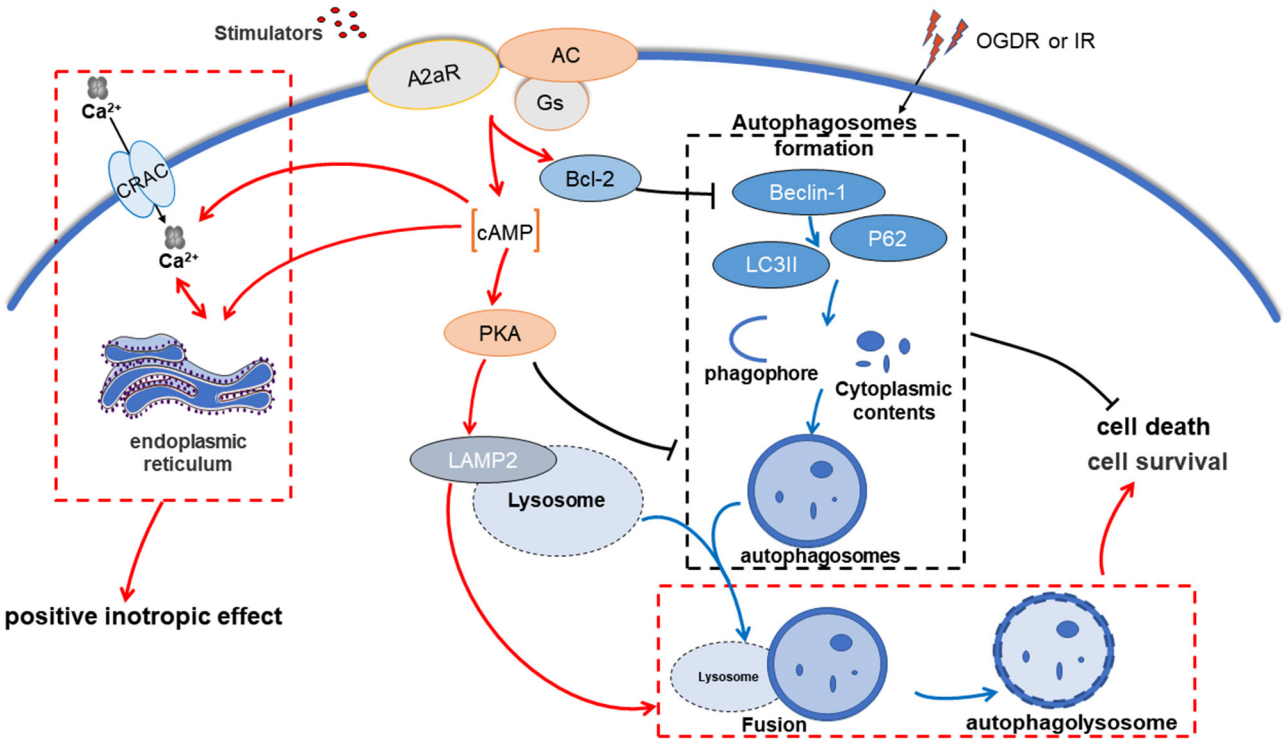

FIGURE 8 | A2aR regulates autophagy and apoptosis to alleviate myocardial ischemia-reperfusion injury via cAMP-PKA. OGDR or IR damage induces intracellular accumulation of autophagosomes, which exacerbates cell death. In contrast, A2aR activation inhibits the generation of autophagosomes and promotes its cleaning process, allowing cells to survive.

shortening. We also observed an improvement in QT interval prolongation following activation of A2aR with CGS21680. The cellular mechanisms of A2aR-mediated global ventricular repolarization and QT interval changes may refer to an augment in outward K^+ current (37, 76, 81).

In summary, A2aR activation before reperfusion can effectively inhibit apoptosis, reduce the formation of autophagosomes, and restore the impaired autophagy flux, thereby weakening ventricular dysfunction, improving QT interval prolongation, and reducing MIRI damage. This protective effect achieves by activating the cAMP-PKA pathway and Beclin-1-Bcl-2 complex related mechanisms (**Figure 8**).

DATA AVAILABILITY STATEMENT

The original contributions presented in the study are included in the article/**Supplementary Material**, further inquiries can be directed to the corresponding author/s.

ETHICS STATEMENT

The animal study was reviewed and approved by the Animal Experiment Committee of Wuhan University (China, Approval No. WP2020–01108).

AUTHOR CONTRIBUTIONS

YXia, YXio, JZ, and HL: designed the study. YXia, MM, HZ, and JL: conducted experiments, collected, and analyzed data. YXia: wrote the manuscript. JK and YW: revised the manuscript. FH: supplemented the experiments. All authors read and final approval of manuscript.

FUNDING

This work was supported by the National Natural Science Foundation of China (81871553).

ACKNOWLEDGMENTS

All authors genuinely appreciate Chengjun Hu and Yihao Tian (Department of Human Anatomy, School of Basic Medical Sciences, Wuhan University) for the guidance and help to the experimental technology.

SUPPLEMENTARY MATERIAL

The Supplementary Material for this article can be found online at: https://www.frontiersin.org/articles/10.3389/fcvm.2022.755619/full#supplementary-material

REFERENCES

1. Piccolo R, Giustino G, Mehran R, Windecker S. Stable coronary artery disease: revascularisation and invasive strategies. *Lancet.* (2015) 386:702–13. doi: 10.1016/S0140-6736(15)61220-X
2. Virani SS, Alonso A, Benjamin EJ, Bittencourt MS, Callaway CW, Carson AP, et al. Heart disease and stroke statistics-2020 update: a report from the american heart association. *Circulation.* (2020) 141:e139–596. doi: 10.1161/CIR.0000000000000746
3. Mubagwa K, Flameng W. Adenosine, adenosine receptors and myocardial protection: an updated overview. *Cardiovasc Res.* (2001) 52:25–39. doi: 10.1016/S0008-6363(01)00358-3
4. Zhang Y, Wernly B, Cao X, Mustafa SJ, Tang Y, Zhou Z. Adenosine and adenosine receptor-mediated action in coronary microcirculation. *Basic Res Cardiol.* (2021) 116:22. doi: 10.1007/s00395-021-00859-7
5. Gaudry M, Vairo D, Marlinge M, Gaubert M, Guiol C, Mottola G, et al. Adenosine and its receptors: an expected tool for the diagnosis and treatment of coronary artery and ischemic heart diseases. *Int J Mol Sci.* (2020) 21:5321. doi: 10.3390/ijms21155321
6. Mehaffey JH, Money D, Charles EJ, Schubert S, Piñeros AF, Wu D, et al. Adenosine 2A receptor activation attenuates ischemia reperfusion injury during extracorporeal cardiopulmonary resuscitation. *Ann Surg.* (2019) 269:1176–83. doi: 10.1097/SLA.0000000000002685
7. Ke JJ, Yao B, Li T, Cui SS, Ding H. A2 adenosine receptor-mediated cardioprotection against reperfusion injury in rat hearts is associated with autophagy downregulation. *J Cardiovasc Pharmacol.* (2015) 66:25–34. doi: 10.1097/FJC.0000000000000239
8. Ashton KJ, Reichelt ME, Mustafa SJ, Teng B, Ledent C, Delbridge LM, et al. Transcriptomic effects of adenosine 2A receptor deletion in healthy and endotoxemic murine myocardium. *Purinergic Signal.* (2017) 13:27–49. doi: 10.1007/s11302-016-9536-1
9. Boknik P, Eskandar J, Hofmann B, Zimmermann N, Neumann J, Gergs U. Role of cardiac A2A receptors under normal and pathophysiological conditions. *Front Pharmacol.* (2021) 11:627838. doi: 10.3389/fphar.2020.627838
10. Borg N, Alter C, Görldt N, Jacoby C, Ding Z, Steckel B, et al. CD73 on T cells orchestrates cardiac wound healing after myocardial infarction by purinergic metabolic reprogramming. *Circulation.* (2017) 136:297–313. doi: 10.1161/CIRCULATIONAHA.116.023365
11. Yang Z, Day YJ, Toufektsian MC, Xu Y, Ramos SI, Marshall MA, et al. Myocardial infarct-sparing effect of adenosine A2A receptor activation is due to its action on CD4+ T lymphocytes. *Circulation.* (2006) 114:2056–64. doi: 10.1161/CIRCULATIONAHA.106.649244
12. Rork TH, Wallace KL, Kennedy DP, Marshall MA, Lankford AR, Linden J. Adenosine A2A receptor activation reduces infarct size in the isolated, perfused mouse heart by inhibiting resident cardiac mast cell degranulation. *Am J Physiol Heart Circ Physiol.* (2008) 295:H1825–33. doi: 10.1152/ajpheart.495.2008
13. Zhao ZQ, Budde JM, Morris C, Wang NP, Velez DA, Muraki S, et al. Adenosine attenuates reperfusion-induced apoptotic cell death by modulating expression of Bcl-2 and bax proteins. *J Mol Cell Cardiol.* (2001) 33:57–68. 10.1006/jmcc.2000.1275. doi: 10.1006/jmcc.2000.1275
14. Sciaraffia E, Riccomi A, Lindstedt R, Gesa V. Cirelli Elisa, Patrizio Mario, et al. Human monocytes respond to extracellular cAMP through A2A and A2B adenosine receptors. *J Leukoc Biol.* (2014) 96:113–22. doi: 10.1189/jlb.3A0513-302RR
15. Batty NJ, Fenrich KK, Fouad K. The role of cAMP and its downstream targets in neurite growth in the adult nervous system. *Neurosci Lett.* (2017) 652:56–63. doi: 10.1016/j.neulet.2016.12.033
16. Delaunay M, Osman H, Kaiser S, Diviani D. The role of cyclic AMP signaling in cardiac fibrosis. *Cells.* (2019) 9:69. doi: 10.3390/cells9010069
17. Chung YW, Lagranha C, Chen Y, Sun JH, Tong G, Hockman SC, et al. Targeted disruption of PDE3B, but not PDE3A, protects murine heart from ischemia/reperfusion injury. *Proc Natl Acad Sci U S A.* (2015) 112:E2253–62. doi: 10.1073/pnas.1416230112
18. Choi AMK, Ryter SW, Levine B. Autophagy in human health and disease. *N Engl J Med.* (2013) 368:651–62. doi: 10.1056/NEJMra1205406
19. Kroemer G. Autophagy: a druggable process that is deregulated in aging and human disease. *J Clin Invest.* (2015) 125:1–4. doi: 10.1172/JCI78652
20. Al-Bari MAA, Xu P. Molecular regulation of autophagy machinery by mTOR-dependent and -independent pathways. *Ann N Y Acad Sci.* (2020) 1467:3–20. doi: 10.1111/nyas.14305
21. Levine B, Kroemer G. Biological functions of autophagy genes: a disease perspective. *Cell.* (2019) 176:11–42. doi: 10.1016/j.cell.2018.09.048
22. Ma S, Wang Y, Chen Y, et al. The role of the autophagy in myocardial ischemia/reperfusion injury. *Biochim Biophys Acta.* (2015) 1852:271–6. doi: 10.1016/j.bbadis.2014.05.010
23. Aghaei M, Motallebnezhad M, Ghorghanlu S, Jabbari A, Enayati A, Rajaei M, et al. Targeting autophagy in cardiac ischemia/reperfusion injury: a novel therapeutic strategy. *J Cell Physiol.* (2019) 234:16768–78. doi: 10.1002/jcp.28345
24. Dong Y, Chen H, Gao J, Liu Y, Li J, Wang J. Molecular machinery and interplay of apoptosis and autophagy in coronary heart disease. *J Mol Cell Cardiol.* (2019) 136:27–41. doi: 10.1016/j.yjmcc.2019.09.001
25. Xie M, Cho GW, Kong Y, Li DL, Altamirano F, Luo X, et al. Activation of autophagic flux blunts cardiac ischemia/reperfusion injury. *Circ Res.* (2021) 129:435–50. doi: 10.1161/CIRCRESAHA.120.318601
26. Hamacher-Brady A, Brady NR, Gottlieb RA. Enhancing macroautophagy protects against ischemia/reperfusion injury in cardiac myocytes. *J Biol Chem.* (2006) 281:29776–87. doi: 10.1074/jbc.M603783200
27. Hamacher-Brady A, Brady NR, Logue SE, Sayen MR, Jinno M, Kirshenbaum LA, et al. Response to myocardial ischemia/reperfusion injury involves Bnip3 and autophagy. *Cell Death Differ.* (2007) 14:146–57. doi: 10.1038/sj.cdd.4401936
28. Simpson P, Savion S. Differentiation of rat myocytes in single cell cultures with and without proliferating nonmyocardial cells. cross-striations, ultrastructure, and chronotropic response to isoproterenol. *Circ Res.* (1982) 50:101–16. doi: 10.1161/01.RES.50.1.101
29. Gu S, Tan J, Li Q, Liu S, Ma J, Zheng Y, et al. Downregulation of LAPTM4B contributes to the impairment of the autophagic flux via unopposed activation of mTORC1 signaling during myocardial ischemia/reperfusion injury. *Circ Res.* (2020) 127:e148–65. doi: 10.1161/CIRCRESAHA.119.316388
30. Grisanti LA, Thomas TP, Carter RL, de Lucia C, Gao E, Koch WJ, et al. Pepducin-mediated cardioprotection via β-arrestin-biased β2-adrenergic receptor-specific signaling. *Theranostics.* (2018) 8:4664–78. doi: 10.7150/thno.26619
31. Imarisio C, Alchera E, Sutti S, Valente G, Boccafosch i F, Albano E, et al. Adenosine A2a receptor stimulation prevents hepatocyte lipotoxicity and non-alcoholic steatohepatitis (NASH) in rats. *Clin Sci (Lond).* (2012) 123:323–32. doi: 10.1042/CS20110504
32. Yang Y, Yan X, Xue J, Zheng Y, Chen M, Sun Z, et al. Connexin43 dephosphorylation at serine 282 is associated with connexin43-mediated cardiomyocyte apoptosis. *Cell Death Differ.* (2019) 26:1332–45. doi: 10.1038/s41418-019-0277-x
33. Su Q, Lv XW, Sun YH, Ye ZL, Kong BH, Qin ZB. MicroRNA-494 Inhibits the LRG1 expression to induce proliferation and migration of VECs in rats following myocardial infarction. *Mol Ther Nucleic Acids.* (2019) 18:110–22. doi: 10.1016/j.omtn.2019.08.007
34. Nah J, Zhai P, Huang CY, Fernández ÁF, Mareedu S, Levine B, et al. Upregulation of rubicon promotes autosis during myocardial ischemia/reperfusion injury. *J Clin Invest.* (2020) 130:2978–91. doi: 10.1172/JCI132366
35. Kin H, Zatta A, Lofye M, Amerson BS, Halkos ME, Kerendi F, et al. Postconditioning reduces infarct size via adenosine receptor activation by endogenous adenosine. *Cardiovasc Res.* (2005) 67:124–33. doi: 10.1016/j.cardiores.2005.02.015
36. Li D, Wang X, Huang Q, Li S, Zhou Y, Li Z. Cardioprotection of CAPE-oNO2 against myocardial ischemia/reperfusion induced ROS generation via regulating the SIRT1/eNOS/NF-κB pathway *in vivo* and *in vitro*. *Redox Biol.* (2018) 15:62–73. doi: 10.1016/j.redox.2017.11.023
37. Batchu SN, Law E, Brocks DR, Falck JR, Seubert JM. Epoxyeicosatrienoic acid prevents postischemic electrocardiogram abnormalities in an isolated heart model. *J Mol Cell Cardiol.* (2009) 46:67–74. doi: 10.1016/j.yjmcc.2008.09.711
38. Zhang X, Wei M, Fan J, Yan W, Zha X, Song H, et al. Ischemia-induced upregulation of autophagy preludes dysfunctional lysosomal storage and

associated synaptic impairments in neurons. *Autophagy*. (2021) 17:1519–42. doi: 10.1080/15548627.2020.1840796
39. Hou Y, Wang J, Feng J. The neuroprotective effects of curcumin are associated with the regulation of the reciprocal function between autophagy and HIF-1α in cerebral ischemia-reperfusion injury. *Drug Des Devel Ther*. (2019) 13:1135–44. doi: 10.2147/DDDT.S194182
40. Sanada S, Asanuma H, Tsukamoto O, Minamino T, Node K, Takashima S, et al. Protein kinase A as another mediator of ischemic preconditioning independent of protein kinase C. *Circulation*. (2004) 110:51–7. doi: 10.1161/01.CIR.0000133390.12306.C7
41. Ye Y, Qian J, Castillo AC, Ling S, Ye H, Perez-Polo JR, et al. Phosphodiesterase-3 inhibition augments the myocardial infarct size-limiting effects of exenatide in mice with type 2 diabetes. *Am J Physiol Heart Circ Physiol*. (2013) 304:H131–41. doi: 10.1152/ajpheart.00609.2012
42. Nah J, Zablocki D, Sadoshima J. Autosis: a new target to prevent cell death. *JACC Basic Transl Sci*. (2020) 5:857–69. doi: 10.1016/j.jacbts.2020.04.014
43. Wu X, Qin Y, Zhu X, Liu D, Chen F, Xu S, et al. Increased expression of DRAM1 confers myocardial protection against ischemia via restoring autophagy flux. *J Mol Cell Cardiol*. (2018) 124:70–82. doi: 10.1016/j.yjmcc.2018.08.018
44. Zech ATL, Singh SR, Schlossarek S, Carrier L. Autophagy in cardiomyopathies. *Biochim Biophys Acta Mol Cell Res*. (2020) 1867:118432. doi: 10.1016/j.bbamcr.2019.01.013
45. Patel P, Karch J. Regulation of cell death in the cardiovascular system. *Int Rev Cell Mol Biol*. (2020) 353:153–209. doi: 10.1016/bs.ircmb.2019.11.005
46. Del Re DP, Amgalan D, Linkermann A, Liu Q, Kitsis RN. Fundamental mechanisms of regulated cell death and implications for heart disease. *Physiol Rev*. (2019) 1:1765–1817. doi: 10.1152/physrev.00022.2018
47. Jia C, Chen H, Zhang J, Zhou K, Zhuge Y, Niu C, et al. Role of pyroptosis in cardiovascular diseases. *Int Immunopharmacol*. (2019) 67:311–18. doi: 10.1016/j.intimp.2018.12.028
48. Ye B, Chen X, Dai S, Han J, Liang X, Lin S, et al. Emodin alleviates myocardial ischemia/reperfusion injury by inhibiting gasdermin D-mediated pyroptosis in cardiomyocytes. *Drug Des Devel Ther*. (2019) 25:975–90. doi: 10.2147/DDDT.S195412
49. Han Y, Sun W, Ren D, Zhang J, He Z, Fedorova J, et al. SIRT1 agonism modulates cardiac NLRP3 inflammasome through pyruvate dehydrogenase during ischemia and reperfusion. *Redox Biol*. (2020) 34:101538. doi: 10.1016/j.redox.2020.101538
50. Zhang M, Lei YS, Meng XW, Liu HY, Li LG, Zhang J, et al. Iguratimod alleviates myocardial ischemia/reperfusion injury through inhibiting inflammatory response induced by cardiac fibroblast pyroptosis via COX2/NLRP3 signaling pathway. *Front Cell Dev Biol*. (2021) 25; 9:746317. doi: 10.3389/fcell.2021.746317
51. Chen Y, Fan H, Wang S, Tang G, Zhai C, Shen L. Ferroptosis: A novel therapeutic target for ischemia-reperfusion injury. *Front Cell Dev Biol*. (2021) 10:688605. doi: 10.3389/fcell.2021.688605
52. Jiang X, Stockwell BR, Conrad M. Ferroptosis: mechanisms, biology and role in disease. *Nat Rev Mol Cell Biol*. (2021) 22(4):266–82. doi: 10.1038/s41580-020-00324-8
53. Feng Y, Madungwe NB, Imam Aliagan AD, Tombo N, Bopassa JC. Liproxstatin-1 protects the mouse myocardium against ischemia/reperfusion injury by decreasing VDAC1 levels and restoring GPX4 levels. *Biochem Biophys Res Commun*. (2019) 10:606–11. doi: 10.1016/j.bbrc.2019.10.006
54. Lin JH, Yang KT, Lee WS, Ting PC, Luo YP, Lin DJ, et al. Xanthohumol protects the rat myocardium against ischemia/reperfusion injury-induced ferroptosis. *Oxid Med Cell Longev*. (2022) 17 2022: 9523491. doi: 10.1155/2022/9523491
55. Shan X, Lv ZY, Yin MJ, Chen J, Wang J, Wu QN. The protective effect of cyanidin-3-glucoside on myocardial ischemia-reperfusion injury through ferroptosis. *Oxid Med Cell Longev*. (2021) 6:2021:8880141. doi: 10.1155/2021/8880141
56. Song Y, Wang B, Zhu X, Hu J, Sun J, Xuan J, et al. Human umbilical cord blood-derived MSCs exosome attenuate myocardial injury by inhibiting ferroptosis in acute myocardial infarction mice. *Cell Biol Toxicol*. (2021) 37:51–64. doi: 10.1007/s10565-020-09530-8
57. Tang LJ, Zhou YJ, Xiong XM, Li NS, Zhang JJ, Luo XJ, et al. Ubiquitin-Specific protease 7 promotes ferroptosis via activation of the p53/TfR1 pathway in the rat hearts after ischemia/reperfusion. *Free Radic Biol Med*. (2021) 162:339–52. doi: 10.1016/j.freeradbiomed.2020.10.307
58. Cherra SJ, Kulich SM. Uechi Guy, Balasubramani M, Mountzouris J, Day BW, et al. Regulation of the autophagy protein LC3 by phosphorylation. *J Cell Biol*. (2010) 190:533–9. doi: 10.1083/jcb.201002108
59. Pankiv S, Clausen TH, Lamark T, Brech A, Bruun JA, Outzen H, et al. p62/SQSTM1 binds directly to Atg8/LC3 to facilitate degradation of ubiquitinated protein aggregates by autophagy. *J Biol Chem*. (2007) 282:24131–45. doi: 10.1074/jbc.M702824200
60. Ma XC, Liu HY, Foyil SR, Godar RJ, Weinheimer CJ, Hill JA, et al. Impaired autophagosome clearance contributes to cardiomyocyte death in ischemia/reperfusion injury. *Circulation*. (2012) 125:3170–81. doi: 10.1161/CIRCULATIONAHA.111.041814
61. Hariharan N, Zhai P, Sadoshima J. Oxidative stress stimulates autophagic flux during ischemia/reperfusion. *Antioxid Redox Signal*. (2011) 14:2179–90. doi: 10.1089/ars.2010.3488
62. Ma H, Guo R, Yu L, Ren J. Aldehyde dehydrogenase 2 (ALDH2) rescues myocardial ischaemia/reperfusion injury: role of autophagy paradox and toxic aldehyde. *Eur Heart J*. (2011) 32:1025–38. doi: 10.1093/eurheartj/ehq253
63. Maiuri MC, Le Toumelin G, Criollo A, Rain JC, Gautier F, Juin P, et al. Functional and physical interaction between Bcl-X(L) and a BH3-like domain in Beclin-1. *EMBO J*. (2007)26: 2527–39. doi: 10.1038/sj.emboj.7601689
64. Bai H, Zhao L, Liu HX, Guo H, Guo W, Zheng LL, et al. Adiponectin confers neuroprotection against cerebral ischemia-reperfusion injury through activating the cAMP/PKA-CREB-BDNF signaling. *Brain Res Bull*. (2018) 143:145–54. doi: 10.1016/j.brainresbull.2018.10.013
65. Khedr RM, Ahmed AEA, Kamel R, Raafat EM. Sitagliptin attenuates intestinal ischemia/reperfusion injury via cAMP/PKA, PI3K/Akt pathway in a glucagon-like peptide 1 receptor-dependent manner. *Life Sci*. (2018) 211:31–9. doi: 10.1016/j.lfs.2018.09.013
66. Ji HF, Zhang Y, Shen XD, Gao F, Huang CY, Abad C, et al. Neuropeptide PACAP in mouse liver ischemia and reperfusion injury: immunomodulation by the cAMP-PKA pathway. *Hepatology*. (2013) 57:1225–37. doi: 10.1002/hep.25802
67. Nakamura A, Miyagawa M, Yanagawa Y. Modulation of 11β-hydroxysteroid dehydrogenase 1 by β2-adrenoceptor in the ischaemia-reperfused rat kidney. *Nephrol Dial Transplant*. (2012) 27:3456–64. doi: 10.1093/ndt/gfr701
68. Stephan JS, Yeh YY, Ramachandran V, Deminoff SJ, Herman PK, et al. The Tor and PKA signaling pathways independently target the Atg1/Atg13 protein kinase complex to control autophagy. *Proc Natl Acad Sci U S A*. (2009) 106:17049–54. doi: 10.1073/pnas.0903316106
69. Budovskaya YV, Stephan JS, Deminoff SJ, Herman PK. An evolutionary proteomics approach identifies substrates of the cAMP-dependent protein kinase. *Proc Natl Acad Sci U S A*. (2005) 102:13933–8. doi: 10.1073/pnas.0501046102
70. Budovskaya YV, Stephan JS, Reggiori F, Klionsky DJ, Herman PK. The Ras/cAMP-dependent protein kinase signaling pathway regulates an early step of the autophagy process in saccharomyces cerevisiae. *J Biol Chem*. (2004) 279:20663–71. doi: 10.1074/jbc.M400272200
71. Torres-Quiroz F, Filteau M, Landry CR. Feedback regulation between autophagy and PKA. *Autophagy*. (2015) 11:1181–3. doi: 10.1080/15548627.2015.1055440
72. Wang J, Whiteman MW, Lian H, Wang GX, Singh A, Huang DY, et al. A non-canonical MEK/ERK signaling pathway regulates autophagy via regulating Beclin-1. *J Biol Chem*. (2009) 284:21412–24. doi: 10.1074/jbc.M109.026013
73. Ugland H, Naderi S, Brech A, Collas P, Blomhoff HK. cAMP induces autophagy via a novel pathway involving ERK, cyclin E and Beclin 1. *Autophagy*. (2011) 7:1199–211. doi: 10.4161/auto.7.10.16649
74. Takahashi T, Tang T, Lai NC, Roth DM, Rebolledo B, Saito M, et al. Increased cardiac adenylyl cyclase expression is associated with increased survival after myocardial infarction. *Circulation*. (2006) 114:388–96. doi: 10.1161/CIRCULATIONAHA.106.632513
75. Marie-Claire Toufektsian, Zequan Yang, Konkal M Prasad, Overbergh L, Ramos SI, Mathieu C, et al. Stimulation of A2A-adenosine receptors after myocardial infarction suppresses inflammatory activation and attenuates contractile dysfunction in the remote left ventricle. *Am J Physiol Heart Circ Physiol*. (2006) 290:H1410–8. doi: 10.1152/ajpheart.00860.2005

76. Ke QG, Xiao YF, Bradbury JA, Graves JP, Degraff LM, Seubert JM, et al. Electrophysiological properties of cardiomyocytes isolated from CYP2J2 transgenic mice. *Mol Pharmacol.* (2007) 72:1063–73. doi: 10.1124/mol.107.035881
77. Liang BT, Morley JF, A. New cyclic AMP-independent, Gs-mediated stimulatory mechanism via the adenosine A2a receptor in the intact cardiac cell. *J Biol Chem.* (1996) 271:18678–85. doi: 10.1074/jbc.271.31.18678
78. Kerfant BG, Zhao DL, Lorenzen-Schmidt I, Wilson LS, Cai S, Chen SR W, et al. PI3Kgamma is required for PDE4, Not PDE3, activity in subcellular microdomains containing the sarcoplasmic reticular calcium ATPase in cardiomyocytes. *Circ Res.* (2007) 101:400–8. doi: 10.1161/CIRCRESAHA.107.156422
79. Baumert M, Porta A, Vos MA, Malik M, Couderc JP, Laguna P, et al. QT interval variability in body surface ECG: measurement, physiological basis, and clinical value: position statement and consensus guidance endorsed by the european heart rhythm association jointly with the ESC working group on cardiac cellular electrophysiology. *Europace.* (2016) 18:925–44. doi: 10.1093/europace/euv405
80. Diez ER, Sánchez JA, Prado NJ, Zumino AZP, García-Dorado D, Miatello RM, et al. Ischemic postconditioning reduces reperfusion arrhythmias by adenosine receptors and protein kinase C activation but is independent of K(ATP) channels or connexin 43. *Int J Mol Sci.* (2019) 20:5927. doi: 10.3390/ijms20235927
81. Chen L, Sampson KJ, Kass RS. Cardiac delayed rectifier potassium channels in health and disease. *Card Electrophysiol Clin.* (2016) 8:307–22. doi: 10.1016/j.ccep.2016.01.004

Conflict of Interest: The authors declare that the research was conducted in the absence of any commercial or financial relationships that could be construed as a potential conflict of interest.

Publisher's Note: All claims expressed in this article are solely those of the authors and do not necessarily represent those of their affiliated organizations, or those of the publisher, the editors and the reviewers. Any product that may be evaluated in this article, or claim that may be made by its manufacturer, is not guaranteed or endorsed by the publisher.

frontiers | Frontiers in Cardiovascular Medicine

ORIGINAL RESEARCH
published: 17 May 2022
doi: 10.3389/fcvm.2022.818585

Differential Gene Expression and Immune Cell Infiltration in Carotid Intraplaque Hemorrhage Identified Using Integrated Bioinformatics Analysis

Xiaoshuo Lv[1,2], Feng Wang[1,2], Mingsheng Sun[1,3], Congrui Sun[1,3], Xueqiang Fan[1], Bo Ma[1], Yuguang Yang[1], Zhidong Ye[1], Peng Liu[1,2] and Jianyan Wen[1,2]**

[1] Department of Cardiovascular Surgery, China-Japan Friendship Hospital, Beijing, China, [2] Graduate School of Peking Union Medical College, Beijing, China, [3] Peking University China-Japan Friendship School of Clinical Medicine, Beijing, China

OPEN ACCESS

Edited by:
A. Phillip Owens III, University of Cincinnati, United States

Reviewed by:
Frank Davis, University of Michigan, United States
Zhensen Chen, Fudan University, China

***Correspondence:**
Jianyan Wen
jianyanwen@sina.com
Peng Liu
liupeng5417@163.com

Specialty section:
This article was submitted to Atherosclerosis and Vascular Medicine, a section of the journal Frontiers in Cardiovascular Medicine

Received: *19 November 2021*
Accepted: *11 March 2022*
Published: *17 May 2022*

Citation:
Lv X, Wang F, Sun M, Sun C, Fan X, Ma B, Yang Y, Ye Z, Liu P and Wen J (2022) Differential Gene Expression and Immune Cell Infiltration in Carotid Intraplaque Hemorrhage Identified Using Integrated Bioinformatics Analysis. Front. Cardiovasc. Med. 9:818585. doi: 10.3389/fcvm.2022.818585

Background: Intraplaque hemorrhage (IPH) is an important feature of unstable plaques and an independent risk factor for cardiovascular events. However, the molecular mechanisms contributing to IPH are incompletely characterized. We aimed to identify novel biomarkers and interventional targets for IPH and to characterize the role of immune cells in IPH pathogenesis.

Methods: The microarray dataset GSE163154 which contain IPH and non-IPH plaque samples was obtained from the Gene Expression Omnibus (GEO). R software was adopted for identifying differentially expressed genes (DEGs) and conducting functional investigation. The hub genes were carried by protein-protein interaction (PPI) network and were validated by the GSE120521 dataset. CIBERSORT deconvolution was used to determine differential immune cell infiltration and the relationship of immune cells and hub genes. We confirmed expression of proteins encoded by the hub genes by immunohistochemistry and western blotting in 8 human carotid endarterectomy samples with IPH and 8 samples without IPH (non-IPH).

Results: We detected a total of 438 differentially expressed genes (DEGs), of which 248 were upregulated and 190 were downregulated. DEGs were mainly involved in inflammatory related pathways, including neutrophil activation, neutrophil degranulation, neutrophil-mediated immunity, leukocyte chemotaxis, and lysosomes. The hub genes found through the method of degree in the PPI network showed that *ITGB2* and *ITGAM* might play an important role in IPH. Receiver operating characteristic (ROC) results also showed a good performance of these two genes in the test and validation dataset. We found that the proportions of infiltrating immune cells in IPH and non-IPH samples differed, especially in terms of M0 and M2 macrophages. Immunohistochemistry and western blotting analysis showed that expression levels of *ITGB2* and *ITGAM* increased significantly in carotid atherosclerotic plaques with IPH.

Conclusion: *ITGB2* and *ITGAM* are key hub genes of IPH and may play an important role in the biological process of IPH. Our findings advance our understanding of the underlying mechanisms of IPH pathogenesis and provide valuable information and directions for future research into novel targets for IPH diagnosis and immunotherapy.

Keywords: intraplaque hemorrhage, immune cell infiltration, bioinformatics, GEO, atherosclerosis

INTRODUCTION

Carotid atherosclerotic disease is a key risk factor for ischemic stroke, which remains an important cause of mortality and disability worldwide (1). Improvement of atherosclerotic imaging capabilities revealed important new insights, suggesting that the vulnerability of atherosclerotic plaques depends more on their composition than on their size or degree of lumen narrowing (2). Intraplaque hemorrhage (IPH), lipid-rich necrotic cores, thin fibrous caps, and inflammation are considered important features of high-risk atherosclerotic lesions (3). In particular, there is a well-established relationship between IPH and adverse cardiovascular outcomes. Recent studies confirmed that IPH is an independent risk factor for stroke and coronary heart disease, and that the risk of ipsilateral ischemic events in existing IPH patients is increased 4 to 12 times (4–6).

IPH is thought to originate from new, immature vessels that respond to hypoxia or inflammatory stimuli (7, 8). During plaque advancement, intraplaque angiogenesis provides oxygen and nourishment to maintain plaque growth. However, these neovessels are usually immature, characterized by increased permeability caused by a discontinuous basement membrane, underdeveloped interendothelial connections and poor pericyte coverage (9–11). Leaky neovessels tend to rupture and permit extravasation of blood components such as erythrocytes, inflammatory cells, lipoproteins, and plasma, resulting in IPH (9). IPH rapidly enlarges the volume of the necrotic core of the plaque and promotes deposition of free cholesterol by accumulating cholesterol-rich erythrocyte membranes. These processes trigger an inflammatory response and initiate a vicious cycle that destabilizes atherosclerotic plaques (12, 13). Further, accumulated erythrocytes can attract inflammatory cells to exudate from neovessels and release a large amount of cytokines, growth factors, and matrix metalloproteinases (MMPs), thus creating a highly immune-responsive environment and further triggering the formation of new immature intraplaque microvessels (14, 15).

While histopathological and experimental studies improved our understanding of the pathogenesis of IPH, the molecular mechanisms remain unclear. Toward filling this gap, recent advances in gene chip technology have helped identify new and important genes related to disease mechanisms. However, although bioinformatics studies have described gene expression and immune cell infiltration patterns during atherosclerosis occurrence and progression, there are few studies comparing atherosclerotic plaques in tissues with and without IPH (non-IPH) (16–18).

As the flowchart showed in **Figure 1**, we downloaded array dataset GSE163154 from the Gene Expression Omnibus (GEO) to study differentially expressed genes (DEGs) and pathways between IPH and non-IPH carotid plaques by bioinformatics methods including DEG screening, functional enrichment analysis, protein–protein interaction (PPI) analysis and identification of hub genes. The GSE120521 dataset was used to validate the hub genes and CIBERSORT was used to further analyze immune cell infiltration in these two types of plaques. Finally, the protein expression associated with the important hub genes was verified in carotid endarterectomy specimens by immunochemical staining and western blotting. Our results contribute to understanding the molecular mechanisms underlying IPH development and highlight the importance of immune cells in the pathogenesis of IPH.

MATERIALS AND METHODS

Microarray Data

mRNA expression profiles of GSE163154, which were assayed on the GPL6104 platform (Illumina humanRef-8 v2.0 expression beadchip), were obtained from the GEO database. The dataset contains 43 carotid atherosclerotic plaques, including 16 non-IPH plaque samples and 27 IPH plaque samples, which were collected from symptomatic patients undergoing carotid endarterectomy (CEA) surgery. Meanwhile the dataset GSE120521 obtained from the GEO was used as an external validation dataset, including 4 stable plaques (macroscopically normal) and 4 unstable plaques (plaque rupture with IPH).

Test for Correlation and Variation of Samples

Pearson's correlation analysis and principal component analysis (PCA) were performed for the mRNA expression profile in GSE163154 dataset to examine the correlation and variation of the samples. All statistical computing and graphics were performed using R software. Pearson's correlation test was used to evaluate the correlation among all samples, and a correlation heatmap was drawn to visualize correlations between samples using the pheatmap package of R (version 4.1.0, https://www.r-project.org/). PCA was used to visualize the variation and clustering of samples. If the samples within the group can be clustered or have high correlation, the data was considered to have good quality and reliability for bioinformatics analysis.

Identification of DEGs

The limma package in R was used to normalize and screen DEGs between non-IPH samples and IPH samples. DEGs with

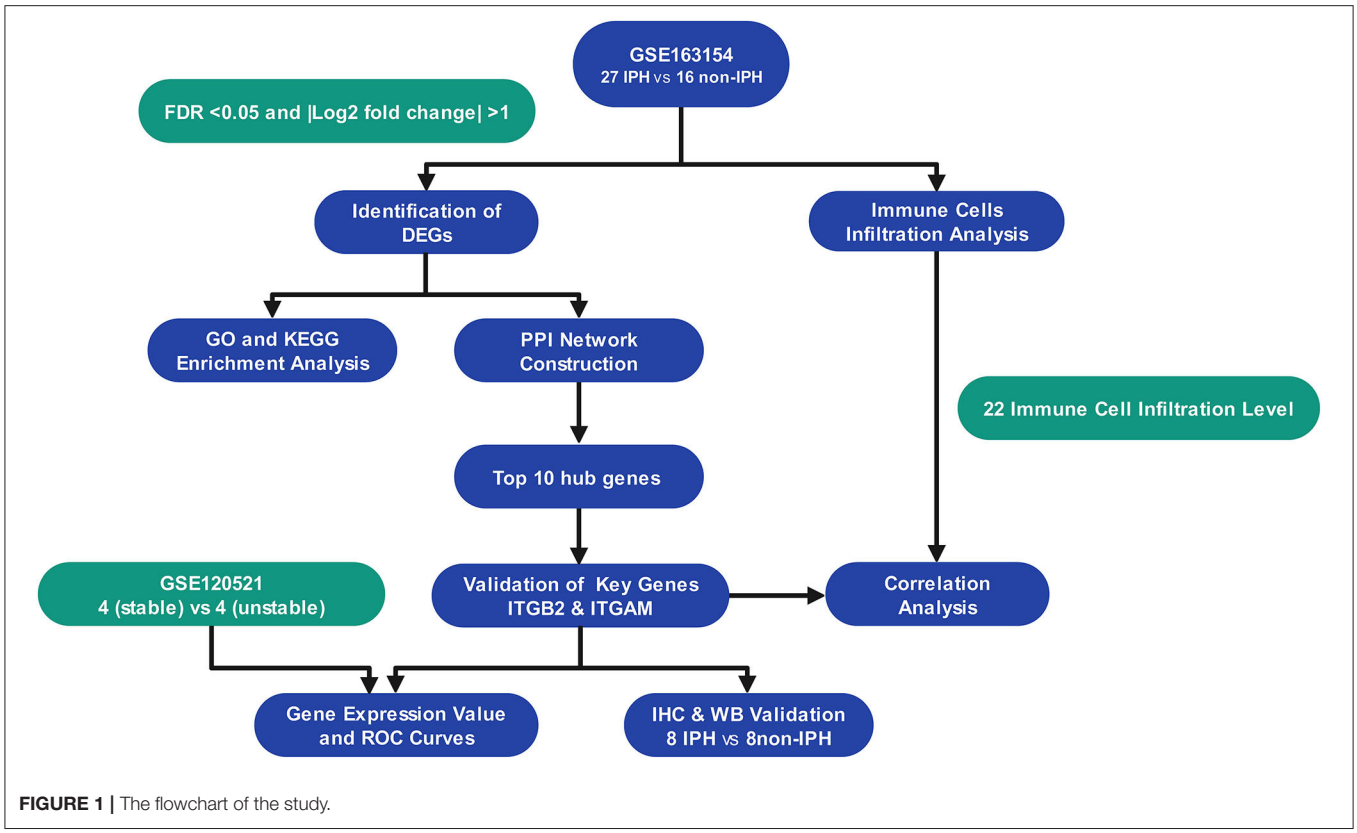

FIGURE 1 | The flowchart of the study.

an adjusted false discovery rate (FDR) $p < 0.05$ and |log2 fold change (FC)| >1 were considered significant. A heatmap was drawn using the pheatmap package for visualizing DEGs.

Enrichment Analysis

Gene Ontology (GO) term and Kyoto Encyclopedia of Genes and Genomes (KEGG) pathway enrichment analyses were performed for DEGs using the clusterProfiler package, and the *p*-value cutoff and q-value cutoff were set to 0.05.

Construction of the PPI Network and Identification of Hub Genes

The online Search Tool for the Retrieval of Interacting Genes (STRING, https://www.string-db.org/) database was used to construct the DEG PPI network, with a PPI score threshold (medium confidence) ≥0.4. The Cytohub plugin in Cytoscape (version 3.8.2, https://cytoscape.org/) was used to identify hub genes using the degree method (Top 10 genes). Moreover, we verified the expression of the crucial genes and evaluated the accuracy of crucial genes using receiver operating characteristic (ROC) curves in internal dataset GSE163154 and external dataset GSE120521.

CIBERSORT Analysis of Immune Cell Infiltration

The CIBERSORT (https://cibersortx.stanford.edu/) deconvolution algorithm was used to evaluate differential immune cell infiltration between IPH and non-IPH samples. CIBERSORT is an analysis tool that uses gene expression data to estimate the abundances of member cell types in a mixed cell population. The LM22 gene file provided by CIBERSORT was used to define and infer the relative proportions of 22 types of infiltrating immune cells in the IPH and non-IPH plaque gene expression data.

The default signature matrix of 100 permutations was used in this algorithm. To ensure confidence in the results, CIRBERSORT uses Monte Carlo sampling to derive the deconvolution *p*-value for each sample, and only data with *p*-values <0.05 were retained. After data processing and filtering, 14 cases of non-IPH data and 27 cases of IPH data were included in the subsequent analysis. The results obtained by CIBERSORT were visualized using the corplot, vioplot, and ggplot2 packages in R. We then performed correlation analysis between the 22 immune cells and the key genes using Spearman's rank correlation test.

Sample Collection and Classification

From December 2020 to September 2021, we collected 37 carotid plaques during CEA surgery in China-Japan Friendship Hospital. Through preliminary macroscopic observation, we intentionally selected 8 IPH plaques and 8 non-IPH plaques for analyze and retrospectively collected clinical characteristic information of patients. The collected specimens were cut into 5–8-mm-thick parallel sections, and each alternate section was quickly frozen in liquid nitrogen and stored at −80°C for subsequent protein extraction, while the rest of the sections were fixed in

4% polyoxymethylene for 24 h, and then embedded in paraffin. Histological examination was performed on 5-mm-thick serial sections. Sections from different segments of each sample were taken for hematoxylin-eosin (H&E) and Perls staining (Solarbio, G1424) to reconfirm the presence of IPH. This study was approved by the Medical Ethics Committee of the China-Japan Friendship Hospital of Beijing, China (2019-25-1), and we received informed consent from all patients.

Immunohistochemistry

Sections were deparaffinated, blocked, and incubated with the primary anti-*ITGB2* antibody (Proteintech, 10554-1-AP) or anti-*ITGAM* antibody (Proteintech, 21851-1-AP) at 4°C overnight. Image-Pro Plus 6.0 software (IPP 6.0, Media Cybernetics, United States) was utilized to measure the total tissue area and integrated optic density (IOD) of the target gene, which was stained yellow-brown. The intensity of gene expression was presented as IOD per unit area.

Protein Extraction and Western Blotting Analysis

Plaque samples were washed twice with cold phosphate-buffered saline and lysed with RIPA buffer (Beyotime Technology; Cat: P0013C) containing proteinase inhibitors. Total protein concentrations were measured using a BCA Protein Assay Kit (Invitrogen; Cat: 23227). Equal amounts of protein were separated by SDS-PAGE and transferred to a PVDF membrane. Blot membranes were blocked with 5% non-fat milk, and incubated with primary antibodies (*ITGAM*, 1:2000, Proteintech; *ITGB2*, 1:1000, Proteintech) followed by suitable peroxidase-conjugated secondary antibody. Immunoreactive bands were detected with Pierce ECL Western Blotting Substrate (Thermo Scientific; Cat: 32209). β-actin was used as an internal control and blots were quantified by Image J.

Statistical Analysis

R version 4.1.0 was used to perform bioinformatics analyses and a p-value or adjusted p-value < 0.05 was considered statistically significant. SPSS version 26 and GraphPad Prism 6.0 software were used to analyze clinical and experimental data. Unpaired Student's t-test was used to compare the two sets of data. $P < 0.05$ was considered statistically significant.

RESULTS

Dataset Validation

Pearson's correlation test and PCA were used to validate the dataset. The correlation heatmap of the GSE163154 dataset showed that there were strong correlations among samples within the IPH group and also between samples within the non-IPH group (**Figure 2A**). PCA of GSE163154 showed that the 43 samples in the two groups could be distinguished, as the distances between the samples in the IPH group were close in the dimensions of PC1 and PC2 and the distance between samples in the non-IPH group were also close (**Figure 2B**).

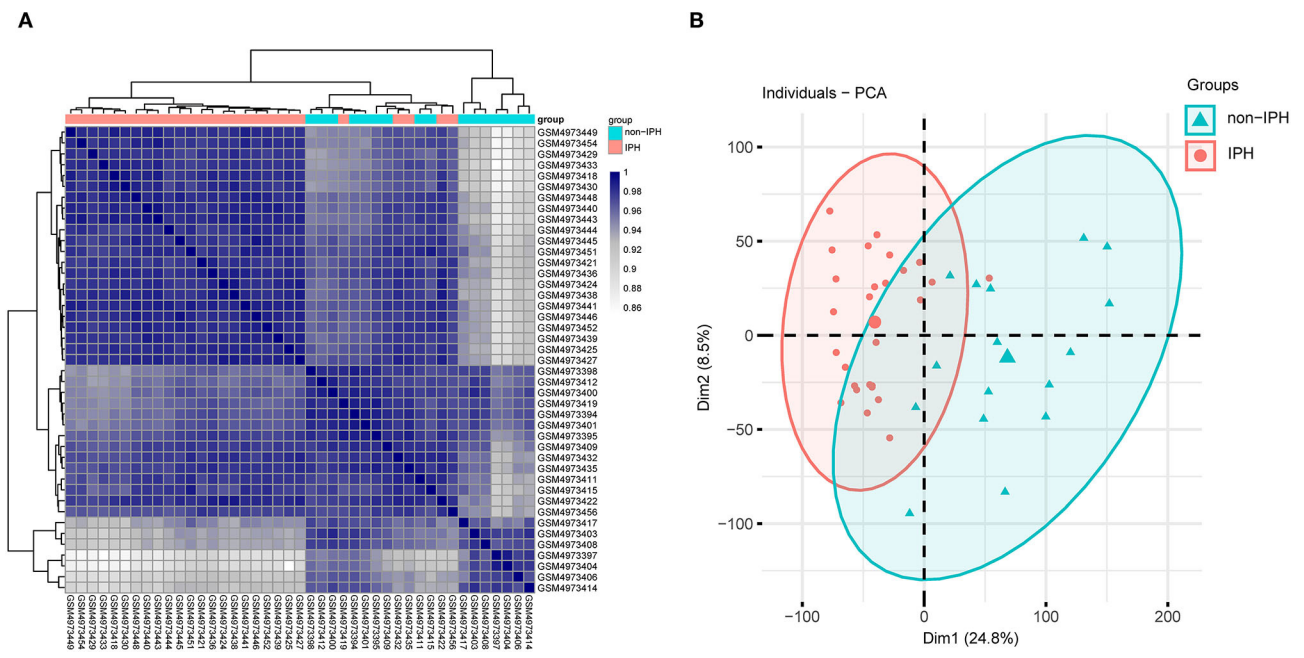

FIGURE 2 | Validation of the dataset GSE163154 by Pearson's correlation analysis and PCA. **(A)** Pearson's correlation analysis of samples from the GSE163154 dataset. The correlation coefficient is reflected by the colors in the heatmap. **(B)** PCA of samples from the GSE163154 dataset. PC1 and PC2 are represented on the x-axis and y-axis, respectively. PCA, principal component analysis; PC1, principal component 1; PC2, principal component 2.

Identification of DEGs

A total of 438 DEGs were screened, with an adjusted *p*-value of <0.05 and | log2 (fold-change) | >1 as thresholds. A total of 248 upregulated and 190 downregulated DEGs were identified in IPH samples when compared to non-IPH samples, as shown by volcano plot (**Figure 3A**) and heatmap (**Figure 3B**), while a detailed summary was listed in **Supplementary Table S1**.

Functional and Pathway Enrichment Analysis

GO analysis classified DEGs into three categories: biological process (BP), molecular function (MF), and cellular component (CC). DEGs linked with BP were significantly enriched in neutrophil activation, neutrophil degranulation, and neutrophil activation involved in immune response. DEGs linked with CC were significantly enriched in collagen-containing extracellular matrix, secretory granule membrane, and cell-substrate junction. DEGs linked with MF were significantly enriched in actin binding, collagen binding, and cargo receptor activity (**Figure 4A**). KEGG pathway enrichment analysis revealed that DEGs were mainly enriched in lysosome, pertussis, cholesterol metabolism, and phagosome pathways (**Figure 4B**). The detatiled results were listed in **Supplementary Table S2**.

Construction of the PPI Network and Screening of Hub Genes

The top ten genes *ITGB2*, *ITGAM*, TYROBP, SPI1, CSF1R, MMP9, CXCL8, IL1B, CYBB, and CD53 obtained by PPI analysis and Cytoscape were regarded as hub genes, of which *ITGB2* and *ITGAM* were in the most critical positions and became the focus of subsequent analyses (**Figure 5**).

Different Immune Cell Infiltrative Patterns Between IPH and Non-IPH Samples

GO and KEGG analysis identified multiple pathways related to the immune process. Therefore, we used CIBERSORT software to reveal the pattern of immune cell infiltration in carotid atherosclerotic plaques with hemorrhage. After data processing and screening, 14 cases of non-IPH data and 27 cases of IPH data were included in the subsequent analysis, and a heatmap was used to show the proportion of 22 immune cells in these two groups of samples (**Figure 6A**). M2 macrophages, M0 macrophages, resting mast cells, gamma delta T cells, and monocytes represented the top five highest infiltrating fractions in both groups of plaques. Compared with the non-IPH group, the proportion of M0 macrophages was higher in the IPH group, while the proportion of M2 macrophages was lower (**Figure 6B**). Furthermore, we

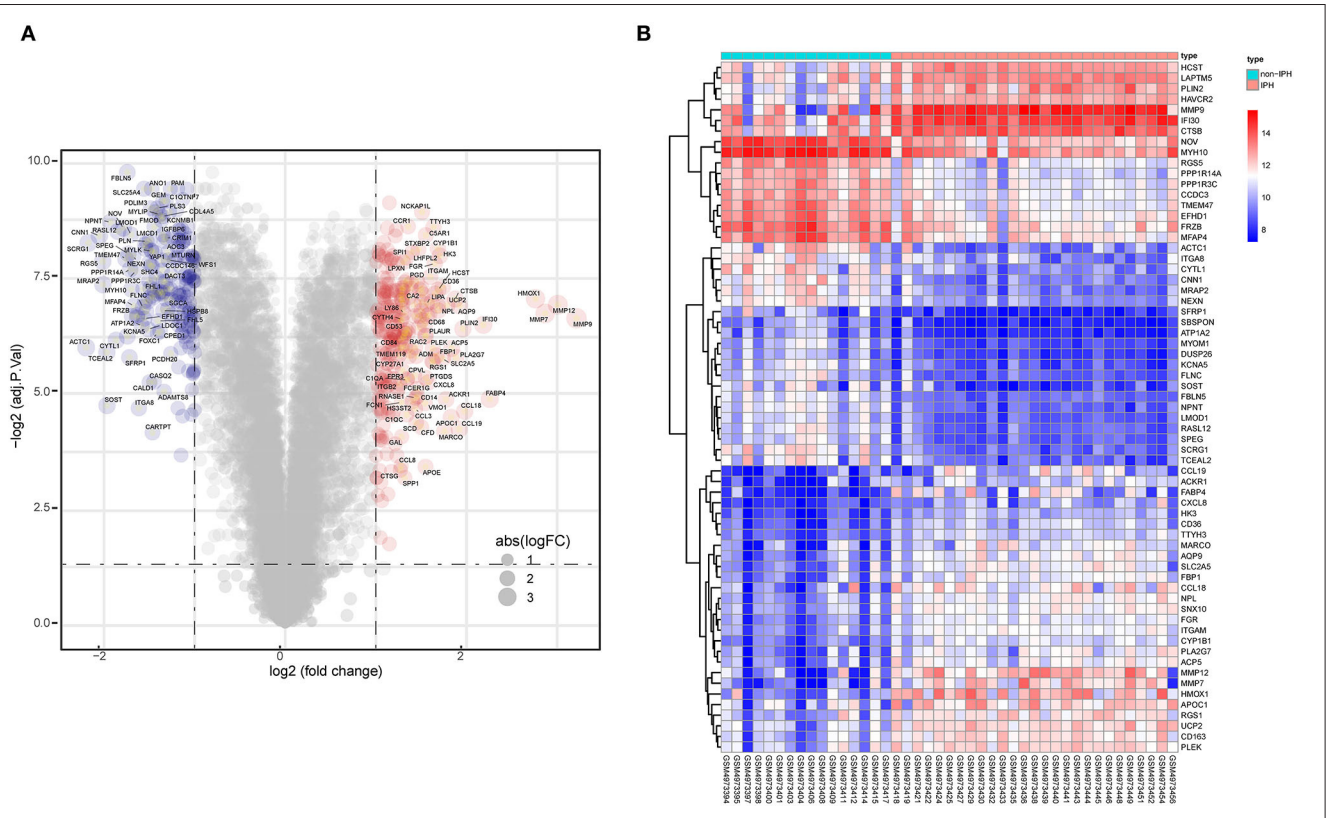

FIGURE 3 | Identification of DEGs between non-IPH samples and IPH samples. **(A)** Volcano plot showing the DEGs between non-IPH and IPH groups after analysis of the GSE163154 dataset with R software. The x-axis represents the fold-change (log-scaled) and the y-axis represents the *p*-value (log-scaled). Red symbols represent upregulated genes, blue symbols represent downregulated genes, and gene name symbols represent the DEGs with the greatest magnitude of fold-change. **(B)** A heatmap showing the DEGs between the two groups. Upregulated genes are labeled in red and downregulated genes are shown in blue.

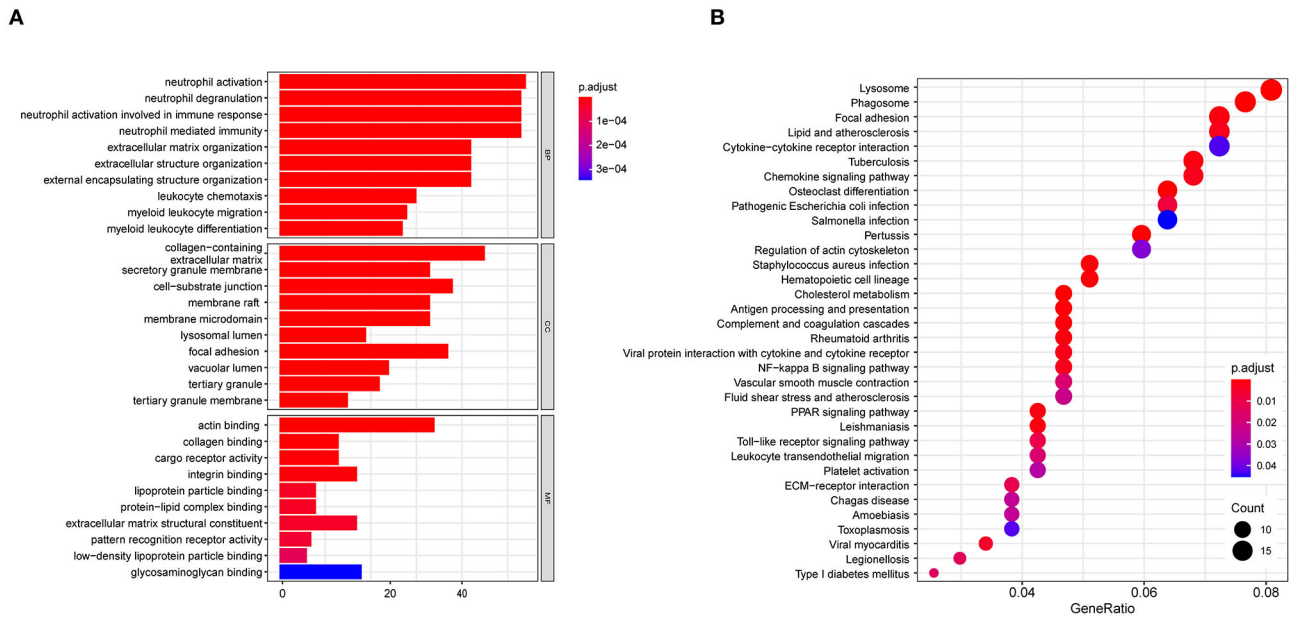

FIGURE 4 | Biofunctional enrichment analysis of DEGs. **(A)** GO functional enrichment analyses of DEGs and the top 10 BP, CC, and MF terms (BP, Biological Process; CC, Cellular Component; MF, Molecular Function). **(B)** KEGG pathway enrichment analyses of DEGs.

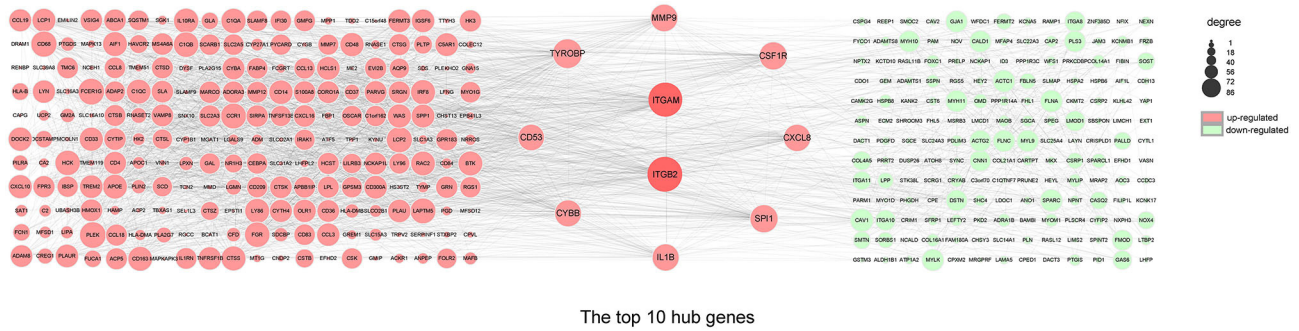

FIGURE 5 | PPI network and hub genes. The PPI network analyzed by the STRING database. The top 10 hub genes screened by the degree method using CytoHubba plugin (Cytoscape). The size of the circle from small (lower) to large (higher) represents the ranking. Red and green represent upregulated and downregulated genes, respectively. DEGs, differentially expressed genes; *ITGB2*, integrin subunit beta 2; *ITGAM*, integrin subunit alpha M; *TYROBP*, transmembrane immune signaling adaptor TYROBP; *SPI1*, Spi-1 proto-oncogene; *CSF1R*, colony stimulating factor 1 receptor; *MMP9*, matrix metallopeptidase 9; *CXCL8*, C-X-C motif chemokine ligand 8; *IL1B*, interleukin 1 beta; *CYBB*, cytochrome b-245 beta chain; *CD53*, CD53 molecule.

performed a correlation analysis of infiltrated immune cells in the plaques, with scores representing the degree of correlation (**Figure 6C**). The correlation heatmap indicated that activated dendritic cells and neutrophils showed the most synergistic effect, while M0 macrophages and M2 macrophages showed the most competitive effect.

Analysis Between Crucial Genes and Immune Cells

As indicated from the correlation analysis, *ITGAM* displayed a significant positive correlation with M0 macrophages ($r = 0.678$, $p < 0.001$), and a significant negative correlation with resting mast cells ($r = -0.423$, $p = 0.006$), M2 macrophages ($r = -0.410$, $p = 0.008$), and resting mast cells ($r = -0.423$, $p = 0.006$) (**Figure 7A**). *ITGB2* displayed a significant positive correlation with M0 macrophages ($r = 0.576$, $p < 0.001$), and a significant negative correlation with resting mast cells ($r = -0.419$, $p = 0.006$), neutrophils ($r = -0.424$, $p = 0.006$), as well as CD4 memory resting T cells ($r = -0.487$, $p = 0.001$) (**Figure 7B**). A detailed summary was listed in **Supplementary Table S3.**

Internal and External Validation of Key Genes

We validated expression of the two key genes and performed ROC analysis on internal dataset GSE163154 and external dataset GSE120521. Results revealed that *ITGAM* and *ITGB2* were

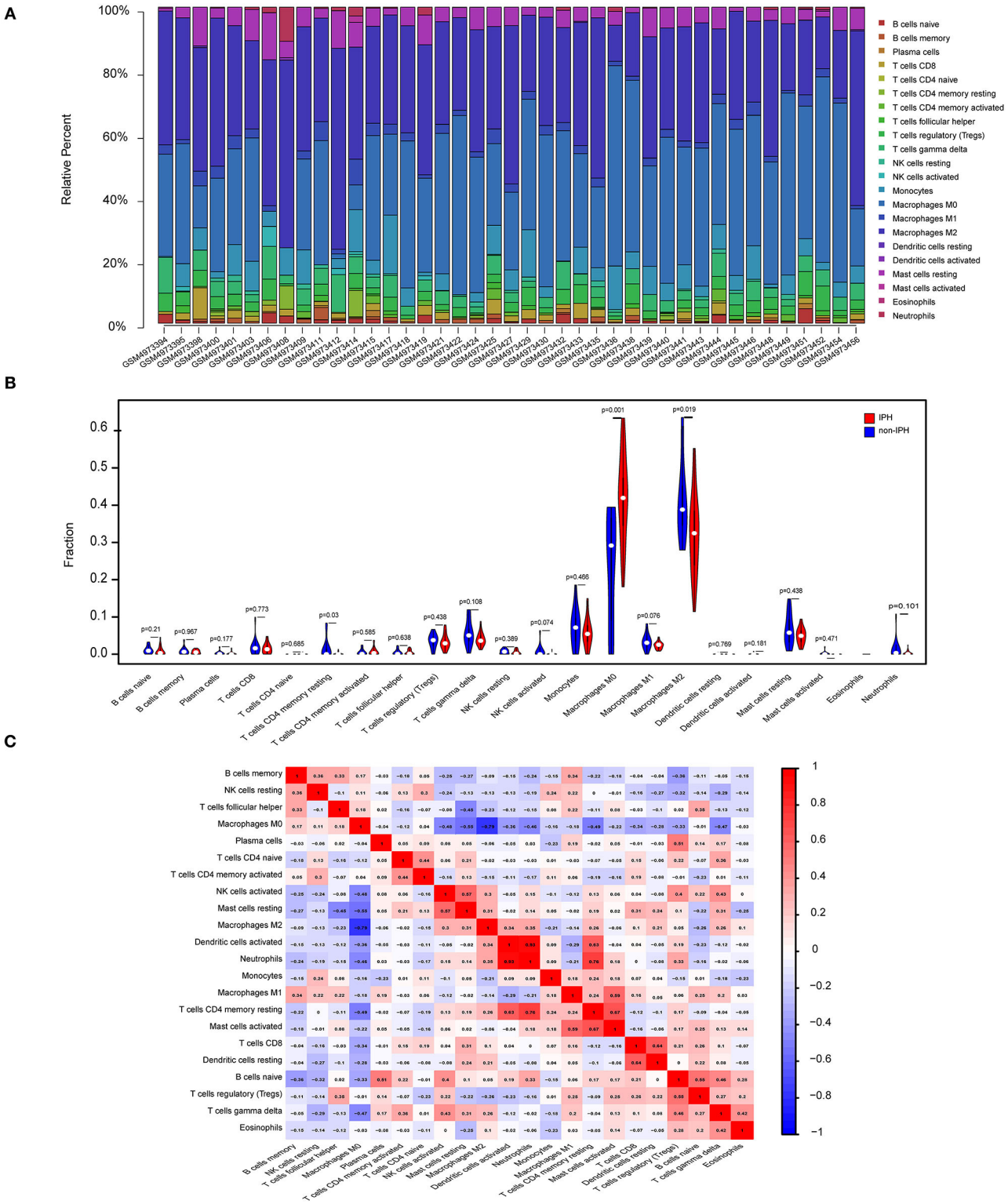

FIGURE 6 | Immune cell infiltration patterns in IPH samples and non-IPH samples. **(A)** Histogram of the proportions of 22 immune cell subpopulations in each IPH and non-IPH sample. x-axis: GEO samples; y-axis: percentage of each immune cell type. **(B)** Violin plot showing the differentially infiltrated immune cells between the two groups. Blue represents the non-IPH plaque group and red represents the IPH plaque group. **(C)** Correlation heatmap of all immune cells. Numbers in the small square represent Pearson's correlation coefficient between the two immune cells on the horizontal and vertical coordinates; red squares indicate positive correlation, and blue squares indicate negative correlation.

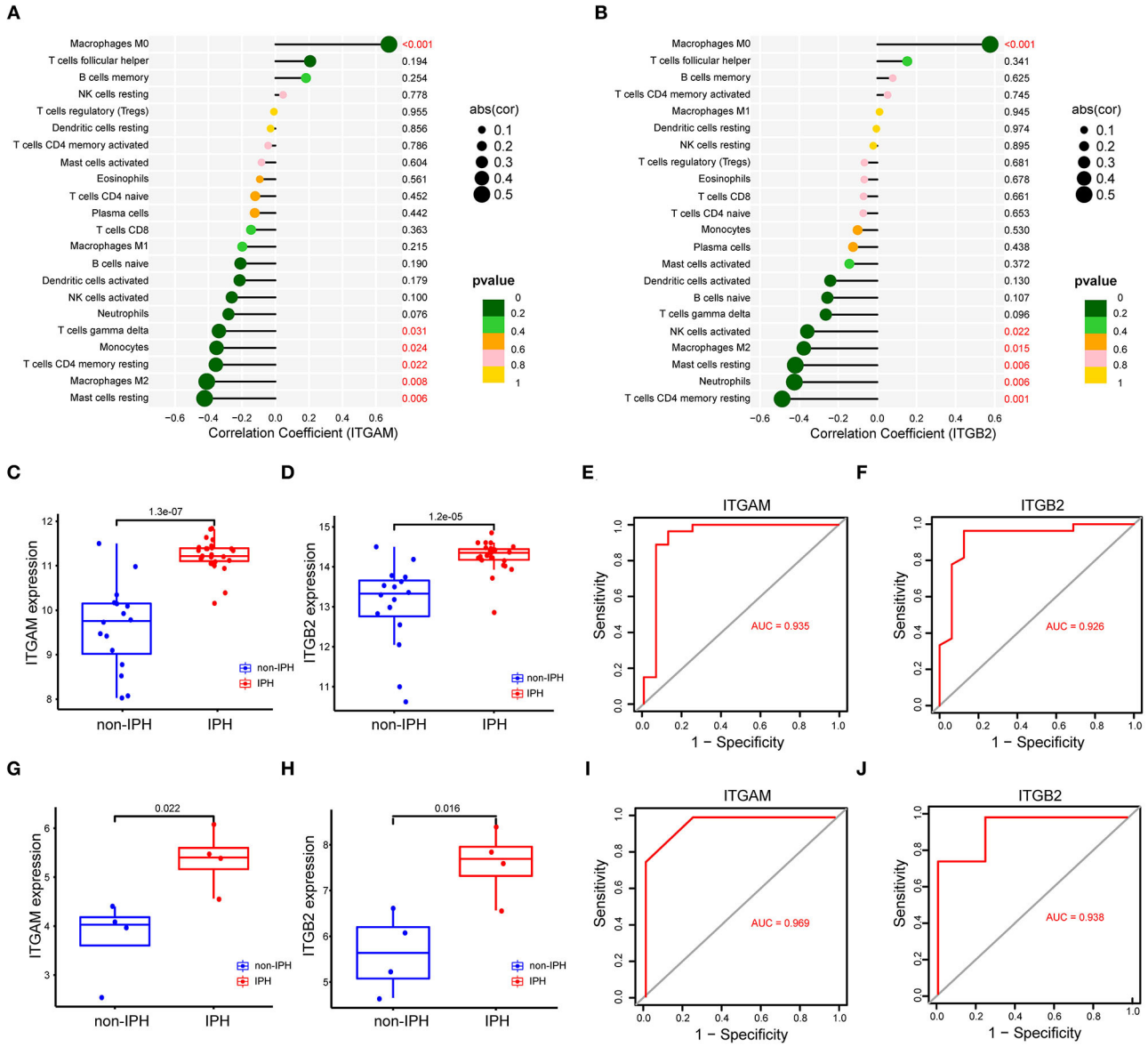

FIGURE 7 | (A,B) Correlation between the hub genes (*ITGAM, ITGB2*) and infiltrating immune cells. The size of the dots represents the strength of the correlation between genes and immune cells, and the color of the dots represents the *p*-value. $p < 0.05$ was considered statistically significant. **(C,D)** The expression level of two genes between IPH and non-IPH samples in dataset GSE163154. **(E,F)** ROC curves for evaluating the accuracy of logistic regression analysis of dataset GSE163154. **(G,H)** The expression level of two genes between IPH and non-IPH samples in validation dataset GSE120521. **(I,J)** ROC curves for evaluating the accuracy of logistic regression analysis of validation dataset GSE120521. ROC, receiver operating characteristic.

significantly upregulated in IPH or advanced atheroma plaques (**Figures 7C,D,G,H**). The ROC curves revealed the probability of *ITGAM* and *ITGB2* as valuable biological markers with AUCs of 0.935 and 0.926 (**Figures 7E,F**); the ROC analysis of external data sets also showed good diagnostic effects of *ITGAM* and *ITGB2*, with AUCs of 0.820 and 0.825, respectively (**Figures 7I,J**). Differences in expression levels of the remaining 8 hub genes (TYROBP, SPI1, CSF1R, MMP9, CXCL8, IL1B, CYBB, and CD53) and their correlation with immune cells were detected in dataset GSE163154 (**Supplementary Figure S1**).

Demographic Data of the Patients and the Expression of *ITGB2* and *ITGAM*

The plaques were divided into IPH plaques and non-IPH plaques by macroscopic examination (**Figure 8A**), H&E and Perls staining of tissue sections. Perls staining showed hemosiderin in hemorrhagic plaques in blue color and revealed the accumulation of erythrocytes in the hemorrhagic area within a plaque (**Figure 8B**). After screening and pathologic confirmation, 8 IPH plaques and 8 non-IPH plaques were intentionally selected for subsequent analysis. Patients' clinical characteristics including

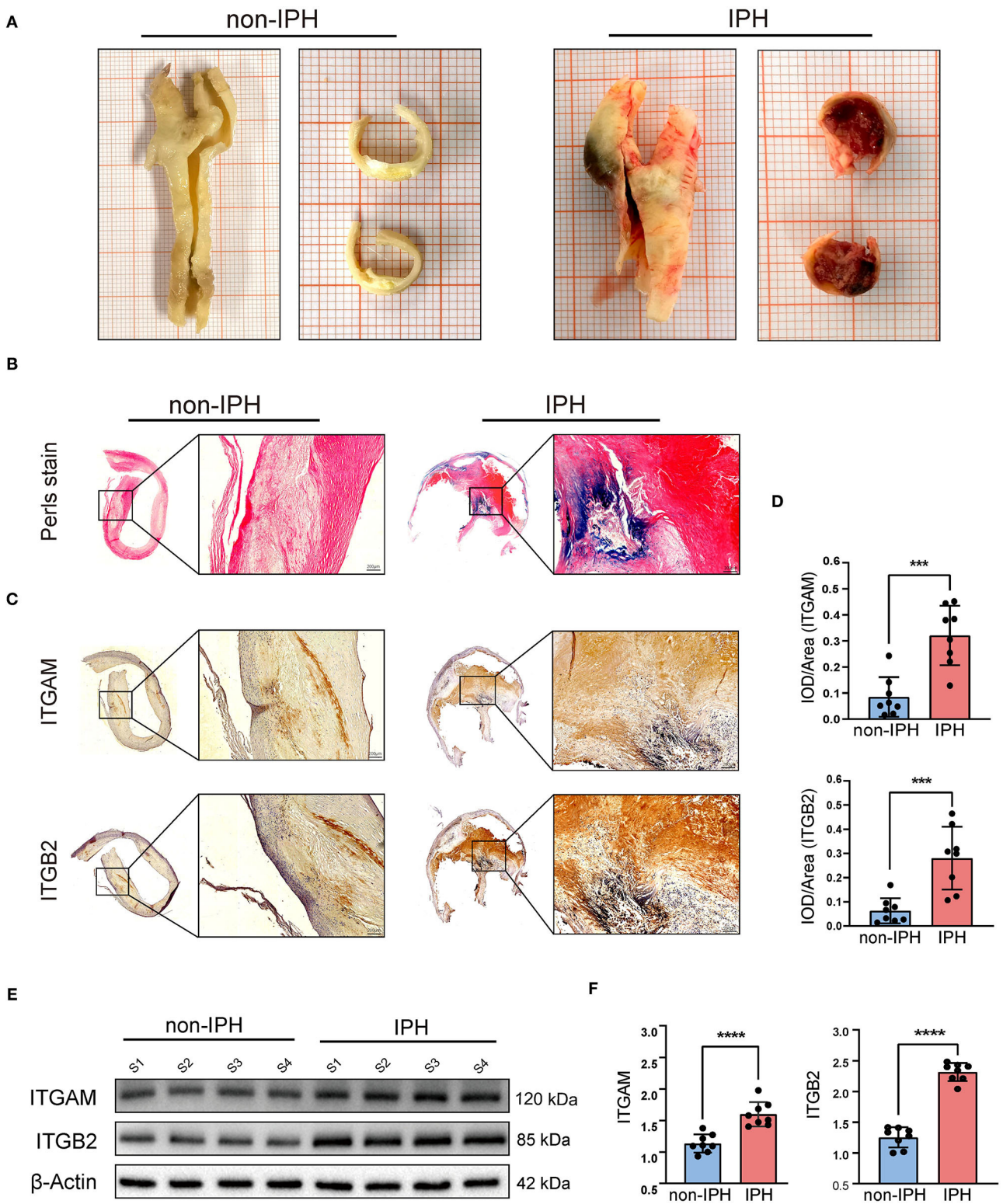

FIGURE 8 | Validation of the hub genes (*ITGAM* and *ITGB2*). **(A)** Fresh human carotid atherosclerotic plaque specimens were collected from carotid endarterectomy. Plaque features can be preliminarily observed in gross specimens and cross sections. From left to right, atherosclerotic plaques without IPH and with IPH are shown. **(B)** Perls staining was used to further identify the plaques. The IPH plaque section showed obvious blue staining and infiltration of erythrocytes by light microscopy. **(C)** Typical micrographs of *ITGAM* and *ITGB2* immunohistochemical staining, macroscopic, and microscopic views of the cross sections from left to right. **(D)** Histograms

(Continued)

FIGURE 8 | show the quantitative results of immunohistochemical staining. *ITGAM* and *ITGB2* expression were significantly increased in the IPH group. **(E)** Western blotting was used to determine the protein expression levels. Quantitative results **(F)** show that the expression of *ITGB2* and *ITGAM* in the IPH group was significantly higher than that in the non-IPH group. ***$p < 0.001$, ****$p < 0.0001$.

TABLE 1 | Patient demographic data.

	Total	Non-IPH	IPH	*p*-Value
Patients	16	8	8	–
Male (*n* [%])	11 (68.7%)	5 (62.5%)	6 (75%)	1
Age (years)	65.31 ± 8.42	65.00 ± 8.452	65.63 ± 8.975	0.888
BMI (kg/m^2)	27.31 ± 1.968	27.977 ± 1.966	26.655 ± 1.854	0.188
Hypertension Yes	13 (81.2%)	7 (87.5%)	6 (75%)	1
Diabetes mellitus Yes	7 (43.7%)	2 (25%)	5 (62.5%)	0.315
CHD Yes	3 (18.7%)	0 (0%)	3 (37.5%)	0.2
TC (mmol/L)	3.48 ± 0.43	3.332 ± 0.240	3.63 ± 0.537	0.181
Smoker Yes	10 (62.5%)	4 (50%)	6 (75%)	0.608

Values are shown as mean ± SD or n (%). IPH, intraplaque hemorrhage; BMI, body mass index; CHD, coronary heart disease; TC, serum total cholesterol (TC).

age, gender, body mass index (BMI), hypertension, diabetes mellitus, coronary heart disease (CHD), serum total cholesterol (TC), and smoking were retrospectively collected and compared between groups. None of the clinical characteristics differed significantly between the two groups (**Table 1**).

Immunohistochemistry was used to assess *ITGB2* and *ITGAM* expression and tissue distribution. *ITGB2* and *ITGAM* expression was significantly higher in IPH samples, especially in the hemorrhagic area (**Figure 8C**). Quantitative analysis by IPP software showed that the mean DOI of the tissue area (DOI/Area) of IPH samples was significantly higher than that of non-IPH samples (**Figure 8D**). Western blotting was used to evaluate the protein expression levels of *ITGB2* and *ITGAM* in 8 samples from each group, and band densities were quantified using Image J software. The expression levels of the two molecular proteins in the IPH group were significantly higher than those in the non-IPH group (**Figures 8E,F**).

DISCUSSION

Increasing evidence indicates that IPH is associated with high risk of atherosclerotic plaques. In fact, IPH is not only a marker of unstable plaques, but also a trigger of plaque instability (13). IPH leads to a series of subsequent pathological processes, such as accumulation of cholesterol-rich erythrocyte membranes (19), expansion of necrotic cores, promotion of oxidant and proteolytic activity, infiltration of leukocytes, and a highly inflammatory plaque environment (8, 20, 21). Therefore, preventing the occurrence and progression of IPH is of great significance for increasing plaque stability and preventing stroke. However, IPH is a complex multifactorial disease with unclear pathologic mechanisms, and valuable biomarkers are needed to predict and prevent IPH-related stroke.

The key hub genes identified in this study, *ITGB2* (also known as *CD18*) and *ITGAM* (also known as *CD11b*), belong to the integrin family, which is an important transmembrane protein family that mediates cell-cell adhesion and cell-extracellular matrix (ECM) adhesion (22). Previous studies have demonstrated that *ITGAM* (integrin αM) and *ITGB2* (integrin β2) can promote leukocyte transendothelial migration and disrupt endothelial barrier function through animal and cultured cells experiments (23, 24), and some studies have reported that *ITGB2* and *ITGAM* may be involved in the progression of atherosclerosis through bioinformatics analysis (25, 26). However, few studies have directly reported the relationship between these two genes and IPH. Different from the *in vivo* and *in vitro* experimental methods in previous studies, and also different from the genomic analysis of unclassified atherosclerotic plaques, this study directly conducted bioinformatics analysis on high-throughput gene chip data of human IPH plaques. Through differential gene screening, PPI analysis and ROC verification, *ITGAM* and *ITGB2* were identified as key hub genes of IPH, and further histological examination proved for the first time that *ITGB2* and *ITGAM* were highly expressed in IPH plaques. In addition, we revealed for the first time the correlations between *ITGB2*/*ITGAM* and various types of immune cells in atherosclerosis plaques by immune cell infiltration analysis. These results provided a new comprehensive perspective for understanding the pathogenesis of IPH and provided valuable clues for finding potential therapeutic targets for IPH and IPH-related stroke.

ITGB2 (also known as *CD18*) and *ITGAM* (also known as *CD11b*) encode the integrin β2 subunit and αM subunit, respectively. Integrins are heterodimers formed by specific non-covalent binding of α and β subunits, and have traditionally been considered important regulators of cell survival, proliferation, adhesion, and migration (22, 27). *ITGB2* encodes the integrin β2 subunit, which is non-covalently coupled to different α subunits to form the β2 integrin family (including αLβ2, αMβ2, αXβ2, and αDβ2) (28). β2 integrin is a major receptor family on many leukocyte subsets and plays an important adhesion function in the process of leukocyte recruitment, antigen presentation, pathogen clearance and thrombosis (29).

In addition, recent studies showed that β2 integrin controls various cellular metabolic signals and pathways. Zhang et al. reported that *ITGB2* enhances the glycolysis activity of cancer-associated fibroblasts through the PI3K/AKT/mTOR pathway, thus playing a key role in promoting cancer cell proliferation (30). Furthermore, Liu et al. found that *ITGB2* expression of cancer cells can be induced by YAP to promote cancer cell invasion of cancer cells in a manner similar to that of leukocytes (31).

The integrin αM (CD11b) subunit encoded by *ITGAM* is coupled with the β2 subunit (CD18) to form αMβ2 integrin, also known as Mac-1 (CD11b/CD18). It is expressed mainly on cells of the myeloid lineage, such as monocytes and neutrophils, and certain lymphocyte subsets and is therefore often regarded as a marker of circulating monocytes (32). Mac-1 is involved in phagocytosis, adhesion, and trans-endothelial cell migration, as well as other functions such as regulating apoptosis and degranulation (23, 29). As a major member of the β2 integrin family, CD11b contains an inserted domain that facilitates binding of many ligands, including the adhesion ligands intercellular adhesion molecule-1 and−2 (ICAM-1 and−2), the blood coagulation protein fibrinogen, complement protein iC3b, and the recently discovered MMP9 (33). During leukocyte migration across endothelial cells, Mac-1 promotes adhesion of leukocytes to the ligand ICAM-1 expressed on endothelial cells, and mediates leukocyte crawling on the vascular wall (34, 35). In addition, studies reported that when integrin on immune cells binds to ligands on endothelial cells, it will activate downstream signaling pathways and destroys the intercellular link molecule VE-cadherin (14, 36, 37). This may be a key step in the occurrence of IPH and immune cell infiltration in atherosclerotic lesions.

The results of this study are consistent with previous studies. Meng et al. reported that *ITGB2* and *ITGAM* are involved in the progression of carotid atherosclerotic plaques (25). In addition, high expression of *ITGAM* is associated with unstable atherosclerotic plaques (26), and *ITGAM* knockout reduces macrophage infiltration, MMP9 expression, and elastin and collagen degradation in mouse abdominal aortic aneurysm models (38). This suggests that *ITGAM* and *ITGB2* may play an important role in the occurrence of IPH, immune cell infiltration, and the progression of atherosclerosis.

To further investigate the effect of immune cells in atherosclerotic hemorrhagic plaques, we performed a comprehensive analysis of immune cell infiltration. In this analysis, M2 macrophages, M0 macrophages, resting mast cells, gamma delta T cells, and monocytes represented the top five highest infiltrating fractions in carotid atherosclerotic plaques, which is consistent with previous studies using CIBERSORT analysis and single cell sequencing (16, 39).

Immune cells, especially macrophages, play a critical role in atherogenesis. A recent single-cell sequencing study found that CD4+ T cells, CD8+ T cells, and macrophages dominate the human carotid atherosclerotic plaque immune landscape, while mass-cytometry analysis also revealed two macrophage clusters corresponding to classically activated M1 and alternately activated M2 phenotypes. Nevertheless, plaque macrophages had higher resolution at the single-cell level of transcription, suggesting that these cells have different functional heterogeneity in plaques (39). In a mouse model, aortic atherosclerotic lesions are mainly composed of macrophages, monocytes, and T cells, while the adventitial tissue is dominated by B cells (40). However, few studies have revealed the immune cell landscape of hemorrhagic plaques, so we used CIBERSORT to reveal the differences in infiltrating immune cells between IPH and non-IPH samples. This novel analysis showed a higher proportion of M0 macrophages and a lower proportion of M2 macrophages in IPH samples compared with non-IPH samples. IPH is regarded as a potentially important inflammatory stimulus that promotes macrophage influx into atherosclerotic lesions (41, 42), whereas the reduction of M2 macrophage expression (considered an anti-inflammatory phenotype) in IPH plaques is reasonable (38).

Previous evidence showed that erythrocyte lysis in the IPH region releases free hemoglobin, which can be absorbed by macrophages through CD163 receptors (43). On the other hand, macrophages secrete MMPs and angiogenic factors, including TGF- β, VEGF, and EGF, which undoubtedly further promote the occurrence of new angiogenesis and IPH within plaques (44, 45). This evidence and our results suggest that macrophages and their specific differentiation phenotypes play an important role in intraplaque hemorrhage. However, the specific mechanisms involving macrophages in the process of IPH and the precise signals that trigger macrophage differentiation remain unclear and require further study. Interestingly, the results of this study showed that *ITGB2* and *ITGAM* have positive correlation with M0 macrophages and negative correlation with M2 macrophages. In addition, M0 macrophages were significantly negatively correlated with M2 macrophages, and activated dendritic cells were significantly positively correlated with neutrocytes. These results provide a new direction for future research on the role of macrophages in IPH.

Immunohistochemistry and western blotting showed that the protein expression levels associated with hub genes *ITGB2* and *ITGAM* were significantly higher in the IPH group than in the non-IPH group. Since *ITGAM (CD11b)* is also a marker of macrophages, we concluded that there were more infiltrated macrophages in the IPH group. Notably, immunohistochemistry showed that *ITGB2* and *ITGAM* expression was mainly concentrated in the IPH region or around neovessels (**Figure 8C**), which may be caused by IPH-induced inflammatory stimulation or neovessel leakage.

These results provide valuable clues for further study on the pathophysiological mechanism of IPH.

This study has several limitations. Firstly, because information on specific clinical characteristics of samples in public datasets could not be collected, we could not rule out the potential impact of heterogeneity in patient populations and clinical characteristics on the results of this study. Secondly, the sample size used for analysis and validation was small, which may affect the accuracy of the analysis results. Future studies need to expand the sample size of IPH plaques prospectively and explore the specific mechanisms of *ITGB2* and *ITGAM* in the development of IPH needs to be further studied through *in vivo* and *in vitro* experiments.

CONCLUSION

This study used *in silico* analysis to identify key genes and pathways closely related to the occurrence of IPH. In addition, we described the immune landscape in detail, revealing the underlying immune infiltration patterns of carotid atherosclerotic plaques in the absence or presence of IPH. We validated the key genes *ITGB2* and *ITGAM* experimentally, confirming that the proteins encoded by these genes are highly expressed in IPH plaques. Our findings advance our understanding of the underlying mechanisms of IPH pathogenesis and provide valuable information and directions for future research into novel targets for IPH immunotherapy and diagnosis.

DATA AVAILABILITY STATEMENT

The datasets presented in this study can be found in online repositories. The names of the repository/repositories and accession number(s) can be found in the article/**Supplementary Material**.

ETHICS STATEMENT

This study was approved by the Medical Ethics Committee of the China-Japan Friendship Hospital of Beijing, China (2019-25-1). The patients/participants provided their written informed consent to participate in this study.

AUTHOR CONTRIBUTIONS

JW and PL designed, guided, and funded the study. XL conducted most of the experimental work. FW, MS, and CS performed the data analysis. XL and BM drafted the manuscript. YY, XF, ZY, JW, and PL critically revised the manuscript. All authors contributed to the article and approved the submitted version.

FUNDING

This work was supported by grants from the National Natural Science Foundation of China (nos. 81670275, 81670443, and 82170066) and the International S&T cooperation program (2013DFA31900).

SUPPLEMENTARY MATERIAL

The Supplementary Material for this article can be found online at: https://www.frontiersin.org/articles/10.3389/fcvm.2022.818585/full#supplementary-material

REFERENCES

1. Song P, Fang Z, Wang H, Cai Y, Rahimi K, Zhu Y, et al. Global and regional prevalence, burden, and risk factors for carotid atherosclerosis: a systematic review, meta-analysis, and modelling study. *Lancet Global Health.* (2020) 8:e721–9. doi: 10.1016/S2214-109X(20)30117-0
2. Underhill HR, Hatsukami TS, Fayad ZA, Fuster V, Yuan C. MRI of carotid atherosclerosis: clinical implications and future directions. *Nat Rev Cardiol.* (2010) 7:165–73. doi: 10.1038/nrcardio.2009.246
3. Saba L, Saam T, Jäger HR, Yuan C, Hatsukami TS, Saloner D, et al. Imaging biomarkers of vulnerable carotid plaques for stroke risk prediction and their potential clinical implications. *Lancet Neurology.* (2019) 18:559–72. doi: 10.1016/S1474-4422(19)30035-3
4. Bos D, Arshi B, van den Bouwhuijsen QJA, Ikram MK, Selwaness M, Vernooij MW, et al. Atherosclerotic carotid plaque composition and incident stroke and coronary events. *J Am Coll Cardiol.* (2021) 77:1426–35. doi: 10.1016/j.jacc.2021.01.038
5. Alkhalil M, Choudhury RP. Intraplaque hemorrhage as a marker of stroke risk. *JACC Cardiovasc Imaging.* (2020) 13(Pt. 1):407–9. doi: 10.1016/j.jcmg.2019.05.004
6. Schindler A, Schinner R, Altaf N, Hosseini AA, Simpson RJ, Esposito-Bauer L, et al. Prediction of stroke risk by detection of hemorrhage in carotid plaques: meta-analysis of individual patient data. *JACC Cardiovasc Imaging.* (2020) 13(Pt. 1):395–6. doi: 10.1016/j.jcmg.2019.03.028
7. Parma L, Baganha F, Quax PHA, de Vries MR. Plaque angiogenesis and intraplaque hemorrhage in atherosclerosis. *Eur J Pharmacol.* (2017) 816:107–15. doi: 10.1016/j.ejphar.2017.04.028
8. Michel J-B, Martin-Ventura JL, Nicoletti A, Ho-Tin-Noé B. Pathology of human plaque vulnerability: mechanisms and consequences of intraplaque haemorrhages. *Atherosclerosis.* (2014) 234:311–9. doi: 10.1016/j.atherosclerosis.2014.03.020
9. Sluimer JC, Kolodgie FD, Bijnens APJJ, Maxfield K, Pacheco E, Kutys B, et al. Thin-Walled microvessels in human coronary atherosclerotic plaques show incomplete endothelial junctions. *J Am Coll Cardiol.* (2009) 53:1517–27. doi: 10.1016/j.jacc.2008.12.056
10. de Vries MR, Parma L, Peters HAB, Schepers A, Hamming JF, Jukema JW, et al. Blockade of vascular endothelial growth factor receptor 2 inhibits intraplaque haemorrhage by normalization of plaque neovessels. *J Intern Med.* (2019) 285:59–74. doi: 10.1111/joim.12821
11. Xu J, Lu X, Shi GP. Vasa vasorum in atherosclerosis and clinical significance. *Int J Mol Sci.* (2015) 16:11574–608. doi: 10.3390/ijms160511574
12. Guo L, Harari E, Virmani R, Finn AV. Linking hemorrhage, angiogenesis, macrophages, and iron metabolism in atherosclerotic vascular diseases. *Arterioscler Thromb Vasc Biol.* (2017) 37:e33–9. doi: 10.1161/ATVBAHA.117.309045
13. Michel JB, Virmani R, Arbustini E, Pasterkamp G. Intraplaque haemorrhages as the trigger of plaque vulnerability. *Eur Heart J.* (2011) 32:1977–85:85a, 85b, 85c. doi: 10.1093/eurheartj/ehr054
14. Sluiter TJ, van Buul JD, Huveneers S, Quax PHA, de Vries MR. Endothelial barrier function and leukocyte transmigration in atherosclerosis. *Biomedicines.* (2021) 9:328. doi: 10.3390/biomedicines9040328
15. de Vries MR, Quax PHA. Plaque angiogenesis and its relation to inflammation and atherosclerotic plaque destabilization. *Curr Opin Lipidol.* (2016) 27:499–506. doi: 10.1097/MOL.0000000000000339
16. Tan L, Xu Q, Shi R, Zhang G. Bioinformatics analysis reveals the landscape of immune cell infiltration and immune-related pathways participating in the progression of carotid atherosclerotic plaques. *Artif Cells Nanomed Biotechnol.* (2021) 49:96–107. doi: 10.1080/21691401.2021.1873798
17. Jin H, Goossens P, Juhasz P, Eijgelaar W, Manca M, Karel JMH, et al. Integrative multiomics analysis of human atherosclerosis reveals a serum response factor-driven network associated with intraplaque hemorrhage. *Clin Transl Med.* (2021) 11:e458. doi: 10.1002/ctm2.458
18. Yang Y, Cai Y, Zhang Y, Yi X, Xu Z. Identification of molecular subtypes and key genes of atherosclerosis through gene expression profiles. *Front Mol Biosci.* (2021) 8:628546. doi: 10.3389/fmolb.2021.628546
19. Koskinas KC, Giannoglou GD. Intraplaque hemorrhage, RBC-derived cholesterol, and plaque progression: time to move

from conjecture to evidence? *JACC Cardiovasc Imaging.* (2012) 5:1185–6. doi: 10.1016/j.jcmg.2012.09.003
20. Tziakas DN, Chalikias G, Pavlaki M, Kareli D, Gogiraju R, Hubert A, et al. Lysed erythrocyte membranes promote vascular calcification. *Circulation.* (2019) 139:2032–48. doi: 10.1161/CIRCULATIONAHA.118.037166
21. Jeney V, Balla G, Balla J. Red blood cell, hemoglobin and heme in the progression of atherosclerosis. *Front Physiol.* (2014) 5:379. doi: 10.3389/fphys.2014.00379
22. Zhang Y, Wang H. Integrin signalling and function in immune cells. *Immunology.* (2012) 135:268–75. doi: 10.1111/j.1365-2567.2011.03549.x
23. Fagerholm SC, Varis M, Stefanidakis M, Hilden TJ, Gahmberg CG. alpha-Chain phosphorylation of the human leukocyte CD11b/CD18 (Mac-1) integrin is pivotal for integrin activation to bind ICAMs and leukocyte extravasation. *Blood.* (2006) 108:3379–86. doi: 10.1182/blood-2006-03-013557
24. Dunne JL, Collins RG, Beaudet AL, Ballantyne CM, Ley K. Mac-1, but not LFA-1, uses intercellular adhesion molecule-1 to mediate slow leukocyte rolling in TNF-alpha-induced inflammation. *J Immunol.* (2003) 171:6105–11. doi: 10.4049/jimmunol.171.11.6105
25. Meng Y, Zhang C, Liang L, Wei L, Wang H, Zhou F, et al. Identification of potential key genes involved in the carotid atherosclerosis. *Clin Interv Aging.* (2021) 16:1071–84. doi: 10.2147/CIA.S312941
26. Zhou S, Liu S, Liu X, Zhuang W. Bioinformatics gene analysis of potential biomarkers and therapeutic targets for unstable atherosclerotic plaque-related stroke. *J Mol Neurosci.* (2021) 71:1031–45. doi: 10.1007/s12031-020-01725-2
27. Shen B, Zhao X, O'Brien KA, Stojanovic-Terpo A, Delaney MK, Kim K, et al. A directional switch of integrin signalling and a new anti-thrombotic strategy. *Nature.* (2013) 503:131–5. doi: 10.1038/nature12613
28. Tan SM. The leucocyte beta2 (CD18) integrins: the structure, functional regulation and signalling properties. *Biosci Rep.* (2012) 32:241–69. doi: 10.1042/BSR20110101
29. Rosetti F, Mayadas TN. The many faces of Mac-1 in autoimmune disease. *Immunol Rev.* (2016) 269:175–93. doi: 10.1111/imr.12373
30. Zhang X, Dong Y, Zhao M, Ding L, Yang X, Jing Y, et al. ITGB2-mediated metabolic switch in CAFs promotes OSCC proliferation by oxidation of NADH in mitochondrial oxidative phosphorylation system. *Theranostics.* (2020) 10:12044–59. doi: 10.7150/thno.47901
31. Liu H, Dai X, Cao X, Yan H, Ji X, Zhang H, et al. PRDM4 mediates YAP-induced cell invasion by activating leukocyte-specific integrin beta2 expression. *EMBO Rep.* (2018) 19:e45180. doi: 10.15252/embr.201745180
32. Podolnikova NP, Podolnikov AV, Haas TA, Lishko VK, Ugarova TP. Ligand recognition specificity of leukocyte integrin αMβ2 (Mac-1, CD11b/CD18) and its functional consequences. *Biochemistry.* (2015) 54:1408–20. doi: 10.1021/bi5013782
33. Stefanidakis M, Bjorklund M, Ihanus E, Gahmberg CG, Koivunen E. Identification of a negatively charged peptide motif within the catalytic domain of progelatinases that mediates binding to leukocyte beta 2 integrins. *J Biol Chem.* (2003) 278:34674–84. doi: 10.1074/jbc.M302288200
34. Marchini T, Mitre LS, Wolf D. Inflammatory cell recruitment in cardiovascular disease. *Front Cell Dev Biol.* (2021) 9:635527. doi: 10.3389/fcell.2021.635527
35. Vestweber D. How leukocytes cross the vascular endothelium. *Nat Rev Immunol.* (2015) 15:692–704. doi: 10.1038/nri3908
36. Allingham MJ, van Buul JD, Burridge K. ICAM-1-mediated,, Src- and Pyk2-dependent vascular endothelial cadherin tyrosine phosphorylation is required for leukocyte transendothelial migration. *J Immunol.* (2007) 179:4053–64. doi: 10.4049/jimmunol.179.6.4053
37. Wessel F, Winderlich M, Holm M, Frye M, Rivera-Galdos R, Vockel M, et al. Leukocyte extravasation and vascular permeability are each controlled *in vivo* by different tyrosine residues of VE-cadherin. *Nat Immunol.* (2014) 15:223–30. doi: 10.1038/ni.2824
38. Zhou M, Wang X, Shi Y, Ding Y, Li X, Xie T, et al. Deficiency of ITGAM attenuates experimental abdominal aortic aneurysm in mice. *J Am Heart Assoc.* (2021) 10:e019900. doi: 10.1161/JAHA.120.019900
39. Fernandez DM, Rahman AH, Fernandez NF, Chudnovskiy A, Amir ED, Amadori L, et al. Single-cell immune landscape of human atherosclerotic plaques. *Nat Med.* (2019) 25:1576–88. doi: 10.1038/s41591-019-0590-4
40. Winkels H, Ehinger E, Vassallo M, Buscher K, Dinh HQ, Kobiyama K, et al. Atlas of the immune cell repertoire in mouse atherosclerosis defined by single-cell RNA-sequencing and mass cytometry. *Circ Res.* (2018) 122:1675–88. doi: 10.1161/CIRCRESAHA.117.312513
41. Finn AV, Nakano M, Polavarapu R, Karmali V, Saeed O, Zhao X, et al. Hemoglobin directs macrophage differentiation and prevents foam cell formation in human atherosclerotic plaques. *J Am Coll Cardiol.* (2012) 59:166–77. doi: 10.1016/j.jacc.2011.10.852
42. Jinnouchi H, Guo L, Sakamoto A, Torii S, Sato Y, Cornelissen A, et al. Diversity of macrophage phenotypes and responses in atherosclerosis. *Cell Mol Life Sci.* (2020) 77:1919–32. doi: 10.1007/s00018-019-03371-3
43. Guo L, Akahori H, Harari E, Smith SL, Polavarapu R, Karmali V, et al. CD163+ macrophages promote angiogenesis and vascular permeability accompanied by inflammation in atherosclerosis. *J Clin Invest.* (2018) 128:1106–24. doi: 10.1172/JCI93025
44. Pourcet B, Staels B. Alternative macrophages in atherosclerosis: not always protective! *J Clin Invest*. (2018) 128:910–2. doi: 10.1172/JCI120123
45. Kalucka J, Bierhansl L, Wielockx B, Carmeliet P, Eelen G. Interaction of endothelial cells with macrophages—linking molecular and metabolic signaling. *Pflügers Arch Eur J Physiol.* (2017) 469:473–83. doi: 10.1007/s00424-017-1946-6

Conflict of Interest: The authors declare that the research was conducted in the absence of any commercial or financial relationships that could be construed as a potential conflict of interest.

Publisher's Note: All claims expressed in this article are solely those of the authors and do not necessarily represent those of their affiliated organizations, or those of the publisher, the editors and the reviewers. Any product that may be evaluated in this article, or claim that may be made by its manufacturer, is not guaranteed or endorsed by the publisher.

Frontiers in
Cardiovascular Medicine

Innovations and improvements in cardiovascular treatment and practice

Focuses on research that challenges the status quo of cardiovascular care, or facilitates the translation of advances into new therapies and diagnostic tools.

Discover the latest Research Topics

See more →

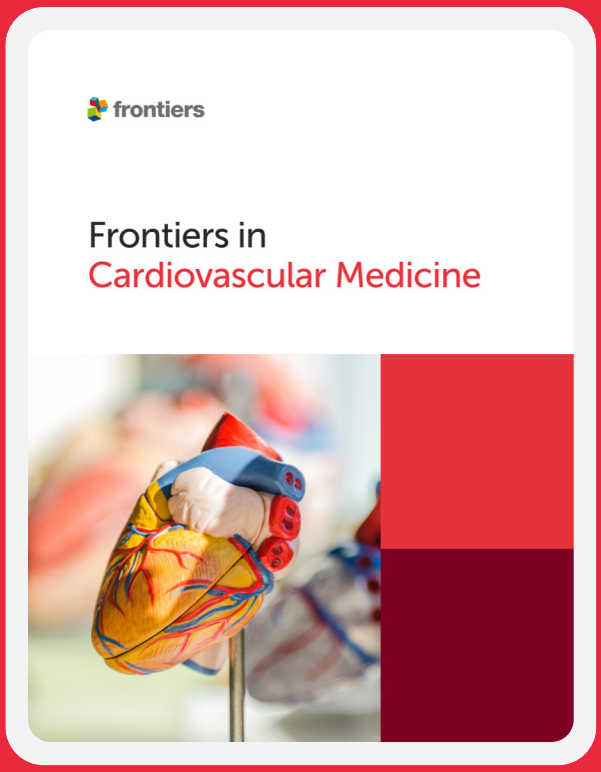

Frontiers

Avenue du Tribunal-Fédéral 34
1005 Lausanne, Switzerland
frontiersin.org

Contact us

+41 (0)21 510 17 00
frontiersin.org/about/contact